

Radiation Physics and Radionuclide Decay

Michael F. L'Annunziata

The Montague Group, P.O. Box 5033, Oceanside, CA 92052-5033, USA

Chapter Outline

I. Introduction	2	C. Internal Conversion Electrons	68
II. Discovery and Early Characterization of Radioactivity	2	D. Auger Electrons	70
III. Basic Units and Definitions	13	E. Neutron Radiation	72
A. Properties of Atomic Constituents	13	1. Discovery of the Neutron	72
B. Nuclides, Isotopes, Isobars, Isomers, and Isotones	13	2. Neutron Classification	73
C. Mass and Energy	14	3. Sources of Neutrons	76
IV. Properties of the Nucleus	16	4. Interactions of Neutrons with Matter	84
A. Nuclear Radius and Density	16	5. Neutron Attenuation and Cross Sections	87
B. Nuclear Forces	17	6. Neutron Decay	90
C. Binding Energy	19	IX. Electromagnetic Radiation – Photons	90
1. Nuclear Fission	21	A. Dual Nature: Wave and Particle	90
2. Nuclear Fusion	21	B. Gamma Radiation	92
D. Nuclear Models	23	C. Annihilation Radiation	94
1. Liquid Drop Model	23	D. X-Radiation	94
2. Shell Model	26	1. X-rays Characterized by Discrete Spectral Lines	95
3. Collective Model	29	2. Bremsstrahlung	97
E. Cluster Radioactivity	31	3. X-rays from Beta-particle Emissions	101
V. Naturally Occurring Radionuclides	32	E. Cherenkov Radiation	102
A. Radionuclides of Cosmogenic Origin	32	X. Interaction of Electromagnetic Radiation with Matter	105
B. Long-lived Radionuclides	32	A. Photoelectric Effect	105
C. Natural Radioactive Decay Chains	33	B. Compton Effect	105
VI. Artificially Produced Radionuclides	33	C. Pair Production	107
VII. Nuclear Reactions	37	D. Combined Photon Interactions	109
A. Reactions Types	37	XI. Radioactive Nuclear Recoil	113
B. Notation	39	A. Relativistic Expressions	114
C. Energy of Reactions (<i>Q</i> Value)	39	B. Nonrelativistic Expressions	115
D. Reaction Cross Section	41	1. Nuclear Recoil Energy from Alpha-particle Emissions	115
VIII. Particulate Radiation	42	2. Nuclear Recoil Energy from Gamma-ray, X-ray, and Neutrino Emissions	116
A. Alpha Decay	42	C. Sample Calculations	116
1. Energy and Half-life Relationship	42	1. Nuclear Recoil from Alpha Emissions	116
2. Decay Energy	43	2. Nuclear Recoil from Beta Emissions	116
3. Alpha-particle Interactions with Matter	45	3. Nuclear Recoil from Gamma-ray Photon, X-ray Photon, or Neutrino Emissions	117
B. Beta Decay	49	D. Radioactive Recoil Effects	118
1. Negatron (β^-) Emission	49	1. Szilard–Chalmers Process	118
2. Positron (β^+) Emission	54	2. Radioactive Disequilibrium	120
3. Electron Capture (EC)	57	XII. Cosmic Radiation	120
4. Branching β^- , β^+ , and EC Decay	60	A. Classification and Properties	121
5. Double-Beta ($\beta\beta$) Decay	62	B. Showers of the Cosmic Radiation	123
6. Beta-particle Interactions with Matter	65		
7. Beta-particle Absorption and Transmission	67		

C. Cosmic Rays, Underground	127	D. Transient Equilibrium	143
D. Origins of Cosmic Radiation	128	E. No Equilibrium	145
XIII. Radiation Dose	128	F. More Complex Decay Schemes	145
XIV. Stopping Power and Linear Energy Transfer	130	XVI. Radioactivity Units and Radionuclide Mass	146
A. Stopping Power	130	A. Units of Radioactivity	146
B. Linear Energy Transfer	133	B. Correlation of Radioactivity and Radionuclide Mass	147
XV. Radionuclide Decay, Ingrowth, and Equilibrium	135	1. ^{32}P , half-life = 14.3 days	147
A. Half-Life	135	2. ^{14}C , half-life = 5730 years	147
B. General Decay Equations	141	C. Carrier-Free Radionuclides	148
C. Secular Equilibrium	141	References	148

I. INTRODUCTION

Radioactivity is the emission of radiation originating from a nuclear reaction or as a result of the spontaneous decay of unstable atomic nuclei. The term radioactive decay refers to the process whereby unstable atomic nuclei decay with the loss of energy by the emission of elementary particles (*e.g.*, alpha particles, beta particles, neutrons, and gamma-ray photons) directly from the nucleus or the atomic electron shells (*e.g.*, Auger electrons and x-ray photons) within which the nucleus resides. The rate of decay or disintegration rate of a radionuclide (*i.e.*, a specific isotope of an element), as we shall see in this chapter, is directly proportional to the mass of the radionuclide. Thus, radioactivity analysis is essentially the quantitative analysis of radionuclides. Methods of radioactivity analysis have, for the most part, two approaches, namely, the determination of the disintegration rate of a radionuclide by the counting of the atoms of a radionuclide disintegrating per unit time or by measuring the mass of a radionuclide, such as is done using mass spectrometry. Thus, we can calculate the mass of the radionuclide from its disintegration rate and vice versa.

The analysis of radioactivity is a challenging field. Both the sources of radioactivity (*i.e.*, radionuclides) and the media within which the radionuclides may be found can present themselves in a wide range of complexities. Also, nuclear radiation resulting from the decay of radionuclides can occur in various types, percent abundances or intensities, and energies. Furthermore, a given radionuclide may have more than one mode of decay. The presence of appreciable activities of more than one radionuclide in a sample can further complicate analysis. In addition, the different parent–daughter nuclide decay schemes, equilibria between parent and daughter radionuclides, and the rates of decay that radioactive nuclides undergo may facilitate or complicate the analysis of a given radionuclide. The problem of radioactivity analysis may be confounded further by the wide range of chemical and/or physical media (*i.e.*, sample matrices) from which the nuclear radiation may emanate.

As we will find in this book, there are many modern methods of radioactivity analysis. The types of detectors available for the measurement of radioactivity are numerous, and they may be designed in the gaseous, liquid, or solid state. They will differ not only in their physical state but also in chemistry. The instrumentation and electronic circuitry associated with radiation detectors will also vary. As a result, the detectors and their associated electronic instrumentation will perform with varying

efficiencies of radiation detection depending on many factors, including the characteristics of the instrumentation, the types and energies of the radiation, as well as sample properties.

The proper selection of a particular radiation detector or method of radioactivity analysis requires a good understanding of the properties of nuclear radiation, the mechanisms of interaction of radiation with matter, half-life, decay schemes, decay abundances, and energies of decay. This chapter covers these concepts as a prelude to the various chapters that follow on radioactivity analysis. Throughout the book, reference will be made to the concepts covered in this introductory chapter. For the experienced radioanalytical chemist, this chapter may serve only as a review. However, the newcomer in this field should find this introductory chapter essential to the understanding of the concepts of radiation detection and measurement. He or she will find that the concepts covered in this introductory chapter will facilitate the selection of the most suitable radiation detector and instrumentation required for any particular case.

The properties of nuclear radiation and the mechanisms whereby nuclear radiation dissipates its energy in matter, dealt with in this chapter, form the basis for the methods of detection and measurement of radionuclides.

II. DISCOVERY AND EARLY CHARACTERIZATION OF RADIOACTIVITY

A brief history of radioactivity and the pioneers, who have contributed much to our understanding of this fascinating field of science, is resented here. The history of the science is important to our understanding of how we have arrived to where we are today in this science, and it serves as a source of motivation to future pioneers in this field. For a more detailed treatment of the history of radioactivity, the reader is invited to peruse a previous work by the author (L'Annunziata, 2007).

Radioactivity was discovered in 1896 by Henri Becquerel. At the beginning of 1896, on the very day that news reached Paris of the discovery of x-rays, Henri Becquerel thought of carrying out research to see whether or not natural phosphorescent materials emitted similar rays. He was then professor of the École Polytechnic in Paris where he went to work on some uranium salts that he had inherited from his father, who had previously studied phosphorescence as professor of applied physics at the Polytechnic. Henri Becquerel placed samples of uranium sulfate onto photographic plates, which were enclosed in black paper or aluminum sheet to protect the plates from exposure to light. After developing the photographic plates, he

discovered that the uranium salts emitted rays that could pass through the black paper and even a metal sheet or thin glass positioned between the uranium salts and the photographic plates. Becquerel reported his findings to the French Academy of Sciences in February and March of 1896 (Becquerel, 1896a,b) and summarized his discovery in 1901 in the journal *Nature* as follows:

At the commencement of the year 1896, in carrying out some experiments with the salts of uranium.... I observed that these salts emitted an invisible radiation, which traversed metals and bodies opaque to light as well as glass and other transparent substances. This radiation impressed a photographic plate and discharged from a distance electrified bodies – properties giving two methods of studying the new rays.

At first he thought the rays were a result of phosphorescence, that is, excitation of the crystals by sunlight forcing the crystals to give off their own rays. However, Henri Becquerel carried out further tests demonstrating that the rays emanating from the uranium salts were independent of any external source of excitation including light, electricity, or heat, and the intensity of the rays did not diminish appreciably with time. "We were thus faced with a spontaneous phenomenon of a new order", which were his words during his Nobel Lecture (Becquerel, 1903) given on December 11, 1903.

Becquerel provided evidence that all uranium salts emitted the same radiation and that this was a property of the uranium atom particularly since uranium metal gave off much more intense radiation than the salts of that element. The new radiation produced ionization, and the intensity of the radioactivity could be measured by this ionization. Not only did these rays produce ionization, but he was able to demonstrate that a large portion of these rays could be deflected by a magnetic field and were charged particles of property similar to cathode rays. It was J. J. Thomson, Cavendish Professor of Experimental Physics at Trinity College, Cambridge, who discovered in 1897 that the cathode rays were electrons (Thomson, 1897). Thus, Becquerel was the first to provide evidence that some of the radiation emitted by uranium and its salts were similar in properties to electrons. It would be years later that Ernest Rutherford (1903) would name the electrons originating from nuclear decay as beta particles.

Following Becquerel's discovery of spontaneous radiation from uranium, Marie Curie, who was born Maria Sklodowska in

Warsaw, Poland, decided to study the mysterious rays emitted by uranium and to apply the work for a doctorate degree in the laboratory of her husband Pierre Curie, who was Professor of the Municipal School of Industrial Physics and Chemistry in Paris, France. In 1898 Marie Curie discovered that not only uranium gave off the mysterious rays discovered by Becquerel, but thorium did as well; this was independently discovered by Gerhard Schmidt in Germany the same year. Pierre and Marie Curie observed that the intensity of the spontaneous rays emitted by uranium or thorium increased as the amount of uranium or thorium increased. They concluded that these rays were a property of the atoms of uranium and thorium; thus, they decided to coin these substances as "radioactive". The emanation of such spontaneous rays from atoms would now be referred to as "radioactivity". Through tedious chemical separations and analyses, Marie and Pierre Curie worked as a team and found that another radioactive element with chemical properties similar to bismuth was present in pitchblende. She named this new element "polonium" in honor of her native country. They found yet a second new radioactive element in the pitchblende ore with chemical properties close to that of barium, and they named that new element "radium" from the Latin word *radius* meaning "ray" (Curie, 1905, 1911).

The discovery of a highly penetrating radiation that was nondeviable in an external magnetic field, which is now known as gamma radiation, was discovered by Paul Villard at the Ecole Normal in Paris, France in 1900. Villard's discovery of gamma radiation was reported to the French Academy of Sciences (Villard, 1900a,b) and at the Meetings of the French Society of Physics (1900c). Villard did not provide any diagrams of his experimental arrangements, which led to the discovery of gamma rays; however, the writer sketched Fig. 1.1 to facilitate the description of his experiment. Villard placed a sample of barium chloride containing radium sealed in a glass ampoule within a lead shield that contained an opening, which essentially provided a collimated beam of the radiation from the radium source as illustrated in Fig. 1.1. To the radiation beam, he exposed two photographic plates wrapped in black light-tight protective paper. Between the two plates was sandwiched a 0.3 mm thick lead barrier. A magnetic field was applied to the collimated beam to deflect the deviable rays. Alpha particles emitted by the radium are ignored, because these are absorbed by the protective paper wrapping of the photographic plates. The magnetic field caused a deviation of

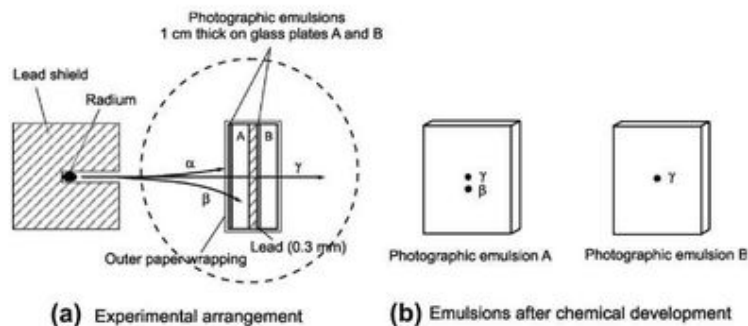


FIGURE 1.1 Paul Villard's (a) experimental arrangement and (b) experimental results that lead to his discovery of gamma rays in 1900. Photographic plates A and B consisting of emulsion set on 1 cm thick glass supports were separated from each other by a 0.3 mm thick lead barrier and wrapped in an envelope of light-tight paper. The dashed circle represents the pole of a magnet from which the lines of force are directed into the plane of the page perpendicular to the path of radiation emitted by the radium source.

the beta particles whereas a very penetrating radiation remained unaffected or undeviable by the magnetic field as evidence from the images produced by the radium emanations on the developed photographic emulsions. The developed photographic emulsion A, which was the first to receive the nuclear radiations from the radium, showed two spots produced by two types of radiation, one deviable (marked β) and the other undeviable (marked γ) in the magnetic field. The second photographic emulsion B, which was placed behind a 0.3 mm thick lead barrier, yielded only one spot produced by a highly penetrating radiation unaffected by the magnetic field. The intensity of the spot on emulsion B was the same as that on emulsion A indicating that its intensity remained unaffected to any observable extent by the lead barrier. The spot was also more clearly discernable, because it was not clouded by the deviable beta particles. Villard concluded that his experimental evidence demonstrated a radiation of property similar to x-rays, but with a greater penetrating power than x-radiation. In the journal *Nature*, Becquerel (1901) acknowledged Villard's discovery of gamma rays, which had not yet been named as such, with the following statement:

...there exists two kinds of radiations, one not capable of deviation [in a magnetic field] and of which the nature is still unknown, the other capable of deviation, which later experiments have identified with the cathode rays [later identified as beta particles]...I might add that recently Mr. Villard has proved the existence in the radium radiation of very penetrating rays, which are not capable of deviation.

Villard did not venture to name this newly discovered highly penetrating radiation. He was a modest person possibly uninterested in fame or in the highly competitive pursuits of his fellow scientists in this new frontier.

Ernest Rutherford (1903), who is considered by many as the best experimental physicist of the 20th century, was first to name the highly penetrating radiation discovered by Villard as gamma rays. A few years prior to Villard's discovery, Rutherford (1899) had already named two types of nuclear radiation as "alpha" and "beta", which he characterized on the basis of their relative penetrative power in matter, that is, alpha radiation would be more easily absorbed by matter than beta radiation. In harmony with this nomenclature, Rutherford assigned the term gamma rays to the yet more penetrating radiation. In the *Philosophical Magazine*, Rutherford (1903) named and characterized the three types of nuclear radiation on the basis of their penetration power in matter as follows:

"Radium gives out three distinct types of radiation:

1. The α rays, which are very easily absorbed by thin layers of matter, and which give rise to the greater portion of the ionization of the gas observed under the usual experimental conditions.
2. The β rays, which consist of negatively charged particles projected with high velocity, and which are similar in all respects to cathode rays produced in a vacuum-tube.
3. The γ rays, which are nondeviable by a magnetic field, and which are of a very penetrating character.

These rays differ very widely in their power of penetrating matter. The following approximate numbers, which show the

thickness of aluminum traversed before the intensity is reduced to one-half, illustrate this difference:"

Radiation	Thickness of aluminum
α rays	.0005 cm
β rays	.05 cm
γ rays	8 cm

As noted by Rutherford in the above quotation, ionization in a gas was one of the principal properties of nuclear radiation, which helped distinguish the radiation type. It was well understood at the time that the three rays possessed different powers of ionization in matter. The number of ion pairs formed in a gas by α -, β -, and γ -rays of given energy per path length of travel would differ according to the relationship α -rays > β -rays > γ -rays. Consequently, the property of ionization power of a given radiation was used to also measure the intensity of that radiation.

In addition to the different penetrating powers of α -, β -, and γ -radiation, other properties were used to identify these mysterious radiations, such as the differing deflections that the three radiations undergo in electric or magnetic fields. Rutherford (1903) contributed much to the understanding of these properties during the early years of research on radioactivity. Alpha radiation was known to possess a positive charge, because it would be deflected toward the negative electrode in an electric field potential, while beta particles were known to be negatively charged due to their deflection in the opposite direction toward the anode or positive electrode. However, gamma radiation would not undergo any deflection whatsoever as illustrated in Fig.1.2. Likewise, the alpha and beta radiations, when traveling in a path perpendicular to the lines of force of a magnetic field, will be deflected in opposite directions, which is a characteristic of charged particles. Gamma radiation, which

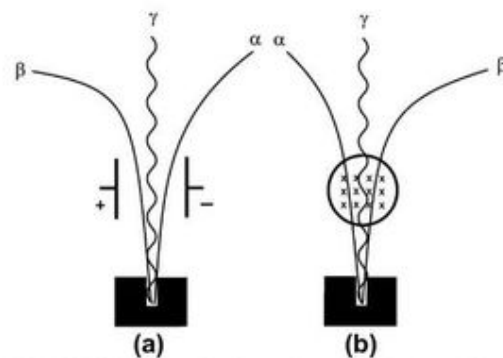


FIGURE 1.2 Paths of travel of collimated beams of alpha-, beta-, and gamma radiation in (a) electric and (b) magnetic fields. Beam collimation is provided by placing the radiation source in a hole drilled within shielded containers (e.g., lead) of which cross sections are illustrated. The electric field in (a) is illustrated by positive and negatively charged electrodes separated by a space through which the radiations pass; and the magnetic field in (b) is illustrated by the circle to depict the pole of a magnet through which the lines of force of magnetic flux (marked by the symbol x) are directed into the plane of the page (z-axis) perpendicular to the radiation paths in the xy-axis.

carries no electric charge, would continue along a straight undeviating path in either electric or magnetic fields.

After three years at the Cavendish Laboratory, University of Cambridge, Ernest Rutherford, originally from New Zealand, moved in 1898 to McGill University in Montreal at the age of 27 to take on the position of Professor of Physics. It is at McGill University where he began to make his major discoveries in the field of nuclear physics. The first of these was the discovery that radioactive atoms emitting α -particles or β -particles disintegrate into atoms of lighter weight; in other words, atoms of an element such as radium that emit α -particles undergo transformations to atoms of a lighter and consequently different element. Rutherford and coworkers demonstrated that the alpha particle was an atom of helium (later to be determined to be a nucleus of helium) and that helium gas would accumulate or be entrapped in minerals that contained radium. Furthermore, he demonstrated that the lighter atom produced as a product of the decay of radium would likewise be radioactive and, in turn, decay to another even lighter atom, and so on until the final product atom was stable. It was for this work that Rutherford received the 1908 Nobel Prize in Chemistry.

Rutherford's work in conjunction with numerous collaborators, including Frederick Soddy (Rutherford and Soddy, 1902, Rutherford, 1908), led to the conclusion that one chemical element can transform into other elements, which was previously only a centuries-old belief of alchemists, who tried to change lead into gold. Prof. Hasselberg (1908), in his speech of the 1908 Nobel Prize presentation, had foresight when he added further

[Rutherford's] disintegration theory [of atoms] and the experimental results upon which it is based, are synonymous with a new department of chemistry.

We can thus give credit to Rutherford for giving birth to the field of radiochemistry. It was, however, Frederick Soddy, who established the "displacement law" or "periodic law" of radionuclides. While at Glasgow University in 1913, he published in the journal *Nature* (Soddy, 1913a) the law in the following words:

The successive expulsion of one α and two β particles in three radioactive changes in any order brings the inter-atomic charge of the element back to its initial value, and the element back to its original place in the (Periodic) Table, though its atomic mass is reduced by four units.

An example of Soddy's displacement law can be taken from a part of Fig. 1.19 of the thorium decay series, which is illustrated here in Fig. 1.3.

As illustrated in Fig. 1.3, Soddy demonstrated that the emission of an α -particle would produce an element that is two atomic numbers lower, while the emission of a β -particle would displace an atom one atomic number higher. In the illustration above we see that the radioactive atom of thorium-232 emits an α -particle to become an atom of radium-228, which in turn decays by the emission of a β -particle to become radioactive actinium-228. The actinium atom also decays by the emission of a β -particle to become thorium, the same element of atomic number 90 from which it had originated, but with a mass number of four units less. The emission of an α -particle from

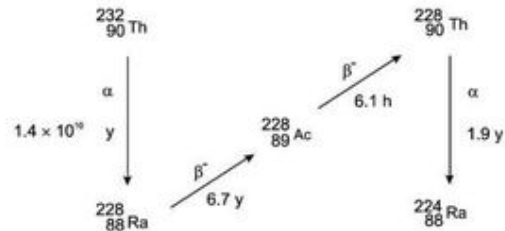
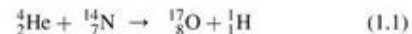


FIGURE 1.3 Soddy's displacement or periodic law as illustrated with thorium and radium isotopes.

the thorium-228 brings the atom back to the element radium with four mass units less than the atom of radium-228. The parent and product atoms of atomic number 90 are of the same element thorium, but of different mass. These two distinct atoms of thorium ($^{232}_{90}\text{Th}$ and $^{228}_{90}\text{Th}$) and radium ($^{228}_{88}\text{Ra}$ and $^{224}_{88}\text{Ra}$) illustrated above are today known as "isotopes", because Soddy (1913a,b) coined the word "isotopes" to refer to such atoms that occupy the same place (from the Greek) in the Periodic Table. Isotopes have the same atomic number (*i.e.*, the number of protons in the nucleus), but different mass number (*i.e.*, number of protons plus neutrons in the nucleus).

One of Ernest Rutherford's greatest discoveries came in 1919 when he reported the first evidence of a man-made nuclear reaction, that is, the splitting of the atom. This he was able to demonstrate when a high-speed alpha particle would strike the nucleus of an atom and rearrange it into two different atoms. Rutherford observed that when alpha particles would strike air, he could detect scintillation on a zinc sulfide screen produced at a distance well beyond the distance of alpha-particle range of travel, which corresponded to the range of travel of hydrogen atoms (protons). He demonstrated that the production of high-speed protons, by collision of alpha particles with air, arose from the collision of the alpha particles with nitrogen atoms only, because the effect would not occur with other constituents of air such as oxygen or carbon dioxide. Furthermore, when pure nitrogen was the target, the scintillations produced by the product hydrogen nuclei (protons) were greater than when air was bombarded with alpha particles (air contains 79% nitrogen). Rutherford was also able to show that the number of swift atoms of oxygen produced by the alpha-particle collisions was about the same as the corresponding number of hydrogen nuclei (protons). This first man-made nuclear reaction is written as follows:



The historic nuclear reaction occurs when the colliding alpha particle, equivalent to a nucleus of helium (${}^4_2\text{He}$), interacts with an atom of nitrogen-14 (the most abundant isotope of nitrogen, denoted as ${}^{14}_7\text{N}$, because its nucleus contains 7 protons and 7 neutrons). In the collision, a proton (${}^1_1\text{H}$) is ejected and two protons and two neutrons from the alpha particle can coalesce with the remaining nucleons of the original nitrogen to yield a nucleus having 8 protons and 9 neutrons, namely, the isotope oxygen-17 denoted above as ${}^{17}_8\text{O}$. This was the very first artificial transformation of one element into another, which was the age-old dream of alchemists.

As a result of the above man-made nuclear reaction where protons were emitted as a product, Rutherford has been given the honor of discovering the third elementary particle in matter, the proton. To put this discovery in perspective, the first elementary particle to be discovered was the electron from the work of J.J. Thomson in 1897, and the second elementary particle to be discovered was the photon from the work of Albert Einstein in 1905. Einstein's discovery of the photon came in the heels of Max Planck's quantum theory of radiation (Planck, 1900), which was presented by Planck on December 14, 1900 at a meeting of the Physikalische Gesellschaft in Berlin. Thus, the world came to know that radiation is emitted at discrete energies corresponding to differences in energy states of a body. Planck defined the discrete energies of emitted radiation as the product of Planck's constant, h , and the radiation frequency, ν , or

$$E = h\nu \quad (1.2)$$

Planck referred to this discrete radiation energy as "the quantum" from the Latin *quantus* meaning "how great". Thus, Planck's discovery of the energy quantum in 1900 and Einstein's interpretation of the photoelectric effect in 1905, where he explained that light traveled not only as waves of electromagnetic radiation but also as discrete packets of energy, namely "light quanta" or photons. This opened a new door to radiation physics, referred to as quantum physics, and Eqn (1.2) is now often referred to as the Planck-Einstein relation (Woan, 2000). If electromagnetic radiation, such as x-rays, gamma rays, and visible light, had the properties of a particle, that is, the energy quantum or photon, Louis Victor de Broglie at Paris University reasoned, in turn, that all particles in motion would have properties of a wave (de Broglie, 1923a,b,c, 1924, 1925). He reasoned that all particles of known rest mass would, in motion, have a dual nature, that of a particle and that of a wave. Thus, the electron, neutron, proton, and alpha particle, etc, could display this dual nature. He derived the fundamental relation for the wavelength of a particle in motion as

$$\lambda = h/p \quad (1.3)$$

where λ is the wavelength of the particle, that is, the distance between two consecutive peaks of the particle wave, h is Planck's constant, and p is the particle momentum. This dual nature of particles (matter and wave) has been proven many times over and remains vital to applications in particle diffraction.

Another contribution, among many others made by Rutherford, deserves mention. This is the development, together with Hans Geiger, of the electronic means of detecting and counting individual alpha-particle emissions from radioactive atoms. The alpha-particle emissions were allowed to travel through a small opening or window into a vessel containing air or other gas exposed to an electric potential. The vessel is referred to today as an ionization chamber. Upon entering the vessel the alpha particle, which carries a double positive charge, would cause ionization of the gas, and the ions produced by the alpha particle would accelerate toward electrodes of the chamber, thereby magnifying the ionization within the gas. The positive and negative ions produced by the alpha particle would be collected by their apposing electrodes and thereby produce a pulse that

would cause a deflection of the electrometer needle. This instrument was the precursor of more modern Geiger counters, but it served its purpose, as Rutherford and Geiger were able to count each alpha-particle emission from a radium sample and calculate its specific activity, in the words of Rutherford on his 1908 Nobel Lecture, "In this way it was shown that 3.4×10^{10} alpha particles are expelled per second from one gram of radium." This was very close to the real value of 3.7×10^{10} , which is used today to define the unit of radioactivity known as the Curie (Ci), where $1 \text{ Ci} = 3.7 \times 10^{10}$ disintegrations per second.

Rutherford's best work was yet to come after the Nobel Prize. In 1907 he moved to England to fill the position of Professor of Physics at Manchester University. It was at Manchester where Rutherford had a list of research topics to explore, and one of these was the deflection that alpha particles would undergo when passing through thin foils (approx. 5×10^{-5} cm thick) of materials such as mica, aluminum, gold, etc. He knew that the alpha particles, as they travel at high speed, would traverse the very thin foils as if the foil material was not even in the alpha-particle path, and that the flux of alpha-particle radiation would undergo only a very slight dispersion upon exiting the foils. This was understandable to him as strong electrical charges, expected to occur in atoms, could cause the slight deflection of the positively charged alpha particles.

The story goes that Rutherford was approached by one of his students at Manchester, Dr. Hans Geiger (best known as the person who developed the Geiger counter still used today for the monitoring of radioactivity). Geiger had asked Rutherford "What do you suggest we give the new student Ernest Marsden to do? Rutherford proposed that they try to see if any alpha particles would bounce back, that is, not traverse the foil but be deflected by over 90° back toward the particle direction of travel. Rutherford did not expect to see any such deflection, but it had to be investigated. They could discern the alpha-particle direction of travel and count the deflections by means of a zinc sulfide screen that would produce a microscopic fluorescence (flash of light scintillation) in the dark when each individual alpha particle hit the screen. They used radium as the source of the alpha-particle beam to bombard a thin foil of gold. Geiger later informed Rutherford that they could see the occasional deflection by greater than 90° of one alpha particle for every 8000 particles traversing the gold foil. In a presentation given by Rutherford years later, he described his reaction to this discovery by stating

It was quite the most incredible event that ever happened to me in my life. It was as incredible as if you fired a 15-inch shell at a piece of tissue paper and it came back and hit you.

Rutherford grasped this discovery to conclude that there had to be a massive core or nucleus in the atoms of materials that would cause colliding alpha particles to bounce back. By using high-energy (7.7 MeV) alpha particles, that would travel at highest speeds available at that time, Rutherford was able to calculate the distance of closest approach and consequently the radius of the atomic nucleus to be approx. 5×10^{-15} meters (Rutherford, 1906, 1913, 1919, 1920a,b).

In a Letter to the Editor of *Nature*, concerning the structure of the atom, published on December 11, 1913, Rutherford

postulated correctly the atomic nucleus as the origin of α - and β -radiation. In his letter, he stated the following:

There appears to me no doubt that the α particle does arise from the nucleus, and I have thought for some time that the evidence points to the conclusion that the β particle has a similar origin. This point has been discussed in some detail in a recent paper by Bohr (Phil. Mag., September 1913). The strongest evidence in support of this view is, to my mind, (1) that the β ray, like the α ray transformations, are independent of physical and chemical conditions, and (2) that the energy emitted in the form of β and γ rays by the transformation of an atom of radium C is much greater than could be expected to be stored up in the external electronic system.

From here on, Rutherford was able to begin to formulate the structure of atoms with a central massive nucleus (Rutherford, 1929, 1936), the structure that holds today. Rutherford's findings were the initial step that provided the foundation upon which other physicists such as Niels Bohr, Werner Heisenberg, and others to elaborate the structure of the atom as we know it today.

Following Rutherford's alpha-scattering experiment, which provided evidence for a massive central nucleus, Niels Bohr (1913, 1914, 1921a,b, 1922) formulated the structure of the atom, known as the Bohr atom, consisting of a positively charged nucleus with electron orbitals about the nucleus, the number of which were sufficient to neutralize the positive charge on the nucleus (*i.e.*, the number of electrons in each atom equaled the number of protons in the nucleus or its atomic number). Also, the dimensions of the nucleus were very small in comparison to the size of the atom defined by the electron orbits, and almost all of the mass of the atom was concentrated in the nucleus. By taking Rutherford's atom, Max Planck's quantum theory of energy, and the simplest of all atoms hydrogen, Niels Bohr was able to launch his quantum theory of atomic structure, referred to as the Bohr atom. With his quantum theory of atomic structure, Bohr was able to explain the spectra of radiation emitted by atomic electrons and the chemical properties of the elements based on electron groupings in quantum orbits. Bohr proposed that electrons would exist in orbits about the nucleus at discrete distances and each orbit would represent specific quantized energies. Thus, when an atom absorbs energy, from an external form of excitation, an atomic electron would jump from one orbit to another further away from the atomic nucleus. Energy absorbed by the atom could be emitted from the atom as radiation when an electron falls from an outer to an inner orbit. Bohr explained that energy can be absorbed or emitted by an atom only as a single quantum of energy or light photon ($h\nu$) equal to the energy differences of specific orbitals. The difference between two such energy levels ($E_2 - E_1$), divided by Planck's constant h , would define the oscillation frequency of a spectral line that can be emitted by the atom, as described by the following:

$$\nu = \frac{E_2 - E_1}{h} \quad (1.4)$$

With his quantum theory of atomic structure, Bohr derived and explained fully the Rydberg formula, which was a formula devised by the Swedish physicist Janne Rydberg (1854–1919)

to calculate and predict the wavelengths of light photons emitted by hydrogen and later applied to the other elements of the periodic table to include, in addition to visible light, other types of electromagnetic radiation emitted by atoms.

The use of electron orbits about a central atomic nucleus as depicted by Bohr (*i.e.*, the Bohr atom) was not considered or intended as an accurate depiction of the atom; however, it remains to this day a very didactic method to illustrate the atom and explain radiation emission and absorption of electron origin and the chemical properties of the elements. Because electrons have properties of both particles and waves, that is, a dual nature as described by de Broglie, Werner Heisenberg (1926a,b,c, 1929) demonstrated that we cannot always assign to an electron a position in space at a given time, nor follow it in its orbit; therefore, we cannot assume that the planetary orbits postulated by Niels Bohr actually exist. Heisenberg thus established the uncertainty principle (Heisenberg, 1927), which states that it is not possible to accurately measure both the atomic particle (*e.g.*, electron) velocity or momentum and its location. Heisenberg's derivation from quantum mechanics showed that it is not possible to determine, in any given instant in time, both the velocity and the position of an atomic particle. It was demonstrated that the more accurately one tries to determine the velocity of the particle, the more uncertain becomes the determination of its position, and vice versa. Niels Bohr (1928) presented his complementarity argument that the clearest analysis that can be derived from quantum mechanics must include both the corpuscular and wave nature of atomic particles, that is, both the particulate and wave nature of the electron are needed to complement each other in providing a complete description of the atomic particle.

Erwin Schrödinger (1926a,b,c,d,e) took the dual nature of the electron to describe the electron and its properties with wave equations. Schrödinger's wave mechanics provided scientists with a visual picture of the space coordinates occupied by the electron, which Heisenberg's mathematical matrix equations could not provide. Thus, we may also picture atomic electrons as possessing energy levels, rather than occupying definite orbits. Schrödinger had interpreted his wave function Ψ as the electron's matter-wave density distribution, that is, he wanted to dispense with the particulate properties of the electron and consider them to possess a continuous density distribution $|\Psi|^2$ meaning that the electron as a wave could have a high density in some regions of space and lower density in other regions. Max Born, however, interpreted the wave function Ψ as providing a picture of the electron with its coordinates in space, and $|\Psi|^2$ as the probability density of the electron (Born, 1926a,b,c,d, Born, Heisenberg and Jordan, 1926, Born and Oppenheimer, 1927 and Born and Fock, 1928). Born's probability density interpretation is widely accepted today as that which gives the probability of finding the electron particle at particular coordinates in space.

At the time that Heisenberg, Schrödinger, and Born were studying the atomic electron, the Austrian physicist Wolfgang Pauli postulated the exclusion principle for which he received the 1945 Nobel Prize in Physics, as this proved to be a vital contribution to nuclear and atomic physics. The exclusion principle (Pauli, 1924, 1925, 1946) stated that no two electrons

in an atom could exist in the same quantum or energy state. Pauli's exclusion principle enabled the assignment of electrons to different quantum levels K, L, M, N , etc., and our subsequent understanding of x-ray spectra that often follows nuclear decay. The Pauli exclusion principle also proved to be a vital tool decades later to explain the structure of protons and neutrons in the nucleus, particularly what is referred to as the shell structure of the nucleus, and the stability of particular nuclei to decay. Like the electrons, which are assigned to various quantum levels or orbitals on the basis of Pauli's exclusion principle, no two nucleons may possess the same quantum or energy state and are assigned to specific shells. Certain filled shells of protons and neutrons in the nucleus were found to be unusually stable by Maria Goeppert-Mayer at the Argonne National Laboratory and J. Hans D. Jensen at the University of Heidelberg (Goeppert-Mayer and Jensen, 1955). Maria Goeppert-Mayer and J. Hans D. Jensen were awarded the 1963 Nobel Prize for Physics for their work on nuclear structure, which they shared with Eugene Wigner for his work on the mechanics of proton-neutron interaction.

One of the greatest conundrums of modern physics was beta decay. It was understood that the kinetic energy of a particle emitted by a decaying nucleus was a manifest of the decay energy of that nucleus. However, it was observed that beta particles are emitted from decaying nuclei with a broad spectrum of energies over a range between zero and a maximum energy or E_{\max} . In other words, it was observed that most of the beta particles emitted possessed an energy less than the nuclear decay energy. Only a very small number of the beta particles of the maximum energy of the beta-particle energy spectrum would correspond to the nuclear decay energy. In desperation for an answer, some physicists proposed that possibly the laws of conservation of energy did not apply in this particular case. However, Wolfgang Pauli could not agree to any exceptions to the laws of energy conservation, and he took a bold step. He proposed that during beta decay, there exists another particle of zero charge and very small rest mass that would be created at the time of beta decay, and this particle would share the decay energy with the beta particle. While he was professor of theoretical physics at the Swiss Federal Institute of Technology in Zurich (Eidgenössische Technische Hochschule or ETH, Zurich), Pauli sent an Open Letter dated December 4, 1930 to the Radioactivity Group at their Regional Meeting at Tübingen, Germany. In this letter Pauli wrote

Dear Radioactive Ladies and Gentleman,

I beg you to most favorably listen to the carrier of this letter. He will tell you... of the continuous beta spectrum, I have hit upon a desperate remedy to save... the law of conservation of energy. There is the possibility that electrically neutral particles exist... in nuclei, which have a spin $\frac{1}{2}$ and obey the exclusion principle, and which differ from the photons also in that they do not move with the velocity of light. The continuous beta spectrum would then be understandable if one assumes

that during beta decay with each electron a [neutrino]¹ is emitted in such a way that the sum of the energies of the [neutrino]¹ and electron (i.e., beta-particle) is constant.

I admit that my remedy may seem incredible... But only he who dares can win and the difficult situation caused by the continuous beta spectrum... Henceforth every possible solution must be discussed. So, dear radioactive people, because I am indispensable here due to a ball which will take place in Zurich during the night from December 6 to 7. With my best regards to you...

Your humble servant,

W. Pauli

The writer believes that Wolfgang Pauli used the ball in Zurich as an excuse not to attend the scientific conference, because he wanted his letter to be read to the participants of the conference; and it is very understandable that he would not want to listen to any ridiculous arguments against his theory, particularly any that would suggest an exception to the law of conservation of energy.

Wolfgang Pauli's prediction in 1930 of the neutrino as a particle that would be produced in beta decay and share the decay energy with the beta particle was only the beginning of the elucidation of a more complex scheme for beta decay. Two years earlier Paul A.M. Dirac, as a Fellow at St. John's College in Cambridge and a researcher at the Cavendish Laboratory, published the quantum theory of the electron (Dirac, 1928a,b, 1933). A result of Dirac's quantum theory of the electron was the prediction of the electron spin and the occurrence of a new electron, one of positive charge, known as the positron, the antiparticle of the negatron or negative electron. Dirac also predicted the phenomenon of annihilation, when a particle and its antiparticle (e.g., negatron and positron) come into contact and are annihilated by the conversion of their electron masses into electromagnetic radiation. He also predicted pair production, which would be the converse of annihilation, that is, the creation of a positron and negatron pair from electromagnetic radiation. In his Nobel Lecture Dirac explained

From our theoretical picture, we should expect an ordinary electron, with positive energy, to be able to drop into a hole and fill up this hole, the energy being liberated in the form of electromagnetic radiation. This would mean a process in which an electron and a positron annihilate one another. The converse process, namely the creation of an electron and a positron from electromagnetic radiation, should also be able to take place. Such processes appear to have been found experimentally, and are at present being more closely investigated by experimenters.

The existence of the positron was experimentally discovered in 1932 by Carl D. Anderson while carrying out research on cosmic rays for which he was awarded the Nobel Prize in Physics 1936 (Anderson, 1932, 1933a,b). Anderson also demonstrated together with his graduate student, Seth

¹ The actual naming of the particle as the neutrino, while not included in Pauli's letter, is included here for clarification with the reader as to the real particle referred to by Pauli. Enrico Fermi later coined the name of this neutral particle of near-zero rest mass as the "neutrino" from the Italian meaning 'little neutral one'. Due to the particle's neutral charge and near-zero rest mass, it was very difficult to detect the neutrinos, so difficult, that it was not until over 25 years later (June 1956) did technology permit Frederick Reines and Clyde Cowan, Jr. to finally achieve the detection of the neutrino.

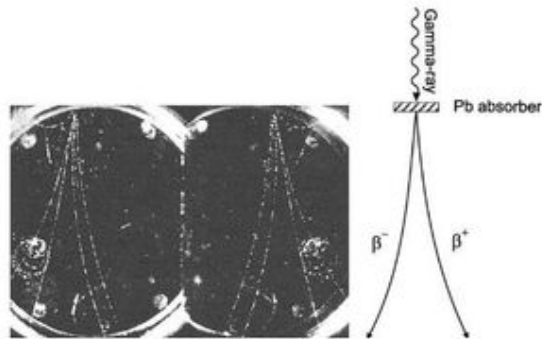


FIGURE 1.4 Photograph of cloud chamber tracks of positrons (curved tracks on the right) and negatrons (curved tracks on the left) originating from a common point of origin where gamma-ray photons of cosmic origin were absorbed by a lead barrier. The magnetic field was applied in the direction of the page of this book. The photograph was presented as a stereoscopic pair, and the direct image is at the left. (From Anderson and Neddermeyer, 1936). A drawing to the right illustrates pair-production, that is, the production of a negatron-positron pair from the energy of a gamma-ray photon in the region of the nucleus of an absorber material such as lead. The curved tracks illustrate the direction of the negatron-positron pair by the magnetic field. (Reprinted with permission © 1936 American Physical Society.)

Neddermeyer, that gamma rays from “ThC” (*i.e.*, ^{212}Bi) would generate positrons, by pair production, after passing through substances such as lead (Anderson and Neddermeyer, 1933). Pair production, as predicted by Dirac, is the creation of an electron and positron pair by the conversion of the energy of electromagnetic gamma radiation into the masses of two electrons of opposite charge. A cloud chamber photograph of positron–negatron pair production is illustrated in Fig. 1.4.

If negative and positive electrons (*i.e.*, beta particles) were known to exist and these were products of beta decay, the mystery remained how beta particles, which are equivalent to electrons, could originate and be expelled from an atomic nucleus. The beta decay process of radioisotopes, often referred to as “Fermi Beta Decay”, was elaborated in 1934 by Enrico Fermi (1934a,b) only two years following the discovery of the neutron by James Chadwick (1932a, b). Fermi proposed that within the nucleus of a radioactive atom, the neutron may decay to a proton and vice versa, a proton into a neutron. He proposed the existence of a weak interaction as a new force, within the nucleus, that permits a neutron to decay into a proton and a negatively charged electron (*i.e.*, negatron) and antineutrino ($n \rightarrow p^+ + e^- + \bar{\nu}$) or vice versa, a proton could decay into a neutron and a positively charged electron (*i.e.*, positron) and neutrino ($p^+ \rightarrow n + e^+ + \nu$). The weak interaction would allow a nucleon (proton or neutron) to transform itself into the other to achieve nuclear stability. This force would be weaker than the strong nuclear force or strong interaction that binds the nucleons together in the nucleus. The weak interaction proposed by Fermi advanced into a unified electroweak theory for which the Nobel Prize in Physics 1979 was awarded to Sheldon L. Glashow, Abdus Salam, and Steven Weinberg “for their contributions to the theory of unified weak and electromagnetic interaction between elementary particles...”, as it has subsequently been discovered that the weak interactions and electromagnetic

interactions are of similar strengths at short distances typical of nucleons (10^{-18} meters). These two forces can be combined into what is called the electroweak force.

Fermi’s original manuscript on the transformations of nucleons within the nucleus was rejected by the editors of the journal *Nature* because of its theoretical nature, and therefore his first reports on the beta decay theory were published in the Italian and German languages (Fermi 1934a,b). Evidence for these transformations was provided years later by Snell and Miller (1948), who demonstrated that the neutron, when outside the protective confines of a nucleus, would decay to a proton and an electron with a lifetime of ~15 minutes according to the scheme



Although Fermi is well remembered for his beta decay theory, the Nobel Prize was awarded to him in 1938 for his contribution to the application of neutron radiation to the production of many new radioactive isotopes and to his discovery that certain nuclear reactions are brought about by slow neutrons. In his Nobel Lecture (December 12, 1938) Fermi acknowledged that Rutherford was the first to start the technique of nuclear bombardments using high-energy alpha particles to enable the transmutation of one element into another in 1919. Fermi further noted that immediately after the discoveries of the artificial production of radioactive elements (radioisotopes) by the Joliot-Curies in 1934 by alpha-particle induced nuclear reactions (Joliot-Curie and Joliot 1934a–c), he thought that alpha particles might not be the only type of bombarding projectiles that could produce artificial radioactivity, particularly for atoms with atomic number greater than 20, and began then to investigate the effects of bombarding various elements with neutrons.

Fermi observed that neutrons having no electric charge should be able to reach the nuclei of all atoms without having to overcome the Coulombic barrier of the target nucleus. He knew that the neutron would not be hindered by the atomic electrons or the positive charge of the atomic nucleus, and that the probability of nuclear collisions by neutrons would be higher than that achievable with charged projectiles such as alpha particles or protons. The initial results obtained by Fermi in early 1934 (Fermi 1934c,d and Fermi et al, 1934) and his coworkers during 1934–1940 including H. Anderson, E. Amaldi, O. D’Agostino, F. Rasetti, E. Segré, and L. Szilard (Amaldi and Fermi, 1935, 1936a,b, Amaldi et al, 1935, Anderson, et al, 1939a,b, Fermi and Amaldi (1936), Fermi (1940a,b) and Fermi et al, (1934, 1938) yielded 63 artificial radioisotopes.

Only about six months after their first experiment with neutron bombardment Fermi made a great discovery. Fermi found that the neutron irradiation of elements became more effective in producing new radioisotopes when the neutrons were made to slow down, by allowing the neutron beam to pass through a given barrier of water or paraffin. By so doing the fast neutrons are slowed down to become thermal neutrons or, in other words, neutrons corresponding to thermal agitation. In his Nobel Lecture, Fermi explained the properties of thermal neutrons

After their energy is reduced to a value corresponding to thermal agitation, the neutrons go on diffusing without further change of their average energy. All of the processes of capture of slow neutrons by any nucleus are generally accompanied by the emission of gamma rays: Immediately after the capture of the neutron, the nucleus remains in a state of high excitation and emits one or more gamma-quanta, before reaching the ground state.

The idea of slowing down neutrons to improve the efficiency of neutron capture was contrary to what one would believe at that time, because previously only charged particles were used to bombard atomic nuclei and the higher the speed of the charged particle, the greater the probability of penetrating the Coulombic barrier of the target atom. Because neutrons have no difficulty diffusing into close proximity of atomic nuclei, Fermi and his coworkers were able to produce more than 400 new radioisotopes using slow neutron bombardment of all known elements with the exception of hydrogen and helium.

The work of Enrico Fermi on neutron reactions up to 1938 was the final precursor needed for the discovery of nuclear fission by Otto Hahn and Fritz Strassmann in 1939 with the collaboration of Lise Meitner (Hahn and Strassman, 1939a,b, Meitner and Frisch, 1939 and Meitner et al, 1938). Fermi's next great achievement would be the construction of the first nuclear reactor.

Enrico Fermi collaborated with Leo Szilard and a team of scientists in the construction of the first nuclear reactor. Leo Szilard was a renowned theoretical physicist and lifelong friend of Albert Einstein. Fermi's great knowledge of neutron physics and Szilard's determination to beat Germany to the production of a nuclear fission chain reaction were an excellent combination for the successful working reactor. In the words of Richard Rhodes (1986)

In 1939, still official enemy aliens, Fermi and Szilard co-invented the nuclear reactor at Columbia University, sketching out a three-dimensional lattice of uranium slugs dropped into holes in black, greasy blocks of graphite moderator, with sliding neutron-absorbing cadmium control rods to regulate the chain reaction.

As soon as it became known that neutron-induced fission of uranium-235 would yield more than one neutron per fission Fermi, Szilard, and others knew that a fission chain reaction would be possible, which would release large amounts of energy. Walter Zinn and Leo Szilard (1939) determined that 2.4 neutrons were emitted on the average for neutron-induced ^{235}U fission, and it was understood that each fission reaction would yield a high amount of energy, ~200 MeV. The reactor, that was built under the direction of Enrico Fermi, was given the name of an "atomic pile", coined by Fermi, because the unique apparatus had the appearance of a pile of uranium fuel, graphite moderator, and cadmium control elements. Fermi knew from his previous work with neutrons that cadmium has a very high efficiency for absorbing slow (thermal) neutrons and should serve to control the chain reaction, and that fission in ^{235}U is optimal at thermal incident neutron energies. They assembled the pile in such a way that neutrons would be produced with the correct energy needed to create fission in the uranium whereby the splitting of uranium nuclei would create additional neutrons

and keep the chain reaction going to produce energy with the application of cadmium rods to control the reaction. The reactor "pile" was assembled by Fermi and his team on a squash court under the stands of the University of Chicago's Stagg (football) Field in late 1942. On December 2, 1942, under the direction of Enrico Fermi, the reactor went critical, that is, the chain reaction was sustained with the production of a neutron for every neutron absorbed by the uranium nucleus. Fermi allowed the reactor to continue as a carefully controlled chain reaction for 4.5 minutes at one-half watt of power. A plaque, at the site of the first "atomic pile", commemorates this historic event with the words "On December 2, 1942, man achieved here the first self-sustaining chain reaction and thereby initiated the controlled release of nuclear energy."

On December 19, 1944 Enrico Fermi and Leo Szilard jointly filed for a highly classified patent as co-inventors of the atomic pile, describing how the self-sustained nuclear chain reaction had been achieved. The patent (U.S. Patent No. 2,708,656 entitled "Neutronic Reactor") was not issued until May 18, 1955. The invention of the nuclear reactor for the peaceful application of nuclear energy capable of providing electric power to cities was declared by some to be one of the most significant inventions of all time comparable to those of communication, the telegraph and telephone, by Samuel Morse and Alexander Graham Bell.

The first nuclear reactor was a giant step for mankind, as it has had since Fermi's "atomic pile" and continues to have a vital role in development with peaceful applications including (1) the production of isotopes for medical, biological, and other vital sciences; (2) the production of heat that can drive steam turbines and generate enormous amounts of electricity; and (3) the production of neutrons for research. A fourth ominous application of the nuclear reactor is, of course, for the production of plutonium for nuclear weapons. The peaceful applications of nuclear power have an enormous impact on our daily lives. This is underscored in an article by ElBaradei (2004), then IAEA Director General, where he noted

At the end of last year there were 440 nuclear power units operating worldwide. Together, they supply about 16% of the world's electricity. That percentage has remained relatively steady for almost 20 years—meaning that nuclear electricity generation has grown at essentially the same rate as total electricity use worldwide.

About the same time that Enrico Fermi was producing radionuclides by nuclear reactions with neutrons, Ernest O. Lawrence at the University of California, Berkeley, invented the cyclotron, which could accelerate charged particles to high energies capable of penetrating the Coulombic barrier of atoms resulting in nuclear reactions that produced numerous radionuclides. Lawrence visualized an accelerator, not consisting of a large number of cylindrical accelerating electrodes in a straight line, but one that had only two electrodes, which would be used over and over again by sending the positive ions back and forth through the electrodes in a circular fashion in a magnetic field. He concluded that two hollow electrodes would be needed with a relatively low voltage (e.g., 4000 volts) and oscillating positive and negative potential so that each instant the accelerating ions exit one electrode and enter the

other, the charges on the electrodes would change in accord with the proper frequency providing a 'push' to the ions as they exit an electrode and thereby increase their energy and velocity.

The experimental work on the development of the cyclotron began in 1930 and, in the Spring of that year, Lawrence's first graduate student at Berkeley, Nels Edlefsen, constructed a crude model, which gave evidence of working. In September 1930 they gave a preliminary report before a meeting of the National Academy of Sciences (Lawrence and Edlefsen, 1930). In the fall of the same year another graduate student M. Stanley Livingston improved on the model, which was only 4.5 inches (11.43 cm) in diameter. The diameter of the accelerator refers to the size of the chamber in which the ions move in a circular path of increasing radius. The first working cyclotron produced 80,000 volt protons with less than 1,000 volts applied to the semi-circular accelerating electrode. This was reported before the American Physical Society (Lawrence and Livingston, 1931a) as a demonstration of the cyclotron as a practical apparatus for the acceleration of ions. The same year Lawrence and Livingston (1931b) reported the acceleration of protons to 0.5 MeV with only 5000 volts potential applied to the electrodes.

Lawrence and Livingston (1932) described the basic design and principle of the cyclotron, with a simple diagram such as that illustrated in Fig. 1.5. The cyclotron utilizes the principle of repeated acceleration of ions by means of resonance with an oscillating field. The ions circulate from the interior of one electrode to the interior of another back and forth with increasing speed in a circular fashion. The hollow electrodes *A* and *B* of Fig. 1.5 are placed between the poles of a magnet, and the magnetic field normal to the plane of the hollow plates causes the ions to deflect in a circular fashion with a radius of curvature dependent on the mass, charge, and velocity of the ions.

The oscillating electric field between the electrodes is vital to the operation of the cyclotron. For example, as Lawrence and Livingston (1932) explained, if at one instant there is an ion in the region between the electrodes, and if electrode *A* is negative with respect to electrode *B*, the ion will be 'pushed' and accelerated to the interior of electrode *A*. Within the hollow electrode, the ion will travel along a circular path under the effect of the magnetic field. After completing a semi-circular path in electrode *A*, as illustrated by the arc *a...b* in Fig. 1.5, the ion emerges again between the electrodes. If the time consumed in the travel of this semi-circular path (e.g., from point *a* to point *b* of Fig. 1.5) is equal to the half-period of the electric oscillations, the electric field will have reversed and the ion will receive a second 'push' and be accelerated into the interior of electrode *B* with higher velocity. The ion continues to travel in a circular path in electrode *B* and completes another semi-circular path with greater velocity and greater radius of curvature. Upon completion of the semi-circular path in electrode *B* at point *c*, the ion again emerges between the electrodes, and the ion is again accelerated by the oscillating electric field to travel at a greater speed into the interior of the opposing electrode with a path of greater radius of curvature. The process of acceleration repeats itself over and over until the ion achieves a radius of curvature whereby it emerges from the cyclotron.

A vital characteristic of the cyclotron principle is that time of travel of an ion to complete a semi-circular path is independent of the ion's velocity and thus independent of the radius of the ion path. This was demonstrated and explained by Lawrence and Livingston (1932) following their demonstration of an 11-inch (28-cm) diameter cyclotron:

...the radius of the path is proportional to the velocity, so that the time required for the travel of a semi-circular path is independent of the ion's velocity. Therefore, if the ion travels its first half-circle in

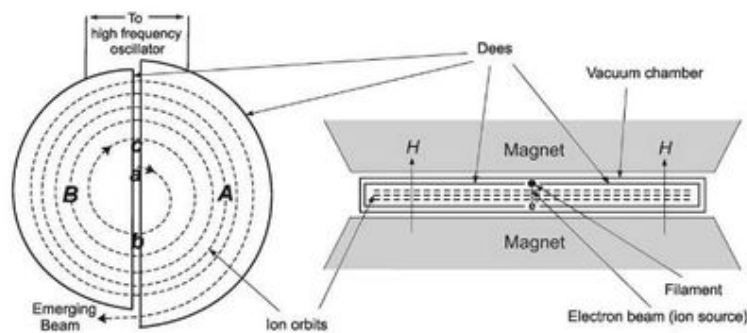


FIGURE 1.5 Diagrams illustrating the cyclotron method of multiple acceleration of ions. On the left is a drawing of the top or bottom of the cyclotron electrodes and on the right is a drawing of a view from the side with the electrodes between magnet poles. Two electrodes *A* and *B* in the form of semi-circular hollow plates (called Dees' because they have the shape of the letter D) are mounted in a vacuum chamber with their diametral edges adjacent. The electrodes of the early cyclotron of Lawrence and Livingston measured only 24 cm in diameter; and their hollow semi-circular chambers, through which the ions traveled, had a width of only 1 cm. The system is placed between the poles of a magnet whereby the magnetic field *H* is introduced normal to the plane of the plates. High frequency electric oscillations are applied to the plates so that there results an oscillating electric field in the diametral region between them. A filament placed above the diametral region creates a stream of electrons that produce the needed positive ions, which are pulled out sideways by the oscillating electric field. The electrons are not drawn out into the cyclotron electrodes because of their very small radii of curvature in the magnetic field. The positive ions (e.g., protons, deuterons, or helium nuclei) are accelerated by the oscillating electric field and travel with increasing speed and energy in a circular fashion of increasing radius in the magnetic field as described in the text. The beam of positive ions emerges from the cyclotron to collide with specific targets creating new elements, stable isotopes, and radioisotopes, etc. (Adapted from Lawrence and Livingston, 1932.)

a half-cycle of the oscillations, it will do likewise on all succeeding paths. Hence it will circulate around on ever widening semi-circles from the interior of one electrode to the interior of the other, gaining an increment of energy on each crossing of the diametral region that corresponds to the momentary potential difference between the electrodes. Thus, if, as was done in the present experiments, high frequency oscillations having peak values of 4000 volts are applied to the electrodes, and protons are caused to spiral around in this way 150 times, they will receive 300 increments of energy, acquiring thereby a speed corresponding to 1,200,000 volts.

The 1.2 million-volt hydrogen ions produced by Lawrence and Livingston in their early 11-inch (28-cm.) diameter accelerator were of sufficient energy to disintegrate the light lithium nucleus; but much higher energies would be needed to penetrate larger atomic Coulombic barriers and disintegrate the heavier elements. Larger-diameter cyclotrons would require larger magnets, because the spiraling path taken by the ions in the cyclotron are produced by a uniform magnetic field normal to their plane of travel. Thus, the pole faces of the magnets had to be at least as large as the diameter of the cyclotron vacuum chamber.

With a larger magnet at hand, Lawrence then proceeded to build a 27-inch (69 cm.) diameter cyclotron with the electrodes ('dees') measuring 20 inches (51 cm) having a width of 1.12 inches (2.8 cm). With the new and larger cyclotron, Lawrence and Livingston (1934) were able to accelerate protons (${}^1_1\text{H}$) to 5 MeV energy. With yet further modification by essentially increasing the size of the electrodes 'dees' to a diameter of 24.5 inches (62 cm) and width of 1.75 inches (4.4 cm), Lawrence and Cooksey (1936) produced deuterium (heavy hydrogen, ${}^2_1\text{H}$) ions and helium ions (${}^4_2\text{He}$) of 5- and 10-MeV energy, respectively. The helium ions would be accelerated to twice the energy of the deuterons, explained by Lawrence and Cooksey (1936) as follows:

...The helium ions having twice the charge and mass relative to deuterons, receive twice the increments in energy each time they pass between the dees and arrive at the periphery with twice as much energy. Thus, apart from difficulties of producing doubly charged helium ions at the center, the cyclotron produces 10 MeV alpha particles as readily as 5 MeV deuterons.

The most significant outcome of the new and improved cyclotron demonstrated by Lawrence and Cooksey (1936) was the production of neutrons and artificial radioactive isotopes. Neutron fluxes higher than ever achieved were reported. For example, the neutron flux by the deuteron bombardment of various elements including beryllium was 10^5 times greater than that produced by a mixture of 1 curie of radon and beryllium. Lawrence began to produce many new radioisotopes as noted by Lawrence and Cooksey (1936):

With 5 MeV deuterons, it has been found possible (Lawrence, 1935) to produce radioactive isotopes of many of the elements throughout the periodic table. In many cases, the yields of the radioactive substances are quite large; as for example, a day's bombardment of sodium metal with 20 microamperes of 5 MeV deuterons produces more than 200 milligrams — equivalent of radio sodium.

By 1939, the year Lawrence received the Nobel Prize, he and coworkers (Lawrence et al., 1939) at the Berkeley lab

completed the construction of a larger 60-inch (1.5 meter) cyclotron that produced 16 MeV deuterons. It had a magnet weighing 200 tons. In his Nobel Lecture at Stockholm, Lawrence (1951) commented about the larger cyclotron

...the cyclotron for the first time began to look like a well-engineered machine. It was with this machine that the discoveries of the transuranium elements were made, which have been rewarded this year by the award of the Nobel Prize in Chemistry [1951] to Edwin M. McMillan and Glenn T. Seaborg.

Using the 60-inch cyclotron at the University of California, Berkeley, McMillan and Abelson (1940) created neptunium (Np) a new element of atomic number 93. He moved to the Massachusetts Institute of Technology, and Glenn T. Seaborg continued research on the creation of new radioactive elements with the 60-inch cyclotron. By bombarding U-238 with 16-MeV deuterons from the 60-inch cyclotron, Seaborg et al. (1946a,b) discovered element 94 (*i.e.*, atomic number 94). The new element was named plutonium after the planet Pluto, because McMillan had suggested the name neptunium after the planet Neptune, the planet immediately beyond Uranus. Thus, Seaborg noted that it would be proper to name the new element plutonium (Pu) after what was then considered the next planet Pluto. In the summer of 1944, Seaborg and coworkers bombarded ${}^{239}\text{Pu}$ with 32 MeV helium ions (equivalent to alpha particles) in the Berkeley 60-inch cyclotron and created the new radioactive element 96, named curium, according to the reaction ${}^{239}\text{Pu}(\alpha,n){}^{242}\text{Cm}$, which is an abbreviation for the nuclear reaction that reads 'target nucleus(projectile, particle emitted) product nucleus'. A few months later they identified a new element 95, named americium, created by the bombardment of ${}^{239}\text{Pu}$ with neutrons produced in a nuclear reactor. The resulting ${}^{241}\text{Pu}$ would decay by negative beta emission to yield ${}^{241}\text{Am}$. By December 1949, they were able to identify new elements 97 and 98 created by bombarding americium and curium with 37 MeV helium ions in the 60-inch cyclotron according to the reactions ${}^{241}\text{Am}(\alpha,2n){}^{243}\text{Bk}$ and ${}^{242}\text{Cm}(\alpha,2n){}^{244}\text{Cf}$, respectively. The new elements berkelium (Bk) and californium (Cf) were named after the city and the university and state, respectively, where the discovery was made. This work laid the foundation for Seaborg's formulation of the 'actinide' transition series of elements in the Periodic Table, which begins with the radioactive element actinium with a tripositive oxidation state. Included in the series are elements 99–103, namely, einsteinium, fermium, mendelevium, nobelium, and lawrencium. In recognition of this work, element 106 among the transuranium elements, was named 'seaborgium' in 1997, which was the first time an element was named after a living person, less than two years before the passing of Glenn T. Seaborg. For a detailed description of this work, see Seaborg's Nobel Lecture (Seaborg, 1951) and a more recent paper published by him four years before his passing (Seaborg, 1995).

The cyclotron remains to this day an invaluable instrument for the production of radionuclides. Many short-lived nuclides are needed for the diagnosis and treatment of various types of cancer. Particularly the radionuclides used by medical physicians for positron emission tomography (PET) are short-lived; and only with the cyclotron is it possible to produce these

radionuclides on-site at hospitals where patients can be diagnosed and treated. There are currently more than 350 cyclotrons in 39 countries of the world (IAEA, 2006, 2007), many of these are in hospitals, which produce short-lived radionuclides for medical use.

III. BASIC UNITS AND DEFINITIONS

A. Properties of Atomic Constituents

The properties of the atomic constituents that are relevant to topics dealt with in this chapter are rest mass, charge, spin, magnetic moment, and stability. Several units of rest mass are given, as these are used throughout the chapter, including the expression of mass in terms of energy, the electron volt (eV) or joule (J), the unit of energy established by the International System of units (SI). A brief description of the terms used for the properties of the atomic constituents is as follows:

Rest Mass: The rest mass, which is the mass of the particle at rest relative to an observer, is expressed in four units, namely, kilograms (kg) or atomic mass units (u), and the energy equivalence of the rest mass ($E = mc^2$) in joules (J) or electron volts (eV). The atomic mass unit is defined in terms of the stable carbon nuclide ^{12}C , which is assigned an atomic mass of exactly 12 u where $1 \text{ u} = 1.660540 \times 10^{-27} \text{ kg}$. The rest mass of the proton or neutron is approximately 1840 times that of the electron.

Charge: The charge on the particle is expressed on the basis of the unit electron charge $+e$ or $-e$ or in units of the coulomb (C). The neutron is neutral or without charge. A neutral atom would be one that possesses a number of external electrons equal to the number of protons in the nucleus. It may be expressed as ^A_ZX , where Z is the nuclear charge or number of protons in the nucleus and A is the mass number of the nucleus or the sum of the number of protons and neutrons in the nucleus. The number of electrons that the atom possesses is assumed to equal that of Z when the atom is a neutral atom.

Spin: The proton, neutron, and electron possess half-integer spin states that belong to a class of particles called fermions (named after Enrico Fermi). Fermions obey the Pauli exclusion principle, which states that no fermion can occupy the same quantum state (energy state) at any given time, as described further on in this chapter. The property of spin and the Pauli exclusion principle enable the assignment of protons and neutrons to specific quantum levels or shells within the nucleus and electrons to specific orbitals away from the nucleus.

Magnetic moment: The nuclear magnetic moments of the proton and neutron are about a thousand-fold smaller than that of the electron. Although the neutron is of neutral charge, it possesses a magnetic moment due to its underlying quark constituents that possess charge. The positive or negative signs designated to the magnetic moments indicate that the spin vectors and the magnetic moments are in opposite direction. The magnetic moments are important properties that establish the basis for magnetic resonance imaging and spectroscopy.

Stability: The neutron is unstable outside the confines of the nucleus. Once outside the nucleus, a neutron has a mean half-life of 10.2 minutes.

B. Nuclides, Isotopes, Isobars, Isomers, and Isotones

The fact that the atom contained a massive center was discovered by Ernest Rutherford (1911) following experiments that revealed the backscattering of α -particles by atoms of gold, which was discussed previously in Section II. Reference to the "nucleus" as a massive positively charged center of the atom was proposed by Rutherford (1913) and Niels Bohr (1913) in their classic papers on the structure of the atom. However, it was not until James Chadwick (1932a,b, 1935) discovered the neutron and determined its mass, could the structure of an atomic nucleus be explained to contain a definite number of protons and neutrons. Consequently, the term nuclide and radionuclide could then be derived, which are defined as follows:

Nuclide: A nuclide is a species of an atom that is characterized by the number of protons (Z) and number of neutrons (N) in its nucleus and by the energy state of the nucleus. A symbol for a nuclide can be written in the form ^A_ZX , where X is the symbol for the chemical element, Z is the atomic number or number of protons in the nucleus, A is the mass number or the number of protons plus neutrons in the nucleus, and N is the number of neutrons in the nucleus. Generally when A and Z are noted with the nuclide symbol, the neutron number N is not written, as it is deduced (*i.e.*, $N = A - Z$). For example, the nuclide written as $^{90}_{38}\text{Sr}$ represents an atom of the element strontium with a nucleus containing 38 protons and 52 neutrons and a mass number of 90. The nuclide may also be written in a more abbreviated form as ^{90}Sr , since the atomic number of the element strontium is known and is an invariable number for that element. There are 266 stable nuclides and 83 unstable or radioactive nuclides that exist naturally on Earth. More than 3000 radioactive nuclides are known that are artificially produced. The radioactive nuclides are referred to as **radio-nuclides**. All of the nuclides, both stable and radioactive, are organized in "the Chart of the Nuclides". The chart provides a block containing the properties of each nuclide, which is plotted according to its Z versus N . A small part of the Chart of the Nuclides is illustrated in Fig. 1.35 in this chapter. The entire Chart of the Nuclides and the nuclear data for each nuclide can be viewed on-line on the website of the National Nuclear Data Center of the Brookhaven National Laboratory (<http://www.nndc.bnl.gov/nudat2/>), or on the website of the International Atomic Energy Agency (<http://www-nds.iaea.org/relnsd/vcharhtml/VChartHTML.html>). The term isotope, which is frequently and erroneously used for the term nuclide, is discussed and defined below.

Isotopes: Nobel Laureate Frederick Soddy coined the word "isotopes" (Soddy 1913a,b) to refer to such atoms that have the same atomic number (*i.e.*, the number of protons in the nucleus) but different mass number (*i.e.*, number of protons plus neutrons in the nucleus). Soddy recognized that these are atoms of the same element in the periodic table but of different mass. In his words, Soddy (1913a) explained

I call (them) "isotopes" or "isotopic elements", because they occupy the same place (from the Greek) in the periodic table. They are chemically identical, and save only as regards the relatively few

physical properties which depend on atomic mass directly, physically identical also.

Soddy went further by alluding to the fact that not only can we consider the radioactive atoms of specific elements as "isotopes", but that many, if not most, of the stable elements may actually consist of a mixture of isotopes. In his Nobel Lecture, Soddy (1922) gave credit to the Swedish scientists Strömholm and Svedberg (1909a,b) by quoting them as follows:

Perhaps, one can see, as an indication in this direction, the fact that the Mendeleev scheme (Periodic Table of Elements) is only an approximate rule as concerns the atomic weight, but does not possess the exactitude of a natural law; this would not be surprising if the elements of the scheme were mixtures of several homogeneous elements of similar but not completely identical atomic weight.

Isotopes are nuclides that have the same atomic number (Z), that is, the same number of protons; but they differ in their number of neutrons (N). Thus, they differ in their mass number (A), which is the sum of the number of protons and neutrons in the nucleus. Because isotopes have the same atomic number, they are nuclides of the same chemical element. For example, the following are isotopes of the chemical element carbon: ${}^{10}_6\text{C}$, ${}^{11}_6\text{C}$, ${}^{12}_6\text{C}$, ${}^{13}_6\text{C}$, ${}^{14}_6\text{C}$, where the subscript and superscript represent the atomic number Z and mass number A , respectively, whereby the number of neutrons in the nucleus, N , is calculated as $A - Z$. Among the five isotopes of carbon listed above, ${}^{10}_6\text{C}$, ${}^{11}_6\text{C}$, and ${}^{14}_6\text{C}$ are radioactive, and thus referred to as **radioisotopes**. The other two isotopes of carbon listed above, namely, ${}^{12}_6\text{C}$ and ${}^{13}_6\text{C}$ are stable isotopes of carbon.

Isotope natural abundance: Isotopes of the elements, that are found in nature, occur at a particular **natural abundance**. The term natural abundance refers to the relative abundance of an isotope that occurs naturally on earth. For example, among the five isotopes of carbon listed above, ${}^{12}_6\text{C}$ and ${}^{13}_6\text{C}$ occur naturally at natural abundances of 98.90 % and 1.10 %. The isotope ${}^{14}_6\text{C}$ is naturally occurring in only a small trace ($\sim 10^{-10}$ % natural abundance), as it is formed continuously by the interaction of cosmic-ray protons with nuclides in the upper atmosphere. The isotope ${}^{14}_6\text{C}$ is radioactive, and thus a radioisotope of carbon. The percent natural abundances of the isotopes for each element should add up to 100 percent. Another example is the naturally occurring isotopes of potassium, namely, ${}^{39}_19\text{K}$, ${}^{40}_19\text{K}$, and ${}^{41}_19\text{K}$, which occur at natural abundances of 93.2581%, 0.0117%, and 6.7302%, respectively. The isotopes ${}^{39}_19\text{K}$ and ${}^{41}_19\text{K}$ are stable isotopes; however, the isotope ${}^{40}_19\text{K}$ is a radioisotope that decays with a half-life of 1.26×10^9 years. Since the naturally occurring isotopes are remnants of the nucleosynthesis of the earth, which is 4.54×10^9 years of age (Dalrymple, 2001), the isotope ${}^{40}_19\text{K}$ has had time to decay since the earth's creation. When only one isotope of an element exists naturally on earth, its natural abundance is expressed as 100%. Examples are ${}^{19}_9\text{F}$, ${}^{27}_{13}\text{Al}$, ${}^{31}_{15}\text{P}$, ${}^{45}_{21}\text{Sc}$, ${}^{55}_{25}\text{Mn}$, ${}^{59}_{27}\text{Co}$, ${}^{89}_{39}\text{Y}$, ${}^{127}_{53}\text{I}$, ${}^{133}_{55}\text{Cs}$, ${}^{209}_{83}\text{Bi}$, and ${}^{232}_{90}\text{Th}$.

Further up the Chart of the Nuclides are found the last of the natural isotopes, namely, isotopes of uranium. Three of the isotopes of uranium are found naturally on earth, namely, ${}^{234}_{92}\text{U}$, ${}^{235}_{92}\text{U}$, and ${}^{238}_{92}\text{U}$, at abundances of 0.0055%, 0.720%, and

99.2745%, respectively. The isotope ${}^{238}_{92}\text{U}$, which is the most abundant, has a half-life of 4.5×10^9 years. It has not undergone even a half-life of decay since the formation of the earth. However, the isotopes ${}^{234}_{92}\text{U}$ and ${}^{235}_{92}\text{U}$ with half-lives of 2.4×10^5 years and 7.1×10^8 years, respectively, have undergone considerable decay since the formation of the earth. All nuclides of atomic number greater than that of uranium do not occur naturally and have been produced artificially by man as described in Section II.

Isobars: Isobars are nuclides that possess the same mass number (A), but different atomic number (Z). For example, ${}^{56}_{28}\text{Ni}$, ${}^{56}_{27}\text{Co}$, ${}^{56}_{26}\text{Fe}$, ${}^{56}_{25}\text{Mn}$, and ${}^{56}_{24}\text{Cr}$ are isobars. In mass spectrometry where nuclides are separated and analyzed according to their mass, isobars can cause interference, and special techniques may be required to discriminate between nuclides of the same mass number (Kusnir et al., 2004, Litherland et al., 2007, Plaß et al., 2008). In beta decay, discussed further on in this chapter, the parent and daughter nuclides are always isobars.

Isomers: Nuclear isomers are different energy states of the same nucleus, having different half-lives and even different modes of decay. A well-known example is that of ${}^{99}_{42}\text{Tc}$, which may have two isomeric states. The isomers of ${}^{99}_{42}\text{Tc}$ are the following: ${}^{99}_{42}\text{Tc}$, which decays by negatron emission to ${}^{99}_{41}\text{Ru}$ with a half-life of 2.14×10^5 years, and ${}^{99m}_{42}\text{Tc}$, which decays by gamma emission to ${}^{99}_{42}\text{Tc}$ with a half-life of 6.00 hours. Isomeric states of nuclides other than the ground state are represented with a superscript 'm' following the mass number. The isomer ${}^{99m}_{42}\text{Tc}$ is commonly used in the field of nuclear medicine as a diagnostic imaging source injected into the human body (L'Annunziata, 2007). When more than two excited isomeric states of a nuclide exist, the nuclear isomers are labeled as m_1 , m_2 , etc. in order of increasing excitation energy. For example, the isomers of ${}^{152}_{63}\text{Eu}$ are identified as follows: ${}^{152}_{63}\text{Eu}$ of 13.2 year half-life, ${}^{152m1}_{63}\text{Eu}$ of 9.3 hour half-life, and ${}^{152m2}_{63}\text{Eu}$ of 1.6 hour half-life. There are over 950 isomeric states known to exist among the nuclides. They are not considered as individual nuclides, but rather as isomers of individual nuclides.

Isotones: Nuclides that have the same number of neutrons, but different mass numbers are isotones. For example, ${}^{33}_{15}\text{P}$, ${}^{34}_{16}\text{S}$, ${}^{35}_{17}\text{Cl}$, ${}^{36}_{18}\text{Ar}$, and ${}^{37}_{19}\text{K}$ are isotones; their nuclei all contain 18 neutrons. Isotones may be found in the Chart of the Nuclides, which plots the nuclides according to their Z versus N , as the column of nuclides having the same number N .

C. Mass and Energy

The rest masses of the proton and neutron are of the order of 10^{-27} kg (see Table 1.1), and consequently the masses of the atomic nuclei are also very small. Due to the very small masses, most calculations involving atomic nuclei, such as nuclear decay energy, binding energy, and energies of nuclear reactions, make use of a more convenient scale of unit, namely, the atomic mass unit (u).

The atomic mass unit is defined in terms of the stable carbon nuclide ${}^{12}_6\text{C}$, which is assigned an atomic mass of exactly 12.000000 u. Thus, the atomic mass unit is by definition exactly $1/12$ the rest mass of ${}^{12}_6\text{C}$ or

$$1 \text{ u} = 1.66053873 \times 10^{-27} \text{ kg.} \quad (1.6)$$

TABLE 1.1 Properties of Atomic Constituents

Property	Proton	Neutron	Electron
Rest mass	1.67262×10^{-27} kg	1.67492×10^{-27} kg	9.10938×10^{-31} kg
	1.50327×10^{-10} J	1.50534×10^{-10} J	8.18710×10^{-14} J
	938.271 MeV	939.565 MeV	0.510998 MeV
	1.007276466 u	1.008664915 u	0.0005485799 u
Charge	+e	zero	-e
	$+1.602 \times 10^{-19}$ C		-1.602×10^{-19} C
Spin	1/2	1/2	1/2
Magnetic moment	1.410×10^{-26} J T ⁻¹	-0.966×10^{-26} J T ⁻¹	928.476×10^{-26} J T ⁻¹
Stability	stable	10.2 min, half-life	stable

The mass of all of the nuclides in atomic mass units is available in reference tables, such as those listed in the Handbook of Chemistry and Physics (Lide, 2010) and the following NIST website: <http://physics.nist.gov/constants>.

The International System of units (SI) for energy is the joule (J); however, the electron volt (eV) remains a very popular unit for expressing energy in nuclear decay, nuclear reactions, nuclear binding, etc. The electron volt (eV) is, by definition, the amount of kinetic energy gained by an electron when accelerated through a potential difference of 1 volt. The electron volt is equivalent to the following units:

$$1 \text{ eV} = 1.602176462 \times 10^{-19} \text{ J} = 1.602176462 \times 10^{-12} \text{ erg} \quad (1.7)$$

The erg is a unit of energy in the centimeter–gram–second (CGS) system of units, and less commonly used in nuclear energy calculations. From the above relation, the erg is equivalent to 10^{-7} J or 6.2415097×10^{11} eV.

Calculations concerning nuclear decay energy, nuclear reaction energy, or nuclear binding energy, etc. generally require the conversion of mass to energy. A common factor that is used in such calculations is one that can convert atomic mass units (u) to the units of the electron volt (eV). The conversion factor is found using Einstein's equation to convert the mass of 1 u to energy or

$$E = m_0 c^2 \quad (1.8)$$

where E is energy in joules, m_0 is the rest mass in kilograms, and c is the velocity of light in a vacuum or 2.99792458×10^8 m/s. If by definition, the mass of 1 u = $1.66053873 \times 10^{-27}$ kg, the energy equivalent to 1 u is calculated as

$$\begin{aligned} E &= (1.66053873 \times 10^{-27} \text{ kg/u})(2.99792458 \times 10^8 \text{ m/s})^2 \\ &= 14.92417783 \times 10^{-11} \text{ J/u} \end{aligned} \quad (1.9)$$

The energy in units of joules is then converted to units of electron volts, as $1 \text{ eV} = 1.602176462 \times 10^{-19} \text{ J}$ or

$$\begin{aligned} E &= \frac{14.92417783 \times 10^{-11} \text{ J/u}}{1.602176462 \times 10^{-19} \text{ J/eV}} \\ &= 9.31494013 \times 10^8 \text{ eV/u} \\ &= 931.494013 \text{ MeV/u} \end{aligned} \quad (1.10)$$

Thus, $1 \text{ u} = 931.494013 \text{ MeV}$ or $931.494013 \text{ MeV}/c^2$. The latter units of MeV/c^2 are used conveniently when converting atomic mass units to MeV energy in Einstein's equation according to the following:

$$E = mc^2 = [(\text{atomic mass units})(931.494013 \text{ MeV}/c^2)]c^2 \quad (1.11)$$

Eqn (1.11) is used to convert conveniently atomic mass units (u) to units of energy in MeV. Examples are given throughout this chapter in calculations of nuclear decay energy, nuclear reaction energy, and nuclear binding energy.

Energy of nuclear reactions is calculated by the mass difference of the nuclear reactants and nuclear products, and this energy is denoted as the Q value of the reaction: or

$$Q = E_{\text{Reactants}} - E_{\text{Products}} = m_R - m_P \quad (1.12)$$

where m_R and m_P are the rest masses of the reactants and products of the nuclear reaction. As nuclear reactions involve the reactions between nuclear particles and nuclei of atoms, we would need to know the masses of the nuclei or nuclear particles involved in the reaction to calculate a reaction Q value. In lieu of using rest masses of the atomic nuclei, it is common to use the atomic masses (u) which are available in reference tables, such as that of the Handbook of Chemistry and Physics. However, it is important to keep in mind that atomic masses include the masses of the atomic electrons. To eliminate error that might occur from the added masses of the atomic electrons, it is important to assure that the number of electrons added to either side of the reaction are equal, whereby the difference of the electron masses of the reactants and products would be zero according to Eqn (1.12). Let us take an example and calculate the Q value of the first man-made nuclear reaction whereby

Earnest Rutherford discovered the proton described earlier in Part II. The reaction is as follows:



In this reaction the alpha particle interacts with an atom of ${}^{14}\text{N}$ to form an atom of ${}^{17}\text{O}$ with the ejection of a proton from the nucleus. The atomic masses may be used to calculate the Q value of the reaction as follows:

$$\begin{aligned} Q &= (M_{{}^4\text{He}} + M_{{}^{14}\text{N}}) - (M_{{}^{17}\text{O}} + M_{{}^1\text{H}}) \\ &= (4.00260325 \text{ u} + 14.00307401 \text{ u}) \\ &\quad - (16.9991315 \text{ u} + 1.007825032 \text{ u}) \\ &= -0.001279272 \text{ u} \end{aligned} \quad (1.14)$$

By using atomic masses, we have added nine electron masses to each side of the reaction, and their difference is zero from Eqn (1.14). Converting atomic mass units to energy according to Eqn (1.11) gives the Q value in units of MeV energy or

$$\begin{aligned} Q \text{ value} &= E = mc^2 \\ &= [(-0.001279272)(931.494013 \text{ MeV}/c^2)]c^2 \end{aligned} \quad (1.15)$$

$$Q \text{ value} = -1.192 \text{ MeV}$$

Atomic masses are conveniently used in such calculations, in lieu of nuclear masses, provided an equal number of electrons are added to either side of Eqn (1.14). The negative energy value above demonstrates that the reaction is endoergic or endothermic, that is, the reaction requires a net energy input of 1.192 MeV. When the Q value is positive, the nuclear reaction is exoergic or exothermic, resulting in a net release of energy. There are small differences in the binding energies of the electrons when using atomic masses; however, the differences in the binding energies are negligible and ignored.

IV. PROPERTIES OF THE NUCLEUS

A. Nuclear Radius and Density

Ernest Rutherford (1911, 1919, 1920a,b) was the first to discover the atomic nucleus and to measure the size of the nucleus of an atom. A detailed accounting of this work is given in a previous book (L'Annunziata, 2007). In brief, Rutherford bombarded very thin gold foil (4×10^{-5} cm thick) with alpha particles. Most of the alpha particles traversed the gold foil almost as if the foil was not in the path of the alpha particles; however, one alpha particle for every 20,000 particles would bounce back from the foil by more than 90° from the direction of travel. Rutherford concluded that within much empty space of the atom, there exists a massive central nucleus capable of knocking back the alpha particle to the direction from which it came. Rutherford expressed his reaction to the observed alpha-particle backscattering with the following statement, related by N. Feather (1940) in a biographical essay a few years following his death:

It was quite the most incredible event that ever happened to me in my life. It was almost as incredible as if you fired a 15-inch shell at a piece of tissue paper and it came back and hit you. On consideration, I

realized that the scattering backwards must be the result of a single collision, and when I made calculations I saw that it was impossible to get anything of that order of magnitude unless you took a system in which the greater part of the mass of the atom was concentrated in a minute nucleus.

Rutherford went even further to make use of this interaction to determine the nuclear radius of aluminum. By selecting a metal foil of low Z (aluminum, $Z = 13$) and thus low Coulomb barrier to alpha penetration, and applying alpha particles of high energy (7.7 MeV) whereby defined alpha-particle scattering at acute angle due to Coulombic repulsion would begin to fail, Rutherford (1919, 1920a,b) was able to demonstrate that the distance of closest approach of these alpha particles to the atom center according to Coulomb's law was equivalent to the nuclear radius of aluminum, $\sim 5 \times 10^{-15}$ m or 5 fm (*i.e.*, 5 femtometer or 5 fermi).

Since Rutherford's pioneering alpha-particle scattering experiment numerous nuclear scattering experiments have been carried out to measure the size of atomic nuclei including electron scattering (Jansen et al, 1971 and Sick, 1982), electron-proton scattering (Klarsfeld et al, 1986), electron-deuteron scattering (Sick and Trautmann, 1998), and high-energy beam interactions (Tanihata et al, 1985 and Suzuki et al, 1999). The radius of an atomic nucleus obeys the general empirical formula:

$$R = r_0 A^{1/3} \quad (1.16)$$

where r_0 is a constant, referred to as the radius parameter, and A is the mass number of the nucleus (Tolhoek and Brussaard, 1954, Elton, 1958, Angeli and Csatlós, 1977). A detailed derivation of Eqn (1.16) is provided by Elton (1958). The value of the radius parameter, r_0 was confirmed by Royer (2008) to be 1.22 fm. Obviously, the radius of the nucleus will increase with mass number. For a small nucleus, such as the nucleus of ${}^4_2\text{He}$ (equivalent to an alpha particle), the radius is calculated to be 1.9×10^{-15} m or 1.9 fm. For larger nuclei, such as ${}^{27}_{13}\text{Al}$, ${}^{197}_{79}\text{Au}$, and ${}^{235}_{92}\text{U}$, the nuclear radii is calculated to be 3.6, 6.9 and 7.4 fm, respectively.

Treating the nucleus as a sphere permits the calculation of the nuclear volume; and from the mass of the nucleus, we can calculate the nuclear density ρ_N as

$$\rho_N = \text{mass/volume} = m_n A / \left(\frac{4}{3} \pi R^3 \right) \quad (1.17)$$

where m_n is the mass of a nucleon (proton or neutron), A is the mass number, and R is the nuclear radius. The mass of either nucleon (the proton or neutron) may be used, as the two nucleons are very similar in mass and may be considered equal in mass, when only three significant figures are used, namely, 1.67×10^{-27} kg. Substituting $r_0 A^{1/3}$ for R in Eqn (1.17) gives

$$\rho_N = m_n / \left(\frac{4}{3} \pi r_0^3 \right) \quad (1.18)$$

The value of the nuclear density calculated according to Eqns (1.17) or (1.18) gives the value of $\rho_N = 2.3 \times 10^{17}$ kg/m³. Treating the nucleus as a sphere facilitates the density calculation and provides a good estimate as provided in current

textbooks; however, most nuclei are not spherical and some may exhibit oscillations such as depicted by the liquid-drop model of the nuclei. Some nuclei described by Gould et al (2004) exhibit football-shaped quadrupole deformations and even pear-shaped octupole deformations (Krappe and Wahsweiler, 1967, Vogel, 1967, 1968, Aponik et al, 1970 and Cline, 1993). Gould et al (2004) describe the interior of a large nucleus as uniform ($0.17 \text{ nucleons/fm}^3$); but that the density falls off smoothly at the surface of the nucleus, dropping from 90% to 10% of the interior density over a distance of $\sim 2.5 \text{ fm}$.

The density of the nucleus is extraordinarily high when compared with elements and materials consisting of atoms. For example, the atomic nucleus is 2.0×10^{13} times the density of lead ($11.3 \times 10^3 \text{ kg/m}^3$) or 1.2×10^{13} times the density of depleted uranium ($19.1 \times 10^3 \text{ kg/m}^3$). While the density of the nucleus is amazingly high, the nucleus consists of closely packed nucleons and, thus, the nucleons themselves and even subnuclear particles, particularly leptons, would even have higher densities.

Subnuclear particles are classified into two groups, the leptons and hadrons. The word leptons comes from the Greek "lepto" meaning "refined" or "thin". Leptons are particles with no apparent substructure and thus considered to be truly elementary or point particles, such as the electron, muon, and their respective neutrinos and quarks. **Leptons**, with the exception of quarks, participate in electromagnetic and weak interactions. **Hadrons**, on the other hand, are more complex in subnuclear structure and they participate in the strong nuclear force. Hadrons are classified into two groups, namely, the **mesons** containing two quarks (e.g., pion and kaon) and the **baryons** (from the Greek "barys" meaning "heavy"), which are of higher mass and contain three quarks (e.g., proton and neutron). The role of mesons as particles, that mediate the strong nuclear force between the nucleons, is discussed in the next section.

The high density of the nucleus and its constant value from nuclide to nuclide underscores the importance of a strong short-range nuclear force that exists between the nucleons (i.e., protons and neutrons) keeping them closely packed regardless of the repulsive forces of the positively charged protons or the Z/N ratios of the nucleus and among the thousands of nuclides that exist.

B. Nuclear Forces

In the 1930s, question arose concerning the force that was capable of holding the protons and neutrons together in the nucleus. It was unusual to find that the like positive charge of the protons, together with neutrally charged neutrons, did not repel each other, but rather were held tightly together into a very dense nucleus. It was expected that the force holding the

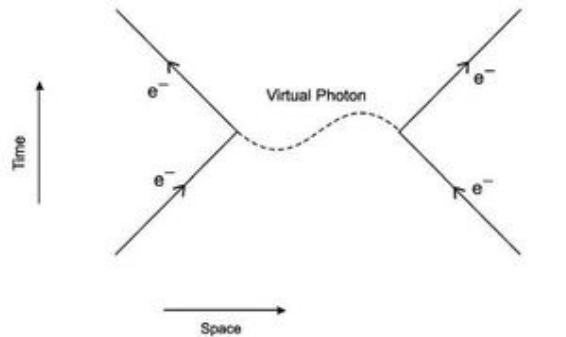


FIGURE 1.6 Feynman diagram illustrating the photon as a particle that mediates the electromagnetic force between two electrons. The electromagnetic interaction results in the absorption of the photon particle by an electron providing it with momentum to be repelled. The electron emitting the photon undergoes recoil. The photon is illustrated as a dashed wave. It is referred to as virtual photon, because it is emitted and absorbed without being detected.

nucleons together would be a strong force. Nobel Laureate Hideki Yukawa (1935, 1949) first postulated the strong force between nucleons. Before doing this, Yukawa understood that charged particles would interact through the exchange of photon particles. He noted that such a force, known as the electromagnetic force, would become manifest when the particles collide. For example, electrons would interact via the exchange of virtual photons as illustrated by the Feynman diagram² of Fig. 1.6. Yukawa explained the strong force between the nucleons by proposing a new particle, which would mediate the strong force between the nucleons. He predicted that the new particle would have a mass inversely proportional to the force between the nucleons and that the mass of the particle would be intermediate of the proton and electron masses ($\sim 200 \times$ the electron mass). The new particle was named the meson, which was taken from the Greek "meso" meaning "middle". The prediction of Yukawa was verified by the discovery of the π meson or pion by Ochiaiini and Powell (1947, 1948). The strong force keeping the nucleons together is mediated by the exchange of π mesons between the nucleons. The pion is the carrier of Yukawa's nuclear force. It is found in three charge states, π^+ , π^- , and π^0 . They have the mass predicted by Yukawa and are unstable, e.g., the π^+ has a mass of $139.5 \text{ MeV}/c^2$ and a mean lifetime of $2.6 \times 10^{-8} \text{ s}$ (Sundaeson, 2001). The mediation of the strong force between a neutron and a proton in the nucleus is illustrated by the Feynman diagram in Fig. 1.7, which illustrates a neutron converting into a proton and a proton converting into a neutron and, in the process, a π^+ is exchanged between the two nucleons.

Pion exchange between nucleons, as the particle mediating the strong force, is explained on the basis of the subnuclear

² A convenient way to illustrate the interactions and exchange forces between the elementary particles is with Feynman diagrams, which were devised by Nobel laureate Richard Feynman (1918–1988). When he was a young scientist, he introduced the diagrams as a means of depicting, through sketches, the interactions among nuclear particles as shorthand for the equations that are used to put the interactions into more complex mathematical terms. Feynman diagrams show particle interactions in coordinates of space and time. The axis are not quantitative, that is, the length of the lines or spacing between particles are not measures of relative time or distance. Particles are illustrated by solid lines with arrows giving the particle direction. Virtual particles are illustrated as dashed waves for particles with zero rest mass (i.e., photons or gluons) and dashed straight lines for particles with a rest mass.

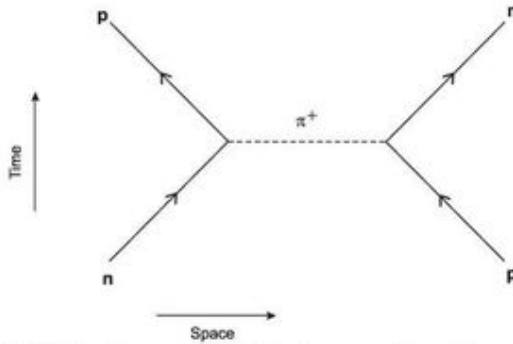


FIGURE 1.7 A Feynman diagram illustrating the mediation of the strong nuclear force between nucleons in the nucleus. A neutron (lower left) is transformed into a proton (upper left) and a proton (lower right) is transformed into a neutron (upper right) via the intermediary pi meson.

structure of the proton, neutron, and meson. The 1969 Nobel Laureate in Physics, Murray Gel-Mann (1964) and George Zweig (1964) independently proposed the idea of a substructure to mesons and baryons, now universally referred to as quarks, which would possess quantum numbers and fractional charge. The mesons (*e.g.*, pion and kaon), which are of intermediate mass between that of the electron and proton, contain two quarks; whereas, the baryons (*e.g.*, proton, neutron, lambda, etc.), which are of higher mass, contain three quarks. The quark compositions of pi mesons (pions) and of the nucleons (proton and neutron), and the properties of the quarks are provided in Table 1.2. In the table, it is seen that the π^+ contains an up quark (u) with charge of $+2/3e$ and an antidown (\bar{d}) quark with charge of $+1/3e$ yielding a total charge on the π^+ of $+1$. The π^- consists of a down quark (d) of charge $-1/3e$ and antiup quark (\bar{u}) of charge $-2/3e$ yielding an overall particle charge of -1 . The π^0 is a mixture or superposition of $u\bar{u}$, $d\bar{d}$ quark pairs referred to as mixing of quark pairs with overall neutral charge.

The proton, neutron, and all of the baryons, which are particles of higher mass than the mesons, contain three quarks. The quark content of the proton, as listed in Table 1.2, is two up quarks and one down quark (uud) with respective charges of $+2/3e$, $+2/3e$, and $-1/3e$ or a total charge of $+1$; whereas the neutron contains two down quarks and one up quark (ddu) with a total charge of zero.

Quarks possess another property called color or color charge. The property of color or color charge has no relation to visible radiation as we see color; but rather, color charge is a quantum number and source of force that quarks and antiquarks possess. Color charge was proposed by Greenberg (1964) as a quantum number, and as a source of force between quarks by Han and Nambu (1965). To satisfy the Pauli exclusion principle, that states no two particles can exist in the same energy or quantum state, the concept of color charge was introduced as a quantum state and force between quarks. Three color-charge quantum states carried by quarks are red, blue, and green; and those carried by antiquarks are antired, antiblue, and antigreen. In the baryons, all of which possess three quarks such as the proton (uud) and the neutron (ddu), there would exist three quarks of color charge, red, blue, and green. Quarks of different color charge possess an attractive force between each other, whereas quarks of like color would repel each other. Mesons, which possess only two quarks, a quark and antiquark (See Table 1.2), would display red and antired, blue and antiblue, or green and antigreen quantum states. There is an attractive force between quarks of a given color and its anticolor quantum state in mesons.

There are yet other particles in addition to quarks, called gluons, which exist in mesons and in baryons. A gluon is a field particle like the electromagnetic photon, which has zero rest mass. Gluons differ from photons, because they interact directly with quarks and with each other; and they carry, similar to quarks, a color charge quantum state. Quarks emit and absorb gluons. When a quark either emits or absorbs a gluon, the

TABLE 1.2 Quark Compositions and Properties of Quark Components of Pi Mesons and Nucleons

Particle	Quark composition	Properties of quarks ^a			
		Name ^b	Symbol	Charge	Mass
Mesons					
π^+	$u\bar{d}$	up	u	$+2/3e$	$\approx 300\text{MeV}/c^2$
π^-	$d\bar{u}$	down	d	$-1/3e$	$m_d \approx m_u$
π^0	$u\bar{u}, d\bar{d}$	antiup	\bar{u}	$-2/3e$	$m_{\bar{u}} = m_u$
Nucleons/Baryons					
p	uud	antidown	\bar{d}	$+1/3e$	$m_{\bar{d}} = m_d$
n	udd				

^aData from Martin and Shaw (2004).

^bOther quarks exist, such as the strange (s), charmed (c), bottom (b), and top (t) quarks, which are component quarks of other mesons and baryons.

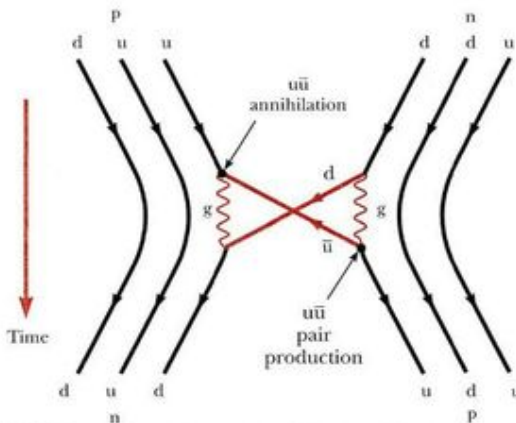


FIGURE 1.8 A Feynman diagram illustrating the mediation by a π^+ meson of the strong nuclear force between a proton and neutron in the nucleus with the interaction of quarks and gluons as follows: down quark (d) of a neutron (upper right, ddu) emits a gluon (center right wave, g) that creates an up-antiup ($u\bar{u}$) pair of quarks. The created up quark (u) forms a proton (lower right, udu); whereas the antiup quark (\bar{u}) annihilates in contact with an up quark (u) of the proton (p) from the upper left (duu) of the diagram with the creation of a gluon (center left wave, g) and the down quark (d) of the neutron (from the upper right) is captured to form a neutron (lower left). (Diagram is from SERWAY/MOSES/MOYER, *Modern Physics*, 3E. © 2005 Brooks/Cole, a part of Cengage Learning, Inc. Reproduced by permission. www.cengage.com/permissions.)

quantum state of the quark changes and, thus, the color charge of the quark also changes. The process of emission and absorption of gluons by quarks, which is discussed subsequently, is part of the mechanism by which the strong nuclear forces keep the protons and neutrons closely packed in the atomic nucleus. The force that exists between quarks of different quantum color states is called color force; and the theory that these forces play in the strong interactions is called quantum chromodynamics (QCD).

In summary, mesons mediate the strong forces between the protons and neutrons in the nucleus, and it is the energy exchange or quantum state changes between quarks and gluons of the mesons and nucleons that enable the strong nuclear forces to hold the protons and neutrons together in the nucleus. An example of a process, whereby the strong nuclear forces between the nucleons come into play, is illustrated by the Feynman diagram of Fig. 1.8. The figure illustrates the involvement of quarks and gluons in the transformation of a proton into a neutron and a neutron into a proton via the mediation of a pi meson (π^+).

The mass of the nucleons as well as that of the mesons arise from the interaction of their quarks with the gluon field particles. Because gluons have a zero rest mass, the creation and absorption of gluons is a constant process in the nucleons attributing mass to the nucleons. As described by Gould et al (2004), the mass of the nucleons comes from the interaction of the quarks with the nucleon field; and the nucleon is described as consisting of a core of three quarks confined within a sphere of radius $\sim 0.5\text{--}1.0$ fm. Surrounding the core is a cloud of

pions (pi mesons), which are themselves composed of quark-antiquark pairs.

The range of the strong nuclear force is very close to that of the radius of the nucleon core. We can use Heisenberg's uncertainty principle to calculate the range of interaction of the strong nuclear force mediated by the pi meson or pion. Nobel Laureate Werner Heisenberg published the uncertainty principle (Heisenberg, 1927), which is a basic concept of quantum physics. In terms of energy and time variables, Heisenberg's uncertainty principle can be expressed as

$$\Delta E \Delta t \geq \frac{\hbar}{4\pi} \geq \frac{\hbar}{2} \quad (1.19)$$

which states that the precision with which we measure the energy of an atomic particle (ΔE) is limited by the time available (Δt) to measure the particle energy, where \hbar is Planck's constant ($\hbar = 6.626 \times 10^{-34}$ J s) and h is a reduced form of Planck's constant ($\hbar = h/2\pi = 1.055 \times 10^{-34}$ J s = 6.582×10^{-22} MeV s). We can accurately calculate the energy of the pion from its mass; and from the Heisenberg uncertainty principle expressed by Eqn (1.19), we can state that the pion would violate the conservation of energy if it lasted for a period of time exceeding

$$\Delta t \approx \frac{\hbar}{2\Delta E} \quad (1.20)$$

where ΔE is the energy needed to create a pion of mass m_π defined by Einstein's equation of mass and energy as

$$\Delta E = m_\pi c^2 \quad (1.21)$$

and Δt is the time it would take for the pi meson to travel from one nucleon to the other (e.g., from a proton to a neutron or vice versa). The mass m_π of the π^+ or $\pi^- = 139.5$ MeV/ c^2 . Since the pi meson cannot travel faster than the speed of light c , its distance (d) of travel is defined as

$$d = c\Delta t \quad (1.22)$$

Thus, the maximum distance, that the pi meson could travel, is calculated as

$$\begin{aligned} d &= c\Delta t = c \left(\frac{\hbar}{2m_\pi c^2} \right) \\ &= 2.99 \times 10^8 \text{ m/s} \left(\frac{6.582 \times 10^{-22} \text{ MeV s}}{2(139.5 \text{ MeV}/c^2)c^2} \right) \\ &= 7.0 \times 10^{-16} \text{ m} \approx 1 \times 10^{-15} \text{ m} \approx 1 \text{ fm} \end{aligned} \quad (1.23)$$

The range of the strong nuclear force mediated by the pion is thus ~ 1 fm similar to that of the radius of the proton or neutron.

For a more in-depth reading on subnuclear structure and its role in the strong nuclear force, see books by Sundaresan (2001), Heyde (2004), Martin and Shaw (2004), and Serway et al (2005).

C. Binding Energy

The difference in the total energy of the nucleus with its bound nucleons is always less than the total energy of the separate

protons and neutrons, and this difference in energy is the binding energy (E_b) of the nucleus. The binding energy is equivalent to the energy required to pull a bound system apart, such as a bound nucleus, leaving its component protons and neutrons free of attractive forces. The binding energy is described by the equation

$$E_b = \sum_{i=1}^n m_i c^2 - M c^2 \quad (1.24)$$

where m_i are the free component particles (protons and neutrons) of the nucleus numbered $i = 1$ to n , and M is the mass of the bound nucleus. We may use atomic mass units (u) to calculate the nuclear binding energies according to Eqn (1.24) for any nuclide, ${}^A_Z X$, of Z number of protons, A number of protons + neutrons, and $N = A - Z$ number of neutrons as follows:

$$E_b = [(Zm_{1H} + Nm_n - M_{ZX})931.494\text{MeV}/c^2]c^2 \quad (1.25)$$

where m_{1H} is the atomic mass of hydrogen, m_n is the neutron mass, and M_{ZX} is the atomic mass of the nuclide of atomic number Z and mass number A , i.e., ${}^A_Z X$, and by definition $1\text{u} = 931.494\text{MeV}/c^2$. Atomic mass units are used in Eqn (1.25), because the number of electrons of the Z hydrogen atoms are the same as the electrons included in the atomic mass of the nuclide ${}^A_Z X$. The differences in electron-binding energies of the hydrogen atoms and that of the nuclide are negligible and ignored. Let us take an example and use atomic mass units to calculate the binding energy for the helium

nucleus, i.e., ${}^4_2\text{He}$, which is equivalent to an alpha particle, as follows:

$$\begin{aligned} E_b &= [(2m_{1H} + 2m_n - M_{{}^4_2\text{He}})931.494\text{MeV}/c^2]c^2 \\ &= [(2)(1.007825\text{u}) + (2)(1.008665\text{u}) \\ &\quad - 4.002603\text{u})931.494\text{MeV}/c^2]c^2 \\ &= 28.296\text{MeV} \end{aligned} \quad (1.26)$$

Because nuclei vary in their number of nucleons or mass number (A), it is common to express the nuclear binding energy in terms of the number of nucleons in the nucleus, that is, the binding energy per nucleon or E_b/A . In the case of the nuclide, ${}^4_2\text{He}$, the binding energy per nucleon is

$$E_b/A = 28.296\text{MeV}/4 = 7.07\text{MeV} \quad (1.27)$$

The values of the binding energies per nucleon for all of the nuclides provides a measure of how tightly bound the nucleons are within a particular nucleus. Fig. 1.9 illustrates graphically the difference in the values of the binding energy per nucleon (E_b/A) as a function of the mass number (A) of the nucleus for nuclides over the entire range of mass numbers.

From Fig. 1.9 it is seen that the highest nuclear stability is found in the region of mass number $A = 50-70$; and the most stable nuclei, that is, those nuclei that are most tightly bound, belong to the "iron group" including ${}^{62}\text{Ni}$, ${}^{58}\text{Fe}$, and ${}^{56}\text{Fe}$ with binding energies per nucleon at a maximum of approximately 8.8 MeV. On either side of this maximum, illustrated in Fig. 1.9,

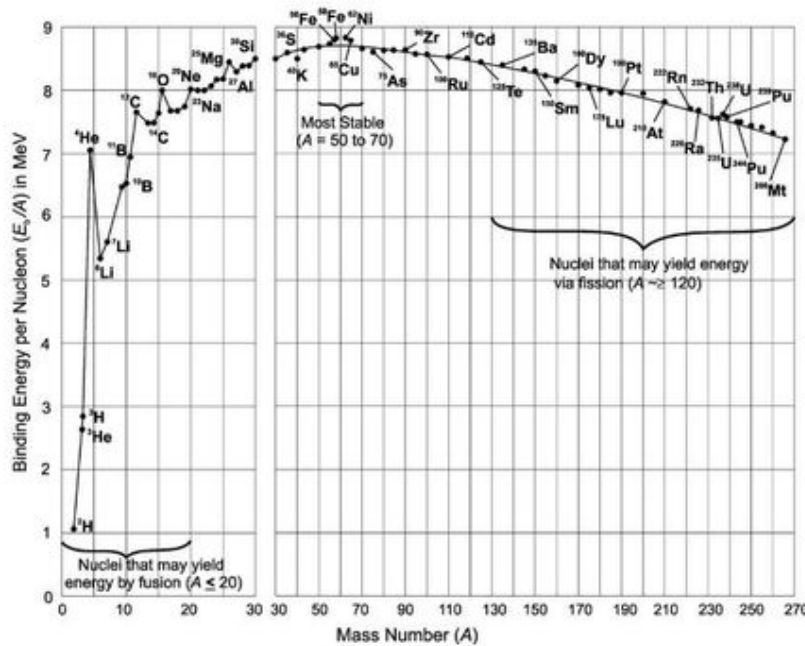
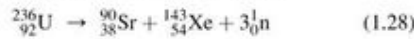


FIGURE 1.9 Binding energy per nucleon as a function of mass number. The scale between mass number 0 and 30 is broader than that illustrated for mass numbers 30–270. Several nuclides are identified along the curve. The most stable nuclei are ${}^{62}\text{Ni}$, ${}^{58}\text{Fe}$, and ${}^{56}\text{Fe}$ with E_b/A values of 8.794, 8.792 and 8.790 MeV, respectively. Notice the small peak of highest stability at the top of the curve.

are: (i) the smaller nuclei in the range of $A = 2-20$ with lower binding energies per nucleon, which could fuse to yield larger and more stable nuclei with the release of energy or (ii) the very large nuclei in the range of about $A \geq 120$, which could break apart into approximately equal mass number by fission to form smaller and more stable nuclei with the release of energy. Consequently, the size of the nucleus and its binding energy per nucleon will govern whether nuclear fusion or fission would be feasible; and the energy released in both cases can be estimated directly from Fig. 1.9 or by calculation. Let us take examples of both cases, fission and fusion.

1. Nuclear Fission

The nuclide ^{236}U , which results from the capture of a slow neutron by ^{235}U , is unstable. It takes on the characteristic of an unstable oscillating droplet. The nuclear droplet, which oscillates with the opposing forces of two positively charged nuclides, splits into two fragments with the liberation of an average energy of 193.6 MeV (Koch, 1995). The mass numbers of the fission fragments vary between 70 and 160; and the following is just one example, illustrating the fission of ^{236}U into the nuclide fragments ^{90}Sr and ^{143}Xe with the emission of 3 neutrons:



The binding energy (E_b) of the ^{236}U nucleus, *i.e.*, the difference in mass of the ^{236}U nucleus and the combined mass of its free component nucleons, is calculated as follows:

$$E_b = (M_{92 \text{ protons}} + M_{144 \text{ neutrons}}) - M_{^{236}\text{U}} \quad (1.29)$$

where $M_{92 \text{ protons}}$ is the mass of 92 protons, $M_{144 \text{ neutrons}}$ is the mass of 144 neutrons, and $M_{^{236}\text{U}}$ is the mass of the bound nucleus of ^{236}U . Using atomic mass units for the masses of the ^{236}U nucleus and its constituent nucleons, we calculate the binding energy (E_b) in atomic mass units (u) as

$$\begin{aligned} E_b &= [92(1.007825 \text{ u}) + 144(1.008665 \text{ u})] - 236.045561 \text{ u} \\ &= 237.96766 \text{ u} - 236.045561 \text{ u} = 1.922099 \text{ u} \end{aligned} \quad (1.30)$$

Although the masses of the electrons are included in the atomic masses, the electron masses can be ignored since these are the same for the ^{236}U and the 92 hydrogen atoms. Using Einstein's equation for the equivalence of mass and energy, we can convert the binding energy to MeV or

$$\begin{aligned} E &= mc^2 = [(1.922099 \text{ u})(931.494 \text{ MeV}/c^2)]c^2 \\ &= 1790.42 \text{ MeV} \end{aligned} \quad (1.31)$$

Dividing the binding energy by the number of nucleons in the nucleus (mass number, $A = 236$) will provide the binding energy per nucleon for ^{236}U or

$$(E_b/A)_{^{236}\text{U}} = 1790.42 \text{ MeV}/236 = 7.58 \text{ MeV/nucleon} \quad (1.32)$$

Similar calculations for the binding energies of the fission fragments ^{90}Sr and ^{143}Xe yield $E_b/A = 8.69 \text{ MeV/nucleon}$ for ^{90}Sr and 8.19 MeV/nucleon for ^{143}Xe . Estimated values for the

binding energies per nucleon (E_b/A) as a function of mass number (A) can be obtained from Fig. 1.9. Because the binding energies per nucleon for the two fission products are slightly different, we could average the two values simply to get an estimated figure for the amount of energy released. We can now estimate the energy released from ^{236}U fission or the Q value, using as an example the fission reaction of Eqn (1.28) as follows:

$$\begin{aligned} &^{236}_{92}\text{U} \rightarrow ^{90}_{38}\text{Sr} + ^{143}_{54}\text{Xe} + 3^1_0\text{n} \\ Q &= [(E_b/A)_{\text{fission products}} - (E_b/A)_{^{236}\text{U}}] \\ &\quad \times 236 \text{ nucleons} \\ Q &= \left[\left(\frac{(E_b/A)_{^{90}\text{Sr}} + (E_b/A)_{^{143}\text{Xe}}}{2} \right) - (E_b/A)_{^{236}\text{U}} \right] \\ &\quad \times 236 \text{ nucleons} \quad (1.33) \\ Q &= \left[\left(\frac{8.69 \text{ MeV/nucleon} + 8.19 \text{ MeV/nucleon}}{2} \right) \right. \\ &\quad \left. - 7.58 \text{ MeV/nucleon} \right] \times 236 \text{ nucleons} \\ Q &= 202 \text{ MeV} \end{aligned}$$

Thus, approximately 200 MeV is the amount of energy released from ^{236}U fission, *i.e.*, neutron-induced fission of ^{235}U . The magnitude of the energy released from neutron-induced fission of ^{235}U would be an average figure, because the actual amount of energy released would depend on the fission reaction, and there are many possible ways that the ^{236}U could break into two nuclides.

There are about 100 radionuclides of high mass number $A \geq 230$, which decay by spontaneous fission (SF), which involves the spontaneous noninduced splitting of the nucleus into two nuclides or fission fragments. A rough estimate of the energy released by fission reactions can be estimated quickly from Fig. 1.9. For example, ^{252}Cf undergoes spontaneous fission in 3% of the decay events as an alternative to alpha decay. A rough estimate of the energy released in the spontaneous fission is found by reading from Fig. 1.9 the binding energy per nucleon for a nuclide of mass number $A \approx 250$, which would be about 7.5 MeV, and the binding energy per nucleon for fission fragments that would have a mass number (A) in the range of 80–150, which varies between 8.5 and 8.3 or an average of ~8.4 MeV. The following calculation, in accord with Eqn (1.33), would give the approximate energy released as

$$\begin{aligned} Q &\approx [(8.4 \text{ MeV/nucleon}) - (7.5 \text{ MeV/nucleon})] \\ &\quad \times 252 \text{ nucleons} \approx 230 \text{ MeV} \end{aligned} \quad (1.34)$$

Nuclear fission is discussed in more detail further on in this chapter.

2. Nuclear Fusion

Nuclides of very low mass number ($A < 20$) have nuclei (See Fig. 1.9) with relatively low binding energies, and if these nuclei could coalesce, a larger more tightly bound nucleus would form, and the overall process would release energy as described by Eqn (1.24). For example, if two nuclei of deuterium (^2_1H) were

to fuse into a nucleus of helium (${}^4_2\text{He}$), equivalent to an alpha particle, the energy released by the nuclear fusion could be estimated from Fig. 1.9. Taking the values of binding energy per nucleon (E_b/A) from Fig. 1.9 for ${}^2_1\text{H}$ to be ~ 1 MeV and that for ${}^4_2\text{He}$ to be ~ 7 MeV, the energy released would be estimated from the following as

$$Q = [(E_b/A)_{\text{He}} - (E_b/A)_{\text{H}}] \times 4 \text{ nucleons} \quad (1.35)$$

$$Q \approx [(\sim 7 \text{ MeV/nucleon}) - (\sim 1 \text{ MeV/nucleon})] \times 4 \text{ nucleons} \approx 24 \text{ MeV}$$

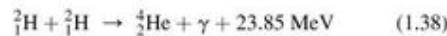
The energy released is more precisely determined by calculating the binding energy, E_b , for the ${}^4_2\text{He}$ nucleus and for the ${}^2_1\text{H}$ nucleus according to Eqn (1.25). The nuclear binding energy for ${}^4_2\text{He}$ was previously calculated (see Eqn (1.26)) to be 28.296 MeV, and the binding energy per nucleon would be $(E_b/A)_{\text{He}} = 28.296 \text{ MeV}/4 = 7.074 \text{ MeV}$. The nuclear binding energy for ${}^2_1\text{H}$ according to Eqn (1.25) is calculated as

$$\begin{aligned} E_b &= [(m_{\text{H}} + m_n - M_{\text{He}})931.494 \text{ MeV}/c^2]c^2 \\ &= [(1.007825032\text{u} + 1.00866492\text{u} - 2.014101778\text{u}) \\ &\quad \times 931.494 \text{ MeV}/c^2]c^2 \\ &= 2.225 \text{ MeV} \end{aligned} \quad (1.36)$$

The binding energy per nucleon for ${}^2_1\text{H}$ would be $(E_b/A)_{\text{H}} = 2.225 \text{ MeV}/2 = 1.112 \text{ MeV}$. The energy released in the fusion of two nuclei of deuterium to a nucleus of helium would be calculated according to Eqn (1.25) as

$$Q = [7.074 \text{ MeV} - 1.112 \text{ MeV}] \times 4 \text{ nucleons} = 23.85 \text{ MeV} \quad (1.37)$$

The deuterium fusion reaction is written as



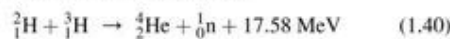
The energy released in the deuterium fusion may be calculated according to Eqns (1.12) and (1.15) as

$$Q = (m_R - m_P)931.494 \text{ MeV}/\text{u} \quad (1.39)$$

where m_R and m_P are the rest masses of the reactants and products, respectively, in atomic mass units (u). For the fusion of two deuterium nuclei, the energy released is calculated as

$$Q = [2(2.014101778\text{u}) - 4.00260325\text{u}]931.494 \text{ MeV}/\text{u} = 23.85 \text{ MeV}$$

The nuclear fusion reaction described by Eqn (1.38) is one that releases a relatively large amount of energy, but it has a low reaction cross section or low probability of occurrence, and the energy not easily captured, because most of the energy would be carried off by the gamma radiation. A more practical source of energy by nuclear fusion would be the fusion of deuterium and tritium nuclei according to the reaction



When comparing the energy released from neutron-induced fission of ${}^{235}\text{U}$ (~ 200 MeV, see Eqn (1.33)) and that produced by the fusion of deuterium and tritium nuclei (17.6 MeV, see

Eqn (1.40)), we can immediately see that there is more than a 10-fold greater magnitude of energy released by the neutron-induced fission reaction. However, if we evaluate the reactions in terms of fuel mass, we will find that the above deuterium–tritium fusion reaction is the most efficient for energy production. For example, let us now calculate and compare the energy yields per kilogram of fuel for both nuclear fission and nuclear fusion.

Neutron-induced ${}^{235}\text{U}$ Fission energy yield:

$$\begin{aligned} E \text{ yield}_{\text{D-T fusion}} &= \frac{\text{Reaction energy release}}{\text{Fuel mass}} \\ &= \frac{200 \text{ MeV}}{(M_{\text{D-T}} + M_{\text{neutron}})(1.660 \times 10^{-27} \text{ kg/u})} \\ &= \frac{200 \text{ MeV}}{(235.04392 \text{ u} + 1.00866 \text{ u})(1.660 \times 10^{-27} \text{ kg/u})} \\ &= 0.5104 \times 10^{27} \text{ MeV/kg} \end{aligned} \quad (1.41)$$

Deuterium–tritium (D–T) fusion:

$$\begin{aligned} E \text{ yield}_{\text{D-T fusion}} &= \frac{\text{Reaction energy release}}{\text{Fuel mass}} \\ &= \frac{17.6 \text{ MeV}}{(M_{\text{D}} + M_{\text{T}})(1.660 \times 10^{-27} \text{ kg/u})} \\ &= \frac{17.6 \text{ MeV}}{(2.01410 \text{ u} + 3.016049 \text{ u})(1.660 \times 10^{-27} \text{ kg/u})} \\ &= 2.1077 \times 10^{27} \text{ MeV/kg} \end{aligned} \quad (1.42)$$

In Eqns (1.41) and (1.42), the notation $M_{\text{D-T}}$, M_{neutron} , M_{D} , and M_{T} refer to the masses of ${}^{235}\text{U}$, the neutron, deuterium, and tritium in atomic mass units (u). Taking the ratio of energy yields of nuclear fusion over fission yields

$$\frac{E \text{ yield}_{\text{D-T fusion}}}{E \text{ yield}_{\text{D-T fission}}} = \frac{2.1077 \times 10^{27} \text{ MeV/kg}}{0.5104 \times 10^{27} \text{ MeV/kg}} = 4.13 \quad (1.43)$$

Thus, deuterium–tritium (D–T) nuclear fusion is more than four times as efficient than neutron-induced nuclear fission in terms of energy yield per mass of fuel consumption.

D–T fusion offers great promise as a future energy source, which would be more efficient and more environmentally friendly than neutron-induced fission. There are 438 nuclear power plants in 31 countries of the world operating on the basis of nuclear fission, which provides 14% of the energy needs of these countries (IAEA, 2009). However, nuclear fusion is still in the developmental stage. The fusion of light nuclei is not possible under normal temperature and pressure, because the repulsive Coulombic forces between atomic electrons and between positive charges of atomic nuclei prevent the nuclei from mingling into the required close proximity for them to coalesce into one nucleus. However, at temperatures of about 100×10^6 °C, the nuclei of atoms become plasmas in which nuclei and electrons move freely with high kinetic energy sufficient for the nuclei to overcome their repulsive forces and combine. Because of the high temperatures required, the process is referred to as thermonuclear fusion.

In summary, the fusion of the light nuclei, such as those of deuterium (${}^2\text{H}$) and tritium (${}^3\text{H}$), release an energy per nucleon

(MeV/u) or energy per unit of material considerably greater than can be achieved by nuclear fission as calculated above. Thermonuclear fusion requires a large energy input to achieve high temperatures and maintain nuclear plasma; but once achieved, the energy output is greater than the input. An additional advantage of the nuclear fusion of deuterium and tritium is that no hazardous radioactive wastes are direct products of the reaction. The products of the thermonuclear fusion of deuterium and tritium nuclei are alpha particles and neutrons. The neutrons can produce some radioactive isotopes in the surrounding reactor shielding material, but most would be short-lived and there would be no need to store radioactive waste in geological deposits for long periods of time as is the custom with nuclear fission.

Nuclear fusion reactors or controlled thermonuclear reactors (CTRs) are under development to achieve nuclear fusion as a practical energy source. The reactors are based on maintaining plasmas through magnetic or inertial confinement. A deuterium–tritium (D–T) plasma burning experiment was performed with 0.2 g of tritium fuel with the Joint European Torus (JET) reactor in the UK in 1991, and a higher power D–T experimental program with 20–30 g of tritium was continued on the Tokamak Fusion Test Reactor (TFTR) at Princeton in 1993. The International Thermonuclear Experimental Reactor (ITER) was established under the auspices of the International Atomic Energy Agency to develop a prototype fusion reactor by the year 2030. In February 2008, the ITER International Fusion Energy Organization (ITER Organization) applied formally for a construction permit to build the ITER reactor in Cadarache, France (IAEA, 2009). The prototype reactor has the purpose of demonstrating that fusion can produce useful and relatively safe energy. Fusion energy production via a commercial reactor is assumed to start around the year 2050 (Sheffield, 2001). For further reading on fission and fusion, see articles by Brink (2005) and Fiore (2006).

D. Nuclear Models

Since Ernest Rutherford's alpha-scattering experiment that led to the discovery of the atomic nucleus (Rutherford, 1911), physicists have used experimental and empirical data to establish nuclear models to describe the nucleus. The nuclear models, that have been established, provide insight into the stability of the atomic nucleus and an understanding of the processes of nuclear decay.

1. Liquid Drop Model

During a meeting of the Royal Society in London on February 7, 1929, the Russian-born physicist George Gamow (1904–1968) presented his thoughts on the properties of the nucleus and that the nucleus would possess forces similar to those of a liquid drop (Gamow, 1929). A very complete and detailed account of Gamow's conception of the liquid-drop model of the nucleus is given by Stuewer (1997). The writer will give here a small portion of this historical account, which provides the reasoning used by Gamow. At the time Gamow first presented his ideas on the liquid-drop characteristics of the nucleus, the neutron had

not been discovered; and the alpha particle was thought to be the building block of the nucleus. In the discussion, Gamow (1929) commented

Such an assembly of alpha particles with attractive forces between them, which vary rapidly with the distance may be treated somewhat as a small drop of water in which the particles are held together by surface tension.

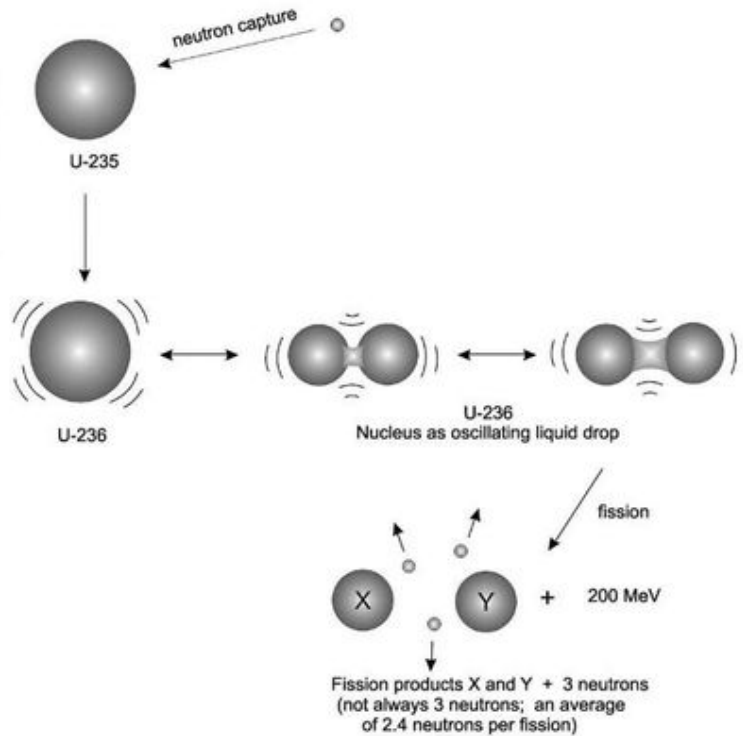
Gamow (1930) continued his development of the liquid-drop model, still yet before the neutron was discovered by James Chadwick (1932a,b) to be a component particle of the nucleus. After the discovery of the neutron, Werner Heisenberg (1934) presented his analysis of exchange forces and general theory of nuclear structure at the 7th Solvay Conference in Brussels in October 1933. At the meeting, Heisenberg reported theory on nuclear structure, which could be "considered as corresponding to a form of Gamow's drop model made precise by the neutron hypothesis" (Stuewer, 1997). Only a year later, Heisenberg's student Carl Friedrich von Weizsäcker (1935) derived an empirical equation, that would yield the binding energy of the nucleus as a function of its mass number (A), incorporating into the equation the various properties of the nucleus characteristic of a liquid drop. Von Weizsäcker's equation for the liquid-drop model of the nucleus gained notoriety when Hans Bethe and Robert Bacher (Bethe and Bacher, 1936, Bethe, 1937) from Cornell University reworked Weizsäcker's equation to include a pairing energy, which was referred to subsequently as the Bethe–Weizsäcker mass formula.

Gamow's original conception of the nucleus with the physical properties of a liquid drop soon became useful in the interpretation of nuclear fission. In December 1938, Otto Hahn and Fritz Strassman (1939a,b) had confirmed that barium ($Z = 56$) was a product of neutron bombardment of uranium ($Z = 92$). Hahn could not arrive at an explanation of how a nuclide of lower atomic number would result from the reaction of a neutron with a nucleus of much higher atomic number. Hahn asked his former colleague and collaborator, Lise Meitner, for an explanation. Lise Meitner and Otto Frisch (1939) considered the recently developed concept of the nucleus having the properties of a liquid drop. They arrived at the conclusion that the capture of a neutron by the uranium nucleus attributed to the nucleus a degree of instability, whereby it would oscillate like a liquid drop forming a dumbbell shape (See Fig. 1.10) and that the apposing Coulomb forces of the fat sections of the dumbbell would cause the nucleus to split apart into two nuclides (fission fragments) of smaller atomic number, and that the sum of the atomic numbers of the two fission fragments would equal that of the original uranium ($Z = 92$). They concluded that if barium ($Z = 56$) was a product (fission fragment) of neutron bombardment of uranium ($Z = 92$), the other fission fragment would be krypton ($Z = 36$), as described by the following reaction:



They coined the word "fission" by borrowing the word from biology, a word used to describe the splitting of bacteria cells.

FIGURE 1.10 Neutron capture by uranium-235 and subsequent fission of unstable uranium-236. The capture of a slow neutron by uranium-235 yields the nuclide uranium-236, which is unstable, capable of oscillating like a liquid drop and breaking into two smaller nuclides X and Y generally of different masses and of atomic numbers that add up to $Z = 92$ (the atomic number of the parent uranium) plus the emission of an average of 2.4 neutrons and energy (approximately 200 MeV). The emission of three neutrons is illustrated. The uranium-236 nuclides break into two fission fragments in as many as 30 different possible ways producing, therefore, 60 different nuclide fission fragments.



The liquid-drop model remains to this day an excellent means of describing nuclear fission, and the liquid-drop model formula has been used to predict spontaneous fission half-lives (Ronen, 2004).

Today the liquid-drop model formula is referred to often as the Weizsäcker liquid-drop model formula or the semi-empirical mass formula. It has been refined by many researchers to include theory with empirical measurements, including those described by Evans (1955), Friedlander et al (1964), Ronen (2004), Serway et al (2005), Mahboub (2008), and Royer (2008), and the formulas vary slightly among research reports; however, all have the basic mathematical structure as the equation first reported by von Weizsäcker. The liquid-drop formula described by Evans (1955), Friedlander et al (1964), Choppin et al (2002), Gould et al (2004), and Serway et al (2005) is basically the following:

$$E_b = a_v A - a_s A^{2/3} - a_c \frac{Z(Z-1)}{A^{1/3}} - a_{sy} \frac{(N-Z)^2}{A} \pm \delta_p(Z, N) \tag{1.45}$$

where E_b is the nuclear binding energy in MeV, A is the mass number, N is the neutron number, Z is the atomic number, a_v , a_s , a_c , and a_{sy} are coefficients for the volume energy, surface energy, Coulomb energy, and the symmetry energy, respectively, and $\delta(Z, N)$ is a pairing energy term described subsequently. The values of the coefficients a_v , a_s , a_c , and a_o reported

by Woan (2000) are $a_v \approx 15.8$ MeV, $a_s \approx 18.0$ MeV, $a_c \approx 0.72$ MeV, and $a_{sy} \approx 23.5$ MeV. The coefficients vary slightly among research reports depending on the data used to obtain the mathematical best fit of the equation to measured values of nuclear binding energy, and the equation generally agrees with measured values to within a few percent for nuclides of $A > 40$. The various terms of the liquid-drop equation (Eqn (1.45)) are described as follows:

Volume Energy, $a_v A$. The volume energy term assigns a direct proportionality of the nuclear volume to the total binding energy of the nucleus, *i.e.*, the nuclear volume increases in proportion to the number of nucleons. The extension of the binding energy throughout the entire volume of the nucleus is a consequence of the short range and saturation characteristics of the nuclear forces. The strong nuclear forces binding neutrons and protons in the nucleus extend throughout the nuclear volume.

Surface Energy, $a_s A^{2/3}$. The surface energy term is negative, as the nuclear forces binding the nucleons are unsaturated at the surface similar to the surface tension effect that occurs with a liquid drop (See Fig. 1.11) and there is thus a reduction of binding at the surface. The nucleons at the surface have fewer neighboring nucleons with which to bind resulting in a reduction in binding energy as a function of surface area. The surface effect will increase with surface area; and surface area of a sphere is defined as πr^2 . Since the radius of the nucleus is proportional to the mass number ($r \propto A^{1/3}$) as defined by

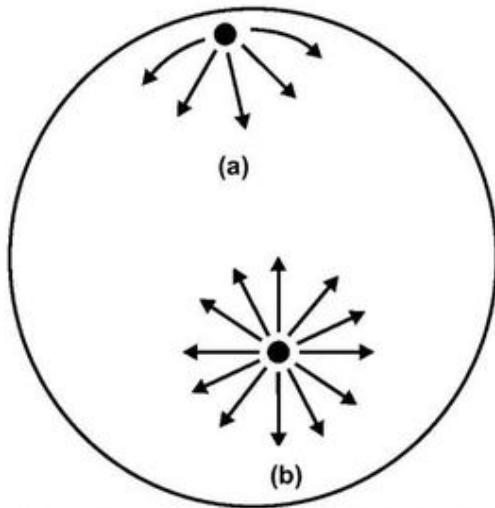


FIGURE 1.11 Nuclear forces (arrows) binding a nucleon at the nuclear surface (a) and a nucleon within the nucleus (b). The binding forces of the nucleon at the surface are unsaturated, as there are fewer neighboring nucleons with which to bind compared to nucleons within the nucleus. The phenomenon is similar to that which occurs in the binding of molecules of a liquid drop resulting in surface tension.

Eqn (1.16), the surface area term can be written as being proportional to $A^{2/3}$.

Coulomb Energy, $a_c(Z(Z-1)/A^{1/3})$. The Coulomb energy term takes into account the repulsive Coulomb forces of the protons in the nucleus. The nucleus contains Z protons and their long-range Coulomb forces interact with the remaining $Z-1$ protons. The Coulomb force therefore extends throughout the nucleus with radius proportional to $A^{1/3}$ (see Eqn (1.16)), which is included in this Coulomb energy term of the liquid-drop model.

The strong nuclear-binding forces between neutrons and protons in the nucleus, which are of short range, counteract the Coulomb repulsive forces. Thus, throughout the Chart of the Nuclides among the stable nuclei with $Z > 20$, we will find that their nuclei contain more neutrons than protons. If we look throughout the Chart of the Nuclides, we will notice that the stable nuclides of low atomic number ($Z \leq 20$) will have an N/Z ratio of ~ 1 . However, as the atomic number increases ($Z > 20$), the N/Z ratio of the stable nuclides increases gradually and reaches as high as ~ 1.5 (e.g., $^{209}_{83}\text{Bi}$, $Z = 83$, $N/Z = 1.518$). Furthermore, there are no stable nuclides of atomic number greater than 83.

In brief, the importance of the N/Z ratio to nuclear stability is explained on the basis of the existence of strong short-range nuclear binding forces, which are charge independent and the long-range repelling Coulomb forces between protons. The short-range strong nuclear forces extend to a distance of ≈ 2 fm (2 fermi or 2×10^{-15} m), which is close to the radius of a small nucleus, such as that of ^4_2He (See Section IV.A). These attractive strong nuclear forces are binding exchange forces that have charge independence (see Section IV.B). The binding exchange forces exist, therefore, regardless of charge on the particles, between two protons, two neutrons, and a proton and neutron. Thus, at short distances within 2 fm, the strong forces between $n-n$, $n-p$, and $p-p$ are equal and charge independent. However, at distances beyond 2 fm, there exists repelling Coulombic forces between the positively charged protons that act to force them apart. For nuclides of low Z , the attractive nuclear forces exceed the repelling Coulombic forces when $N \approx Z$. However, increasing the number of protons (e.g., $Z > 20$) further increases the strength of the repelling Coulombic forces over a larger nucleus, which will tend to force the nucleus apart. Therefore, additional neutrons, $N > Z$, provide additional strong attractive nuclear forces needed to overcome the repelling forces of the larger proton population. Fig. 1.12 illustrates a plot of the stable nuclides as a function of their N and Z numbers. The N/Z ratio of the stable nuclides, as

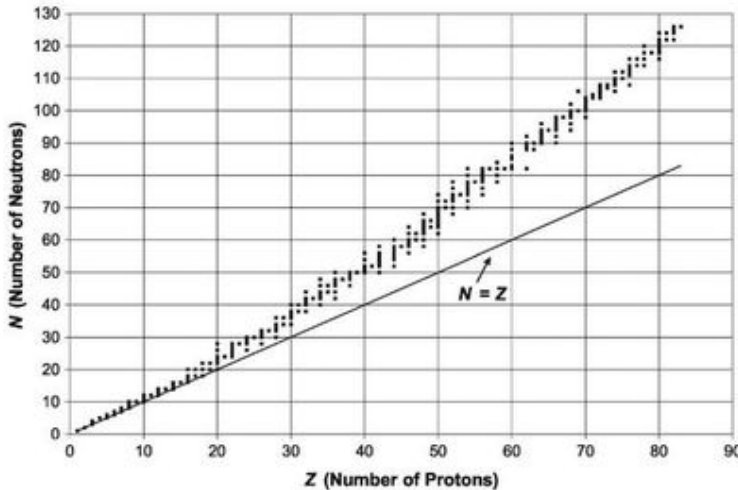


FIGURE 1.12 Plot of stable nuclides. The number of neutrons (N) is plotted against the number of protons (Z) in the nuclei of the stable atoms. The straight line represents $N = Z$. Only 13 nuclides in the region $Z \leq 20$ are stable with an equal number of neutrons and protons ($N = Z$).

illustrated in Fig. 1.12, increases significantly as a function of Z for nuclides of $Z > 20$. As the atomic number increases further, $Z > 83$, all nuclides are unstable. Even though N/Z ratios reach 1.5, nuclear stability is not achieved, when the number of protons in the nucleus exceeds 83.

Volume Symmetry, $a_{sy}((N-Z)^2/A)$. The volume symmetry term quantifies the contribution of nuclear symmetry to the binding energy. Among the light nuclei, the unstable nuclei reside on either side of the symmetrical term $N=Z$. Thus, a negative sign is assigned to this symmetry term, which increases according to $(N-Z)$. Nuclear stability among the larger nuclei is achieved by an increase in the N/Z ratio (See Fig. 1.12) as the strong short-range binding nuclear forces between neutrons and protons (See Section IV.B) are needed to hold the nucleus together over the entire volume of the nucleus. As these short-range n-p binding forces do not reach throughout the volume of the nucleus, the probability of occurrence of n-p binding within a nucleus would be inversely proportional to the nuclear volume or A^{-1} .

Pairing Energy, $\pm\delta_p(Z, N)$. The pairing energy term may have appositive sign whereby the term adds to the nuclear binding energy, or a negative sign diminishing the nuclear binding energy. Nuclei that have an even number of protons and even number of neutrons (even Z , even N) are known to be the most stable of all nuclei due to proton-proton spin coupling and neutron-neutron spin coupling (see Section IV.D.2 below). The pairing energy term for the binding energy of these nuclei is assigned a value of $+34/A^{3/4}$ MeV. Nuclides with even Z , odd N or odd Z , even N are generally less stable than even-even nuclides, and thus the even-odd and odd-even (*i.e.*, odd A) nuclides are assigned a value of zero to the pairing energy term. The least stable of the nuclides are those with odd Z and odd N (*i.e.*, odd-odd nuclides), and these are assigned a pairing energy term of $-34/A^{3/4}$ MeV. The negative value of this term would diminish the total binding energy of Eqn (1.45) for the liquid-drop model. Thus, the pairing energy term would have the following values as summarized by Woan, (2000) and Gould et al. (2004):

$$\pm\delta_p(Z, N) \approx \frac{34}{A^{3/4}} \begin{cases} +1 & \text{for even-even} \\ 0 & \text{for } A \text{ odd} \\ -1 & \text{for odd-odd} \end{cases} \quad (1.46)$$

The liquid-drop model is useful in describing certain properties that may attribute stability or instability to atomic nuclei, and it has proved to be successful in explaining nuclear fission in large nuclei. However, the liquid-drop model does not provide insight into the fine organized structure and spin coupling of protons and neutrons in the nucleus that attribute stability to certain nuclei as provided by the shell model described subsequently.

2. Shell Model

Our knowledge of the shell structure of the atomic nucleus has its beginnings with the independent work of Maria Goeppert-Mayer while at the Argonne National Laboratory in the USA (Goeppert-Mayer, 1948a,b, 1949) and J. Hans D. Jensen, from the University of Heidelberg, Germany (Haxel et al., 1949). They subsequently collaborated with a book on nuclear shell structure (Goeppert-Mayer and Jensen, 1955). For this work

they were awarded the 1963 Nobel Prize in Physics, which they shared with Eugene Paul Wigner. This award made Maria Goeppert-Mayer the 2nd woman to receive the Nobel Prize in physics since Marie Curie.

Maria Goeppert-Mayer's opportunity for discovery came while voluntarily collaborating at the University of Chicago's Institute for Nuclear Studies (now known as the Enrico Fermi Institute). At the institute she collaborated with Edward Teller in a search for the cosmological model of the origin of the universe. While compiling data she studied the abundance of the elements and found that there were certain elements that were highly abundant, and she found a correlation between the abundance of these elements and specific numbers of neutron and protons in their nuclei. J. Hans D. Jensen at the Institute of Theoretical Physics in Heidelberg together with his collaborators Otto Haxel at the Max Planck Institute in Göttingen and Hans E. Suess of the Institute of Physical Chemistry at Hamburg came to a similar conclusion that certain elements with particular numbers of neutrons and protons were particularly stable. It is interesting to note that at both sides of the globe, the discoveries were made simultaneously and independently. When the stage is set, the discoveries will be made.

The numbers of protons and neutrons, correlated to particularly stable nuclei, were called the "magic numbers". In the words of Goeppert-Mayer in her Nobel Lecture,

What makes a number magic is that a configuration of a magic number of neutrons, or of protons, is unusually stable whatever the associated number of the other nucleons." The magic numbers, as we know them today, are:

2, 8, 20, 28, 50, 82, 126

And most importantly, they are the same for neutrons and protons.

Nuclides containing a magic number of neutrons and/or protons are listed in Table 1.3. Goeppert-Mayer (1963, 1964) pointed out that Sn ($Z=50$) is the element with the largest number of stable isotopes among all of the elements in the Periodic Table. There are six stable nuclides with 50 neutrons and 7 stable nuclides with 82 neutrons, whereas normally one will find only 2 or 3 stable nuclei in the Chart of the Nuclides having identical numbers of neutrons.

Some nuclides are called "doubly magic", because they have equal numbers of protons and neutrons that are magic numbers. The nuclide ${}^4_2\text{He}$ has a high binding energy, *i.e.*, it is very tightly bound (See Fig. 1.9), and an extra proton or neutron cannot be attached to its nucleus, as evidenced by the fact that ${}^4_3\text{Li}$ and ${}^5_2\text{He}$ do not exist. In addition, ${}^{16}_8\text{O}_8$, which is also "doubly magic", is very stable. A large amount of energy would be required to remove a neutron from the ${}^{16}_8\text{O}_8$ nucleus; whereas the addition of an extra neutron to its nucleus to form ${}^{17}_8\text{O}_9$ would result in a weakly bound neutron, which is evidenced by the low natural abundance of ${}^{17}\text{O}$ (0.04%) compared to ${}^{16}\text{O}$ (99.76%).

The breakthrough in the development of the nuclear shell model came with the conclusion that the protons and neutrons in the nucleus exhibit nuclear spin-coupling effects, which result in shifts in their energy levels within the nucleus, similar to what occurs with electrons in their orbitals about the atom. Pauli's exclusion principle, which was applied to atomic electrons, is

TABLE 1.3 Magic Number Nuclides

Number of protons	2	8	20	28	50	82	126
	⁴ He	¹⁶ O	⁴⁰ Ca	⁵⁰ Ni	¹¹² Sn	²⁰⁴ Pb	
		¹⁷ O	⁴² Ca	⁶⁰ Ni	¹¹⁴ Sn	²⁰⁶ Pb	
		¹⁸ O	⁴³ Ca	⁶¹ Ni	¹¹⁵ Sn	²⁰⁷ Pb	
			⁴⁴ Ca	⁶² Ni	¹¹⁶ Sn	²⁰⁸ Pb	
			⁴⁶ Ca	⁶⁴ Ni	¹¹⁷ Sn		
			⁴⁸ Ca		¹¹⁸ Sn		
					¹¹⁹ Sn		
					¹²⁰ Sn		
					¹²² Sn		
					¹²⁴ Sn		
Number of neutrons	2	8	20	28	50	82	126
	⁴ He	¹⁵ N	³⁶ S	⁴⁸ Ca	⁸⁶ Kr	¹³⁶ Xe	²⁰⁰ Pb
		¹⁶ O	³⁷ Cl	⁵⁰ Ti	⁸⁷ Rb	¹³⁸ Ba	²⁰⁹ Bi
			³⁸ Ar	⁵¹ V	⁸⁸ Sr	¹³⁹ La	
			³⁹ K	⁵² Cr	⁸⁹ Y	¹⁴⁰ Ce	
			⁴⁰ Ca	⁵⁴ Fe	⁹⁰ Zr	¹⁴¹ Pr	
					⁹² Mo	¹⁴² Nd	
						¹⁴⁴ Sm	

(Goepfert-Mayer, 1963; reprinted with permission © The Nobel Foundation 1958)

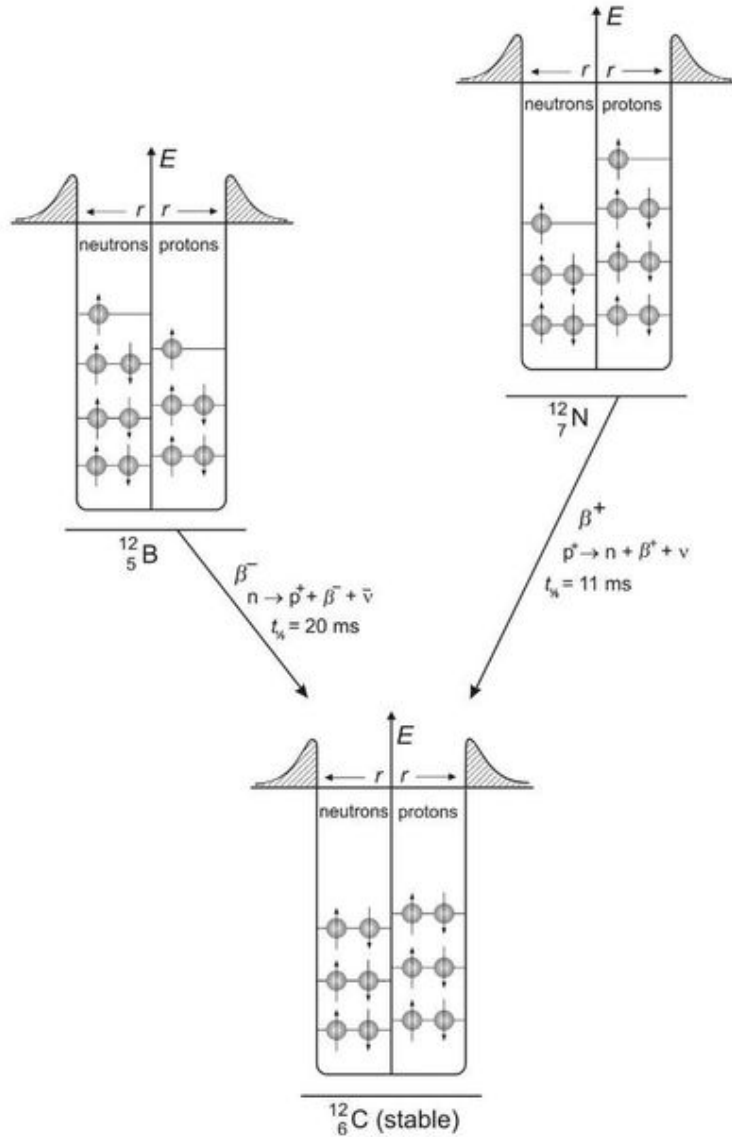
also applied to the nucleons in the nucleus. The exclusion principle states that no two protons or two neutrons in a nucleus could exist in the same quantum or energy state. The proton or neutron can exist in two spin quantum states, namely $+1/2$ (i.e., spin-up) or $-1/2$ (i.e., spin-down). Goepfert-Mayer explained in her Nobel Lecture that there is a strong interaction between spin and orbital angular momentum, whereby spin-up and spin-down refer to the spin being parallel or anti-parallel to the orbital angular momentum. She provided evidence that this spin interaction raised considerably the energy levels of nuclei that contained 9, 21, 29, 51, or 83 protons or neutrons, or 127 or 128 neutrons, thereby attributing a high degree of stability to nuclei that contain 8, 20, 28, 50, 82 protons or neutrons, or 126 neutrons. The numbers 8, 20, 28, 50, 82, and 126 refer to closed shells of protons or neutrons attributing a high degree of stability to nuclei with these nucleon numbers. The closed shells of nucleons in the highly stable nuclei are analogous to the closed electron shells of the noble gases, which attribute to these gases a high degree of chemical inertness. Thus, protons and neutrons exist in the nucleus in different energy states in structured orbitals similar to the external electron orbitals of the atom. In Section IV.D.1 it was discussed how stability is achieved in the light nuclei ($Z < 20$) when $Z = N$, and this was illustrated previously in Fig. 1.12. In accord with the exclusion principle, the nucleons are packed in the nucleus according to energy levels with two protons of opposite spin and two

neutrons of opposite spin per energy level. As a proton or neutron is added to the nucleus, it will occupy the next highest energy state; and the increase in energy state of the nucleus can decrease its stability. Fig. 1.13 illustrates how the additional proton in ¹²N compared to ¹²C attributes a higher energy state to the ¹²N nucleus, whereby it decays to the stable ¹²C by the conversion of a proton to a neutron via positive beta decay. Also, an extra neutron in the nucleus of ¹²B places that nucleus in a higher energy state compared to ¹²C. The ¹²B achieves stability by conversion of the excess neutron to a proton to form stable ¹²C via negative beta decay.

In her Nobel Lecture Maria Goepfert-Mayer provided evidence for the increased instability of nuclei when additional neutrons are added to nuclei above the magic numbers, which represent closed shells at 2, 8, 20, 28, 50, 82, and 126 nucleons. Fig. 1.14 illustrates the β^- decay energies of various nuclides with $N-Z = 3$ to $N-Z = 2$. Maria Goepfert-Mayer explained the curve as follows:

One would expect to find a smooth curve, sloping downward. Except for one point it is indeed so. This point is ³⁹Ar with 21 neutrons and 18 protons. A smooth interpolation of the curve would predict ³⁹Ar to be stable ... However, ³⁹Ar is unstable against β^- emission by about 0.5 MeV. The explanation of this anomaly is the low binding energy of the 21st neutron, while the 19th proton into which it is transformed has the higher binding energy of the proton shell which closes at 20. That

FIGURE 1.13 Nuclear potential energy-well illustrations of the pairing of nucleons in the isobars ^{12}N , ^{12}B , and ^{12}C . The neutrons and protons are illustrated with arrows to represent opposite spin states, spin up (\uparrow) and spin down (\downarrow). Only two nucleons of opposite spin state are allowed per energy level (E) in accord with the Pauli Exclusion Principle. The protons are illustrated at a higher energy level than the neutrons, because of the added positive Coulomb potential of the protons. The ridge, above the energy-well, represents the Coulomb potential barrier to charged particles from entering or escaping the nucleus. The nuclear radius is represented by r . (See Fig. 1.26 for a detailed description of the nuclear energy-well.)



the energies drop again sharply is due to the fact that now $Z = 20$ is involved. These types of discontinuity occur at all magic numbers.

A similar discontinuity of the β^- decay energies in the neighborhood of $N = 50$ is illustrated in Fig. 1.15. The addition of a single neutron to the nucleus of $N = 50$ increases the energy state of that nucleus illustrated by the higher decay energy of the nucleus of ^{89}Sr with $N = 51$ compared to ^{85}Kr with $N = 49$. This is only one of several examples given by Goepfert-Mayer (1972) of nuclear stability attributed to the closing of a neutron shell at $N = 50$.

The highest magic number of 126 occurs only for the closing of a neutron shell. Thus, it would be expected that the 127th and 128th neutrons would be less tightly bound and that these nuclides would be at higher and less stable energy states compared to nuclides with 126 neutrons. This is just the case, as illustrated in Fig. 1.16. In the case of α -decay, there is the emission of two neutrons together with two protons. As illustrated in Fig. 1.16, the α -particle decay energy is the highest for nuclides with 128 neutrons, and this drops sharply when the 128th and 127th neutron is removed from the nucleus.

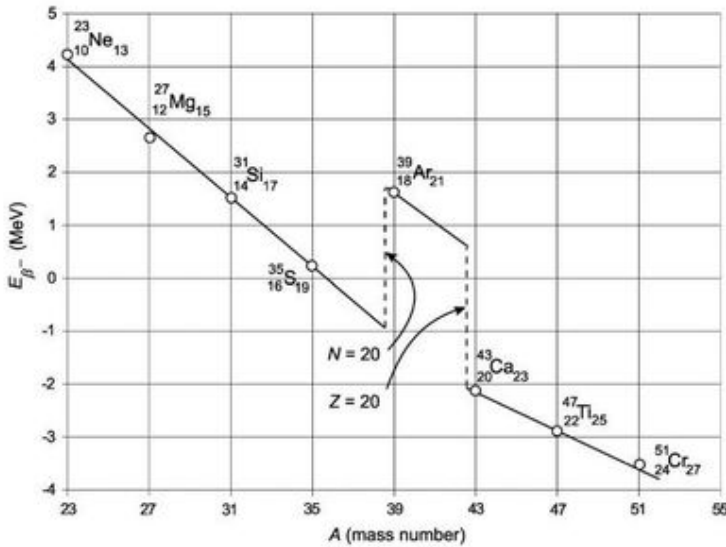


FIGURE 1.14 Beta decay energies in the neighborhood of $N = 20$. (Goepfert-Mayer, 1963; reprinted with permission © The Nobel Foundation 1958.)

For further information on this subject matter, the reader is invited to peruse works by Goepfert-Mayer and Jensen (1955, 1965), Goepfert-Mayer (1965), Choppin et al (2002), and Rowe and Wood, (2010).

3. Collective Model

The collective model of the nucleus combines aspects of the liquid-drop and shell models, which provides a description of the collective properties of the nucleus. The oldest model was the liquid-drop model described previously. This model was very useful in describing certain nuclear reactions, such as nuclear fission. After the liquid-drop model came the shell model, which

gave an organized picture of the nucleons in different energy states in structured orbitals. This provided an explanation for the stability of the nucleus with certain “magic numbers”. However, neither model could provide an explanation for excited states of the nucleus, which are a result or consequence of the collective action of the nuclei. The collective model, for which Aage Bohr (son of Niels Bohr), Ben Mottelson, and James Rainwater received the 1975 Nobel Prize in physics, depicts the nucleus with both the properties of a liquid drop and the ordered structure of the nucleons providing an explanation of excited states of the nucleus as a consequence of its rotations and vibrations.

Certain nuclei, particularly heavy nuclei ($A > 150$), exhibit large electric quadrupole moments. This property is a charge

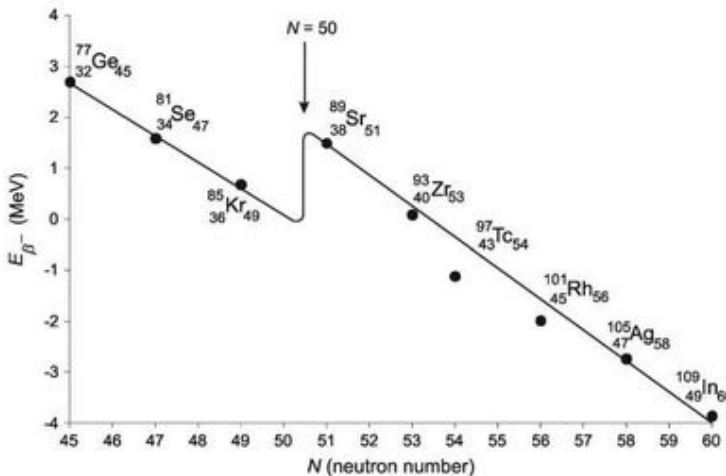
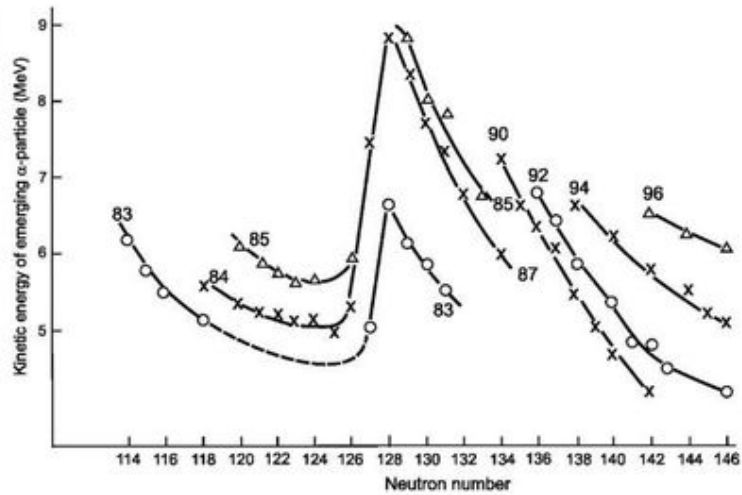


FIGURE 1.15 Beta decay energies in the neighborhood of $N = 50$. Source: Goepfert-Mayer, 1963; reprinted with permission © The Nobel Foundation 1958.

FIGURE 1.16 Energy release in alpha decays. (Goepfert-Mayer, 1972; reprinted with permission © The Nobel Foundation 1958.)



distribution that deviates from what one would encounter with a symmetrical spherical nucleus. This property clearly indicated that certain nuclei were not spherical in shape, but that they were deformed or ellipsoidal in shape. Rainwater (1950) provided a solution by considering that there was an interaction between an inner core and outer surface of valence nucleons whereby the valence nucleons could influence the shape of the nucleus. The movement of the valence nucleons with respect to the core would cause a polarizing effect, resulting in a deformed nucleus as what would be expected in the liquid-drop model. Aage Bohr (1951) published ideas similar to those of Rainwater in a paper that was submitted prior to the publication of Rainwater's paper demonstrating their independent discoveries. Bohr linked the movement of nucleons on the nuclear surface to oscillations of the nuclear shape, which would account for the large nuclear quadrupole moments. Bohr predicted collective excitations of the nucleus, namely vibrational excitations resulting in the periodic change in the shape of the nucleus and rotational excitations, which entails the rotation of the entire nucleus not as a single body, but that the motion consists of a surface wave of nucleons that propagates. In his words during his Nobel address, Aage Bohr stated "The rotational motion resembles a wave traveling across the nuclear surface and the moment of inertia is much smaller than for a rigid rotation." The moment of inertia of the nucleus will change as its shape changes. This is analogous to the actions of a figure skater, who with outstretched arms will pull in his or her arms, thereby reducing their moment of inertia resulting in a faster spin. In his Nobel Lecture Aage Bohr (1975) illustrated the differences between the rotation of a rigid nucleus and one which has a nonrigid surface as depicted in Fig. 1.17.

Thus, nuclear excitations would be expected from the nucleus rotating not as rigid body, but resulting from the movement of a surface wave of nucleons propagating about and around the surface of the nucleus. The nuclear deformations (ellipsoidal shapes) would result from numerous nucleons acting

in a collective manner as a wave about the surface of a more rigid inner nuclear core. The differing ellipsoidal shapes or rotational states of the nucleus are manifested as rotational bands in gamma emission spectra as subsequently discussed.

Bohr and Mottelson (1953a,b) were able to correlate the energy of rotational states with gamma-ray emission spectra. The energy (E) of the rotational states for even-even nuclei would be defined by the equation

$$E = h^2 \frac{I(I+1)}{2\vartheta} \quad (1.47)$$

where I is the nuclear spin and ϑ is the moment of inertia. Some of the first examples of energy spectra proportional to $I(I+1)$ are

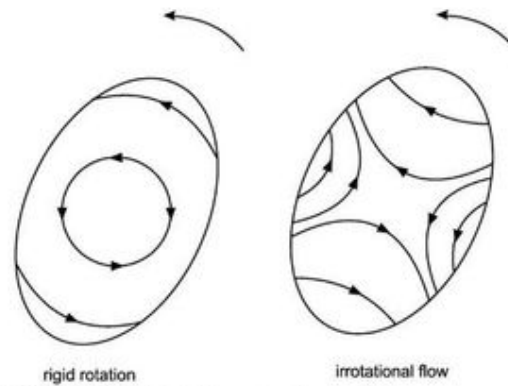


FIGURE 1.17 Velocity fields for rotational motion. For the rotation generated by irrotational flow, the velocity is proportional to the nuclear deformation (amplitude of the traveling wave). Thus for a spheroidal shape, the moment of inertia is $\vartheta = \mathfrak{I}_{rig}(\Delta R/R)^2$ where \mathfrak{I}_{rig} is the moment for rigid rotation, while R is the mean radius and ΔR (assumed small compared to R) is the difference between major and minor semi-axes (From Bohr, A., 1992; reprinted with permission © The Nobel Foundation 1958.)

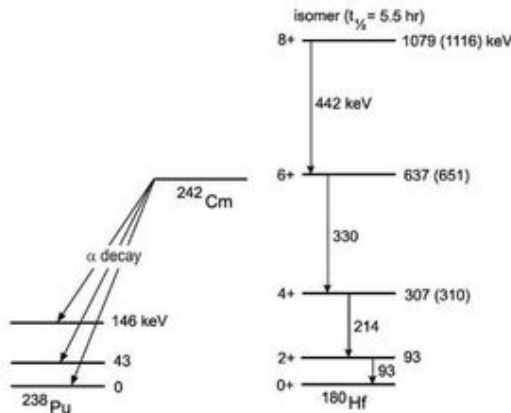


FIGURE 1.18 Rotational spectra for ^{238}Pu and ^{180}Hf . The spectrum of ^{180}Hf was deduced from the observed γ lines associated with the decay of the isomeric state. The nuclear spin states (0, 2, 4...) and parity (+) are given at the left of each energy plateau of ^{180}Hf , and the energies in keV are given to the right of each energy plateau. The vertical arrows pointing downward in the decay of ^{180}Hf represent the energy differences between plateau and the magnitudes of the gamma-ray photon energies. The numbers in parenthesis are calculated from the energy of the first excited state, assuming the energies to be proportional to $I(I+1)$. (From Bohr, A., 1992; reprinted with permission © the Nobel Foundation 1958.)

illustrated in Fig. 1.18. For example, the ratio of spin state 4 to spin state 2 is $4(4+1)/2(2+1) = 3.33$, and the product of this ratio and the observed energy at spin state 2 yields $(3.33)(93 \text{ keV}) = 310 \text{ keV}$ as given in parenthesis for the calculated energy at spin state 4 in Fig. 1.18.

Similar calculations can be made to arrive at the calculated energy levels of 651 and 1116 keV of ^{180}Hf illustrated in Fig. 1.18. In his Nobel Lecture Bohr stated "The spectrum of ^{238}Pu was established by Asaro and Perlman (1953) from measurements of the fine structure in the α -decay of ^{242}Cm . Subsequent evidence showed the spin-parity sequence to be $0+$, $2+$, $4+$, and the energies are seen to be closely proportional to $I(I+1)$." These findings were the first to demonstrate that certain nuclear energy states can be explained on the basis that they constitute a nuclear rotational spectrum, thus providing convincing evidence for the collective model of the nucleus.

E. Cluster Radioactivity

Cluster radioactivity is nuclear decay with the spontaneous emission of a particle heavier than an alpha particle with $Z \geq 6$. It is included in this part of the chapter, because cluster radioactivity is an important phenomenon not in the analysis of radionuclides, but rather in the study of the properties of the nucleus.

Cluster radioactivity was first predicted by Sandulesco and Greiner (1977) and discovered by Rose and Jones (1984), who were the first to observe the emission of ^{14}C from the nucleus of ^{223}Ra . Since the discovery in 1984, intense experimental research at numerous institutions (See reviews by Price, 1989 and 1994, Ronen, 1997, Bonetti and Guglielmetti, 1999, and Santhosh et al, 2010) have uncovered numerous radionuclides

of high mass number ($A \geq 221$) that emit clusters, including ^{14}C , ^{20}O , ^{23}F , ^{24}Ne , ^{28}Mg , or ^{32}Si . Radionuclides, that exhibit cluster radioactivity, are listed in Table 1.4 with their cluster decay modes and decay properties.

Cluster decay is a rare event that competes with alpha-particle emission, i.e., alpha decay. The probabilities of cluster decay for observed decay modes (i.e., branching ratios) range from 10^{-9} to 10^{-17} of the alpha-decay probability. All of the decay modes listed in Table 1.4 yield product nuclei that possess magic numbers of protons ($Z = 82$) and/or neutrons $N = 126$) with the exception of ^{211}Bi ($Z = 83$, $N = 128$), which is accompanied with the ^{14}C cluster in the decay of ^{225}Ac . However, in this exceptional case, the ^{14}C cluster has the highest binding energy (BE) per cluster. Ronen (1997) compared the magic numbers, binding energies per cluster, and Q values of the cluster decays as listed in Table 1.4. From these comparisons, Ronen (1997) concluded the following:

1. *The most likely mode of cluster radioactivity is when the light cluster has the highest BE per cluster and the daughter product is the doubly magic nucleus ^{208}Pb . We can see from Table 1.4 that, among the isotopes of Ra, which yield the ^{14}C cluster, the decay mode yielding the doubly magic ^{208}Pb has the highest Q value. Also, among the isotopes of U and Pu, the decay modes that yield the doubly magic ^{208}Pb also have the highest Q values.*
2. *Nuclei that decay by cluster radioactivity have either a daughter that is magic ($N = 126$ or $Z = 82$) or a light emitted cluster with the highest BE per cluster. Nuclei that obey both conditions (magic number and highest BE per cluster for the emitted cluster) have shorter half-lives.*

Because of the rarity of cluster radioactivity in comparison to alpha decay, the detection of emitted clusters must be done with a relatively high alpha activity. Certain solid-state nuclear track detectors insensitive to alpha particles (Durrani and Bull, 1987 and Ilić and Durrani, 2003) serve as good means of detecting cluster radioactivity. However, Bonetti et al (2001) point out that track detectors may not have enough A resolution to offer unambiguous identification. Thus, to decide in favor of one of the most probable Ne clusters, Bonetti et al (2001) resorted to theoretical calculations.

An important outcome of the discovery of cluster radioactivity was the reconfirmation of the magic numbers of closed shells of magic numbers of protons and neutrons in the nucleus that yield exceptional stability to atomic nuclei discussed previously in this chapter. Numerous works have been devoted to explaining the cluster decay process. These are summarized by Santhosh et al (2010). There are two approaches to explaining the cluster decay process, namely, (1) fission-like and (2) alpha-like. In the fission model (Sandulescu et al, 1985, Greiner et al, 1985, Poenaru et al, 1985 and 1986, Shi and Swiatecki, 1985, and Shanmugam and Kamalaharan, 1988), the nucleus deforms continuously as the cluster penetrates the nuclear barrier. This would be somewhat similar to the nuclear fission process discussed previously in this chapter. In the alpha-like or cluster model of decay (Blendowske et al, 1987, Landowne and Dasso, 1986, Buck and Merchant, 1989, and Malik and Gupta, 1989), the cluster is assembled in the nucleus in

TABLE 1.4 Cluster Decay Modes and Properties^a

Decay mode ^b	Magic number(s) ^c	E or Q value (MeV)	Half-life (log T _{1/2} (s))
²³¹ Fr → ²⁰⁷ Tl + ¹⁴ C	N = 126	29.28	14.5 ± 0.12
²²³ Ra → ²⁰⁷ Pb + ¹⁴ C	Z = 82	30.34	13.0 ± 0.2
²²² Ra → ²⁰⁸ Pb + ¹⁴ C	Z = 82, N = 126	30.97	11.0 ± 0.06
²²³ Ra → ²⁰⁹ Pb + ¹⁴ C	Z = 82	29.85	15.2 ± 0.05
²²⁴ Ra → ²¹⁰ Pb + ¹⁴ C	Z = 82	28.63	15.8 ± 0.12
²²⁵ Ac → ²¹¹ Bi + ¹⁴ C	None	28.57	17.16 ± 0.06
²²⁶ Ra → ²¹² Pb + ¹⁴ C	Z = 82	26.46	21.3 ± 0.2
²²⁸ Th → ²⁰⁸ Pb + ²⁰ O	Z = 82, N = 126	44.72	20.7 ± 0.08
²³³ Pa → ²⁰⁸ Pb + ²³ F	Z = 82, N = 126	46.68	26.0
²³⁰ Th → ²⁰⁶ Hg + ²⁴ Ne	N = 126	51.75	24.6 ± 0.07
²³³ Pa → ²⁰⁷ Tl + ²⁴ Ne	N = 126	54.14	22.9 ± 0.05
²³² U → ²⁰⁸ Pb + ²⁴ Ne	Z = 82, N = 126	55.86	20.5 ± 0.03
²³⁴ U → ²¹⁰ Pb + ²⁴ Ne	Z = 82	52.81	25.9 ± 0.2
²³⁴ U → ²⁰⁶ Hg + ²⁸ Mg	N = 126	65.26	25.7 ± 0.2
²³⁶ Pu → ²⁰⁸ Pb + ²⁸ Mg	Z = 82, N = 126	70.22	21.7 ± 0.3
²³⁸ Pu → ²⁰⁸ Pb + ³⁰ Mg	Z = 82, N = 126	67.00	25.7 ± 0.25
²³⁸ Pu → ²⁰⁶ Hg + ³² Si	N = 126	78.95	25.3 ± 0.16

^aDecay mode, energy (E) and half-life data are from Price (1994) and Ronen (1997).

^bOther cluster decays, not listed in the table, are ²³⁶U → ²⁰⁶Hg (N = 126) + ³⁰Mg, ²³⁶Pu → ²¹²Pb (Z = 82) + ²⁴Mg, and ²⁴²Cm → ²⁰⁸Pb (Z = 82, N = 126) + ³⁴Si reported by Tretyakova (1995) and ²³⁰U → ²⁰⁷Pb (Z = 82, N = 126) + ²³Ne and ²²⁶Th → ²⁰⁸Pb (Z = 82, N = 126) + ¹⁸O reported by Bonetti et al. (2001). The magic numbers of the product nuclei are in parenthesis where the nucleus of ²⁰⁸Pb is "doubly magic".

^cThe magic numbers are those of the cluster-decay product nuclei.

a similar fashion as the alpha particle is assembled (see alpha decay in this chapter) before the cluster penetrates the nuclear potential barrier.

V. NATURALLY OCCURRING RADIONUCLIDES

If we take into account the age of the earth, which is 4.5×10^9 years, and the characteristic property of radionuclide half-life decay, one of the following conditions would have to be met for a natural radioactive nuclide to occur on earth: (1) the radionuclide would be produced continuously on earth or its atmosphere by a natural phenomenon, (2) the radionuclide would be very long-lived, that is, it would have a half-life of the order of $\geq 10^9$ years, or (3) a short-lived radionuclide would be in equilibrium with a naturally occurring long-lived parent radionuclide. The above categories of naturally occurring radionuclides will be subsequently discussed.

A. Radionuclides of Cosmogenic Origin

A number of radionuclides are produced on a continuous basis by the interaction of cosmic-ray particles with nuclei in the earth's atmosphere. The cosmogenic isotopes are created by the interactions of high-energy primary and secondary particles of

cosmic radiation with nuclei of gaseous molecules of the atmosphere (e.g., N₂, O₂, Ar, etc.), resulting in the fragmentation of the target nuclei or by the capture of thermal neutrons of the cosmic radiation showers with target nuclei of the atmosphere (see Section XII.B for additional information on cosmic-ray interactions in the earth's atmosphere). As reported by Lal (2009), most of the cosmic-ray energy (>98%) is dissipated in the earth's atmosphere. Secondary particles of cosmic radiation produce nuclear reactions at a much-reduced rate with the earth's superficial reservoirs, including the hydrosphere, cryosphere, and lithosphere. Cosmogenic radionuclides are produced, therefore, to the greatest extent in the earth's atmosphere. Table 1.5 provides a list of cosmogenic nuclides, their half-lives, rate of production in the atmosphere, and the global mass of these naturally occurring nuclides. Short-lived radionuclides are not included here. Once produced in the atmosphere, radionuclides, such as ³H, ⁷Be, ¹⁰Be, ²⁶Al, and ³⁶Cl, will find their way to the earth's surface; whereas radionuclides in gaseous form, such as ¹⁴CO₂, ³⁷Ar, ³⁹Ar, and ⁸¹Kr, find their way into oceans and rivers via air exchange.

B. Long-lived Radionuclides

Based on the age of the earth (4.5×10^9 years), we can expect that all noncosmogenic radionuclides with a half-life $< 10^8$ years, that were formed during the formation of the earth and

TABLE 1.5 Production Rates of Several Isotopes in the Earth's Atmosphere, Arranged in Order of Decreasing Half-Lives^a

Isotope	Half-life	Production rate (atoms cm ⁻² s ⁻¹)		Global inventory
		Troposphere	Total atmosphere	
³ He	Stable	6.7×10^{-2}	0.2	3.2×10^3 tons ^b
¹⁰ Be	1.5×10^6 y	1.5×10^{-2}	4.5×10^{-2}	260 tons
²⁶ Al	7.1×10^5 y	3.8×10^{-5}	1.4×10^{-4}	1.1 tons
⁸¹ Kr ^c	2.3×10^5 y	5.2×10^{-7}	1.2×10^{-6}	8.5 kg
³⁶ Cl	3.0×10^5 y	4.0×10^{-4}	1.1×10^{-3}	15 tons ^d
¹⁴ C	5730 y	1.1	2.5	75 tons
³⁹ Ar ^e	268 y	4.5×10^{-3}	1.3×10^{-2}	52 kg
³² Si	~ 150 y	5.4×10^{-5}	1.6×10^{-4}	0.3 kg
³ H	12.3 y	8.4×10^{-2}	0.25	3.5 kg
²² Na	2.6 y	2.4×10^{-5}	8.6×10^{-5}	1.9 g
³⁵ S	87 d	4.9×10^{-4}	1.4×10^{-3}	4.5 g
⁷ Be	53 d	2.7×10^{-2}	8.1×10^{-2}	3.2 g
³⁷ Ar	35 d	2.8×10^{-4}	8.3×10^{-4}	1.1 g
³³ P	25.3 d	2.2×10^{-4}	6.8×10^{-4}	0.6 g
³² P	14.3 d	2.7×10^{-4}	8.1×10^{-4}	0.4 g

^aBased on Lal and Peters (1967).^bThe inventory of this stable nuclide is based on its atmospheric inventory, which includes an appreciable contribution from crustal degassing of ³He.^cBased on atmospheric ⁸¹Kr/Kr ratio of $(5.2 \pm 0.4) \times 10^{-15}$.^dIncludes a rough estimate of ³⁶Cl produced by the capture of neutrons at the earth's surface.^eBased on atmospheric ³⁹Ar/Ar ratio of (0.107 ± 0.004) dpm/L Ar (STP).

(From Lal, 2009, Reprinted with permission from Elsevier Publishers)

are not in equilibrium with a parent nuclide in a naturally occurring decay chain (See Section V.C below), would have decayed to an undetectable level. Table 1.6 lists the naturally occurring long-lived radionuclides according to increasing atomic number (Z) together with their half-lives, relative isotope abundances, decay modes, and decay products. Two decay products are listed when there are two modes of decay. All of the decay products are stable with the exception of the decay products of ¹⁴⁸Sm and ¹⁵²Gd, which decay to the very long-lived ¹⁴⁴Nd and ¹⁴⁸Sm, respectively, and ²³²Th, ²³⁵U, and ²³⁸U, which are long-lived parent radionuclides of the thorium, uranium, and actinium decay chains described in Section V.C. Not listed in the table are 10 radionuclides that are exceptionally long-lived. These decay via a double-beta ($\beta\beta$) decay mode with half-lives ranging between 10^{18} and 10^{24} years. Double-beta decay, which is the rarest form of nuclear decay, is discussed further on in this chapter.

C. Natural Radioactive Decay Chains

There are three naturally occurring decay chains, which begin with one of three long-lived parent nuclides. The three decay chains, namely, the ²³²Th or thorium decay chain ($4n$), the ²³⁸U or uranium decay chain ($4n+2$), and the ²³⁵U decay chain or also referred to as the actinium decay chain ($4n+3$) are illustrated in Figs 1.19, 1.20, and 1.21, respectively. The notations

$4n$, $4n+2$, and $4n+3$ refer to the mass number A for all nuclides in the respective decay chains where n is a positive integer between 50 and 60. The notations are derived from the fact that the mass number (A) for all radionuclides in a given decay chain is a multiple of 4, because α -decay results in a mass reduction of 4, whereas the mass number between parent and daughter does not change in β -decay. Thus, the mass numbers in the respective series agree with the relations $4n=A$, $4n+2=A$, and $4n+3=A$, where n is an integer between 50 and 60. There are radionuclides in the decay chains with very short half-lives (of the order of minutes and seconds). These short-lived nuclides have survived the billions of years since the formation of the earth due to an equilibrium that develops between a long-lived parent and its shorter-lived daughters. Equilibrium between parent and daughter nuclides are discussed in detail further on in this chapter. All radionuclides in the thorium, uranium, and actinium decay chains terminate with a stable isotope of lead, namely, ²⁰⁸Pb, ²⁰⁶Pb, and ²⁰⁷Pb, respectively.

VI. ARTIFICIALLY PRODUCED RADIONUCLIDES

There are over 1300 artificially produced radionuclides. These are made by nuclear reactions often facilitated by a nuclear reactor or particle accelerator. A brief historical account of the

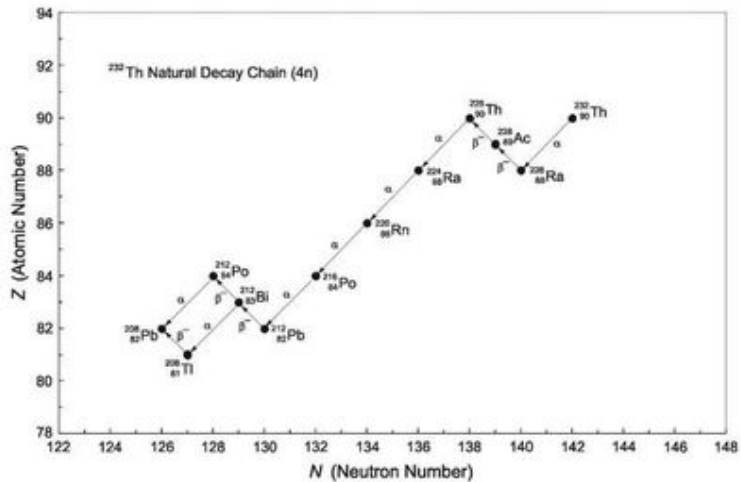
TABLE 1.6 Long-lived Naturally Occurring Radionuclides^a

Nuclide	Half-life (years)	Isotope abundance (%)	Decay mode(s)	Decay product(s)
⁴⁰ ₁₉ K	1.26 × 10 ⁹	0.0117	β ⁻ , EC	⁴⁰ ₂₀ Ca(β ⁻), ⁴⁰ ₁₉ Ar (EC)
⁵⁰ ₂₃ V	1.4 × 10 ¹⁷	0.250	β ⁻ , EC	⁵⁰ ₂₄ Cr(β ⁻), ⁵⁰ ₂₂ Ti (EC)
⁸⁷ ₃₇ Rb	4.88 × 10 ¹⁰	27.835	β ⁻	⁸⁷ ₃₈ Sr
¹¹³ ₄₈ Cd	9.0 × 10 ¹⁵	12.22	β ⁻	¹¹³ ₄₉ In
¹¹⁵ ₄₈ In	4.4 × 10 ¹⁴	95.71	β ⁻	¹¹⁵ ₅₀ Sn
¹²³ ₅₂ Te	1.3 × 10 ¹³	0.908	EC	¹²³ ₅₃ Sb
¹³⁸ ₅₇ La	1.06 × 10 ¹¹	0.0902	β ⁻ , EC	¹³⁸ ₅₈ Ce(β ⁻), ¹³⁸ ₅₆ Ba (EC)
¹⁴² ₅₈ Ce	5.0 × 10 ^{16b}	11.08	α	¹³⁸ ₅₆ Ba
¹⁴⁴ ₆₀ Nd	2.1 × 10 ¹⁵	23.80	α	¹⁴⁰ ₅₈ Ce
¹⁴⁷ ₆₂ Sm	1.06 × 10 ¹¹	15.0	α	¹⁴³ ₆₀ Nd
¹⁴⁸ ₆₂ Sm	7.0 × 10 ¹⁵	11.3	α	¹⁴⁴ ₆₀ Nd
¹⁵² ₆₂ Gd	1.1 × 10 ¹⁴	0.20	α	¹⁴⁸ ₆₂ Sm
¹⁷⁶ ₇₁ Lu	3.8 × 10 ¹⁰	2.59	β ⁻	¹⁷⁶ ₇₂ Hf
¹⁷⁴ ₇₂ Hf	2.0 × 10 ¹⁵	0.162	α	¹⁷² ₇₀ Yb
¹⁸⁰ ₇₃ Ta	>1.2 × 10 ¹⁵	0.012	β ⁻ , EC	¹⁸⁰ ₇₄ W(β ⁻), ¹⁸⁰ ₇₂ Hf (EC)
¹⁸⁷ ₇₅ Re	4.4 × 10 ¹⁰	62.60	β ⁻	¹⁸⁷ ₇₆ Os
¹⁸⁶ ₇₆ Os	2.0 × 10 ¹⁵	1.58	α	¹⁸² ₇₄ W
¹⁹⁰ ₇₈ Pt	6.5 × 10 ¹¹	0.01	α	¹⁸⁶ ₇₆ Os
²³² ₉₀ Th	1.4 × 10 ¹⁰	100.0	α	²²⁸ ₈₈ Ra
²³⁵ ₉₂ U	7.04 × 10 ⁸	0.720	α	²³¹ ₉₀ Th
²³⁸ ₉₂ U	4.46 × 10 ⁹	99.27	α	²³⁴ ₉₀ Th

^aData from Lide (2010).

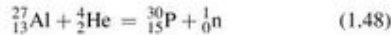
^bHalf-life from Mactarlane and Kohman (1961).

FIGURE 1.19 The ²³²Th natural decay chain.



alpha particles with the aluminum foil produced a new radioactive isotope of short half-life, yet unknown to mankind.

The Joliot-Curies were able to demonstrate that the new isotope was chemically equivalent to elemental phosphorus, and it was radioactive phosphorus. By balancing the transformation of the nuclear reaction between alpha particles and aluminum yielding neutrons, they could write the reaction



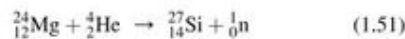
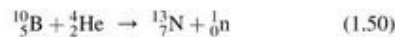
They used the equal sign rather than an arrow for the above reaction to demonstrate that the sum of the mass numbers and atomic numbers on one side of the nuclear reaction should equal those on the other side, *i.e.*, $27 + 4 = 30 + 1$ for the mass numbers and $13 + 2 = 15 + 0$ for the atomic numbers. Expressing nuclear reactions was not a practice at that time. The Joliot-Curies were one of the first to introduce the practice.

The Joliot-Curies demonstrated that the new radioactive isotope of phosphorus emitted positrons. The new radioisotope, phosphorus-30, decays to stable silicon-30 with positron emission and a short half-life of 2.5 minutes according to the following:



Thus, the Joliot-Curies not only produced a previously nonexistent radioisotope, but they were the first to produce positrons in the laboratory as well.

By irradiating other metals, such as boron and magnesium, with alpha particles the Joliot-Curies were able to produce radioactive nitrogen and radioactive silicon according to the following reactions (Joliot-Curie and Joliot, 1934a,b,c):



The radioisotopes of nitrogen and silicon above decay by positron emission.

The Joliot-Curies were awarded the Nobel Prize in Chemistry the very year following the report of these discoveries. The rapid award of the Nobel Prize underscored the impact this discovery had on the scientific community and the advancement of science. Their work established firmly a new branch of chemistry called "radiochemistry". As explained by Frédéric Joliot in his part of the Nobel Lecture

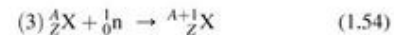
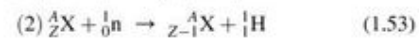
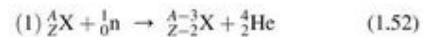
The succession of radioactive transformations provides numerous examples in which the quantities of radio-elements are extremely small and not capable of being weighed, yet nevertheless, by the methods of radiochemistry it has been possible to examine correctly their chemical properties, and identify some of them as being isotopes of elements... This special kind of chemistry in which one handles unweighable quantities, sometimes of the order of 10^{-16} g. is made possible thanks to the fact that one can determine and follow by measuring the radiation emitted, infinitesimal traces of radioactive matter dispersed in the midst of other matter.

While this work established firmly "radiochemistry" as a new branch of chemistry, the Joliot-Curies were the first to coin the terminology, which we are very accustomed to, when

referring to radioactive elements. In their Nobel Lecture, Frédéric Joliot stated

We have proposed that these new radio-elements (isotopes, not found in nature, of known elements) be called radio-nitrogen (for radioactive isotopes of nitrogen), radio-phosphorus (for radioactive isotopes of phosphorus), ...

Only two years after the Joliot-Curies reported the synthesis of radionuclides by the alpha-particle bombardment of nuclei, Enrico Fermi and his coworkers reported the synthesis of new radionuclides by neutron bombardment of nuclei. This work, which was cited earlier in this chapter, yielded 63 previously unknown artificial radionuclides by the following three nuclear reactions:



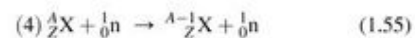
where ${}_Z^AX$ is a symbol for any element X with atomic number Z and mass number A , and n is the symbol for the neutron. Fermi found reactions (1) and (2) to occur chiefly among the light elements, and the reaction of type (3) was found to occur most often among the heavy elements. More than one of the above reactions would sometimes occur when elements were bombarded with neutrons. In Fermi's words at his Nobel Lecture

In many cases the three processes are found at the same time in a single element. For instance, neutron bombardment of aluminum that has a single isotope ${}^{27}\text{Al}$, gives rise to three radioactive products: ${}^{24}\text{Na}$, with a half-life of 15 hours by process (1); ${}^{27}\text{Mg}$, with a period (half-life) of 10 minutes by process (2); and ${}^{28}\text{Al}$ with a period (half-life) of 2 to 3 minutes by process (3).

In addition to the above three neutron reactions described by Fermi, he and his coworkers were also able to observe the production of artificial radioactive isotopes by a fourth process that he described:

The primary neutron does not remain bound in the nucleus, but knocks off instead, one of the nuclear neutrons out of the nucleus; the result is a new nucleus, that is isotopic with the original one and has an atomic weight less by one unit.

This fourth neutron interaction, where the mass number is reduced by one (loss of a neutron) and the atomic number remains unaltered, can be written as follows:



Fermi knew that neutrons, because of their neutral charge, did not have to overcome the Coulombic barrier to penetrate the nucleus of an atom. Furthermore, he discovered that reducing the neutron energy or slowing the neutron down by placing a water or paraffin barrier between a neutron source and its target nuclei, the energy of the neutrons could be reduced to that corresponding to thermal agitation. At this energy state, the slow neutrons could diffuse through target atoms and be captured by the target nuclei. Thus, using slow neutron bombardment, Fermi and his coworkers were able to produce

more than 400 new radioisotopes of all known elements with the exception of hydrogen and helium.

At the same time that Enrico Fermi was producing radionuclides by means of neutron bombardment of target nuclei, Ernest Lawrence was developing the cyclotron capable of accelerating protons, deuterons, and helium nuclei to very high energies. This work, discussed previously in this chapter, yielded many new artificial radionuclides, as the high energy of the accelerated ions could easily penetrate the Coulombic barrier of target nuclei.

The discovery of nuclear fission by Otto Hahn and Fritz Strassman with collaboration of Lise Meitner in 1939 led to the discovery of the first nuclear reactor in 1942 by Enrico Fermi and coworkers. This work was discussed previously in more detail in Section II. Today, the nuclear reactor and the cyclotron are the main instruments for the artificial production of radionuclides. There are now more than 1300 artificially produced radionuclides. Many of these radionuclides are vital for medical diagnosis and treatment, the sterilization of medical implements and supplies, industry, and scientific research.

Elements with atomic number $Z > 92$, which are elements with atomic number higher than that of uranium, are artificially produced. They are all radioactive. By means of the cyclotron, Glenn T. Seaborg pioneered the synthesis of many artificial elements. This work is described in detail in Section II. There are no natural elements beyond $Z = 92$, because they all have half-lives too short to have survived since the formation of the earth. Also, there is the $4n+1$ naturally occurring decay chain. The $4n+1$ decay chain, illustrated in Fig. 1.22, consists of artificially produced radionuclides. It is called the neptunium decay chain after ^{237}Np , which is the longest-lived nuclide of the chain with a half-life of 2.1×10^6 years. There are currently over 20 artificially produced elements.

VII. NUCLEAR REACTIONS

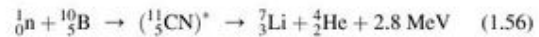
A nuclear reaction is an interaction between two nuclear particles or two nuclei that yields products which are different

from the reactants, that is, new nuclei are formed. If the interacting particles or nuclei only collide and separate without change, the process is referred to as **elastic scattering**. When a nuclear particle collides with a nucleus, but the nucleus only undergoes excitation to a higher energy state, the process is referred to as an **inelastic collision**.

A. Reactions Types

The term nuclear reaction generally refers to the interaction of a projectile particle and a target nucleus that results in the production of a residual (product) nucleus and an ejected particle.

An example of a nuclear reaction, which is also discussed in Chapter 16, is as follows:



In the example provided by Eqn (1.56), a neutron, ${}_0^1n$, collides with the target nucleus ${}_5^{10}\text{B}$, whereby they coalesce to form an excited and unstable compound nucleus (abbreviated as CN^*). The compound nucleus generally is not written, as it is very short-lived ($\sim 10^{-16}$ seconds). In this example, the compound nucleus decays to yield the product nucleus ${}_3^7\text{Li}$ and an ejected alpha particle, ${}_2^4\text{He}$. The sum of the proton numbers and mass numbers must be equal on both sides of the reaction. For example, in Eqn (1.56) the proton numbers $0 + 5 = 3 + 2$ and mass numbers $1 + 10 = 7 + 4$ are equal on both sides of the reaction. As illustrated in Eqn (1.56), there is kinetic energy released in this reaction to the amount of 2.8 MeV. This nuclear reaction is a very practical one, because it is used for the detection of thermal neutrons. The nuclide ^{10}B has a high natural abundance of 20%, and when incorporated into the crystalline structure of a solid scintillator detector, the crystal becomes a sensitive detector for thermal neutrons. The alpha particles ejected as a product of the reaction have a very short range of travel in the crystalline detector. The kinetic energy of the alpha particles is in the MeV range, and they dissipate their

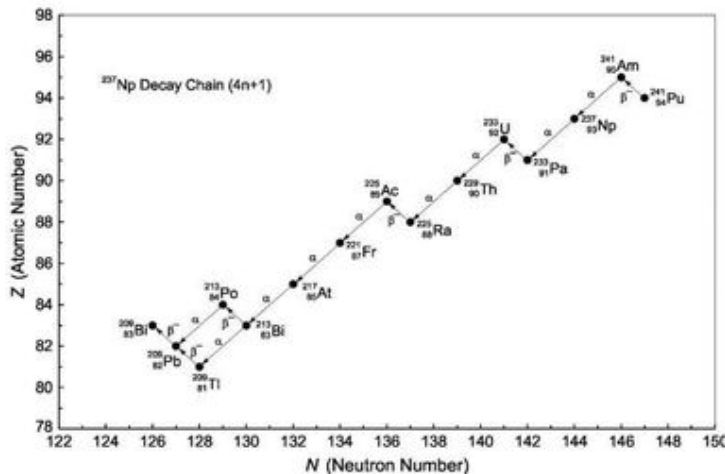


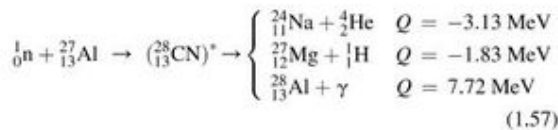
FIGURE 1.22 The Neptunium decay chain.

energy close to the point of neutron interaction. Solid scintillators of this type serve as good thermal neutron detectors.

Nuclear reactions between a specific projectile and target nucleus may result in more than one set of reaction products. For example, in his Nobel Lecture, Enrico Fermi noted the following:

"Neutron bombardment of aluminum, that has a single isotope ^{27}Al , gives rise to three radioactive products: ^{24}Na , with a half-life of 15 h...; ^{27}Mg , with a half-life of 10 min...; and ^{28}Al with a half-life of 2 to 3 min..."

The three reactions described by Fermi may be written as follows:



An intermediary compound nucleus is illustrated as decaying into three possible decay products. The above reactions, that leave behind the residual nuclei of ^{24}Na and ^{27}Mg , have negative Q values. These reactions are endoergic or endothermic. In these two cases, the neutron projectile must possess additional kinetic energy for the reaction to proceed. The reaction, that produces the ^{28}Al residual nucleus, has a positive Q value. This reaction is exoergic or exothermic resulting in a release of energy. Low-energy neutrons, classified as slow or thermal neutrons, are sufficient for this reaction to proceed. The capture of slow neutrons by nuclei is accompanied generally with the immediate emission of one or more gamma-ray photons. The nuclei are left in a state of excitation after the neutron capture; and their ground state is reached after the emission of the gamma-ray quanta. The Q value, as a measure of reaction energy, is discussed in more detail further on in this section.

The above reactions were described as possessing a compound nucleus, and those reactions may be referred to as **compound nuclear reactions**. Two other types of nuclear

reactions are classified as **pickup** and **stripping reactions**. When high-energy nuclear projectiles are used to bombard a target nucleus, the interaction can be more direct whereby the projectile does not interact with all of the nucleons of the target and thus do not reside in a compound nucleus; but rather, the projectile may interact only with a few nucleons in specific nuclear shell-model orbits of the target. In such cases, the projectile may pick up or gain nucleons from the target nucleus in pickup reactions, or the projectile may lose nucleons to the target in stripping reactions. Some early studies of pickup and stripping reactions that may occur in specific nuclear shell-model orbits are the works of Kaschl et al (1970) and Brien et al (1972). Examples of pickup and stripping reactions and the projectile energies at which these reactions were observed are listed in Table 1.7.

Spallation reactions are another class of nuclear reaction, which is gaining increased interest worldwide. Spallation occurs when a high-energy ($> 100 \text{ MeV}$) charged particle, such as a proton, strikes a nucleus whereby it initially "knocks out" several nucleons from the target nucleus within a duration of about 10^{-22} seconds leaving the residual nucleus in an excited state. The excited residual nucleus may then immediately break up into numerous smaller components of smaller nucleons such as helium and lithium nuclei, deuterons, mesons, and individual protons and neutrons, etc. In general, numerous neutrons are emitted from each spallation reaction making this reaction a good neutron source. Nobel Laureate Glenn T. Seaborg is credited with coining the term "nuclear spallation" in his doctoral dissertation in 1937 deriving the word from the verb "spall" meaning to chip or crumble.

Nuclear spallation is a common occurrence in our atmosphere when high-energy cosmic-ray particles of energies ranging from 10^8 to $>10^{20}$ eV strike nuclei in the atmosphere resulting in the fragmentation of nuclei into smaller nucleons constituting the cosmic-ray showers discussed further on in this chapter. Spallation reactions resulting from the interaction of high-energy particles in the cosmic-ray showers colliding with

TABLE 1.7 Examples of Pick-up and Stripping Reactions

Reaction	Condensed notation ^a	Projectile energy	Reference
Pick-up reactions:			
${}^{12}_6\text{C} + {}^1_1\text{H} \rightarrow {}^{13}_6\text{C} + {}^1_1\text{H}$	${}^{12}_6\text{C}(p, d){}^{13}_6\text{C}$	12 MeV	Glover and Jones (1966)
${}^{12}_6\text{C} + {}^1_1\text{H} \rightarrow {}^{11}_5\text{B} + {}^4_2\text{He}$	${}^{12}_6\text{C}(t, \alpha){}^{11}_5\text{B}$	10 MeV	Honda et al. (1965)
${}^{20}_{10}\text{Ne} + {}^1_1\text{H} \rightarrow {}^{19}_9\text{F} + {}^2_1\text{H}$	${}^{20}_{10}\text{Ne}(d, h){}^{19}_9\text{F}$	52 MeV	Kaschl et al. (1970)
${}^{89}_{39}\text{Y} + {}^1_1\text{H} \rightarrow {}^{87}_{38}\text{Sr} + {}^2_1\text{H}$	${}^{89}_{39}\text{Y}(d, \alpha){}^{87}_{38}\text{Sr}$	12 MeV	Brien et al. (1972)
Stripping reactions:			
${}^{12}_6\text{C} + {}^1_1\text{H} \rightarrow {}^{11}_6\text{C} + {}^1_1\text{H}$	${}^{12}_6\text{C}(d, p){}^{11}_6\text{C}$	12 MeV	Glover and Jones (1966)
${}^{12}_6\text{C} + {}^1_1\text{H} \rightarrow {}^{12}_6\text{C} + {}^1_1\text{H}$	${}^{12}_6\text{C}(t, d){}^{12}_6\text{C}$	12 MeV	Glover and Jones (1966)
${}^{27}_{13}\text{Al} + {}^4_2\text{He} \rightarrow {}^{26}_{14}\text{Si} + {}^1_1\text{H}$	${}^{27}_{13}\text{Al}(h, d){}^{26}_{14}\text{Si}$	41 MeV	Munger and Peterson (1978)
${}^{198}_{78}\text{Pt} + {}^4_2\text{He} \rightarrow {}^{195}_{79}\text{Au} + {}^1_1\text{H}$	${}^{198}_{78}\text{Pt}(h, d){}^{195}_{79}\text{Au}$	41 MeV	Munger and Peterson (1978)

^aThe condensed form of writing nuclear reactions is discussed subsequently in this chapter.

nuclei in mineral deposits on the earth's surface are attributed to the cosmogenic production of nuclides, such as, ^{36}Cl (Stone et al, 1996 and Licciardi et al, 2008).

There is current worldwide interest in the artificial production of spallation reactions as neutron sources referred to as spallation neutron sources (SNS). Spallation neutron sources are accelerator-driven systems whereby protons are accelerated to high energies (1 GeV and above), which then collide with heavy metal targets resulting in nuclear spallation with the emission of neutrons useful in research (Słowiński, 2003, Mason et al, 2006, Thomsen, 2007, and Zamani et al, 2008).

Two other nuclear reactions that are very important sources of energy are nuclear fission and nuclear fusion. These are discussed in much detail in other parts of this chapter.

B. Notation

The nuclear reaction, illustrated by the above in Eqn (1.56), may be abbreviated as follows:



which is written in the sequence

target nucleus(projectile, ejected particle)product nucleus. (1.59)

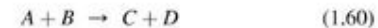
This condensed form of writing the nuclear reaction, as written above in Eqn (1.58), reads as follows: a ^{10}B target nucleus bombarded by neutrons ejects an alpha particle leaving the residual ^7Li nucleus. Particles, which are often projectiles or ejected particle, in nuclear reactions are the following in name and abbreviation in parenthesis: proton (^1_1H or p), neutron (n), deuteron (^2_1H or d), triton (^3_1H or t), helium-3 (^3_2He or h), and helium-4, *i.e.*, the alpha particle (^4_2He or α). Neutrons as projectiles for nuclear reactions with target nuclei are easily available from alpha-particle-induced nuclear reactions, such as the alpha-particle bombardment of beryllium (*i.e.*, $^9_4\text{Be}(\alpha, n)^{12}_6\text{C}$), which provide neutrons with average energies of 5.5 MeV. The nuclear fission reactor is another excellent source of neutrons available as projectile particles to induce nuclear reaction. Accelerators are also good sources of neutrons via spallation reactions induced by high-energy particle collisions with target nuclei. Various sources of neutrons are described further on in this chapter. The cyclotron is an excellent source of high-energy positively charged particles and nuclei, such as protons, deuterons, triton ions, and helium-3 and helium-4 ions. In the cyclotron, target material is placed in the path of the accelerating ion, and numerous radionuclides are made via the nuclear reactions initiated by the bombardment of the positively charged projectiles with the target nuclei.

C. Energy of Reactions (Q Value)

The Q value of a nuclear reaction is a measure of the reaction energy. It is the difference between the kinetic energy of the reaction products and the kinetic energy of the original particles of the nuclear reaction. The Q value for the reaction illustrated above in Eqn (1.56) is reported in the literature to be 2.8 MeV.

The Q values for all nuclear reaction are readily available online at the following website of the National Nuclear Data Centre, Brookhaven National Laboratory: <http://www.nndc.bnl.gov/qcalc/> (NNDC, 2010a,b). At this website it is only needed to identify the projectile, target nucleus and the ejected particle. There is no need to input or identify the residual nucleus on this website, because the calculator can easily deduce the proton number and mass number of the residual nucleus by difference. The calculations made at this website are based on the data maintained by the Atomic Mass Data Center and on atomic mass evaluations reported by Audi et al (2003), Wapstra et al (2003), and Möller, et al (1995). Q values for nuclear reactions are easy to calculate, and the calculation of Q values will be discussed subsequently in this section. The Q value is an important property of a nuclear reaction, because it will tell us whether a reaction will release kinetic energy ($Q > 0$) or lose kinetic energy ($Q < 0$). When $Q = 0$, the reaction is referred to as **elastic scattering** whereby the projectile and target nucleus collide and exchange energy, but they do not undergo any change. When the projectile and target nucleus collide, and part of the kinetic energy of the projectile is transferred to the target nucleus leaving the target at an excited energy state, the reaction is referred to as **inelastic scattering**. There is only energy transfer, but no change in atomic or mass number of the projectile or target nucleus in inelastic scattering reactions.

To arrive at the equation for the calculation of reaction Q values, let us abbreviate the nuclear reaction of Eqn (1.56) in the form



where projectile A bombards nucleus B , which leaves behind a residual nucleus C and ejected particle D . If the total energy of the reactants and products are conserved, we can write

$$E_A + E_B = E_C + E_D \quad (1.61)$$

Also, the total energy (E) of a particle or nucleus is the sum of its kinetic energy (K) and its rest energy (m_0c^2), that is

$$E = K + m_0c^2 \quad (1.62)$$

where m_0 is the particle or nuclear rest mass, and c is the speed of light in a vacuum. Furthermore, if we assume that the target nucleus is at rest, *i.e.*, it has zero kinetic energy, we can transform Eqn (1.61) to

$$K_A + m_Ac^2 + m_Bc^2 = K_C + m_Cc^2 + K_D + m_Dc^2 \quad (1.63)$$

The total kinetic energy released or absorbed in the reaction, Q , is the difference of the kinetic energies of the products and the reactants. In other words, it is the differences in the kinetic energies gotten out of the reaction versus what was put into the reaction, or

$$Q = K_{\text{out}} - K_{\text{in}} \quad (1.64)$$

Then from Eqn (1.63), we can write

$$Q = (K_C + K_D) - K_A = (m_A + m_B)c^2 - (m_C + m_D)c^2 \quad (1.65)$$

In accord with $E = mc^2$, Eqn (1.65) simply states

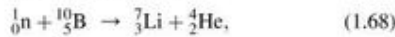
$$Q = E_{0, \text{reactants}} - E_{0, \text{products}} \quad (1.66)$$

where $E_{0, \text{reactants}}$ and $E_{0, \text{products}}$ are the rest energies of the nuclear reactants and products, respectively. Eqns (1.65) and (1.66) may be simplified to read

$$Q = (m_{\text{reactants}})c^2 - (m_{\text{products}})c^2 \quad (1.67)$$

where $m_{\text{reactants}}$ and m_{products} are the combined masses of the nuclear reactants and products, respectively.

For example, in accord with Eqns (1.65) and (1.67), the Q value for the nuclear reaction described previously in Eqn (1.56) and rewritten here in condensed form



would be calculated as follows:

$$Q = (M_{\text{n}} + M_{\text{B}})c^2 - (M_{\text{Li}} + M_{\text{He}})c^2 \quad (1.69)$$

where M_{n} , M_{B} , M_{Li} , and M_{He} are the masses of the neutron and ${}^{10}\text{B}$ reactants and the ${}^7\text{Li}$ and ${}^4\text{He}$ product nuclei, respectively, and c is the speed of light in a vacuum. We may use atomic mass units (u) taken from standard reference tables since the 5 atomic electron masses of the reactants and the product nuclides are included on both sides of the equation. Thus, using atomic mass units in Eqn (1.69) gives

$$Q = \left\{ \begin{array}{l} (1.00866492 \text{ u} + 10.012937 \text{ u})(931.494 \text{ MeV/u}) \\ - (7.016004 \text{ u} + 4.00260325 \text{ u})(931.494 \text{ MeV/u}) \end{array} \right\}$$

$$Q = 2.79 \text{ MeV}$$

The Q value is positive. Thus, energy is released in the nuclear reaction. When Q is positive, the reaction is called **exoergic**. In such a case, the reaction releases kinetic energy by conversion of some of the rest mass to kinetic energy according to

$$E_{\text{Total}} = E_K + m_0c^2 \quad (1.70)$$

Reactions with a positive Q value ($Q > 0$) are also called **exoergic** or **exothermic**, since kinetic energy is released. When the Q value is negative ($Q < 0$) the reaction is called **endoergic** or **endothermic**, as kinetic energy would be absorbed in the reaction. In such a case, the reaction could not take place unless energy is added to the reactant particle or projectile. For example, let us calculate the Q value of the following nuclear reaction used by Ernest Rutherford (1919) whereby he discovered the proton:



$$Q = (M_{\text{He}} + M_{\text{N}})c^2 - (M_{\text{O}} + M_{\text{H}})c^2$$

$$Q = \left\{ \begin{array}{l} (4.00260325 \text{ u} + 14.00407401 \text{ u})(931.494 \text{ MeV/u}) \\ - (16.9991315 \text{ u} + 1.007825031 \text{ u})(931.494 \text{ MeV/u}) \end{array} \right\}$$

$$Q = -1.192 \text{ MeV} \quad (1.72)$$

The reaction is endoergic ($Q < 0$) or endothermic, that is, energy is absorbed in the reaction. The reaction would require at least 1.192 MeV of energy to occur. Since the target nucleus is at rest, it is the projectile particle or nucleus that would carry the

kinetic energy needed for the reaction to take place. Furthermore, there is a threshold energy (E_{th}), which is by definition the minimum bombarding energy that the projectile particle must possess when Q is negative ($Q < 0$) for the reaction to take place. The threshold energy is calculated by the following equation, derived by Evans (1955):

$$E_{\text{th}} = -Q \left(\frac{M_1 + M_2}{M_2} \right) \quad (1.73)$$

where M_1 and M_2 are the masses of the projectile particle and target nucleus, respectively, as illustrated in Fig. 1.23. Using the Q value of -1.192 MeV, we can calculate the threshold energy of the alpha-particle projectile for Reaction (1.71) to take place as follows:

$$E_{\text{th}} = -(-1.192 \text{ MeV})$$

$$\times \left[\frac{(4.00260325 \text{ u} + 14.00307401 \text{ u})(931.494 \text{ MeV/u})}{(14.00307401 \text{ u})(931.494 \text{ MeV/u})} \right]$$

$$= 1.533 \text{ MeV} \quad (1.74)$$

The calculated threshold alpha-particle projectile energy of 1.533 MeV would be required for Reaction 1.71 to take place. Rutherford (1919) used alpha particles from radium C', which is today known as ${}^{214}\text{Po}$. The alpha particles from ${}^{214}\text{Po}$ have energies of 7.8 MeV well above the threshold energy for Reaction 1.71 to take place.

The projectile particle M_1 of Eqn (1.73) is illustrated in Fig. 1.23 traveling in the direction of the target nucleus M_2 , which forms an intermediate compound nucleus M_C , which has a mass equivalent to the combined masses of the projectile particle and target nucleus. The compound nucleus then dissociates into an ejected particle M_3 and a residual nucleus M_4 . Due to the very short lifetime of the combined nucleus ($\sim 10^{-22}$ seconds) or of an intermediate system that does not consist of the formation of a compound nucleus, Evans (1955) reports that M_C loses no appreciable energy due to ionization prior to dissociation into M_3 and M_4 . When particle M_3 is ejected at an

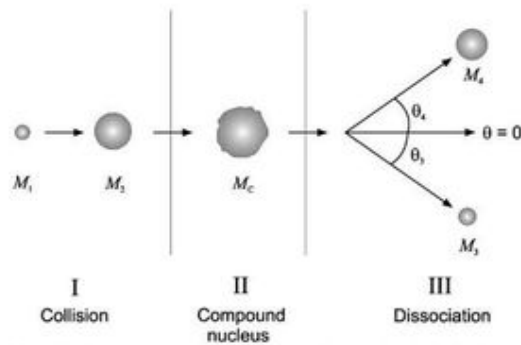


FIGURE 1.23 Three stages of a nuclear reaction, namely, (I) Collision where a projectile particle of mass M_1 collides with a target nucleus of mass M_2 forming a (II) Compound or intermediate nucleus M_C of mass equivalent to the combined masses of the projectile and target nucleus, and (III) Dissociation of the compound nucleus resulting in an ejected particle of mass M_3 and residual nucleus of mass M_4 expelled at angles θ_3 and θ_4 , respectively.

angle $\theta_3 = 0$, the energy of the projectile particle is at the minimum or threshold energy E_{th} . As the projectile particle energy is raised over the threshold energy, the ejected particles M_3 begin to appear at $\theta_3 > 0$.

D. Reaction Cross Section

The reaction cross section is, by definition, the measure of the probability that a nuclear reaction or process will occur. The cross section has units of area (cm^2), and the term reaction cross section is used, because it is a term that depicts the effective area of the target nucleus. It is not a measure of the true cross section of a target nucleus; rather, it is a measure of the effectiveness of the target nucleus to increase or reduce the probability of a nuclear reaction with a projectile particle. The larger the measured effective area or cross section of the target nucleus, the greater will be the probability that a projectile particle will hit or interact with the target nucleus. The probability, that a projectile particle collides with a target nucleus, will depend on the rate at which the projectile particles are bombarding the target material, that is, the particle beam intensity ($I = \text{projectile particles/second}$), the number of target nuclei in the target material or the target nuclei density ($n = \# \text{ of nuclei/cm}^3$), the effective area of the target nucleus, that is, the cross section (σ) of the target nucleus (cm^2), and the thickness of the target material (cm). The variables affecting the probability of a nuclear reaction and consequently the rate of the reaction are illustrated in Fig. 1.24

The rate of a nuclear reaction is a function of the effective target area exposed to the projectile particle beam. The effective target area is a product of the total number of target nuclei in the target material and the reaction cross section (σ) of the target nuclei. The number ($\#$) of target nuclei in the target material is dependent on the density of the target nuclei and the target volume, that is,

$$\# \text{ of target nuclei} = n(Ax) \quad (1.75)$$

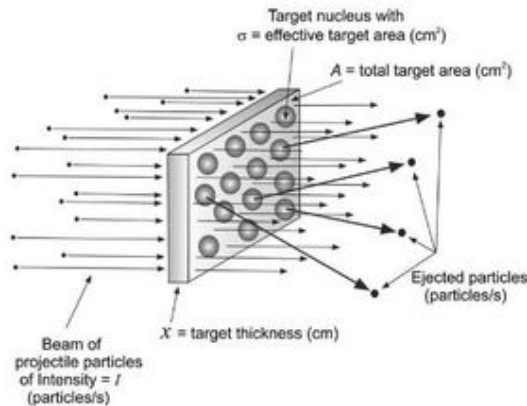


FIGURE 1.24 Reaction target area. A beam of projectile particles bombards a material containing target nuclei of cross section (σ). Some of the projectile particles react with the target nuclei resulting in the ejection of particles as products of the nuclear reaction. The reaction rate is measured by a detector sensitive to the ejected particles.

where n in the target nuclei density ($\# \text{ of nuclei/cm}^3$), A is the target area (cm^2), and x is the target thickness (cm). The effective target area is then calculated as

$$\text{Effective target area} = (\# \text{ of target nuclei})(\sigma) \quad (1.76)$$

$$= n(Ax)\sigma \quad (1.77)$$

We can reason that the rate of the reaction is related to the particle beam intensity as the effective target area is to the total target area, or

$$\frac{\text{Rate of reaction (particles/s)}}{\text{Beam intensity (particles/s)}} = \frac{\text{Effective target area (cm}^2\text{)}}{\text{Total target area (cm}^2\text{)}} \quad (1.78)$$

or

$$\frac{R}{I} = \frac{n(Ax)\sigma}{A} \quad (1.79)$$

and

$$R = In\sigma x \quad (1.80)$$

where R in the rate of the reaction (ejected particles/s), I is the projectile beam intensity (projectile particles/s), n is the density of target nuclei ($\# \text{ of target nuclei/cm}^3$), σ is the reaction cross section (cm^2), and x is the target thickness (cm). The cross section may be determined experimentally from the reaction rate, projectile beam intensity, target nuclei density, and the target thickness. As described in the previous section on reaction Q value, the rate of a nuclear reaction will depend also on the energy of the projectile particles bombarding the target nuclei. Thus, reaction cross sections are reported together with the projectile particle energy (Kelly et al, 2005, He et al, 2006, Janczyszyn et al, 2006, Zhou et al, 2010, and Madani et al, 2010). Thorough treatments of reaction cross section are given by Evans (1955), Friedlander et al (1964), and Serway et al (2005).

The common unit of measure for the reaction cross section is the barn where $1 \text{ barn} = 1 \times 10^{-24} \text{ cm}^2$. This measure of cross section was first used by Baker et al (1943) and proposed by Marshall P. Holloway and Charles P. Baker (1944) as the unit of measure for the cross section in secret technical reports of the Los Alamos National Libraries during the Manhattan Project. Holloway and Baker (1944, 1972) reported that, while measuring reaction cross sections at Purdue University, they tried to come up with a suitable unit of measure. They thought of the word "Oppenheimer", but discarded the idea because of the word's length. They also considered the "Bethe", but discarded that, because of possible confusion with the widespread use of "beta". They also considered using the name "John" after John Manley, who headed the Purdue Project, and also discarded that because that word had widespread use for purposes other than the name of a person. One of the authors had a rural background, and on farms in the countryside, the barn was always the largest building, which could be seen at a distance. There was then the very common colloquial term "big as a barn", and the term is still used today. It was a common saying then to sportsmen, who had poor aim such as poor marksman,

archers, or golfers, that “they couldn’t hit the side of a barn”. Barns were built generally longer than they were wide, and thus the side or length of a barn was the largest part of a barn. They reported then that the unit “barn” was appropriate, because a cross section of 10^{-24} cm² for nuclear processes was very large and really “as big as a barn”. Submultiples and multiples of the barn are also used, such as the millibarn (mb = 10^{-3} barns) and the kilobarn (kb = 10^3 barns).

Two very important nuclear reactions that are vital energy sources are nuclear fission and fusion. These are discussed in detail in other parts of this chapter.

VIII. PARTICULATE RADIATION

All types of nuclear radiation over all ranges of energy will have a dual nature, that of a particle and a wave. Earlier in this chapter the work of Louis Victor de Broglie was described, whereby he demonstrated that all particles of known rest mass (e.g., alpha particles, beta particles, neutrons, etc.) would, in motion, display the properties of a wave with a wavelength inversely proportional to the particle momentum. For the purpose of classifying radiation in this chapter, particulate radiation will be all types of radiation that have a known mass at rest.

A. Alpha Decay

Alpha decay is the nuclear decay process whereby the parent nucleus emits an alpha particle. The alpha particle, structurally equivalent to the nucleus of a helium atom and denoted by the Greek letter α , consists of two protons and two neutrons. Alpha particles are emitted as decay products of many radionuclides predominantly of atomic number greater than 83 (See Appendix A, Table of Radioactive Isotopes).

1. Energy and Half-life Relationship

Alpha particles are emitted by radionuclides with distinct energies that range between 4 and 10 MeV; and half-lives of the nuclides will vary over a wide range of time from 10^{10} years to microseconds. Radionuclides emitting alpha particles of low energy decay with long half-lives, whereas those emitting alpha particles of high energy have short half-lives.

A relationship between alpha-decay energy and the half-life of the nuclide was recognized very early in the history of the study of radionuclide decay. German physicist Hans (Johannes Wilhelm) Geiger, best known for the Geiger–Müller counter, and British physicist John Mitchell Nuttall (Geiger and Nuttall, 1911) were the first to measure a relationship between alpha-particle energy and half-life decay of even-Z even-A radionuclides, that is, radionuclides that had an even number of protons and even atomic number. By correlating half-life measurements with the range of alpha particles emitted by several radionuclides, Geiger and Nuttall (1911) determined the best-fit linear relationship between the two variables and reported the following equation, which is known as the Geiger–Nuttall law:

$$\log \lambda = a \log R + b \quad (1.81)$$

where λ is the radionuclide decay constant, R is the alpha-particle range (cm), and a and b are constants that provided the best fit to the experimental data. Since $\lambda = 0.693/t_{1/2}$, where $t_{1/2}$ is the half-life (see Eqn (1.420) in this chapter), it is clear from Eqn (1.81) that for shorter values of $t_{1/2}$ there are correspondingly increasing magnitudes of the alpha-particle range (R). The range of travel of the alpha particle is proportional to its energy. Consequently, the Geiger–Nuttall law provided a correlation between radionuclide decay half-life and alpha decay energy. Other variations of the best fit equation were reported subsequently to the work of Geiger and Nuttall, which provided best-fit empirical equations for specific radionuclide decay series (Beckerly, 1945), but the correlation of half-life decay and decay energy remained the same.

Alpha-decay energy and half-life of heavy elements of even Z even A were studied by Perlman and Ypsilantis (1950) on the basis of the shell structure of nuclei. They found a direct and exponential relationship between half-life and alpha-decay energy for many even Z even A radioisotopes of the heavy elements, which is illustrated in Fig. 1.25

Radionuclides that are not even Z and even A (i.e., even Z odd N , odd Z even N , or odd Z odd N) also obey the general rule whereby nuclides with low alpha-decay energy exhibit long half-lives, and nuclides with high alpha decay energy exhibit short half-lives. However, these nuclides exhibit longer half-lives than even–even nuclides, because these nuclides must first transition to an excited state prior to the formation of the alpha particle, which is an even–even nucleus of two protons and two neutrons. The alpha particle must be assembled within the nucleus from proton and neutron nuclear shells; and the transition to the excited nuclear state will prolong the nuclear decay to yet longer half-lives (Perlman et al, 1950, Evans, 1955 and Loveland, 2004).

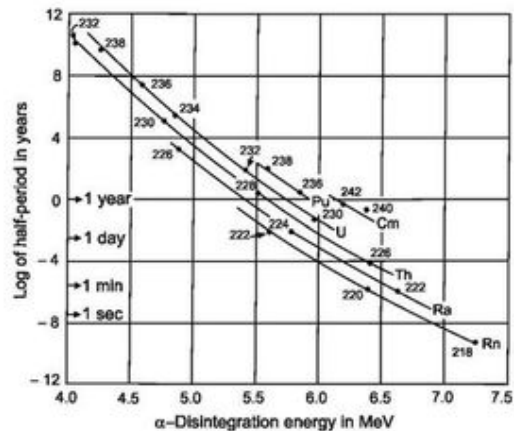


FIGURE 1.25 Observed values of half-life (half-period) and total alpha decay energy for each nuclide. The mass number of the radioactive parent nuclide is given at each point. The curves represent the theoretical values for radioactive parents having the same atomic number (isotopes). The range in half-life for the radionuclides in the curves provided are 35 ms for ²¹⁸Rn to 1.4×10^{10} y for ²³²Th. (From Perlman and Ypsilantis, 1950; reprinted with permission © 1950 American Physical Society.)

The shorter half-lives exhibited by radionuclides with high alpha-decay energies compared to the longer half-lives of nuclides with lower decay energies are explained on the basis of the nuclear potential barrier, that the alpha particle must overcome to penetrate or escape from the nucleus. By bombarding a thin foil of uranium with 8.75 MeV alpha particles, Ernest Rutherford (1927) demonstrated that the high-energy alpha particles were scattered by the uranium nuclei at a distance of 30×10^{-13} cm from the center of the nucleus, as illustrated in Fig. 1.26. A Coulomb potential barrier, which is inversely proportional to the distance from the center of the nucleus, repels incoming alpha particles as well as inhibits their escape from the nucleus. Question therefore arose as to how alpha particles, which are emitted from decaying nuclei with energies as low as 4 MeV, escape from the nucleus. George Gamow (1928) and Gurney and Condon (1928) independently used Schrödinger's wave mechanics to demonstrate that, within the nucleus, the alpha particle as a wave need not pass over the Coulomb barrier, but that the alpha-particle wave could tunnel its way through the potential barrier and escape from the nucleus. The probability of the alpha-particle escape will be a function of the energy of the alpha particle and the amount of potential barrier that the alpha particle must overcome. Alpha-decay energies, among all of the alpha-decaying radionuclides, vary between approximately 4 and 10 MeV. A high alpha-decay energy yields alpha particles with less Coulomb barrier to overcome, which augments the probability for alpha-particle escape resulting in a shorter half-life. The opposite would be the case for a low alpha decay energy, which would yield alpha particles with a greater Coulomb barrier or reduced

penetrability and thus lower probability of escape, resulting in a longer decay time or half-life.

2. Decay Energy

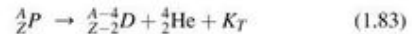
The decay energy is a common term used for all modes of nuclear decay, and it is the energy released in nuclear decay. The energy released in alpha decay will be reviewed in this section and the decay of ^{241}Am will be taken as an example.

The radionuclide americium-241 decays by alpha particle emission to yield the daughter nuclide ^{237}Np according to the following scheme:



The loss of two protons and two neutrons from the americium nucleus results in a mass reduction of four and a charge reduction of two on the nucleus. In nuclear equations such as the preceding one, the subscript denotes the charge on the nucleus (*i.e.*, the number of protons or atomic number, also referred to as the *Z* number) and the superscript denotes the mass number (*i.e.*, the number of protons plus neutrons, also referred to as the *A* number). The energy liberated during nuclear decay is referred to as the decay energy. Many reference books report the precise decay energies of radioisotopes. The value reported by Holden (1997a) in the Table of Isotopes for the decay energy of ^{241}Am , illustrated in Eqn (1.82), is 5.638 megaelectron volts (MeV).

The alpha decay equation may be described in general terms as follows:



where $^A_Z P$ is the parent nucleus of atomic number *Z* and mass number *A*, $^{A-4}_{Z-2} D$ is the daughter nucleus of atomic number *Z* - 2 and mass number *A* - 4, $^4_2 \text{He}$ is the alpha particle equivalent to a helium nucleus, and K_T is the total kinetic energy released in the alpha decay. The total kinetic energy released, also referred to as the decay energy (Q_α), is shared between the alpha particle, recoil daughter nucleus, and gamma radiation or

$$Q_\alpha = K_T = E_\alpha + E_{\text{recoil}} + E_\gamma \quad (1.84)$$

where E_α is the kinetic energy of the alpha particle, E_{recoil} is the kinetic energy of the recoil daughter nucleus, and E_γ is the energy lost as gamma radiation from the daughter nucleus, when the daughter nucleus is left at an excited energy state and decays to its ground state. We will use the symbol "E" for kinetic energy, rather than "K", when referring to the kinetic energy of particulate radiation and recoil nuclei, as it is the symbol most commonly used, and the kinetic energy is inferred. The decay energy is represented by *Q* as the "Q value" described previously in this chapter. The decay energy of 5.638 MeV of Eqn (1.82) above may be written as Q_α for alpha-decay energy, which may be composed of the energies of the alpha-particle, recoil daughter nucleus, and gamma radiation described in Eqn (1.84). Energy and mass are conserved in the decay process; that is, the energy liberated in radioactive decay is equivalent to the loss of mass by the parent radionuclide (*e.g.*, ^{241}Am) or, in other words, the difference in masses between the parent radionuclide and the product nuclide and particle.

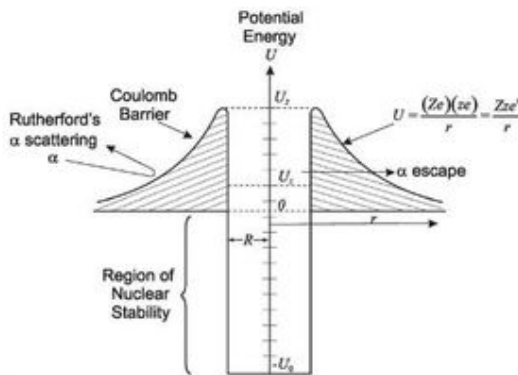


FIGURE 1.26 Nuclear potential barrier and potential energy well based on schematics of Gamow (1950) and Evans (1955). The nuclear radius is from 0 to *R*; and the distance from the center of the nucleus is *r*. The potential energy of the bound nucleus within the well is considered constant from $-U_0$ to 0. The Coulomb potential barrier *U* is inversely proportional to the distance from the center of the nucleus according to $U = (Ze)(ze)/r$ or Zze^2/r where *Z* is the atomic number or charge on the nucleus and *z* is the proton number of the alpha particle (*z* = 2). Excess energy of the unstable nucleus, required for alpha-particle emission, is represented by the energy level U_1 along the potential energy scale; and the height of the potential barrier occurs at U_2 where $r = R$. For a perspective on the nuclear dimensions, data from Evans (1955) for the uranium nucleus (*Z* = 92) are the following: $R \approx 9.3 \times 10^{-13}$ cm, $U_1 \approx 4$ MeV, and $U_2 \approx 28$ MeV.

We can calculate the energy liberated in the decay of ^{241}Am , as well as for any radionuclide decay, by accounting for the mass loss in the decay equation. Using Einstein's equation for equivalence of mass and energy

$$E = mc^2 \quad (1.85)$$

we can write the general equation for the energy equivalence to mass loss as

$$Q = (\text{mass of parent nuclide} - \text{mass of decay products})c^2 \quad (1.86)$$

For the decay of ^{241}Am described in Eqn (1.82) above, we can write Eqn (1.86) as

$$Q_\alpha = (M_{^{241}\text{Am}} - M_{^{237}\text{Np}} - M_\alpha)c^2 \quad (1.87)$$

where Q_α is the disintegration or alpha-decay energy, $M_{^{241}\text{Am}}$, $M_{^{237}\text{Np}}$, and M_α are the masses of ^{241}Am , ^{237}Np , and the alpha particle, and c is the speed of light in a vacuum. We may use atomic mass units (u) for the calculation, because the electron masses included with atomic mass units may be ignored. The number of electrons on both sides of the decay Eqns (1.82) and (1.83) are equal, and we can ignore the negligible differences in the binding energies of the electrons. When the nuclide masses are expressed in the more convenient atomic mass units (u), the energy liberated in decay equations can be calculated in units of megaelectron volts according to the equation

$$Q_\alpha = (M_{^{241}\text{Am}} - M_{^{237}\text{Np}} - M_\alpha)(931.494 \text{ MeV/u}) \quad (1.88)$$

The precise atomic mass units obtained from reference tables (Holden, 1997a) can be inserted into Eqn (1.88) to obtain

$$\begin{aligned} Q_\alpha &= (241.056822\text{u} - 237.048166\text{u} - 4.00260325\text{u}) \\ &\times (931.494 \text{ MeV/u}) = (0.00605275\text{u})(931.494 \text{ MeV/u}) \\ &= 5.638 \text{ MeV} \end{aligned}$$

The energy liberated is shared between the daughter nucleus and the α -particle. If the parent nuclide (e.g., ^{241}Am) is at rest when it decays, most of the decay energy will appear as kinetic energy of the liberated less-massive α -particle and only a small fraction of the kinetic energy remaining with the recoiling massive daughter nuclide (e.g., ^{237}Np). The kinetic energy of the recoiling daughter nuclide is comparable to that of a recoiling canon after a shell is fired, with the shell being analogous to that of the α -particle shooting out of the nucleus. Fig. 1.27 illustrates the transitions involved in the decay of ^{241}Am . The interpretation of this figure is given in the following paragraph. There are five major α -particle transitions in the decay of ^{241}Am , each involving an α -particle emission at different energies and relative intensities. These are illustrated in Fig. 1.27. The decay energy of 5.638 MeV for ^{241}Am calculated above and reported in the literature is slightly higher than any of the α -particle energies provided in Fig. 1.27. This is because there remains also the recoil energy of the daughter nucleus and any gamma-ray energy that may be emitted by the daughter, when its nucleus remains at an excited state. The emission of gamma radiation often accompanies radionuclide decay processes that occur by alpha-particle emission. Gamma

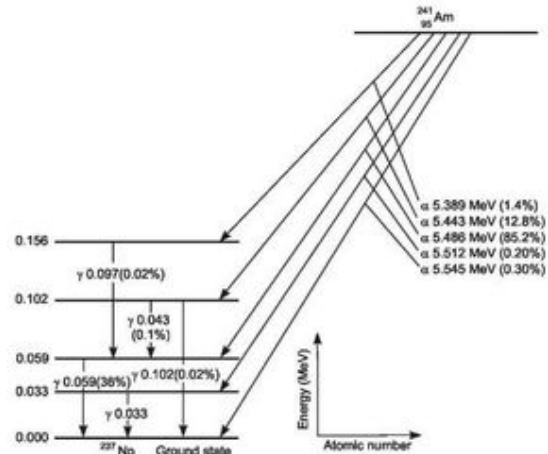


FIGURE 1.27 Decay scheme of ^{241}Am . The relative intensities of alpha-particle and gamma-ray emissions are expressed in percent beside the radiation energy values in MeV.

radiation is described in Section IX.B. The recoil energy, E_{recoil} , of the daughter nucleus can be calculated by the equation

$$E_{\text{recoil}} = (M_\alpha/M_{\text{recoil}})E_\alpha \quad (1.89)$$

which is derived in Section XI.A.2.a, where M_α is the mass of the alpha particle as defined in Eqn (1.87), M_{recoil} is the mass of the recoil nucleus, and E_α is the α -particle energy. For example, the recoil energy of the ^{237}Np daughter nucleus for the transition of the 5.545 MeV alpha particle (Fig. 1.27) can be calculated according to Eqn (1.89) as

$$\begin{aligned} E_{\text{recoil}} &= (4.00260325\text{u}/237.048166\text{u})5.545\text{MeV} \\ &= (0.0168851897)(5.545 \text{ MeV}) \\ &= 0.0936 \text{ MeV} \end{aligned}$$

The transition energy, E_{trans} , for the above α -particle emission is the sum of the α -particle and recoil nuclear energies or

$$\begin{aligned} E_{\text{trans}} &= E_\alpha + E_{\text{recoil}} = 5.545 \text{ MeV} + 0.0936 \text{ MeV} \\ &= 5.638 \text{ MeV} \end{aligned} \quad (1.90)$$

In the above case, the transition energy turns out to be equal to the reported and calculated decay energy, because as illustrated in Fig. 1.27, the ^{241}Am radionuclides decay directly to the ground state whenever 5.545 MeV α -particles are emitted. This is not the case when α -particles of other energies are emitted from ^{241}Am . If we take, for example, the 5.486 MeV α -particle transition of Fig. 1.27, the decay energy, E_{decay} , would be the sum of the transition energy plus gamma-ray energy, E_γ , emitted from the daughter nucleus or

$$\begin{aligned} E_{\text{decay}} &= E_{\text{trans}} + E_\gamma = E_\alpha + E_{\text{recoil}} + E_\gamma \\ &= E_\alpha + (M_\alpha/M_{\text{recoil}})E_\alpha + E_\gamma \\ &= 5.486 \text{ MeV} + (4.00260325\text{u}/237.048166\text{u}) \\ &\times (5.486 \text{ MeV}) + 0.059 \text{ MeV} \\ &= 5.486 \text{ MeV} + 0.0926 \text{ MeV} + 0.059 \text{ MeV} \\ &= 5.638 \text{ MeV} \end{aligned} \quad (1.91)$$

The gamma-ray energy emitted from the daughter nucleus for the 5.486 MeV α -particle transition in ^{241}Am decay is found in Fig. 1.27. Gamma-ray energy values of other radionuclides are available from Appendix A and reference tables (Browne et al. 1986, Firestone et al. 1996 and Lederer and Shirley et al. 1978).

As described in the previous paragraphs, alpha particles are emitted with a certain quantum of energy as the parent nuclide decays to a lower energy state. The energy emitted from radionuclides as nuclear radiation can be described by a decay scheme such as that given in Fig. 1.27. Decay schemes are written such that the energy levels of the nuclides are plateaus along the ordinate, and these energy plateaus are distributed along the abscissa according to atomic number. The alpha particles, as the example shows (Fig. 1.27), are emitted with certain magnitudes of kinetic energy, which is most often expressed in units of kiloelectron volts (keV) or mega-electron volts (MeV). The definition of the electron volt (eV) is given in Section III.C. The energies of alpha particles from most nuclear decay reactions fall within the range 1–10.5 MeV.

Alpha particles are emitted from unstable nuclei with discrete quanta of energy, often leaving the daughter nuclide at an excited energy state. In such cases, when the daughter nuclide occurs at an elevated energy state, it may reach the ground state via the emission of energy in the form of electromagnetic gamma radiation as illustrated in Fig. 1.27.

The nuclei of daughter atoms of alpha particle-emitting nuclides are often unstable themselves and may decay by further alpha- or beta-particle emission. Thus, alpha particle-emitting nuclides may consist of a mixture of radionuclides, all part of a decay chain, as illustrated in Figs 1.19–1.22 described previously in this chapter. Additional reading on radionuclide alpha decay is available from Das and Ferbel (1994).

3. Alpha-particle Interactions with Matter

Now consider what happens to an alpha particle that dissipates its kinetic energy by interaction with matter. Alpha particles possess a double positive charge due to the two protons present. This permits ionization to occur within a given substance (solid, liquid, or gas) by the formation of ion pairs due to Coulombic attraction between a traversing alpha particle and atomic electrons of the atoms within the material the alpha particle traverses. The two neutrons of the alpha particle give it additional mass, which further facilitates ionization by Coulombic interaction or even direct collision of the alpha particle with atomic electrons. The much greater mass of the alpha particle, 4 atomic mass units (u), in comparison with the electron (5×10^{-4} u) facilitates the ejection of atomic electrons of atoms through which it passes, either by direct collision with the electron or by passing close enough to it to cause its ejection by Coulombic attraction. The ion pairs formed consist of the positively charged atoms and the negatively charged ejected electrons. The alpha particle continues along its path suffering, for the most part, negligible deflection by these collisions or Coulombic interactions because of the large difference in mass between the particle and the electron. An exception will be a less common (~ one in a few thousand) deflection or scattering of the alpha particle due to a direct collision with the Coulombic

barrier of an atomic nucleus. Thus, an alpha particle travels through matter producing thousands of ion pairs (see the following calculation) in such a fashion until its kinetic energy has been completely dissipated within the substance it traverses.

In air, an alpha particle dissipates an average of 35 eV (electron volts) of energy per ion pair formed. Before it stops, having lost most of its energy, an alpha particle produces many ion pairs. For example, as a rough estimate, a 5-MeV alpha particle will produce 1.4×10^5 ion pairs in air before coming to a stop:

$$\frac{5 \times 10^6 \text{ eV}}{35 \text{ eV/ion pair}} = 1.4 \times 10^5 \text{ ion pairs in air} \quad (1.92)$$

The thousands of interactions between a traveling alpha particle and atomic electrons can be abstractly compared with a rolling bowling ball colliding with stationary ping-pong balls. Because of the large mass difference of the two, it will take thousands of ping-pong balls to stop a bowling ball. The additional stopping power of electrons is the binding energy of the atomic electrons.

The amount of energy required to produce ion pairs is a function of the absorbing medium. For example, argon gas absorbs approximately 25 eV per ion pair formed and a semiconductor material requires only 2–3 eV to produce an ion pair. Ionization is one of the principal phenomenon utilized to detect and measure radionuclides; and it is treated in more detail in subsequent chapters. The energy threshold for ion-pair formation in semiconductor materials is approximately 10 times lower than in gases, which gives semiconductor materials an important advantage as radiation detectors (see Chapter 5) when energy resolution in radioactivity analysis is an important factor.

In addition to ionization, another principal mechanism by which alpha particles and charged particles, in general, may impart their energy in matter is via electron excitation. This occurs when the alpha particle fails to impart sufficient energy to an atomic electron to cause it to be ejected from the atom. Rather, the electrons of atoms of a given material may absorb a portion of the alpha particle energy and become elevated to a higher energy state. Depending on the absorbing material, the excited atoms of the material may immediately fall back to a lower energy state or ground state by dissipating the absorbed energy as photons of visible light. This process, referred to as fluorescence, was first observed by Sir William Crookes in London in 1903 and soon confirmed by Julius Elster and Hans Geitel the same year in Wolfenbüttel, Germany (Elster and Geitel, 1903). They observed fluorescence when alpha particles emitted from radium bombarded a zinc sulfide screen. In darkness, individual flashes of light were observed and counted on the screen with a magnifying glass with the screen positioned a few millimeters from the radium source. The phenomenon of fluorescence and its significance in the measurement of radionuclides are discussed in subsequent chapters. Thus, as described in the previous paragraphs, alpha particles as well as other types of charged particles dissipate their energy in matter mainly by two mechanisms, ionization and electron excitation.

Because the atomic "radius" is so very much bigger ($\approx 10^{-10}$ m) than the "radius" of the nucleus ($\approx 10^{-14}$ m), the

interactions of alpha particles with matter via direct collision with an atomic nucleus are few and far between. In this case, though, the large mass of the nucleus causes deflection or ricocheting of the alpha particle via Coulombic repulsion without generating any change within the atom. Such a deflection was discovered in the early part of this century by Ernest Rutherford and his students Hans Geiger and Ernest Marsden in an experiment discussed previously in detail in Section II.

Scattering of alpha particles at angles of less than 90° may occur by Coulombic repulsion between a nucleus and a particle that passes in close proximity to the nucleus. These deflected particles continue traveling until sufficient energy is lost via the formation of ion pairs. The formation of ion pairs remains, therefore, the principal interaction between alpha particles and matter.

The high mass and charge of the alpha particle in relation to other forms of nuclear radiation give it greater ionization power, but a poorer ability to penetrate matter. In air, alpha particles may travel only a few centimeters. This short range of travel varies depending on the initial energy of the particle. For example, a 5.5-MeV alpha particle, such as that emitted by the radionuclide ²⁴¹Am previously described, has a range of approximately 4 cm in dry air at standard temperature and pressure, as estimated by empirical formulas, such as Eqns (1.93) and (1.94) provided below:

$$R_{\text{air}} = (0.005E + 0.285)E^{3/2} \quad (1.93)$$

where R is the average linear range in cm of the alpha particle in air and E is the energy of the particle in MeV. The empirical formula is applied for alpha particles in the energy range 4–15 MeV. According to calculations of Fenyves and Haiman (1969), the ranges of alpha particles with energies between 4 and 7 MeV can be estimated by using a simplified version of Eqn (1.93) as follows:

$$R_{\text{air}} = 0.3E^{3/2} \quad (1.94)$$

Ranges of alpha particles in air over a more wide range of alpha-particle energy can be obtained from Figs B.1 and B.2 of Appendix B. A thorough treatment of range calculations for charged particles is available from Fenyves and Haiman (1969). The approximate 4-cm range of 5.5-MeV alpha particles in air is illustrated in Fig. 1.28. There is no abrupt drop in the number of alpha particles detected at the calculated range of 4 cm owing to statistical variations in the number of collisions that the particles may have with air molecules and to variations in the amount of energy loss by the particles for each ion pair formed. After being halted, an alpha particle acquires two free electrons through Coulombic attraction and is converted to helium gas.

In materials other than air, such as liquids and solids, the range of alpha particles is obviously much shorter owing to their higher densities, which enhance the number of collisions a particle may undergo per path length of travel. The range of alpha particles in liquids and solids may be approximated by comparison with ranges in air according to the empirical formula

$$R_{\text{cm}} = 0.00032(A^{1/2}/\rho)R_{\text{air}} \quad (1.95)$$

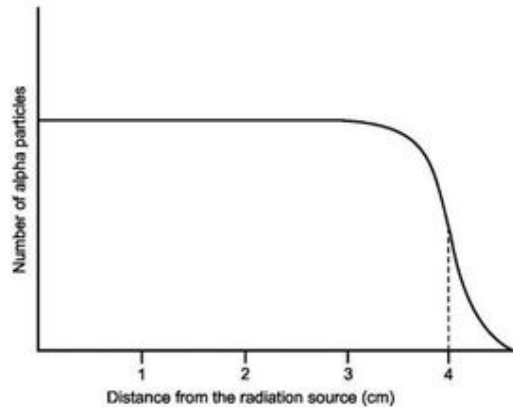


FIGURE 1.28 Range of 5.5 MeV alpha particles in air.

described in a previous text (L'Annunziata, 1987), where R_{cm} is the average range in cm of the alpha particle in an absorber other than air, A is the atomic weight of the absorber, ρ is the absorber density in g/cm^3 , and R_{air} is the calculated average linear range of the alpha particle in air (from Eqn (1.93) or Eqn (1.94)). For example, the 5.5-MeV alpha particles emitted by ²⁴¹Am have a calculated linear range of only 2.4×10^{-3} cm or 24 μm in aluminum ($A = 27$ and $\rho = 2.69 \text{ g}/\text{cm}^3$).

The linear ranges of alpha particles in liquids and solid materials are too short to measure with conventional laboratory instrumentation. The alternative is to express range in units of weight of absorber material per unit area, such as mg/cm^2 , which is a measure of milligrams of absorber per square centimeter in the absorption path or, in other words, a measure of absorber thickness. If we multiply the linear range of the alpha particle measured in cm of absorber material by the density of the absorber in units of mg/cm^3 , the range of the alpha particle in an absorber will be expressed in terms of the weight of absorber per unit area (mg/cm^2) as described by Eqn (1.96), as follows:

$$R_{\text{mg}/\text{cm}^2} = (R_{\text{cm}})(\rho) \quad (1.96)$$

where $R_{\text{mg}/\text{cm}^2}$ is the range of alpha particles of a given energy in units of mg/cm^2 , also referred to as mass thickness units or material surface density, R_{cm} is the linear range of the alpha particles, and ρ is the absorber density. For example, the linear range of the 5.5 MeV alpha particles in aluminum, calculated above with Eqn (1.95), is converted to range in mass thickness units according to Eqn (1.96) as follows:

$$R_{\text{mg}/\text{cm}^2} = (2.4 \times 10^{-3} \text{ cm})(2690 \text{ mg}/\text{cm}^3) = 6.4 \text{ mg}/\text{cm}^2$$

Therefore, the mass thickness of 6.4 mg/cm^2 of aluminum absorber is sufficient to absorb alpha particles of 5.5 MeV energy.

Ranges of alpha particles as well as other charged particles such as protons and deuterons of a given energy in absorber elements of atomic number $Z > 10$ in units of absorber mass thickness can be calculated directly by comparison to the calculated range of the same charged particles of the same

energy in air according to the following formula described by Friedlander et al (1964):

$$\frac{R_Z}{R_{air}} = 0.90 + 0.0275Z + (0.06 - 0.0086Z)\log \frac{E}{M} \quad (1.97)$$

where R_Z is the range of the charged particle in mass thickness units, mg/cm^2 , R_{air} is the range of the charged particle in air in the same mass thickness units, Z is the atomic number of the absorber element, E is the particle energy in MeV, and M is the mass number of the particle (i.e., 1 for protons, 2 for deuterons, and 4 for alpha particles). For example, if we use the empirical formula provided above (Eqn (1.97)) to calculate the range of 5.5 MeV alpha particles ($M=4$) in aluminum ($Z=13$), we obtain the value of $R_Z=6.1 \text{ mg}/\text{cm}^2$, which is in close agreement to the mass thickness range calculated previously with Eqns (1.95) and (1.96). In this example, Eqn (1.97) requires the value of R_{air} for 5.5 MeV alpha particles, which is determined according to Eqn (1.96) as the product of the 5.5 MeV alpha-particle linear range in air (previously calculated) and the density of air at STP ($\rho=1.226 \text{ mg}/\text{cm}^3$), that is, $R_{air}=(4 \text{ cm})(1.226 \text{ mg}/\text{cm}^3)=4.90 \text{ mg}/\text{cm}^2$. The formula provided by Eqn (1.97) is applicable to charged particles over a wide range of energies (approximately over the range 0.1–1000 MeV) and to absorber elements of $Z > 10$. For lighter absorber elements, the term $0.90 + 0.0275Z$ is replaced by the value 1.00 with the exception of hydrogen and helium, where the values of 0.30 and 0.82 are used, respectively (Friedlander et al, 1964).

Where alpha particles alone are concerned, the range in mass thickness units can be calculated according to Eqn (1.98) described by Ehman and Vance (1991), as follows:

$$R_{\text{mg}/\text{cm}^2} = 0.173E^{3/2}A^{1/3} \quad (1.98)$$

where E is the energy of the alpha particle in MeV and A is the atomic weight of the absorber. If we continue to use the 5.5 MeV alpha particles emitted from ^{241}Am as an example, we can calculate their range in mass thickness units in aluminum according to Eqn (1.98) as follows:

$$R_{\text{mg}/\text{cm}^2} = 0.173(5.5)^{3/2}(27)^{1/3} = 6.6 \text{ mg}/\text{cm}^2.$$

Ranges reported in mass thickness units (mg/cm^2) of absorber can be converted to linear range (cm) in that same absorber material from the absorber density (ρ) from the relationship described in Eqn (1.96) or

$$R_{\text{cm}} = R_{\text{mg}/\text{cm}^2}/\rho \quad (1.99)$$

For example, the linear range of the 5.5 MeV alpha particles in aluminum ($\rho=2.69 \text{ g}/\text{cm}^3$) is calculated as

$$R_{\text{cm}} = \frac{6.6 \text{ mg}/\text{cm}^2}{2690 \text{ mg}/\text{cm}^3} = 0.0024 \text{ cm} = 24\mu\text{m}$$

When the absorber material is not a pure element, but a molecular compound (e.g., water, paper, polyethylene, etc) or mixture of elements, such as an alloy, the ranges of alpha particles in the absorber are calculated according to Eqn (1.100) on the basis of the atomic weights of the elements and their

percent composition in the absorber material or, in other words, the weight fraction of each element in the complex material. Thus, the range in mass thickness units for alpha particles in absorbers consisting of compounds or mixtures of elements is calculated according to the equation

$$\frac{1}{R_{\text{mg}/\text{cm}^2}} = \frac{w_1}{R_1} + \frac{w_2}{R_2} + \frac{w_3}{R_3} + \dots + \frac{w_n}{R_n} \quad (1.100)$$

where $R_{\text{mg}/\text{cm}^2}$ is the range of the alpha particles in mass thickness of the complex absorber material, and $w_1, w_2, w_3, \dots, w_n$ are the weight fractions of each element in the absorber, and $R_1, R_2, R_3, \dots, R_n$ are the ranges in mg/cm^2 of the alpha particle of defined energy in each element of the absorber. For example, the range of 5.5 MeV alpha particles in Mylar (polyethylene terephthalate) in units of mass thickness is calculated as follows:

$$\frac{1}{R_{\text{mg}/\text{cm}^2}} = \frac{w_C}{R_C} + \frac{w_H}{R_H} + \frac{w_O}{R_O}$$

where $w_C, w_H,$ and w_O are the weight fractions of carbon, hydrogen, and oxygen, respectively, in Mylar and $R_C, R_H,$ and R_O are the mass-thickness ranges of the alpha particles in pure carbon, hydrogen, and oxygen, respectively. The ranges of 5.5 MeV alpha particles in carbon, hydrogen, and oxygen are calculated according to Eqn (1.98) as

$$R_C = 0.173(5.5)^{3/2}(12)^{1/3} = 5.10 \text{ mg}/\text{cm}^2$$

$$R_H = 0.173(5.5)^{3/2}(1)^{1/3} = 2.23 \text{ mg}/\text{cm}^2$$

$$R_O = 0.173(5.5)^{3/2}(16)^{1/3} = 5.62 \text{ mg}/\text{cm}^2$$

The weight fractions of the carbon, hydrogen, and oxygen in Mylar [$-(\text{C}_{10}\text{H}_8\text{O}_4)_n-$] are calculated as

$$w_C = (12 \times 10)/192 = 0.625$$

$$w_H = (1 \times 8)/192 = 0.042$$

$$w_O = (16 \times 4)/192 = 0.333$$

The calculated ranges of the 5.5 MeV alpha particles in each element and the values of the weight fractions of each element in Mylar can now be used to calculate the alpha-particle range in Mylar in mass thickness units according to Eqn (1.100) as

$$\frac{1}{R_{\text{Mylar}}} = \frac{0.625}{5.10} + \frac{0.042}{2.23} + \frac{0.333}{5.62} = 0.200$$

$$R_{\text{Mylar}} = 1/0.200 = 5.0 \text{ mg}/\text{cm}^2$$

The linear range of these alpha particles in Mylar are obtained from range in mass thickness units and the density of Mylar ($\rho=1.38 \text{ g}/\text{cm}^3$) as

$$R_{\text{cm}} = \frac{5.0 \text{ mg}/\text{cm}^2}{1380 \text{ mg}/\text{cm}^3} = 0.0036 \text{ cm} = 36\mu\text{m}$$

To provide illustrative examples, the values of the ranges of 5.5 MeV alpha particles in units of mass thickness of various absorber materials are provided in Table 1.8. These values

TABLE 1.8 Ranges of 5.5-MeV Alpha Particles in Various Absorbers in Units of Surface Density or Mass Thickness

Water ^a	Paper ^{a,b}	Aluminum ^c	Copper ^c	Gold ^c
4.8 mg/cm ²	4.9 mg/cm ²	6.6 mg/cm ²	8.9 mg/cm ²	12.9 mg/cm ²

^aCalculated with empirical formula provided by Eqn (1.100) on the basis of the weight fraction of each element in the absorber.

^bCellulose, (C₆H₁₀O₅)_n, calculated on the basis of the weight fraction of each element in the monomer.

^cCalculated with empirical formula provided by Eqn (1.98).

TABLE 1.9 Linear Ranges of 5.5-MeV Alpha Particles in Various Absorbers in Units of cm and μm or 10⁻⁶ m

Air ^a	Water ^b	Mylar ^{b,c}	Paper ^{b,d}	Aluminum ^b	Copper ^b	Gold ^b
4 cm	0.0048 cm	0.0036 cm	0.0034 cm	0.0024 cm	0.001 cm	0.00075
40,000 μm	48 μm	36 μm	34 μm	24 μm	10 μm	7.5 μm

^aCalculated with empirical formula provided by Eqns (1.93) and (1.94).

^bCalculated by dividing the range in mass thickness by the absorber density according to Eqn (1.99).

^cPolyethylene terephthalate, ρ = 1.38 g/cm³.

^dCellulose, (C₆H₁₀O₅)_n, ρ = 1.45 g/cm³.

represent the milligrams of absorber per square centimeter in the alpha-particle absorption path. It can be difficult to envisage alpha-particle distance of travel from the values of range when expressed in units of mass thickness. However, it is intuitively obvious that the greater the charge on the nucleus of the absorber (*i.e.*, absorber atomic number, *Z*), the greater the atomic weight of the absorber (*A*), and the greater the absorber density (*ρ*), the shorter will be the path length of travel of the alpha particle through the absorber. This is more evident from the calculated values of linear range of 5.5 MeV alpha particles in various gaseous, liquid, and solid absorbers provided in Table 1.9. From the linear ranges, we can see that 5.5 MeV alpha particles could not pass through fine commercial aluminum or copper foils, 0.0025 cm thick. Although commercial paper varies in thickness and density, the linear range in paper calculated in Table 1.9 illustrates that 5.5 MeV alpha particles would not pass through 0.0034 cm thick paper, which has an average density value of 1.45 g/cm³. Also, the alpha particles of the same energy would not pass through a layer of Mylar only 0.0036 cm thick. Mylar is a polymer sometimes used as a window for gas ionization detectors. From our previous calculations in this chapter, we can see that a Mylar window of mass thickness 5 mg/cm² would not allow 5.5 MeV alpha particles to pass into the gas ionization chamber. A sample emitting such alpha particles would have to be placed directly into the chamber in a windowless fashion to be detected and counted.

From the above treatment, it is clear that the range of alpha-particle travel depends on several variables including (i) the energy of the alpha particle, (ii) the atomic number and atomic weight of the absorber, and (iii) the density of the absorber. The higher the alpha particle energy, the greater will be its penetration power into or through a given substance as more Coulombic interactions of the alpha particle with the electrons of the absorber will be required to dissipate its energy before coming to rest. Also, if we consider an alpha particle of given

energy, its range will be shorter in absorbers of higher atomic number or atomic weight, as the absorber atoms will contain a higher number of atomic electrons, which would consequently increase the number of Coulombic interactions of the alpha particle per path length of travel.

As the alpha particle travels through air and undergoes energy loss via numerous collisions, the velocity of the particle obviously diminishes. At reduced velocity and consequently reduced momentum, an alpha particle is more affected by Coulombic attraction within the vicinity of a given atom. Progressive reduction in the velocity of travel of the alpha particle therefore results in an increase in the number of ion pairs produced per millimeter of path length of travel. The increase in ionization per path length of travel of an alpha particle is illustrated in Fig. 1.29. The highest specific ionization (number of ion pairs formed per millimeter of path) occurs shortly before termination of the alpha particle's travel, nearly 2 or 3 mm before the end of its range.

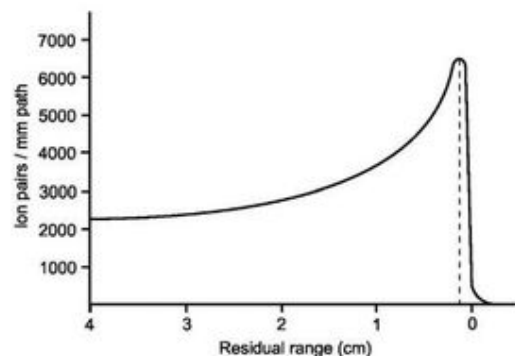


FIGURE 1.29 Specific ionization of an alpha particle in air along its range of travel.

B. Beta Decay

Beta decay may be defined as any nuclear decay process whereby the mass number (*A*) of the nucleus remains the same and the atomic number (*Z*) changes. There are three main types of beta decay: (i) negatron (β^-) emission, which involves the emission of a negative beta particle or negative electron from the nucleus; (ii) positron (β^+) emission whereby a positive beta particle or positively charged electron is emitted; and (iii) electron capture (EC), which does not result in the emission of any beta particle. Each of these beta-decay processes will be treated in detail in the following sections.

1. Negatron (β^-) Emission

Negatron emission can be described by the general equation

$${}^A_ZP \rightarrow {}^A_{Z+1}D + \beta^- + \bar{\nu} + K_T \tag{1.101}$$

where A_ZP is the parent nuclide of atomic number *Z* and mass number *A*, ${}^A_{Z+1}D$ is the daughter nuclide of atomic number *Z*+1 and same mass number as the parent, β^- is the negatron or negative beta particle, $\bar{\nu}$ is the antineutrino, and K_T is the total kinetic energy released in the beta-decay process. The total kinetic energy released, also referred to as the decay energy (Q_{β^-}), is shared between the negatron, antineutrino, recoil daughter nucleus, and any gamma radiation that may be emitted by the daughter nucleus. Gamma-ray emission can occur when the daughter nuclide is left in an excited energy state and decays to a lower energy state or ground (stable) state with the emission of energy as gamma-ray photons. Gamma-ray emission does not occur in all cases of negatron emission. There are some nuclides described further on in this section that decay with the emission of negatrons directly to the stable ground state without the emission of gamma radiation. The decay energy, Q_{β^-} , may be defined as

$$Q_{\beta^-} = K_T = E_{\beta^-} + E_{\bar{\nu}} + E_{\gamma} + E_{recoil} \tag{1.102}$$

where E_{β^-} is the kinetic energy of the negatron, $E_{\bar{\nu}}$ is the kinetic energy of the antineutrino, E_{γ} is the gamma-ray energy, which is emitted when the daughter nucleus is at an elevated energy state and drops to a more stable or ground state, and E_{recoil} is the kinetic energy of the recoil daughter nucleus. The recoil energy may be ignored in most calculations of beta-decay energy, because it may be only a few electron volts (eV) compared to the fractional or multiple magnitudes of million electron volts (MeV) energy possessed by the beta particle, antineutrino, and gamma radiation (see the Section on Nuclear Recoil in this chapter). We should keep in mind that there is a maximum energy shared by the beta particle and antineutrino ($E_{\beta^-} + E_{\bar{\nu}}$), which is often referred to as the E_{max} of the beta particle.

a. Basic Principles

A negatron or negative beta particle (β^-) is an electron emitted from the nucleus of a decaying radionuclide that possesses an excess of neutrons or, in other words, a neutron/proton (*n/p*) imbalance. The nuclear instability, caused by the *n/p* imbalance, results in the conversion of a neutron to a proton within the

nucleus. The balance of charge is conserved by the simultaneous formation of an electron (negatron) according to the equation

$$n \rightarrow p^+ + \beta^- + \bar{\nu} \tag{1.103}$$

A neutrino (ν), which is a particle of zero charge, accompanies beta-particle emission. The neutrino can be identified further as two types with opposite spin, namely, the antineutrino ($\bar{\nu}$), which accompanies negative beta-particle (negatron) emission, and the neutrino (ν), which accompanies positive beta-particle (positron) emission. Because the neutrino and antineutrino have similar properties with the exception of spin, it is common to use the word "neutrino" to simplify references to both particles. The explanation for the neutrino and its properties, also emitted from the decaying nucleus, is given further on in this section. The electron formed cannot remain within the nucleus; and it is thus ejected as a negatron or negative beta particle, β^- , with an energy equivalent to the mass difference between the parent and daughter atoms, less the energy of antineutrino or neutrino in the case of positron emission, and any gamma-ray energy that may be emitted by the daughter nucleus, if the nucleus is left in an excited energy state, and recoil energy of the daughter nucleus as described by Eqn (1.102). Tritium (${}^3\text{H}$), for example, decays with β^- emission according to the following:

$${}^3_1\text{H} \rightarrow {}^3_2\text{He} + \beta^- + \bar{\nu} + 0.0186 \text{ MeV} \tag{1.104}$$

The ${}^3\text{H}$ nucleus decays directly to the ground state of ${}^3\text{He}$. Thus, there is no gamma-ray energy emission in this case. The value of 0.0186 MeV (mega-electron volts) is the maximum energy the beta particle may possess. The unstable tritium nucleus contains two neutrons and one proton. The transformation of a neutron to a proton within the tritium nucleus results in a charge transfer on the nucleus from +1 to +2 without any change in the mass number. Although there is no change in the mass number, the mass of the stable helium isotope produced is slightly less than that of its parent tritium atom. Eqns (1.105)–(1.110) illustrate other examples of β^- decay, which decay to stable daughter nuclides whereby no gamma-ray emission occurs; and many beta particle-emitting nuclides are listed in the Appendix:

$${}^{14}_6\text{C} \rightarrow {}^{14}_7\text{N} + \beta^- + \bar{\nu} + 0.156 \text{ MeV} \tag{1.105}$$

$${}^{32}_{15}\text{P} \rightarrow {}^{32}_{16}\text{S} + \beta^- + \bar{\nu} + 1.710 \text{ MeV} \tag{1.106}$$

$${}^{35}_{16}\text{S} \rightarrow {}^{35}_{17}\text{Cl} + \beta^- + \bar{\nu} + 0.167 \text{ MeV} \tag{1.107}$$

$${}^{36}_{17}\text{Cl} \rightarrow {}^{36}_{18}\text{Ar} + \beta^- + \bar{\nu} + 0.714 \text{ MeV} \tag{1.108}$$

$${}^{45}_{20}\text{Ca} \rightarrow {}^{45}_{21}\text{Sc} + \beta^- + \bar{\nu} + 0.258 \text{ MeV} \tag{1.109}$$

$${}^{89}_{38}\text{Sr} \rightarrow {}^{89}_{39}\text{Y} + \beta^- + \bar{\nu} + 1.490 \text{ MeV} \tag{1.110}$$

The energies of beta-particle decay processes are usually reported as the maximum energy, E_{max} , that the emitted beta particle or antineutrino may possess. The maximum energy is reported because beta particles are emitted from radionuclides with a broad spectrum of energies. A typical spectrum is illustrated in Fig. 1.30. The shape of the beta-particle energy spectra will vary among the beta-emitting radionuclides, but all

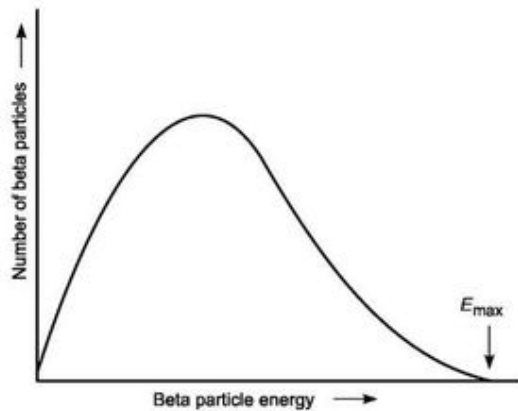


FIGURE 1.30 General beta-particle energy spectrum.

beta-emitting radionuclides will display a wide spectrum of energies between zero and E_{max} . Unlike alpha particles, which have a discrete energy, beta particles are emitted with a wide spectrum of energies ranging from zero to E_{max} .

The majority of beta particles emitted have energies of approximately $\frac{1}{3} E_{max}$. Only a very small portion of the beta particles is emitted with the maximum possible energy from any radionuclide sample. In 1930 Wolfgang Pauli was the first to postulate why beta particles were not emitted with fixed quanta of energy, quite the contrary to what is observed in alpha-particle emission. He proposed the existence of an elusive, neutral particle of near-zero rest mass in a letter to the participants of a Regional Meeting on Radioactivity at Tübingen, Germany. The neutrino was considered elusive, because if it existed, its zero charge and near-zero rest mass would make the neutrino undetectable by conventional means and allow a neutrino to penetrate matter easily and even pass through the entire earth without causing a single interaction. The neutrino would be emitted simultaneously with the beta particle from the decaying nucleus and share the energy of decay with the beta particle. For example, if a beta particle was emitted from tritium (decay energy = 0.0186 MeV) with an energy of 0.0086 MeV, the accompanying neutrino would possess the remaining energy of 0.01 MeV, that is, the decay energy less the beta-particle energy (0.0186 MeV - 0.0086 MeV). Consequently, if we observe any number of beta particles emitted from a tritium sample or other beta-emitting nuclide sample (e.g., ^{14}C , ^{32}P , and ^{90}Sr), they would possess different energies and display an energy spectrum from zero to E_{max} as illustrated in Fig. 1.30.

b. Inverse Beta Decay

With Pauli's postulation of the neutral particle, Enrico Fermi elaborated the beta-decay theory in 1934 and coined the neutrino from the Italian language meaning "little neutral one". The particle remained elusive until the observation of the neutrino was demonstrated by Reines and Cowan in 1956 (see Reines and Cowan 1956, 1957, Cowan et al, 1956 and Reines, 1960, 1979 and 1994). They confirmed the existence of the

neutrino by demonstrating inverse beta decay where an anti-neutrino interacts with a proton to yield a neutron and positron:



They used a tank of water containing a solution of $^{113}\text{CdCl}_2$ illustrated schematically in Fig. 1.31. Neutrinos interacted with the protons of the water to produce neutrons and positrons. Some of the neutrons produced would be absorbed by the ^{113}Cd with the concomitant emission of characteristic gamma radiation. In coincidence, they observed two 511 keV gamma rays, which originate when a positron comes to rest in the vicinity of an electron, its antiparticle, which results in the annihilation of two electrons into two gamma-ray photons of energy equivalent to the electron masses, 0.511 MeV. In the same year, Lee and Yang (1956) proposed that neutrinos and antineutrinos possessed left-handed and right-handed spins, respectively. Inverse beta decay remains an important nuclear process utilized in the measurement of solar neutrinos today (Gratta and Wang, 1999, Zuber, 2003, Ianni et al, 2005, and Fukuda et al, 2010).

An inverse beta decay, first proposed by Raghaven (1976), which involves the interaction of a neutrino with the neutron of ^{115}In , is as follows:



which can be written in general terms illustrating only the nucleons as

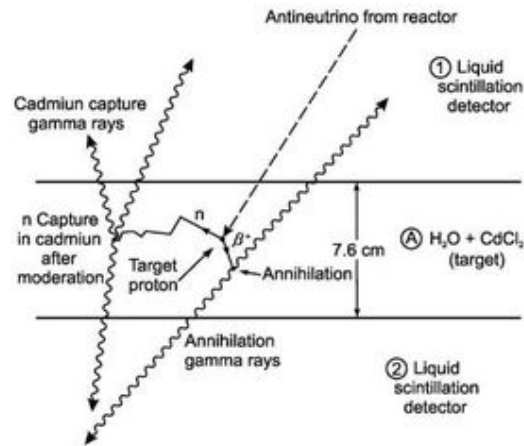


FIGURE 1.31 Detection scheme used by Reines and Cowan for the antineutrino signature signal (From Reines (1995) Nobel Lecture with permission © The Nobel Foundation 1995.) An antineutrino is illustrated entering the tank of aqueous CdCl_2 solution and striking a target proton. The proton converts to a neutron and positron. The positron annihilates on an electron with the emission of two 0.511 MeV gamma rays in opposite direction detected by the liquid scintillator in tanks above and below the water target tank. The neutron produced by the antineutrino interaction slows down in the water and is captured by a cadmium nucleus; and the resulting gamma rays are detected by the liquid scintillator in the adjacent tanks approximately 10 μs after the positron annihilation.

The superscript asterisk in Eqn (1.112) represents an excited state of ^{115}Sn , which decays into the ground state with a lifetime of 4.76 μs and emits two gamma-ray photons of 116 and 497 keV. This provides a triple coincidence signal, namely the emitted electron together with the two gamma-ray photons, that can be detected among huge backgrounds (Fukuda, 2010). Also, the neutrino energy may be calculated from the energy of the prompt electron according to the equation

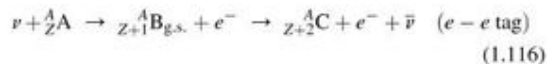
$$E_{e^-} = E_\nu - (E_f - E_i) \quad (1.114)$$

where E_{e^-} is the energy of the electron produced, E_ν is the neutrino energy, and E_f and E_i are the final and initial energies of the nuclear state involved in the transition (Zuber, 2003). In the case of neutrino interactions with ^{115}In , Eqn (1.114) may be written, according to Fukuda et al (2010), as

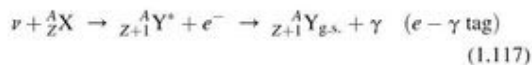
$$E_{e^-} = E_\nu - 118 \text{ keV} \quad (1.115)$$

Thus, neutrino spectroscopy is possible.

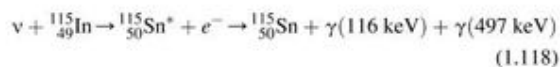
In general, the detection principle of solar neutrinos involving the inverse beta-decay reaction of Eqn (1.113), as described by Zuber (2003), may involve one of the following two reactions:



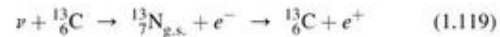
or



The reaction described in Eqn (1.116) involves the interaction of a neutrino with a neutron of nuclide ${}^A_Z\text{A}$ of atomic number Z and mass number A producing a nuclide ${}^A_{Z+1}\text{B}_{g.s.}$ at its ground state and a beta particle (e^-). The nuclide ${}^A_{Z+1}\text{B}_{g.s.}$ undergoes beta decay to nuclide ${}^A_{Z+2}\text{C}$ with the emission of a beta particle (e^-) and antineutrino ($\bar{\nu}$). This reaction has an $e-e$ tag whereby a coincidence signal between the two electron emissions provides the signature for the neutrino detection. The following reaction described by Eqn (1.117) depicts a neutrino interacting with a neutron of nuclide ${}^A_Z\text{X}$ producing nuclide ${}^A_{Z+1}\text{Y}^*$ at an excited energy state indicated by the superscript asterisk plus an electron or beta particle (e^-). The nuclide ${}^A_{Z+1}\text{Y}^*$ then undergoes deexcitation to its ground state ${}^A_{Z+1}\text{Y}_{g.s.}$ with the emission of a gamma-ray photon. This reaction has an $e-\gamma$ tag whereby a coincidence signal between the electron and one or more gamma-ray photon emissions provides the signature for the neutrino detection. The neutrino energies are determined by Eqn (1.114). Zuber (2003) provides a review of these two approaches to neutrino detection and spectroscopy. The interaction of a neutrino with ^{115}In previously discussed Eqn (1.112), utilized by Fukuda et al (2010), is an example of the generic reaction yielding an $e-\gamma$ tag depicted by Eqn (1.117), which is specifically



An example of the generic reaction depicted in Eqn (1.116) is the following:



This reaction was utilized by Ianni et al (2005) for the detection of neutrinos. The reaction provides an $e-e$ tag as the beta particle (e^-) produced in the reverse beta decay yields one signal while the positron produced in the subsequent decay of ^{13}N provides a time and space coincidence signal and signature for the neutrino detection.

c. Neutrino Mass

Since its inception by Pauli in 1930 up to recent years, the neutrino or antineutrino had been thought to have no rest mass or to possess a near-zero rest mass. It was not until June 5, 1998 that it was announced by the Super-Kamiokande Collaboration, including scientists from 23 institutions in Japan and the United States, at the "Neutrino 98" International Physics Conference in Takayama, Japan, that neutrinos possessed a definite mass (Gibbs, 1998, Kesterbaum, 1998, Kearns et al 1999, and Nakahata, 2000). The mass was not reported, but evidence was provided that the neutrino did possess mass although it was considered to be "very small", at least 0.07 eV, which would be less than a millionth of the electron mass. Evidence for the neutrino mass was provided by demonstrating that neutrinos can "oscillate" from one type into another (*i.e.*, electron-, muon-, and tau-neutrinos) as they travel through space and matter. Oscillation is the changing of neutrino types back and forth from one type to another, and this could occur only if the neutrino possessed mass. Experimental research on neutrino oscillation is reviewed by Messier (2006).

At the "Neutrino 2000" Conference held at Sudbury, Canada June 16–21, 2000, groups from the University of Mainz, Germany (Bonn et al, 2001) and Institute for Nuclear Research, Moscow (Lobashev et al, 2000) reported the mass of the neutrino to be between 2.2 and 2.5 eV/c^2 , respectively, at 95% confidence levels. It is common to express subatomic particle mass in units of energy based on equivalence of mass and energy ($E = mc^2$), so that the particle mass m is measured in units of E/c^2 or eV/c^2 . Neutrino mass experiments are reviewed by Kraus et al (2005), Otten and Weinheimer (2008), Beck (2010), and Kristiansen (2010). Beck (2010) underscores that results from previous research reported by the Triosk (Russia) and Mainz (Germany) neutrino mass experiments (See Lobashev et al, 1999a,b,c, and 2000, and Kraus et al, 2005) have set the best upper limits of 2.3 eV/c^2 with a 95% confidence limit on the neutrino mass. Beck (2010) also reports that the KATRIN experiment (KARlsruhe TRItium Neutrino experiment) is under preparation to search for the mass of the electron neutrino with a sensitivity of 0.2 eV/c^2 . With this objective, the KATRIN experiment will perform a precision measurement of the endpoint region of the β -decay spectrum of tritium, the shape of which depends highly on the neutrino mass. A windowless gaseous tritium source is used in a transport system that guides the beta particles of tritium without energy loss to PIN diode detectors described by Wüstling et al (2006). A pre-spectrometer rejects all beta particles with energy <200 eV below the β -spectrum endpoint, and the beta-particle energies can be measured with a resolution of 0.93 eV.

The collection of data to obtain the neutrino mass will start in 2012 and will proceed for five years.

To put the mass of the neutrino in perspective, we can take the current experimental value of the upper limit to the neutrino rest mass, $m_\nu = 2.3 \text{ eV}/c^2$, and convert this to kilograms as follows:

By definition $1 \text{ eV} = 1.60 \times 10^{-19} \text{ J}$ and, from the equation $E = mc^2$, we can calculate the neutrino rest mass in kilograms as

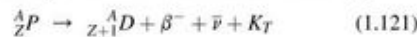
$$\begin{aligned} m_\nu &= E/c^2 \\ &= (2.3 \text{ eV})(1.6 \times 10^{-19} \text{ J/eV}) / (3.0 \times 10^8 \text{ m/s})^2 \quad (1.120) \\ &= 4.1 \times 10^{-36} \text{ kg} \end{aligned}$$

If we compare the rest mass of the neutrino, m_ν , to that of the miniscule electron, m_e , we see that the neutrino rest mass is approximately 4 millionths that of the electron or

$$m_\nu/m_e = 4.1 \times 10^{-36} \text{ kg} / 9.1 \times 10^{-31} = 4.5 \times 10^{-6}$$

d. Negatron Decay Energy

The general reaction for negatron emission was described previously by Eqn (1.101). It is provided here again for a treatment on negatron decay energy calculations, and it is the following:



where ${}^A_Z P$ is the parent nuclide of atomic number Z and mass number A , ${}^A_{Z+1} D$ is the daughter nuclide of atomic number $Z+1$ and same mass number as the parent, β^- is the negatron or negative beta particle, $\bar{\nu}$ is the antineutrino, and K_T is the total kinetic energy released in the beta-decay process.

In terms of nuclear masses, we may write Eqn (1.121) as

$${}_Z M_P = {}_{Z+1} M_D + m_e + K_T \quad (1.122)$$

where ${}_Z M_P$ and ${}_{Z+1} M_D$ are the masses of the parent and daughter nuclei of atomic numbers Z and $Z+1$, respectively, and m_e is the mass of the beta particle (*i.e.*, one electron mass). We may use atomic mass units (u) to calculate the mass difference of the parent and daughter nuclei by adding firstly Z atomic electron masses to each side of Eqn (1.122) to give

$${}_Z M_P + Z m_e = {}_{Z+1} M_D + (Z+1) m_e + K_T \quad (1.123)$$

The mass difference of the parent and daughter nuclei is equivalent to the decay energy (Q_{β^-}). We can now calculate the decay energy Q_{β^-} by the difference of the parent and daughter

nuclide atomic masses, after adding Z atomic electrons to each side of the equation, ignoring the small difference in the binding energies of the electrons in the two nuclides as

$$Q_{\beta^-} = ({}_Z M_P - {}_{Z+1} M_D) c^2 = K_T = E_{\beta^-} + E_{\bar{\nu}} + E_\gamma + E_{\text{recoil}} \quad (1.124)$$

where c is the velocity of light in a vacuum and the product Mc^2 yields the energy equivalence of the mass, E_{β^-} is the kinetic energy of the negatron, $E_{\bar{\nu}}$ is the kinetic energy of the antineutrino, E_γ is the gamma-ray energy, which only appears with the decay of a daughter nucleus when left at an excited energy state, and E_{recoil} is the kinetic energy of the daughter recoil nucleus. As previously described, the recoil energy, E_{recoil} , is generally relatively very small (a few electron volts) and will be ignored here. Also, if there is no gamma radiation emitted by the daughter nucleus, we can exclude the term E_γ . The remaining decay energy ($E_{\beta^-} + E_{\bar{\nu}}$) is shared as kinetic energy between the beta particle and antineutrino, most often referred to as the E_{max} .

A simple example would be that of the radionuclide ${}^{14}\text{C}$, which decays by negatron emission without the emission of gamma radiation to the stable daughter nuclide ${}^{14}\text{N}$ according to the following:



The decay scheme is illustrated in Fig. 1.32.

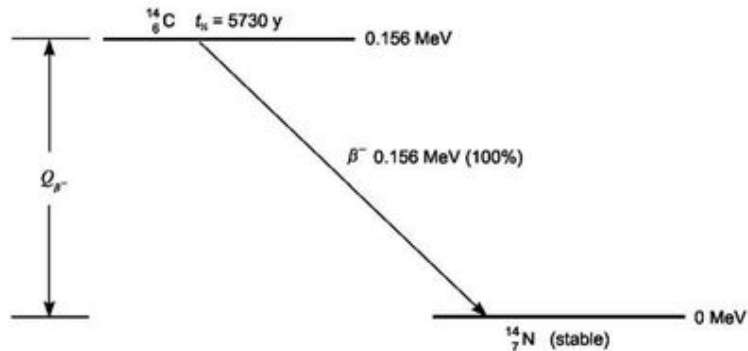
The decay energy of ${}^{14}\text{C}$ can be calculated according to Eqn (1.124) using atomic mass units (u) of the parent and daughter atoms as follows:

$$\begin{aligned} Q_{\beta^-} &= (M_{14\text{C}} - M_{14\text{N}}) c^2 \\ &= (14.00324199 \text{ u} - 14.00307401 \text{ u})(931.494 \text{ MeV/u}) \\ &= 0.156 \text{ MeV} \end{aligned} \quad (1.126)$$

where 931.494 is the energy equivalence of 1 atomic mass unit as derived previously in this chapter. The energy of 0.156 MeV, calculated above, is shared between the beta particle and antineutrino. Thus, the maximum energy that the beta particle or antineutrino may possess is 0.156 MeV. The calculated decay energy may be found in Appendix A, which lists the decay energies of many radioactive nuclides.

We may now look at yet a more complex example of ${}^{137}\text{Cs}$ decay where negatron β^- emission occurs with more than one

FIGURE 1.32 Negatron beta decay scheme of ${}^{14}\text{C}$. The radionuclide ${}^{14}\text{C}$ decays to stable ${}^{14}\text{N}$ by negatron emission. Nuclear decay occurs entirely (100%) by emission of a negatron (β^-) and antineutrino ($\bar{\nu}$) with an energy maximum of 0.156 MeV, which is shared by the negatron and antineutrino.



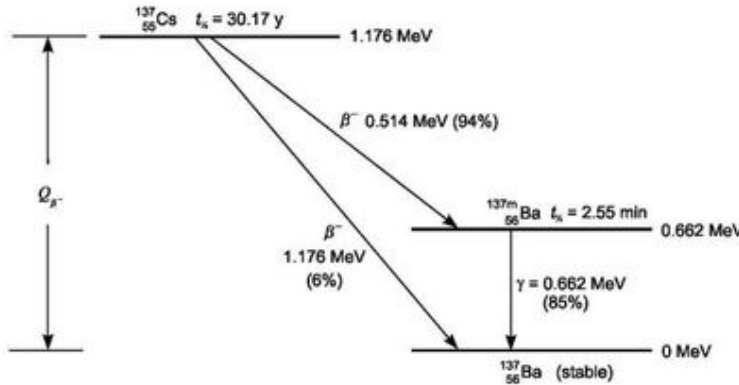
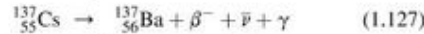


FIGURE 1.33 Negatron beta decay scheme of ^{137}Cs . The radionuclide ^{137}Cs decays to stable ^{137}Ba via two branching negatron emissions with energy maxima of 1.176 MeV at a relative intensity of 6% and 0.514 MeV at an intensity of 94%. Negatrons with energy maxima of 0.514 MeV produce metastable ^{137m}Ba daughter, which decays to stable ^{137}Ba with the emission of a gamma-ray photon of 0.662 MeV at an 85% intensity.

energy maxima, or via what is referred to as a branching decay mode, and which decays with the emission of gamma radiation from the nucleus of the daughter nuclide ^{137}Ba . The decay equation is the following:



The decay scheme of ^{137}Cs to stable ^{137}Ba is illustrated in Fig. 1.33.

The decay energy of ^{137}Cs is calculated as follows:

$$\begin{aligned} Q_{\beta^-} &= (M(^{137}\text{Cs}) - M(^{137}\text{Ba}))c^2 = E_{\beta^-} + E_{\bar{\nu}} + E_{\gamma} + E_{\text{recoil}} \\ &= (136.907085 \text{ u} - 136.905822 \text{ u})(931.494 \text{ MeV/u}) \\ &= 1.176 \text{ MeV} \end{aligned} \quad (1.128)$$

The 1.176 MeV decay energy is the energy liberated from ^{137}Cs decay to the ground state of stable ^{137}Ba . One branch of this decay occurs at a 94% intensity (abundance) via the emission of a negatron and antineutrino with an E_{max} of 0.514 MeV followed by the emission of gamma radiation of 0.662 MeV from the daughter nuclide ^{137m}Ba , which is metastable decaying to the stable ^{137}Ba (See Fig. 1.33). The remaining 6% of the negatron emissions (*i.e.*, 100–94%) arise from the decay of ^{137}Cs directly to the ground state of stable ^{137}Ba with the entire 1.176 MeV of decay energy shared by the negatron (β^-) and antineutrino ($\bar{\nu}$).

More complex negative beta-decay schemes occur such as that of the radionuclide ^{131}I to stable ^{131}Xe , which is illustrated in Fig. 1.34.

The decay energy of ^{131}I to stable ^{131}Xe is calculated as

$$\begin{aligned} Q_{\beta^-} &= (M(^{131}\text{I}) - M(^{131}\text{Xe}))c^2 = E_{\beta^-} + E_{\bar{\nu}} + E_{\gamma} + E_{\text{recoil}} \\ &= (130.906125 \text{ u} - 130.905083 \text{ u})(931.494 \text{ MeV/u}) \\ &= 0.971 \text{ MeV} \end{aligned} \quad (1.129)$$

In summary, if we ignore the relatively very small nuclear recoil energy, we will find that the β^- energy maxima and the gamma-ray emission energies for the three beta decay branches of ^{131}I decay, illustrated in Fig. 1.34, yield the total decay energy of 0.971 MeV as follows:

β^- Branch 1 of 13% Intensity:

$$\begin{aligned} E_{\beta_1^-} + E_{\bar{\nu}} + \gamma_1 &= E_{\text{max}} \text{ of } 0.336 \text{ MeV} + \gamma_1 \text{ of } 0.635 \text{ MeV} \\ &= 0.971 \text{ MeV} \end{aligned}$$

β^- Branch 2 of 86% Intensity:

$$\begin{aligned} E_{\beta_2^-} + E_{\bar{\nu}} + \gamma_2 &= E_{\text{max}} \text{ of } 0.607 \text{ MeV} + \gamma_2 \text{ of } 0.364 \text{ MeV} \\ &= 0.971 \text{ MeV} \end{aligned}$$

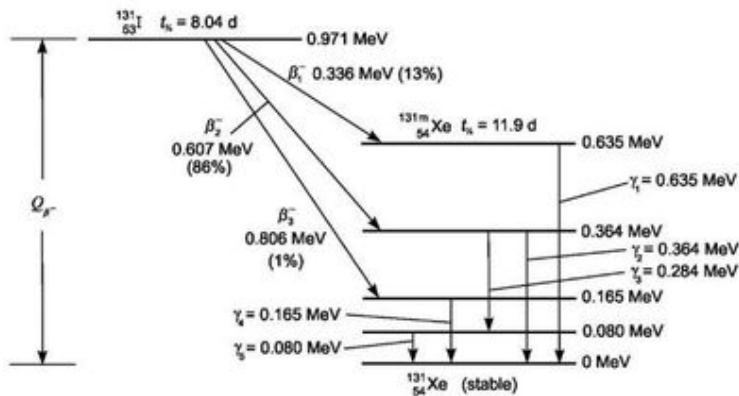


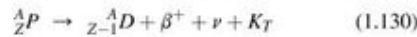
FIGURE 1.34 Negatron decay scheme of ^{131}I . The radionuclide ^{131}I decays to stable ^{131}Xe with three branching negatron emissions with energy maxima at 0.336 MeV, 0.607 MeV, and 0.806 MeV producing metastable ^{131m}Xe at three energy levels yielding several gamma ray lines of emissions, namely, $\gamma_1 = 0.635 \text{ MeV}$, $\gamma_2 = 0.364 \text{ MeV}$, $\gamma_3 = 0.284 \text{ MeV}$, $\gamma_4 = 0.165 \text{ MeV}$, and $\gamma_5 = 0.080 \text{ MeV}$.

β^- Branch 3 of 1% Intensity:

$$E_{\beta_3} + E_{\bar{\nu}} + \gamma_4 = E_{\max} \text{ of } 0.806 \text{ MeV} + \gamma_3 \text{ of } 0.165 \text{ MeV} = 0.971 \text{ MeV}$$

2. Positron (β^+) Emission

Positron emission can be described by the general equation



where ${}^A_Z P$ is the parent nuclide of atomic number Z and mass number A , ${}^A_{Z-1} D$ is the daughter nuclide of atomic number $Z-1$ and same mass number as the parent, β^+ is the positron or positive beta particle, ν is the neutrino, and K_T is the total kinetic energy released in the best-decay process.

a. Basic Principles

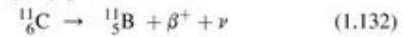
In contrast to negatron emission from nuclei having neutron/proton (n/p) ratios too large for stability, positrons, which consist of positively charged electrons (positive beta particles), are emitted from nuclei having n/p ratios too small for stability, that is, those which have an excess of protons.

To attain nuclear stability, the n/p ratio is increased. This is realized by a transformation of a proton to a neutron within the nucleus. The previously discussed alteration of a neutron to a proton in a negatron-emitting nuclide Eqn (1.103) may now be

considered in reverse for the emission of positrons. Eqn (1.31) illustrates such a transformation:



The decay of the radionuclide ${}^{11}\text{C}$ may be cited as an example of a nuclide that decays by positron emission:



Note that the mass number does not change, but the charge on the nucleus (Z number) decreases by 1. As in negatron emission, a neutrino, ν , is emitted simultaneously with the positron (beta particle) and shares the decay energy with the positron. Thus, positrons, like negatrons emitted from a given radionuclide sample, may possess a broad spectrum of energies from near zero to E_{\max} , as illustrated in Fig. 1.30.

Decay by positron emission can occur only when the decay energy is significantly above 1.02 MeV. This is because two electrons of opposite charge are produced (β^+ , β^-) within the nucleus, and the energy equivalence of the electron mass is 0.51 MeV (see Section X.C). The positive electron, β^+ , is ejected from the nucleus and the negative electron, β^- , combines with a proton to form a neutron:



From the Chart of the Nuclides, it is possible to cite specific examples of the n/p imbalance in relation to negatron and positron emission. Fig. 1.35 illustrates a segment of the Chart of

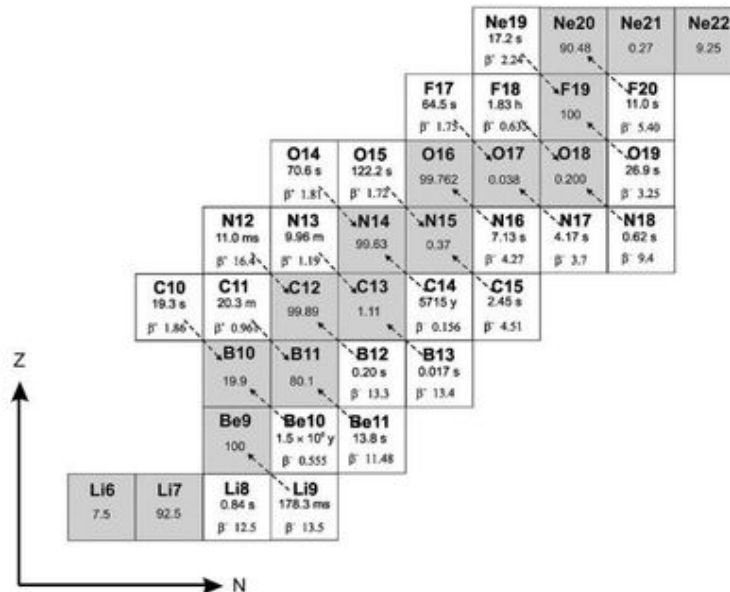
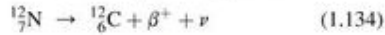


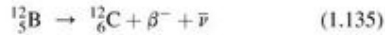
FIGURE 1.35 A Segment of the Chart of the Nuclides showing the relative positions of some stable (shaded) and unstable nuclides. The ordinate Z and abscissa N represent the number of protons (atomic number) and the number of neutrons (neutron number) within the nucleus, respectively. The mass number (number of protons + neutrons) in the nucleus of an isotope is provided alongside the abbreviation of the element. For example, the isotope ${}^{14}\text{C}$ (carbon-14) is written in the Chart as C14. Radionuclides that undergo positron emission (β^+) are illustrated with arrows pointing downward to stable nuclide products of lower atomic number; and radionuclides undergoing negatron (β^-) emission are illustrated with arrows pointing upward to stable nuclide products of higher atomic number. The maximum beta-particle energy in units of MeV is provided alongside the positron or negatron symbol. Numbers in shaded areas are the percent natural abundances of the stable isotopes, which for each element should add up to 100%. For example, the element lithium (Li) exists in nature as a combination of two stable isotopes, namely, ${}^6\text{Li}$ and ${}^7\text{Li}$ with abundances of 7.5 and 92.5%, respectively. When only one stable isotope of an element exists, its natural abundance will be expressed as 100%, such as is the case for ${}^9\text{Be}$ and ${}^{19}\text{F}$ illustrated above. The half-lives of the unstable nuclides are given in units of seconds (s), milliseconds (ms), minutes (m), hours (h) and years (y).

the Nuclides and the relative positions of the stable nuclides (shaded areas) and of their neighboring radionuclides. The nuclides are positioned as a function of the number of protons, Z , and the number of neutrons, N , in their respective nuclei. Dashed arrows are placed through the blocks that segregate radionuclides interrelated with common daughter nuclides resulting from β^- or β^+ decay processes. For example, the stable nuclide ^{12}C of atomic number 6 has a nucleus with an n/p ratio of 6/6. However, the nuclide ^{12}N of atomic number 7 has an unstable n/p ratio of 5/7, an excess of protons. Thus, this radionuclide ^{12}N decays to ^{12}C via positron emission according to the equation



as indicated by a dashed arrow of Fig. 1.35.

The nuclide ^{12}B of atomic number 5 has the unstable n/p ratio of 7/5, an excess of neutrons. This nuclide thus decays to ^{12}C by negatron emission according to the equation



Similar reasoning may be used to explain positron and negatron decay of the unstable nuclides shown in Fig. 1.35 to the stable products ^{13}C , ^{14}N , ^{15}N , etc. The interrelationship between β^- and β^+ decay leading to the formation of stable nuclides is to be found throughout the Chart of the Nuclides. Nuclear stability with n/p ratios close to unity only exists with nuclides of low atomic number ($Z \leq 20$), as discussed in Section IV.D.1 and in the following section.

b. N/Z Ratios and Beta Decay

In Sections VIII.B.1.a and VIII.B.2.a, we discussed negatron and positron decay as processes whereby unstable nuclei may achieve stability via neutron or proton transformations in negatron and positron beta-decay processes, respectively. These processes in the nucleus of the radionuclide result in a change in the neutron/proton or N/Z ratio of the nucleus.

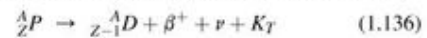
If we look throughout the Chart of the Nuclides, we will notice that the stable nuclides of low atomic number will have an N/Z ratio of approximately 1. However, as the atomic number increases ($Z > 20$), the N/Z ratio of the stable nuclides increases gradually and reaches as high as approximately 1.5 (e.g., $^{209}_{83}\text{Bi}$, $Z = 83$, $N/Z = 1.518$). This was illustrated previously in Fig. 1.12. Furthermore, there are no stable nuclides of atomic number greater than 83.

The nature of nuclear forces and the relationship of N/Z ratio to nuclear stability are discussed in detail in Part IV.D.1, and by Serway et al (2005) and Sundaresan (2001). In brief, the importance of N/Z ratio to nuclear stability is explained by the fact that there exists a short-range attractive nuclear force, which extends to a distance of ≈ 2 fm (2 fermi or 2×10^{-15} m). This attractive force has charge independence and is a consequence of the relative spins of the protons and neutrons and their relative positions in the nucleus. Therefore, these binding exchange forces exist regardless of charge on the particles, between two protons, two neutrons, and a proton and neutron. While the attractive nuclear forces will tend to hold the nucleus together, there exists, at the same time, repelling Coulombic forces between the positively charged protons that act to force them apart. For nuclides of low Z , the

attractive nuclear forces exceed the repelling Coulombic forces when $N \approx Z$. However, increasing the number of protons (e.g., $Z > 20$) further increases the strength of the repelling Coulombic forces over a larger nucleus, which will tend to force the nucleus apart. Therefore, additional neutrons, $N > Z$, provide additional attractive nuclear forces needed to overcome the repelling forces of the larger proton population. As the atomic number increases further, $Z > 83$, all nuclides are unstable. Even though N/Z ratios reach 1.5, nuclear stability is not achieved when the number of protons in the nucleus exceeds 83.

c. Positron Decay Energy

The general reaction for positron emission was described previously by Eqn (1.130). It is provided here again for a treatment on positron decay energy, and it is the following:



where $^A_Z P$ is the parent nuclide of atomic number Z and mass number A , $^A_{Z-1} D$ is the daughter nuclide of atomic number $Z-1$ and same mass number as the parent, β^+ is the positron or positive beta particle, ν is the neutrino, and K_T is the total kinetic energy released in the beta-decay process.

In terms of nuclear masses, Eqn (1.136) may be written as

$${}_Z M_P = {}_{Z-1} M_D + m_e + K_T \quad (1.137)$$

where ${}_Z M_P$ and ${}_{Z-1} M_D$ are the masses of the parent and daughter nuclei of atomic number Z and $Z-1$, respectively, and m_e is the mass of the positron (i.e., one electron mass). Atomic mass units (u) may be used to calculate conveniently the mass difference of the parent and daughter, if we add Z atomic electron masses to each side of Eqn (1.137) and ignore the negligible difference in electron-binding energies of the parent and daughter atoms. Adding Z atomic electrons to each side of Eqn (1.137) gives

$${}_Z M_P + Z m_e = {}_{Z-1} M_D + (Z + 1) m_e + K_T \quad (1.138)$$

and

$${}_Z M_P = {}_{Z-1} M_D + 2 m_e + K_T \quad (1.139)$$

The mass difference of the parent and daughter nuclei is equivalent to the decay energy, Q_{β^+} . The decay energy, Q_{β^+} , may be calculated now using atomic mass units and taking the product of mass and c^2 to determine the energy equivalence of mass using Eqn (1.139) to give

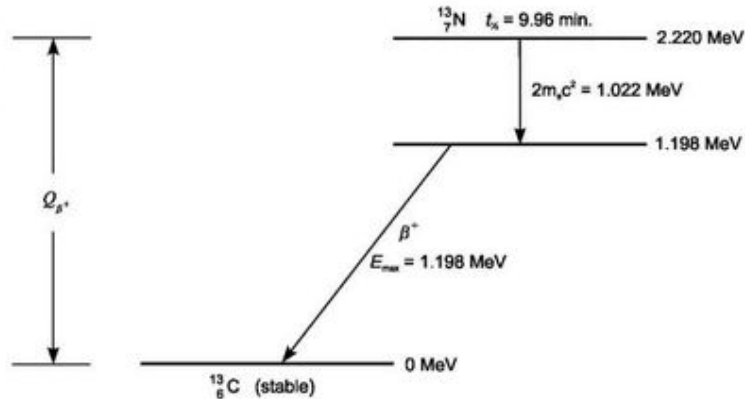
$$Q_{\beta^+} = ({}_Z M_P - {}_{Z-1} M_D) c^2 = 2 m_e c^2 + K_T \quad (1.140)$$

or

$$Q_{\beta^+} = ({}_Z M_P - {}_{Z-1} M_D) c^2 = 2 m_e c^2 + K_{\beta^+} + E_\nu + E_{\text{recoil}} \quad (1.141)$$

where ${}_Z M_P - {}_{Z-1} M_D$ is the mass difference of the parent and daughter nuclides, c is the speed of light in a vacuum, and $2 m_e c^2$ is the energy equivalence of two electron masses or 1.022 MeV, which is the energy required for the creation of the $e^+ e^-$ pair in the positron decay process described previously in this section. The terms $E_{\beta^+} + E_\nu$ are the shared positron and neutrino kinetic energies, which when combined is referred often to as the E_{max} of the beta decay. The term E_γ is gamma-ray energy that may be

FIGURE 1.36 Beta decay of ^{13}N to stable ^{13}C by positron (β^+) emission. The scheme illustrates the energy equivalence (1.022 MeV) of two electron masses (e^+e^-) required for positron emission. The remaining 1.198 MeV energy is shared by the β^+ and ν .



emitted by the daughter nucleus, and E_{recoil} is the nuclear recoil energy, which is relatively small (measured in eV) and can be ignored as negligible when calculating the overall decay energy (measured in MeV).

We may take an example of a simple case of positron emission in the decay of ^{13}N where there is no gamma radiation from the daughter nucleus, that is, the ^{13}N nucleus decays directly to ^{13}C at its stable ground state with the emission of a positron and neutrino with maximum energy 1.198 MeV. The scheme for the decay of ^{13}N is illustrated in Fig. 1.36.

The E_{max} is the combined energy of the positron and neutrino ($E_{\beta^+} + E_{\nu}$), that is, the energy shared by the positron and neutrino. In other words, the E_{max} is the maximum energy of the positron when the neutrino is at its minimum energy or vice versa.

The decay energy, Q_{β^+} , for ^{13}N decay is calculated as

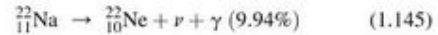
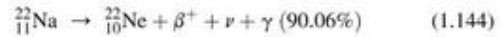
$$\begin{aligned}
 Q_{\beta^+} &= (M_{^{13}\text{N}} - M_{^{13}\text{C}})c^2 \\
 &= (13.0057386 \text{ u} - 13.0033548 \text{ u})(931.494 \text{ MeV/u}) \\
 &= 2.2204 \text{ MeV}
 \end{aligned}
 \tag{1.142}$$

which is the magnitude of the decay energy for ^{13}N listed in standard reference tables (e.g., Table of the Isotopes in Lide, 2010). The maximum energy of the β^+ or neutrino in this case

may be calculated easily according to Eqn (1.141) by ignoring the nuclear recoil energy (E_{recoil}), because of its small value and ignoring the gamma-ray energy (E_{γ}), because, in this example, no gamma-ray energy arises from the daughter nucleus following beta decay. Thus, the maximum energy of the β^+ or neutrino is

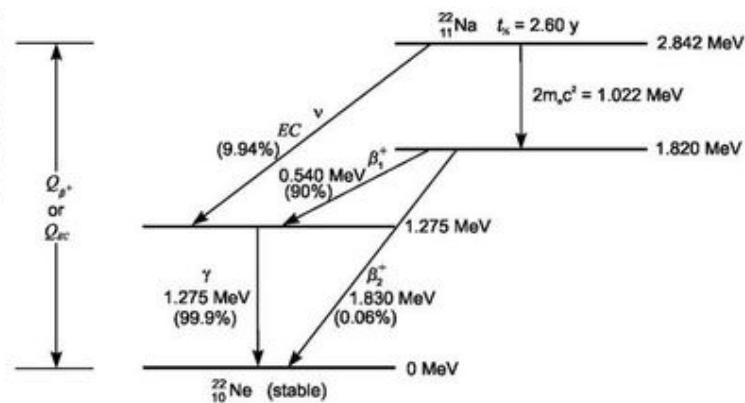
$$\begin{aligned}
 E_{\text{max}} &= E_{\beta^+} + E_{\nu} = Q_{\beta^+} - 2m_e c^2 \\
 &= 2.220 \text{ MeV} - 1.022 \text{ MeV} \\
 &= 1.198 \text{ MeV}
 \end{aligned}
 \tag{1.143}$$

A more complex example would be that of the decay of ^{22}Na , which decays by positron (β^+) emission and electron capture (EC) decay with the emission of gamma radiation according to the decay Eqns (1.144) and (1.145) and the decay scheme illustrated in Fig. 1.37:



As illustrated in Fig. 1.37, the radionuclide ^{22}Na may decay by electron capture (EC) in addition to positron emission. Electron capture is a decay mode that competes with positron emission as discussed in the following section. In this case, 90% of the ^{22}Na

FIGURE 1.37 Beta decay scheme of ^{22}Na by competing positron (β^+) and electron capture (EC) decay. Positron emission occurs in 90.06% of the nuclear decays and EC on the remaining 9.94%. Decay by EC involves the emission of a mono-energetic neutrino of 1.567 MeV (i.e., $E_{\nu} = 2.842 \text{ MeV} - 1.275 \text{ MeV}$) to metastable ^{22}Ne . Positron emission occurs with the consumption of the energy equivalence of two electron masses (i.e., $2m_e c^2$) followed by two branching positron emissions with intensities of 90% and 0.06%.



radionuclides decay via positron emission and the remaining 10% decay via electron capture. When the decay energy, Q_{β^+} , is well above 1.022 MeV (the minimum energy required for e^+e^- pair production), positron emission will predominate over electron capture decay.

The decay energy for ^{22}Na may be calculated according to Eqn (1.141) as

$$\begin{aligned} Q_{\beta^+} &= (M_{^{22}\text{Na}} - M_{^{22}\text{Ne}})c^2 \\ &= (21.994437 \text{ u} - 21.9913855 \text{ u})(931.494 \text{ MeV/u}) \\ &= 2.842 \text{ MeV} \end{aligned} \tag{1.146}$$

which is in agreement with the magnitude of the decay energy for ^{22}Na listed in standard reference tables (e.g., Table of the Isotopes in Lide, 2010). The calculated decay energy corresponds to the theoretical value described by Eq. 1.141, that is,

$$Q_{\beta^+} = 2m_e c^2 + E_{\beta^+} + E_{\nu} + E_{\gamma} + E_{\text{recoil}} \tag{1.147}$$

where $E_{\beta^+} + E_{\nu} = \beta_{\text{max}}^+$ and, if we ignore the relatively very small value of E_{recoil} , we calculate

$$\begin{aligned} Q_{\beta^+} &= 2m_e c^2 + \beta_{\text{max}}^+ + E_{\gamma} \\ &= 1.022 \text{ MeV} + 0.540 \text{ MeV} + 1.275 \text{ MeV} \\ &= 2.84 \text{ MeV} \end{aligned} \tag{1.148}$$

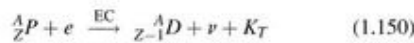
which is in accord with the β_1^+ transition illustrated in Fig. 1.37, and

$$\begin{aligned} Q_{\beta_2^+} &= 2m_e c^2 + \beta_{\text{max}}^+ \\ &= 1.022 \text{ MeV} + 1.830 \text{ MeV} \\ &= 2.85 \text{ MeV} \end{aligned} \tag{1.149}$$

which is in agreement with the β_2^+ transition illustrated in Fig. 1.37 whereby ^{22}Na decays directly to the stable ground state of ^{22}Ne without gamma emission in 0.06% of the nuclear decays.

3. Electron Capture (EC)

The electron capture (EC) decay process is described by the following general equation:



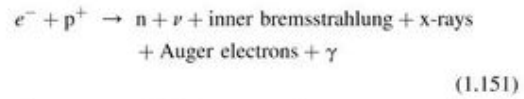
where ${}^A_Z P$ is the parent nuclide of atomic number Z and mass number A , e is an orbital electron captured by the nucleus of the parent nuclide, ${}^A_{Z-1} D$ is the daughter nuclide of atomic number $Z-1$ and same mass number as the parent, ν is the neutrino, and K_T is the total kinetic energy released in the beta-decay process.

a. Basic Principles

Electron capture (EC) is another form of beta decay. The change in atomic number is the same as occurs with positron (β^+) emission. Electron capture competes with positron emission and most radionuclides that decay by positron emission also decay by electron capture to the same daughter nuclide.

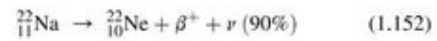
Another mechanism by which an unstable nucleus can increase its n/p ratio is via the capture by the nucleus of a proximate atomic electron (e.g., K - or L -shell electron). The

absorbed electron combines with a proton to yield a neutron within the nucleus as follows:

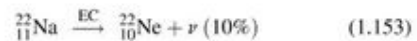


The decay process is known as electron capture (EC), or sometimes referred to as K -capture, because most of the electrons are captured from the K -shell, which is closest to the nucleus. A neutrino, ν , is emitted and this is accompanied by the emission of internal bremsstrahlung, which is a continuous spectrum of electromagnetic radiation that originates from the atomic electron as it undergoes acceleration toward the nucleus. Unlike the beta-decay process, which results in the emission of a neutrino from the nucleus with a broad spectrum of energies, the neutrino emitted from the EC-decay process does not share the transition energy with another particle and, therefore, it is emitted with a single quantum of energy equal to the transition energy less the atomic electron binding energy. The capture of an atomic electron by the nucleus leaves a vacancy in an electron shell, and this is filled usually by an electron from an outer shell, resulting in the production of x-radiation (see Sections IX.D.c). The electron that fills the vacancy leaves yet another vacancy at a more distant shell. A cascade of electron vacancies and subsequent filling of vacancies from outer electron shells occurs with the production of x-rays characteristic of the daughter atom. The x-rays will either travel out of the atom or the energy emitted by the electron transition will be transferred to an outer orbital electron causing the electron to be ejected as an Auger electron. Gamma radiation is illustrated in Eqn (1.151), because it is emitted only when the daughter nuclide is left at an unstable elevated energy state (see Figs 1.37 to 1.39).

The electron-capture decay process may compete with β^+ emission. That is, some radionuclides may decay by either electron capture or β^+ -emission. As discussed previously, positron emission requires a transition energy of at least 1.022 MeV, the minimum energy required for pair production in the nucleus (i.e., two electron rest mass energies or $2 \times 0.511 \text{ MeV}$). Positron emission, therefore, will not compete with electron capture for decay transitions less than 1.022 MeV. In general, positron emission will predominate when the transition energy is high (well above 1.022 MeV) and for nuclides of low atomic number, while the EC decay process will predominate for low transition energies and nuclides of higher atomic number. The decay transitions of ^{22}Na and ^{65}Zn serve as examples. In the case of ^{22}Na , decay by β^+ -emission predominates (90 %) as compared with decay via electron capture (10 %):



and



The transition energy of ^{22}Na is 2.842 MeV (Holden, 1997a), well above the 1.022 MeV minimum required for positron emission. Thus, positron emission predominates. On the other

FIGURE 1.38 Beta decay scheme of ^{44}Sc by competing EC decay and positron (β^+) emission. The high decay energy of 3.653 MeV favors β^+ emission, as it is well above the minimum 1.022 MeV or $2m_e c^2$ required for positron emission. EC decay occurs in only 5% of the nuclear decays and β^+ emission in the remaining 95%. Both EC and β^+ decay yield meta-stable ^{44m}Ca , which decays to stable ^{44}Ca with gamma-ray emission of 1.159 MeV.

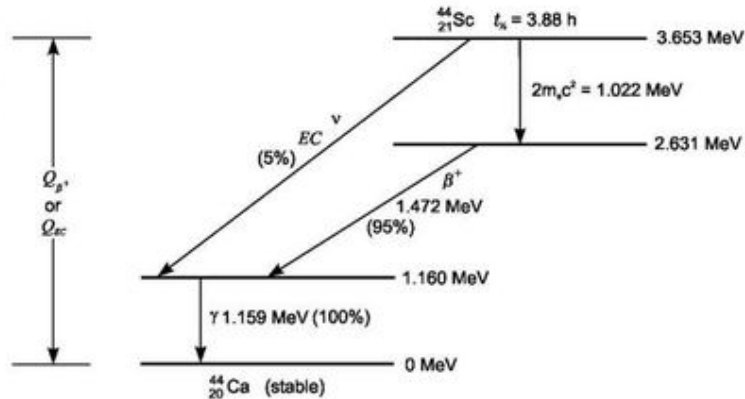
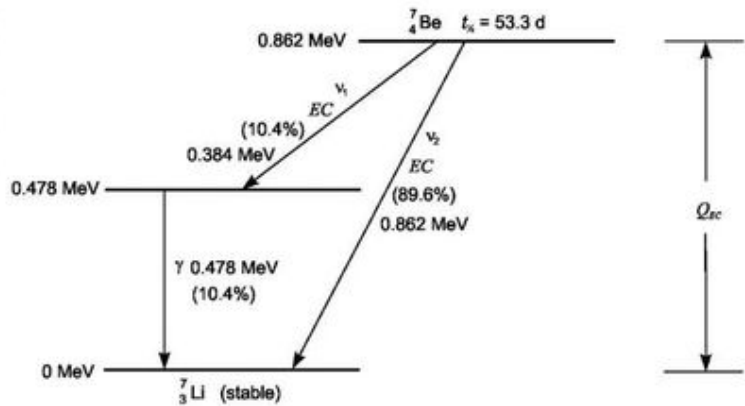
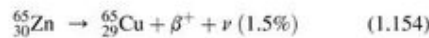


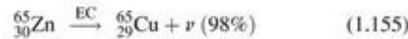
FIGURE 1.39 Decay scheme of ^7Be . The decay occurs exclusively by branching electron capture. In 10.4% of the transitions, ^7Be emits a mono-energetic neutrino of 0.384 MeV (i.e., 0.862 MeV – 0.478 MeV) followed by the emission of a 0.478 MeV gamma-ray photon. The remaining EC decay events occur with the emission of a mono-energetic neutrino of 0.862 MeV directly to the ground state of stable ^7Li in 89.6% of the decay transitions.



hand, taking the following example of the nuclide ^{65}Zn , we see that electron capture predominates over β^+ emission:



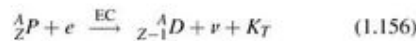
and



In the case of ^{65}Zn , the transition energy is only 1.35 MeV (Holden, 1997a), not much above the minimum energy of 1.02 MeV required for positron emission. Consequently, EC decay predominates.

b. EC Decay Energy

The general decay equation for electron capture was described previously by Eqn (1.150). It is provided here again for a treatment of electron capture decay calculations, and it is as follows:



where $^A_Z P$ is the parent nuclide of atomic number Z and mass number A , e is an orbital electron captured by the nucleus of the parent nuclide, $^A_{Z-1} D$ is the daughter nuclide of atomic number

$Z-1$ and same mass number as the parent, ν is the neutrino, and K_T is the total kinetic energy released in the beta decay process.

In mass and energy terms, Eqn (1.156) can be written as

$${}_Z M_P + m_e = {}_{Z-1} M_D + K_T \quad (1.157)$$

where ${}_Z M_P$ is the mass of the parent nuclide of atomic number Z , m_e is the mass of the atomic electron captured by the nucleus, and ${}_{Z-1} M_D$ is the mass of the daughter nucleus of atomic number $Z-1$. We may use atomic mass units (u) to calculate conveniently the mass difference of the parent and daughter nuclei and arrive at the decay energy by firstly adding $Z-1$ atomic electrons to each side of Eqn (1.157), which yields

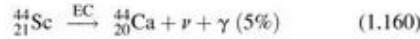
$${}_Z M_P = {}_{Z-1} M_D + K_T \quad (1.158)$$

The mass difference of the parent and daughter nuclei is equivalent to the decay energy (Q_{EC}). We can now calculate the decay energy Q_{EC} by the difference of the parent and daughter nuclide atomic masses ignoring the small difference in the binding energies of the electrons in the two nuclides as

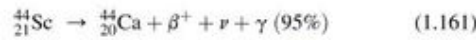
$$Q_{EC} = ({}_Z M_P - {}_{Z-1} M_D) c^2 = K_T = E_\nu + E_\gamma + E_{\text{recoil}} \quad (1.159)$$

where c is the velocity of light in a vacuum and the product Mc^2 yields the energy equivalence of the mass. E_ν is the kinetic energy of the neutrino, E_γ is the gamma-ray photon energy, which only appears with the decay of the daughter nucleus when it is left at a metastable or excited energy state, and E_{recoil} is the kinetic energy of the daughter recoil nucleus. As in previously described beta-decay processes, we will ignore the relatively very small recoil energy when calculating the overall decay energy.

As an example, let us look at the decay scheme of ^{44}Sc , which decays by EC and positron emission. The decay equations are the following:



and



The decay scheme is illustrated in Fig. 1.38.

The scheme in Fig. 1.38 illustrates that 5% of the ^{44}Sc nuclides decay by electron capture and the remaining 95% of the nuclides decay with positron emission with a positron E_{\max} of 1.472 MeV. The ^{44}Ca product nuclides then decay to a stable ground state with the emission of gamma radiation of 1.159 MeV energy.

The decay energy for either mode of decay (EC or β^+ emission) is calculated according to Eqns (1.159) and (1.146), respectively, as follows:

For Electron Capture

$$\begin{aligned} Q_{\text{EC}} &= ({}_Z M_P - {}_{Z-1} M_D)c^2 = E_\nu + E_\gamma + E_{\text{recoil}} \\ &= (M^{44}\text{Sc} - M^{44}\text{Ca})c^2 \\ &= (43.959403 \text{ u} - 43.955481 \text{ u})(931.494 \text{ MeV/u}) \\ &= 3.653 \text{ MeV} \end{aligned} \quad (1.162)$$

which is in agreement with the decay energy provided in the standard reference tables (e.g., Holden, 1997a). As we know that the gamma-ray energy $E_\gamma = 1.159$ MeV (see Fig. 1.38) and, if we disregard the very small magnitude of the recoil energy, we can calculate the neutrino energy in this case as

$$E_\nu = Q_{\text{EC}} - E_\gamma = 3.653 \text{ MeV} - 1.159 \text{ MeV} = 2.494 \text{ MeV} \quad (1.163)$$

The neutrino energies are monoenergetic in the case of the EC decay mode.

For Positron Emission

$$\begin{aligned} Q_{\beta^+} &= ({}_Z M_P - {}_{Z-1} M_D)c^2 \\ &= 2m_e c^2 + E_{\beta^+} + E_\nu + E_\gamma + E_{\text{recoil}} \\ &= (M^{44}\text{Sc} - M^{44}\text{Ca})c^2 = 3.653 \text{ MeV} \end{aligned} \quad (1.164)$$

as calculated in Eqn (1.162).

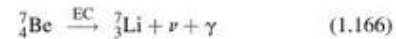
If we again ignore the very small daughter nucleus recoil energy and combine the positron and neutrino energies as

$E_{\max} = E_{\beta^+} + E_\nu$, we can arrive at the decay energy taking the values from Fig. 1.38 as

$$\begin{aligned} Q_{\beta^+} &= 2m_e c^2 + E_{\max} + E_\gamma \\ &= 1.022 \text{ MeV} + 1.472 \text{ MeV} + 1.159 \text{ MeV} \\ &= 3.653 \text{ MeV} \end{aligned} \quad (1.165)$$

The decay energy of 3.653 MeV is well above the minimum energy for e^+e^- pair production ($2m_e c^2$ or 1.022 MeV) required for positron emission. Thus, the EC decay does not compete well against positron emission in the case of ^{44}Sc , which decays via positron emission in 95% of the disintegrations and by EC decay in the remaining 5%.

Let us take another example, which is that of ^7Be decaying exclusively by electron capture according to the following equation:



The decay energy is calculated as

$$\begin{aligned} Q_{\text{EC}} &= (M_{^7\text{Be}} - M_{^7\text{Li}})c^2 \\ &= (7.016929 \text{ u} - 7.016004 \text{ u})(931.494 \text{ MeV/u}) \\ &= 0.862 \text{ MeV} \end{aligned} \quad (1.167)$$

which is in agreement with the magnitude of the decay energy reported in standard reference tables (e.g., Holden, 1997a). The decay energy is not sufficient to satisfy the minimum energy requirement of 1.022 MeV for positron emission in this case. Thus, there is no competition here between EC and β^+ decay modes, and the ^7Be nuclides decay exclusively by EC according to the decay scheme illustrated in Fig. 1.39.

The daughter nuclide, ^7Li , emits a gamma ray of 0.478 MeV in 10.4% of the transitions. The neutrino energy from the EC decay of ^7Be in these transitions would be derived from the difference of the decay energy and gamma-ray energy while ignoring the relatively very small recoil energy according to Eqn (1.163), or

$$\begin{aligned} E_\nu &= Q_{\text{EC}} - E_\gamma \\ &= 0.862 \text{ MeV} - 0.478 \text{ MeV} \\ &= 0.384 \text{ MeV} \end{aligned} \quad (1.168)$$

The remaining 89.6% of the transitions would be due to a neutrino emission of 0.862 MeV directly to the stable ground state of the daughter nuclide without any gamma-ray emission. Neutrinos emitted in the EC decay process are monoenergetic. They do not possess any broad spectrum of energies, contrary to the neutrinos emitted during β^+ or β^- emission, because the neutrinos emitted from the nucleus in EC decay do not share the decay energy with any other particle.

There is nuclear recoil of the parent nucleus during EC decay resulting from the emission of the neutrino. The nuclear recoils in EC decay have been measured by researchers confirming the monoenergetic character of the emitted neutrino. The calculation of nuclear recoil energies is discussed in detail in Section XI.

The ^7Li ion will recoil at two energy maxima corresponding to the neutrino emissions of 0.862 and 0.384 MeV calculated

above. The maximum recoil energy corresponding to the neutrino emission of 0.862 MeV is calculated, according to Eqns (1.345) and (1.351), to be 56.84 eV. This agrees with the experimental measurement of the ${}^7\text{Li}$ recoil energy reported by 2002 Nobel Laureate Raymond Davis Jr. (1952) to be 56 ± 1 eV. The recoil energy in this case is relatively high (>10 eV), because of the relatively low mass of the ${}^7\text{Li}$ nucleus. Nevertheless, the recoil energy here may be ignored as negligible when calculating the decay energy, which has units of MeV.

c. Chemical and Pressure Effects on EC Decay Rates

In general, the chemical and physical environment of radionuclides do not control nuclear decay processes. However, because the electron-capture decay process involves the capture of an orbital electron by the nucleus, atomic- or molecular-binding effects, which vary with chemical structure, can influence the electron-capture decay process. Also, external pressure that may alter electron densities in the vicinity of the nucleus could also have an altering effect on the EC decay rate.

Emilio Segré (1947) at the Los Alamos Laboratories in the USA and R. Daudel (1947) at the Curie Laboratories of the Radium Institute in Paris, France, were the first to independently suggest that the rate of disintegration of nuclei decaying by electron capture or internal conversion would be subject to extra-nuclear environments. Numerous works were published from 1948 to the 1970's confirming the effect of chemical environment on the decay rate of ${}^7\text{Be}$, and these are reviewed by Huh (1999). The effect of pressure on the decay constant of ${}^{99}\text{Tc}$ was first confirmed by Bainbridge (1952), and the mathematical expression for the shift in the binding energy of the atomic electron under pressure, that would affect EC decay rates, was derived by Mukoyama and Shimizu (1974).

During the last two decades or so, much attention has been given to experimentation related to chemical and pressure effects on radionuclide EC decay rates due to the technological advances in detector instrumentation with improved detection efficiencies and energy resolution of semiconductor detectors that can now yield more precise decay-rate measurements. Utilizing a 100% efficiency high-purity germanium detector, Huh (1999) was able to determine the decay constant of ${}^7\text{Be}$ in three chemical environments, namely, $\text{Be}^{2+}(\text{OH})_4$, $\text{Be}(\text{OH})_2$, and BeO with a precision of 0.01% resulting in a $\sim 1.5\%$ difference in the decay rates of ${}^7\text{Be}$ in $\text{Be}(\text{OH})_2$ and BeO . Also, Ray et al (1999) found the decay rate of ${}^7\text{Be}$ implanted in Au was $0.72 \pm 0.07\%$ lower than ${}^7\text{Be}$ implanted in Al_2O_3 . The variation in decay rates of the ${}^7\text{Be}$ was considered a result of the change in the electron density around the nucleus of ${}^7\text{Be}$ due to its association with different anions, and atomic electron affinity and geometry of the lattice within which the ${}^7\text{Be}$ was implanted. Electron capture occurs mostly with electrons in closest proximity to the nucleus, such as electrons from the *K*-shell, and any chemical bond or environment that would force atomic electrons closer to the nucleus or reduce the electron binding energy would increase the electron-capture decay rate.

The combination of chemical environment and pressure can affect electron-capture decay rates. Liu and Huh (2000) found a steady increase in the decay constant of ${}^7\text{Be}$ in $\text{Be}(\text{OH})_2$ as a function of pressure over the range of 1 atm to 441 kbar. The

decay constant increased by 1% at 441 kbar compared to the decay constant at 1 atm, which corresponded to a change in half-life from 53.414 ± 0.003 days at 1 atm to 52.884 ± 0.022 days at 441 kbar pressure. These results were consistent with calculations made by Tossell (2002) on the effects of Be–O bond compression in $\text{Be}(\text{OH})_4^{2-}$ on the energy and the electron density at the nucleus of ${}^7\text{Be}$, which indicates that several hundred kbar pressure could increase the electron density by 1% or more. This would expectedly facilitate the capture of an orbital electron by the nucleus and increase the decay rate. Lee and Steinle-Neumann (2008) demonstrated a 0.1–0.2% increase in the decay constant of ${}^7\text{Be}$ as a metal, chloride, or oxide under a pressure of 25 GPa. The radionuclides ${}^{22}\text{Na}$ and ${}^{40}\text{K}$ in metallic form showed an increase of 0.06% and 0.025% in their decay constants, respectively, at 25 GPa pressure. Ray et al (2009) also observed an increase in the orbital electron capture rates of ${}^{109}\text{In}$ and ${}^{110}\text{Sn}$ by $1.00 \pm 0.17\%$ and $0.48 \pm 0.25\%$, respectively, when implanted in the smaller Au lattice compared to implantation in a larger Pb lattice. They interpret the increased decay rates as due to an increase in the eigenstate energies of an atom under spatial confinement. This effect would increase the electron density of the orbital electrons at the nucleus and thus increase the decay rate of an electron capturing radioactive nucleus.

While the fluctuations in the observed electron-capture decay rates may appear small, Zito and Schifnerl (1987) indicate that the effects may be significant in terms of stellar energetics. They note that pressure-dependent decay may be an important source of heat generation in Jovian planets where central pressures may reach megabars. They give the example of Jupiter's rock-ice core, which contains as much potassium as Earth's continental crust, and that ${}^{40}\text{K}$ decay accounts for about 11.5% of the total excess energy output of Jupiter. This energy divided into two parts gives 9.3% due to normal (zero-pressure) beta and EC decay, and the remaining 2.2% would be due to pressure effects alone on the EC decay rate. Also, they surmise that pressure effects on the EC decay rate of ${}^{90m}\text{Nb}$ could account for 14% of the total energy output of Jupiter's core. Also, the high pressures in Saturn, Uranus, and Neptune could have a role in pressure-accelerated EC decay as an important heat source in these planets. Zito and Schifnerl (1987) also provide convincing arguments in support of the role of ${}^{50}\text{V}$, ${}^{123}\text{Te}$, ${}^{138}\text{La}$, ${}^{40}\text{K}$, ${}^{26}\text{Al}$, and ${}^{36}\text{Cl}$, which undergo EC decay, in stellar energetics. They note that peculiar A stars are enriched in La isotopes by a factor of 600 over normal stars, and other stars breed significant amounts of ${}^{26}\text{Al}$ and ${}^{36}\text{Cl}$. They point out that sudden pressure changes in the interior of these stars could result in EC outbursts.

4. Branching β^- , β^+ , and EC Decay

It is a common practice to characterize radionuclide beta decay according to (i) negatron (β^-) emission and (ii) positron (β^+) emission and/or electron capture (EC). However, there exists also several radionuclides of odd atomic number *Z* and even mass number *A* that decay via all beta decay modes, namely β^- , β^+ , and EC decay to varying degrees yielding two daughter nuclides that differ by two units of atomic number. Their decay may be described by the branching pathways illustrated in Fig. 1.40 where

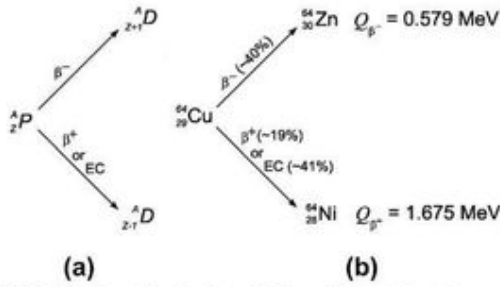


FIGURE 1.40 Branching β^- , β^+ and EC decay illustrated by (a) the general decay reaction of a parent nuclide ${}^A_Z P$ to daughter nuclides ${}^{A}_{Z+1} D$ and ${}^{A}_{Z-1} D$, and (b) the decay of ${}^{64}_{29} \text{Cu}$ to the daughter nuclide ${}^{64}_{30} \text{Zn}$ by negatron (β^-) emission and to the daughter nuclide ${}^{64}_{28} \text{Ni}$ by positron (β^+) emission or electron-capture (EC) decay. The intensities of the three modes of decay, that is, their branching ratios are ~40% for negatron emission, ~19% for positron emission and ~41% for electron capture decay.

the parent nuclide ${}^A_Z P$ decays in two directions, namely, by β^- emission to a daughter nuclide ${}^{A}_{Z+1} D$ of atomic number $Z+1$ and by β^+ emission and by EC decay to a daughter nuclide of atomic number $Z-1$. This decay phenomenon is also referred to as “dual beta decay”; however, it should not be confused with “double beta decay”, which is an altogether different and more elusive decay process described in a subsequent section.

Radionuclides that decay by means of this branching β^- , β^+ , and EC decay are listed in Table 1.11 together with the relative intensity (%) to which these three beta-decay modes occur, along with the decay energies of each mode, and their daughter nuclides. These radionuclides can be found in the Chart of the Nuclides together with their neighboring isobars that are stable. A segment of the Chart of the Nuclides illustrating the positions of ${}^{36}\text{Cl}$ and ${}^{40}\text{K}$, which decay by the three

β^- , β^+ and EC modes, and their neighboring stable daughter isobars is provided in Fig. 1.41.

The decay schemes of ${}^{36}\text{Cl}$ and ${}^{40}\text{K}$ exhibit very low relative occurrences of their β^+ decay modes, namely 0.002% and 0.3%, respectively (See Table 1.10), which may be due to their relatively low decay energies (Q_{EC,β^+}) of 1.142 and 1.505 MeV, respectively (see Table 1.10). Positron decay will compete and predominate over the EC decay mode when the decay energy is well above 1.022 MeV, which is the energy required for the production of an e^+e^- pair needed for the positron decay mode. The following two nuclides listed in Table 1.10, namely ${}^{64}\text{Cu}$ and ${}^{74}\text{As}$, have higher decay energies (Q_{EC,β^+}) of 1.675 and 2.562 MeV, respectively, yielding more significant intensities of 19 and 31%, respectively, for their β^+ decay modes as listed in Table 1.10.

There are an additional 25 radionuclides that decay by branching negatron (β^-) and electron capture (EC) decay modes, whereas positron (β^+) emission does not occur. These radionuclides decay according to the general scheme provided in Fig. 1.40 with the exception that the positron (β^+) decay mode does not occur. The properties of these radionuclides, their decay modes, and product nuclides are included in the Table of Radioactive Isotopes listed in Appendix A. They can be easily identified by the fact that both β^- and EC decay modes are listed and there are two product nuclides rather than the customary one nuclide product. Although positron emission does not occur in these cases, the parent nuclide of atomic number Z decays to two daughter nuclides of atomic numbers $Z-1$ and $Z+1$. These nuclides, which do not decay by positron emission, have mostly low decay energies ($Q_{\text{EC}} < 1.0 \text{ MeV}$). The decay energies are below the minimum decay energy equivalent to two electron masses (1.022 MeV) for the production of an e^+e^- pair required in the positron decay mode.

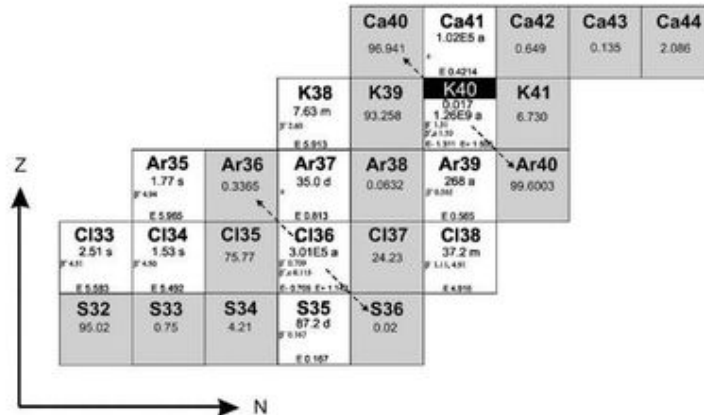


FIGURE 1.41 A segment of the Chart of the Nuclides illustrating the location of ${}^{36}_{17}\text{Cl}$ and ${}^{40}_{19}\text{K}$, which decay to neighboring stable isobars (indicated by arrows via negatron (β^-) emission with increasing Z and via positron (β^+) emission and EC with decreasing Z). The stable and naturally occurring nuclides are shaded blocks, and the percent natural abundance of the isotope is included in the center of the shaded block. ${}^{40}\text{K}$ is a naturally occurring, but radioactive isotope of potassium, and it is thus displayed differently with a black bar over the symbol of the element and the mass number of the isotope. Units of half-life are abbreviated as ‘s’, ‘m’, ‘d’, or ‘a’ for seconds, minutes, days, or anni (years). Beta decay modes are abbreviated as β^- , β^+ , and ϵ for negatron, positron, and electron capture, respectively, with decay energies in MeV. The decay energy of a radionuclide is in MeV at the bottom of each block alongside the letter E. Two decay energies are given for the radionuclides, ${}^{36}\text{Cl}$ and ${}^{40}\text{K}$, because of their branching beta decay modes. The value after the negative sign (E-) is the decay energy for the negatron decay mode and the other with a positive sign (E+) is the decay energy for the positron and EC decay modes.

TABLE 1.10 Radionuclides that Decay via Branching β^- , β^+ , and Electron Capture (EC)^a

Radionuclide	Decay modes (%)	Decay energies (MeV)	Product nuclides
³⁶ ₁₇ Cl	β^- (98%)	Q_{β^-} , 0.708	³⁶ ₁₈ Ar(β^-)
	β^+ (0.002%)	Q_{β^+EC} , 1.421	³⁶ ₁₆ S(β^+ , EC)
	EC (1.9%)		
⁴⁰ ₁₉ K	β^- (89%)	Q_{β^-} , 1.311	⁴⁰ ₂₀ Ca(β^-)
	β^+ (0.3%)	Q_{β^+EC} , 1.505	⁴⁰ ₁₈ Ar(β^+ , EC)
	EC (10.7%)		
⁶⁴ ₂₉ Cu	β^- (40%)	Q_{β^-} , 0.579	⁶⁴ ₃₀ Zn(β^-)
	β^+ (19%)	Q_{β^+EC} , 1.675	⁶⁴ ₂₈ Ni(β^+ , EC)
	EC (41%)		
⁷⁴ ₃₃ As	β^- (32%)	Q_{β^-} , 1.353	⁷⁴ ₃₄ Se(β^-)
	β^+ (31%)	Q_{β^+EC} , 2.562	⁷⁴ ₃₂ Ge(β^+ , EC)
	EC (37%)		
⁸⁰ ₃₅ Br	β^- (92%)	Q_{β^-} , 2.004	⁸⁰ ₃₆ Kr(β^-)
	β^+ (2.6%)	Q_{β^+EC} , 1.871	⁸⁰ ₃₄ Se(β^+ , EC)
	EC (5.7%)		
⁸⁴ ₃₇ Rb	β^- (3%)	Q_{β^-} , 0.894	⁸⁴ ₃₈ Sr(β^-)
	β^+ (22%)	Q_{β^+EC} , 2.681	⁸⁴ ₃₆ Kr(β^+ , EC)
	EC (75%)		
¹⁰² ₄₅ Rh	β^- (22%)	Q_{β^-} , 1.150	¹⁰² ₄₆ Pd(β^-)
	β^+ (14%)	Q_{β^+EC} , 2.323	¹⁰² ₄₄ Ru(β^+ , EC)
	EC (64%)		
¹⁰⁸ ₄₇ Ag	β^- (97%)	Q_{β^-} , 1.650	¹⁰⁸ ₄₈ Cd(β^-)
	β^+ (0.2%)	Q_{β^+EC} , 1.922	¹⁰⁸ ₄₆ Pd(β^+ , EC)
	EC (2.8%)		
¹²⁶ ₅₁ I	β^- (47.3%)	Q_{β^-} , 1.258	¹²⁶ ₅₄ Xe(β^-)
	β^+ (1%)	Q_{β^+EC} , 2.155	¹²⁶ ₅₃ Te(β^+ , EC)
	EC (51.7%)		
¹³⁰ ₅₅ Cs	β^- (1.6%)	Q_{β^-} , 0.370	¹³⁰ ₅₆ Ba(β^-)
	β^+ (43.6%)	Q_{β^+EC} , 2.979	¹³⁰ ₅₄ Xe(β^+ , EC)
	EC (54.8%)		

^aData from Lide (2010), Firestone et al. (1996), and National Data Center, Brookhaven National Laboratory: <http://www.nndc.bnl.gov/nudat2/>.

5. Double-Beta ($\beta\beta$) Decay

Double-beta decay is the rarest of all radioactive decay processes ever observed. It may be described by the following general equation:

$${}^A_ZP \rightarrow {}^A_{Z+2}D + 2\beta^- + 2\bar{\nu} \quad (1.169)$$

The parent nucleus transforms to a daughter nucleus of the same mass number A, but with an increase in atomic number Z by

two. In accord with the beta-decay scheme, within the nucleus of the parent nuclide, two neutrons decay to two protons with the simultaneous emission of two beta particles and two anti-neutrinos, or

$$2n \rightarrow 2p^+ + 2\beta^- + 2\bar{\nu} \quad (1.170)$$

a. Discovery and Current Research

Double-beta decay was first predicted by Nobel Laureate Maria Goeppert-Mayer (1935) at Johns Hopkins University, who calculated a predicted half-life of over 10^{17} years. It was not until 1987 did Steven R. Elliott, Alan A. Hahn, and Michael K. Moe at the University of California, Irvine report the first observation of double-beta decay in a sample of ⁸²Se enriched from its natural abundance of 8.7 % to an isotope abundance of 97% to provide more source material for the double beta decay as well as reduce contamination in the sample from other sources (Elliott et al, 1986, 1987, Moe, 1986 and Moe and Rosen, 1989).

The rarity of this decay process is manifested by the very large half-lives (from 10^{18} to 10^{24} years) of the nuclides that decay by this process. Because of the rarity of double-beta decay, its observation in the laboratory is extremely difficult requiring highly enriched radionuclide sources and sophisticated coincidence (double-beta) counting instrumentation capable of extreme suppression or vetoing of background radiation (Elliott, et al, 2006, Gómez, et al, 2007, Campbell, et al, 2008, Gehman, et al, 2010, and McGrath, et al, 2010). Thus, double-beta decay is not measured routinely and not relevant to the general measurement of radioactivity. Nevertheless, double-beta decay is discussed briefly here, because our knowledge of its existence helps us understand more fully the beta decay process.

b. $\beta\beta$ -Decay Energy

The double-beta decay of ⁸²Se, as observed by Elliott, Hahn, and Moe (1987), can be written as follows:

$${}^{82}_{34}\text{Se} \xrightarrow{t_{1/2} = 9.2 \times 10^{21} \text{ years}} {}^{82}_{36}\text{Kr} + 2\beta^- + 2\bar{\nu} \quad (1.171)$$

The decay equation illustrated above would only be possible if the daughter nucleus, ⁸²Kr, is lighter than the nucleus of its parent ⁸²Se. As explained by Moe and Rosen (1989), the mass of the daughter nucleus is diminished by the mass equivalent to its binding energy, the energy needed to pull the nucleus apart. Thus, a more tightly bound nucleus is lighter than a more loosely bound nucleus containing the same number of nucleons. The number of nucleons or mass number (82) in the above equation remains the same; however, the nucleus of ⁸²Kr is lighter than its parent ⁸²Se, and the difference in mass of the two nuclei would yield the mass equivalent to the decay energy, $Q_{\beta\beta}$. In mass terms, Eqn (1.171) may be written as

$${}_Z M_P = {}_{Z+2} M_D + 2m_e \quad (1.172)$$

where ${}_Z M_P$ and ${}_{Z+2} M_D$ are the masses of the parent and daughter nuclei of atomic numbers Z and Z+2, respectively, and $2m_e$ is the mass of two beta particles (i.e., two electron masses). We may use atomic mass units (u) to calculate the mass

difference of the parent and daughter nuclei by adding firstly Z atomic electron masses to each side of Eqn (1.172) to give

$${}_Z M_P + Z m_e = {}_{Z+2} M_D + (Z + 2) m_e \quad (1.173)$$

The decay energy, $Q_{\beta\beta}$, may then be calculated by the difference in parent and daughter nuclide atomic mass units ignoring the small difference in the binding energies of the electrons in the two nuclides or

$$\begin{aligned} Q_{\beta\beta} &= (M_{\text{Se}} - M_{\text{Kr}})c^2 \\ &= (81.916700 \text{ u} - 81.913485 \text{ u})(931.494 \text{ MeV/u}) \\ &= 2.99475 \text{ MeV} \end{aligned} \quad (1.174)$$

The above calculated value is in agreement with the decay energy reported by the National Nuclear Data Center of the Brookhaven National Laboratory, which is 2.995 MeV (NNDC, 2010a: <http://www.nndc.bnl.gov/qcalc/>). The decay scheme of ^{82}Se is illustrated in Fig. 1.42. The scheme illustrates the decay of ^{82}Se of higher mass to ^{82}Kr of lower mass, and the mass difference of the two is equivalent to the decay energy, $Q_{\beta\beta}$. The decay energy is shared as energy of four particles, namely, two beta particles and two antineutrinos. Single beta decay of ^{82}Se to ^{82}Br , a nuclide of higher mass, is energetically forbidden as depicted in Fig. 1.42.

The National Nuclear Data Center of the Brookhaven National Laboratory currently lists ten nuclides that are known to undergo double-beta decay. These are the following: ^{48}Ca , ^{76}Ge , ^{82}Se , ^{96}Zr , ^{100}Mo , ^{116}Cd , ^{128}Te , ^{130}Te , ^{150}Nd , and ^{238}U . These nuclides have an even number of protons and even number of neutrons. They exhibit a significant stability to beta decay with half-lives that vary over the range of 10^{19} – 10^{24} years. The stability of these nuclei, as described by Moe and Rosen (1989), may be due to their “even–even” characteristic, that is, their nuclei consist of an even number of protons and neutrons versus a neighboring “odd–odd” nucleus in the Chart of the Nuclides with the same number of nucleons consisting of an odd number of protons and neutrons. The strong nuclear force that holds the nucleus together binds pairs of like particles

more tightly than unlike particles. Thus, a nucleus with even number of protons and even number of neutrons can pair and be bound more tightly than a nucleus with the same mass number but with an odd number of protons and odd number of neutrons. For example, the nucleus of $^{82}_{34}\text{Se}$ contains 34 protons and 48 neutrons, whereas its neighboring isobar, $^{82}_{35}\text{Br}$, contains the odd numbers of 35 protons and 47 neutrons. The mass of the ^{82}Br nucleus is slightly higher than that of ^{82}Se , as illustrated in Fig. 1.42. The diminished mass of the ^{82}Se is due to its higher binding energy. Thus, the ^{82}Se is a more tightly bound nucleus than the ^{82}Br , and the transition by beta decay from ^{82}Se to ^{82}Br is forbidden energetically as illustrated in Fig. 1.42.

As discussed in previous parts of this chapter, beta decay is not confined to negatron emission. There also exist positron- and electron-capture decay processes, which are other forms of beta decay. Thus, there may exist theoretically double $\beta^+\beta^+$ - and double EC-decay processes, and research is underway to observe these alternative double-beta decay processes (Barabash et al 2007, 2008, Kolhinen et al, 2010). In single positron emission a minimum decay energy of 1.022 MeV was discussed previously (see Section VIII.B.2). Double $\beta^+\beta^+$ would then require a minimum of 2.044 MeV decay energy.

c. Neutrinoless $\beta\beta$ Decay

There is much research currently underway on double-beta decay particularly with respect to the search for neutrinoless double-beta decay by many research groups in the world; and only a few of the research papers are cited here (Elliott and Vogel, 2002, Kazkaz and the Majorana Collaboration, 2005, Fiorini, 2007, 2008, Rahaman, et al, 2008, Daraktchieva and the NEMO Collaboration, 2009, Dracos, 2009, Avignone III, 2010, Freitas, et al, 2010, Majorovits, 2010, and Šimkovic, 2010). In accord with the standard model, which explains the continuous spectrum of beta energies emitted from decaying nuclei, the neutrino always accompanies beta emission, that is, specifically the antineutrino accompanies negatron (β^-) emission and the neutrino accompanies positron (β^+) emission, and accordingly two antineutrinos would accompany double $\beta^-\beta^-$ decay and

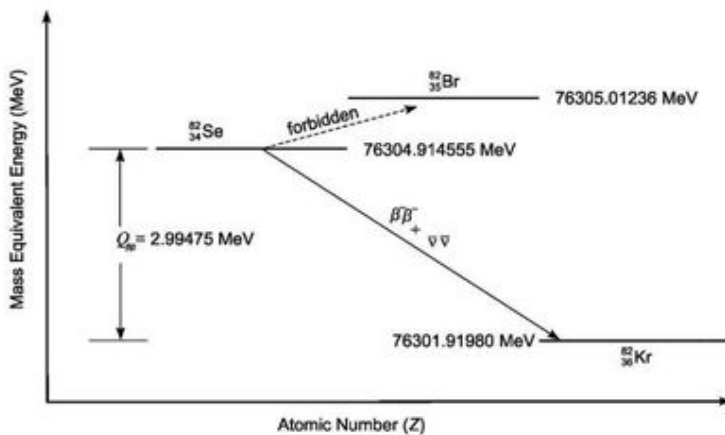
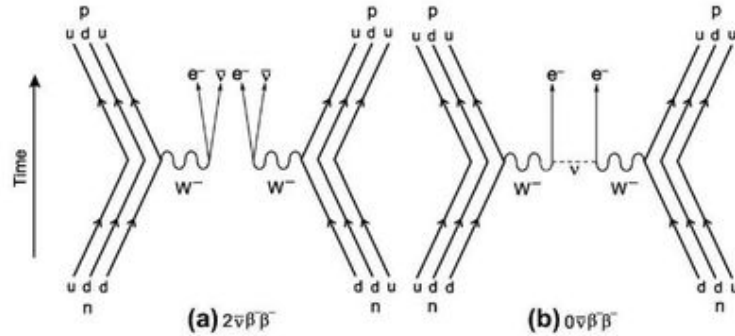


FIGURE 1.42 Double-beta decay of $^{82}_{34}\text{Se}$ to $^{82}_{36}\text{Kr}$. The decay energy, $Q_{\beta\beta}$, of 2.99475 MeV (equivalent to the mass difference between the ^{82}Se and ^{82}Kr) is shared by the two beta particles and two antineutrinos created in the process from the two protons of the parent nucleus $^{82}_{34}\text{Se}$. Transition via beta decay of ^{82}Se to ^{82}Br is forbidden energetically, as the mass of ^{82}Br is greater than that of ^{82}Se . The double-beta decay occurs with the simultaneous emission of two beta particles and two antineutrinos.

FIGURE 1.43 Feynmann diagrams illustrating double-beta decay via (a) two antineutrino double-beta decay ($2\nu\beta\beta^-$), and (b) neutrinoless double-beta decay ($0\nu\beta\beta^-$).



two neutrinos would accompany $\beta^+\beta^+$ emission. However, beyond this Standard Model there exists the possibility that the neutrino could be its own antiparticle referred to as a Majorana neutrino in honor of the exceptionally gifted Italian mathematician and theoretical physicist Ettore Majorana (1906—presumed year of death 1938), who first postulated the possibility. According to this theory, if the neutrino possesses a mass (now estimated to have a mass upper limit of $2.3 \text{ eV}/c^2$) and is its own antiparticle, a neutrino emitted in one beta decay could be reabsorbed in the second beta decay resulting in a double-beta decay in which no neutrinos are emitted, *i.e.*, a neutrinoless double-beta decay often abbreviated as $0\nu\beta\beta$. The search for the neutrinoless double-beta decay is important, because it would reaffirm the mass of the neutrino, as only a particle with a definite rest mass can oscillate from one form into another.

Diagrams illustrating the double-beta decay processes that would occur in a decaying nucleus for the two neutrino double beta-decay ($2\nu\beta\beta$) and the, yet to be observed, neutrinoless double-beta decay ($0\nu\beta\beta$) are illustrated in Fig. 1.43. In both cases, two neutrons (n) transform into two protons (p) in the nucleus when two down quarks (d) in the two neutrons change into two up quarks (u) with the emission of two W bosons. The W^\pm bosons were discovered at the super-proton synchrotron (SPS) proton-antiproton collider at CERN in 1983 by the UA1 and UA2 collaborators (Arnison et al, 1983a,b, Banner et al, 1983 and Bagnaia et al, 1983). These particles are the carriers of the weak interactions between elementary particles and are responsible for the weak decays of the particles (Sundaresan, 2001). As illustrated in Fig. 1.43, the two W bosons transform into two high-energy electrons (beta particles) and two antineutrinos. In the case of neutrinoless double-beta decay (yet to be observed), the Majorana neutrino emitted in one stage of the decay is reabsorbed in the second stage and two high-energy electrons are emitted without neutrinos.

In the $2\nu\beta\beta$ process, the two beta particles that are emitted simultaneously share the total decay energy, $Q_{\beta\beta}$, with the two neutrinos. Thus, the decay energy is shared between four particles, namely, the two neutrinos and two beta particles. In the $0\nu\beta\beta$ process, the two beta particles emitted share the entire decay energy, as there would be no neutrinos emitted with which to share the decay energy. The beta-particle energy spectra for $2\nu\beta\beta$ and $0\nu\beta\beta$ decay are illustrated in

Fig. 1.44. The two beta-particle spectra are very distinct. In the $2\nu\beta\beta$ decay process the numbers of beta particles (N) vary over a wide range of energy plotted as the sum of the two beta-particle energies divided by the decay energy, *i.e.*, $\Sigma(E_{\beta_1} + E_{\beta_2})/Q_{\beta\beta}$. The beta-particle energy spectrum for the $2\nu\beta\beta$ decay would encompass the continuous energy range with a spectral shape similar to that of the single beta-particle emission, because they share the decay energy with neutrinos. Notice in Fig. 1.44 that the endpoint of the continuous beta-particle spectrum of the $2\nu\beta\beta$ decay does not reach the value of 1.0. This is due to the fact that the two beta particles emitted in the $2\nu\beta\beta$ decay process must share decay energy with two neutrinos, and thus the sum of the two beta particle energies can never equal the decay energy, $Q_{\beta\beta}$. However, the beta-particle energy spectrum for the $0\nu\beta\beta$ decay, where neutrinos do not escape with any of the decay energy, would display a single energy line for the sum of the two beta particle energies, and this line would occur at $\Sigma(E_{\beta_1} + E_{\beta_2})/Q_{\beta\beta} = 1$. Current research is underway in the search for the sum of the two beta particles to equal the decay energy, $Q_{\beta\beta}$, or where $\Sigma(E_{\beta_1} + E_{\beta_2})/Q_{\beta\beta} = 1$, which would confirm $0\nu\beta\beta$ decay.

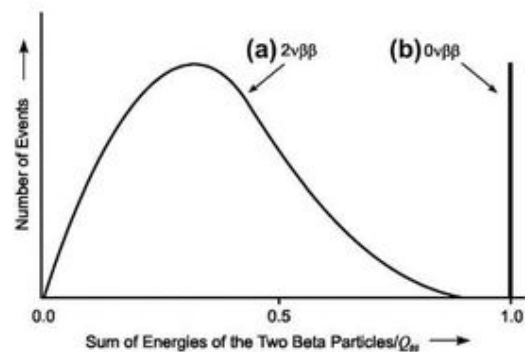


FIGURE 1.44 Beta-particle energy spectra for (a) two-neutrino double-beta decay ($2\nu\beta\beta$), and (b) neutrinoless double-beta decay ($0\nu\beta\beta$). In the $2\nu\beta\beta$ decay process, the sum of the two beta particle energies divided by the decay energy, $\Sigma(E_{\beta_1} + E_{\beta_2})/Q_{\beta\beta}$, displays a continuous spectrum and the maximum will never reach 1.0; whereas, the spectrum for $0\nu\beta\beta$ would display a single line at $\Sigma(E_{\beta_1} + E_{\beta_2})/Q_{\beta\beta} = 1$.

6. Beta-particle Interactions with Matter

Owing to the very low mass of the beta-particle (*i.e.*, electron) compared with the alpha particle, it travels at a much higher velocity than an alpha particle of equivalent energy. Because of its greater velocity, lower mass, and lower charge, the specific ionization produced in air by the traveling beta particle is much lower (by a factor of a thousand) than that of an alpha particle of equivalent energy.

Like the alpha particle, the beta particle interacts with matter via (i) ionization and (ii) electron orbital excitation as it dissipates its kinetic energy. A third mechanism of interaction with matter, which distinguishes the beta particle, is radiative energy dissipation via bremsstrahlung production (see Section IX.D.2). Thus, as described by Turner (1995), the stopping power for beta particles (β^- or β^+) is the sum of the collisional and radiative contributions or

$$\left(-\frac{dE}{dx}\right)_{\text{tot}}^{\pm} = \left(-\frac{dE}{dx}\right)_{\text{col}}^{\pm} + \left(-\frac{dE}{dx}\right)_{\text{rad}}^{\pm} \quad (1.175)$$

where the superscript \pm refers to positively or negatively charged electrons. The radiative contribution, that is, the absorption of beta-particle energy with the concomitant emission of bremsstrahlung radiation is significant with high-energy beta particles (*e.g.*, ^{32}P or ^{90}Y beta-particle emissions) in absorbers of high atomic number (*e.g.*, Pb-glass). Bremsstrahlung radiation is discussed in Section IX.D.2.

Collisional interactions of beta particles are somewhat different from those that occur with alpha particles. A beta particle may collide with an orbital electron or come into close proximity to it and cause the electron to be ejected, resulting in the formation of an ion pair. Considerable scattering of beta particles occurs in such collisions, because the mass of the beta particle is equivalent to that of an atomic electron. This is in direct contrast to the alpha particle, which, for the most part, retains a relatively undeviating path while passing through matter and interacting with atomic electrons. The mass equivalence of beta particles and electrons is an important factor that gives bombarding beta particles the power to impart a major portion of their kinetic energy to atomic electrons in a single collision. The atomic electrons ejected upon beta particle collisions themselves cause ionization in a similar fashion. This is referred to as secondary ionization, and the ionization caused by initial beta particle–electron collisions is classified as primary ionization. Because the major portion of beta particle energy may be imparted to an atomic electron upon collision, secondary ionization may account for as much as 80 % of the total ionization produced in a given material bombarded by beta particles.

The probability of beta-particle interactions with atomic electrons increases with the density of the absorbing material. Beta particle absorption is consequently proportional to the density and thickness of an absorber. Fig. B.3 of Appendix B provides a curve where the range of negatrons (β^-) in units of g/cm^2 in substances of low atomic number can be estimated for particles of energies from 0.01 to 10 MeV. The range of negatrons expressed in terms of surface density or mass thickness (g/cm^2) of absorber can be converted to absorber thickness (cm)

when the absorber density (g/cm^3) is known. Several empirical formulas exist for calculating negatron ranges and are solved based on the E_{max} of the beta particle. The formulas reported by Glendenin (1948) are

$$R = 0.542E - 0.133 \quad \text{for } E > 0.8 \text{ MeV} \quad (1.176)$$

and

$$R = 0.407E^{1.38} \quad \text{for } 0.15 \text{ MeV} < E < 0.8 \text{ MeV} \quad (1.177)$$

where R is the beta particle range in g/cm^2 and E is the energy of the beta particle (*i.e.*, E_{max}) in MeV. In addition, the following empirical formula of Flammersfield (1946) described by Paul and Steinwedel (1955) can be used:

$$R = 0.11 \left(\sqrt{1 + 22.4E^2} - 1 \right) \quad \text{for } 0 < E < 3 \text{ MeV} \quad (1.178)$$

This formula provides calculated ranges in units of g/cm^2 in close agreement to those obtained from Eqns (1.176) and (1.177) or those found from Fig. B.3 in Appendix B. For negatrons or electrons exceeding 2.5 MeV up to ~20 MeV, the following empirical formula from Katz and Penfold (1952) and the U.S. Public Health Service (1970) may be used:

$$R = 0.530E - 0.106 \quad \text{for } 2.5 \text{ MeV} < E < \sim 20 \text{ MeV} \quad (1.179)$$

where R is the negatron or electron range in g/cm^2 . Eqn (1.179) is derived from the experimentally determined energy-range correlation provided in Fig. B.3 of Appendix B.

According to Eqn (1.176), a 1.0 MeV negatron has a calculated range of $0.409 \text{ g}/\text{cm}^2$. This value may be divided by the density, ρ , of the absorber material to provide the range in centimeters of absorber thickness. Thus, it can be estimated that a 1.0 MeV negatron travels approximately 334 cm in dry air ($\rho = 0.001226 \text{ g}/\text{cm}^3$ at STP), 0.40 cm in water ($\rho = 1.00 \text{ g}/\text{cm}^3$), and 0.15 cm in aluminum ($\rho = 2.7 \text{ g}/\text{cm}^3$). The effect of absorber density on beta particle range is obvious from the foregoing examples, which demonstrate that 1 cm of dry air has about the same stopping power as 0.004 mm of aluminum.

The range of beta particles in matter is considerably greater than that of alpha particles of the same energy. Again, this is due to the lower mass, lower charge, and higher velocity of travel of the beta particle in comparison with an alpha particle of equivalent energy. The significance of this difference may be appreciated by reference to Table 1.11, in which the alpha particle and beta particle and/or electron ranges in air as a function of particle energy are compared.

To put the data of Table 1.11 into historical perspective, it is interesting to recall the origin of the names “alpha- and beta-radiation”. Before alpha- and beta particles were characterized fully, Ernest Rutherford (1899) carried out experiments that demonstrated two types of radiation existed: one radiation that was most easily absorbed by matter and another that possessed a greater penetrating power. Out of convenience, he named these radiations as “alpha” and “beta”. Not much later Paul Villard (1900b,c) in France discovered a yet more penetrating radiation. In harmony with the nomenclature assigned to the

TABLE 1.11 Ranges of Alpha- and Beta Particles (or Electrons) of Various Energies in Air

Energy (MeV)	Range (mg/cm ² Air)		Range (cm Air) ^c	
	Alpha particle ^a	Beta particle ^b	Alpha particle	Beta particle
0.1	0.17	16	0.1	13
0.5	0.42	200	0.3	163
1.0	0.67	490	0.5	400
1.5	0.95	790	0.7	644
2.0	1.3	1010	1.1	824
2.5	1.7	1400	1.4	1142
3.0	2.1	1700	1.7	1386
4.0	3.1	2200	2.5	1794
5.0	4.4	2700	3.6	2202
6.0	5.8	3200	4.7	2610
7.0	7.3	3700	5.9	3010
8.0	9.0	4200	7.3	3425

^aFrom the range-energy relationship provided in Fig. B.1 of Appendix B. More accurate values can be obtained from data provided by the National Institute of Standards and Technology (NIST) Database ASTAR (2010) for CSDA (continuous slowing down approximation) ranges: <http://www.nist.gov/pml/data/star/index.cfm>

^bFrom the range-energy relationship provided in Fig. B.2 of Appendix B. More accurate values can be obtained from data provided by the National Institute of Standards and Technology (NIST) Database ASTAR (2010) for CSDA (continuous slowing down approximation) ranges: <http://www.nist.gov/pml/data/star/index.cfm>

^cCalculated from the range in mass thickness units (mg/cm²) and the density of dry air at STP, $\rho_{\text{air}} = 1.226 \text{ mg/cm}^3$ according to Eqn (1.99).

“alpha” and “beta” radiation, Rutherford (1903) coined the term “gamma rays” to the yet more penetrating radiation. In the *Philosophical Magazine*, Rutherford (1903) named and characterized the three types of nuclear radiation on the basis of their penetration power in matter as follows:

Radium gives out three distinct types of radiation:

(1) The α rays, which are very easily absorbed by thin layers of matter, and which give rise to the greater portion of the ionization of the gas observed under the usual experimental conditions.

(2) The β rays, which consist of negatively charged particles projected with high velocity, and which are similar in all respects to cathode rays produced in a vacuum-tube.

(3) The γ rays, which are non-deviable by a magnetic field, and which are of a very penetrating character.

These rays differ very widely in their power of penetrating matter. The following approximate numbers, which show the thickness of aluminum traversed before the intensity is reduced to one-half, illustrate this difference:

Radiation	Thickness of Aluminum (cm)
α rays	.0005
β rays	.05
γ rays	8.

It is important to emphasize that, although all beta particles can be completely absorbed by matter, the shields we select can be

of great consequence. Hazardous bremsstrahlung radiation can be significant when high-energy beta particles interact with shields of high atomic number. The phenomenon of bremsstrahlung production is discussed further in Section IX.D.2.

Positrons dissipate their energy in matter via the same mechanisms as previously described for negatrons, which is understandable, as both are electrons. The scattering of positrons by atomic nuclei (*i.e.*, elastic scattering) is less than that for negatrons of the same energy when traveling through matter of a given atomic number Z as demonstrated by Fowler and Oppenheimer (1938), Lipkin and White (1950), and Feshbach (1952). The mass attenuation coefficients of positrons in the energy range of $0.3 \text{ MeV} < E_{\text{max}} < 3.6 \text{ MeV}$ are always slightly lower than that of negatrons of the same energy when traveling through matter of the same atomic number as demonstrated by Singh and Batra (1987). Calculated and observed mass attenuation coefficients for positrons and negatrons over the energy range of 0.3–3.6 MeV in absorber materials of atomic number 10–90 are provided by Singh and Batra (1987). The role of mass attenuation coefficients in the absorption and transmission of negatrons and positrons in various materials is discussed in more detail in the next section on beta-particle absorption and transmission. Two equations Eqn (1.393) and Eqn (1.394) are cited in Section XIV.A for calculating the ionization-excitation stopping powers for negatrons and positrons due to collision interactions with absorbers; their difference as noted by Tsoulfanidis (1995) is due only to the second term in the brackets of these two equations, which is much smaller than the logarithmic term, and consequently the differences

between negatron and positron stopping powers do not exceed 10%. However, positrons are unique in that these particles produce annihilation gamma radiation in matter discussed in Section IX.C.

7. Beta-particle Absorption and Transmission

Early research work on measuring the range of beta particles involved placing absorbers of increasing thickness between the radioactive source and the detector. The detector would measure the beta particles transmitted through the absorber. Increasing the absorber thickness would increasingly diminish the number of beta particles transmitted on to the detector. The transmission of beta particles was then plotted against absorber thickness, as illustrated in Fig. 1.45, in an attempt to determine the thickness of absorber required to stop all of the beta particles. Unfortunately, the plots could not be used directly to determine accurately beta-particle ranges; rather, they had to be compared to an absorption curve of a beta-emitter of known range by what became known as Feather analysis (Feather, 1938 and Glendenin, 1948). An auspicious outcome of this work was the observation that the plots of beta-particle absorption had more or less an exponential character. When plotted logarithmically against absorber thickness, the beta-particle absorption and/or transmission through the absorber was linear or near linear as illustrated in Fig. 1.45. This was a fortuitous outcome of the continuous energy spectrum of beta particles emitted from any given source. These findings are quite the contrast to the absorption curve of alpha particles discussed previously (Fig. 1.28), where the alpha particle intensity remains constant and then comes to an almost abrupt stop.

The curve illustrated in Fig. 1.45 is characteristic of beta particles. The linear segment of the semi-logarithmic plot of activity transmitted versus absorber thickness levels off horizontally (not illustrated in Fig. 1.45) due to a background of bremsstrahlung radiation. Negatrons and positrons both display a linear semi-logarithmic plot with the exception that, in the case of positrons, the plot has an added background due to annihilation radiation (Glendenin, 1948). Because beta particles have a definite range in matter, beta-particle transmission is not a purely logarithmic one as we shall see is the case for gamma radiation (see Section IX.D). The curves may not display a purely exponential character and the plots may have a degree of concavity to them depending on the distance of the source and detector to the absorber and on the shape of the beta-particle continuous energy spectrum. The greater the atomic number of the beta-particle emitter, and the more the beta spectrum is displaced toward the lower energies, the more nearly exponential (linear) will be the absorption curve (Glendenin, 1948). It is common to express the amount of absorber in mass thickness units, that is, mass per unit area (e.g., g/cm²), which is the product of absorber thickness and density, as it is easier to measure accurately very thin absorbers simply from their weight.

Based on the exponential character of beta-particle absorption, we can describe the transmission of beta particles through the absorber as

$$I = I_0 e^{-\mu x} \tag{1.180}$$

where *I* is intensity of the beta particles (DPM) transmitted through the absorber, *I*₀ is the initial intensity of beta particles (DPM) incident on the absorber, μ is the linear absorption

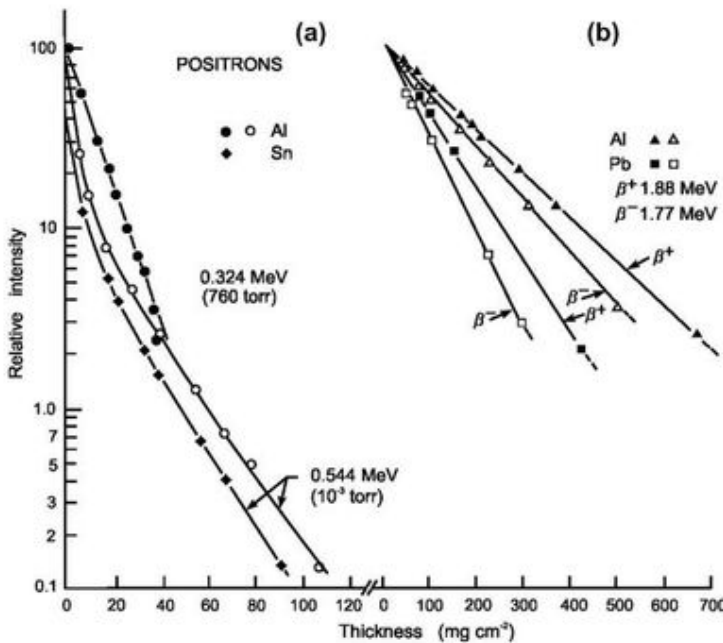


FIGURE 1.45 The relative measured transmission ($I/I_0 \times 100$ of Eqn (1.180)) of positrons of 0.324, 0.544, 1.77 and 1.88 MeV in Al, Sn, and Pb and negatrons of 1.77 and 1.88 MeV in Al and Pb. The semi-logarithmic plot is linear over a specific range of absorber thickness. For the set of curves in (b), the scale along the x-axis is different. (From Singh and Batra (1987) reprinted with permission from Elsevier © 1987.)

coefficient in units of cm^{-1} , and x is the absorber thickness in cm. If we express absorber thickness in mass thickness units (e.g., mg/cm^2 or g/cm^2), we can rewrite Eqn (1.180) as

$$I = I_0 e^{-(\mu/\rho)(\rho x)} \quad (1.181)$$

or

$$\frac{I}{I_0} = e^{-(\mu/\rho)(\rho x)} \quad (1.182)$$

and

$$\ln \frac{I}{I_0} = -(\mu/\rho)(\rho x) \quad (1.183)$$

where μ/ρ is the mass absorption coefficient (also referred to as mass attenuation coefficient) in units of cm^2/g , that is, the linear absorption coefficient divided by the absorber density, and ρx is the absorber thickness in mass thickness units g/cm^2 , that is, the product of the absorber density and absorber thickness. Mass attenuation coefficients for positrons are calculated by Singh and Batra (1987) over the energy range of 0.1–5.0 MeV in various absorbers of atomic number ranging from Al ($Z = 13$) to Pb ($Z = 82$). The mass attenuation coefficients of negatrons are higher than those of positrons over the energy range of 0.3–3.6 MeV as illustrated in Fig. 1.46.

Eqn (1.183) can be used to determine experimentally the unknown thickness of absorber materials. A standard curve is plotted with the ratio I/I_0 on a logarithmic scale versus mass thickness (ρx) of the absorber on a linear scale as illustrated in Fig. 1.45. A value for I in units of DPM is determined with a detector by measuring the beta-particle intensity transmitted through a given absorber thickness. This is repeated with absorbers of different thickness. The magnitude of the

incident beta-particle intensity, I_0 , is a constant value and determined with the detector in the absence of absorber. The linear portion of the plot has a negative slope, such as that illustrated in Fig. 1.45, and from least-squares analysis the mass attenuation coefficient μ/ρ is determined (Singh and Batra, 1987 and Yi et al, 1999). Consequently, the thickness of an unknown similar material can be determined from the measured intensity, I , of the transmitted beta-particle radiation after placing the material between the beta-particle source and detector without altering the counting geometry. The sample thickness is calculated or determined directly from the aforementioned curve (Tumul'kan, 1991 and Clapp et al, 1995).

Beta-particle transmission has many practical applications today in industrial manufacturing. Beta-particle sources and detectors are placed on the production line to test for thickness, uniformity, and defects in the manufacture of paper, metal, and plastic films (Yoshiyuki and Hiroshi, 1999 and Gardner et al, 2004) as well as on-line inspection of sewn seams or fabric density in the textile industry (Ogando, 1993, Clapp et al, 1995, Mapleston, 1997, Titus et al, 1997, and Kim et al, 2009) and in agronomic research to measure leaf water content (Mederski, 1961, 1968, Nakayama, 1964, Jones, 1973, Obregewitsch, 1975 and Barthakur, 1983) or to measure the biomass of a prairie (Knapp et al, 1985). These are commonly referred to as beta transmission thickness gauges. The beta-particle sources used depend on the absorber thickness to be measured and the E_{max} of the beta particles. The sources commonly used include ^{14}C ($E_{\text{max}} = 0.156$ MeV), ^{147}Pm ($E_{\text{max}} = 0.224$ MeV), ^{85}Kr ($E_{\text{max}} = 0.672$ MeV), ^{204}Tl ($E_{\text{max}} = 0.763$ MeV), and ^{90}Sr (^{90}Y) in secular equilibrium (E_{max} of ^{90}Sr and $^{90}\text{Y} = 0.546$ and 2.280 MeV, respectively). A source of low beta-particle E_{max} (e.g., ^{14}C or ^{147}Pr) is used to measure the finest thickness of material (Jaklevic et al, 1983, Balasubramanian, 1997, 1998), and the sources are changed according to beta-particle energy and material density and thickness to be tested. A practical reference for radioisotope thickness gauge measurements is provided by Johansen and Jackson (2004).

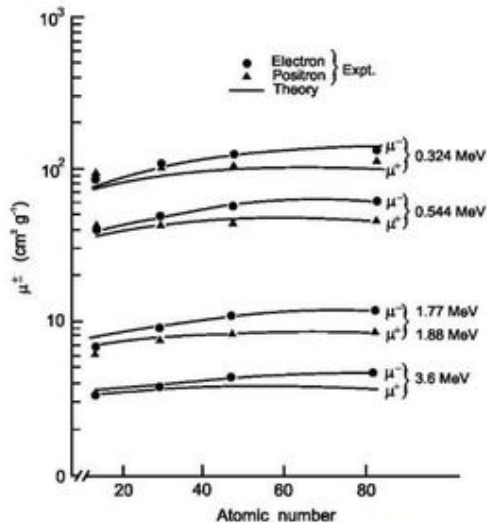


FIGURE 1.46 Mass attenuation coefficient μ (or μ/ρ of Eqn (1.182)) versus atomic number Z for positrons and negatrons (electrons) at different energies. (From Singh and Batra (1987) reprinted with permission from Elsevier © 1987.)

C. Internal Conversion Electrons

Decay by internal conversion (IC) results in the emission of an atomic electron. This electron, called the internal conversion electron, is emitted from an atom after absorbing the excited energy of a nucleus. In this decay process, an unstable nucleus decaying to a lower more stable state transmits its decay energy to an atomic electron, which is emitted from the atom with an energy corresponding to the nuclear decay energy less the binding energy of the atomic electron. This mode of decay accompanies and even competes with gamma-ray emission as a deexcitation process of unstable nuclei.

The kinetic energy of the electron emitted is equivalent to the energy lost by the nucleus (energy of transition of the excited nucleus to its ground or lower energy state) less the binding energy of the electron. This is illustrated by the following equation:

$$\xi_e = (E_i - E_f) - E_b \quad (1.184)$$

where ξ_e is the kinetic energy of the internal conversion electron, $(E_i - E_f)$ is the energy of transition between the initial, E_i , and the final, E_f , nuclear energies normally associated with gamma-ray emission, and E_b is the binding energy of the atomic electron. Lise Meitner and Otto Hahn in Germany (Meitner, 1924 and Hahn and Mettner, 1924) were the first to interpret the origin of this monoenergetic electron energy as derived from the internal conversion of the gamma-decay energy. Nobel Laureate Luis W. Alvarez at the University of California, Berkeley was the first to provide experimental evidence of internal conversion of artificially produced radioactive atoms (Alvarez, 1938).

An example of radionuclide decay by internal conversion is found in Fig. 1.47, which illustrates the decay of the parent-daughter nuclides ^{109}Cd ($^{109\text{m}}\text{Ag}$). Note that the $^{109\text{m}}\text{Ag}$ daughter decays by internal conversion with a 96% probability (i.e., 45% for IC from the K-shell + 48% from the L shell + 3% from higher electron shells – the latter is not illustrated in Fig. 1.47) and decay occurs also via gamma emission with the remaining 4% probability (Rachinhas et al., 2000).

Because the emission of internal-conversion electrons competes with gamma-ray emission as an alternative mode of

nuclear deexcitation, many radioactive nuclei that emit gamma radiation will also emit internal conversion electrons. The degree to which this competition occurs is expressed as the total internal-conversion coefficient (α), which is the ratio of the rate of emission of internal conversion electrons to the rate of emission of gamma rays of equivalent energy or

$$\alpha = e/\gamma = N_e/N_\gamma \tag{1.185}$$

where N_e and N_γ are the number of electrons and number of gamma-ray photons, respectively, emitted by a radionuclide sample in a given time interval for a given decay energy transition.

In other words, the internal-conversion coefficient is a quantitative measure of the number of internal-conversion electrons divided by the number of gamma rays emitted from a radionuclide sample for a given radionuclide energy transition.

Internal-conversion electrons may be emitted from specific electron shells of atoms and may be expressed in terms of internal-conversion electrons and gamma rays of the same energy less the energy difference resulting from the binding energy of the electron as described by Eqn (1.184). When expressed in terms of electrons emitted from specific shells, the shell-conversion coefficients are written with a subscript denoting the electron shell of origin, for example, α_K or e_K/γ , α_L or e_L/γ , and α_i or e_i/γ , where $i = K, L, M$, and so on electron shells, where the total internal-conversion coefficient would be the sum of the shell-conversion coefficients or

$$\alpha = \alpha_K + \alpha_L + \alpha_M + \dots \alpha_i \tag{1.186}$$

where $\alpha_K, \alpha_L, \alpha_M$, and α_i are the shell-conversion coefficients for the K, L, M electrons, etc.

Values of internal-conversion coefficients are provided in reference tables on isotope decay, such as those found in Lederer and Shirley et al (1978). In general, internal-conversion coefficients are small for gamma ray-emitting nuclides of low Z and high-energy transitions and larger for nuclides of high Z and low-energy transitions. This relationship is illustrated in Table 1.12, which lists a few radionuclides selected at random as examples in order of increasing Z. As can be seen, large internal-conversion coefficients occur when internal-conversion electrons are emitted with low-energy nuclear transitions as indicated by the large values of α associated with low gamma-ray energies and high Z. Also, it should be pointed out that the internal-conversion electron (e^-) energies listed are slightly lower than the gamma-ray energies. This is because the energy of the internal conversion electron is equal to the energy absorbed from the decaying nucleus (transition energy) less the binding energy of the atomic electron described previously in Eqn (1.184). On the other hand, gamma-ray energies serve as a measure of the exact quanta of energies lost by a nucleus.

The loss of atomic electrons through the emission of internal-conversion electrons leaves vacancies in atomic electron shells. The vacancies are filled by electrons from outer higher-energy shells, whereby there is a concomitant loss of electron energy as x-radiation. Emission of x-radiation resulting from electron filling of vacancies in electron shells (K, L, M,...)

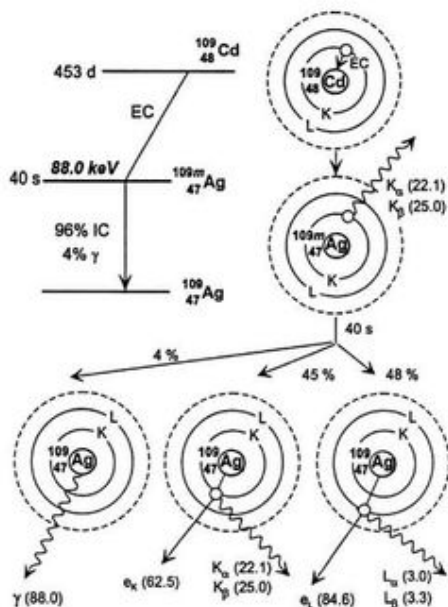


FIGURE 1.47 Decay scheme of ^{109}Cd ($^{109\text{m}}\text{Ag}$). The numbers in parenthesis indicate energy values in keV. The electron capture (EC) process occurs from K, L and outer shells with probabilities of 79%, 17% and 4%, respectively, but only K-capture is represented above. The $^{109\text{m}}\text{Ag}$ daughter decays by emission of 88.0 keV gamma rays with a 4% probability or by internal conversion (IC) with the probabilities of 45% and 48% for K and L shells. Internal conversion from shells higher than L contribute the remaining 3% (not illustrated). The K and L IC decay illustrated involve the ejection of a conversion electron with energy $e_K = 62.5$ keV or $e_L = 84.6$ keV, accompanied by the emission of a Ag K- or L-fluorescence x-ray photon ($K_\alpha = 22.1$, $K_\beta = 25.0$ keV, or $L_\alpha = 3.0$, $L_\beta = 3.3$ keV) or by the emission of Auger electrons (not represented) and x-ray photons following Auger electron emissions. (From Rachinhas et al., 2000, reprinted with permission from Elsevier Science.)

TABLE 1.12 Relationship between Gamma Radiation and Internal-conversion Electron Radiation, e^- , Associated with Several Nuclides Listed in Order of Increasing Z

Nuclide	Gamma radiation (MeV) ^a	e^- (MeV)	$\alpha = e/\gamma$	X-rays ^a
^7_4Be	0.477(10%)		7.0×10^{-7}	
$^{22}_{11}\text{Na}$	1.275(100%)		6.7×10^{-6}	
$^{44}_{22}\text{Ti}$	0.068(90%)	0.065	0.12	Sc K
	0.078(98%)	0.073	0.03	
$^{57}_{27}\text{Co}$	0.014(9%)	0.013	8.2	Fe K (55%)
	0.122(87%)	0.115	0.02	
	0.136(11%)	0.129	0.15	
$^{64}_{29}\text{Cu}$	1.34(0.6%)	1.33	1.3×10^{-4}	Ni K (14%)
$^{87m}_{38}\text{Sr}^b$	0.388(80%)	0.386	0.21	Sr K (9.4%)
$^{90m}_{38}\text{Sr}^b$	0.024(16%)	0.020	5.13	Sn K (28%)
$^{125}_{53}\text{I}$	0.035(7%)	0.030	13.6	Te K (138%)
$^{129}_{53}\text{I}$	0.040(9%)	0.034	22	Xe K (69%)
$^{169}_{68}\text{Er}$	0.008(0.3%)	0.006	220	Tm M
$^{181}_{74}\text{W}$	0.006(1%)	0.004	46	Ta K (65%)
$^{203}_{80}\text{Hg}$	0.279(82%)	0.275	0.23	Tl K (13%)
$^{209}_{84}\text{Po}$	0.039(0.01%)	0.033	461	U K (0.012%)
	0.052(0.02%)	0.047	269	

^aValues in per cent are radiation intensities or abundances.^bm denotes a metastable state.

is also listed in Table 1.12. This is a process that occurs in the daughter atoms; the x-rays are a characteristic of the daughter rather than of the parent.

Internal-conversion electrons are identical in their properties to beta particles. They differ, however, in their origin. Beta particles originate from the nucleus of an atom as a result of beta decay, whereas internal-conversion electrons originate from atomic electron shells. A characteristic difference between these two types of electron is their energy spectra. Beta particles, as discussed previously, are emitted from nuclei with a broad spectrum or smear of energies ranging from near zero to E_{max} . However, internal-conversion electrons are emitted from the atoms of decaying nuclei with discrete lines of energy of a magnitude equivalent to that of the energy lost by the nucleus less the electron binding energy. The energy of an internal-conversion electron can be used to estimate the energy lost by a nucleus.

Like beta particles, internal-conversion electrons dissipate their energy by ionization they cause in matter. The abundance of internal-conversion electrons emitted from some nuclide samples can be significant and should not be ignored. In certain cases, IC can play a significant role in radionuclide detection and measurement. Internal-conversion electron energies are slightly lower than the true gamma-decay energy because of the

energy consumed in the ejection of the bound atomic electron (E_b in Eqn (1.184)).

D. Auger Electrons

An Auger (pronounced OH-ZHAY) electron can be considered as the atomic analog of the internal conversion electron. In the electron-capture (EC) decay processes, vacancies are left in electron shells (K, L, M, \dots) that can be filled by atomic electrons from higher energy levels. In the process of falling to a lower energy shell to fill a vacancy, electron energy is lost as a photon of x-radiation (see Section IX.D). This x-radiation may travel on to be emitted from the atom or the energy emitted in the electron transition may be transferred to an outer atomic electron, resulting in the emission of the electron referred to as an Auger electron.

At the young age of 24 years, Pierre Victor Auger at the Ecole Normale Supérieure de Paris discovered the emission of electrons from atoms excited by x-rays (Auger, 1923, 1925a,b). Pierre Auger irradiated krypton and argon gas with x-rays and discovered the emission of electrons. He reasoned that an x-ray photon causes the ejection of an atomic electron from a given shell or quantum level leaving a vacancy behind. He further reasoned that an electron from the next outer shell could fill the vacancy causing the emission of electromagnetic radiation that would correspond to the difference in the energy levels of the electrons in the outer and inner shells. For example, Auger noted that, if an electron in the K shell was ejected by an artificially produced x-ray photon, an electron from the next outer L shell could fill the vacancy resulting in the emission of energy, E , as electromagnetic radiation, which he described by the following equation:

$$E_{x\text{-ray}} = h\nu = E_L - E_K \quad (1.187)$$

where h is Planck's constant ($h = 6.62 \times 10^{-27}$ erg s = 4.14×10^{-15} eV s = 6.62×10^{-24} J s), ν is the photon frequency in units of s^{-1} , and E_L and E_K are the energy levels of the electrons in the L and K shells, respectively. The transition energy $h\nu$ may be emitted as an x-ray photon characteristic of the atom or, alternatively, the transition energy may be absorbed by an atomic electron resulting in its emission from the atom. The electron emitted in this fashion is identified as an Auger electron in the name of Pierre Auger for his discovery and interpretation of this phenomenon. Lise Meitner (1923) also independently discovered Auger electrons the same year as Pierre Auger; however, the Auger electrons and the phenomenon that gives rise to these electrons, the Auger Effect, are named after Pierre Auger.

Auger electrons are defined as atomic electrons that are emitted from atoms after acquiring energy from an atomic electron transition within the atom. Electron transitions will occur when an atom becomes ionized by the loss of an electron from an inner shell. For example, an atom may become ionized by the ejection of an electron from an inner shell by one of several mechanisms such as (i) irradiation with artificial external x-rays or irradiation with external electron beams, (ii) the emission of an internal conversion electron such as K -shell

internal conversion, or (iii) electron capture also known as *K* capture. The vacancy left in the *K* shell can be filled by an electron from an outer *L* shell. In turn, the vacancy left in the *L* shell could be filled by another electron from the outer *M* shell, etc. The process of nonradiative rearrangement of atomic electrons as a result of the ionization of the atom in one of its inner shells is defined as the Auger effect (Borisenko and Ossicini, 2004). In the process of falling to a lower energy shell to fill a vacancy, electron energy may be lost as a photon of x-radiation. The energy of the photon radiation is equivalent to the differences in the energy levels of the electrons in the outer and inner shells as described by Eqn (1.187). The x-ray photon may be emitted from the atom, or alternatively the energy released in the electron transition will be transferred to an electron of an outer shell and cause its emission from the atom as an Auger electron. The energy of the Auger electron would be that defined by Eqn (1.187) less the binding energy, E_b , of the electron or

$$E_{\text{Auger}} = (E_L - E_K) - E_b \quad (1.188)$$

The energy of the Auger electron is thus equivalent to the energy of the x-ray photon less the binding energy of the electron or

$$E_{\text{Auger}} = (E_{x\text{-ray}} - E_b) \quad (1.189)$$

Values of the binding energies of electrons in various shells (*K*, *L*, *M*,...) are found in references texts such as Lide (2010). Either of two processes, the emission of an x-ray photon or the emission of an Auger electron, can occur as a result of electron energy-level transitions from higher to lower energies. Auger electron emission competes with x-ray emission. An example of the Auger effect and the resultant emission of an Auger electron as compared to x-ray emission are illustrated in Fig. 1.48. The emission of an Auger electron from an atom will occur as a consequence of the following transitions: (i) an atom loses an atomic electron from an inner shell leaving a hole or vacancy in that shell, (ii) an electron from a higher energy level fills the vacancy, and (iii) the energy emitted in the transition of the electron from the higher to lower energy levels is transferred to an outer atomic electron causing the electron to be emitted from the atom.

Whenever an x-ray photon causes the ejection of an atomic electron, another electron falls from an outer shell to a lower one to fill the vacancy, and there is a cascading effect of electrons falling from yet more distant shells to fill vacancies left behind until the atom reaches the ground or stable state. The downward transitions of electrons in this fashion produce additional x-ray photons of lower energy than the initial x-ray photon. The production of x-ray photons in this fashion is referred to as x-ray fluorescence.

Auger electron emission competes with x-ray emission, and it can accompany any nuclear decay process that results in the production of x-rays, such as a consequence of electron capture (EC) decay or nuclides that have internal conversion (IC) in their decay. Like internal-conversion electron emission described previously, the electron-capture decay process also results in the emission of appreciable quantities of x-radiation.

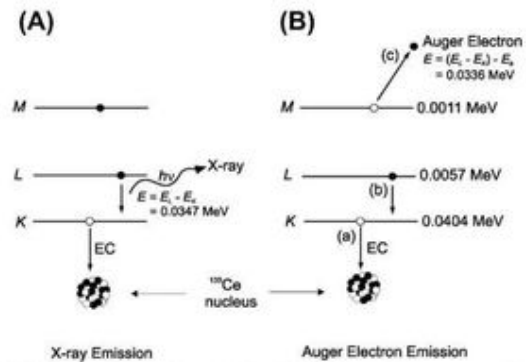


FIGURE 1.48 Decay of the radionuclide ^{139}Ce by electron capture (EC) resulting in (A) X-ray emission or (B) Auger electron emission. An electron vacancy in a shell is illustrated as an empty circle and an electron as a filled circle. Specific binding energies for Cerium atomic electrons in *K*, *L* and *M* shells were obtained from Lide (2010) and are provided along the right-hand side of lines illustrating the various electron energy levels. The Auger effect or process by which an Auger electron is emitted from an atom occurs according to the following sequence as noted in the figure: (a) an atom loses an atomic electron from an inner shell leaving a hole or vacancy, (b) an electron from a higher energy level fills the vacancy, and (c) the energy emitted in the electron transition in step (b) is transferred to an outer atomic electron causing the electron to be emitted from the atom. The energy of the *K* x-ray illustrated above is equal to the electron transition ($E_{x\text{-ray}} = \hbar\nu = E_L - E_K = -0.0057 - (-0.0404) = 0.0347$ MeV. The energy of the Auger Electron is equal to the electron transition energy ($E_L - E_K$) less the binding energy of the electron (E_b), or, in other words, the x-ray energy less the binding energy of the electron ($E_{\text{Auger}} = 0.0347 - 0.0011 = 0.0336$ MeV. The daughter nucleus of the ^{139}Ce remains in an excited state after electron capture and emits a gamma-ray (not illustrated). Also the loss of an Auger electron will leave an electron vacancy, which can be filled by an electron of an outer shell. This will produce another x-ray, which is not illustrated here. The electron filling the vacancy will, in itself leave another vacancy, which could be filled by yet another electron in an outer shell. The production of x-rays by this cascading effect of electron transitions from outer to inner shells is known as x-ray fluorescence.

Auger electron emission can reduce appreciably the abundance of x-ray emission normally expected to accompany radionuclide decay processes. The two competing processes of Auger-electron emission and x-ray emission are important to consider in the detection and measurement of nuclides that decay by electron capture. This is measured by both the fluorescence yield and Auger yield. The fluorescence yield is the fraction of vacancies in a given electron shell that is filled with accompanying x-ray emission, and Auger yield is the fraction of vacancies that is filled resulting in the emission of Auger electrons (Friedlander et al, 1964). For example, as described by Burhop and Asaad (1972), an initial vacancy in the *K* shell may be filled by the emission of either *K* series x-radiation (fluorescence yield ω_K) or *K* Auger electrons (Auger yield a_K) where

$$\omega_K + a_K = 1 \quad (1.190)$$

Fig. 1.49 illustrates the *K*-shell fluorescence yield as a function of nuclide atomic number. The *L*-shell, which consists of subshells, such as L_1 , L_2 , and L_3 , can exhibit fluorescence yields characteristic of the subshells. The *L*-shell fluorescence yield also varies similarly with atomic number as the *K*-shell

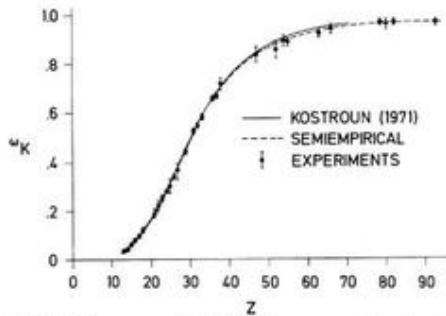


FIGURE 1.49 Fluorescence K -shell yields, ω_K , as a function of atomic number, Z : (a) according to Kostroun *et al.*, (1971); (b) a best fit to selected experimental data; and (c) critically evaluated experimental results. (From Bambynek *et al.*, 1972, reprinted with permission ©1972 The American Physical Society.)

fluorescence yield, but it is several times lower in magnitude (Friedlander *et al.*, 1964). When an Auger electron is emitted as a result of an electron transition from a higher subshell to a lower subshell of the same shell, it is referred to as a Coster–Kronig transition, which is a special type of Auger effect named in honor of Dirk Coster and Ralph Kronig from the Netherlands (Coster and Kronig, 1935). The ejected electrons in Coster–Kronig transitions are of very low energy (≤ 1 keV), and in x-ray spectroscopy, they cause the broadening and lowering of intensities of corresponding x-ray lines.

Auger electron emission energies and intensities, including those arising from Coster–Kronig transitions, are measured and accounted for in radionuclide standardization by liquid scintillation counting (Grau Carles and Grau Malonda, 2006, Grau Malonda *et al.*, 2006, Bé *et al.*, 2006, Kossert and Grau Carles, 2008, 2010, and Grau Carles and Kossert, 2009). As described previously, both Auger and internal conversion (IC) electron emissions possess discrete energies, and these energy lines can be envisaged by the electron emission spectra illustrated in Fig. 1.50. The emission spectra illustrated in Fig. 1.50 provide an excellent picture of the energy magnitudes and monoenergetic character of Auger and IC electrons. Certain radionuclides, such as ^{123}I , ^{125}I , ^{111}In , and ^{119}Sb , which decay by electron capture with significant intensities of Auger electrons emissions, are receiving much attention for their applications in cancer therapy (Behr, *et al.*, 2000, Janson *et al.*, 2000, Bodei *et al.*, 2003, Capello *et al.*, 2003, Michel *et al.*, 2003, Chen *et al.*, 2006, Constantini *et al.*, 2007, and Thisgaard and Jensen, 2009). The low energies of the Auger electrons emitted by these radionuclides, and consequently their short range in the human body, can increase the highly localized radiation-induced kill of cancer cells.

Another auspicious outcome of the discovery of the Auger effect is the development of Auger electron spectroscopy (AES). The technique of AES involves irradiating the surface of a sample with an electron beam of energy sufficient to ionize the inner orbitals of atoms, thereby inducing the concomitant emission of Auger electrons. The Auger electron energy spectra drawn from the induced emissions serve as fingerprints of different atoms to enable their identification and quantitative

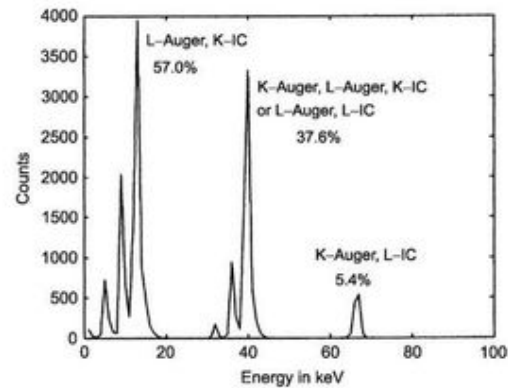


FIGURE 1.50 Simulation of the electron emission spectrum (Auger and IC) of ^{123}I . The 36-keV γ -transition of ^{123}I is highly converted with a probability of 93.3%. As described by Grau Carles and Kossert (2009), three regions characterize the spectrum. The first region below 20 keV comprises about 57% of the spectral events. The peaks are created by the emission of K -IC electrons with about 3.7 keV, which may occur in coincidence with one or two L -Auger electrons stemming from the subsequent rearrangement processes of the preceding EC decay. Thus, the region shows three sharp peaks. The second region at about 40 keV contains about 37.6% of the counts. It corresponds to the coincident interaction of K -IC and K -Auger electrons or the interaction of L -IC electrons. K -Auger electrons may have energies between ~ 21.8 and 31.8 keV. The energy of L -IC electrons is about 31 keV. Again, the emissions can be in coincidence with one or two L -Auger electrons yielding the subdivision into three peaks. The third region above 60 keV contains coincidences of L -IC and K -Auger electron emissions and encompasses $\sim 5.4\%$ of the total spectral events. (From Grau Carles and Kossert, 2009 reprinted with permission from Elsevier © 2009.)

analysis (Chourasia and Chopra, 1997, Mehlhorn, 1998, and Vandendael, 2010).

E. Neutron Radiation

The neutron is a neutral particle, which is stable only in the confines of the nucleus of the atom. Outside of the nucleus the neutron decays with a mean lifetime of about 15 min. Its mass, like that of the proton, is equivalent to 1 u (atomic mass unit). Unlike the particulate alpha and beta nuclear radiation previously discussed, neutron radiation is not emitted in any significant quantities from radionuclides that undergo the traditional nuclear decay processes with the exception of a few radionuclides such as ^{252}Cf and ^{248}Cm , which decay to a significant extent by spontaneous fission (see Section VIII.E.3.b). Significant quantities of neutron radiation occur when neutrons are ejected from the nuclei of atoms following reactions between the nuclei and particulate radiation. Due to its lack of charge, the neutron cannot produce directly any ionization in matter, again unlike alpha and beta radiation. The various sources, properties, and mechanisms of interaction of neutrons with matter are described subsequently.

1. Discovery of the Neutron

The discovery of the neutron had eluded humanity until as late as 1932. The particle's neutral charge and high penetrating

power when traveling through matter made its discovery more difficult during the early years of research on radioactivity. In 1932, J. Chadwick provided evidence for the existence of the neutron (see Chadwick, 1932a,b). He placed a source of alpha-particle radiation in close proximity to beryllium. It was known that bombarding beryllium with alpha radiation would produce another source of radiation, which had a penetration power through matter even greater than that of known gamma radiation. Chadwick observed that, when a sheet of paraffin (wax) was placed in the path of travel of this unknown radiation, he could detect a high degree of ionization in a gas ionization chamber caused by protons emitted from the paraffin. This phenomenon would not occur when other materials such as metals and even lead were placed in the path of this unknown radiation. Based on further measurements of the proton velocities and scattering intensities, it was concluded that the unknown radiation had a mass similar to that of the proton, but with a neutral charge. Only a particle with neutral charge would have a high penetration power through matter. A very detailed account of the experimental technique and calculations that Chadwick used to prove the existence of the neutron is given in a previous text by the writer (L'Annunziata, 2007). As noted in the previous discussion of beta particle decay, the neutron possesses a mass similar to that of the proton and, within the nucleus of an atom, the particle is a close union between a proton and an electron.

2. Neutron Classification

Neutrons are generally classified according to their kinetic energies. There is no sharp division or energy line of demarcation between the various classes of neutrons; however, the following is an approximate categorization according to neutron energy:

*	Cold neutrons	<0.003 eV
*	Slow (thermal) neutrons	0.003–0.4 eV
*	Slow (epithermal) neutrons	0.4–100 eV
*	Intermediate neutrons	100 eV–200 keV
*	Fast neutrons	200 keV–10 MeV
*	High energy (relativistic) neutrons	>10 MeV

The slow (thermal) neutrons are classified above within the encompassing energy range of 0.003–0.4 eV; however, many reference tables may provide the thermal neutron cross sections of the elements and their isotopes at the specific thermal neutron energy of room temperature neutrons (20.43 °C) corresponding to a thermal neutron energy of 0.0253 eV and a neutron velocity of 2200 meters per second (Holden, 1997b).

The energies of neutrons are also expressed in terms of velocity (meters per second) as depicted in the terminology used to classify neutrons. A neutron of specific energy and velocity is also described in terms of wavelength, because particles in motion also have wave properties. It is the wavelength of the neutron that becomes important in studies of neutron diffraction. The values of energy, velocity, and wavelength of the neutron, as with all particles in motion, are interrelated. The

velocity of neutrons increases according to the square root of the energy, and the wavelength of the neutron is inversely proportional to its velocity. Knowing only one of the properties, either the energy, velocity, or wavelength of a neutron, we can calculate the other two. We can relate the neutron energy and velocity using the kinetic energy equation

$$E = \frac{1}{2}mv^2 \text{ or } v = \sqrt{2E/m} \tag{1.191}$$

where E is the particle energy in joules ($1 \text{ eV} = 1.6 \times 10^{-19} \text{ J}$), m is the mass of the neutron ($1.67 \times 10^{-27} \text{ kg}$), and v is the particle velocity in meters per second. The wavelength is obtained from the particle mass and velocity according to

$$\lambda = \frac{h}{p} = \frac{h}{mv}, \tag{1.192}$$

where λ is the particle wavelength in meters, h is Planck's constant ($6.63 \times 10^{-34} \text{ J sec}$), p is the particle momentum, and m and v are the particle mass and velocity as previously defined. The correlation between neutron energy, velocity, and wavelength is provided in Fig. 1.51, which is constructed from the classical Eqns (1.191) and (1.192) relating particle mass, energy, velocity and wavelength. However, calculations involving high-energy particles that approach the speed of light will contain a certain degree of error unless relativistic calculations are used, as the mass of the particle will increase according to the particle speed. In Section X.C, we used the Einstein equation $E = mc^2$ to convert the rest mass of the positron or negatron to its rest energy (0.51 MeV). When gauging particles in motion, the total energy of the particle is the sum of its kinetic (K) and rest energies (mc^2) or

$$E = K + mc^2 = \gamma mc^2 \tag{1.193}$$

Thus, the kinetic energy of the particle would be the difference between the total energy of the particle and its rest energy or

$$K = \gamma mc^2 - mc^2 \tag{1.194}$$

where

$$\gamma = \frac{1}{\sqrt{1 - (u^2/c^2)}}, \tag{1.195}$$

u is the particle speed, and $u < c$. If we call the particle rest mass m_0 , then the relativistic mass, m_r , which is the speed-dependent mass of the particle is calculated as

$$m_r = \frac{m_0}{\sqrt{1 - (u^2/c^2)}} \tag{1.196}$$

and from Eqn (1.194) the kinetic energy of the particle can be written as

$$K = \frac{m_0}{\sqrt{1 - (u^2/c^2)}} c^2 - m_0 c^2 \tag{1.197}$$

Eqn (1.197) can be transformed to read

$$K + m_0 c^2 = \frac{m_0 c^2}{\sqrt{1 - (u^2/c^2)}} \tag{1.198}$$

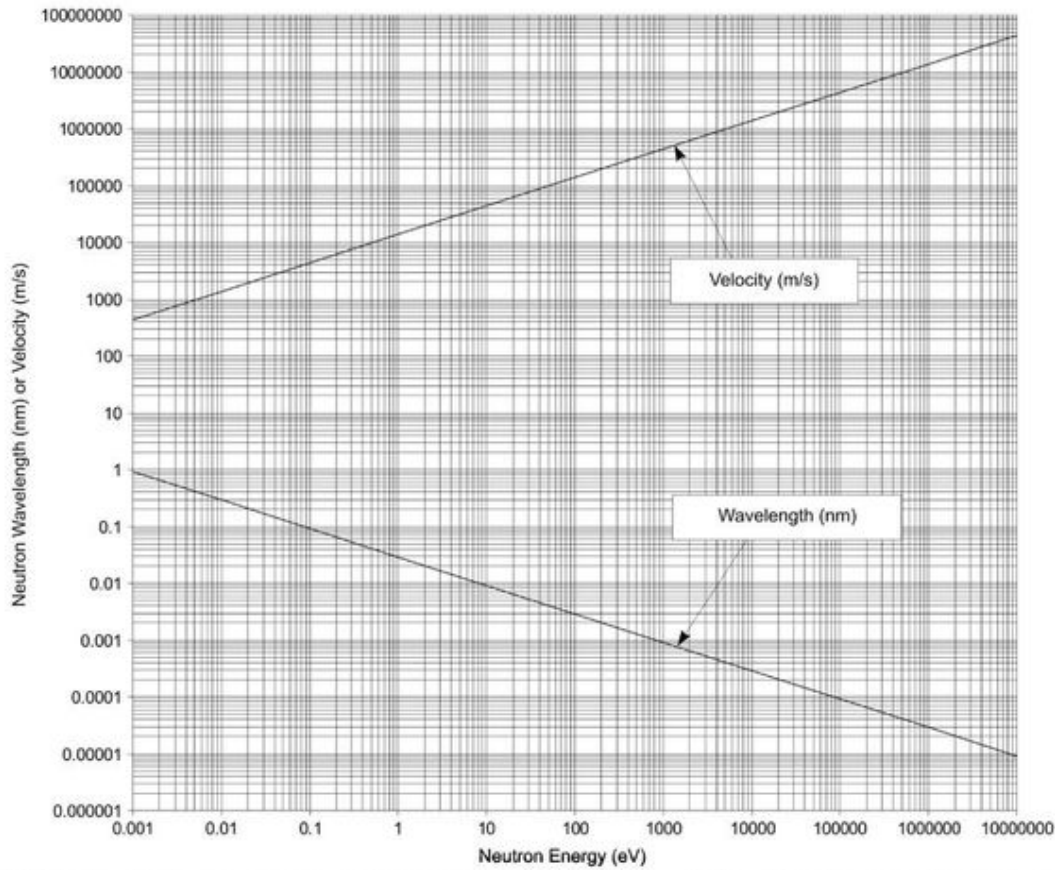


FIGURE 1.51 Correlation between neutron energy in electron volts (eV), velocity (m/sec), and wavelength (nm). From the energy of the neutron in eV on the abscissa, a line is drawn vertically to cross the wavelength and velocity curves. The values of neutron wavelength and velocity are obtained directly from the ordinate. For example, to determine the wavelength and velocity of 0.025 eV thermal neutrons, the value of 0.025 eV is found on the abscissa. A line is then drawn vertically from the point of 0.025 eV to cross the values of 0.18 nm wavelength and 2200 m/sec velocity.

and

$$\frac{K + m_0c^2}{m_0c^2} = \frac{1}{\sqrt{1 - (u^2/c^2)}} \quad (1.199)$$

and

$$\left(\frac{K}{m_0c^2} + 1\right)^2 = \frac{1}{1 - (u^2/c^2)} \quad (1.200)$$

which can be transformed to read

$$\frac{u^2}{c^2} = 1 - \frac{1}{(K/m_0c^2 + 1)^2} \quad (1.201)$$

From Eqn (1.201), the relativistic speed of the particle can be defined as

$$u_r = c\sqrt{1 - (K/m_0c^2 + 1)^{-2}} \quad (1.202)$$

where K is the kinetic energy, and the particle speed u is always less than c (Serway et al. 2005). The nonrelativistic speed is that described by Eqn (1.191) or $u_{nr} = \sqrt{2E/m_0}$.

To confirm the validity of the use of nonrelativistic calculations of particle speed for the construction of Fig. 1.51, let us use Eqns (1.191) and (1.202) to compare the differences between the nonrelativistic and relativistic speeds of a neutron of 10 MeV kinetic energy. This energy was selected, because it is the highest neutron energy included in Fig. 1.51, and differences between nonrelativistic and relativistic calculations increase with particle energy. The difference between the two calculated speeds is defined by the ratio of the two or

$$\frac{u_{nr}}{u_r} = \frac{\sqrt{2E/m_0}}{c\sqrt{1 - (K/m_0c^2 + 1)^{-2}}} \quad (1.203)$$

The rest energy of the neutron, mc^2 , is first calculated as

$$mc^2 = (1.6749 \times 10^{-27} \text{ kg})(2.9979 \times 10^8 \text{ m/s})^2 = 1.505 \times 10^{-10} \text{ J}$$

and

$$\frac{1.505 \times 10^{-10} \text{ J}}{1.602 \times 10^{-19} \text{ J/eV}} = 939.5 \text{ MeV}$$

since by definition, $1 \text{ eV} = 1.602 \times 10^{-19} \text{ J}$. From Eqn (1.203) the ratio of the nonrelativistic and relativistic speeds is calculated as

$$\begin{aligned} \frac{u_{nr}}{u_r} &= \frac{\sqrt{2(10 \text{ MeV})(1.602 \times 10^{-13} \text{ J/MeV})/1.6749 \times 10^{-27} \text{ kg}}}{c\sqrt{1 - ((10 \text{ MeV}/939.5 \text{ MeV}) + 1)^{-2}}} \\ &= \frac{4.3737 \times 10^7 \text{ m/s}}{0.1447751c} = \frac{4.3737 \times 10^7 \text{ m/s}}{(0.1447751)(2.9979 \times 10^8 \text{ m/s})} \\ &= \frac{4.3737 \times 10^7 \text{ m/s}}{4.340 \times 10^7 \text{ m/s}} = 1.0079 = 0.79\% \text{ error.} \end{aligned}$$

The error between the nonrelativistic and relativistic calculations is small at this high neutron energy. However, if we consider higher neutron energies in excess of 10 MeV, the error of making nonrelativistic calculations increases.

As we observed above in the case of particle speed, we will also see that particle wavelength will also differ for nonrelativistic and relativistic calculations. In 1923, Louis Victor de Broglie first postulated that all particles or matter in motion should have wave characteristics just as photons display both a wave and particle character. We therefore attribute the wavelength of particles in motion as de Broglie wavelengths. Let us then compare calculated nonrelativistic and relativistic wavelengths. From Eqn (1.192), we can describe the nonrelativistic wavelength, λ_{nr} , as

$$\lambda_{nr} = \frac{h}{p} = \frac{hc}{pc} = \frac{hc}{cmv} = \frac{hc}{cm\sqrt{2E/m}} = \frac{hc}{\sqrt{2mc^2E}} \quad (1.204)$$

where $p = mv = m\sqrt{2E/m}$. For relativistic calculations, the value of pc is calculated according to the following equation derived by Halpern (1988):

$$pc = \left[2m_0c^2K \left(1 + \frac{K}{2m_0c^2} \right) \right]^{1/2} \quad (1.205)$$

and the calculation for the relativistic de Broglie wavelength, λ_r , then becomes

$$\lambda_r = \frac{hc}{pc} = \frac{hc}{[2m_0c^2K(1 + (K/2m_0c^2))]^{1/2}} \quad (1.206)$$

We can then compare the difference between the nonrelativistic and relativistic wavelengths for the 10 MeV neutron as follows:

$$\begin{aligned} \frac{\lambda_{nr}}{\lambda_r} &= \frac{hc/\sqrt{2m_0c^2E}}{hc/[2m_0c^2K(1 + (K/2m_0c^2))]^{1/2}} \\ &= \frac{\left\{ \frac{[(6.626 \times 10^{-34} \text{ J s})(2.9979 \times 10^8 \text{ m/s})/1.602 \times 10^{-13} \text{ J/MeV}]}{\sqrt{2(939.5 \text{ MeV})(10 \text{ MeV})}} \right\}}{\left\{ \frac{[(6.626 \times 10^{-34} \text{ J s})(2.9979 \times 10^8 \text{ m/s})/1.602 \times 10^{-13} \text{ J/MeV}]}{\sqrt{2(939.5 \text{ MeV})(10 \text{ MeV})[1 + (10 \text{ MeV}/2(939.5 \text{ MeV})]}} \right\}} \\ &= \frac{12.3598 \times 10^{-4} \text{ MeV nm}/\sqrt{18790 \text{ MeV}^2}}{12.3598 \times 10^{-4} \text{ MeV nm}/\sqrt{18890 \text{ MeV}^2}} \\ &= \frac{9.0430 \times 10^{-6} \text{ nm}}{9.0190 \times 10^{-6} \text{ nm}} = 1.0026 = 0.26\% \text{ error} \end{aligned} \quad (1.207)$$

From the above comparison of nonrelativistic and relativistic calculations of neutron wavelength and velocity, we see that the data provided in Fig. 1.51 based on nonrelativistic calculations are valid with less than 1% error for the highest energy neutron included in that figure. However, if we consider higher energies beyond 10 MeV, where we classify the neutron as relativistic, the errors in making nonrelativistic calculations will increase with neutron energy. It will be clearly obvious to the reader that factors in Eqn (1.207) can be canceled out readily and the equation simplified to the following, which provides a quick evaluation of the effect of particle energy on the error in nonrelativistic calculation of the de Broglie wavelength:

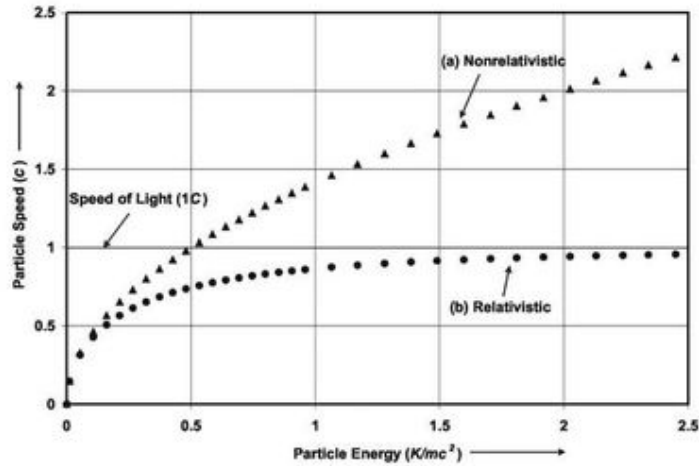
$$\frac{\lambda_{nr}}{\lambda_r} = \sqrt{1 + \frac{K}{2m_0c^2}} \quad (1.208)$$

where K is the particle kinetic energy in MeV and m_0c^2 is the rest energy of the particle (e.g., 939.5 MeV for the neutron and 0.511 MeV for the beta particle). For example, a nonrelativistic calculation of the wavelength of a 50 MeV neutron would have the following error:

$$\frac{\lambda_{nr}}{\lambda_r} = \sqrt{1 + \frac{50 \text{ MeV}}{2(939.5 \text{ MeV})}} = 1.0132 = 1.32\% \text{ error.}$$

Note that the above-computed errors in nonrelativistic calculations of the de Broglie wavelength increased from 0.26% for a 10 MeV neutron to 1.31% for a 50 MeV neutron, and the error will increase with particle energy. Errors in nonrelativistic calculations are yet greater for particles of smaller mass (e.g., beta particles) of a given energy compared to neutrons of the same energy. This is due obviously to the fact that particles of lower mass and a given energy will travel at higher speeds than particles of the same energy but higher mass. This is illustrated in Fig. 1.52 where the particle speed, u , is a function of the particle kinetic energy, K , and its mass or rest energy, mc^2 . The particle energy in Fig. 1.52 is expressed as K/mc^2 to permit the reader to apply the curves for nonrelativistic and relativistic calculations to particles of different mass. For example, from the abscissa of Fig. 1.52, the values of K/mc^2 for a 2 MeV beta particle is $2 \text{ MeV}/0.51 \text{ MeV} = 3.9$ and that for a 2 MeV neutron is $2 \text{ MeV}/939.5 \text{ MeV} = 0.0021$. From Fig. 1.52 we see that the nonrelativistic calculation of the speed of a 2-MeV beta particle

FIGURE 1.52 A graph comparing particle speeds derived from (a) nonrelativistic and relativistic interpretations of the particle speed as a function of the particle kinetic energy. The particle speeds in units of the speed of light ($c = 2.9979 \times 10^8$ m/s) are plotted versus particle energy expressed as a ratio of its kinetic energy (K) over its rest energy (mc^2). In the nonrelativistic case, the particle kinetic energy is defined as $K = 1/2mv^2$ and its speed is calculated according to $v = \sqrt{2K/m}$; whereas in the relativistic case, the particle kinetic energy is the difference between the total energy of the particle and its rest energy ($K = \gamma mc^2 - mc^2$), where $\gamma = 1/\sqrt{1 - (v^2/c^2)}$ and its speed $v = c\sqrt{1 - (K/mc^2 + 1)^{-2}}$ is always less than c .



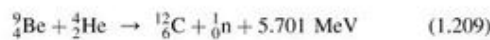
would be erroneously extreme (well beyond the speed of light), while there would be only a small error in the relativistic calculation of the speed of the massive neutron of the same energy.

3. Sources of Neutrons

Neutron sources are vital to our development and well-being. They serve to produce the energy we need and many of the radionuclides required for medical diagnosis and treatment of many forms of cancer as well as numerous applications in industry including nondestructive testing and analysis. A review of current practical applications of neutrons and nuclear radiation is provided by the writer in a previous text (L'Annunziata, 2007). There are several sources of neutrons, including (i) alpha-particle-induced (α,n) nuclear reactions; (ii) radionuclides that decay by spontaneous fission; (iii) neutron-induced fission; (iv) photoneutron (γ,n) sources; (v) charged-particle accelerator sources; and (vi) nuclear fusion. A basic list of these sources is provided in Table 1.13, and a more detailed description of the sources of neutrons will be provided subsequently.

a. Alpha Particle-Induced Nuclear Reactions

It is interesting to note that the method used by Chadwick in 1932 in his discovery of the neutron, namely by an alpha particle-induced reaction, described in Section VIII.E.1, remains an important method for producing a neutron source, particularly when a relatively small or easily transportable neutron source is required. The source may be prepared by compressing an alpha-particle-emitting radioisotope substance with beryllium metal. The nuclear reaction, which occurs between the alpha particle and the beryllium nucleus, terminates with the emission of a neutron and the production of stable carbon as follows:



where 5.701 MeV is the energy released in the reaction. The kinetic energy released in the reaction is determined by calculating the Q value of the reaction according to Eqn (1.67), namely:

$$Q = (m_{\text{reactants}})c^2 - (m_{\text{products}})c^2 \quad (1.210)$$

which for the above reaction is written as

$$\begin{aligned} Q &= (M_{\text{Be}} + M_{\text{He}})c^2 - (M_{\text{C}} + M_{\text{n}})c^2 \\ &= \left[(9.012182 \text{ u} + 4.00260325 \text{ u})931.494 \text{ MeV/u} - \right. \\ &\quad \left. (12.000000 \text{ u} + 1.00866492 \text{ u})931.494 \text{ MeV/u} \right] \\ &= 5.701 \text{ MeV} \end{aligned} \quad (1.211)$$

The calculated value agrees with the Q -value Calculator (QCalc) of the National Nuclear Data Center, Brookhaven National Laboratory: (NNDC, 2010a: <http://www.nndc.bnl.gov/qcalc/>). The neutrons emitted from the reaction will have an average energy of ~5.5 MeV, as the kinetic energy released in the reaction is shared between the neutron and ${}^{12}\text{C}$ nucleus, and the neutron may possess varying energies and velocities as a consequence of the various directions of emission of neutrons from the nucleus.

Several alpha particle sources are used to produce neutrons via the preceding (α,n) reaction. Among these are the alpha emitters ${}^{241}\text{Am}$, ${}^{242}\text{Cm}$, ${}^{210}\text{Po}$, ${}^{239}\text{Pu}$, and ${}^{226}\text{Ra}$. The alpha-radiation source selected may depend on its half-life as well as its gamma-ray emissions. As noted previously in this chapter, gamma radiation often accompanies alpha decay. The use of an alpha source, which also emits abundant gamma radiation, requires additional protection for the user against penetrating gamma rays. For example, Am-Be sources are preferred over the Ra-Be sources of neutrons used in soil moisture probes (Nielsen and Cassel, 1984; O'Leary and Incerti, 1993), because the latter have a higher output of gamma radiation and require more shielding for operator protection.

The energies of the neutrons emitted from these sources will vary over the broad spectrum of 0–10 MeV. The neutrons

TABLE 1.13 Processes for Production of Neutrons and Short Description of Corresponding Spectral Fluence

Process	Example	Neutron fluence energy distribution
Spontaneous fission	$^{252}\text{Cf} \rightarrow n + \text{FP}$	Maxwellian, $E_{\text{mean}} \sim 2 \text{ MeV}$
Neutron-induced fission	$^{235}\text{U}(n, f)$	
Radioisotope (α, n) sources	$\alpha + {}^9\text{Be} \rightarrow {}^{12}\text{C} + n$	Mono ^a or polyenergetic neutrons
Photon reaction	${}^A\text{X}(\gamma, n){}^{A-1}\text{X}$ $\gamma + {}^9\text{Be} \rightarrow {}^9\text{Be} + n$	Mono ^a or polyenergetic neutrons (short half-life of γ -ray emitters)
Charged particle direct reaction	${}^2\text{H}(d, n){}^3\text{He}$	Monoenergetic ^a neutrons $E_{\text{mean}} \sim 0.5 E_d$
Charged particle break-up reaction	${}^2\text{H}(d, np){}^2\text{H}$	Broad energy distribution $E_n \text{ max} \sim E_p$
Spallation reaction	${}^{238}\text{U}(p, 20n)$	Broad energy distribution

^aDefinition of monoenergetic neutron source from ICRU Report 63 (2000): "A neutron source can be considered "monoenergetic" if the energy spectrum consists of a single peak, which has an energy spread which is much less than the energy of the peak. The ideal source has a small energy spread and negligible neutron intensity at lower and higher energies."
(From Lacoste (2010) reprinted with Permission of Elsevier © 2010)

produced by these sources vary in energy as a consequence of several factors, including the sharing of the liberated energy between the neutron and the daughter nucleus, the varying directions of emission of neutrons from the nucleus with consequent varying energies and velocities, and the variations in kinetic energies of the bombarding alpha particles.

The neutron activities available from these sources increase up to a maximum as a function of the amounts of alpha emitter and beryllium target material used. For example, as explained by Bacon (1969), the Ra–Be source, prepared by mixing and compressing radium bromide with beryllium powder, increases steadily in neutron activity (neutrons per second) for each gram of radium used as the amount of beryllium is increased to about 10 g, but no significant increase in neutron output is achieved if more beryllium is used. The maximum neutron output achieved is approximately 2×10^7 neutrons per second per gram of radium. Because alpha decay from any alpha particle-emitting source occurs by means of random events, the production of neutrons by (α, n) reactions is also a random event. Therefore, these reactions can be referred to as "not time correlated." This is contrary to the case of neutron sources provided through fission, discussed subsequently.

Beryllium is not the exclusive element that may be used for the alpha particle-induced neutron source. Other low Z elements may be packed with an alpha emitter (e.g., boron or carbon) but their neutron yields is about six times lower than Be (Lacoste, 2010). For example, Skidmore et al (2009) tested oxygen enriched with ^{18}O packed with ^{241}Am as a possible neutron energy source for planetary research. The neutron flux and energy yield from this source are compared to conventional sources of alpha emitters with Be as well as the ^{252}Cf spontaneous fission neutron source in Table 1.14.

Switchable neutron generators, that is generators that may be turned on or off, of the (α, n) type are possible when the alpha emitter and target are not packed intimately. The alpha emitter need not be packed intimately with the target material, but both must be close enough to allow the alpha particles to be absorbed by the target. Hertz et al (2003) studied many

combinations of alpha emitter and target materials for switchable neutron sources, and they found the ${}^9\text{Be}(\alpha, n)$ generator with an ^{241}Am alpha-emitting source the most suitable as a switchable neutron source. In the "off" position, a mechanical device is used to prevent the alpha particles from reaching the Be target. These switchable neutron sources are classified as micromachines, because they can be constructed to have the dimensions of the same order of magnitude as the alpha-particle range.

b. Spontaneous Fission

About 100 radionuclides are known to decay by spontaneous fission (SF) with the emission of neutrons (Karelin et al, 1997) as an alternative to another decay mode, such as alpha decay. Spontaneous fission involves the spontaneous noninduced splitting of the nucleus into two nuclides or fission fragments and the simultaneous emission of more than one neutron on the average. This phenomenon occurs with radionuclides of high mass number, $A \geq 230$. The radionuclide ^{252}Cf is a good example of a commercially available spontaneous fission neutron source. It decays with a half-life of 2.65 years primarily by alpha emission

TABLE 1.14 The Total Flux Emitted by the Neutron Sources per Second Integrated over Energy

Neutron source	Integrated flux ($\text{s}^{-1}\text{g}^{-1}$)	Approximate source mass required for 100 W thermal power generation (g)
^{252}Cf	2.3×10^{12}	0.05
Am–Be	1.4×10^6	2000
Enriched AmO_2	3.7×10^5	2000
Pu–Be	7.2×10^6	2000

(from Skidmore et al. (2009) reprinted with permission of Elsevier © 2009)

(96.91% probability); the remaining of the ^{252}Cf decay processes occur by spontaneous fission with a probability of 3.09% (Martin et al, 2000, see also Appendix A). Decay of ^{252}Cf by spontaneous fission produces an average number of 3.7 neutrons per fission. Because the sizes of the two fragments resulting from fission are not predictable, average sizes of the two fragments are determined. Consequently, the numbers of neutrons emitted from individual fissions are not the same; and an average number of neutrons produced per fission is determined. The fission rate of ^{252}Cf is 6.2×10^5 SF/s/ μg (Isotope Products Laboratories, 1995). The neutron emission from ^{252}Cf in units of neutrons per second per unit mass is reported to be 2.314×10^6 neutrons/s/ μg with a specific activity of 0.536 mCi/ μg (Martin et al, 2000, Skidmore et al, 2009). Thus, one milligram of ^{252}Cf would emit 2.314×10^9 neutrons per second. If we know the radionuclide specific activity and the % probability of decay by spontaneous fission, we can calculate the fission rate. For example, taking the specific activity and % probability of spontaneous fission reported above for ^{252}Cf , we can calculate the fission rate as the product of decay rate and probability of SF per decay or

$$(0.536 \text{ mCi}/\mu\text{g})(3.7 \times 10^7 \text{ dps/mCi})(0.0309) \\ = 6.13 \times 10^5 \text{ SF/s}/\mu\text{g} \quad (1.212)$$

which is in close agreement with the value cited above. See Section XVI.A for a discussion on radioactivity units and calculations.

The variations in fission fragment sizes and number of neutrons emitted per fission provide variable neutron energies over the range 0–5.5 MeV with an average neutron energy from ^{252}Cf of approximately 2.3 MeV. Small sources of ^{252}Cf are commercially available for a wide range of applications such as prompt-gamma neutron activation analysis of coal, cement, minerals, interplanetary analysis, petroleum contamination analysis in soil, detection of explosives and land mines, neutron radiography, and cancer therapy (Mercer et al, 2007, Skidmore et al, 2009). There is an increasing interest in the use of ^{252}Cf neutron sources in radiation therapy or specifically neutron brachytherapy treatment of various types of cancer (Melhus and Rivard, 2006, Wang et al, 2008, and Ghassoun et al, 2010). Small commercial sources are described by Martin et al (1997, 2000) among which 50-mg sources of ^{252}Cf providing a neutron intensity $> 10^{11}$ /s and measuring only 5 cm in length \times 1 cm diameter are included. They report also larger sources of mass > 100 mg of ^{252}Cf that approach reactor capabilities for neutrons.

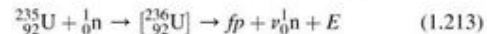
Another standard nuclide source of neutrons is ^{248}Cm , which provides spontaneous fission intensity of only 4.12×10^4 /s/mg and decays with a half-life of 3.6×10^5 years (Radchenko et al, 2000). The lower neutron flux intensity of this source limits its application, although it has the advantage of a very long half-life providing invariability of sample intensity with time.

Some radionuclides of interest in nuclear energy and safeguards also decay by spontaneous fission. The isotopes of plutonium of even mass number, namely ^{238}Pu , ^{240}Pu , and ^{242}Pu , decay principally by alpha particle emission but can also undergo spontaneous fission to a lesser extent at rates of 1100, 471, and 800 SF/s/g, respectively. The average number of neutrons emitted per fission is between 2.16 and 2.26 of broad

energy spectrum (Canberra Nuclear, 1996). Because the neutrons produced with each fission occurrence are emitted simultaneously, we can refer to these emissions as “time correlated.” Other isotopes of uranium and plutonium also undergo spontaneous fission, but at a much lower rate.

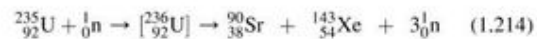
c. Neutron-Induced Fission

When the naturally occurring isotope of uranium, ^{235}U , is exposed to slow neutrons, it can absorb the neutron to form the unstable nuclide ^{236}U . The newly formed nucleus may decay by alpha-particle and gamma-ray emission with the long half-life of 2.4×10^7 years. This occurs in approximately 14% of the cases when ^{235}U absorbs a slow neutron. However, in the remaining 86% of the cases, the absorption of a slow neutron by ^{235}U results in the production of the unstable ^{236}U nuclide, which takes on the characteristics of an unstable oscillating droplet (see Fig. 1.10 of Section IV.D.1). This oscillating nuclear droplet with the opposing forces of two positively charged nuclides splits into two fragments, not necessarily of equal size, with the liberation of an average energy of 193.6 MeV. The general ^{235}U fission reaction may be written as



which represents the reaction of one atom of ^{235}U with one thermal neutron ${}_0^1\text{n}$ to yield the release of fission products *fp* of varying masses plus an average yield of $\nu = 2.42$ neutrons and an overall average release of energy $E = 193.6$ MeV (Koch, 1995). The intermediate nuclide ^{236}U is shown in brackets in the above reaction. Most of this energy (over 160 MeV) appears in the form of kinetic energy of the two fission fragments. The remaining energy is shared among the neutrons emitted, with prompt gamma radiation accompanying fission and also beta particles and gamma radiation from decaying fission fragments and neutrinos accompanying beta decay. When a sample of ^{235}U is bombarded with slow neutrons, the fission fragments produced are rarely of equal mass. The ^{236}U intermediate nuclide breaks into fragments in as many as 30 different possible ways, producing, therefore, 60 different nuclide fission fragments. In a review Koch (1995) provides a list of the fission fragments and their relative abundances as produced in a typical pressurized water reactor (PWR). The most common fission fragments have a mass difference in the ratio 3:2 (Bacon, 1969). Neutrons emitted from this fission process vary in energy over the range 0–10 MeV with an average neutron energy of 2 MeV, which are classified as fast neutrons.

Let us take one of many possible examples of ^{236}U fission to calculate the magnitude of energy liberated. One example of many possible fission reactions, that may be written conserving mass and charge of the ^{236}U nucleus with the emission of three neutrons, is the following:



The energy liberated in the above fission reaction can be determined from its *Q* value, which is calculated from Eqns (1.66) and (1.67) of Section VII.C, as follows:

$$Q = E_{0, \text{reactants}} - E_{0, \text{products}} \quad (1.215)$$

where $E_{0, \text{reactants}}$ and $E_{0, \text{products}}$ are the rest energies of the nuclear reactants and products, respectively. Eqn (1.215) may be written as

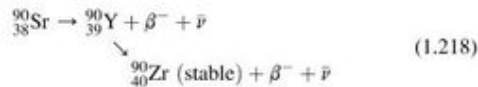
$$Q = (M_{\text{reactants}})c^2 - (M_{\text{products}})c^2 \quad (1.216)$$

where $M_{\text{reactants}}$ and M_{products} are the combined masses of the nuclear reactants and products, respectively, and c is the velocity of light in a vacuum. For the fission reaction (1.213), we can calculate its Q value as

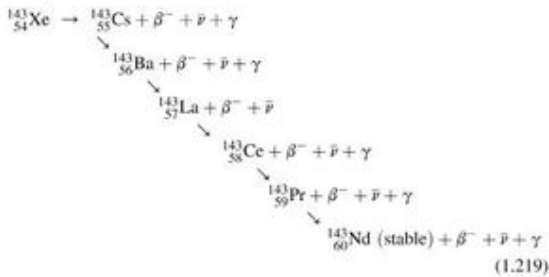
$$\begin{aligned} Q &= (M_{^{235}\text{U}} + M_n)c^2 - (M_{^{90}\text{Sr}} + M_{^{143}\text{Xe}} + 3M_n)c^2 \\ &= \left[(235.043922 \text{ u} + 1.00866492 \text{ u}) - \right. \\ &\quad \left. (89.907738 \text{ u} + 142.9352 \text{ u} + 3(1.00866492 \text{ u})) \right] \\ &\quad \times 931.494013 \text{ MeV/u} \\ &= 171.1 \text{ MeV}, \end{aligned} \quad (1.217)$$

which is in agreement with the computer calculated Q value determined with QCalc provided by the National Nuclear Data Center, Brookhaven National Laboratory (NNDC, 2010a: <http://www.nndc.bnl.gov/qcalc/>). As noted previously, most of the energy released appears as kinetic energy of the fission fragments (~165 MeV). The neutrons carry off about 2 MeV each on the average. Additional energy is released from fission via gamma radiation and beta decay of the fission products and the neutrino radiation that accompanies beta decay. The total energy released by the neutron-induced fission of ^{235}U , in the example given by Eqn (1.214), to the ultimate decay of the fission products ^{90}Sr and ^{143}Xe to their stable ground states is calculated by determining firstly the decay schemes of the two fission products as follows:

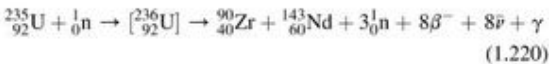
Decay of ^{90}Sr :



Decay of ^{143}Xe :



Thus, the final reaction to the stable nuclides can be written as



If we use atomic mass units to calculate the Q value of the above reaction, the eight additional atomic electrons of the $^{90}\text{Zr} + ^{143}\text{Nd}$ (100 atomic electrons) over the ^{235}U (92 atomic electrons) force the eight electrons represented by the eight beta

particles ($8\beta^-$) to drop out of the equation. Thus, we can calculate the Q value as

$$\begin{aligned} Q &= (M_{^{235}\text{U}} + M_n)c^2 - (M_{^{90}\text{Zr}} + M_{^{143}\text{Nd}} + 3M_n)c^2 \\ &= \left[(235.043922 \text{ u} + 1.00866492 \text{ u}) - \right. \\ &\quad \left. (89.904702 \text{ u} + 142.909810 \text{ u} + 3 \times 1.00866492 \text{ u}) \right] \\ &\quad \times 931.494013 \text{ MeV/u} \\ &= 197.55 \text{ MeV} \end{aligned} \quad (1.221)$$

The calculated Q value of 197.55 MeV represents the total energy released in the example of the neutron-induced fission of ^{235}U to the unstable ^{90}Sr and ^{143}Xe fission products, followed by the decay of these fission products, to the stable ^{90}Zr and ^{143}Nd nuclides. This calculated value is close to the estimated value of ~202 MeV using average binding energies of the parent and daughter nuclides found in Section IV.C.

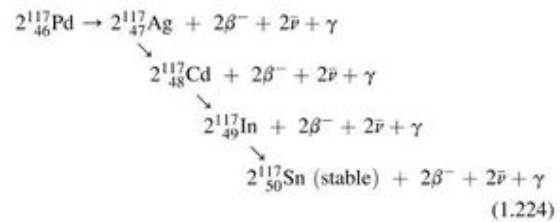
Let us take another example of many possible fission possibilities of the neutron-induced fission of ^{235}U . This example is one where the two fission products are of the same mass number, which is the following:



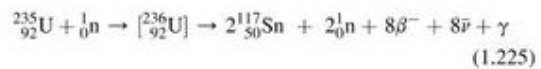
The fission products in this case are two nuclides of ^{117}Pd and two neutrons. The energy released by the neutron-induced fission is calculated as

$$\begin{aligned} Q &= (M_{^{235}\text{U}} + M_n)c^2 - (2M_{^{117}\text{Pd}} + 2M_n)c^2 \\ &= \left[(235.043922 \text{ u} + 1.00866492 \text{ u}) \right. \\ &\quad \left. - (2 \times 116.9178 \text{ u} + 2 \times 1.00866492 \text{ u}) \right] \\ &\quad \times 931.494013 \text{ MeV/u} \\ &= 185.9 \text{ MeV}, \end{aligned} \quad (1.223)$$

which agrees with the value calculated by the National Nuclear Data Center's QCalc, Brookhaven National Laboratory (NNDC, 2010a,b: <http://www.nndc.bnl.gov/qcalc/>). The total energy yield, that includes the decay of the radioactive ^{117}Pd , can be calculated after firstly determining the decay scheme of two nuclides of ^{117}Pd to final stable daughter nuclides. The decay scheme is the following:



From the above reaction schemes, the total reaction of the neutron-induced fission of ^{235}U to two nuclides of ^{117}Sn can be written as follows:



The total energy released from this example of neutron-induced fission of ^{235}U is calculated as

$$Q = (M_{^{235}\text{U}} + M_{\text{n}})c^2 - (2M_{^{137}\text{Sn}} + 2M_{\text{n}})c^2$$

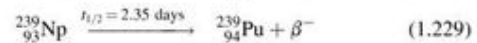
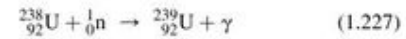
$$= \left[(235.043922 \text{ u} + 1.00866492 \text{ u}) \right. \\ \left. - (2 \times 116.902955 \text{ u} + 2 \times 1.00866492 \text{ u}) \right] \\ \times 931.494013 \text{ MeV/u} = 213.6 \text{ MeV} \quad (1.226)$$

Thus, from the two examples of possible fission reactions taken above Eqns (1.220) and (1.225), which include the decay of the fission products to stable nuclides, we calculated the energy released by the two fission processes as 197.5 MeV Eqn (1.221) and 213.6 MeV Eqn (1.226). We can see that approximately 200 MeV is the amount of energy released from the two examples taken of the neutron-induced fission of ^{235}U . The magnitude of the energy released from neutron-induced fission of ^{235}U would be an average figure, because the actual amount of energy released would depend on the fission reaction, and there are many possible ways that the ^{236}U could break into two nuclides. Some of the energy arises from fission product radioactivity including gamma-ray emission as fission product nuclides decay to lower energy states, beta-particle emission from fission product decay, and the emission of neutrinos that accompany beta decay. The energy released can be itemized into the various energy categories listed in Table 1.15, which are tallied to provide an approximate average figure for the energy released in neutron-induced fission of ^{235}U .

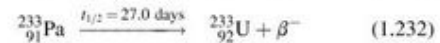
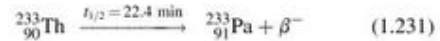
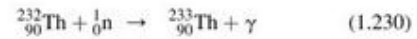
Because more than one neutron is released per fission, a self-sustaining chain reaction is possible with the liberation of considerable energy, forming the basis for the nuclear reactor as a principal source of neutrons and energy. In the case of ^{235}U , slow neutrons are required for neutron capture and fission to occur. The nuclear reactor, therefore, will be equipped with a moderator such as heavy water (D_2O) or graphite, which can reduce the energies of the fast neutrons via elastic scattering of the neutrons with atoms of low atomic weight. The protons of

water also serve as a good moderator of fast neutrons, provided the neutrons lost via the capture process $^1\text{H}(n,\gamma)^2\text{H}$ can be compensated by the use of a suitable enrichment of the ^{235}U in the nuclear reactor fuel (Byrne, 1994).

The previously described fission of ^{235}U represents the one and only fission of a naturally occurring radionuclide that can be induced by slow neutrons. The radionuclides ^{239}Pu and ^{233}U also undergo slow neutron-induced fission; however, these nuclides are man-made via the neutron irradiation and neutron capture of ^{238}U and ^{232}Th , as illustrated in the following equations (Murray, 2009). The preparation of ^{239}Pu occurs by means of neutron capture by ^{238}U followed by beta decay as follows:



The preparation of ^{233}U is carried out via neutron capture of ^{232}Th followed by beta decay according to the following:



Nuclides that undergo slow neutron-induced fission are referred to as fissile materials. Although ^{235}U is the only naturally occurring fissile radionuclide, it stands to reason that, if an excess of neutrons is produced in a thermal reactor, it would be possible to produce fissile ^{239}Pu or ^{233}U fuel in a reactor in excess of the fuel actually consumed in the reactor. This is referred to as "breeding" fissile material, and it forms the basis for the new generation of breeder reactors (Murray, 2009).

Other heavy isotopes, such as ^{232}Th , ^{238}U , and ^{237}Np , undergo fission but require bombardment by fast neutrons of at least 1 MeV energy to provide sufficient energy to the nucleus for fission to occur. These radionuclides are referred to as fissionable isotopes.

d. Photoneutron (γ,n) Sources

Many nuclides emit neutrons upon irradiation with gamma or x-radiation; however, most elements require high-energy electromagnetic radiation in the range 10–19 MeV. The gamma or x-ray energy threshold for the production of neutrons varies with target element. Deuterium and beryllium metal are two exceptions, as they can yield appreciable levels of neutron radiation when bombarded by gamma radiation in the energy range of only 1.7–2.7 MeV. The target material of D_2O or beryllium metal is used to enclose a β^- -emitting radionuclide, which also emits gamma rays. The gamma radiation bombards the targets deuterium and beryllium to produce neutrons according to the photoneuclear reactions $^2\text{H}(\gamma,n)^1\text{H}$ and $^9\text{Be}(\gamma,n)^8\text{Be}$, respectively. The photoneutron source $^{124}\text{Sb} + \text{Be}$ serves as a good example of a relatively high-yielding combination of gamma emitter with

TABLE 1.15 Approximate Energy Released from Neutron-induced ^{235}U Fission

Type	Energy released (MeV)
Prompt Energy	
Fission product kinetic energy	165
Neutrons (2.5 n/fission on average, -2 MeV/n on average)	5
Gamma-ray emissions	7
Energy from fission-product decay	
Gamma-ray emissions	7
Beta radiation	6
Neutrinos	10
Total	200 MeV

beryllium target. The ^{124}Sb gamma radiation of relevance in photoneutron production is emitted with an energy of 1.69 MeV at 50% abundance (*i.e.*, one-half of the ^{124}Sb radionuclides emit the 1.69 MeV gamma radiation following beta decay). A yield of 5.1 neutrons per 106 beta disintegrations per gram of target material has been reported (Byrne, 1994). The half-life ($t_{1/2}$) of ^{124}Sb is only 60.2 days, which limits the lifetime of the photoneutron generator; nevertheless, this isotope of antimony is easily prepared in the nuclear reactor by neutron irradiation of natural stable ^{123}Sb . An excellent example is that reported by Fantidis et al (2009), whereby a SbBe neutron source was demonstrated to be very useful as a transportable neutron source applicable to a neutron radiography system. The particular advantage of such a neutron source is the ability to effectively have an on/off switching capability, because the production of neutrons can be stopped by simply removing the beryllium target from the antimony gamma-ray source. A unique application of the $^9\text{Be}(\gamma,n)^8\text{Be}$ reaction is reported by Moussavi-Zarandi (2008), who used the gamma emissions from a ^{124}Sb source to survey for the Be content of minerals in the exploration of potential beryllium mines. The neutrons emitted from the Be nucleus via the (γ,n) reaction are detected by a BF_3 neutron counter providing a survey meter for Be exploration.

An alternative to a gamma source for the (γ,n) reaction is the use of electrostatic and linear accelerators (LINACs). Commercially available linear accelerators are capable of accelerating electrons against a high Z element, such as tungsten, to produce bremsstrahlung radiation. The bremsstrahlung photons interact with a converter material such as Be or BeD_2 , which converts the photon beam to a neutron beam via the reactions $^9\text{Be}(\gamma,n)^8\text{Be}$ and $^2\text{H}(\gamma,n)^1\text{H}$. The symbol γ is used here to denote the nuclear reaction projectile, although bremsstrahlung photons (x-rays), rather than gamma-rays, are the projectiles. This is done out of convenience, as bremsstrahlung and gamma-rays are photons which differ only in their origins. The target and converter materials are arranged with respect to the electron beam in a fashion such as illustrated in Fig. 1.53. Alternatively, the electron beam may be directed to impinge immediately onto a Be or BeD_2 target material, whereby the bremsstrahlung photons, that are produced, interact directly with the Be or BeD_2 target to yield neutrons (Auditore, 2005).

In such an arrangement, as illustrated in Fig. 1.53, neutrons are produced by means of the electron accelerator. The process, as described by Eshwarappa et al (2007), entails the

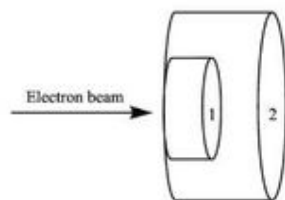
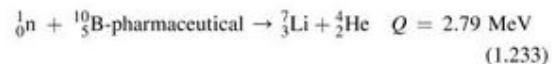


FIGURE 1.53 A photoneutron assembly consisting of (1) a disc of tungsten (W) target embedded within (2) a photoneutron converter consisting of Be or BeD_2 . Typical dimensions are 2×8 cm (thickness \times radius W target) and 10×12 cm or 60×60 cm Be or BeD_2 target. (From Rahmani and Shahriari (2010). Reprinted with permission from Elsevier © 2010.)

acceleration of electrons to impinge on a high Z target (*e.g.*, tungsten, W), which generates a cascade shower of bremsstrahlung photons with an energy spectrum having an end point equal to the electron beam energy. The photons, produced in this fashion, travel through a suitable photoneutron target (*e.g.*, Be or BeD_2), producing excited compound nuclei of energy equal to the sum of the binding energy of the last neutron and the energy of the bremsstrahlung x-rays. When the excitation energy is larger than the binding energy of the last neutron in the compound nucleus, a neutron is emitted. Any excess energy is shared as kinetic energy of the neutron and the residual nucleus (Eshwarappa et al, 2007). Essentially, the energy conversion follows the path of $e-\gamma-n$, that is, the accelerated electron energy is converted to bremsstrahlung photons, which subsequently yields neutrons.

LINACs producing high-energy (15–25 MeV) photon beams are becoming widespread (Bevilacqua et al, 2007). Low-energy LINACs (< 10 MeV) are found to be useful for neutron radiography and radiation boron-neutron-capture therapy (BNCT) in radiation oncology. A 5 MeV electron LINAC with Be and BeD_2 targets can lead to thermal neutron beams of 8.48×10^7 n/cm²/s/mA and 1.23×10^8 n/cm²/s/mA, respectively (Auditore, 2005).

The use of LINACs for $e-\gamma-n$ conversions as neutron sources in cancer therapy using boron-neutron-capture therapy (BNCT) is under development (Bevilacqua et al, 2007, Mameli et al, 2008, Martínez et al, 2010, and Rahmani and Shahriari, 2010). BNCT entails the use of thermal neutrons to kill individual cancer cells (*e.g.*, brain tumors) with minimal damage to cancer-free cells. The principle and technique of BNCT are firstly the administration of a ^{10}B -loaded pharmaceutical to a cancer patient followed by the irradiation of the tumor with thermal neutrons, produced as previously described with the LINAC $e-\gamma-n$ conversion. The ^{10}B -loaded pharmaceutical concentrates in the cancer cells, and the neutrons react with the ^{10}B to yield ^7Li and alpha particles within the cancer cell according to $^{10}\text{B}(n,\alpha)^7\text{Li}$, that is,



The ^7Li and alpha particles share the kinetic energy liberated in the reaction. Their high mass attributes a high linear energy transfer (LET), high relative biological effectiveness (RBE), and short range of travel of 4.1 and 7.7 μm for the ^7Li and alpha particles, respectively (Eskandari and Kashian, 2009, Tanaka et al, 2009a, and Rahmani and Shahriari, 2010). The total range of 11.8 μm is equivalent to the dimensions of a cell in the human body, thus providing BNCT with the advantage of cell selectivity over other methods of radiotherapy.

Accelerated electron-generated neutrons via the (γ,n) reactions have been reported to yield in a uranium target as many as 10^{-2} neutrons per accelerated electron at an electron energy of 30 MeV with a total yield of 2×10^{13} neutrons per second (Byrne, 1994). The accelerator is a good neutron source for the potential generation of nuclear fuels. Some other applications of photoneutrons produced by x-rays from electron accelerators are the detection of explosives by the measurement of

photon-neutron-induced gamma rays (Yang et al, 2007), photon-neutron assay of highly enriched uranium via neutron-induced fission (Lakosi and Nguyen, 2008), and the elemental analysis of short-lived activation products (Patil et al, 2010a,b).

e. Charged-particle Accelerator Sources

The accelerator utilizes electric and magnetic fields to accelerate beams of charged particles such as protons, electrons, and deuterons into target materials. Nuclear reactions are made possible when the charged particles have sufficient kinetic energy to react with target nuclei. Some of the reactions between the accelerated charged particles and target material can be used to generate neutrons.

When electrons are accelerated, they gain kinetic energy as a function of the particle velocity. This kinetic energy is lost as bremsstrahlung electromagnetic radiation when the accelerated electrons strike the target material. Bremsstrahlung radiation is described in Section IX.D.2. It is the bremsstrahlung photons that interact with nuclei to produce neutrons according to the mechanisms described in the previous section under photon-neutron (γ, n) sources.

Accelerated deuterons can be used to produce high neutron yields when deuterium and tritium are used as target materials according to the reactions ${}^2\text{H}(d, n){}^3\text{He}$ and ${}^3\text{H}(d, n){}^4\text{He}$, respectively. In the deuterium energy range of 100–400 keV, it is possible to obtain neutron yields of the order of 10^{11} neutrons per second from these (d, n) reactions with relatively small electrostatic laboratory accelerators (Byrne 1994, Kim et al, 2008, Eskandari and Kashian, 2009 and Park et al, 2009). The ${}^2\text{H}(d, n){}^3\text{He}$ and ${}^3\text{H}(d, n){}^4\text{He}$ reactions are referred to as the D–D and D–T neutron sources. When low-energy deuterons are used as projectiles, the D–D and D–T reactions yield 2.4 and 14.1 MeV fast monoenergetic neutrons, respectively (Eskandari and Kashian, 2009, Tracz et al, 2009, and Sharma et al, 2010). The Q values for the D–D and D–T reactions are 3.27 and 17.58 MeV, respectively, which explains the energy of the neutrons liberated in these reactions. The remaining energy not carried away by the neutrons remains with the residual ${}^3\text{He}$ and ${}^4\text{He}$ nuclei of the D–D and D–T reactions. The two (d, n) reactions are the same as the fusion reactions discussed in the subsequent section. The low energies of the deuteron projectiles required for the D–D and D–T reactions are advantageous when small accelerators are used in facilities that utilize neutrons for radiation therapy such as BNCT described in the earlier sections. Neutrons of higher energy (14–30 MeV) may be obtained from the D–T reactions by increasing the deuteron projectile energy, as the neutron energy is a function of the deuteron energy (Eskandari and Kashian, 2009). By means of a low-energy (350 keV) deuteron beam and a tritium target of 0.37 TBq of ${}^3\text{H}$, Ochiai et al (2007) report the D–T reaction yielding a neutron fluence of 1.5×10^{11} n/s, which was determined by counting the 3.5 MeV alpha particles. The neutron flux from this generator could be increased 10-fold by increasing the thickness of the ${}^3\text{H}$ target (Csikai, 1987 and Eskandari and Kashian, 2009).

By accelerating deuterons and protons to energies between 1.8 and 4 MeV, neutron generation using beryllium and lithium targets via the following reactions: ${}^9\text{Be}(d, n){}^{10}\text{B}$, ${}^7\text{Li}(p, n){}^7\text{Be}$,

and ${}^9\text{Be}(p, n){}^9\text{B}$ are routine (Bayanov et al, 2009a,b, 2010, Eskandari and Kashian, 2009, Feinberg et al, 2009, and Iwashita et al, 2010). A higher-energy 30 MeV proton beam against a beryllium target was used by Tanaka et al (2009b), and the fast neutrons were moderated for boron–neutron capture therapy.

The acceleration of protons in the energy range of ~0.5–5 GeV against targets of high atomic number will result in nuclear spallation with the emission of typically 20–30 high-energy neutrons per incoming proton, depending on the energy of the proton beam and the nature of the target material (Samec et al, 2009 and Krása et al, 2010). Even higher yields of 40–50 neutrons emitted per proton projectile are possible at the very high proton energies of 4 and 5 GeV (Krása et al, 2010). Nuclear spallation is the process that occurs when a nucleus of high atomic number emits a large number of neutrons following impact by a high-energy projectile. Such reactions are abbreviated often with the notation (p, xn) which signifies a proton projectile with the emission of an x number of neutrons (See Table 1.12). Such high-power neutron sources can yield a neutron flux of up to 10^{14} n/cm²/s at the surface of the source. Some typical targets of high mass number, which have favorable spallation-neutron production characteristics, are Hg, W, ${}^{238}\text{U}$, Pb, and Th (Aydin et al, 2008). Practical implications of neutron sources for the generation of nuclear fuels were noted previously in Section VIII.E.3.c. Murray (2009) pointed out that a yield of as many as 50 neutrons per single charged-particle projectile could be used to produce new nuclear fuels via neutron capture by ${}^{238}\text{U}$ and ${}^{232}\text{Th}$ according to reactions 1.226 to 1.231 described previously.

When protons are accelerated at lower energies of 20–60 MeV against targets of intermediate mass number (e.g., Cr and Cu), the spallation-neutron production characteristics are less favorable, that is, the yield of number of neutrons emitted per proton projectile is lower. Aydin et al (2008) measured the spallation reaction cross sections for protons in the energy range of up to 100 MeV against target nuclei consisting of isotopes of Cr and Cu. The neutrons emitted per proton projectile ranged from (p, n) at the low 20–30 MeV proton energies to (p, 4 n) at the higher 50–60 MeV proton energies. Thus, a cyclotron capable of accelerating protons to 20–60 MeV was found suitable for the production of neutrons from these target materials.

f. Thermonuclear Fusion

The fusion of two atomic nuclei into one nucleus is not possible under standard temperature and pressure. This is because the repulsing Coulombic forces between the positive charges of atomic nuclei prevent them from coming into the required close proximity of 10^{-15} m before they can coalesce into one. However, as described by Kudo (1995) in a review on nuclear fusion, if temperatures are raised to 100 million degrees, nuclei can become plasmas in which nuclei and electrons move independently at a speed of 1000 km/s, thereby overcoming the repulsing forces between nuclei. Nuclear fusion reactors or controlled thermonuclear reactors (CTRs) are under development to achieve nuclear fusion as a practical energy source. The reactors are based on maintaining plasmas through magnetic or

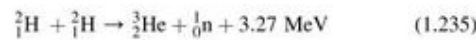
inertia confinement as described by Dolan (1982), Hawryluk et al (1994), Strachan et al (1994), Kudo (1995) Brink (2005), Fiore (2006), and IAEA (2009). Some fusion reactions also produce neutrons.

The energy liberated during nuclear fusion is derived from the fact that the mass of any nucleus is less than the sum of its component protons and neutrons. This is because protons and neutrons in a nucleus are bound together by strong attractive nuclear forces discussed previously in Section IV.C. As described by Eqn (1.24), earlier in this chapter, the total energy of the nucleus with its bound nucleus is always less than the total energy of the separate protons and neutrons, and this difference is the binding energy of the nucleus. The binding energy is equivalent to the energy required to pull a bound system apart, such as a bound nucleus, leaving its component protons and neutrons free of attractive forces. From Eqn (1.24) we can see that, if it is possible to overcome the repulsive forces of protons in nuclei and fuse the nuclei into a new nucleus of lower mass, energy will be liberated.

Nuclear fusion reactions of two types emit neutrons, and these are of prime interest in man-made controlled thermonuclear reactors. The first type is fusion between deuterium and tritium nuclei according to



and the other type involves fusion between two deuterium nuclei according to either of the following equations, which have approximately equal probabilities of occurring (Kudo, 1995):



and



The fusion reaction between deuterium and tritium or D-T reaction Eqn (1.234) gives rise to a 14.06 MeV neutron and a 3.52 MeV alpha particle. The D-D fusion reaction of Eqn (1.235) gives rise to a 0.82 MeV ${}^3\text{He}$ nucleus and a 2.45 MeV neutron, while the D-D fusion reaction of Eqn (1.236) gives rise to 1.01 MeV ${}^3\text{H}$ nucleus and 3.03 MeV proton (${}^1\text{H}$).

g. Inertial Electrostatic Confinement Fusion (IECF)

Under development are compact neutron sources, which utilize either D-D or D-T fusion reactions as well as D- ${}^3\text{He}$ fusion. One instrument described by Miley and Sved (1997) is the inertial electrostatic confinement fusion (IECF) device, which accelerates deuteron ions producing fusion reactions as the ions react with a pure deuterium or deuterium-tritium plasma target. The device is compact measuring 12 cm in diameter and 1 m in length and provides a neutron flux of 10^6 – 10^7 2.5 MeV D-D n/s or 10^8 – 10^9 14 MeV D-T n/s. As described by Noborio et al. (2006), IECF involves a basically simple device, which can cause the fusion reaction, and it is expected to be used as a compact neutron-beam generator. The basic IECF device is illustrated in Fig. 1.54. The device consists of a spherical grounded anode and a grid cathode. Ions are generated by glow discharge in low

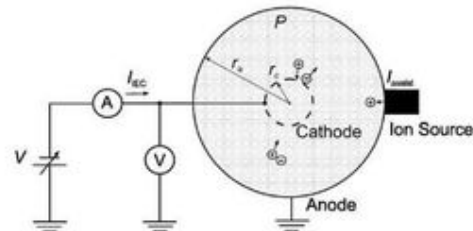
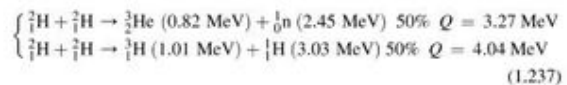


FIGURE 1.54 A schematic diagram of an IECF device and its geometrical and electrical parameters, namely, r_a = anode radius (17.10 cm), r_c = cathode radius (3 cm), P = gas pressure (0.07–0.2 Pa), V = discharge voltage (60–120 kV), I_{DC} = discharge current (2 mA–4 A), and I_{ion} = injected ion current (2–200 mA). (From Noborio et al., (2006) reprinted with permission of Elsevier © 2006.)

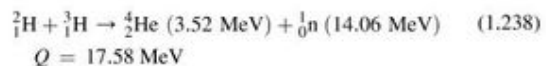
pressure deuterium gas ($< \sim 2$ Pa), and the ions are accelerated toward the center region by a high electric field. Within the center cathode, concentrated energetic ions collide with each other or with background neutral gases resulting in the fusion reaction.

As described by Tomiyasu et al (2010), ions are accelerated to fusion-relevant energies by the electric field between concentric electrodes and circulate inside the outer anode through the inner-gridded cathode. The inner cathode consists of a spherical wire grid, which is highly transparent to ions. The objective, as described by Khachan and Samarian (2007), is to create a deep potential well in order to trap ions and confine them for a long enough time, for which reason the concept was called inertial electrostatic confinement (IEC). The first effective device of this type was reported by Hirsch (1967), who obtained a neutron output of $\sim 10^8$ D-D n/s and 10^{10} D-T n/s from a gridded IECF device driven by six ion guns. In addition to the D-D and D-T fusion reactions as neutron sources described by Eqns (1.234) to (1.236), the IECF device is also a portable proton source yielding 10^8 protons/s utilizing the D- ${}^3\text{He}$ fusion reaction as described by Ashley et al (2000) and Masuda et al (2006). In summary, the fusion reactions that may yield neutrons and/or protons are the following:

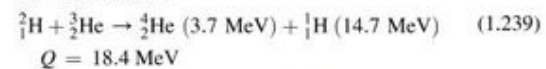
D – D fusion :



D – T fusion :



D – ${}^3\text{He}$ fusion :



The D-D fusion, as illustrated in Eqn (1.237), may occur via two possible reactions that have equal probabilities of occurrence yielding either 2.45 MeV neutrons or 3.03 MeV protons. The D-T and D- ${}^3\text{He}$ fusion reactions yield high-energy (14 MeV) neutrons or protons respectively, according to Eqns (1.238) and (1.239).

Although the concept of inertial electrostatic confinement fusion had an early beginning, only in the last several years has intense research been devoted to making this a compact portable neutron and proton source. In a review by Tomiyasu et al (2010), two approaches have been taken to improve the IECF reaction rates, namely, (i) to increase the ion density by increasing the input current (Yamauchi et al, 2006, Ohnishi et al, 2007, and Radel et al, 2007) and (ii) to increase the ion energy by reducing the background gas pressure, which reduces the energy loss due to collisions with background neutral ions (Higashi et al, 2003, Piefer et al, 2005, Miley et al, 2005, and Takamatsu et al, 2006). Tomiyasu et al (2010) proposed a magnetic assisted electrostatic confinement whereby the ion motion can be controlled, as illustrated in Fig. 1.55. With the application of an appropriate magnetic field, the ions are forced to an azimuthal direction by Lorentz force as they are accelerated toward the center of the electric field.

In addition to efforts to increase the reaction rates achieved with the IECF device, research is conducted toward the practical applications of the device as a portable neutron source in light of its simple configuration and compact size. Applications of such a portable neutron and proton source include the detection and measurement of highly enriched uranium (Radel et al, 2007), the detection of explosives including landmine detection (Yoshikawa et al, 2007a,b and Takahashi et al, 2010), and isotope production (Cipiti and Kulcinski, 2005). Because of the simplicity and compact size of the IECF device, Yoshikawa et al (2007a) list numerous applications subject to the expected improvements in reactions rates achieved by this neutron/proton source. These applications are listed in Fig. 1.56

Another similar device is described by Tsybin (1997), which utilizes laser irradiation to create a plasma in an ion source. Compact neutron sources of these types can become competitive with other neutron sources previously described such as ^{252}Cf and accelerator solid-target sources, because of advantages, including (i) on-off capability, (ii) longer lifetime without

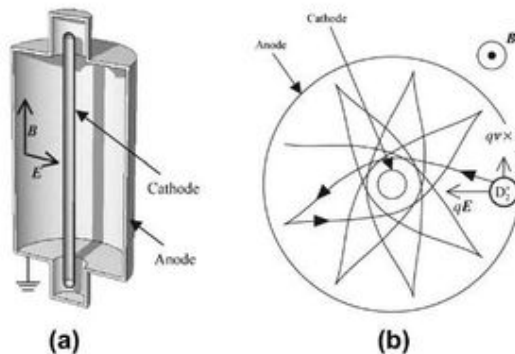


FIGURE 1.55 Schematic of (a) magnetic-assisted electrostatic confinement device, and (b) the motion of deuterium molecular ion under the influence of the applied axial magnetic field. (From Tomiyasu et al. (2010). Reprinted with permission of Elsevier © 2010.)

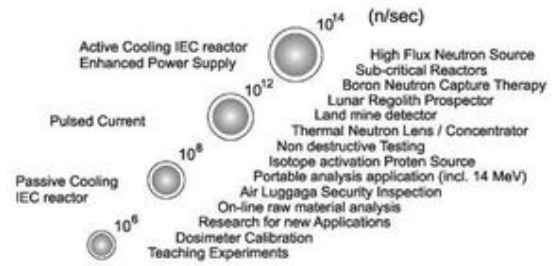


FIGURE 1.56 Applications of Inertial-Electrostatic Confinement Fusion (IECF) devices. (From Yoshikawa et al., 2007a, reprinted with permission from Elsevier © 2007.)

diminished neutron flux strength, and (iii) minimum handling of radioactivity.

4. Interactions of Neutrons with Matter

If a neutron possesses kinetic energy, it will travel through matter much more easily than other nuclear particles of similar energy, such as alpha particles, negatrons, positrons, protons, or electrons. In great contrast to other nuclear particles, which carry charge, the neutron, because it lacks charge, can pass through the otherwise impenetrable barrier of the atomic electrons and actually collide with nuclei of atoms and be scattered in the process or be captured by the nucleus of an atom. Collision of neutrons with nuclei can result in scattering of the neutrons and recoil nuclei with conservation of momentum (elastic scattering) or loss of kinetic energy of the neutron as gamma radiation (inelastic scattering). The capture of a neutron by a nucleus of an atom may result in the emission of other nuclear particles from the nucleus (nonelastic reactions) or the fragmentation of the nucleus into two (nuclear fission). A brief treatment of the various types of neutron interactions, which are based on their scattering or capture by atomic nuclei, is provided next.

a. Elastic Scattering

The elastic scattering of a neutron by collision with an atomic nucleus is similar to that of billiard-ball collisions. A portion of the kinetic energy of one particle is transferred to the other without loss of kinetic energy in the process. In other words, part of the kinetic energy of the neutron can be transferred to a nucleus via collision with the nucleus, and the sum of the kinetic energies of the scattered neutron and recoil nucleus will be equal to the original kinetic energy of the colliding neutron. This process of interaction of neutrons with matter results only in scattering of the neutron and recoil nucleus. It does not leave the recoil nucleus in an excited energy state. Elastic scattering is a common mechanism by which fast neutrons lose their energy when they interact with atomic nuclei of low atomic number, such as hydrogen (^1H) in light water or paraffin, deuterium (^2H) in heavy water, and ^{12}C in graphite, which may be encountered in nuclear reactor moderators. It is easy to conceptualize what would occur when particles of equal or similar mass collide; the event would result in energy transfer and scattering without any

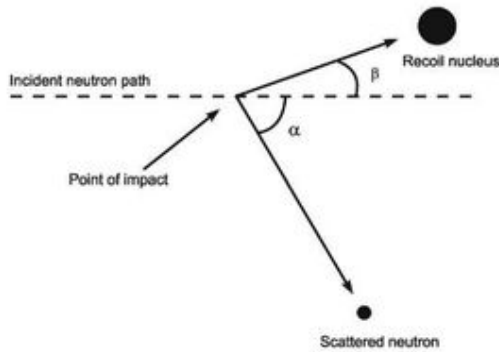


FIGURE 1.57 Elastic scattering of a neutron by collision of the neutron with an atomic nucleus. The neutron is scattered at an angle α and the nucleus recoils at an angle β to the direction of travel of the incident neutron.

other secondary effects, similar to what occurs in billiard-ball collisions.

Neutron scattering is the principal mechanism for the slowing of fast neutrons, particularly in media with low atomic number. Let us consider what occurs when a neutron collides with a nucleus and undergoes elastic scattering. Figure 1.57 illustrates the direction of travel of an incident neutron with given kinetic energy (dashed line). The neutron collides with the nucleus. The nucleus is illustrated as undergoing recoil at an angle β , while the neutron is scattered at an angle α to the direction of travel of the incident neutron. The kinetic energy (E_k) lost by the neutron in this collision is defined by the equation

$$E_k = \frac{4Mm_n}{(M + m_n)^2} \cos^2\beta \quad (1.240)$$

where M is the mass of the nucleus, m_n is the mass of the neutron, and β is the recoil angle of the nucleus. A derivation of Eqn (1.240) is provided by Bacon (1969). Let us look at two extreme examples of elastic collisions between a neutron and a nucleus. In the first example, it is intuitively obvious from Eqn (1.240) that for a recoil angle $\beta = 90^\circ$, $\cos^2\beta = 0$, and consequently $E_k = 0$.

Under such a circumstance, the neutron is undeflected by the nucleus and there is no energy transfer to the nucleus. The neutron continues along its path undeflected until it encounters another nucleus. For the second case, however, let us consider the other extreme in which the recoil angle $\beta = 0^\circ$, where we have a head-on collision of the neutron with the nucleus of an atom. In this case, the maximum possible energy of the neutron is imparted to the nucleus, where $\cos^2\beta = 1$. For example, Table 1.16 provides the maximum fraction of the kinetic energy, calculated according to Eqn (1.240), that a neutron can lose upon collision with various atomic nuclei. As illustrated in Table 1.16, the neutron can transfer more energy to the nuclei of atoms, which have a low mass; and the highest fraction of its energy can be transferred to the nucleus of the proton, which is almost equal in mass to the neutron. Nuclides of low mass number are, therefore, good moderators for the slowing down of fast neutrons. The substances often used are light water (H_2O), heavy water (D_2O), paraffin (C_nH_{2n+2}), and graphite (C).

b. Inelastic Scattering

We may picture a fast neutron colliding with a nucleus. The neutron is scattered in another direction as described in the previous paragraph; however, part of the neutron's kinetic energy is lost to the recoil nucleus, leaving it in an excited metastable state. Inelastic scattering can occur when fast neutrons collide with nuclei of large atomic number. The recoil nucleus may lose this energy immediately as gamma radiation or remain for a period of time in the excited metastable state. Inelastic scattering occurs mainly with fast neutron collisions with nuclei of large atomic number.

Neutron scattering is a common mechanism by which fast and intermediate neutrons are slowed down to the thermal neutron energy levels. Thermal neutrons have an energy level at which they are in thermal equilibrium with the surrounding atoms at room temperature. There is an energy range for thermal neutrons, as described earlier in this chapter; however, the properties of thermal neutrons are often cited at an energy calculated to be the most probable thermal neutron energy of 0.0253 eV at 20.43 °C corresponding to a velocity of 2200 m/s

TABLE 1.16 The Maximum Fraction of the Kinetic Energy (E_k) that a Neutron Can Lose Upon Collision with the Nucleus of Various Atoms Listed in Increasing Mass in Atomic Mass Units (u)

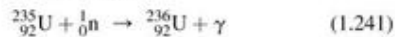
Nuclide	Nuclide Mass, M	Neutron Mass, m_n	$E_k = (4Mm_n / (M + m_n)^2) \cos^2\beta$
1H	1.007825	1.008665	$4.065566 / 4.066232 = 0.999$ or 100%
2H	2.014102	1.008665	$8.126217 / 9.137120 = 0.89$ or 89%
9Be	9.012182	1.008665	$36.36109 / 100.41737 = 0.362$ or 36.2%
^{12}C	12.000000	1.008665	$48.41592 / 169.22536 = 0.286$ or 28.6%
^{16}O	15.994915	1.008665	$64.53404 / 289.12173 = 0.223$ or 22.3%
^{20}Si	27.976927	1.008665	$112.87570 / 840.16454 = 0.134$ or 13.4%
^{55}Mn	54.938047	1.008665	$221.65633 / 3130.0329 = 0.071$ or 7.1%
^{197}Au	196.96654	1.008665	$787.86616 / 39194.175 = 0.020$ or 2.0%

(Gibson and Piesch, 1985 and Holden, 1997b). Fig. 1.51 may be used to find the velocity of the neutron at energy levels over the range 0.001 eV to 10 MeV. For example, if we select the position 0.025 eV on the X-axis and follow up the graph with a straight line to the upper curve, we find the value 2200 m/s. At the thermal energy state, the mechanisms of interaction of neutrons with matter change drastically as discussed in the following section.

c. Neutron Capture

Because of the neutral charge on the neutron, it is relatively easy for slow neutrons, regardless of their low kinetic energy, to "find themselves" in the vicinity of the nucleus without having to hurdle the Coulombic forces of the atom. Once in close proximity to nuclei, it is easy for slow neutrons to enter into and be captured by nuclei to cause nuclear reactions. The capture of thermal neutrons, therefore, is possible with most radionuclides, and neutron capture is the main reaction of slow neutrons with matter. The power of a nucleus to capture a neutron depends on the type of nucleus as well as the neutron energy. The neutron absorption cross section, σ , with units of 10^{-24} cm² or "barns," is used to measure the power of nuclides to absorb neutrons. A more detailed treatment of reaction cross section and its units and application was given earlier in Section VII.D, and this is provided further on in Section VIII.E.5. Because the capture of thermal neutrons is possible with most radionuclides, references will cite the neutron cross sections of the nuclides for comparative purposes at the thermal neutron energy of 0.0253 eV equivalent to a neutron velocity of 2200 m/s. This is also the energy of the neutron, which is in thermal equilibrium with the surrounding atoms at room temperature. For comparative purposes, therefore, Table 1.17 lists the thermal neutron cross sections for neutron capture reactions in barns (10^{-24} cm²) for several nuclides. The nuclides selected for Table 1.17 show a broad range of power for thermal neutron capture. Some of the nuclides listed have practical applications, which are referred to in various sections of this book.

The capture of a slow neutron by a nucleus results in a compound nucleus, which finds itself in an excited energy state corresponding to an energy slightly higher than the binding energy of the neutron in the new compound nucleus. This energy of excitation is generally emitted as gamma radiation. Neutron capture reactions of this type are denoted as (n, γ) reactions. Two practical examples of (n, γ) neutron capture reactions were provided earlier in this chapter in the neutron irradiation of ²³⁸U and ²³²Th for the preparation of fissile ²³⁹Pu and ²³³U Eqns (1.227) and (1.230), respectively. Another interesting example of a (n, γ) reaction is the neutron capture by ²³⁵U according to the following:



This neutron capture reaction is interesting, because the ²³⁶U product nuclide decays by alpha emission with a very long half-life (2.4×10^7 y) in ~14% of the cases and decays by nuclear fission with emission of neutrons in the remaining 86% of the cases, as discussed previously in Section VIII.E.c. The subject of neutron capture is treated in more detail in Section VIII.E.5,

TABLE 1.17 Cross Sections σ in Barns for Thermal Neutron Capture Reactions of Selected Nuclides in Order of Increasing Magnitude

Nuclide	σ (barns)
³ H	<0.000006
¹⁶ O	0.00019
² H	0.00052
¹² C	0.0035
¹ H	0.332
¹⁴ N	1.8
²³⁸ U	2.7
²³² Th	7.4
⁵⁵ Mn	13.3
²³³ U	530
²³⁵ U	586
²³⁹ Pu	752
⁶ Li	940
¹⁰ B	3,840
³ He	5,330
⁴ Be	39,000
¹⁵⁵ Gd	61,000
¹⁵⁷ Gd	254,000

Data from Holden (1997b) and Lide (2010).

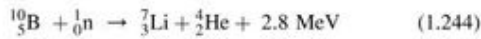
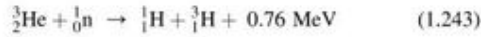
which concerns the neutron cross section and neutron attenuation in matter.

d. Nonelastic Reactions

Neutron capture can occur in nuclei resulting in nuclear reactions that entail the emission of nuclear particles such as protons (n,p), deuterons (n,d), alpha particles (n, α), and even neutrons (n,2n). These reactions may not occur in any specific energy range but may be prevalent at specific resonances, which are energy states of the excited compound nuclei that are specific to relatively narrow energies of the incident neutron. The effect of resonance in neutron capture by nuclei is discussed in more detail subsequently in Section VIII.E.5. The (n,2n) reactions occur at very high incident neutron energies, >10 MeV (Gibson and Piesch, 1985). The (n,p) and (n, α) reactions can occur in the slow neutron capture and reaction with nuclides of low atomic number (low Z), where the Coulomb forces of the electron shells are limited and present less a hurdle for the escape of charged particles from the confines of the atom. Some practical examples of these reactions are the (n,p) reaction used in the synthesis of ¹⁴C by slow (thermal) neutron capture by ¹⁴N



and the (n,p) and (n,α) reactions used to detect neutrons by the interaction of slow neutrons with ³He and ¹⁰B, respectively, according to Eqns (1.243) and (1.244):



Either of these reactions is used to detect neutrons by using gas proportional detectors containing helium-3 gas or a gaseous form of boron (e.g., boron trifluoride). Slow neutrons that penetrate these detectors produce either radioactive tritium Eqn (1.243) or alpha particles Eqn (1.244), which produce ionization in the gas. The ionization events or ion pairs formed can be collected and counted to determine a neutron count rate.

e. Nuclear Fission

The reaction of neutron-induced fission occurs when a neutron interacts with a fissile or fissionable nucleus and the nucleus becomes unstable, taking on the characteristics of an oscillating liquid droplet, which then fragments into two nuclides (fission fragments). At the same time, there is the release of neutrons (2.4 neutrons on the average for neutron-induced ²³⁵U fission) and a relatively high amount of energy (~194 MeV for neutron-induced ²³⁵U fission). Neutron-induced fission of natural ²³⁵U and man-made ²³³U and ²³⁹Pu is optimal at thermal incident neutron energies; whereas neutron-induced fission in ²³²Th, ²³⁸U, and ²³⁷Np requires neutron energies of at least 1 MeV. A more detailed treatment of nuclear fission was provided previously in Sections IV.C and IV.D.

5. Neutron Attenuation and Cross Sections

As we have seen in our previous treatment of the neutron, there are several possible interactions of neutrons with nuclei. Among these are elastic scattering, inelastic scattering, neutron capture, nonelastic reactions, and neutron-induced nuclear fission. As we have seen in several examples, probabilities exist for any of these interactions to occur depending on the energy of the incident neutron and the type of nuclide with which the neutron interacts. We can define this probability of interaction by the term cross section, which is a measure of the capturing power of a particular material for neutrons of a particular energy.

The range of neutrons in matter is a function of the neutron energy and the cross section or capturing power of the matter or medium through which the neutrons travel. To define cross section, let us consider an incident beam of neutrons of given intensity (*I*₀) or number (e.g., neutrons/s), which impinges on a material of unit area (e.g., cm²) and thickness *dx* as illustrated in Fig. 1.58.

The intensity (*I*) of the neutron beam traveling beyond the thickness *dx* will be reduced from the incident beam intensity according to the number of nuclei (*n*) per unit volume in the material and the "area of obstruction" (e.g., cm²) that the nuclei present to the oncoming beam. This area of obstruction is referred to as the cross section of the material. On the basis of the description previously given, we can write the equation

$$dI/dx = -n\sigma I \quad (1.245)$$

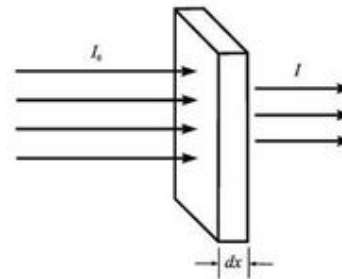


FIGURE 1.58 Attenuation of a neutron beam of intensity *I*₀ by an absorber material of unit area (cm²) and thickness *dx*.

which defines the change in beam intensity (*dI*) with respect to absorber thickness (*dx*) as proportional to the beam intensity (*I*) times a proportionality factor, which we may call the absorption coefficient or "obstruction coefficient" that the nuclei pose to the oncoming beam. The coefficient is a function of the number of nuclei (*n*) in the path of the neutron beam and the stopping power of the nuclei to interact with the neutron beam or, in other words, the neutron cross section (*σ*) of the material through which the neutron beam travels. Eqn (1.245) may be written as

$$dI/I = -n\sigma dx \quad (1.246)$$

Eqn (1.246) is very similar to Eqn (1.303) defining the attenuation of gamma radiation in matter with the exception that the absorption coefficients and attenuation coefficients involved for neutron and gamma radiation, respectively, are very different. The negative sign of Eqns (1.245) and (1.246) denotes the diminishing intensity of the neutron beam as a function of absorption coefficient and absorber thickness. The absorption coefficient *nσ* is the combined effect of the number of nuclei (*n*) in the neutron beam path that might impede the continued travel of neutrons and the power of the nuclei to react with the neutrons. Eqn (1.246) can be integrated over the limits of beam intensity from *I*₀ to *I* and absorber thickness from 0 to *x* as follows:

$$\int_{I_0}^I dI/I = -n\sigma \int_0^x dx \quad (1.247)$$

to give the equation

$$\ln I_0/I = n\sigma x \quad (1.248)$$

or

$$I = I_0 e^{-n\sigma x} \quad (1.249)$$

which is the most simplified expression for the calculated beam intensity (*I*) after passing through an absorber of thickness (*x*) when the absorber material consists of only one pure nuclide and only one type of reaction between the neutron beam and nuclei is possible. If, however, different nuclides are found in the absorber material whereby various reactions between the neutron beam and various different nuclei of the absorber material are possible, we must utilize the sum of the neutron cross sections for all reactions that could take place.

We can use Eqn (1.248) to calculate the half-value thickness ($x_{1/2}$) or the thickness of absorber material needed to reduce the incident neutron beam intensity by one-half. If we give the initial beam intensity (I_0) a value of 1 and the transmitted intensity (I) a value of 1/2, we can write

$$\ln 1/0.5 = n\sigma x_{1/2} \quad (1.250)$$

and

$$\ln 2 = n\sigma x_{1/2} \quad (1.251)$$

or

$$0.693 = n\sigma x_{1/2} \quad (1.252)$$

The half-value thickness for neutron beam attenuation may be written as

$$x_{1/2} = 0.693/n\sigma \quad (1.253)$$

where $n\sigma$ is the number of nuclei per unit volume (cm^{-3}) and σ the neutron cross section in cm^2 . The neutron cross section σ can be defined as the area in cm^2 for which the number of nuclei—neutron reactions taking place is equal to the product of the number of incident neutrons that would pass through the area and the number of target nuclei. The cross section is defined in units of 10^{-24}cm^2 on the basis of the radius of atomic nuclei being about 10^{-12}cm . It provides a measure of the chances for the nuclei of a material being hit by a neutron of a certain energy. The unit of 10^{-24}cm^2 for nuclear cross sections is called the barn. See Section VII.D of this chapter for a more detailed discussion on the barn as a unit of cross section. Tables in reference sources of nuclear data provide the neutron cross sections in units of barns for various nuclides and nuclide energies. An example is the reference directory produced by McLane et al (1988), which provides neutron cross-section values in barns and neutron cross section curves for most nuclides over the neutron energy range from 0.01 eV to 200 MeV.

Let us take an example of 10 eV neutrons incident on a water barrier (*i.e.*, neutrons traveling in water). We may use Eqn (1.253) to estimate the half-value thickness, if we ignore the less significant interactions with oxygen atoms. This is because the neutron cross section for hydrogen at 10 eV is about 20 barns (Fig. 1.59) and that of oxygen is only 3.7 barns (McLane et al, 1988), and there are twice as many hydrogen atoms as oxygen atoms per given volume of water. The half-value thickness may be calculated as follows:

The value of n for the number of hydrogen nuclei per cm^3 of water may be calculated on the basis of Avogadro's number of molecules per mole. If 1 mole of water is equivalent to 18.0 g and the density of water is 1.0g/cm^3 , we can calculate the number of hydrogen nuclei per cm^3 as

$$\begin{aligned} &6.22 \times 10^{23} \text{ molecules H}_2\text{O}/18 \text{ cm}^3 \\ &= 3.45 \times 10^{22} \text{ molecules H}_2\text{O}/\text{cm}^3 \\ n &= (3.45 \times 10^{22} \text{ molecules H}_2\text{O}/\text{cm}^3) \\ &\quad \times (2 \text{ proton nuclei or } 2 \text{ }^1\text{H}/\text{molecule}) \\ &= 6.90 \times 10^{22} \text{ }^1\text{H nuclei}/\text{cm}^3 \end{aligned}$$

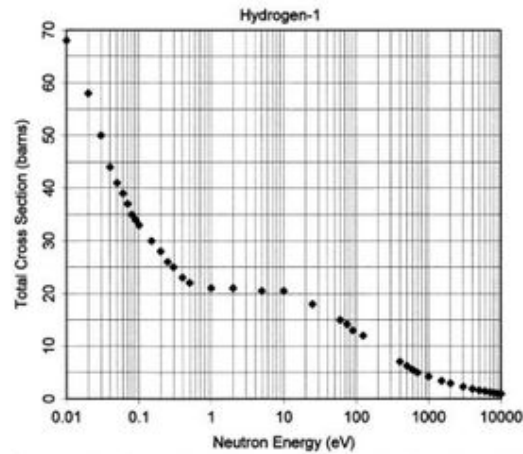


FIGURE 1.59 Total cross section curve for hydrogen-1 over the neutron energy range 0.01 eV–10 keV.

By definition, 20 barns is equal to $20 \times 10^{-24} \text{cm}^2$, and the half-value thickness may then be calculated as

$$\begin{aligned} x_{1/2} &= \frac{0.693}{(6.90 \times 10^{22} \text{ cm}^{-3})(20 \times 10^{-24} \text{ cm}^2)} \\ &= \frac{0.693}{1.38 \text{ cm}^{-1}} \\ &= 0.502 \text{ cm} \end{aligned}$$

If we make the calculation for 1 keV neutrons traversing water and use the value 4.1 barns for the neutron cross section of hydrogen nuclei at this neutron energy (McLane et al, 1988), we calculate a half-value thickness of

$$\begin{aligned} x_{1/2} &= \frac{0.693}{(6.90 \times 10^{22} \text{ cm}^{-3})(4.1 \times 10^{-24} \text{ cm}^2)} \\ &= \frac{0.693}{0.283 \text{ cm}^{-1}} \\ &= 2.45 \text{ cm} \end{aligned}$$

As the examples illustrate in the case of the proton, the neutron cross section (or barns) decreases as the energy or velocity of the neutron increases. That is, the neutron reactions with nuclei obey the general rule of having some proportionality to $1/v$, where v is the velocity of the neutron. This inverse proportionality of cross section and neutron velocity is particularly pronounced in certain regions of energy as illustrated in the total neutron cross section curves for protons and elemental boron in Figs 1.59 and 1.60, respectively. However, this is not always the case with many nuclides at certain neutron energies where there exists a resonance between the neutron energy and the nucleus. At some specific or very narrow neutron energy ranges, certain nuclei have a high capacity for interaction with

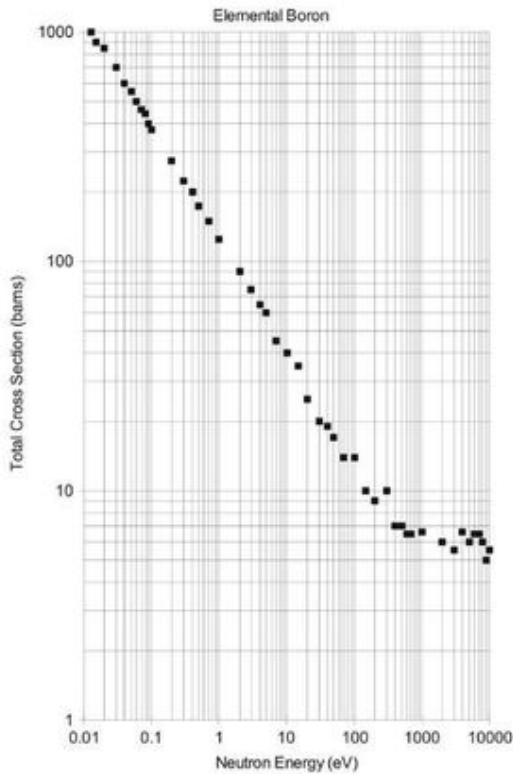


FIGURE 1.60 Total cross section curve for elemental boron over the neutron energy range 0.01 eV–10 keV.

occur with (n,γ) reactions. The high cross sections occur when the energy of the incident neutron corresponds exactly to the quantum state of the excited compound nucleus, which is the newly formed nucleus consisting of a compound between the incident neutron and the nucleus. Most nuclides display both the $1/v$ dependence on neutron cross section and the resonance effects over the entire possible neutron energy spectrum. We should keep in mind that neutron cross sections can be specific and differ in value for certain reactions, such as proton (σ_p)- and alpha particle (σ_α)-producing reactions, fission reactions (σ_f), or neutron capture cross sections (σ_c). The total neutron cross section (σ_{tot}) would be the cross section representing the sum of all possible neutron reactions at that specific neutron energy. For example, the thermal neutron cross section for ^{235}U , which is the neutron cross section at 0.0253 eV neutron energy corresponding to a neutron velocity of 2200 m/s at room temperature, can be given as $\sigma_c = 95$ barns for the neutron capture cross section, $\sigma_f = 586$ barns for the fission cross section, and $\sigma_\alpha = 0.0001$ barns for the neutron cross section for the alpha particle-producing reaction. These neutron cross-section values indicate that neutron fission would predominate at the thermal neutron energy of 0.0253 eV, although some neutron capture would also occur. The total neutron cross section, σ_{tot} , would be the total of the three possible reactions or $\sigma_{tot} = 95$ barns + 586 barns + 0.0001 barns = 681 barns. In our treatment of slow neutron capture by ^{235}U in Section VIII.E.4.c, illustrated by Eqn (1.241), we noted that about 14% of the slow neutron captures by ^{235}U nuclei result in the formation of a long-lived ^{236}U and gamma radiation, and the remaining 86% of the slow neutron captures result in nuclear fission. This is exactly what is predicted by the thermal neutron cross section values just provided, that is, for ^{235}U

$$\sigma_c/\sigma_{tot} = 95 \text{ barns}/681 \text{ barns} = 14\% \text{ neutron capture}$$

and

$$\sigma_f/\sigma_{tot} = 586 \text{ barns}/681 \text{ barns} = 86\% \text{ fission}$$

neutrons. The elevated neutron cross sections at specific neutron energies appear as sharp peaks in plots of neutron cross section versus energy, such as the cross section curve illustrated in Fig. 1.61 for ^{55}Mn . These peaks are called resonances and often

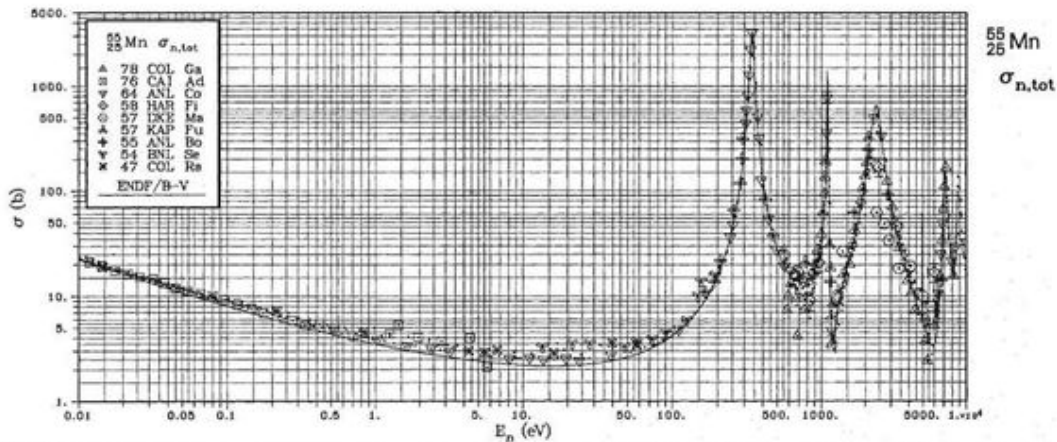


FIGURE 1.61 Total cross section curve for manganese-55 over the neutron energy range of 0.01 eV–10 keV. The columns in the upper left-hand section of the graph provide the number of data points and an abbreviation of the laboratory that provided the data. (From McLane et al. (1988), reprinted with permission from Elsevier © 1988.)

6. Neutron Decay

We have seen that fast neutrons may lose their energy through elastic and inelastic collisions with other nuclei, and if these neutrons do not undergo other reactions with nuclei, they may lose sufficient energy to reach thermal equilibrium with surrounding atoms and possibly be captured by atomic nuclei. The question remains of what would happen to a free neutron that is not absorbed by any atomic nucleus.

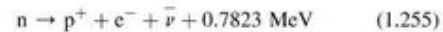
Earlier in this chapter (Section VIII.B.1), we discussed the transformation of the neutron within nuclei of radioactive atoms, which have a neutron/proton ratio too high for stability. In these unstable nuclides, the neutron breaks up into a proton, negatron (negative electron), and antineutrino (See Eqn (1.103)). If the neutron can transform itself in unstable nuclei, it stands to reason that the neutron might be unstable outside the protective boundaries of the stable nucleus. This is just the case, which A. H. Snell and L. C. Miller demonstrated in 1948. This work was followed with further studies by Robson (1950a,b) and Snell et al (1950), that demonstrated that neutrons in free flight in a vacuum would indeed decay with a lifetime in the range of 9–25 minutes with a release of 0.782 MeV of energy. Later more accurate measurements of neutron decay by numerous researchers including Abele (2000), Abele et al (2002), Arzumanov, et al, (2000a,b), Pichlmaier et al, (2000) and Snow et al, (2000), Coakley (2001), Nico et al (2005), and Serebrov et al (2005), among others yielded the neutron lifetime declared by the Particle Physics Group to be 886.7 ± 1.9 s (Caso et al, 1998), which is close to 15 minutes. Much research has been carried out over the past several years to obtain the most accurate measurement of the neutron lifetime (Coakley, 2007, Wilkinson, 2007, Arzumanov et al, 2009, Dewey et al, 2009, Ezhov et al, 2009, Leung and Zimmer, 2009, Materne, et al, 2009, Müller et al, 2009, O'Shaughnessy et al, 2009, and Walstrom et al, 2009), which is an important physical parameter. The most accurate measurement of the neutron lifetime will help answer questions in particle and astrophysics. In particle physics, the neutron lifetime will help us address the weak interaction parameters within baryons, such as the transformation of a d quark into a u quark described in Section IV.B (Walstrom et al, 2009). In astrophysics the neutron lifetime is a key process in establishing the model for the Big Bang primordial nucleosynthesis whereby there was an equilibrium of neutrons and protons a few minutes after the Big Bang described by Paul (2009). A detailed treatment of the Big Bang primordial nucleosynthesis is given in a previous book by the writer (L'Annunziata, 2007).

Various methods are used to measure the neutron lifetime including the trapping and magnetic storage of neutrons followed by the counting of decay products. Paul (2009) provides a very thorough review of the methods used worldwide to determine most accurately the lifetime of the neutron. The present world average of the neutron lifetime of $\tau_n = 885.7 \pm 0.8$ s was reported by the Particle Data Group (Amsler, et al, 2008); however, research to achieve the measurement of the lifetime of the neutron to a precision of ± 0.1 s is currently under intensive research. The decay of elementary particles is

characterized in terms of lifetime. The lifetime, usually symbolized as τ , is related to the term half-life, $t_{1/2}$, the mean time it takes for one-half of the particles to decay (Sundaresan, 2001) according to the relationship

$$t_{1/2} = (\ln 2)\tau = 0.693\tau \quad (1.254)$$

The free neutron decays according to the scheme



The 0.7823 MeV of energy released in the neutron decay corresponds to the difference in mass of the neutron and the sum of the masses of the products of the neutron decay, the proton plus the electron, or

$$\begin{aligned} Q &= m_n - (m_p + m_e) \\ &= [1.008664915 \text{ u} - (1.007276466 \text{ u} + 0.0005485799 \text{ u})] \\ &\quad \times (931.494013 \text{ MeV/u}) \\ &= 0.7823 \text{ MeV} \end{aligned} \quad (1.256)$$

The neutron, therefore, outside the protective confines of the stable nucleus, has a very short lifetime.

IX. ELECTROMAGNETIC RADIATION – PHOTONS

A. Dual Nature: Wave and Particle

In the latter part of the 19th century, Heinrich Hertz (1887) carried out a series of experiments demonstrating that an oscillating electric current sends out electromagnetic waves similar to light waves, but of different wavelength. Hertz proved, thereby, the earlier theory of James Clerk Maxwell, that electric current oscillations would create alternating electric and magnetic fields, and radiated electromagnetic waves would have the same physical properties of light. A subsequent discovery by Nobel Laureate Pieter Zeeman (1897) further linked the properties of light with electricity and magnetism when he discovered that a magnetic field would alter the frequency of light emitted by a glowing gas, which we now refer to as the Zeeman effect. The magnetic field would alter the spectral line corresponding to the frequency of the light into a triplet or even a more complex multiplet of lines. This discovery was significant, because it was the very first to link the properties of light with electricity and magnetism.

Not long after the discoveries of Hertz and Zeeman came the work of Max Planck, who in 1900 proposed a formula to explain that the vibrating particles in the heated walls of a kiln could radiate light only at certain energies. These energies would be defined by the product of a constant having the units of energy \times time and the radiation frequency. The constant, which he calculated, became known as the universal Planck constant, $h = 6.626 \times 10^{-34}$ J s. Therefore, radiation would be emitted at discrete energies, which were multiples of Planck's constant and the radiation frequency, ν . Planck named the discrete radiation energy as the quantum from the Latin *quantus* meaning 'how great'.

In 1905 Einstein grasped the calculations of Planck to explain and provide evidence that light, not only traveled as waves but also existed as discrete packets of energy or particles, which he named “energy quanta”. Today we refer to these energy quanta as photons. Einstein demonstrated the existence of the photon in his explanation of the photoelectric effect (see Section II). He demonstrated that the energy of an electron (photoelectron) ejected from its atomic orbital after being struck by light was not dependent on the light intensity, but rather on the wavelength or frequency of the light. In other words, increasing the light intensity would increase the number of photoelectrons, but not their energy, whereas, altering the frequency, thus energy, of the light would alter the energy of the photoelectron. In summary, Einstein demonstrated that the energy of the photoelectron depended on the energy of the photon that collided with the electron or the product of Planck’s constant times the light frequency according to the formula

$$E = hv = \frac{hc}{\lambda} \quad (1.257)$$

Eqn (1.257) is referred to as the Planck–Einstein relation (Woan, 2000). From this observation, Einstein is credited with discovering the photon as an elementary particle. Also, we may notice from Eqn (1.257) that the product of the photon

frequency, ν , and wavelength, λ , always yields the velocity, c , the speed of light. The photon always travels at the constant speed in a vacuum, $c = 2.9979 \times 10^8$ m/s; it cannot travel at a speed less than c in a vacuum.

From our previous treatment, we see that the photon behaves as a particle, which could knock out an electron from its atomic orbital provided it possessed sufficient energy to do so, that is, an energy in excess of the electron binding energy. Therefore, the photon is considered as another elementary particle. In his explanation of the photoelectric effect, Einstein was the first to demonstrate the particulate nature of light; and it is for this work he won the Nobel Prize. Since these findings of Einstein, electromagnetic radiation is known to have a dual nature as energy that travels as a wave and as a particle.

Electromagnetic radiation may be classified according to its wavelength or origin. For example, we will see in this section of the chapter that gamma rays and x-rays are similar, but have different origins. Gamma rays arise from energy-state transitions of the nucleus of an atom while x-rays come from energy-state transitions of extranuclear electrons. The classification of electromagnetic radiation according to wavelength and frequency is illustrated in Fig. 1.62.

Since electromagnetic radiations or photons have properties of particles, they should also possess momentum. We calculate

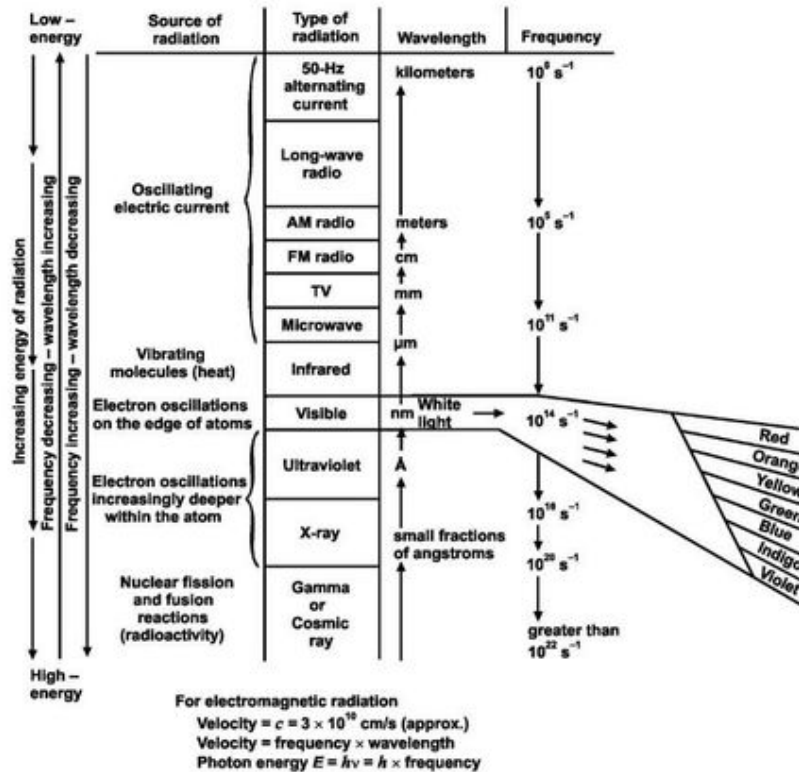


FIGURE 1.62 Electromagnetic radiation spectrum. (From Dean (1995), reproduced with permission from The McGraw-Hill Companies © 1995.)

momentum as the product of mass and velocity. For relativistic conditions, the mass of a particle is a function of its speed according to Eqn (1.196) previously described or

$$m = \frac{m_0}{\sqrt{1 - (u^2/c^2)}} \quad (1.258)$$

where m and m_0 are the particle relativistic and rest masses, u is the particle speed, and c is the speed of light. Gautreau and Savin (1999) transform Eqn (1.258) by squaring both sides and then multiplying each side by $c^2[1 - (u^2/c^2)]$ to yield the equation

$$m^2 c^4 - m^2 u^2 c^2 = m_0^2 c^4 \quad (1.259)$$

By using $E = mc^2$ and $E_0 = m_0 c^2$ to define the relativistic and rest energies and $p = mu$ to define the particle momentum together with the fact that the rest energy of the photon is always zero, i.e., $m_0 = 0$, Eqn (1.259) becomes

$$E^2 - p^2 c^2 = (m_0 c^2)^2 \quad (1.260)$$

$$E^2 - p^2 c^2 = 0 \quad (1.261)$$

and

$$p = \frac{E}{c} \quad (1.262)$$

From Eqns (1.257), (1.261), and (1.262), we can further describe the photon momentum as

$$p = \frac{E}{c} = \frac{h\nu}{c} = \frac{h}{\lambda} \quad (1.263)$$

To illustrate the use of the above equations defining the relationships of photon properties, let us calculate the wavelength, frequency, and momentum of a 2 MeV gamma-ray photon. From Eqn (1.257), we can write the equation for calculating the wavelength as

$$\lambda = \frac{hc}{E} \quad (1.264)$$

Planck's constant, h , can be converted from units of J·s to eV·s as

$$\begin{aligned} h &= \frac{6.626 \times 10^{-34} \text{ J s}}{1.602 \times 10^{-19} \text{ J/eV}} \\ &= 4.136 \times 10^{-15} \text{ eV s} \end{aligned} \quad (1.265)$$

and hc is calculated as

$$\begin{aligned} hc &= (4.136 \times 10^{-15} \text{ eV s})(2.9979 \times 10^8 \text{ m/s}) \\ &= 12.399 \times 10^{-7} \text{ eV m} \\ &= 12.4 \text{ keV}\text{\AA} \end{aligned} \quad (1.266)$$

The wavelength according to Eqn (1.264) becomes

$$\lambda = \frac{hc}{E} = \frac{12.4 \text{ keV}\text{\AA}}{2 \times 10^3 \text{ keV}} = 0.0062 \text{ \AA}$$

The frequency is calculated according to Eqn (1.257) as

$$\begin{aligned} \nu &= \frac{c}{\lambda} = \frac{2.9979 \times 10^8 \text{ m/s}}{0.0062 \times 10^{-10} \text{ m}} = 484 \times 10^{18} \text{ s}^{-1} \\ &= 4.84 \times 10^{20} \text{ Hz} \end{aligned}$$

The momentum is expressed according to Eqn (1.262) as

$$p = \frac{E}{c} = 2.0 \text{ MeV}/c$$

Notice that relativistic calculations of momentum have units of MeV/c, while conventional units of momentum are derived from mass times velocity or kg m/s. Units of MeV/c can be converted to the conventional units with the conversion factor $1 \text{ MeV}/c = 0.534 \times 10^{-21} \text{ kg m/s}$ (Gautreau and Savin, 1999).

B. Gamma Radiation

Radionuclide decay processes often leave the product nuclide in an excited energy state. The product nuclide in such an excited state either falls directly to the ground state or descends in steps to lower energy states through the dissipation of energy as gamma radiation.

A nuclide in an excited energy state is referred to as a nuclear isomer, and the transition (or decay) from a higher to a lower energy state is referred to as isomeric transition. Gamma rays are emitted in discrete energies corresponding to the energy-state transitions a nucleus may undergo when in an excited state. The energy, E_γ , of a gamma ray may be described as the difference in energy states of the nuclear isomers:

$$E_\gamma = h\nu = E_1 - E_2 \quad (1.267)$$

where $h\nu$ is the energy of the electromagnetic radiation described previously in Section IX.A, and E_1 and E_2 represent the energy levels of the nuclear isomers.

Let us consider the decay schemes of some radionuclides to illustrate the process in more detail.

Fig. 1.63 shows the decay scheme of $^{86}_{37}\text{Rb}$ with a half-life of 18.8 days. This nuclide decays by β^- emission with an increase

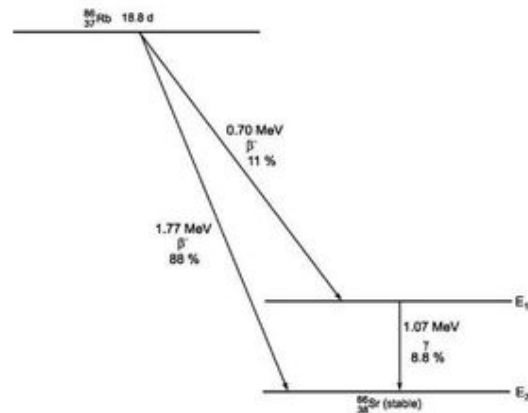


FIGURE 1.63 Decay scheme of $^{86}_{37}\text{Rb}$.

in atomic number to ^{86}Sr . Eighty-eight percent of the beta particles emitted have a maximum energy of 1.77 MeV; the remaining 11 % have a maximum energy of 0.70 MeV. The percentages cited and illustrated in the figure are referred to as transition probabilities or intensities. Obviously, a greater quantum of energy is released by the 1.77 MeV, β^- decay process. As a consequence, the ^{86}Sr product nuclides that result from β^- emission of 0.70 MeV (11 %) are at a higher energy state than those that result from β^- emission of 1.77 MeV. The energy difference of the two ^{86}Sr product nuclide isomers, $E_1 - E_2$, is equivalent to the difference of the two β^- energies, 1.77 MeV - 0.70 MeV = 1.07 MeV. Consequently, the ^{86}Sr nuclide isomers, which are products of the 0.70 MeV β^- -decay process, can emit the remaining energy as 1.07 MeV gamma-ray photons.

As illustrated in Fig. 1.63, 11, % of the parent ^{86}Rb nuclides decay to a ^{86}Sr nuclear isomer at an elevated energy state. Not all of these isomers immediately decay to the ground state. Only 8.8% of the $^{86}\text{Rb} \rightarrow ^{86}\text{Sr}$ disintegrations result in the emission of a gamma-ray photon of 1.07 MeV. For example, a 37 kBq sample of ^{86}Rb by definition would emit 2.22×10^6 beta particles in 1 minute ($37,000 \text{ dps} \times 60 \text{ s/min}$). However, only $(2.22 \times 10^6)(0.088) = 1.95 \times 10^5$ gamma-ray photons of 1.07 MeV can be expected to be emitted in 1 minute from this sample.

Fig. 1.64 shows the somewhat more complicated decay scheme of ^{144}Ce , which has a half-life of 284.5 days. This nuclide decays by β^- -emission with an increase in atomic number to ^{144}Pr . In this case, three distinct β^- -decay processes produce three nuclear isomers of the daughter ^{144}Pr . Seventy-five percent of the beta particles emitted have a maximum energy of 0.31 MeV, 20% have a maximum energy of 0.18 MeV, and the remaining 5 % have a maximum energy of 0.23 MeV. Obviously, a greater amount of energy is released by the 0.31 MeV β^- -decay process. As a consequence, ^{144}Pr nuclides that result from β^- -emission of 0.23 MeV can decay to the ground state with the emission of gamma-ray photons with an energy equivalent to 0.08 MeV, that is, 0.31 MeV - 0.23 MeV.

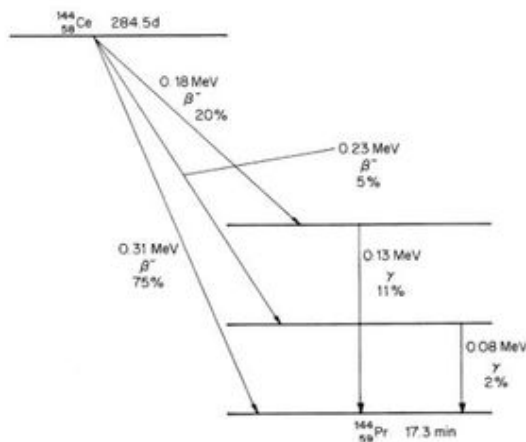


FIGURE 1.64 Decay scheme of ^{144}Ce .

Likewise, ^{144}Pr isomers at an even higher energy state are products of the 0.18 MeV β^- -decay process. These can decay to the ground state with the emission of gamma-ray photons of energy 0.13 MeV, that is, 0.31 MeV - 0.18 MeV. Not all of the product isomers decay with the immediate emission of gamma radiation, and the abundance of these transitions is given in Fig. 1.64.

It is also possible that essentially all of the product nuclides of a decay reaction will be at an excited or elevated energy state and subsequently fall to a lower energy state by the emission of gamma radiation.

The decay scheme of the nuclide ^{22}Na with a 2.6-year half-life serves as an example (see Fig. 1.65). The ^{22}Na nuclides decay by both electron capture (EC) and β^+ -emission, at relative proportions of 10 % and 90 %, respectively, to yield immediate ^{22}Ne product nuclides in an elevated energy state. Only a trace of the ^{22}Na nuclides (0.06 %) decay directly to the ground state. All of the ^{22}Ne isomers in the excited energy state decay immediately with the emission of gamma-ray photons of 1.28 MeV energy, which is equivalent to the difference of the energy levels of the two ^{22}Ne isomers and also equivalent to the difference in energies released by the two beta-decay processes (1.82 MeV - 0.54 MeV).

Isomeric transition, as described earlier, is a decay process in which γ -emission is the sole process of eliminating energy from an excited nucleus. This mode of decay is referred to as isomeric transition because neither the mass number, A , nor the atomic number, Z , of a nuclide (^A_ZX) changes in the decay process, and the nuclides are considered to be in isomeric energy states.

In the previous examples (Figs 1.63, 1.64, and 1.65), the isomeric energy-state transitions are short-lived, that is, they occur virtually immediately after the other decay processes (e.g., β^- , β^+ , and EC) and the half-life of the parent nuclide is dependent on these initial processes. If, however, the isomeric transitions are long-lived, the nuclide is considered to be in a metastable state. These nuclides are denoted by a superscript m beside the mass number of the nuclide. The radionuclide

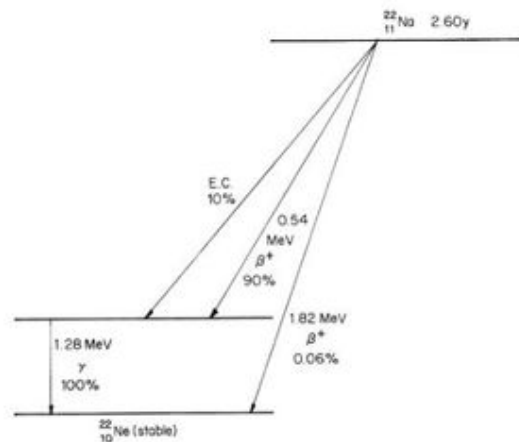
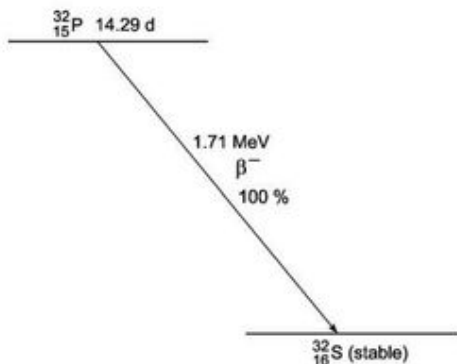
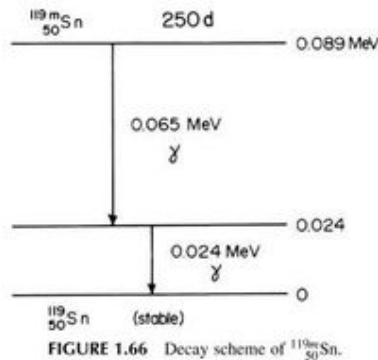


FIGURE 1.65 Decay scheme of ^{22}Na .



$^{119m}_{50}\text{Sn}$ with a 250-day half-life is an example. Its decay scheme, shown in Fig. 1.66, illustrates the emission of two γ -photons of 0.065 and 0.024 MeV energy falling from the 0.089-MeV excited state to the ground (stable) state.

Gamma radiation is not produced in all radionuclide decay processes. Instead, some radionuclides decay by emitting only particulate radiation to yield a product nuclide at an unexcited ground state. An example is the commonly used radionuclide $^{32}_{15}\text{P}$, which decays by the scheme shown in Fig. 1.67.

C. Annihilation Radiation

The negatron or negative beta particle, produced by β decay or by pair production (see Section X.C), will travel through matter until it has completely dissipated its kinetic energy via ionization, electron excitation, or bremsstrahlung. The negatron then at rest acts as an atomic or free electron in matter.

A positron or positive beta particle, however, may be considered an "antiparticle" of an electron and consequently, in the electron environment of atoms, has a definite instability. A given positron emitted by pair production or by β^+ decay will also dissipate its kinetic energy in matter via interactions described previously for the case of the negatron. However, as the positron loses its kinetic energy and comes to a near stop, it comes into contact with an electron (Fig. 1.68) with nearly simultaneous annihilation of the positron and the electron

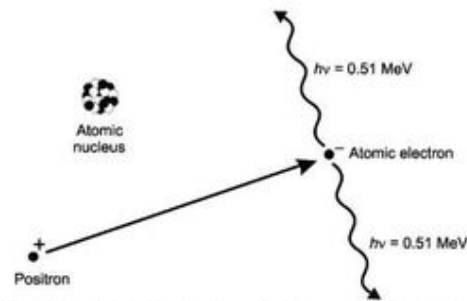


FIGURE 1.68 Annihilation. The interaction between a positron and an electron, and the conversion of their masses into two photons of 0.511 MeV energy.

masses and their conversion into energy. The annihilation involves the formation of positronium, which is a short-lived association of the positron and electron. Its lifetime is only approximately 10^{-10} or 10^{-7} seconds, depending on whether the spin states of the associated particles are parallel (ortho-positronium) or opposed (para-positronium). The para-positronium is the shorter-lived spin state. The energy released in this annihilation appears as two photons emitted in opposite directions. This transformation of mass into energy, considered as the reverse of pair production, is described as

$$e^+ + e^- = 2h\nu = 2E_\gamma \quad (1.268)$$

where a positron, e^+ , and electron, e^- , combine to form two gamma-ray photons of energy E_γ . To maintain the equivalence of mass and energy (see Eqn (1.300)), the equivalent of two electron rest masses (0.511 MeV) must appear as photon energies (see Section X.C). In agreement with Eqns (1.268) and (1.300), the annihilation results in the emission of two 0.511 MeV photons in opposite directions.

D. X-Radiation

X-radiation is electromagnetic radiation similar to gamma (γ) radiation. Both x-rays and γ -rays are identical in their properties. Both x-rays and γ -rays are photons that possess a quantum of energy defined by Eqn (1.257), namely, $E = h\nu$, which is the product of Planck's constant and the frequency of the radiation. X-rays and γ -rays differ only in their origin. X-rays originate from electron energy transitions, and γ -rays originate from the nucleus of an atom as a nucleus at a elevated energy state decays to a lower more stable energy state. There are two types of x-rays, which are the following:

- I. Electromagnetic radiation characterized by discrete spectral lines of energy resulting from electron transitions in shells of the atoms (e.g., K, L, M... shells) from which they originate. These are x-ray emissions produced when an electron from a given shell is ejected from an atom and electron from outer shell fills the vacancy left by the ejected electron. This is followed generally by a cascade of electron transitions from outer electron shells, since the filling of one electron vacancy by the transition of an electron from an outer to inner shell will leave another electron vacancy in the outer

shell. For example, an electron vacancy in the *K* shell created by the capture of an electron by the nucleus (e.g., EC or *K*-capture decay) is filled by an electron in the next outer *L* shell creating an electron vacancy in that shell, which is followed by the filling of that electron vacancy by an electron in the next outer *M* shell, etc. The spectra of these discrete energy lines of electromagnetic radiation are characteristic of the atoms from which they originate.

- Electromagnetic radiation characterized as a broad smear of continuous energies referred to as **bremsstrahlung**, which is produced by electrons or other charged particles, such as protons and alpha particles, as they are accelerated toward an atomic nucleus and are deflected by the Coulomb field of the nucleus. This was the type of x-ray discovered by Wilhelm Röntgen in 1895, who was the first to discover x-rays. Röntgen discovered the mysterious invisible rays on November 8, 1895 when he was studying cathode rays, *i.e.*, the current that would flow through a partially evacuated glass tube (cathode-ray tube then referred to as a Crooke's tube). With such a tube covered in black paper and in a dark room, he noticed that a paper plate covered with the chemical barium platinocyanide would become fluorescent (give off light) even at a distance of two meters from the cathode-ray tube. He was able to demonstrate that the invisible rays came from the collision of the cathode rays (electrons) with the glass surface of the cathode-ray tube or from the collision of the cathode rays with other materials such as aluminum inserted into the glass of the tube. Further studies by Röntgen demonstrated that these rays could travel through various materials to varying extents, when these were placed in the path of the invisible rays, and the transmitted rays could be measured with photographic plates. He gave these mysterious rays the name x-rays, because of their unknown nature and "for the sake of brevity", as he stated in his original papers (Roentgen (1895, 1896).

1. X-rays Characterized by Discrete Spectral Lines

In Section VIII.B.3 we discussed the electron-capture (EC) or *K*-capture decay process whereby an electron from one of the atomic shells (generally the innermost *K*-shell) is absorbed by the nucleus, where it combines with a proton to form a neutron. No particle emission results from this decay process. However, the vacancy left by the electron from the *K*-shell is filled by an electron from an outer shell (generally the adjacent *L* shell). Transitions produced in electron shell energy levels result in the emission of energy as x-radiation (see also Sections VIII.C and VIII.D). This radiation consists of photons of electromagnetic radiation similar to gamma radiation. X-radiation and gamma radiation differ only in their origin. X-rays arise from atomic electron energy transitions and gamma rays from transitions between nuclei of different energy states. Another nuclear decay process that results in the loss of atomic electrons is decay by internal conversion (IC), which competes with gamma-ray emission, discussed in Section VIII.C. Also, Auger electron emission, that may follow EC decay, will leave a vacancy in an

electron shell that would cause electron transitions from outer shells during the filling of that vacancy and the emission of x-rays. The production of x-radiation from atomic electron transitions is illustrated in Figs 1.47, 1.48, 1.69, and 1.70.

When an electron transition occurs from the outer *L* shell to an inner *K*-shell, the energy emitted is equivalent to the difference between the *K* and *L* electron-binding energies. The electron transitions that ensue in the filling of vacancies result in energy lost by the atom as x-radiation, which is equivalent to the difference of the electron-binding energies of the outer, E_{outer} , and its new inner state, E_{inner} , as described by

$$h\nu = E_{outer} - E_{inner} \tag{1.269}$$

The radiation emitted consists of a discrete line of energy characteristic of the electron shell and, consequently, of the atom from which it arises.

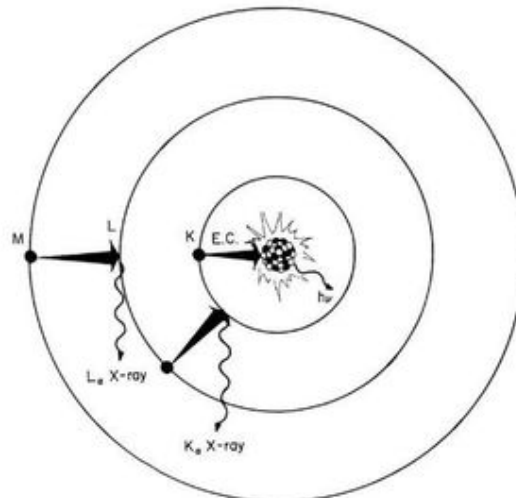


FIGURE 1.69 Electron capture (EC) decay and the accompanying gamma ($h\nu$) and x-radiation.

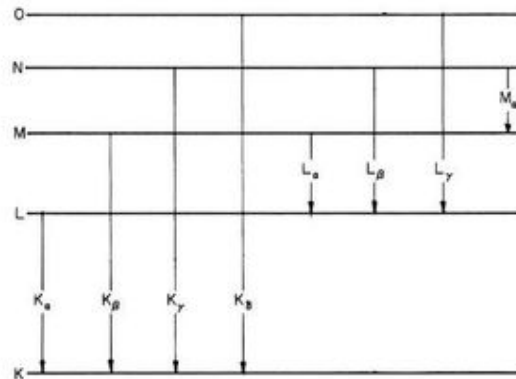


FIGURE 1.70 Atomic electron energy levels or shells (*K*, *L*, *M*, etc.) and lines of transition corresponding to characteristic x-rays (K_α , K_β , K_γ , etc.).

The production of x-rays in radionuclide decay is, however, more complex. The filling of one electron vacancy in an inner shell is followed by a series of electron transitions in an overall adjustment of electrons in outer shells. This gives rise to further x-rays with lines characteristic of outer shells. Such electron transitions, each resulting in the emission of discrete lines of characteristic x-rays, are illustrated in Fig. 1.70. The transitions are identified by a letter corresponding to the shell (*K*, *L*, *M*, etc.) with vacancy giving rise to the x-ray photon and a subscript (α , β , γ , etc.) to identify, from among a series of outer electron shells of the atom, the shell from which the electron vacancy is filled. For example, an x-ray arising from an electron transition from the *L* to the *K*-shell is denoted as K_{α} and that arising from a transition from the *M* to the *K*-shell as K_{β} . Transitions involving the filling of electron vacancies in the *L* shell from outer *M*, *N*, and *O* shells are denoted by L_{α} , L_{β} , and L_{γ} , etc.

The complexity of x-ray lines emitted and their abundances of emission are compounded by the existence of other mechanisms of x-ray production in unstable atoms. One of these mechanisms is the production of Auger electrons. An x-ray emitted from an atom may produce an Auger electron (see Section VIII.D), which results in the emission of an atomic electron from a shell farther away from the nucleus. The vacancy left by the Auger electron gives rise to additional x-rays characteristic of outer shells following the electron readjustments that ensue. Auger electrons can be emitted from a variety of electron shells, followed by an equal variety of characteristic x-rays from subsequent electron adjustments in outer shells.

Any process that would cause the ejection of an atomic electron of an inner shell can result in the production of x-radiation. Other processes, such as radiation-induced ionization within inner electron shells of atoms, will result in the filling of the missing electron from an outer shell and a cascade of electron rearrangements from outer to inner shells. Any radiation source, that can produce ionization, even x-rays that impinge on a target material, will produce additional x-rays as a consequence of the ionization of internal electron shells of atoms, and these x-ray emissions will be characteristic of the elements that were ionized by the external radiation. Nobel Laureate Charles Glover Barkla made this observation in 1917 in his Nobel Lecture where he stated (Barkla, 1917)

Each element when traversed by x-rays emits x-radiations characteristic of the element; each characteristic radiation is unaffected by changes in the physical condition or state of chemical combination of the radiating element, and its quality is independent of that of the exciting primary radiation. But only primary radiations of shorter wavelength are able to excite the characteristic x-radiations... all of the radiations hitherto definitely observed have fallen into three series, the K-, L-, and M-series.

Thus, each element can be characterized by its x-ray emission spectra. It was Henry Moseley, who devised an apparatus whereby he could bombard individually all of the known and available elements with cathode rays and measure the wavelengths of the x-rays emitted by each element (Moseley, 1913, 1914). In his first report, Moseley (1913) measured the x-ray

emission spectra of 21 elements of increasing numbers of the Periodic Table of the Elements from aluminum to silver and determined the wavelengths of the α and lower intensity β lines that belong to Barkla's *K* series. In a subsequent paper, Moseley (1914) measured the wavelengths of the *L* series of x-ray emissions of 24 elements of increasing numbers of the Periodic Table of the Elements from zirconium to gold. Of the *L* series, he measured the wavelengths of α -, β -, γ -, and δ -lines of decreasing wavelengths and decreasing intensities. Moseley then plotted the square root of the radiation frequencies against a characteristic integer (*N*) assigned to each element. Starting with aluminum, being the 13th element in the periodic table, he assigned it the number *N* = 13. The next element, silicon, was assigned the next highest integer *N* = 14, phosphorus *N* = 15, etc. A copy of his plots is illustrated in Fig. 1.71. The plots showed an incredibly straight line relationship between the assigned integer *N* and the x-radiation frequencies for each element. From this relationship, he concluded the following (Moseley, 1914):

Now if either the elements were not characterized by these integers or any mistake had been made in the order chosen, or in the number of places left for unknown elements [places for three unknown elements in the Periodic Table were found. See Fig. 1.71], these irregularities would at once disappear. We can therefore conclude from the evidence of the x-ray spectra alone, without using any theory of atomic structure, that these integers are really characteristic of the elements. Further, as it is improbable that two different stable elements should have the same integer, three, and only three, more elements are likely to exist between Al and Au. As the x-ray spectra of these elements can be confidently predicted, they should not be difficult to find... There is ever reason to suppose that the integer which controls the x-ray spectrum is the same number of electrical units in the nucleus...

In this work Moseley was able to demonstrate that the number of electrons in the atoms of each element are equivalent to what we now refer to as the atomic number *Z* (Moseley's *N*) and that the x-ray emission spectra is a characteristic of each element.

Nobel Laureate Karl Manne Siegbahn provided insight into the energy quanta emitted by the x-rays and consequently the energy states of the electrons in the *K*-, *L*-, *M*-, *N*- and other orbitals of the elements. The impact of Siegbahn's findings was underscored in the Nobel Prize Presentation Speech (Gullstrand, 1925) with the statement

In an element that can emit both K- and L-rays, the former radiation has much shorter wavelengths and consequently greater frequencies than the latter. As the energy quanta are proportional to the frequencies, therefore, the K radiation involves a larger change in the energy of the atom than the L radiation; and in the atomic theory this is as much as to say that an orbit into which an electron falls on emission of a K-line must lie nearer the nucleus than an orbit to which an electron falls on emission of an L-line. In this way it was inferred that there is a K-level nearest the nucleus, outside that a L-level, and after that a M-level and a N-level (and so on ...), all these four being experimentally determined [by Manne Siegbahn].

Because x-radiation is characteristic of the atom from which it arises, it is customary to identify the element along with the

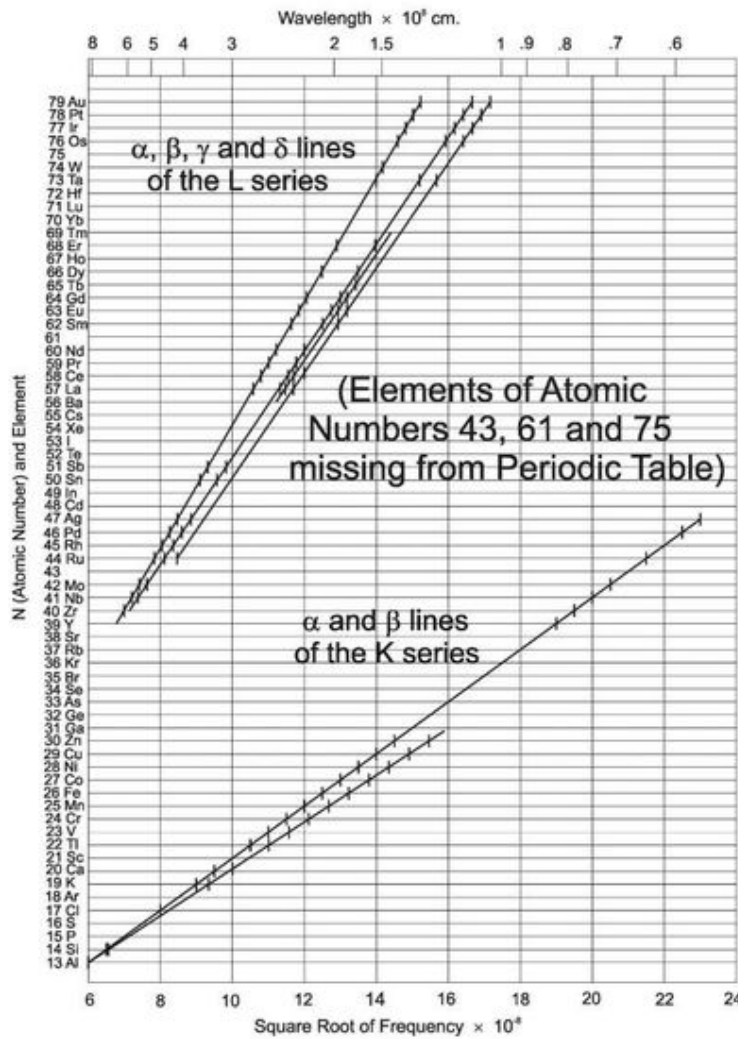


FIGURE 1.71 Artist's portrayal of Moseley's original 1914 graph of the frequencies and wavelengths of x-rays emitted by all of the then known elements plotted against each element and an integer N assigned to each element starting at Aluminum (Al, assigned N = 13) to Gold (Au, assigned N = 79). Three missing and yet unknown elements are listed with blank spaces adjacent to integers N = 43, 61, and 75. The two lines of the lower curves (elements N = 13 to 47) are x-rays resulting from α and β lines of the K series of electron transitions; and the four lines of the upper curves (elements N = 40 to 79) are x-rays resulting from α, β, γ, and δ lines of the L series of electron transitions (From Moseley, 1914). The original Moseley graph, drawn by his own hand, may be seen in the Moseley Room of the Cavendish Laboratory, University of Oxford.)

x-ray photon (e.g., Cr K x-rays, Hg L x-rays, and many examples are listed in Appendix A). In these examples, the fine structure of the x-ray emissions is not given and the lines are grouped together as K and L x-rays. Whenever a nuclide undergoes alpha or beta-decay including EC decay, the daughter nucleus may be left at an excited energy state whereby the daughter nucleus then decays to the ground state with the emission of gamma radiation. The emission of internal conversion electrons often competes with gamma emission, which leaves vacancies in electron shells and the concomitant emission of x-rays. In such cases, the x-ray emissions are characteristic of the daughter atom. See examples throughout Appendix A in the radionuclide decay tables where the x-ray emission intensities are listed as those of the daughter nuclide rather than the parent.

2. Bremsstrahlung

Bremsstrahlung is a type of x-radiation that is characterized by a broad smear of continuous energies of electromagnetic radiation anywhere in the range between zero and an energy maximum. In general, any charged particle that undergoes acceleration will emit electromagnetic radiation; thus, an accelerating charged particle will emit bremsstrahlung when it is made to decelerate upon deflected from its path of travel by collision or near encounter with an atomic nucleus. Charged particles undergoing acceleration, such as beta particles, electrons, protons, deuterons, and alpha particles, can emit bremsstrahlung as these particles decelerate in a series of collisions with atomic nuclei. This mechanism is illustrated in Fig. 1.72, where a beta particle traveling through matter approaches

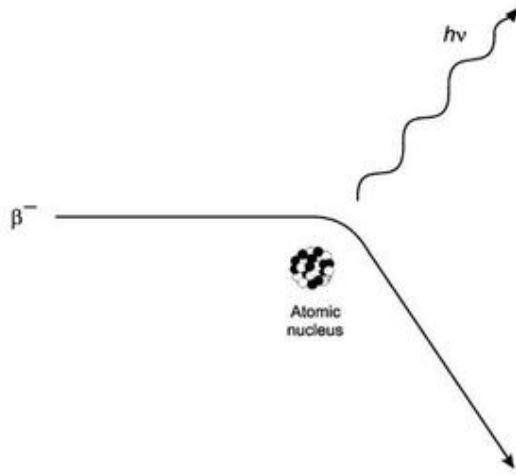


FIGURE 1.72 Bremsstrahlung production. A beta particle is deflected by an atomic nucleus and loses kinetic energy with the emission of a photon of x-radiation.

a nucleus and is deflected by it. This deflection causes a deceleration of the beta particle and consequently a reduction in its kinetic energy with the emission of energy as a photon of bremsstrahlung, which is taken from the German language meaning “braking radiation.” The phenomenon is described by

$$hv = E_i - E_f \quad (1.270)$$

where hv is the energy of the photon of bremsstrahlung, E_i is the initial kinetic energy of the beta particle prior to collision or deflection, producing a final kinetic energy E_f of the electron.

As described by Evans (1955), the acceleration produced by a nucleus of charge Ze on a particle of charge ze and mass M is proportional to Zze^2/M , where Z is the atomic number of the nucleus, e is the elementary charge $= 4.803 \times 10^{-10}$ esu, and z is the particle atomic number or 1 for electrons and protons, 2 for alpha particles. Thus, the bremsstrahlung intensity, which is proportional to the square of the product of the amplitude and the charge ze , will vary according to $Z^2z^4e^6/M^2$ (Evans, 1955). From this relation it is seen that the production of bremsstrahlung per atom of absorber is proportional to the square of the atomic number of the absorber material, and that the total bremsstrahlung is inversely proportional to the square of the mass M of the accelerating charged particle. It is intuitively obvious and it has been demonstrated through experiment that an absorber material of higher atomic number will yield a greater production of bremsstrahlung per atom, because the size of the nucleus as well as its charge increases with atomic number, and thus the probabilities of interaction of the accelerating charged particle with a nucleus will be a function of the magnitude of the charge on the nucleus as well as the nuclear size. For example, a charged particle (e.g., electron or beta particle) of given energy will yield more bremsstrahlung upon interaction with absorber material consisting of pure Pb than one of Cu or C (e.g., graphite), that is, bremsstrahlung in Pb ($Z = 82$) $>$ Cu ($Z = 29$) $>$ C ($Z = 6$). The inverse proportionality of bremsstrahlung to the square of the

mass M of the charged particle yields as an outcome that bremsstrahlung production by electrons ($M = 0.0005485$ u) is the most significant among all other charged particles, which are of much higher mass, e.g., the muon ($M = 0.1134$ u), proton ($M = 1.007$ u), deuteron ($M = 2.014$ u), or the alpha particle ($M = 4.001$ u). For example, the muon, which has a mass equivalent to 206.7 times that of the electron, would yield less bremsstrahlung than an electron of equal energy in the same absorber medium by a factor of more than 42,000, i.e., $M_\mu^2/M_e^2 = 0.1134^2/0.0005485^2 = 42,700$. A proton of the same energy and in the same absorber material would yield yet less bremsstrahlung than that of the electron by a factor of $M_p^2/M_e^2 = 1.007^2/0.0005485^2 = 3.37 \times 10^6$. Nevertheless, bremsstrahlung from accelerated charged particles, such as accelerated protons, is significant (Huisman et al, 2000, Volkerts et al, 2001, Mahjour-Shafiei et al, 2006, Cohen et al, 2008, and Johansson and Wilkin, 2009).

The tremendous difference between the magnitudes of bremsstrahlung production by protons and electrons of the same energy in a given absorber material described in the previous paragraph (i.e., $M_p^2/M_e^2 = 1.007^2/0.0005485^2 = 3.37 \times 10^6$) was utilized by Olzem et al (2007) to measure cosmic-ray positron radiation through bremsstrahlung conversion. A major difficulty in the measurement of cosmic-ray positrons in the energy range of 50 GeV is the high background of cosmic-ray protons, which exceed the number of positrons by a factor of 10^4 (Aguilar et al, 2002, Beatty et al, 2004, and L’Annunziata, 2007). The researchers (Olzem et al, 2007) took advantage of the fact that proton bremsstrahlung is suppressed by a factor of more than 3.37×10^6 with respect to the electron (i.e., positrons). By detecting the bremsstrahlung produced by the high-energy (1–50 GeV) cosmic-ray positrons, the proton background in this same energy range is suppressed by a factor of more than 3×10^6 . Bremsstrahlung by cosmic-ray pions are also significantly suppressed compared to electron bremsstrahlung by a factor of $M_\pi^2/M_e^2 = 0.1485\text{u}^2/0.0005485\text{u}^2 = 7.3 \times 10^4$. A diagram illustrating the process of cosmic-ray positron bremsstrahlung conversion is illustrated in Fig. 1.73.

As illustrated in Fig. 1.73, a primary cosmic-ray positron enters into the detector material from above producing bremsstrahlung photons. The bremsstrahlung photon then converts into a positron–electron pair. Three particles are observed in the tracking detector, namely, the positron and negatron each of 0.511 MeV energy created in the pair production, which are highly deflected in a magnetic field, and the incident high-energy positron, which is only slightly deflected in the magnetic field. Olzem et al (2007) report that additional background rejection of cosmic-ray mesons and protons are provided by the photon emission angles, which are essentially zero for high-energy positrons and significantly larger than zero for mesons and protons due to their higher mass.

a. Bremsstrahlung in Beta-particle Absorbers

When beta particles from a particular radionuclide source strike an absorber material, a wide spectrum of bremsstrahlung photon wavelengths (or energies) will be produced. The bremsstrahlung photon energies will range from zero to a maximum photon

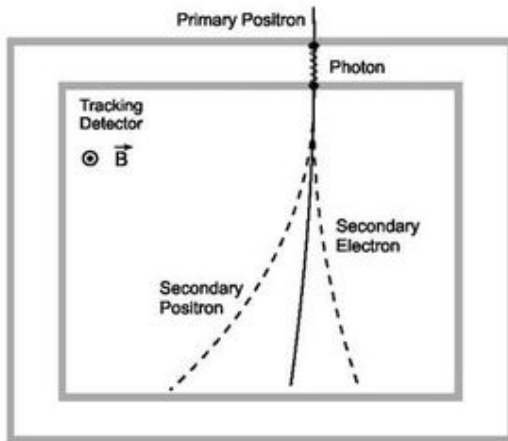


FIGURE 1.73 Signature of pair production by a bremsstrahlung photon. (From Olzem et al., 2007). Reprinted with permission of Elsevier © 2007.)

energy, $h\nu_{\max}$. The broad spectrum of bremsstrahlung is due to the broad possibilities of different interactions, *i.e.*, deflections or collisions, that the beta particles can have with atomic nuclei of the absorber and the broad spectrum of beta-particle energies emitted from any given radionuclide. In a given spectrum of bremsstrahlung, the shortest wavelength, λ_{\min} , is observed when a beta particle or electron undergoes a direct collision with the nucleus of an atom and loses all of its kinetic energy, $h\nu_{\max}$, as bremsstrahlung or x-radiation according to the relation

$$h\nu_{\max} = \frac{hc}{\lambda_{\min}}, \quad (1.271)$$

which follows the energy–wavelength Planck–Einstein relation previously described by Eqn (1.257).

Let us consider an example of a 1.710 keV beta particle from ^{32}P ($E_{\max} = 1.71 \text{ MeV}$) striking a nucleus. If the beta particle

loses all of its energy in the collision, the wavelength of the bremsstrahlung emitted from this interaction according to Eqn (1.271) would be

$$\lambda = \frac{hc}{h\nu_{\max}} = \frac{12.4 \text{ keV}\text{\AA}}{1710 \text{ keV}} = 0.00725 \text{ \AA} \quad (1.272)$$

See Eqn (1.266) for the conversion of the constant hc to convenient units of eV m or eV\AA. Bremsstrahlung production by high-energy beta particles in absorber material of high atomic number is significant (see Section XIV). Consequently, to reduce the production of bremsstrahlung in radiation shielding against the harmful effects of high-energy beta particles, an absorber of low atomic number (*e.g.*, plastic) may be preferred over one of high atomic number (*e.g.*, Pb-glass).

Ionization and electron excitation were previously described as predominant mechanisms by which a traveling beta particle may lose its kinetic energy in matter (see Sections VIII.B.6 and XIV.A). However, the production of bremsstrahlung may also be another significant mechanism for the dissipation of beta-particle energy, particularly as the beta-particle energy and the atomic number of the absorber increase (Kudo, 1995). A more thorough treatment is found in Section XIV.A, which includes examples of calculations involved to determine the degree of bremsstrahlung production as a function of beta-particle energy and absorber atomic number. In general terms, we can state that for a high-energy beta particle such as the beta particle of highest-energy emitted from ^{32}P ($E_{\max} = 1.71 \text{ MeV}$) in a high-atomic-number absorber such as lead ($\text{Pb} = 82$), bremsstrahlung production is significant. In a substance of low atomic number such as aluminum ($\text{Al} = 13$), bremsstrahlung production by a 1.7 MeV beta particle is reduced to more than sixfold as compared to lead (See Table 1.18).

In view of the wide spectrum of beta-particle energies emitted from radionuclides and the wide variations of degree of beta-particle interactions with atomic particles, the production of a broad spectrum, or smear, of photon energies of bremsstrahlung

TABLE 1.18 Approximate Incident Beta-particle Energy Loss (I/E) as Bremsstrahlung in Various Thick Targets^a

Incident energy (E)	Fraction of incident Beta-particle Energy loss (I/E)					
	H ₂ O (Z = 6.6) ^b	Al (Z = 13)	Cu (Z = 29)	Mo (Z = 42)	W (Z = 74)	Pb (Z = 82)
0.1 MeV	0.05 %	0.09 %	0.2 %	0.3 %	0.5 %	0.6 %
0.2	0.09	0.2	0.5	0.6	1.0	1.1
0.5	0.2	0.5	1.0	1.5	2.6	2.9
1.0	0.5	0.9	2.0	2.9	5.2	5.7
1.5	0.7	1.4	3.0	4.4	7.8	8.6
2.0	0.9	1.8	4.1	5.9	10.4	11.5
2.5	1.1	2.3	5.1	7.4	13.0	14.4

^aCalculated according to $I/E = (0.0007 \text{ MeV}^{-1})ZE$ where I is the total bremsstrahlung energy (MeV), E is the incident electron or beta-particle energy (MeV), and Z is the atomic number of the thick-target absorber.

^bFor H₂O, a compound absorber, the effective or modified atomic number is used as calculated by Markowicz and VanGriken (1984) and Manjunatha and Rudraswamy (2009, 2010), namely, $Z_{\text{mod}} = (\sum_i W_i Z_i^2 / A_i) / (\sum_i W_i Z_i / A_i)$ where W_i , Z_i , and A_i are the weight fraction, atomic number, and mass number, respectively, of the i th element.

is characteristic. This contrasts with x-radiation, which is emitted as a result of atomic electron rearrangement processes, resulting in the emission of discrete lines of photon energy.

b. Artificially Produced Bremsstrahlung

An apparatus used to produce artificially x-rays, such as those employed in medical diagnosis or x-ray diffraction, functions on a similar principle of bremsstrahlung described previously. The x-ray apparatus consists of an evacuated tube containing a cathode filament and a metal anode target such as tungsten ($A = 74$). A voltage potential is applied to the tube so that electrons emitted from the cathode accelerate toward the anode. Upon colliding with the tungsten anode, the accelerated electrons lose energy as bremsstrahlung x-radiation. For example, an electron accelerated in an x-ray tube to an energy of 40 keV, which loses all of its energy upon impact with a tungsten nucleus, would produce a single x-ray photon of wavelength calculated as

$$\lambda = \frac{hc}{hv} = \frac{12.4 \text{ keV} \cdot \text{\AA}}{40 \text{ keV}} = 0.31 \text{ \AA} = 0.031 \text{ nm} \quad (1.273)$$

A broad spectrum of bremsstrahlung is produced due to the various degrees of deflection or collision of the accelerated electrons with the target nuclei.

Electron accelerators are a good source of bremsstrahlung currently employed in food irradiation for the preservation and extension of the shelf-life of food (Miller, 2003, 2005, Mehta et al, 2003, Auslender et al, 2004, Farkas, 2004, 2006, L'Annunziata, 2007, and Farkas et al, 2010). Food irradiation is the process where food is exposed to ionizing energy, utilizing gamma photons emitted by ^{60}Co (or less frequently by ^{137}Cs), machine-generated x-rays (bremsstrahlung) of max. 5 MeV, or accelerated electrons of max. 10 MeV kinetic energy (Farkas, 2004). The use of accelerator sources is gradually replacing the use of radioisotope sources for the irradiation of food, mainly because the generation of the radiation can be controlled by a simple on-off switch (Cleland et al, 1998 and Miller, 2003). The accelerators may be used to irradiate food directly with the electron beam or indirectly with the bremsstrahlung radiation produced after the electron beam strikes a converter material. To avoid the possibility of measurable food activation via photo-nuclear reactions, the kinetic energy of the electron beam is limited by regulation to 10 MeV, and the kinetic energy regulation for bremsstrahlung irradiation of foods is limited to 5 MeV.

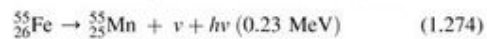
Bremsstrahlung, electron beams, and gamma radiation have numerous industrial applications, which include, in addition to food preservation, the sterilization of health-care products, the irradiation of blood to prevent transfusion-associated graft versus host disease, the sterilization of tissue for transplant surgery, the synthesis of radiation-cured rubber, the manufacture of radiation-cured wood polymer composites, etc. These applications are reviewed in a previous text by the author (L'Annunziata, 2007).

c. Inner or Internal Bremsstrahlung

Bremsstrahlung of very low intensity, referred to as *inner* or *internal bremsstrahlung*, also occurs during the transforming

nucleus in electron-capture decay processes and beta particle emission. This is a continuous spectrum of x-ray photons that originates within the transforming atoms and can be attributed to the sudden change of nuclear charge when the beta particle is emitted or when an orbital electron is captured (Evans, 1955). Internal bremsstrahlung is explained by Cengiz and Almaz (2004) to occur during the emission of a β^- -particle from the nucleus, as the β^- -particle undergoes an acceleration at its birth and emits bremsstrahlung in the field of the emitting nucleus. The magnitude of inner bremsstrahlung was calculated to be approximately 1/137 quantum of internal bremsstrahlung per beta particle emitted from the nucleus (Knipp and Uhlenbeck, 1936 and Evans, 1955). Internal bremsstrahlung spectra for several nuclides that emit β^- particles were calculated by Cengiz and Almaz (2004). This radiation was named inner or internal bremsstrahlung, because it originates from the nucleus the internal part of the atom in contrast to external bremsstrahlung that occurs when an external beta particle approaches an atom external to it from another source and is deflected by the nucleus of that atom.

In the electron-capture decay process, the quantum of energy not carried away by the neutrino is emitted as internal bremsstrahlung. Thus, in electron capture decay, internal bremsstrahlung may possess energies between zero and the maximum, or transition energy of a radionuclide. When gamma radiation is also emitted, the internal bremsstrahlung may be masked by the more intense gamma rays and go undetected. However, in the absence of gamma radiation, the upper limit of the internal bremsstrahlung can be used to determine the transition energy of a nuclide in electron capture decay. Some examples of radionuclides that decay by electron capture without the emission of gamma radiation are as follows:



and



where hv is the internal bremsstrahlung, the upper energy limits of which are expressed in MeV.

d. Nuclear Bremsstrahlung (Nuclear Startstrahlung)

Nuclear bremsstrahlung was recently identified by Nie Luo, Magdi Ragheb, and George Miley at the University of Illinois (Luo et al, 2010). This class of bremsstrahlung refers to electromagnetic radiation of low energy (*i.e.*, soft x-rays of a few hundred eV to a few keV) emitted by a proton or deuteron or both as these undergo acceleration during the fusion of a proton with a neutron or the fusion of a proton with a deuteron. Luo et al (2010) loosely assigned the name of nuclear bremsstrahlung to this phenomenon and have ventured to also call it nuclear startstrahlung from the German meaning "take-off radiation" depicting the acceleration of these nuclear particles as the origin of the soft x-rays. The identification of this class of bremsstrahlung opens the door to new plasma diagnostics such as in the identification of the parasitic D-D fusion reaction in future thermonuclear research based on

D–T fusion. The D–D fusion reaction, previously described by Eqn (1.237), produces protons according to



The D–T thermonuclear reaction is also an excellent source of neutrons, as described previously in this chapter (See Eqn (1.238)). The protons and neutrons generated can, in turn, participate in the thermonuclear process via other reactions including the fusing of a proton with a neutron according to



and the fusion of a proton with un-reacted deuterium fuel according to the reaction



Both of which give rise to the nuclear bremsstrahlung, which are included in the above two reactions.

The process of nuclear bremsstrahlung, in the simplest case of p – n capture, is illustrated in Fig. 1.74. As described by Luo

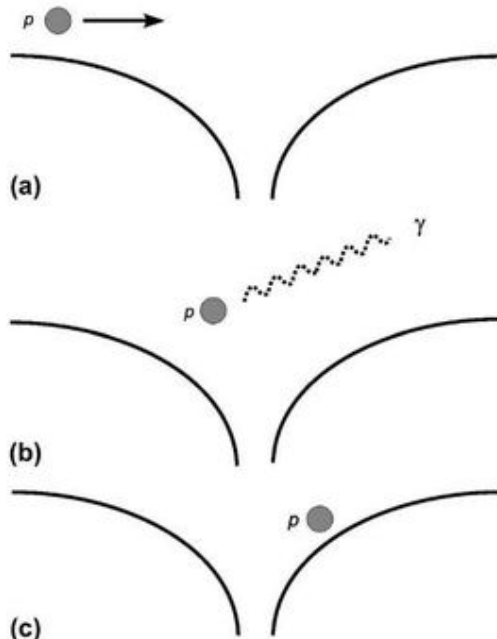


FIGURE 1.74 The nuclear bremsstrahlung process that releases soft x-ray in the proton-neutron capture and proton-deuteron fusion. The solid curves represent the attractive nuclear potential of a neutron (or deuteron) felt by a proton. The length dimension shown is ~ 10 fermi. (a) The proton, having an initial positive kinetic energy of several keV, is moving toward the neutron (or deuteron) due to nuclear attraction. (b) The proton accelerates in the process, and therefore starts radiating electromagnetic waves, *i.e.*, photons. (c) The proton, having lost all of its initial kinetic energy and maybe more, now has a total energy of negative value, *i.e.*, it is now a bound state around the neutron (or deuteron). Afterwards it may emit a gamma of 2.23 MeV for proton-neutron fusion (or 5.49 MeV for proton-deuteron fusion) and then combine with the neutron (or deuteron) to finally form ${}^2\text{H}$ (or ${}^3\text{He}$). The acceleration of the neutron is radiation-free, because the neutron is without charge. In p – d fusion, the accelerating deuteron also radiates, but this is not illustrated in the figure for clarity. (From Luo et al., 2010 with permission of Elsevier © 2010.)

et al. (2010), the proton and neutron are attracted to each other by the strong nuclear force, and this attraction causes both particles to accelerate toward each other. Due to the charge on the accelerating proton, electromagnetic radiation is generated of the bremsstrahlung type. Luo et al (2010) refer to this as a nuclear bremsstrahlung or nuclear startstrahlung to accentuate its origin in acceleration due to the strong nuclear force.

The fusion of the proton with deuterium yields the nuclear bremsstrahlung similar to the case of the proton and neutron fusion. However, Luo et al (2010) explain that the Coulomb repulsion of proton and deuteron adds a degree of complication to the process. They explain that the Coulomb barrier is overcome by quantum mechanical tunneling, and the strong nuclear force still causes both particles to accelerate toward each other, although the particles accelerate at different rates because of their mass difference. As both the proton and deuteron are charged, they radiate quanta of electromagnetic radiation. Because the two charged particles are accelerating toward each other, they travel in opposite directions, the radiation they emit will tend to cancel each other; however, the cancellation is not complete, because the two particles accelerate at different rates due to their mass difference.

3. X-rays from Beta-particle Emissions

All beta-emitting radionuclides, even those radionuclides classified as pure beta emitters that are not the source of any gamma radiation, including ${}^3\text{H}$, ${}^{14}\text{C}$, ${}^{32}\text{P}$, ${}^{35}\text{S}$, ${}^{45}\text{Ca}$, ${}^{63}\text{Ni}$, ${}^{89}\text{Sr}$, ${}^{90}\text{Y}$, and ${}^{123}\text{Sn}$, among others, will produce x-ray photons. For example, the measurement of bremsstrahlung from the beta particles of ${}^3\text{H}$ has been demonstrated as a method for the monitoring of the fuel processing system in the development of thermonuclear fusion reactors (Shu et al. 2004, 2006). This section describes x-ray production by beta particles in thick-target materials. Thick-target materials include any absorber within which a beta particle will come to a complete stop. When beta particles are emitted from decaying nuclei and escape the atom from which they originated, and are absorbed by materials before coming to a stop, x-ray photons are created by several distinct physical phenomena, which are enumerated as follows:

1. **External bremsstrahlung**, which is a continuous spectrum of x-rays produced when the accelerating beta particle traverses atoms of absorber material and is deflected by the Coulomb field of atomic nuclei causing the beta particle to decelerate and emit electromagnetic radiation. This is the major source of x-ray energy that a beta particle will radiate. As discussed previously the energy of the electromagnetic radiation emitted ($E = h\nu$) is proportional to the initial energy of the beta particle and the atomic number (Z) of the absorber. Thus, the bremsstrahlung energy loss (I) in MeV is written as

$$I = kZE^2 \quad (1.280)$$

or

$$I/E \approx kZE \quad (1.281)$$

where I/E is the fraction of incident beta-particle energy lost as bremsstrahlung and $k \approx 0.0007 \text{ MeV}^{-1}$ is a normalization constant (Evans, 1955, and Faw and Shultis, 2004). Table 1.18 illustrates the effect of atomic number Z on the conversion of beta-particle energy to bremsstrahlung in a thick target according to the approximation given by Eqn (1.281).

The estimates of energy conversion for a 1 MeV electron in aluminum and a 2 MeV electron in lead listed in Table 1.18 agree with estimates quoted by Choppin et al (2002) and Faw and Shultis (2004), respectively. Molybdenum (Mo) and tungsten (W), listed in Table 1.18, are relatively high- Z materials with heat stability used as target materials for the production of bremsstrahlung x-rays in commercial medical diagnostic x-ray tubes (Mavunda et al, 2004).

2. **Internal bremsstrahlung** occurs during the emission of the beta particle from the nucleus, as the beta particle accelerates at its birth and emits a continuous spectrum of x-rays in the field of the emitting nucleus (Cengiz and Almaz, 2004). This mechanism of bremsstrahlung production is in direct contrast to that of outer bremsstrahlung whereby the beta particle approaches a nucleus from outside the atom described in the previous section.
3. **X-rays corresponding to line spectra characteristic of the absorber material** are produced when the beta particle traverses the absorber and produces ionization in inner electron shells (K, L, M, \dots shells). The electron vacancies in the inner shells are filled by electrons from outer shells with the concomitant emission of x-rays. These x-rays consist of discrete lines of energy characteristic of x-ray lines of the absorber material.
4. **X-rays corresponding to line spectra characteristic of the emitting atom** are produced when the beta particle produces ionization as it accelerates out of the atom from which is was created. Ionization of internal electron shells (K, L, M, \dots shells) of the emitting atom leaves electron vacancies, which are filled by electrons from outer shells, producing x-rays of discrete energy lines characteristic of the emitting atom. The probability of this internal ionization followed by x-ray emission by the β -emitting atom is of the order of 10^{-4} (Levinger, 1953, Boehm and Wu, 1954, and Evans, 1955).

E. Cherenkov Radiation

Charged particles, when they possess sufficient energy, may travel through a transparent medium (gas, liquid, or solid) at a speed greater than the speed of light in that medium. This occurrence, known as the Cherenkov or Cerenkov effect, causes the emission of photons of light referred to as Cherenkov photons or Cherenkov radiation. These photons extend over a spectrum of wavelengths from the ultraviolet into the visible portion of the electromagnetic radiation spectrum. The photon emission is a result of a coherent disturbance of adjacent molecules in matter caused by the traveling charged particle, which must possess a certain threshold energy. This phenomenon has practical applications including (i) the measurement and detection of radionuclides that emit relatively high-energy beta particles, (ii) the measurement of gamma radiation via the Cherenkov

effect produced by Compton electrons, and (iii) the identification of subatomic particles. The history of discovery, theory, and the applications of Cherenkov photons are discussed in detail in Chapter 15, and only a brief treatment is provided in this chapter.

Cherenkov radiation was discovered by Pavel A. Cherenkov (1934a,b, 1936) while working on his PhD dissertation under the direction of Sergei I. Vavilov, who was director of the P. N. Lebedev Institute of Physics in Moscow. For detailed accounts of the history of this discovery and Cherenkov's experimental technique, see papers by Cherenkov's daughter, Elena Cherenkova (2005, 2008), and a previous book by the author (L'Annunziata, 2007). Once Cherenkov had discovered this unique visible radiation produced by high-energy Compton electrons or high-energy (fast) β -particles, and once Cherenkov found that this light was polarized and that the light emission was asymmetric, that is, it was emitted only in the direction of the fast electrons (Cherenkov, 1934a,b, 1936) did Cherenkov and his doctoral dissertation advisor Sergei I. Vavilov know that they were dealing with a yet unknown phenomenon. Il'ja Frank and Igor Tamm of the Theoretical Physics Division of the same institute noticed and went to work on the interpretation of this new phenomenon. Their findings were published in a joint paper entitled "Coherent Visible Radiation of Fast Electrons Passing through Matter" (Frank and Tamm, 1937). They explained the phenomenon as caused by a charged particle traveling in a medium at a speed in excess of the speed of light in that medium. It was known from Einstein's theory of relativity that matter could not travel in excess of the speed of light in a vacuum ($c = 2.99 \times 10^8 \text{ m/s}$); however, in gaseous, liquid, or solid media, the velocity of light will be less than its velocity in a vacuum, and an elementary charged particle with sufficient energy could travel in such media at speeds exceeding that of light. The charged particle in passing through the electron clouds of a transparent medium (liquid, solid, or gaseous) would create an electromagnetic shock wave analogous to that of a 'sonic boom' created by a jet airplane or projectile traveling in the atmosphere at a speed exceeding that of sound. In the words of Frank and Tamm (1937) with authors remarks in brackets:

We shall consider an electron moving with constant velocity v along [an] axis through a medium characterized by its index of refraction n . The field of the electron may be considered as the result of superposition of spherical waves of retarded potential, which are being continually emitted by the moving electron and are propagated with the velocity (c/n) . [See Fig. 1.75] It is easy to see that all these consecutive waves emitted will be in phase along the directions making the angle θ with the axis of motion [of the particle], if only v , n , and θ do satisfy the condition

$$\cos \theta = \frac{1}{\beta n} \quad (1.282)$$

where $\beta = v/c$. Thus, there will be a radiation emitted in the direction θ , whereas the interference of waves will prevent radiation in any other direction. Now the condition [of radiation emission] can be fulfilled only if

$$\beta n > 1, \quad (1.283)$$

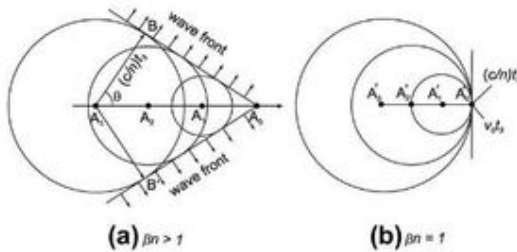


FIGURE 1.75 A Huygens construction of the spherical waves of retarded potential produced by a charged particle traveling along an axis in a refractive medium from points A_3 to A_0 at two velocities, namely, (a) $\beta n > 1$ and (b) $\beta n = 1$. (From Nobel Lecture of Il'ja Frank (1958) with permission © The Nobel Foundation 1958.)

that is, only in the case of fast electrons in a medium, whose index of refraction n for frequencies in question is markedly larger than 1.

The index of refraction, n , is by definition the ratio of the speed of light in a vacuum to its speed in a particular medium, and the value of n will vary from one medium to another. The term ‘fast electrons’ used by Frank and Tamm (1937), quoted above, refers to electrons of such energy that they travel at a speed in excess of the speed of light in a particular medium. Also, the term β is called the relative phase velocity of the particle ($\beta = v/c$) or the velocity of the particle in a medium divided by the speed of light in a vacuum.

Eqn (1.282), derived by Frank and Tamm, can be found from the distance of travel of the spherical wave front relative to the distance traveled by the electron, as depicted in Fig. 1.75. In the words of Frank (1958) in his Nobel Lecture (© The Nobel Foundation):

...We have to consider each point of the particle trajectory as a source of waves. In this case the wave phase is determined by the instant of passage of the particle through a given point. Let us assume that at moment $t = -t_3$ the emitter was at point A_3 , at moment $t = -t_2$ at point A_2 , at moment $t = -t_1$ at A_1 , and, finally, at the moment of observation $t = 0$ at A_0 .

...the velocity of the waves is equal to the phase velocity of light c/n ...The surfaces of the rays are simply spheres whose radii for points A_3 , A_2 , A_1 , and A_0 are $(c/n)t_3$, $(c/n)t_2$, $(c/n)t_1$, and 0, respectively [See Fig. 1.75a]. The envelope of these spheres evidently represents a cone of circular cross section with the apex at A_0 . Its generatrices in the plane of the drawing are A_0B and A_0B' .

According to the Huygens' principle, the directions of the rays are defined by the radius vectors drawn from some centre of the waves to the point of tangency with the envelope. For example, in Fig. 1.75a, it is A_3B and A_3B' coinciding with the generatrices of the wave normal cone...

From Fig. 1.75 it is not difficult to determine the magnitude of the threshold velocity. When the velocity diminishes, the distances between points A decrease. The threshold case arises when point A , occupies the position A_0 on the surface of the sphere (This case is depicted separately in Fig. 1.75b.) At lower velocities, one of the spheres lies completely within the other and they do not have a common envelope.

In the threshold case [$\beta n = 1$], they have only a common point of tangency, A'_0 . Thus evidently $(c/n)t_3 = v_0 t_3$, i.e., $v_0 = c/n$. The cone of wave normals is compressed in the direction of velocity v , and the wave cone transforms into a plane perpendicular to the axis of motion at point A'_0 [Fig. 1.75b].

From Fig. 1.75a the equation defining the angle θ as a function of the particle phase velocity β and index of refraction n , i.e., $\cos \theta = 1/\beta n$, is derived from the distances of travel of the wave front with respect to that traveled by the charged particle. The velocity v of travel of the wave front in a particular medium is a function of the index of refraction n of the medium, since by definition $n = c/v$. The distance traveled by the wave front from A_3 to B of Fig. 1.75a is the product of velocity and time t or $A_3B = vt_3$, and the distance traveled by the charged particle in the same time span from A_3 to A_0 is the product of the particle velocity in the medium v_p and time t_3 or $A_3A_0 = v_p t_3$, which may be written as $A_3A_0 = (v_p/c)ct_3$. Since the particle phase velocity β is defined as v_p/c , the distance A_3A_0 traveled by the charged particle becomes $A_3A_0 = \beta ct_3$. The angle of emission θ of the Cherenkov radiation with respect to the direction of travel of the charged particle is defined as

$$\cos \theta = \frac{AB}{A_3A_0} = \frac{(c/n)t_3}{\beta ct_3} = \frac{1}{\beta n} \quad (1.284)$$

Thus, the Cherenkov photons are anisotropic, that is, the photons are not emitted in all directions; rather, the photons are conical, i.e., they are emitted as a cone at an angle θ . The angle of emission is a function of the phase velocity of the particle (β) and the index of refraction (n) of the medium within which the particle is traveling. If the particle is assigned a maximum velocity, where β approaches unity, there will be a maximum angle of emission θ of the Cherenkov photons in liquids, and the angle would be a function of the index of refraction of the medium or

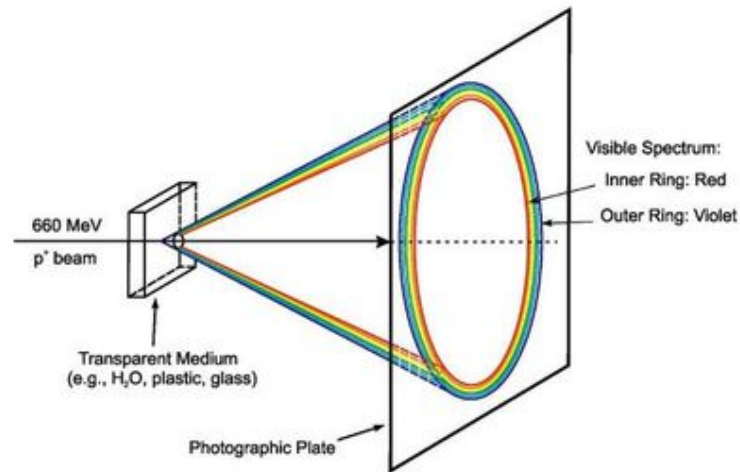
$$\cos \theta_{\max} = \frac{1}{n} \quad \text{when } \beta = 1 \quad (1.285)$$

For example, if an electron traveling in water is assigned a maximum velocity, where $\beta = 1$, and the index of refraction of water at the sodium D line, $n_D^{20} = 1.3330$, the maximum angles of emission of Cherenkov photons in water would be calculated according to Eqn (1.285) as

$$\theta_{\max} = \cos^{-1} \frac{1}{1.3330} = 41.4^\circ \quad (1.286)$$

In another medium such as benzene, where the index of refraction, $n_D^{20} = 1.50108$, the maximum angle of emission of the Cherenkov photons would be 48.2° calculated according to Eqn (1.286). Thus, Cherenkov photons are emitted as a cone at various angles between zero and a maximum value depending on the velocity of the particle and the index of refraction of the medium within which the particle travels. The conical properties of Cherenkov radiation, illustrated in Fig. 1.76, was described by Cherenkov in 1958 in his Nobel Lecture (© 1958

FIGURE 1.76 Diagram of an experimental arrangement for obtaining photographs of the cone section in the plane of a photographic plate placed perpendicular to the path of high-speed (600 MeV) protons in an accelerator beam. (From Cherenkov's Nobel Lecture (1958) with permission © The Nobel Foundation 1958.)



The Nobel Foundation) with the authors comments in brackets as follows:

If we consider the picture [of the radiation] not in the [2-dimensional] plane but spatially, then the radiation must spread out along the surface of a cone whose axis forms the path of an electrically charged particle while the surface line forms with this axis the angle [θ].

If we place [a] photographic plate perpendicular to the beam of high-speed particles [See Fig. 1.76], we shall obtain, in addition to an image of the track of the beam, also a photograph of the radiation in the form of a ring. This photograph was obtained with the aid of a fine beam of protons in the accelerator of the United Institute for Nuclear Research at Dubna.

...we have in our considerations assumed some fixed frequency. In reality, however, the radiation spectrum is continuous. Since the medium exhibits dispersion, i.e., the refractive index is dependent on the frequency, this means that the light of different wavelengths is propagated at angles which, even with strictly constant velocity of the particles, differ somewhat from one another.

Thus, the radiation is broken up as in spectral analysis. The radiation cone will consequently show a definite intensity, and in the case of a medium with normal dispersion the spectral red will lie in the inner part of the cone while the violet is on the outside. That this is actually so was shown by a photograph showing part of the ring with a colour plate.

Cherenkov photon ring imaging has developed into a field of its own. Special ring-imaging-Cherenkov (RICH) detectors have been developed, which are used for particle identification. Such detectors can provide information on the particle velocity, β , and discriminate between very high-energy relativistic particles of different mass, such as protons ($m = 938.27 \text{ MeV}/c^2$), kaons ($m = 493.67 \text{ MeV}/c^2$), pions ($m = 139.56 \text{ MeV}/c^2$), and electrons ($m = 0.511 \text{ MeV}/c^2$). The RICH detectors are specifically capable of discriminating between

kaons and pions of momentum approximately $50 \text{ GeV}/c$. These detectors are discussed in detail in Chapter 15, and advances are reviewed in the proceedings of international workshops on this technique (Engelfried and Paic, 2005, and Bressan et al, 2008).

As noted above and illustrated in Fig. 1.75, the particle phase velocity, β , is a critical factor in the production of Cherenkov photons in a medium of given index of refraction, n , that is, Cherenkov radiation will occur only when $\beta > 1/n$. Consequently, the particle energy, upon which the particle phase velocity is dependent, is a critical factor. Thus, there is a minimum or threshold energy that the charged particle must reach when traveling in a medium of given index of refraction, before Cherenkov photons will be produced. This threshold energy is defined by the equation

$$E_{\text{th}} = m_0 c^2 \left[\left(1 - \frac{1}{n^2} \right)^{-1/2} - 1 \right] \quad (1.287)$$

where m_0 is the particle rest mass and c is the velocity of light in a vacuum ($2.99 \times 10^{10} \text{ cm/s}$). Eqn (1.287) is dealt with in more detail in Chapter 15. Thus, the threshold energy for Cherenkov photon production will vary according to the particle rest mass and index of refraction of the medium. The energy required for the production of Cherenkov photons, E_{th} , increases with particle mass, and it will be lower for media of higher index of refraction.

The counting of Cherenkov photons for the analysis of radionuclides is a common technique, and Eqn (1.287) may be used to assess the potential of a given medium for the detection of beta particles that are emitted by particular radionuclides. For example, the radionuclides ^{33}P and ^{32}P are commonly used as radionuclide tracers in the biosciences, and aqueous solutions are generally the medium within which the radionuclides are used. Eqn (1.287) may be used to determine the threshold energy for the production of

Cherenkov photons by beta particles (*i.e.*, electrons) in water by taking the rest mass of the electron ($m_e = 9.10938 \times 10^{-28}$ g) and the index of refraction of water ($n_D^{20} = 1.3330$) to give

$$\begin{aligned}
 E_{th} &= (9.10938 \times 10^{-28} \text{g})(2.99792 \times 10^{10} \text{cm/sec})^2 \\
 &\times \left[\frac{1}{\sqrt{1 - \frac{1}{(1.333)^2}}} - 1 \right] \\
 &= 8.18707 \times 10^{-7} \text{ergs} \left[\frac{1}{\sqrt{0.43721}} - 1 \right] \\
 &= \left(\frac{8.18707 \times 10^{-7} \text{ergs}}{1.602 \times 10^{-12} \text{ergs/eV}} \right) \left[\frac{1}{0.66121} - 1 \right] \\
 &= (0.5110 \times 10^6 \text{eV})(0.51237) = 0.262 \text{MeV}
 \end{aligned}
 \tag{1.288}$$

Thus, the beta particle must possess a minimum of 0.262 MeV energy to produce Cherenkov photons in water. Comparing the maximum energies of the beta emissions of ^{32}P ($E_{max} = 1.710$ MeV) and ^{33}P ($E_{max} = 0.249$ MeV) clearly indicate that the beta emissions from ^{33}P will not produce any Cherenkov photons in water; and only those beta-particle emission from ^{32}P in water with energies in excess of 0.262 MeV can be detected by Cherenkov photon counting. Thus, the Cherenkov effect may be used to discriminate between ^{32}P and ^{33}P in water by detecting only the ^{32}P fraction. Cherenkov photon counting is discussed in detail in Chapter 15 together with other applications of the Cherenkov effect.

There are numerous applications of the Cherenkov effect, and these are discussed in detail in Chapter 15. Among these applications are (i) the analysis of radionuclides that emit beta particles with sufficient energy to produce Cherenkov photons in the medium in which they are analyzed, (ii) the discrimination of beta-emitting radionuclides by the selection of a medium with an index of refraction that would allow or prevent the Cherenkov effect, and (iii) the measurement of gamma radiation via the detection of photons produced by Compton electrons, and (iv) high-energy particle identification with ring-imaging Cherenkov (RICH) detectors.

X. INTERACTION OF ELECTROMAGNETIC RADIATION WITH MATTER

The lack of charge or rest mass of electromagnetic gamma and x-radiation hinders its interaction with matter and the dissipation of its energy in matter. Consequently, gamma radiation and x-rays have greater penetration power and longer ranges in matter than the massive and charged alpha and beta particles of the same energy. Nevertheless, gamma and x-radiation are absorbed by matter, and the principal mechanisms by which this type of radiation interacts with matter are discussed in this section.

A. Photoelectric Effect

The energy of a photon may be completely absorbed by an atom. Under such circumstances, the entire absorbed photon energy is transferred to an electron of the atom and the electron is released, resulting in the formation of an ion pair (see also Section IX.A). Consequently, the energy of the emitted electron is equal to the energy of the impinging photon less the binding energy of the electron. This is described by the photoelectric equation of Einstein:

$$E_e = h\nu - \phi \tag{1.289}$$

where E_e is the energy of the ejected electron, $h\nu$ is the energy of the incident photon, and ϕ is the binding energy of the electron or the energy required to remove the electron from the atom. The ejected electron is identical to a beta particle and produces ionization (secondary ionization in this case) as it travels through matter as previously described for beta particles.

The photoelectric effect occurs in the inner electron shells, predominately in the *K*-electron shell, of the atom as described in Section X.D. When an electron from an inner atomic *K* or *L* shell is ejected, electrons from outer shells fall from outer electron shells to fill the resulting gap. These transitions in electron energy states require a release of energy by the atomic electrons, which appears as soft (low-energy) x-rays. X-radiation is identical in properties to gamma radiation. The essential difference lies in the origin of the two radiations. As previously described, gamma radiation originates from energy-state transformations of the nucleus of an atom, whereas x-radiation originates from energy-state transformations of atomic electrons.

B. Compton Effect

There is a second mechanism by which a photon (*e.g.*, x-ray or gamma ray) transfers its energy to an atomic orbital electron. In this interaction, illustrated in Fig. 1.77, the photon, E_γ , imparts only a fraction of its energy to the electron and in so doing is deflected with energy E'_γ at an angle Θ , while the bombarded electron is ejected at an angle θ to the trajectory of the primary photon. This interaction is known as the Compton effect and also as Compton scattering. The result of this

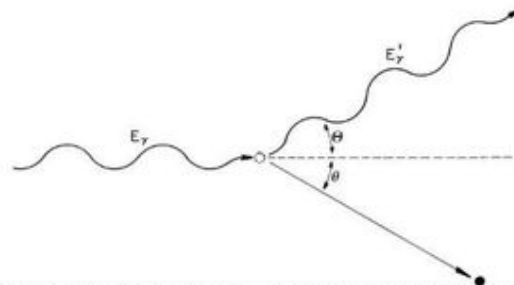


FIGURE 1.77 The Compton effect. An incident photon collides with an atomic electron and imparts energy to it, the photon and electron being deflected at angles Θ and θ , respectively, to the trajectory of the incident photon.

interaction is the formation of an ion pair, as in the case of the photoelectric effect. However, the deflected photon continues traveling through matter until it dissipates its entire kinetic energy by interacting with other electrons in a similar fashion or via other mechanisms of interaction with matter discussed in this section. The ejected electron, being identical in properties to a beta particle, loses its energy through the secondary ionization it causes according to mechanisms previously described.

Our understanding of the Compton effect comes from the original work of Arthur H. Compton (1923a,b), who discovered that x-ray photons scattered by thin foils underwent a wavelength shift. The shift in wavelength of the scattered photon with respect to that of the incident photon was a function of the angle of scatter Θ . To interpret this effect, he treated x-radiation as photon particles or quanta according to the Einstein-Planck relation $E = h\nu$ (see Eqn (1.257)) and the scattering to occur as photon-electron collisions somewhat like billiard-ball collisions as illustrated in Fig. 1.77. Compton derived the equation, which describes the wavelength shift between the incident and scattered photons and angle of scatter as

$$\lambda' - \lambda = \frac{h}{m_0c}(1 - \cos \Theta) \quad (1.290)$$

where λ' and λ are the wavelengths of the incident and deflected photons, h is Planck's constant, m_0 is the rest mass of the electron, c is the speed of light, and Θ is the angle of scatter of the photon relative to its original direction of travel.

The Compton-scatter photon will always be of longer wavelength (lower energy) than the incident photon, because of energy lost in the collision with the electron. For example, let us calculate the wavelength shift and energy loss by an incident photon of wavelength 0.300 nm that collides with an electron, and where the photon is scattered at an angle of 70° . The wavelength of the scattered photon is calculated according to Eqn (1.290) as

$$\begin{aligned} \lambda' &= \lambda + \frac{h}{m_0c}(1 - \cos \Theta) \\ &= 3.0 \times 10^{-10} \text{ m} + \frac{6.626 \times 10^{-34} \text{ J sec}}{(9.109 \times 10^{-31} \text{ kg})(2.997 \times 10^8 \text{ m/sec})} \\ &\quad \times (1 - \cos 70^\circ) \\ &= 3.0 \times 10^{-10} \text{ m} + 2.43 \times 10^{-12} \text{ m}(1 - 0.342) \\ &= 0.3016 \text{ nm} \end{aligned}$$

The energy lost by the incident photon according to the Einstein-Planck relation Eqn (1.257) is given by

$$\begin{aligned} \Delta E &= E_\gamma - E'_\gamma \\ &= \frac{hc}{\lambda} - \frac{hc}{\lambda'} \\ &= \frac{12.4 \text{ keV}\text{\AA}}{3.00 \text{ \AA}} - \frac{12.4 \text{ keV}\text{\AA}}{3.016 \text{ \AA}} \\ &= 4.133 \text{ keV} - 4.111 \text{ keV} = 0.022 \text{ keV} \end{aligned}$$

and the fraction of photon energy lost becomes

$$\frac{\Delta E}{E} = \frac{0.022 \text{ keV}}{4.133 \text{ keV}} = 0.0053 = 0.53\%$$

We can calculate directly the energy of the Compton scatter photon, λ' , if we know the incident x-ray or gamma-ray photon energy and angle of scatter of the photon according to the equation

$$E'_\gamma = \frac{E_\gamma}{1 + (E_\gamma/mc^2)(1 - \cos \Theta)} \quad (1.291)$$

where E'_γ is the energy of the Compton scatter photon, E_γ is the incident photon energy, mc^2 is the rest energy of the electron (511 keV or 0.511 MeV, see Section X.C), and Θ is the Compton photon angle of scatter (Tait, 1980). If we take the data from the previous example, where the incident photon energy was 4.133 keV and the angle of scatter was 70° , we can calculate the energy of the Compton photon according to Eqn (1.291) to be

$$E'_\gamma = \frac{4.133 \text{ keV}}{1 + (4.133 \text{ keV}/511 \text{ keV})(1 - \cos 70^\circ)} = 4.111 \text{ keV}$$

The result is in agreement with the calculations above using Eqn (1.290) derived by Compton.

It has been shown by Compton that the angle of deflection of the photon is a function of the energy imparted to the electron. This angle may vary from just above $\Theta = 0^\circ$ for low Compton electron energies to a maximum $\Theta = 180^\circ$ for the highest Compton electron energy. Compton electrons are thus emitted with energies ranging between zero and a maximum energy referred to as the Compton edge. The Compton edge is the Compton electron energy corresponding to complete backscattering of the gamma-ray photon. With $\Theta = 180^\circ$ or $\cos \Theta = -1$, Eqn (1.291) is reduced to the following equation describing the energy, E'_γ , of the gamma-ray photon at the Compton edge in MeV units:

$$E'_\gamma = \frac{E_\gamma}{1 + (E_\gamma/0.511 \text{ MeV})(1 - \cos 180^\circ)} \quad (1.292)$$

$$E'_\gamma = \frac{E_\gamma}{1 + (2E_\gamma/0.511)} \quad (1.293)$$

$$E'_\gamma = \frac{E_\gamma}{1 + 3.914E_\gamma} \quad (1.294)$$

As an example, the energy of the gamma-ray photon in MeV at the Compton edge for an incident gamma ray from ^{137}Cs ($E_\gamma = 0.662 \text{ MeV}$) is calculated according to Eqn (1.294) to be

$$E'_\gamma = \frac{0.662}{1 + 3.914(0.662)} = 0.184 \text{ MeV}$$

A Compton scatter photon is of longer wavelength and lower energy than the incident photon. Deflected Compton photons occur with a broad spectrum of energies. Spectra of Compton

scattered photon energies contain a peak known as the backscatter peak (see Chapter 16). The backscatter peak arises from Compton scattering into a gamma photon detector [e.g., NaI(Tl) crystal] from the surrounding detector shielding and housing materials. The backscatter peak occurs at increasing values of energy (MeV) in proportion to the incident photon energy and approaches a constant value of 0.25 MeV, according to Eqn (1.294), for incident photon energies greater than 1 MeV (Tait, 1980). The energy of the Compton electron, E_c , may be described by

$$E_c = E_\gamma - E'_\gamma - \phi \quad (1.295)$$

where E_γ and E'_γ are the energies of the incident and deflected photons, respectively, and ϕ is the binding energy of the electron. As the binding energy of the atomic electron is relatively small, the energy of the ejected electron is essentially the difference between the incident and deflected photon energies. Substituting the value of E'_γ from Eqn (1.291) and ignoring the electron binding energy, the Compton electron energy can be expressed as

$$E_c = E_\gamma - \frac{E_\gamma}{1 + (E_\gamma/mc^2)(1 - \cos \Theta)} \quad (1.296)$$

$$E_c = E_\gamma - \frac{E_\gamma}{1 + (E_\gamma/0.511 \text{ MeV})(1 - \cos \Theta)} \quad (1.297)$$

where the electron energies are given in MeV. For example, the energy of a Compton electron, E_c , scattered at 180° (Compton edge: $\cos \Theta = -1$) and originating from an incident gamma-ray photon from ^{137}Cs ($E_\gamma = 0.662 \text{ MeV}$) is calculated according to Eqn (1.297) as

$$\begin{aligned} E_c &= 0.662 - \frac{0.662}{1 + (0.662/0.511)(1 - \cos 180^\circ)} \\ &= 0.478 \text{ MeV} \end{aligned}$$

Alternatively, if we ignore the negligible electron-binding energy and know the incident photon energy and Compton scatter photon energy, we can calculate the Compton electron energy by difference according to Eqn (1.295):

$$E_c = 0.662 \text{ MeV} - 0.184 \text{ MeV} = 0.478 \text{ MeV},$$

which is in agreement with the electron energy calculated above. The Compton edge and backscatter peak due to interactions of Compton electrons and Compton backscatter photons, respectively, in a scintillation crystal detector are described in Chapter 16.

C. Pair Production

The interactions of gamma radiation with matter, considered earlier, involve the transfer of γ energy, in whole or in part, to atomic electrons of the irradiated material. Pair production, as another mechanism of γ -energy dissipation in matter, results in the creation of matter (i.e., electrons) from the γ -energy. The particles produced are a negatron and a positron from an individual gamma-ray photon that interacts with the Coulombic field of a nucleus (see Figs 1.4 and 1.78). Consequently, this phenomenon involves the creation of mass from energy.

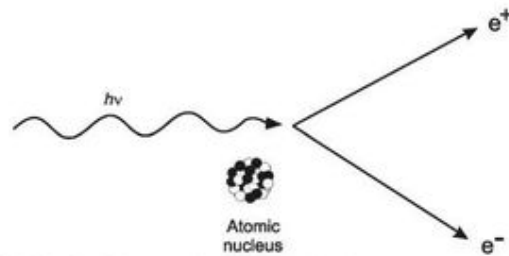


FIGURE 1.78 Pair production. The conversion of a gamma-ray photon into a negatron and positron pair.

Carl D. Anderson at the California Institute of Technology (Caltech) received the 1936 Nobel Prize in physics for his discovery of the positron, the first experimental evidence of antimatter. He and his graduate student Seth Neddermeyer also reported in their findings (Anderson and Neddermeyer, 1933) the first observation of pair production, which they described as follows:

One of the most striking phenomena, which have been observed in this experiment is the occasional simultaneous appearance of paired tracks consisting of one positive particle and one negative with a common point of origin...The process, which gives rise to the positrons is at present not known, but so far as these data go they are in accord with the view expressed by Blackett and Occhialini (1933) that the two particles may be formed by a process in which the energy of approximately 1 MeV required for the formation of a positive and negative electron is supplied by the impinging radiation.

It was Nobel Laureate Patrick Blackett and his coworker G.P.S. Occhialini (1933) who recognized that the two particles, positron and negatron, are formed by the process known as 'pair production' whereby the energy of 1.02 MeV required for the production of the two particles is provided by the gamma radiation. In his Nobel Lecture, Anderson (1936) explained the pair-production phenomena as follows:

...that the appearance of pairs of positive and negative electrons could be understood in terms of this theory [Dirac's theory] as the "creation" of a positive-negative electron pair in the neighborhood of an atomic nucleus. The energy corresponding to the proper mass of both of the particles, as well as to their kinetic energies is supplied, according to this view, by the incident radiation. Since the energy corresponding to the proper mass of a pair of electrons is approximately 1 MeV, one should expect gamma rays of energy greater than this amount to produce positrons in their passage through matter, and further that the sum of the kinetic energies of the positive and negative electrons should be equal to the energy of the radiation producing them diminished by approximately 1 MeV.

In the above statement, Anderson described the process of pair production, first theorized by Dirac (1928a,b), observed through cloud-chamber track photographs by Anderson and Neddermeyer (1933), and interpreted by Blackett and Occhialini (1933). The gamma-ray photon energy required for pair production is, as noted above by Anderson, equivalent to the sum of the masses of the electron and positron described by the equation

$$E_{pair} = m_e c^2 + m_e c^2 = 2mc^2 = 2(0.511 \text{ MeV}) = 1.022 \text{ MeV} \quad (1.298)$$

The gamma-ray photon energy in excess of 1.022 MeV appears as the kinetic energy of the electron and positron created, and the overall pair-production phenomena can be expressed as

$$h\nu = 2mc^2 + E_{e^-} + E_{e^+} \quad (1.299)$$

where $h\nu$ is the gamma-ray photon energy, $2mc^2$ is the energy equivalence of the mass of two electrons, and E_{e^-} and E_{e^+} are the kinetic energies of the electron and positron, respectively. In pair production, gamma-ray energy in excess of 1.02 MeV appears as kinetic energy of the negatron and positron produced. By the time of his Nobel Lecture in 1936, three sources of positrons were known, and Anderson took the opportunity of his lecture to describe these, which are the following: (1) cosmic-ray showers of electron-positron pairs via pair production from cosmic gamma radiation, (2) pair production via the absorption of gamma radiation in excess of 1 MeV from radionuclide sources, and (3) positron emission via beta decay from radioactive elements, such as ^{30}P , ^{13}N , and ^{27}Si , artificially produced by Joliot-Curie and Joliot (1934a,b,c), which decay by positron emission.

The creation of an electron requires a certain quantum of energy of a gamma-ray photon, which may be calculated according to Einstein's equation for the equivalence of mass and energy

$$E = m_e c^2 \quad (1.300)$$

where E is the energy, m_e is the electron rest mass, and c is the speed of light in a vacuum. Thus, the rest energy of the electron (negatron or positron) is calculated as

$$E = (9.109 \times 10^{-31} \text{ kg})(2.997 \times 10^8 \text{ m/sec})^2 = 8.182 \times 10^{-14} \text{ J}$$

Since by definition, $1 \text{ eV} = 1.602 \times 10^{-19} \text{ J}$, the electron rest energy in joules is converted to electron volts as

$$8.182 \times 10^{-14} \text{ J} / 1.602 \times 10^{-19} \text{ J/eV} = 0.511 \text{ MeV}$$

Thus, the creation of an electron (negatron) requires a minimum energy of 0.511 MeV. However, a gamma ray of 0.511 MeV energy cannot alone create a negatron, as there must also be the simultaneous creation of its antiparticle, the positron of equal mass, and opposite charge. The minimum gamma-ray photon energy required for the creation of the negatron-positron pair is, as described by Eqn (1.298) above, $2(0.511)$ or 1.022 MeV. Thus, the absorption by matter of gamma radiation greater than 1.02 MeV may result in pair production. The probability of pair production increases in proportion to the magnitude of gamma-ray photon energy above 1.02 MeV, and pair production is the predominant mechanism of absorption of photons of energies of 5 MeV and above (see Figs 1.81 and 1.82 further on in this chapter).

As discussed previously in Section IX.C, positrons will produce annihilation radiation when they come to rest in the proximity of a negative electron, *i.e.*, their antiparticle, resulting

in the simultaneous conversion of two electron masses into two gamma-ray photons of 0.511 MeV energy.

Pair production does not occur only in the vicinity of atomic nuclei bombarded by gamma radiation. It may also originate from nuclei that emit gamma radiation with transition energies greater than 1.02 MeV. This is referred to as internal pair production, and the mechanism competes to a small extent with the emission of gamma radiation. The degree to which this competition occurs is measured by the ratio of intensities of positron-negatron pairs to gamma radiation or (e^\pm/γ). Some examples of nuclides that emit such positron-negatron pairs and the intensities of these pairs relative to gamma radiation are given in Table 1.19.

A practical application of internal pair production to the nondestructive activity analysis of ^{90}Y and ^{90}Sr was reported by Selwyn et al (2007). The nuclide ^{90}Y decays by negatron emission with a Q value of 2280.1 keV as illustrated in Fig. 1.79. The activity of ^{90}Y is determined traditionally by liquid scintillation or Cherenkov counting of the high-energy negatron emissions, which have an E_{max} of 2280.1 keV as described in Chapters 7, 9, and 15, as this beta transition occurs at an intensity of 99.999% to the ground state of stable ^{90}Zr . There is a very small branching beta transition with an E_{max} of 519.4 keV, which occurs at an intensity of 0.011%, to metastable ^{90}Zr at the energy level of 1760.7 keV (see Fig. 1.79). This is well above the 1022 keV required for internal pair production, that can occur in the transition from 1760.7 keV to the ground state of ^{90}Zr . Selwyn et al (2007) measured the internal pair production branching ratio for this transition to be $(31.86 \pm 0.47) \times 10^{-6}$ by measuring the count rate of the 511 keV peak with a high-purity germanium detector (HPGe) produced by the positron (β^+) annihilation that

TABLE 1.19 Examples of Nuclides that Exhibit Internal Pair Production, Their Gamma Radiations and Relative Intensities of the Positron-Negatron Pairs

Nuclide	Gamma radiations		Pair/gamma ratio (e^\pm/γ)
	Energy (MeV)	Abundance (%)	
^{24}Na	1.369	100	6×10^{-5}
	2.754	100	7×10^{-4}
^{56}Mn	1.81	29	5.6×10^{-4}
	2.11	15	4.6×10^{-4}
^{59}Fe	1.099	57	1.4×10^{-4}
	1.292	43	1.1×10^{-4}
^{60}Co	1.17	100	3.7×10^{-5}
	1.33	100	Combined ^a
^{142}Pr	1.576	4	1.1×10^{-4}
^{144}Pr	1.489	0.3	1.9×10^{-4}
	2.186	0.7	6.7×10^{-4}
^{154}Eu	1.274	37	8.0×10^{-5}

^aThe value of (e^\pm/γ) of 3.7×10^{-5} for ^{60}Co represents the pair/gamma ratio for both gamma emissions combined.

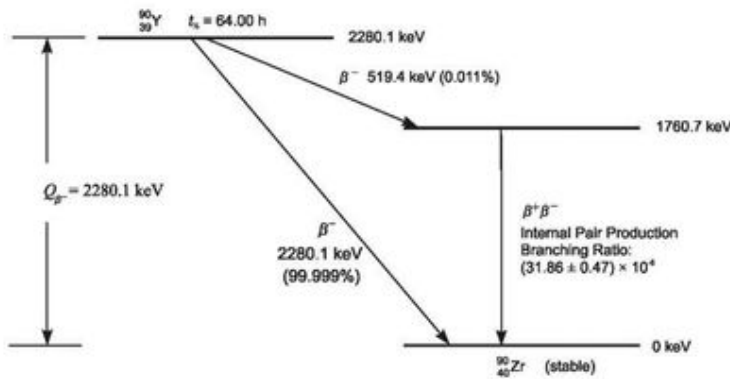


FIGURE 1.79 Decay scheme of ⁹⁰Y.

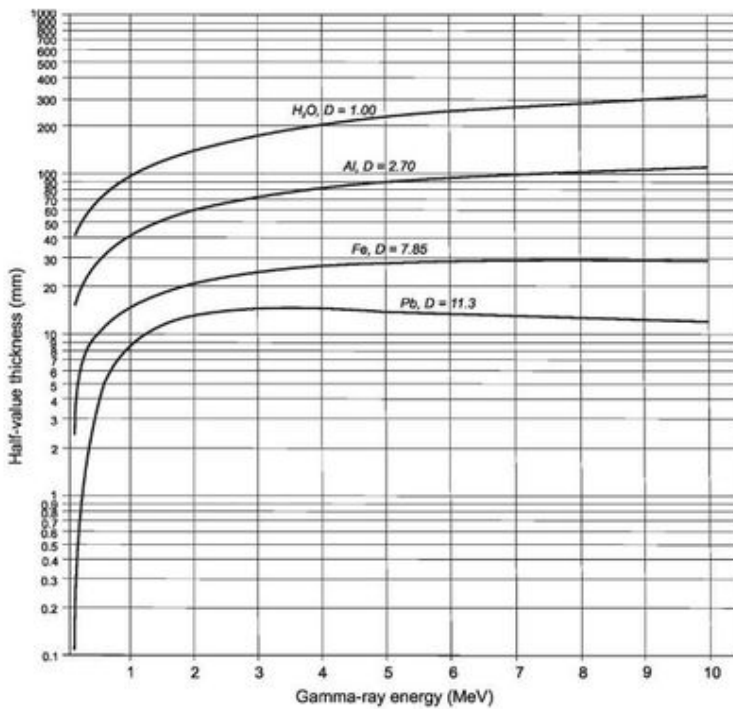


FIGURE 1.80 Half-value thicknesses of various materials as a function of gamma-ray energy, D is the density of each material. (From L'Annunziata (1987) reprinted with permission from Elsevier © 1987 Academic Press.)

follows pair production. The high-energy beta emissions of ⁹⁰Y produce bremsstrahlung background radiation, which had to be subtracted from the overall count rate to get an accurate measurement of the net count rate at the 511 keV peak. With the known branching ratio for the internal pair production, and measurement of the net count rate and detection efficiency of the 511 keV positron (β^+) annihilation photons, the ⁹⁰Y activity of unknown samples can be determined. The activity of ⁹⁰Sr can be calculated from the measured activity of ⁹⁰Y, as their activities are equal when in secular equilibrium (see Section XV.C and Fig. 1.97).

D. Combined Photon Interactions

Because of its zero rest mass and zero charge, gamma radiation has an extremely high penetration power in matter in comparison with alpha and beta particles.

Materials of high density and atomic number (such as lead) are used most often as absorbers to reduce x- or gamma radiation intensity. Radiation intensity, I , is defined here as the number of photons of a radiation beam that traverse a given area per second, the units of which can be photons $\text{cm}^{-2} \text{s}^{-1}$. Suppose a given absorber material of thickness x attenuates or

reduces the intensity of incident gamma radiation by one-half. Placing a similar barrier of the same thickness along the path of the transmitted gamma radiation would reduce the intensity again by one-half. With three barriers each of thickness x and an initial gamma-ray intensity I_0 , there is a progressive drop in the transmitted gamma-ray intensities: $I_1 = \frac{1}{2}I_0$, $I_2 = \frac{1}{2}I_1$, $I_3 = \frac{1}{2}I_2$, and $I_n = \frac{1}{2}I_{n-1}$. Obviously, incident x - or gamma radiation may be reduced from I_0 to I_3 by using a $3x$ thickness of the same material as an absorber. Consequently, the intensity of the transmitted electromagnetic radiation is proportional to the thickness of the absorber material and to the initial intensity of the radiation. An increasing absorber thickness increases the probability of photon removal, because there is a corresponding increase of absorber atoms that may attenuate the incident photons via the photoelectric effect, the Compton effect, and pair production mechanisms.

If gamma-ray attenuation with respect to absorber thickness is considered, the change in gamma-ray intensity, ΔI , with respect to the absorber thickness, Δx , is proportional to the initial gamma-ray photon intensity, I . This may be written as

$$\Delta I/\Delta x = -\mu I \tag{1.301}$$

where μ is the proportionality constant, referred to as the linear attenuation coefficient or linear absorption coefficient. Its value is dependent on the atomic composition and density of the absorber material. The change in intensity over an infinitely thin section of a given absorber material may be expressed as

$$dI/dx = -\mu I \tag{1.302}$$

or

$$dI/I = -\mu dx \tag{1.303}$$

Integrating Eqn (1.303) over the limits defined by the initial intensity, I_0 , to the transmitted intensity, I , and over the limits of absorber thickness from zero to a finite value x , such as

$$\int_{I_0}^I dI/I = -\mu \int_0^x dx \tag{1.304}$$

gives

$$\ln I - \ln I_0 = -\mu x \tag{1.305}$$

or

$$\ln I_0/I = \mu x \tag{1.306}$$

Eqn (1.306) may be written in exponential form as

$$I = I_0 e^{-\mu x} \tag{1.307}$$

which is somewhat similar to the exponential attenuation of neutrons discussed earlier in this chapter.

Because gamma-ray absorption is exponential, the term half-value thickness, $x_{1/2}$, is used to define the attenuation of gamma radiation by matter. Half-value thickness is the thickness of a given material of defined density that can reduce the

intensity of incident gamma radiation by one-half. The half-value thickness may also be defined according to Eqn (1.306), in which the initial gamma-ray intensity, I_0 , is given an arbitrary value of 1 and the transmitted intensity must, by definition, have a value of 1/2, or

$$\ln 1/0.5 = \mu x_{1/2} \tag{1.308}$$

or

$$\ln 2 = \mu x_{1/2} \tag{1.309}$$

and

$$x_{1/2} = 0.693/\mu \tag{1.310}$$

From the linear attenuation coefficient, μ , of a given material and gamma-ray photon energy, it is possible to calculate the half-value thickness, $x_{1/2}$. The linear attenuation coefficient has units of cm^{-1} , so that calculated half-value thickness is provided in units of material thickness (cm). Linear attenuation coefficients for some materials as a function of photon energy are provided in Table 1.20. The table refers to these as total linear attenuation coefficients, because they constitute the sum of coefficients due to Compton, photoelectric, and pair production interactions. Celiktas (2011) reports on the development of the experimental methods that may be used to determine gamma-ray linear attenuation coefficients. Calculated half-value thicknesses of various absorber materials as a function of gamma-ray energy are illustrated in Fig. 1.80 to show some examples of the varying amounts of absorber material required to attenuate gamma-ray photons. The linear attenuation coefficient is a constant for a given absorber material and gamma-ray photon energy and has units of reciprocal length such as cm^{-1} . It is, however, dependent on the state of the absorber or the number of atoms per unit volume of absorber. A more popular coefficient is the mass

TABLE 1.20 Total Linear Attenuation Coefficients (cm^{-1}) for Gamma-Ray Photons in Various Materials^a

Photon energy (MeV)	Water	Aluminum	Iron	Lead
0.1	0.167	0.435	2.704	59.99
0.2	0.136	0.324	1.085	10.16
0.4	0.106	0.2489	0.7223	2.359
0.8	0.0786	0.1844	0.5219	0.9480
1.0	0.0706	0.1658	0.4677	0.7757
1.5	0.0575	0.1350	0.3812	0.5806
2.0	0.0493	0.1166	0.3333	0.5182
4.0	0.0339	0.0837	0.2594	0.4763
8.0	0.0240	0.0651	0.2319	0.5205
10.0	0.0219	0.0618	0.2311	0.5545

^aData from Argonne National Laboratory, ANL-5800 (1963), Hubbell (1969), and Berger et al. (2010).

attenuation coefficient, μ_m , which is independent of the physical state of the absorber material and is defined as

$$\mu_m = \mu/\rho \tag{1.311}$$

where ρ is the density of the absorber in units of g/cm^3 , and μ_m has units of cm^2/g . Some examples of mass attenuation coefficients according to x- and gamma-ray photon energy are provided in Table 1.21. Using the mass attenuation coefficient, Eqn (1.307) transforms to

$$I = I_0 e^{-\mu_m \rho x} \tag{1.312}$$

and the half-value thickness is calculated according to Eqn (1.310) as

$$x_{1/2} = 0.693/\mu_m \rho \tag{1.313}$$

Mass attenuation coefficients for x- or gamma-ray photons over a wide range of energies from 1 keV to 1000 MeV in 100 elements are available from Berger and Hubbell (1997). In addition, mass attenuation coefficients for any element, chemical compound, mixtures of elements, or mixtures of compounds over the x-ray- or gamma-ray photon energy range of 1 keV to 10^5 MeV are available from a database, which can be found at the following National Institute of Standards and Technology (NIST) website: <http://physics.nist.gov/PhysRefData/Xcom/html/xcom1.html>. A sample of mass attenuation coefficients over the range of 5 keV to 10 MeV in a few materials are listed in Table 1.21. The following calculation illustrates the use of the data from Tables 1.20 and 1.21 to calculate half-value thickness and radiation attenuation:

Let us calculate the half-value thickness of lead ($\rho = 11.3 \text{ g}/\text{cm}^3$) for 2.0 MeV gamma radiation, and further calculate what the reduction in radiation intensity would result if we positioned four times the half-value thickness of lead in the path of the radiation beam. First, the linear attenuation coefficient, μ , or mass attenuation coefficient, μ_m , for 2.0 MeV photons in lead are obtained from either Table 1.20 or 1.21 and the half-value thickness of lead for 2.0 MeV photons is calculated as

$$x_{1/2} = \frac{0.693}{\mu} \text{ or } \frac{0.693}{\mu_m \rho} \tag{1.314}$$

or

$$x_{1/2} = \frac{0.693}{0.5182 \text{ cm}^{-1}} \text{ or } \frac{0.693}{(0.0457 \text{ cm}^2/\text{g})(11.3 \text{ g}/\text{cm}^3)}$$

$$x_{1/2} = 1.34 \text{ cm}$$

Thus, a barrier of 1.34 cm thickness of lead is sufficient to reduce the radiation intensity of 2.0 MeV photons by 1/2 or 50%. According to Eqn (1.307), the relation between the initial radiation intensity, I_0 , and the transmitted intensity, I , is

$$\frac{I}{I_0} = e^{-\mu x} \tag{1.315}$$

and for $x = 1.34$, if the initial radiation intensity is given an arbitrary value of 2, the transmitted intensity would be 50% of the initial intensity or equal to 1. We then can write

TABLE 1.21 Total Mass Attenuation Coefficients (cm^2/g) for X- or Gamma-Ray Photons in Various Materials^a

Photon energy (MeV)	Air	Water	Aluminum	Iron	Lead
0.005	38.3	42.0	193	140	730
0.01	4.6	5.1	26.2	171	131
0.05	0.187	0.208	0.368	1.96	8.04
0.1	0.151	0.167	0.170	0.372	5.55
0.2	0.123	0.136	0.122	0.146	0.999
0.4	0.0953	0.106	0.0922	0.0919	0.208
0.8	0.0706	0.0786	0.0683	0.0664	0.0836
1.0	0.0655	0.0706	0.0614	0.0595	0.0684
1.5	0.0517	0.0575	0.0500	0.0485	0.0512
2.0	0.0445	0.0493	0.0432	0.0424	0.0457
4.0	0.0307	0.0339	0.0310	0.0330	0.0420
8.0	0.0220	0.0240	0.0241	0.0295	0.0459
10.0	0.0202	0.0219	0.0229	0.0294	0.0489

^aData from Argonne National Laboratory, ANL-5800 (1963), Hubbell (1969), and Berger and Hubbell (1997), and Berger et al. (2010), available at National Institute of Standards and Technology (NIST): http://physics.nist.gov/cgi-bin/Xcom/xcom3_1.

$$\frac{I}{I_0} = \frac{1}{2} = e^{-1.34\mu} \quad (1.316)$$

If we employ four times the half-value thickness of lead or $4 \times 1.34 \text{ cm} = 5.36 \text{ cm}$, we can calculate that the transmitted radiation would be reduced to the following:

$$\frac{I}{I_0} = (e^{-1.34\mu})^4 = \left(\frac{1}{2}\right)^4$$

or

$$e^{-5.36\mu} = \frac{1}{16} = 0.0625 = 6.25\% \text{ transmitted}$$

The remaining 15/16 or 93.75% of the initial radiation is attenuated by the 5.36 cm lead barrier. In general, we need not know the half-value thickness of the material or shield, but simply obtain the linear or mass attenuation coefficient for a given energy of x- or gamma radiation from reference tables and use Eqns (1.307) or (1.312) to calculate the magnitude of radiation attenuation for any thickness of the absorber material. For example, if we used only 2.5 cm of lead barrier, the attenuation of 2.0 MeV gamma rays could be calculated as

$$\frac{I}{I_0} = e^{-\mu x} = e^{-\mu_m \rho x} \quad (1.317)$$

and

$$\begin{aligned} \frac{I}{I_0} &= e^{-(0.5182 \text{ cm}^{-1})(2.5 \text{ cm})} = e^{-(0.0457 \text{ cm}^2/\text{g})(11.3 \text{ g/cm}^3)(2.5 \text{ cm})} \\ &= e^{-1.29} = 0.275 = 27.5\% \end{aligned}$$

Thus, the 2.0 MeV radiation transmitted through a shield of 2.5 cm of lead would be 27.5% of the initial radiation intensity.

As previously discussed, the absorption of gamma radiation is a process that principally involves three mechanisms of attenuation: the Compton effect, the photoelectric effect, and pair production. The attenuation coefficients just discussed above are also referred to as total attenuation coefficients, because they consist of the sum of three independent coefficients or

$$\mu = \mu_c + \mu_e + \mu_p \quad (1.318)$$

where μ_c , μ_e , and μ_p are attenuation coefficients for Compton, photoelectric, and pair production processes. The attenuation coefficients are proportional to the probabilities of occurrence of these radiation attenuation processes and can be used as a measure of the relative roles these processes play in the absorption of gamma-ray photons.

Accordingly, the total and partial mass attenuation coefficients can be written as

$$\mu_m = \mu/\rho = \mu_c/\rho + \mu_e/\rho + \mu_p/\rho \quad (1.319)$$

Figs 1.81 and 1.82 provide a graphic representation of the relative frequency of occurrence of the Compton,

photoelectric, and pair production processes in aluminum and sodium iodide absorbers as a function of photon energy. From these curves, it is seen that the photoelectric effect plays an increasing role in total gamma-ray attenuation at lower gamma-ray energies and with absorber materials of higher atomic number. We can also note from these figures that pair production becomes significant at photon energies above 1 MeV, as the threshold energy for pair production is 1.022 MeV. Data on the total and partial mass attenuation coefficients as a function of photon energy for any element, chemical compound, mixture of elements, or mixture of compounds over the photon energy range of 1 keV to 10^5 MeV are available from the following website of the National Institute of Standards and Technology (NIST): <http://physics.nist.gov/PhysRefData/Xcom/html/xcom1.html>.

In some absorber materials of relatively high density, absorption edges can be measured for low photon energies, such as the *K* edge illustrated in Fig. 1.81. The absorption edge is a discontinuity in the attenuation coefficient curve for the photoelectric effect that is caused when photon energies are less than the binding energies of electrons of a certain shell (e.g., *K*-shell) and that reduces the number of electrons which may be ejected by the photoelectric effect. When photons possess the threshold binding energy of electrons of that shell, there is a sudden surge in attenuation owing to the ejection of electrons from that shell via photoelectric interactions. The photoelectric effect will occur primarily in the *K*-electron shell. At such photon energies ($>$ *K*-shell binding energy), the probability of the photoelectric effect occurring in the *L* shell is only about 20% and even less probable for outer shells (Friedlander et al, 1964). Such a phenomenon may appear strange, considering that the binding energies of the electrons are lower in shells further away from the nucleus. If one considers only the binding energies of the electrons, it would appear, although incorrectly, that for photon energies in excess of the *K*-shell binding energy, electrons further away from the nucleus (e.g., *L*, *M*, *N* shells) would be ejected as photoelectrons more easily. This is not the case, because energy and momentum must be conserved in the process, and the atom, because of its much higher mass, will carry off the excess momentum while taking away negligible energy in the process. The entire photon energy is transferred to the photoelectron less its binding energy. Consequently, the photoelectric effect cannot occur with a free electron, because there is no atom to carry off excess momentum, as demonstrated by Gautreau and Savin (1999). In the same sense, when the photon energy is much greater than the electron binding energy, the electrons, such as those in the outer shells with very low binding energies, act more like free electrons. These electrons contribute less to photon attenuation by the photoelectric effect. As explained by Lilley (2001), the conservation of energy and momentum is the reason why the most tightly bound electrons contribute most to photoelectric absorption for $E_\gamma > B_K$, where E_γ is the photon energy and B_K is the *K*-shell electron-binding energy, and also why there is a marked dependence of photon attenuation on photon energy and absorber atomic number. The photon absorption in NaI, illustrated in Fig. 1.82, shows a *K* edge at ~ 0.033 MeV or 33 keV. This corresponds to the electron binding energy in the *K*-shell of iodine, which from

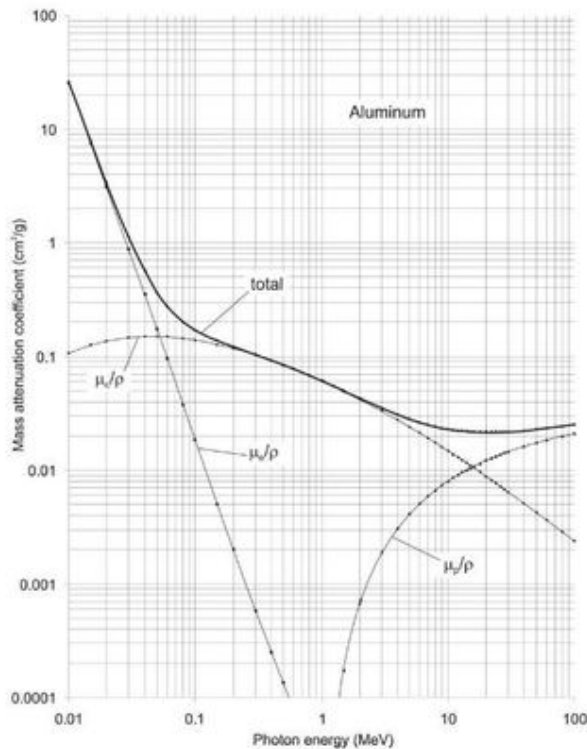


FIGURE 1.81 Mass attenuation coefficients for photons in aluminum. The total attenuation is given by the solid line, which is the sum of the partial attenuations due to the Compton effect, μ_e/ρ ; the photoelectric effect, μ_a/ρ ; and pair production, μ_p/ρ . (Drawn from data of Hubbel et al. (2010) available from the website of the National Institute of Standards and Technology (NIST): <http://physics.nist.gov/PhysRefData/Xcom/html/xcom1.html>)

reference tables (Lide, 2010) is reported to be 33169 eV or 33.1 keV. Photon attenuation by the photoelectric effect for photon energies in excess of 33 keV occur predominantly with the *K*-shell electrons. There is no *K* edge observed for sodium in Fig. 1.82 for the NaI absorber, because the binding energy of the *K* shell of sodium is only 1070 eV or 1.07 keV, a factor of 10 lower than the photon energy scale provided in the figure. At much lower photon energies, corresponding to *L*- and *M*-shell electron-binding energies, characteristic *L* and *M* edges can be observed. The binding energies of electrons in the various atomic electron shells of the elements are listed in reference tables, such as those provided by Lide (2010).

As illustrated in Figs 1.81 and 1.82, the pair production process does not occur at gamma-ray energies below the threshold value of 1.02 MeV, as expected, in accord with the combined positron and negatron rest energies (*i.e.*, 2×0.511 MeV) required for pair production. A thorough treatment of the attenuation and absorption of gamma radiation in matter is available from Hubbell (1969), Krane (1988), Lilley (2001), Serway et al (2005) and Turner (1995).

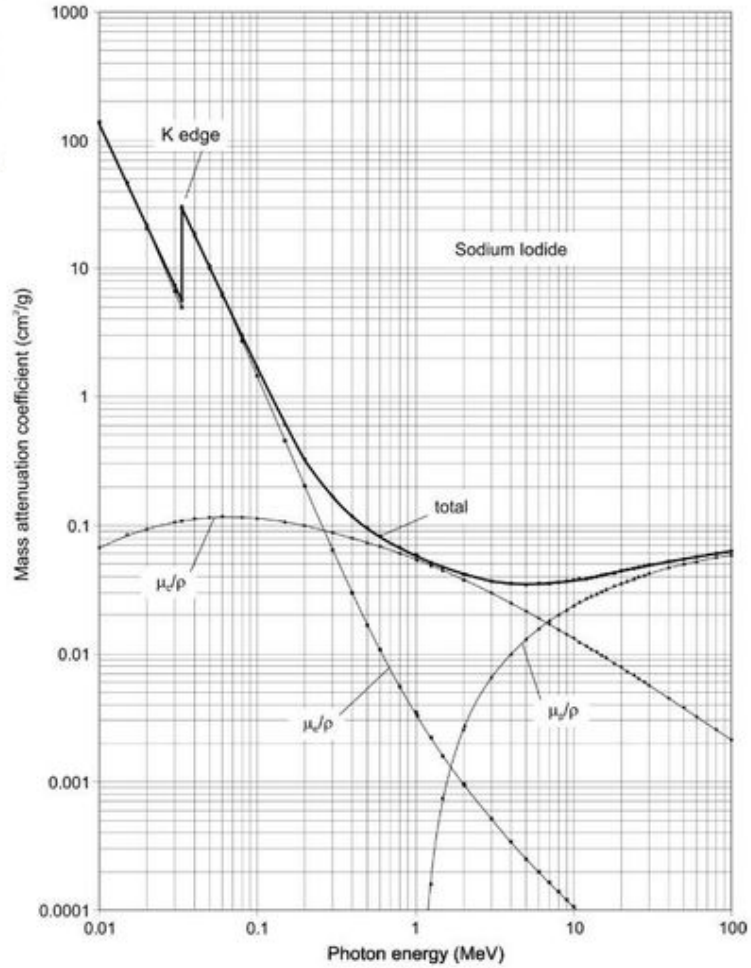
XI. RADIOACTIVE NUCLEAR RECOIL

When a decaying nucleus discharges or emits a particle such as an alpha particle, beta particle, gamma-ray or x-ray photon, or neutrino, the nucleus will recoil in a fashion somewhat like

a cannon recoils when it shoots a cannon ball from its barrel. The energy of recoil is a function of the mass and energy of the particle that is emitted as well as the mass of the nucleus. This may appear intuitively obvious, if we relate the process to that of a cannon, that is, the heavier the cannon for a given mass and velocity of cannon ball, the less will be the recoil energy. Even radionuclides that emit electrons or photons from their atomic shell, such as Auger electrons and x-rays, respectively, will experience some recoil effect, albeit much less than would occur when a heavy particle, such as the alpha particle, is emitted from a nucleus at high energy. Nuclear particles that collide also do so resulting in nuclear recoil. In accord with the principles of conservation of momentum, nuclear recoil will occur in all nuclear decay processes with the conservation of momentum between the emitted particle and the product nucleus, as illustrated in Fig. 1.83.

In various textbooks one can find reference to some equations for calculating nuclear recoil energies for some particular particle emissions. However, van Rooyen et al (2008) and Szucs et al (2009) provide relativistic and nonrelativistic expressions for all particle emissions including alpha particles, beta particles, Auger electrons, neutrinos, and gamma-ray and x-ray photons. Detailed derivations of the equations are not included by these authors, and the derivations will be provided here.

FIGURE 1.82 Mass attenuation coefficients for photons in sodium iodide. The total attenuation is given by the solid line, which is the sum of the partial attenuations due to the Compton effect, μ_c/ρ ; the photoelectric effect, μ_{pe}/ρ ; and pair production, μ_{pp}/ρ . (Drawn from data of Hubbel et al. (2010) available from the website of the National Institute of Standards and Technology (NIST): <http://physics.nist.gov/PhysRefData/Xcom/html/xcom1.html>)



A. Relativistic Expressions

When a particle is emitted by a decaying nucleus, it possesses a kinetic energy (K_p), which is the difference of the total particle energy (E_p) and its rest energy ($m_p c^2$) or

$$K_p = E_p - m_p c^2 \tag{1.320}$$

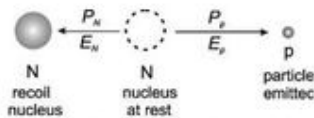


FIGURE 1.83 Nuclear recoil resulting from the energy imparted to a nucleus (N) at rest (dashed circle) by the emission of a particle (p) by the nucleus. Conservation of energy and momentum requires that the energy of the nucleus at rest be equal to the energy of the recoil nucleus + the energy of the emitted particle, i.e., E_N (at rest) = E_N (recoil) + E_p ; and the momentum of the recoil nucleus P_N is equal to the momentum of the emitted particle P_p , i.e., $P_N = P_p$.

And if the expression of energy, momentum, and particle mass is written as (See Eqn (1.260))

$$E_p^2 = p_p^2 c^2 + (m_p c^2)^2 \tag{1.321}$$

where p_p is the particle momentum and c is the speed of light in a vacuum. From Eqns (1.320) and (1.321), we can write

$$(K_p + m_p c^2)^2 = p_p^2 c^2 + (m_p c^2)^2 \tag{1.322}$$

which becomes

$$K_p^2 + 2m_p c^2 K_p + (m_p c^2)^2 = p_p^2 c^2 + (m_p c^2)^2 \tag{1.323}$$

and reduces to

$$K_p^2 + 2m_p c^2 K_p = p_p^2 c^2 \tag{1.324}$$

Solving Eqn (1.324) for the particle momentum gives

$$p_p = \frac{\sqrt{K_p^2 + 2m_p c^2 K_p}}{c} \quad (1.325)$$

According to the laws of conservation of momentum, we can write

$$p_N = p_p \quad (1.326)$$

where p_N is the momentum of the nucleus as a result of the emission of the particle. From Eqns (1.325) and (1.326), we can equate the expressions for the nuclear and particle momentums as

$$\frac{\sqrt{K_N^2 + 2m_N c^2 K_N}}{c} = \frac{\sqrt{K_p^2 + 2m_p c^2 K_p}}{c} \quad (1.327)$$

where K_N and m_N are the kinetic energy and mass, respectively, of the recoil nucleus. If the total energy of the nucleus (E_N), in terms of its momentum and mass, is written according to Eqn (1.321),

$$E_N^2 = p_N^2 c^2 + (m_N c^2)^2 \quad (1.328)$$

and with $p_N = p_p$, we can express the total energy of the nucleus as

$$E_N^2 = \left(\frac{\sqrt{K_p^2 + 2m_p c^2 K_p}}{c} \right)^2 c^2 + (m_N c^2)^2 \quad (1.329)$$

which becomes

$$E_N^2 = K_p^2 + 2m_p c^2 K_p + m_N^2 c^4 \quad (1.330)$$

Eqn (1.330) is reduced to the simple expression of the total energy of the nucleus as

$$E_N = \sqrt{K_p^2 + 2m_p c^2 K_p + m_N^2 c^4} \quad (1.331)$$

If by definition, the kinetic energy of the nucleus K_N , that is, it's recoil energy, is the difference of its total energy, E_N , and its rest energy, $m_N c^2$, then

$$K_N = E_N - m_N c^2 \quad (1.332)$$

From Eqns (1.331) and (1.332), we can arrive at the final expression for the kinetic energy of the recoil nucleus in terms of the particle kinetic energy (K_p), particle mass (m_p), and mass of the recoil nucleus (m_N) to be

$$K_N = \sqrt{K_p^2 + 2m_p c^2 K_p + m_N^2 c^4} - m_N c^2 \quad (1.333)$$

Eqn (1.333) is the fully relativistic expression for the calculation of the nuclear recoil energy for particle emissions that possess nonzero rest mass, such as alpha particles, beta particles, and Auger electrons. For particle emissions consisting of gamma-

ray and x-ray photons, which have a zero rest mass, the term $2m_p c^2 K_p$ will fall out of Eqn (1.333), and in the case of the neutrino, which has a near-zero rest mass, the term $2m_p c^2 K_p$ becomes negligible and can be dropped out of Eqn (1.333) so that it simplifies to

$$K_N = \sqrt{K_p^2 + m_N^2 c^4} - m_N c^2 \quad (1.334)$$

Eqn (1.334) is thus used to calculate the nuclear recoil energies for gamma-ray photon, x-ray photon, or neutrino emissions. We should keep in mind that the recoil nucleus is that of the daughter nucleus, because it is the daughter nucleus that recoils after the nucleus discharges or expels a particle.

B. Nonrelativistic Expressions

1. Nuclear Recoil Energy from Alpha-particle Emissions

For relatively very heavy particles, such as the alpha particle, the more simple nonrelativistic calculation of the nuclear recoil energy may also be used. The nonrelativistic expression of the nuclear recoil energy for alpha-particle emissions is derived subsequently. The nonrelativistic expression of the kinetic energy of the alpha particle is defined as

$$K_\alpha = \frac{1}{2} m_\alpha v^2 \quad (1.335)$$

where m_α and v are the mass and velocity of the particle, respectively. Its nonrelativistic momentum would be simply

$$p_\alpha = m_\alpha v \quad (1.336)$$

Multiplying Eqn (1.335) by $2m_\alpha$ gives

$$2m_\alpha K_\alpha = (m_\alpha v)^2 = p_\alpha^2 \quad (1.337)$$

Eqn (1.337) relates the alpha-particle mass, energy, and momentum. Conservation of momentum of the alpha particle (p_α) and recoil nucleus (p_N) dictates

$$p_\alpha = p_N \quad (1.338)$$

and then from Eqns (1.337) and (1.338), we can write

$$\sqrt{2m_\alpha K_\alpha} = \sqrt{2m_N K_N} \quad (1.339)$$

where m_N and K_N are the mass and kinetic energies of the recoil nucleus. Squaring both sides of Eqn (1.339) and solving for K_N gives

$$K_N = \left(\frac{m_\alpha}{m_N} \right) K_\alpha \quad (1.340)$$

Eqn (1.340) was used in Section VIII.A.2 Eqn (1.89) for the calculation of the recoil energy resulting from the 5.545 MeV alpha particle emitted from ^{241}Am . The relativistic expression, provided in Eqn (1.333), yields the same result.

2. Nuclear Recoil Energy from Gamma-ray, X-ray, and Neutrino Emissions

For gamma-ray photons and x-ray photons, which have zero rest mass, and neutrinos, which have near-zero rest mass, we can express their momentum (See Eqn (1.262)) as

$$p_p = \frac{E_p}{c} \tag{1.341}$$

where p_p is the momentum of the gamma-ray photon, X-ray photon, or neutrino, E_p is the particle energy, and c is the speed of light in a vacuum. If the nonrelativistic expression of the kinetic energy of the recoil nucleus is

$$K_N = \frac{1}{2} m_N v^2 \tag{1.342}$$

where K_N is the kinetic energy of the recoil nucleus, m_N is the mass of the recoil nucleus and v is its velocity. Multiplying both sides of Eqn (1.342) by $2m_N$ gives

$$2m_N K_N = (m_N v)^2 = p_N^2 \tag{1.343}$$

where p_N is the momentum of the recoil nucleus. As momentum is conserved, we can write

$$p_N^2 = p_p^2 = 2m_N K_N = \frac{E_p^2}{c^2} \tag{1.344}$$

Solving Eqn (1.344) for the kinetic energy of the recoil nucleus gives

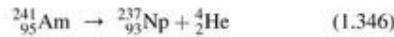
$$K_N = \frac{1}{2} \left(\frac{E_p^2}{m_N c^2} \right) \tag{1.345}$$

where E_p^2 is the energy of the gamma-ray photon, X-ray photon, or neutrino, and m_N is the mass of the recoil nucleus.

C. Sample Calculations

1. Nuclear Recoil from Alpha Emissions

Earlier in this chapter (Section VIII.A.2, Eqn (1.89)), the nonrelativistic expression for the recoil energy was used to determine the recoil energy imparted to a nucleus as a result of alpha-particle emission of 5.545 MeV that occurs in the following decay of ^{241}Am :



The relativistic expression provided by Eqn (1.333) will be used. Since nuclear recoil occurs after the nucleus emits a particle, it is the daughter nuclide that recoils. We will use atomic mass units (u) and the conversion factor of 931.494013 MeV/u to convert mass to energy units. Relevant data from nuclear tables (e.g., Lide, 2010) are the mass of the alpha particle and that of ^{237}Np which are 4.00150617 u

and 237.048166 u, respectively. Thus, from Eqn (1.333), the nuclear recoil energy is calculated as

$$K_N = \sqrt{K_p^2 + 2m_p c^2 K_p + m_N^2 c^4} - m_N c^2$$

$$= \left\{ \begin{aligned} & (5.545 \text{ MeV})^2 + 2(4.00150617 \text{ u}) \\ & \times (931.494013 \text{ MeV/u})(5.545 \text{ MeV}) \\ & + [(237.048166 \text{ u})(931.494013 \text{ MeV/u})]^2 \end{aligned} \right\}^{1/2}$$

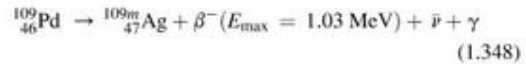
$$- (237.048166 \text{ u})(931.494013 \text{ MeV/u})$$

$$= 0.0936 \text{ MeV} \tag{1.347}$$

The recoil energy of 0.0936 MeV agrees with the nonrelativistic calculation made earlier in Section VIII.A.2 (see Eqn (1.89)). The nuclear recoil energy is 1.68 % of the alpha-particle energy. In general, the nuclear recoil energy resulting from alpha-particle emissions are about 2% of the alpha-particle energy. This is relatively high for recoil energies, which is characteristic of alpha-particle emissions, because the alpha particle is massive. We will notice much smaller nuclear recoil energies resulting from beta-particle emission energies of similar energies to the alpha particle. This is because the alpha particle is massive compared to the electron or beta particle. The mass of the alpha particle is 7294 times that of the electron (i.e., $m_e = 4.00150617 \text{ u}/0.000548579 \text{ u}$). An analogy can be made by comparing the recoil imparted to a cannon upon firing a cannon ball compared to the kick imparted to a pistol upon firing a 0.45 caliber bullet.

2. Nuclear Recoil from Beta Emissions

Let us calculate the recoil energy imparted to a nucleus by the emission of a beta particle. The following decay of ^{109}Pd by beta-particle emission may serve as an example:



Beta particles are emitted with a broad spectrum of energies from zero to E_{max} , because the decay energies are shared with a neutrino. We will select the maximum energy (1.03 MeV) that the negative beta particle may possess when the antineutrino energy is at its minimum (near zero) in order to calculate the maximum recoil energy that the particle may impart to the nucleus. We will not calculate here any nuclear recoil energy that the gamma ray may impart to the nucleus. Again, as in the previous example, the nucleus that undergoes the recoil is that of the daughter nuclide, because it is the daughter that is produced when the beta particle is emitted from the nucleus. Also, we will use the relativistic expression of the recoil energy Eqn (1.333) for the calculation. Relevant data from nuclear reference tables for the calculation are the mass of the beta particle (i.e., electron mass) and that of ^{109m}Ag , which are 0.000548579 u and 108.904756 u, respectively. The nuclear recoil energy is calculated as

$$\begin{aligned}
 K_N &= \sqrt{K_p^2 + 2m_p c^2 K_p + m_N^2 c^4 - m_N c^2} \\
 &= \left\{ \begin{aligned} &\sqrt{(1.03 \times 10^6 \text{ eV})^2 + 2(5.48579 \times 10^{-4} \text{ u})} \\ &\quad (931494013 \text{ eV/u})(1.03 \times 10^6 \text{ eV}) \\ &\quad + [(108.904756 \text{ u})(931494013 \text{ eV/u})]^2} \\ &\quad - (108.904756 \text{ u})(931494013 \text{ eV/u}) \end{aligned} \right\} \\
 &= 10.41 \text{ eV}
 \end{aligned}
 \tag{1.349}$$

As we see from this example, the previous example, and from Table 1.22, the energies imparted by the massive alpha particles to recoil nuclei are measured in the tens of thousands of electron

volts; whereas, energies imparted by the relatively miniscule beta particle range mostly from a few to several hundred electron volts, and energies imparted to nuclei by gamma-ray and x-ray photons and neutrino emissions are yet smaller.

3. Nuclear Recoil from Gamma-ray Photon, X-ray Photon, or Neutrino Emissions

Let us consider an example of a nuclide that decays exclusively by electron capture with the emission of neutrinos and gamma radiation. The nuclide ⁷Be decays to ⁷Li with the emission of neutrinos of 0.862 MeV at 89.6% relative intensity and 0.384 MeV at the remaining 10.4% intensity. The ⁷Li daughter nuclides resulting from the lower 0.384 MeV neutrino

TABLE 1.22 Recoil Energies in Electron Volts (eV) Imparted to Nuclei of Various Masses by Emitted Particles of Various Energies in MeV

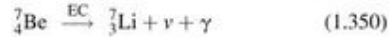
Alpha particles ^a					
Nuclear mass	$E_\alpha = 1.5 \text{ MeV}$	$E_\alpha = 2 \text{ MeV}$	$E_\alpha = 4 \text{ MeV}$	$E_\alpha = 6 \text{ MeV}$	$E_\alpha = 8 \text{ MeV}$
150 u	4.0E4 eV	5.3E4 eV	10.7E4 eV	16.0E4 eV	21.3E4 eV
175	3.4E4	4.6E4	9.1E4	13.7E4	18.3E4
200	3.0E4	4.0E4	8.0E4	12.0E4	16.0E4
225	2.7E4	3.6E4	7.1E4	10.7E4	14.2E4
250	2.4E4	3.2E4	6.4E4	9.6E4	12.8E4
Beta particles ^b					
Nuclear mass	$E_\beta = 0.5 \text{ MeV}$	$E_\beta = 1 \text{ MeV}$	$E_\beta = 2 \text{ MeV}$	$E_\beta = 4 \text{ MeV}$	$E_\beta = 6 \text{ MeV}$
10 u	40.84 eV	108.35 eV	324.42 eV	1078.27 eV	2261.53 eV
20	20.42	54.27	162.21	539.13	1130.76
50	8.17	21.71	64.88	215.65	452.30
100	4.08	10.85	32.44	107.82	226.15
150	2.72	7.23	21.63	71.88	150.77
200	2.04	5.43	16.22	53.91	113.08
250	1.63	4.34	12.98	43.13	90.46
Gamma-ray, x-ray photons or neutrinos ^c					
Nuclear mass	$E_\gamma = 0.5 \text{ MeV}$	$E_\gamma = 1 \text{ MeV}$	$E_\gamma = 2 \text{ MeV}$	$E_\gamma = 4 \text{ MeV}$	$E_\gamma = 6 \text{ MeV}$
10 u	13.42 eV	53.68 eV	214.71 eV	858.83 eV	1932.38 eV
20	6.71	26.84	107.35	429.42	966.19
50	2.68	10.74	42.94	171.77	386.47
100	1.34	5.37	21.47	85.88	193.24
150	0.89	3.58	14.32	57.25	128.82
200	0.67	2.68	10.74	42.94	96.62
250	0.54	2.15	8.59	34.35	77.29

^aNuclear recoil energies resulting from alpha-particle emission are expressed in exponential form. For example, the nuclear recoil energy imparted to a nucleus of mass 150 u by an alpha-particle emitted with energy of 1.5 MeV is 4.0E4 or 4.0×10^4 eV. Also, nuclear recoil energies for nuclear masses of < 150 u are not listed for alpha-particle emissions, because only nuclei of relatively high mass ($A > 140$ u) are unstable to alpha-particle emission. The recoil energies resulting from alpha-particle emissions were calculated by Eqn (1.340), i.e., $K_N = (m_\alpha/m_N)K_\alpha$.

^bThe recoil energies resulting from beta-particle emissions were calculated according to Eqn (1.333), i.e., $K_N = \sqrt{K_\beta^2 + 2m_\beta c^2 K_\beta + m_N^2 c^4} - m_N c^2$.

^cRecoil energies resulting from gamma-ray photon, x-ray photon or neutrino emissions were calculated according to Eqn (1.334), i.e., $K_N = \sqrt{K_\gamma^2 + m_N^2 c^4} - m_N c^2$.

emissions decay to the ground state with the emission of gamma radiation of 0.478 MeV. The decay scheme of ${}^7\text{Be}$ is illustrated in Fig. 1.39 and the decay equation is the following:



We can use Eqn (1.334) to calculate the nuclear recoil energy resulting from the emission of a neutrino or gamma-ray photon. Let us calculate the recoil energy imparted to the ${}^7\text{Li}$ nucleus resulting from the emission of a 0.862 MeV neutrino. The mass of ${}^7\text{Li}$ obtained from physical data tables is 7.016004 u and the constant for conversion of mass units to energy is 931.494013 MeV/u.

$$K_N = \sqrt{K_p^2 + m_N^2 c^4} - m_N c^2$$

$$K_N = \left\{ \sqrt{\frac{(8.62 \times 10^5 \text{ eV})^2 + [(7.016004 \text{ u})(931.494013 \text{ eV/u})]^2}{(7.016004 \text{ u})(931.494013 \text{ eV/u})}} \right\} \quad (1.351)$$

$$= 56.84 \text{ eV}$$

This calculated value is in agreement with the experimental measurement of the ${}^7\text{Li}$ recoil energy of $56 \pm 1 \text{ eV}$ by 2002 Physics Nobel Laureate Raymond Davis Jr. (See Davis, 1952). The recoil energy is higher than that calculated above for the recoil energy imparted by the beta-particle emission to a ${}^{109m}\text{Ag}$ nucleus Eqn (1.349), because of the relatively small mass of the ${}^7\text{Li}$ nucleus. We can see from Table 1.22 that when comparing particle emissions of the same mass and energy, higher recoil energies will result with nuclei of smaller mass.

D. Radioactive Recoil Effects

The implications of nuclear recoil are numerous including applications of hot-atom chemistry where chemical bonds are broken by recoiling nuclei facilitating the preparation of high specific activity radionuclides by means of the Szilard–Chalmers effect. Also, nuclear recoil during radioactive decay of naturally occurring radionuclides can create disequilibrium when the recoil liberates the nuclide from its mineral lattice. These recoil effects will be discussed subsequently.

1. Szilard–Chalmers Process

Prior to discussing the Szilard–Chalmers process, which is important in the preparation of radionuclides with high specific activity, the historical background that led to its discovery is relevant and will be presented briefly. A more thorough account is given in a previous book by the author (L'Annunziata, 2007). On September 12, 1933, Leo Szilard (1898–1964) read a news report in the *The Times* where Ernest Rutherford was interviewed. The reporter had asked Rutherford what were his thoughts concerning nuclear transmutations and nuclear energy. Rutherford replied that charged particles, such as the proton, could eventually be accelerated with sufficient high voltage to eventually transform all of the elements. He added that the

energy released would be too small to produce energy on a large scale for power and anyone who looked for transmutation as a source of power was talking “moonshine”. Szilard agreed with Rutherford's comments concerning accelerated protons that these would not be a useful source of energy. He knew that the proton had to overcome the Coulombic barrier of its repelling positive charge with that of the atomic nucleus. However, he thought that the neutron, because of its neutral charge, should be able to penetrate the Coulombic barrier of an atom and collide with the nucleus without any external force and cause a reaction or transmutation of the nucleus. Szilard's mind was restless, while standing at a street corner in London in the following month of October and during the time that it took a traffic light to change, the idea of the possibility of a neutron-induced nuclear chain reaction hit him. Szilard knew that in chemistry, there existed chain reactions where one reaction could yield two products that could further interact with other reactants to produce four products and these could react to produce eight products, etc. resulting in an exponential increase in reactions. The chain reactions could be very numerous and limited only by the quantity of reactants available. He thought that if a chain reaction with neutrons could occur, that is, if a neutron would be able to interact with an atomic nucleus to produce more than one neutron and the additional neutrons created would interact with other atomic nuclei to produce yet more neutrons, a chain reaction would ensue and a tremendous amount of energy could be liberated. Szilard could foresee that the initial neutron reaction and the resultant multiplication of neutrons should occur in a very short period of time, in microseconds, as nuclear reactions would be fast, producing an explosion of unforeseeable magnitude. Leo Szilard was the first to conceive the possibility of obtaining large amounts of energy and even an explosion from nuclear transmutations.

Having formulated further his initial idea of the potential energy that could be released from neutron-induced chain reactions on March 12, 1934, Szilard filed for a patent, which contained the basic concepts of a nuclear chain reaction, the concept of “critical mass”, that is, the minimum mass of a material required for a sustained nuclear chain reaction, and the “explosion” that could result. He was awarded British Patent No. 630,726 entitled *Improvements in or Relating to the Transformation of Chemical Elements*. In his patent Szilard described the concept of critical mass in his statement “If the thickness is larger than the critical value...I can produce an explosion.” (Feld and Weiss-Szilard, 1972, Loeber, 2002). Otto Hahn, Fritz Strassmann, and Lise Meitner had not discovered nuclear fission until 1939. Consequently, the fissile materials required to produce neutron-induced nuclear chain reactions had not yet been discovered and there is no record of any such nuclear chain reactions ever been discussed prior to Szilard's patent. Szilard was clearly ahead of his time. The patent, as written by Szilard, stated “This invention has for its object the production of radioactive bodies and the liberation of nuclear energy for power production and other purposes through nuclear transmutation.” (Feld and Weiss-Szilard, 1972) Szilard was a pacifist and idealist, and the objective of his patent was not personal gain but for control over the harmful use of nuclear weapons. After a year's time, he convinced the British government to accept the

patent in order to keep the concepts of the patent secret and inaccessible to the world. Later in life Leo Szilard joined the Manhattan Project, which was the secret American project for the production of the atomic bomb, out of fear that Germany could become the first to acquire the weapon. Rhodes (1986) and Loeber (2002) point out that Szilard tried to use his patent as a means to gain control of the decision-making process for the atomic bomb. He felt that the control of the bomb and its use should be in the hands of the wisest scientists and not in the hands of government officials. Rhodes (1986) noted that the U.S. government rejected Szilard's claim to the atomic bomb on simple legalistic grounds, because he did not disclose the existence of his patent before joining the Manhattan Project.

When Szilard first conceived of neutron-induced fission in 1933, he did not know what element or isotope would undergo such fission. His patent had made a slight mention of uranium and thorium, but his thoughts were mistakenly on beryllium. He therefore started a search for the chain-reacting element. With this in mind, Szilard began a collaboration of nuclear research with T. H. Chalmers at the Physics Department of the Medical College of St. Bartholomew's Hospital, London. This research did not lead to the discovery of the neutron-induced chain reaction, but led to other important discoveries, including (i) the discovery of a photoneutron (γ, n) source, that is, the induction of neutron emission by gamma or x-radiation and (ii) the Szilard–Chalmers effect, which is the rupture of a chemical bond between an atom and a molecule of which the atom is a constituent, as a result of nuclear recoil during radioactive decay of that atom. The Szilard–Chalmers effect led to the Szilard–Chalmers process or reaction, which has enabled the isolation of high-specific activities of radionuclides. The two discoveries and their applications will be discussed subsequently.

In his search for neutron emission that might initiate a neutron-induced chain reaction, Leo Szilard and T.H. Chalmers irradiated beryllium with radium gamma rays. They discovered a radiation from the beryllium that would induce radioactivity in iodine and concluded that neutrons were emitted from the beryllium by the gamma rays (Szilard and Chalmers, 1934a,b, 1935). Their report was the first where neutron emission was initiated by gamma radiation, and the reaction that they observed can be abbreviated as



which reads

${}^9\text{Be}$ target nuclide (gamma-ray projectile, neutron emitted) ${}^8\text{Be}$ product nucleus.

This discovery was significant, because today photoneutron (γ, n) sources are useful portable sources of neutrons. A very common neutron source of this nature used today is the mixture of ${}^{124}\text{Sb} + \text{Be}$ where the gamma rays from ${}^{124}\text{Sb}$ yield neutrons via a photoneuclear reaction (see Table 1.13).

Szilard and Chalmers (1934b) used iodine as the indicator for neutrons as the neutrons would induce radioactivity in iodine by creating radioiodine via neutron capture. A subsequent work was reported shortly thereafter by Brasch and coworkers together with Szilard and Chalmers and assistance of Lise Meitner in Berlin (Brasch et al., 1934) whereby the neutron

emission from beryllium was induced by x-ray photons and neutron capture by bromine, and the isolation of the product nuclide, radiobromine, was used as the neutron indicator.

An important outcome of this work was the discovery of the Szilard–Chalmers process whereby radionuclides may be easily separated and isolated from their parent atoms and consequently high specific activities of radionuclides may be obtained which otherwise would be difficult when both the target and product atoms are isotopes. For example, Szilard and Chalmers (1934 a,b.) surrounded 150 mg of radium (gamma-ray source) with 25 g of beryllium in a sealed container of 1-mm-thick platinum. The Ra–Be neutron source was immersed in 100 mL of ethyl iodide. The neutrons produced radioactive ${}^{128}\text{I}$ from stable ${}^{127}\text{I}$ by neutron capture. The ${}^{128}\text{I}$ would precipitate as radioactive silver iodide (Ag^{128}I) after the addition of water containing silver ions (Ag^+). However, a control experiment without the neutron source produced no radioactivity over background in the silver iodide precipitate. This experiment indicated that the chemical bond between the carbon atom of the ethyl group and the ${}^{128}\text{I}$ was broken after ${}^{127}\text{I}$ neutron capture, because free unbound ionic ${}^{128}\text{I}^-$ would precipitate with the Ag^+ to produce radioactive Ag^{128}I precipitate in the aqueous phase according to the sequence illustrated in Fig. 1.84

The energy of bonding between the carbon and iodine atoms is about 2 eV, which is higher than the neutron recoil energy. Consequently, the rupture of this bond is due to the gamma-recoil when the ${}^{128}\text{I}$ undergoes gamma emission upon de-excitation after neutron capture. Some atoms of ${}^{128}\text{I}$ could recombine with the free ethyl group and even exchange with some stable atoms of ${}^{127}\text{I}$, but if these processes are slow and if

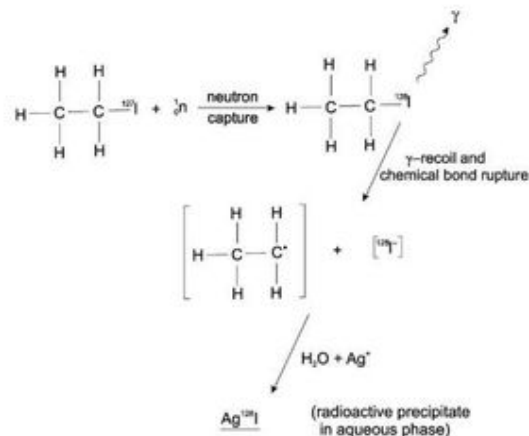


FIGURE 1.84 Szilard–Chalmers Process. High specific activity ${}^{128}\text{I}$ is separated from the stable ${}^{127}\text{I}$ as a result of the Szilard–Chalmers Effect. The capture of a neutron by the stable isotope ${}^{127}\text{I}$ in the ethyl iodide molecule created radioactive ${}^{128}\text{I}$. The neutron capture process leaves the ${}^{128}\text{I}$ nucleus in an excited state, which emits a gamma-ray upon de-excitation. The gamma-recoil causes a rupture of the chemical bond between the carbon atom of the ethyl group and the ${}^{128}\text{I}$ thereby liberating the ${}^{128}\text{I}$ as an anion. The addition of water containing silver cations (Ag^+) to the organic solution enables the ionic ${}^{128}\text{I}^-$ to enter the aqueous phase and separate out as precipitated Ag^{128}I . The radioactivity of ${}^{128}\text{I}$ is detected by its beta-particle emissions; and it decays with a half-life of 25 minutes.

these processes are further reduced by the addition of water or even alcohol to dilute the organic phase, the precipitate of radioactive inorganic iodide proceeds yielding a highly enriched radioactive ^{128}I with minimal ^{127}I .

The Szilard–Chalmers process remains to this day a very practical application to the isolation of high specific activity radioactive sources from the medium in which the radionuclide sources were synthesized. A few examples taken from the literature are an editorial review by Eckelman et al (2008), the isolation of high specific activity radioisotopes after cyclotron production (Bonardi, et al, 2004, Birattari, et al, 2001), the preparation of high specific activity ^{64}Cu (Van Elteren et al, 1999, Gielow, 1990, Barnes et al, 1986, Hetherington, et al, 1986, and Sekine, 1986), the production of high specific activity ^{166}Ho (Zeisler, and Weber, 1998), the preparation of high specific activity $^{117\text{m}}\text{Sn}$ for medical applications (Mausner et al, 1992), high specific activity ^{186}Re (Jia and Ehrhardt, 1997), the optimized production of ^{18}F (Alfassi et al, 1986), high specific activity radiohalonium complexes (Abbe and Marques-Netto, 1975 and Marques-Netto and Abbe, 1975), high specific activity ^{51}Cr (Harbottle, 1954 and Green and Maddock, 1949), high specific activity ^{56}Mn (Zahn, 1967a,b), high specific activity radioisotopes of tin (Spano and Kahn, 1952), the concentration of high specific activities of the radioisotopes of Groups IV and V elements (Murin and Nefedov, 1955), and the production of high specific activity ^{99}Mo and ^{90}Y (Tomar et al, 2010).

2. Radioactive Disequilibrium

When chemical bonds are broken after radioactive nuclear recoil, the recoiling nucleus may be displaced from the chemical structure (e.g., mineral lattice) within which it resided. The liberated nuclide, which may be part of a natural decay chain, may then be leached from mineral deposits into ground water creating disequilibrium among the natural radionuclides. For example, Labidi et al (2010) measured the isotopic levels of $^{234}\text{U}/^{238}\text{U}$ and $^{226}\text{Ra}/^{234}\text{U}$ in waters of Tunisia and found a disequilibrium between the two members of the ^{238}U decay series, which may be due to the direct action of nuclear recoil during radioactive decay and preferential leaching. This decay series was discussed and illustrated previously in Fig. 1.20. The researchers estimated the annual effective radiation doses due to the ingestion of the mineral waters to be well below the 0.1 mSv/year reference dose level. Fernandez et al (2006) studied the radioecological characteristics of a uranium mining site in Brazil and point out that, as suggested by Ivanovich (1994) and Ivanovich and Harmon (1992), disequilibrium between Ra and U isotopes may be due to (i) precipitation/dissolution reactions, (ii) alpha recoil, (iii) diffusion, and (iv) the Szilard–Chalmers effect. The activity ratios of $^{234}\text{U}/^{238}\text{U}$ were studied by Paces et al (2002) for evidence of ground-water flow patterns in the USA and acknowledge that ^{234}U enters solution preferentially from rocks as a result of mechanisms related to its origin by radioactive decay of ^{238}U , including alpha recoil damage of crystal-lattice sites containing ^{234}U and the Szilard–Chalmers effect as well as radiation-induced oxidation of ^{234}U . Similar disequilibrium effects of natural radioactivity, that may be due to nuclear recoil following alpha

decay in the ^{238}U decay series, was observed by Dowell and O’Dea (2002) and Davis and Krogh (2000). Disequilibrium among radionuclides in the natural decay series was underscored by Adloff (1989) to occur by “natural Szilard–Chalmers reactions” all along the radioactive decay series and that this is triggered mostly by nuclear recoil effects after alpha decay. Adloff summarizes that these effects have found a wide range of applications in environmental studies such as geochronology, weathering, sedimental processes, and oceanic chemistry.

XII. COSMIC RADIATION

Stable charged particles and nuclei with lifetimes of 10^6 years or longer originating from space, that strike the top of the atmosphere (TOA) from all directions, constitute what is known as the cosmic radiation. Air showers of the cosmic radiation consist of cascades of subatomic particles and electromagnetic radiation resulting from nucleon–nucleon collisions of high-energy cosmic-ray particles from space with atomic nuclei of the earth’s atmosphere. Cosmic rays are classified according to their origin in space, and the air showers of the cosmic radiation are characterized according to the products of collisions of high-energy cosmic-ray particles and nuclei with atoms of the earth’s atmosphere.

The discovery of cosmic radiation is attributed to Victor Hess, who made seven balloon ascents during 1911–1913 into the atmosphere during the daytime, during the evening darkness, and even during a solar eclipse. On these ascents he took along three electroscopes that would measure the ionization caused by external radiation. He thought it is best to make simultaneous measurements of ionization with more than one instrument to eliminate doubt in the event one instrument might give erroneous readings. Hess found that at an altitude of 500 meters, the ionization dropped to about half that obtained from the soil surface. However, the readings would increase proportionally with altitude as he would ascend beyond 1000 meters. He found that the ionization at 1500 meters would increase to be approximately equal to that at the soil surface, and further ascents to altitudes of 5000 meters would provide ionization readings of several times that at the ground level (Hess, 1912, 1936, 1940). It was obvious to Hess that gamma rays, from radium in air, could not cause any increase in ionization with altitude where air got thinner, and he interpreted his results in the following words:

The only possible way to interpret my experimental findings was to conclude to the existence of a hitherto unknown and very penetrating radiation, coming mainly from above and being most probably of extraterrestrial (cosmic) origin...

Victor Hess was awarded the Nobel Prize in 1936 for his discovery of cosmic radiation.

The dose to the human body from cosmic radiation is of concern to astronauts, airline pilots, and persons living at high altitudes, as our atmosphere attenuates considerably cosmic radiation and the dose to the human body consequently increases with altitude. Cosmic radiation is also of much concern as background interference in the measurement of low levels of radioactivity. The accurate measurement of

radionuclides in our environment requires the suppression and accurate measurement of the background interference from cosmic rays.

A. Classification and Properties

Cosmic radiation incident on the earth's atmosphere is classified into "primary" or "secondary" cosmic rays. As defined by Gaisser and Stanev (2002), primary cosmic rays are stable charged particles and nuclei accelerated at astrophysical sources, and secondary rays are particles produced via the interaction of the primaries with interstellar gas. The nuclear interactions of the accelerated primary cosmic-ray particles with interstellar medium produce stable nuclei of the light elements (e.g., Li, Be, and B), as well as many fundamental particles including pions or π mesons of zero charge (π^0), that decay into gamma rays (see Eqns (1.367) and (1.368)). Galactic gamma radiation has been mapped recently by the Compton Gamma Ray Observatory satellite. The satellite has provided an image of the galaxy produced by gamma rays of approximately 100 MeV (Simpson, 2001). The gamma-ray image compares closely to the visible-light image of the galaxy of which we are most familiar. Galactic gamma rays can cover the full energy range from <100 MeV to >10 TeV.

Primary cosmic-ray particles include protons, helium nuclei, electrons, and nuclei of most elements of the periodic table (e.g., carbon, iron, oxygen, etc) of stellar origin. Nuclei of the light elements lithium, beryllium, and boron ($Z = 3-5$) are classified as secondary radiation. The abundance of these light elements in cosmic radiation is highly enriched over the abundance of these elements in the universe, which is evidence that these are secondary nuclei created via collision (nuclear spallation interactions) with heavier primary particles during the interstellar propagation of primary nuclei. The radionuclide ^{10}Be ($t_{1/2} = 1.6 \times 10^6$ y) is found among other isotopes of the light elements in cosmic rays. From the measured abundance analysis of ^7Be , ^9Be , and the radioactive ^{10}Be in cosmic radiation, it is found that cosmic-ray particles remain contained in galactic magnetic fields for approximately 10^7 years before escaping into our atmosphere or inter-galactic space. The mean interstellar density for propagation of the cosmic radiation is ~ 0.2 atom/cm³ (Simpson, 2001).

Nucleons of practically all elements of the periodic table will be found in cosmic radiation. Free protons account for about 80% of the primary nucleons and approximately 15% are nucleons bound in helium nuclei (equivalent to alpha particles). Electrons constitute about 2% of the primaries. Nuclei of the elements of the periodic table other than the previously mentioned (H and He) make up the remaining components of cosmic radiation. Nuclei of the light elements (Li, Be, and B), which constitute secondary cosmic ray particles, account for a small fraction ($\sim 0.2\%$) of cosmic ray nuclei (see Table 1.23).

The composition of cosmic radiation will vary according to the 11-year solar cycle and the earth's magnetic latitude (Potgieter, 2008a,b). The earth's magnetic field, which extends well into space, affects the composition of the charged particles of cosmic radiation. The geomagnetic latitude effect was

TABLE 1.23 Approximate Composition of Cosmic Radiation of Galactic Origin Incident on the Top of the Atmosphere (TOP)^a

Radiation type	Approximate fraction (%)
H nuclei or protons (p^+ and p^-) ^b	80
He nuclei (equivalent to α particles)	15
Electrons (e^- and e^+) ^c	2
Heavier nuclei (e.g., C, O, Mg, Fe, Si, etc) ^d	1
Lighter nuclei ($Z = 3-5$, i.e., Li, Be, and B) ^e	0.2

^aCosmic radiation incident at the top of the terrestrial atmosphere includes all stable charged particles and nuclei with lifetimes of the order of 10^6 years or longer (Gaisser and Stanev, 2002).

^bThe ratio of antiprotons to protons (\bar{p}/p) is about 2×10^{-4} in the particle energy range of 10–20 GeV.

^cThe ratio of positrons to negatrons (e^+/e^-) varies from ~ 0.2 below 1 GeV to ~ 0.1 around 2 GeV and to ~ 0.05 at higher electron energies of 5–20 GeV.

^dNucleons of all of the elements of the periodic table stripped of their atomic electrons with the exception of the lighter nucleons listed above.

^eThe nuclei of Li, Be, and B are classified as secondary cosmic radiation, that is, particles produced by the interaction of the primaries with interstellar gas.

first reported by Clay (1928) and confirmed by Compton (1932, 1933), who measured cosmic-ray showers with ionization detectors while traversing latitudes onboard ocean vessels. Cosmic-ray particles will concentrate in the earth's Van Allen radiation belts, which extend from about 1000 to 60,000 km from the earth. The sea-level latitude effect of the electromagnetic and meson components of cosmic-ray interactions in the earth's atmosphere measured by Compton corresponded to an approximately 12–15 percent increase between the geometric equator and high latitudes. However, no information was obtained then on the latitude effect on the nucleonic component of cosmic radiation at sea level. Subsequent studies (Simpson, 1948, 1951, 2001) demonstrated a dramatic increase of 300–400 percent in the nucleonic component compared with a 10–15% increase in the meson component of cosmic radiation at sea level as one traveled from 0° to 70° latitude. This is particularly relevant to international airline pilots who are concerned about the cosmic radiation dose they accumulate when they travel frequently at high altitudes (12 km) and high latitudes (40–60 degrees) where the radiation intensities are higher.

Positrons and antiprotons are components of secondary cosmic radiation. Positrons are much lower in abundance than electrons (See Table 1.23). They are produced mainly via proton and nuclei interactions in the interstellar medium (Grimani, 2009). The differential flux of negatrons and positrons incident at the top of the atmosphere from galactic space is a function of particle energy. The positron fraction, measured as $e^+/(e^+ + e^-)$, decreases from ~ 0.2 below 1 GeV, to ~ 0.1 around 2 GeV and to ~ 0.05 at higher energies of 5–20 GeV (Grimani 2009, 2005, Clem and Evenson, 2002, Gaisser and Stanev, 2002 and Sundaresan, 2001). Antiprotons in the cosmic radiation were discovered by Golden et al (1979, 1984). These are classified as secondaries, as antiprotons as well as positrons are produced by

the interactions of primary cosmic radiation, principally protons with the interstellar matter, such as cosmic-ray nuclei (Adriani, et al, 2010, Gaisser and Schaefer, 1992, Webber and Potgieter, 1989 and Gaisser and Maurer, 1973). The proportions of anti-protons to protons (\bar{p}/p) are a function of energy with ratios varying from $\sim 0.3 \times 10^{-5}$ to 1×10^{-5} in the energy range of $\sim 0.2-1$ GeV, from $\sim 2 \times 10^{-5}$ to 1×10^{-4} in the energy range of $\sim 1-10$ GeV, and from $\sim 2 \times 10^{-3}$ to 3×10^{-3} in the energy range of $10-180$ GeV (Adriani, et al, 2010, Beach et al, 2001, Basini et al, 1999, Mitchell et al, 1996, and Hof et al, 1996). In summary, the approximate composition of galactic cosmic-ray particles is provided in Table 1.23.

Most galactic cosmic-ray particles possess energies from about 50 MeV to 10 GeV as illustrated in Fig. 1.85, which provides the energy distributions of some of the major components of primary cosmic radiation for a particular period of the solar cycle. A series of very precise measurements of primary protons and helium nucleon intensities have been made by the AMS Collaboration (2000), Menn et al (2000) and Sanuki et al (2000), Bellotti et al (1999), and Boezio et al (1999). Particle energies up to 10^{15} eV were first observed by

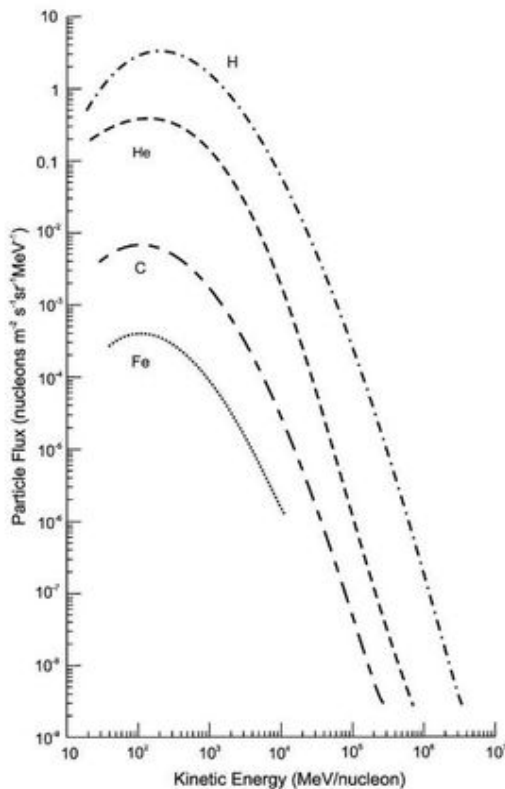


FIGURE 1.85 Approximate flux distributions of major components of primary cosmic radiation. See Simpson (1983) and Gaisser and Stanev (2002) for more precise data on nucleon flux as a function of particle energy.

Auger and Maze (1938, 1939), and a cosmic-ray particle of about 10^{20} eV energy was observed by Linsley (1963).

Protons in the kinetic energy range of 100 MeV to 10 GeV would have relativistic speeds ranging from 42.8% to 99.6% the speed of light (*i.e.*, $0.428c$ to $0.996c$) calculated according to Eqn (1.202). For example, the relativistic speed of a proton with 10 GeV kinetic energy would be calculated according to the following equation:

$$u = c \sqrt{1 - \left(\frac{K}{mc^2} + 1 \right)^{-2}} \quad (1.353)$$

The rest energy of the proton (mc^2) is calculated as

$$\begin{aligned} mc^2 &= (1.6726 \times 10^{-27} \text{ kg})(2.9979 \times 10^8 \text{ m/sec})^2 \\ &= 1.503 \times 10^{-10} \text{ J} \end{aligned} \quad (1.354)$$

which can be expressed in units of eV as follows:

$$\frac{1.503 \times 10^{-10} \text{ J}}{1.602 \times 10^{-19} \text{ J/eV}} = 0.9382 \times 10^9 \text{ eV} = 938.2 \text{ MeV} \quad (1.355)$$

The relativistic speed of the 10 GeV proton can then be calculated as

$$u = c \sqrt{1 - \frac{1}{(10^4 \text{ MeV}/938.2 \text{ MeV} + 1)^2}} = 0.996c \quad (1.356)$$

A higher kinetic energy 100 GeV (10^5 MeV) cosmic-ray proton would have a relativistic speed of

$$u = c \sqrt{1 - \frac{1}{(10^5 \text{ MeV}/938.2 \text{ MeV} + 1)^2}} = 0.999956c \quad (1.357)$$

The speed of the 100 GeV proton may also be calculated on the basis of the definition of the kinetic energy of the particle being the difference between the *total energy* of the particle and its rest energy (See Eqn (1.194)) or

$$K = \gamma mc^2 - mc^2 = (\gamma m - m)c^2 \quad (1.358)$$

or

$$10^5 \text{ MeV} = (\gamma m - m)c^2$$

Converting the units of electron volts in the above equation to joules and imputing the speed of light provides

$$\begin{aligned} (10^{11} \text{ eV})(1.602 \times 10^{-19} \text{ J/eV}) \\ = (\gamma m - m)(2.9979 \times 10^8 \text{ m/sec})^2 \end{aligned} \quad (1.359)$$

from which the differences of the relativistic and rest masses of the proton can be calculated as

$$\gamma m - m = \frac{1.606 \times 10^{-8} \text{ J}}{8.9874 \times 10^{16} \text{ m}^2/\text{sec}^2} = 0.1782495 \times 10^{-24} \text{ kg} \quad (1.360)$$

Inputting the known rest mass m of the proton (1.6726×10^{-27} kg) permits the calculation of the relativistic mass of the 100 GeV proton as

$$\begin{aligned} \gamma m &= 178.2495 \times 10^{-27} \text{ kg} + 1.6726 \times 10^{-27} \text{ kg} \\ &= 179.9221 \times 10^{-27} \text{ kg} \end{aligned} \quad (1.361)$$

Since by definition, $\gamma m = m/\sqrt{1 - (u^2/c^2)}$ (See Eqn (1.195)), we can write

$$\frac{\gamma m}{m} = \frac{1}{\sqrt{1 - (u^2/c^2)}} \quad (1.362)$$

which transforms to read

$$\left(\frac{m}{\gamma m}\right)^2 = 1 - \frac{u^2}{c^2} \quad (1.363)$$

or

$$\frac{u^2}{c^2} = 1 - \left(\frac{m}{\gamma m}\right)^2 \quad (1.364)$$

Inputting the values for the relativistic and rest masses of the proton yields

$$\begin{aligned} \frac{u^2}{c^2} &= 1 - \left(\frac{1.6726 \times 10^{-27} \text{ kg}}{179.9221 \times 10^{-27} \text{ kg}}\right)^2 \\ \frac{u^2}{c^2} &= 1 - (0.00929624)^2 \\ \frac{u^2}{c^2} &= 1 - 8.64200 \times 10^{-5} \\ u^2 &= (0.9999135)c^2 \end{aligned} \quad (1.365)$$

and

$$u = 0.999956c$$

where u is the relativistic speed of the 100 GeV proton exactly as calculated previously by Eqn (1.357).

High-energy cosmic-ray protons, as demonstrated above, approach the speed of light. Primary cosmic-ray nucleon intensity drops rapidly according to energy beyond several GeV as illustrated in Fig. 1.85. The primary nucleon intensity from a few GeV to 100 TeV is described according to the power law

$$I_N(E) = 1.8E^{-\alpha} \text{ nucleons/cm}^2 \text{ sec sr GeV} \quad (1.366)$$

where E is the energy per nucleon (including rest mass energy) and α is approximately 2.7.

As illustrated in Fig. 1.85, primary nucleon energies in excess of 1 TeV (*i.e.*, 10^{12} eV or 10^6 MeV) are relatively few in number, and primary cosmic-ray particles with energies in excess of 10^{20} eV or 10^{14} MeV are very rare, but have been reported (Hörandel, 2010, Pierre Auger Collaboration, 2010, Scherini, 2010, Zavrtanik, 2010, Nagano and Watson, 2000, Bird et al., 1995, Hayashida et al., 1994, and Linsley, 1963). The rarity of such extremely high-energy primary cosmic-ray particles can be visualized with the graph of primary cosmic-ray flux as a function of nucleon energy illustrated in Fig. 1.86.

The cosmic-ray scientific community is studying the knee and ankle regions of the cosmic-ray spectrum illustrated in Fig. 1.86. The knee region at particle energies of 10^{15} – 10^{16} eV shows a decline in the particle flux while the ankle region of the spectrum occurring between 10^{18} and 10^{19} eV shows a rise in particle flux. The origins of the knee and ankle regions of the energy spectrum is not fully understood, and these are now under intense research as described by Chiavassa (2010), Marcelli (2010), Blümer et al. (2009), Giller (2008), and Hörandel (2008a). The knee portion of the energy spectrum at about 4 PeV (*i.e.*, $\sim 4 \times 10^{15}$ eV), as described by Hörandel (2008a), is caused by a break in the energy spectra of the light elements. The mean mass of the cosmic rays is found to increase as a function of energy in the knee region. The knee in the energy spectrum is most likely caused by a combination of the maximum energy reached during acceleration and leakage from the Galaxy during propagation (Hörandel, 2008a). A current thinking for the production of the ankle region of the spectrum is summarized by Sundaesan (2001). It appears that the ankle is caused by a higher-energy cosmic-ray population mixed in with a lower energy population at energies a couple of orders of magnitude below the ankle. The spectrum below 10^{18} eV is considered to be of galactic origin, and the higher-energy population in excess of 5×10^{18} eV is considered to be of extragalactic origin (Marcelli, 2010, Allard et al., 2007, Cronin, 1999, and Sundaesan, 2001).

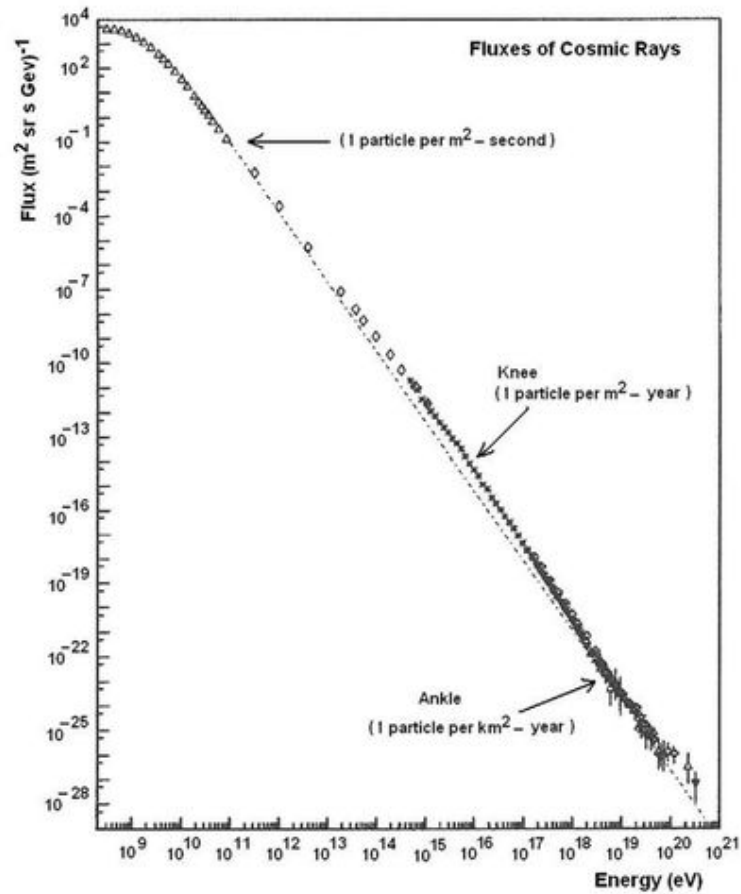
Much attention in the cosmic-ray community is also focused on the mechanisms by which the cosmic-ray nucleons are accelerated in space to energies in excess of 10^{20} eV. Enrico Fermi (1949) proposed and calculated the acceleration of cosmic rays resulting from a series of collisions with magnetic fields or magnetic clouds traversing the universe whereby the cosmic-ray particles gain energy each time they bounce off the magnetic fields. This is now referred to as Fermi acceleration, and Cronin (1999) explains that subsequent work has shown that multiple “bounces” off turbulent magnetic fields associated with supernova shock waves is the more efficient acceleration process (Drury, 1983). The energy spectrum of cosmic rays supports the “standard picture”, as described by Hörandel (2008a), that the bulk of galactic cosmic rays is accelerated in shocks of supernova remnants.

B. Showers of the Cosmic Radiation

Cosmic radiation consisting of high-energy nucleons striking the top of the atmosphere (TOA) collide with atoms of the air to produce a cascade of secondary subatomic particles and electromagnetic radiation referred to as showers of the cosmic radiation. During the years that preceded the development of man-made high-energy particle accelerators, cosmic rays provided much information to the field of high-energy particle physics. The collisions of high-energy nucleons with atomic nuclides of the atmosphere provided natural “atom smashers” that led to the early discovery of sub-atomic particles.

When a cosmic-ray particle strikes an atomic nucleus of a gaseous molecule of the atmosphere (*e.g.*, N_2 , O_2 , etc.),

FIGURE 1.86 Spectrum of cosmic rays greater than 100 MeV. The cosmic rays consist predominantly of nucleons ranging in species from protons to iron nuclei with traces of nuclei of the heavier elements. Not included in the figures are notations for estimated cosmic rays fluxes of about 1 particle/cm²/sec at the low energy end of 10⁸ eV and only of the order of 1 particle/km²/century at the high-energy end of 10²⁰ eV of the spectrum. (This figure was produced by S. Swonfy, University of Chicago from published results of the LEAP, Proton, Akeno, AGASA, Fly's Eye, Haverah Park, and Yakutsk experiments. See Marcelli, 2010 and Bhattacharjee and Sigl, 2000. Reprinted with permission from Elsevier © 2000.)



a nuclear disintegration follows producing high-energy secondary nucleons and charged and neutral π mesons (pions). These secondary nucleons collide with additional atomic nuclei of the atmosphere producing a cascade of particles including mesons, nucleons of various masses, neutrons, and products of meson-nuclear interactions and meson decay, namely, photons of electromagnetic radiation, positrons, negatrons, and neutrinos. Fig. 1.87 provides a good schematic of the various possible nucleon interactions that produce the cascade of secondary cosmic radiation in the atmosphere.

Mesons are strongly interacting particles of mass intermediate between that of the electron ($0.511 \text{ MeV}/c^2$) and the proton ($938 \text{ MeV}/c^2$). Among the mesons produced are (a) kaons (K -mesons), which have a mass of about $490 \text{ MeV}/c^2$, lifetimes of approximately 10^{-10} and 10^{-8} s for the neutral (K^0) and charged (K^\pm) kaon, respectively, decaying to pions and/or muons as illustrated in Fig. 1.88 and (b) the pions (π -mesons) that can decay into muons, such as described by Eqns (1.371) and (1.372). A neutral pion has a mass of $135 \text{ MeV}/c^2$ and a lifetime of 8.3×10^{-17} s. It

decays into two gamma-ray photons, as illustrated in Fig. 1.87, or into a positron-negatron pair and gamma ray with branching ratios of approximately 98.8% and 1.2%, respectively, for the two decay modes (Sundareson, 2001, Glasser et al, 1961) as follows:

$$\pi^0 \rightarrow \gamma + \gamma \quad (98.798 \pm 0.032\%) \quad (1.367)$$

$$\pi^0 \rightarrow e^+ + e^- + \gamma \quad (1.198 \pm 0.032\%) \quad (1.368)$$

The positron and negatron pair (e^+e^-), as products of the neutral pion decay, illustrated by Eqn (1.368), is a result of internal conversion of a gamma-ray photon (*i.e.*, internal pair production). The neutral pion decay may also manifest itself in yet a more rare form of dual internal conversion whereby two gamma-ray photons are converted to two positron-negatron pairs. The decay scheme is illustrated by Eqn (1.369), and the tracks from such a decay scheme produced in a bubble chamber are illustrated in Fig. 1.89:

$$\pi^0 \rightarrow e^+ + e^- + e^+ + e^- \quad (1.369)$$

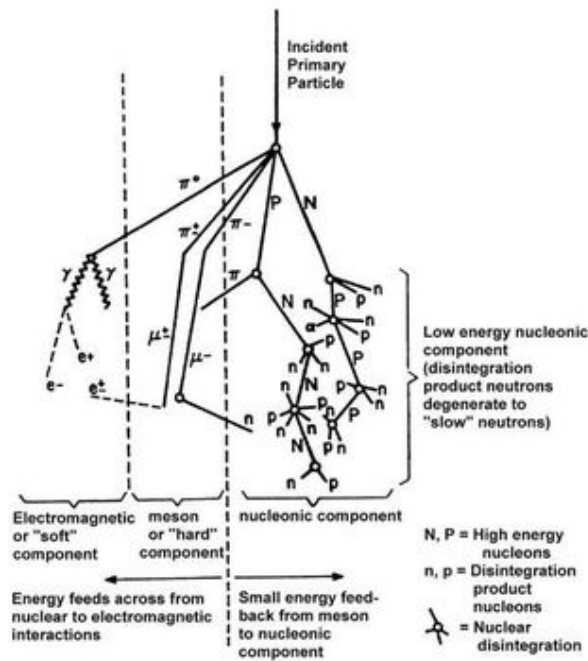


FIGURE 1.87 Schematic representation of the typical development of the secondary cosmic radiations within the atmosphere arising from an incident primary particle. (From Simson et al., 1953, reprinted with permission © 1953 The American Physical Society.)

Out of eight million π^0 decays in 836,000 bubble chamber pictures, Samios et al (1962) were able to find only 206 neutral pion decays with double internal conversion. The numerous neutral pions were produced by Samios et al (1962) by the interactions of π^- mesons from a cyclotron, with protons of the bubble chamber liquid according to the reaction

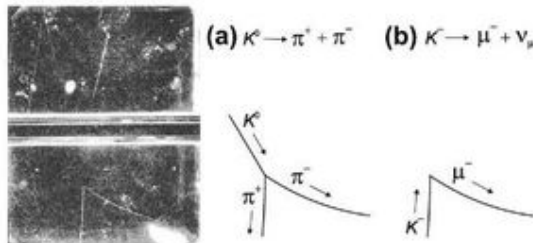
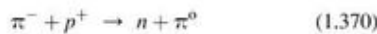


FIGURE 1.88 A cloud-chamber photograph of the tracks of a probable V^0 particle in a magnetic field of 5000 gauss. V particles got their name from the V-shaped tracks, that they formed from a given point in the cloud chamber. The cloud chamber consists of upper and lower chambers separated by the glass walls and copper tubing of a central Geiger counter. The V-shaped track appears left center in the lower-chamber. The track was the result of one of two possible modes of kaon decay, namely, (a) a neutral kaon (K^0) decaying into positive and negative pions where the neutral kaon does not leave a track because of its lack of charge, or (b) a negative kaon (K^-) entering the cloud chamber from below and decaying into a negative muon and neutrino. The neutrino obviously does not leave a track. (Cloud chamber photograph is from the work of Nobel Laureate Carl D. Anderson and coworkers (Leighton et al., 1953) reprinted with permission © 1953 The American Physical Society.)

The π^- mesons were slowed down with a polyethylene absorber and then allowed to stop in the hydrogen bubble chamber. The numerous bubble chamber photographs could be analyzed for the identification of specific tracks by a digitized scanning machine.

Any of the gamma rays can, in turn, produce positron–negatron pairs via pair production, and the positron can undergo annihilation to gamma radiation. The positive and negative pions are antiparticles. Charged pions have a mass of $139.6 \text{ MeV}/c^2$ and a lifetime of $2.6 \times 10^{-6} \text{ s}$, much longer than that of the $\nu_{\mu}e$ neutral pion. The positive pion decays to a positive muon and muon neutrino, whereas the negative pion decays into a negative muon and muon antineutrino as illustrated by the following:



The muon has a mass of $106 \text{ MeV}/c^2$ and lifetime of $2.2 \times 10^{-6} \text{ s}$. The positive muon decays to a positron and muon neutrino, and the negative muon to a negatron and anti-muon neutrino as illustrated in Fig. 1.87 and by the following:



Slow negative muons undergo nuclear absorption by nucleons with sufficient high atomic number ($Z \approx 10$ or greater); however, for low Z nuclides such as carbon ($Z = 6$), slow negative muon decay occurs rather than absorption by the nucleus (Sundareson, 2001).

At sea level muons are the most numerous of the charged particles resulting from cosmic ray interactions with atomic

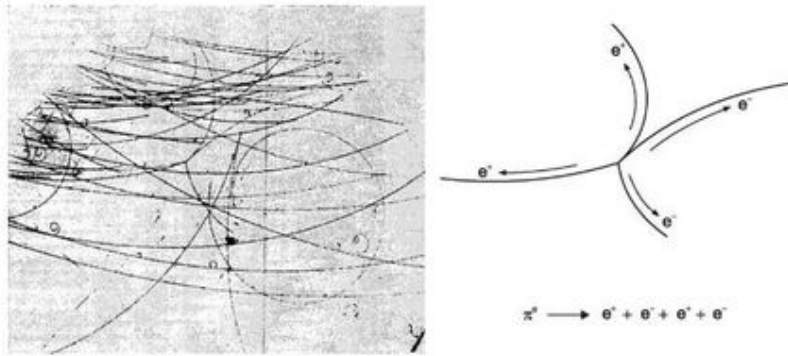


FIGURE 1.89 Photograph of a typical double internal conversion following π^0 decay on the left with a drawing of the specific tracks provided on the right. The tracks were produced in a hydrogen bubble chamber 30.5 cm in diameter and 15.25 cm in depth. A magnetic field of 5.5 gauss produced the curved deflection of the oppositely charged electrons. (From Samios et al., (1962), reprinted with permission © 1962 The American Physical Society.)

nuclei of the atmosphere. These have been measured with an intensity of $100 \text{ m}^{-2} \text{ sec}^{-1}$ at sea level. The relative abundances of the cosmic radiation shower components in the atmosphere at different altitudes with energies in excess of 1 GeV are illustrated in Fig. 1.90. As illustrated in the figure, most muons are produced high in the atmosphere at an altitude of $\sim 15 \text{ km}$ where high-energy cosmic-ray nucleons encounter and undergo collision with nuclei of the

atmospheric gases. Pions likewise are produced high in the atmosphere; however, their number at sea level is highly diminished due to the prompt decay of the neutral pion to gamma radiation and the decay of the charged pions to muons. The muon produced high in the atmosphere loses about 2 GeV of energy to ionization before reaching the ground, and the mean energy of the muon at the ground is $\approx 4 \text{ GeV}$ (Gaisser and Stanev, 2002), and these travel at speeds close to the speed of light ($>0.99c$).

One might ask at this point the following question: If muons of the cosmic radiation showers are produced high in the earth's atmosphere (at altitudes of $\sim 15,000$ meters or higher), travel at speeds close to the speed of light, and have an average lifetime of only 2.2×10^{-6} seconds, how could such muons be detected to reach the earth's surface? The question is an obvious one, as it would appear with classical mathematics that, with such a short lifetime, muons would never be expected to reach the earth. Let's say, for example, a muon is produced at the altitude of 15,000 meters and it travels at the speed v of $0.9993c$, which would correspond to a speed in units of m/sec as

$$0.9993c = (0.9993)(2.9979 \times 10^8 \text{ m/sec}) = 2.9958 \times 10^8 \text{ m/sec} \quad (1.374)$$

The classical calculation of its average distance d of travel during its lifetime would be

$$d = (v)(t) = (2.9958 \times 10^8 \text{ m/sec})(2.2 \times 10^{-6} \text{ sec}) = 659.1 \text{ m} \quad (1.375)$$

Thus, the muon would be expected to decay, according to classical transformations, after traveling only 659 meters on the average and, therefore, never be detected an earth. However, for such a muon viewed by an observer on earth, he or she would view the two events : (A) the creation of the muon and (B) the decay of the muon, to occur in two locations in space-time coordinates. The Lorentz time transformations demonstrate that the two events, A and B, separated by the time interval Δt , will be dilated to the time interval Δt_{earth} , when viewed by an observer on earth. The time dilation is calculated according to

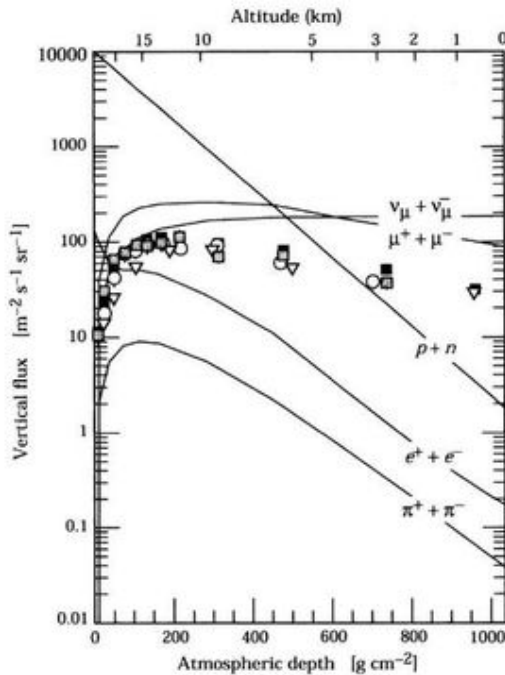


FIGURE 1.90 Vertical fluxes of cosmic rays in the atmosphere with $E > 1 \text{ GeV}$ estimated from the nucleon flux of Eqn (1.366). The points show measurements of negative muons with $E_\mu > 1 \text{ GeV}$. (From Bellotti et al (1996, 1999), Boezio et al (2000a,b), Coniu et al (2000), and Gaisser and Stanev (2002), reprinted with permission © 1996 The American Physical Society.)

the following Lorentz transformation derived by Gautreau and Savin (1999) and Serway et al (2005)

$$\Delta t_{\text{earth}} = \frac{\Delta t}{\sqrt{1 - (v^2/c^2)}} \quad (1.376)$$

where v is the velocity of the particle and c is the invariable speed of light in a vacuum. For the muon traveling at $0.9993c$, we can calculate Δt_{earth} or the dilated lifetime of the muon as follows:

$$\begin{aligned} \Delta t_{\text{earth}} &= \frac{\Delta t}{\sqrt{1 - (v^2/c^2)}} = \frac{2.2 \times 10^{-6} \text{ sec}}{\sqrt{1 - (0.9993)^2}} \\ &= \frac{2.2 \times 10^{-6} \text{ sec}}{0.0374} = 58.8 \times 10^{-6} \text{ sec} \end{aligned} \quad (1.377)$$

According to the dilated time of 58.8×10^{-6} sec, the observer on earth will determine that the muon would travel, before it decays, a distance of

$$\begin{aligned} d &= (v)(\Delta t_{\text{earth}}) = (2.9958 \times 10^8 \text{ m/sec})(58.8 \times 10^{-6} \text{ sec}) \\ &= 17615 \text{ meters} \end{aligned} \quad (1.378)$$

which is well beyond the distance of 15,000 meters elevation when it was created, permitting its detection on earth. The distance is only an average figure, because the muon lifetime of 2.2×10^{-6} seconds is an average lifetime.

The example provided here is a realistic one, and the relativistic time dilation has been demonstrated by Bailey et al (1977, 1979) based on the historical tests of Rossi and Hall (1941).

The historical work of Rossi and Hall entailed the measurement of the muon flux on Mt. Washington in New Hampshire at the altitude of 2,000 meters and at the mountain base. They found that the muon flux at both altitudes did not differ greatly, only by the ratio of 1.4, that is, the muon flux was 1.4 times as high at the altitude of 2,000 meters compared to the ground level. Calculations based on a muon half-life of 1.5×10^{-6} seconds, the muon flux ratio for the two altitudes, should have been approximately 22 even when attributing the highest unrealistic speed of light to the muons. The actual low ratio of 1.4 could only be explained by applying the time dilation calculations for muons traveling at the speed of $0.994c$.

More recent experiments at CERN by Bailey et al (1977, 1979) involved accelerating muons in a storage ring to speeds of up to $0.9994c$. The rates of decay of the accelerated muons were measured by detecting their electron decay-product emissions. The accelerated muons were found to have a lifetime of 29.3 times longer than a muon at rest. This agrees perfectly with the calculated dilated lifetime of the muon according to the Lorentz transformation

$$\Delta t = \frac{\Delta t_0}{\sqrt{1 - (v^2/c^2)}} \quad (1.379)$$

where Δt_0 is the lifetime of the muon at rest, v the speed of the muon, and c the speed of light. The dilated lifetime of the muon at $0.9994c$ is calculated to be

$$\Delta t = \frac{2.2 \times 10^{-6} \text{ sec}}{\sqrt{1 - (0.9994)^2}} = 63.58 \times 10^{-6} \text{ sec} \quad (1.380)$$

The increase in the observed lifetime of the accelerated muons over the muons at rest is

$$\frac{\Delta t}{\Delta t_0} = \frac{63.58 \times 10^{-6} \text{ sec}}{2.2 \times 10^{-6} \text{ sec}} = 28.9 \quad (1.381)$$

This test of time dilation, provided by the muon lifetime measurements, is discussed in papers by Drumm et al (1977), Thompson (2004) and Tomaschitz (2004).

C. Cosmic Rays, Underground

The only significant cosmic radiation with energy sufficient to penetrate considerable depths of earth are charged muons and muon neutrinos. Thus, Tueros and Sciutto (2010) describe muons as the “penetrating component” of the cosmic-ray-induced showers, capable of reaching deep underground without interacting in the atmosphere. High-energy muons will traverse rock and lose energy via either direct ionization or radiative processes. The radiative processes include bremsstrahlung production with concomitant positron–electron pair production and photonuclear interactions. Muon-induced spallation is another mechanism of energy loss. The muon cosmic-ray intensities diminish with depth as expected. This is a subject of concern in the measurement of very low levels of radiation. Consequently, underground laboratories have been built to achieve lowest possible background radiation interference in the counting of very low levels of natural radioactivity. Muon ranges in rock are measured in units of km-water-equivalent (km.w.e) where $1 \text{ km.w.e.} = 10^5 \text{ g/cm}^2$ of standard rock. Average ranges in standard rock ($Z = 11$, $A = 22$, $Z/A = 0.5000$, $\rho = 2.650 \text{ g/cm}^3$) for muons of 10, 100, 1000, and 10,000 GeV are 0.05, 0.41, 2.45, 6.09 km.w.e. The vertical muon intensity versus underground depth of standard rock has been determined. The muon vertical intensity drops from $10^{-6} \text{ cm}^{-2}\text{sr}^{-1}\text{s}^{-1}$ to $10^{-12} \text{ cm}^{-2}\text{sr}^{-1}\text{s}^{-1}$ over the range of rock depths from 1 to 10 km.w.e., respectively (Gaisser and Stanev, 2002).

Radiation from muons of the cosmic-ray showers is significant underground. The mechanisms of muon energy loss are dependent on the muon energy. Tueros and Sciutto (2010) report a Monte Carlo program that simulate high-energy cosmic-ray showers underground. From nuclear data tables of Groom (2001), they calculated the muon energy losses in standard rock by plotting the stopping power versus muon energy illustrated in Fig. 1.91. (Stopping power calculations are discussed in Section XIV.A.) Muons traveling through matter will lose energy by several mechanisms including ionization, bremsstrahlung production, pair production, photonuclear reactions including spallation caused by muon collisions with nuclei. Tueros and Sciutto (2010) demonstrate from Fig. 1.91 that ionization losses are dominate at low muon energies ($< 100 \text{ MeV}$) and ionization losses predominate among the other mechanisms of energy loss and remain fairly constant constant at $1.5\text{--}2.2 \text{ MeV cm}^2/\text{g}$ below 10 GeV (10^4 MeV) muon energy in standard rock. At muon energies ($> 10 \text{ GeV}$) radiative energy losses steadily increase and reach the critical energy at $\sim 0.7 \text{ TeV}$ (693 GeV , see Fig. 1.91), which is the energy at which the ionization loss is equal to the radiative loss. The critical energy for muons in air is much higher 3.6 TeV as reported by Greider (2001). Thus, Tueros and Sciutto

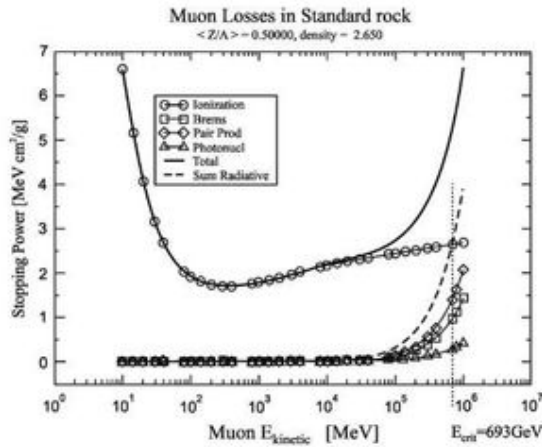


FIGURE 1.91 Muon energy loss versus muon energy in standard rock. (From Taueros and Sciutto (2010), reprinted with permission from Elsevier © 2010.)

(2010) point out that bremsstrahlung and pair production energy losses for muons in air are negligible with the exception of very high muon energies, whereas it is increasingly important underground for muon energies >50 GeV.

Another source of underground background interference from muons of the cosmic radiation showers is the production of gamma-ray photons from radiative neutron capture reactions in hydrogen and elements encountered in rock and other soil materials. Neutrons are produced by muon spallation reactions as well as photonuclear reactions arising from bremsstrahlung radiative energy loss. Araújo et al (2008) and Lindote et al (2009) report a Monte Carlo simulation, which provides a very good estimate of the absolute neutron yield in lead as $(1.31 \pm 0.06) \times 10^{-3}$ neutrons/muon/g/cm² for a mean muon energy of 260 GeV.

D. Origins of Cosmic Radiation

The origins of galactic and extragalactic cosmic rays remains an unsolved problem, and reviews on current research and thinking are provided by Potgieter (2010), Blasi (2008), Hörandel (2008b), and Gaisser (2001). The subject of cosmic-ray origin is somewhat out of scope of this chapter; and the reader is invited to peruse the review papers on this subject cited above. In brief, cosmic rays can originate from (i) energetic particles associated with mass ejections from solar flares and similar energetic solar events, (ii) anomalous cosmic rays, which are particles of interstellar origin accelerated at the edge of the heliopause and accelerated at the termination shock in the solar wind, (iii) high-energy particles of galactic origin far outside the heliosphere or our solar system, and (iv) extragalactic sources, which give rise to particles of the highest energies ~10¹⁸ eV or higher.

XIII. RADIATION DOSE

Radiation dose, also referred to as absorbed radiation dose, is the amount of energy deposited in a given mass of a medium by ionizing radiation. The measurement of radiation dose, i.e., radiation dosimetry, is not a subject of this book. Nevertheless,

the basic units used in the measurement of radiation dose will be mentioned briefly here, as the monitoring of radiation workers for the dose received by the body is essential.

Radiation exposure was historically measured by the roentgen (R), which is a measure of the quantity of radiation deposited in air from the amount of charge or ionization produced by the radiation in air. By definition, 1 R = 2.58 × 10⁻⁴ C/kg of air at STP, that is, one roentgen will produce 2.58 × 10⁻⁴ Coulombs of ion pairs in one kilogram of air. The roentgen is a unit of exposure that is mostly historical and seldom used; it still occasionally appears on some dosimeter readings. Of more significance is the measure of absorbed dose, that is, the energy of radiation absorbed per unit mass of absorber. The original unit of absorbed dose is the rad, which is derived from the term "radiation absorbed dose". The rad has been replaced with the gray (Gy), which is the SI unit of absorbed dose. The use of SI units is recommended by the International Commission on Radiation Units and Measurements (ICRU). The rad and gray have the following equivalents:

$$100 \text{ rad} = 10^4 \text{ erg/g} = 1 \text{ Gy} = 1 \text{ J/kg} \quad (1.382)$$

$$1 \text{ rad} = 10 \text{ mGy} = 100 \text{ erg/g} \quad (1.383)$$

$$1 \text{ mrad} = 10 \mu\text{Gy} \quad (1.384)$$

As 1 eV = 1.602 × 10⁻¹⁹ J, we can convert the gray to units of electron-volt energy deposited in a kg of absorber or

$$1 \text{ Gy} = 6.24 \times 10^{12} \text{ MeV/kg} \quad (1.385)$$

Let us use the following example to illustrate the calculation of radiation dose:

A 1.5 cm² beam of gamma radiation consisting of 1 MeV photons with an emission rate of 5 × 10⁸ photons/sec is irradiated onto human tissue of density 1.1 g/cm³. If 6.25% of the gamma radiation is absorbed by 1.25 cm thickness of the tissue (i.e., 93.75 % transmitted through the tissue), the rate of radiation dose administered to the tissue per second may be calculated as

$$\text{dose} = \frac{\text{energy}}{\text{mass}} \quad (1.386)$$

and

$$\begin{aligned} \text{dose/sec} &= \frac{\text{energy/sec}}{\text{mass}} \\ &= \frac{(5 \times 10^8 \text{ photons/sec})(0.0625)(1 \text{ MeV/photon})}{(1.1 \text{ g/cm}^3)(1.5 \text{ cm}^2)(1.25 \text{ cm})} \\ &= \frac{3.12 \times 10^7 \text{ MeV/sec}}{2.0625 \text{ g}} = 1.51 \times 10^{10} \text{ MeV/sec/kg} \end{aligned} \quad (1.387)$$

If 1 gray (Gy) is equivalent to 6.24 × 10¹² MeV/kg Eqn (1.385), the dose rate in MeV/sec/kg is converted to units of the Gray (Gy) as

$$\text{dose (Gy/sec)} = \frac{1.51 \times 10^{10} \text{ MeV/sec/kg}}{6.24 \times 10^{12} \text{ MeV/kg/Gy}} = 2.42 \text{ mGy/sec} \quad (1.388)$$

Another formerly very common and historical unit of radiation dose is the rem. The rem is a measure of absorbed dose in

biological tissue. This unit of measure is derived from the term “roentgen equivalent for man” or “roentgen equivalent mammal”. The rem was created as a measure of dose of ionizing radiation to body tissue in terms of its estimated biological effect; its SI unit is the sievert (Sv) and

$$100 \text{ rem} = 1 \text{ Sv} \quad \text{and} \quad 1 \text{ rem} = 10 \text{ mSv} \quad (1.389)$$

The rem or Sv (sievert) are referred to as units of equivalent dose, because the dose is measured on the basis of a weighting factor (w_R), which defines the relative hazard of radiation on the basis of the types and energies of the radiations by placing all radiation classes on the same dose level or equivalent (L'Annunziata, 1987). The weighting factor, formerly known as the quality factor (QF), is defined as the ratio of the gamma-ray or x-ray dose to the dose required to produce the same biological effect by the radiation in question. Table 1.24 lists the radiation weighting factors according to radiation type and energy. The weighting factor of a given radiation is a function of the radiation linear energy transfer (LET), that is, the radiation energy loss per path length of travel. As discussed in Section XIV, radiations of high mass and charge, such as alpha particles or fission products, will have a higher LET than electrons or beta particles, muons, or x-ray or gamma-ray photons. Because photons will produce electrons as secondary particles, x- or gamma-ray photons are classified to have the same radiation weighting factor as electrons. According to the weighting factors provided in Table 1.24, alpha particles are considered to be 20 times more damaging to cells of the human body than beta particles, muons, and x- or gamma radiation. However, alpha particles and other heavy nuclei have short ranges in matter compared to other radiation types. Thus, distance provides the best protection from alpha particles and other heavy nuclei. Also, the weighting factors for neutrons in Table 1.24 classify the neutrally charged neutrons as more hazardous to biological tissue than the charged electrons or muons. This is because neutrons will produce recoil protons and ions of higher mass via neutron collisions in body tissue.

TABLE 1.24 Radiation Weighting Factors¹

Radiation	w_R
X- and gamma-rays, all energies	1
Electrons and muons, all energies	1
Neutrons < 10 keV	5
10–100 keV	10
>100 keV to 2 MeV	20
2–20 MeV	10
>20 MeV	5
Protons (other than recoils) > 2 MeV	5
Alphas, fission fragments, and heavy nuclei	20

¹From ICRP (1991) and Donahue and Fassó (2002). Reprinted with permission from ICRP © 1991.

The equivalent dose in Sv can be calculated from the weighting factors as

$$\text{Sv} = \text{absorbed dose in grays} \times w_R \quad (1.390)$$

where the weighting factor expresses potential damage to cells and long-term risk (primarily cancer and leukemia) from low-level chronic exposure, which is dependent on radiation type and other factors (ICRP, 1991 and Donahue and Fassó, 2002). Using the notation of Lilley (2001) for average absorbed dose in tissue, Eqn (1.390) can be written as

$$\text{Sv} = D_{T,R} \times w_R \quad (1.391)$$

where Sv is the equivalent dose in sieverts and $D_{T,R}$ is the average absorbed dose in tissue T from a given type of radiation R. For example, from the weighting factors of Table 1.24 and Eqn (1.391), we can calculate that an average absorbed dose of 0.01 Gy from alpha particles ($w_R = 20$) will produce the same biological effect as a 0.2 Gy dose from x- or gamma radiation ($w_R = 1$). Likewise, a 0.1 Gy dose from 50 keV neutrons ($w_R = 10$) will produce the same biological effect as a 1 Gy dose of electrons ($w_R = 1$). When more than one radiation type contributes to the absorbed dose, the equivalent dose is calculated according to the weighted sum of the contributions from each radiation type.

The ICRP (1991) recommendation for limits of exposure for radiation workers for whole-body dose is 20 mSv/yr (2 rem/yr) averaged over 5 years, with the dose in any one year ≤ 50 mSv (5 rem/yr). It is estimated by the United States National Safety Council that the average person in the United States receives only 3.6 mSv (0.36 rem or 360 mrem) of accumulated radiation dose per year from all sources including cosmic radiation, medical x-rays, and natural radioactivity, etc. In most world, areas the whole-body equivalent dose rate is $\approx 0.4\text{--}4$ mSv/yr or 40–400 mrem/yr, although in certain areas of the world the dose rate can range up to 50 mSv/yr or 5 rem/yr (Donahue and Fassó, 2002).

As discussed previously in Section XII.B, the atmosphere serves as an excellent shield against intense cosmic radiation, as cosmic-ray particles collide with nuclei of nitrogen, oxygen, and other gaseous atoms of the atmosphere and produce the less hazardous particles that constitute the cosmic-ray showers. Exposure to cosmic radiation is of some concern to intercontinental airline pilots, who fly at high altitudes (7–12 km above the earth) and high degrees of latitude and who compile large numbers of flight hours per year over long careers. Hammer et al (2000) report a mean cosmic radiation dose estimate of 35 mSv for 509 pilots, who averaged 26.6 years of employment at an average of 481 flight hours per year. The accumulated cosmic radiation dose of 35 mSv over 26.6 years will yield an average dose rate of 1.3 mSv/y. The dose rates are well within the ICRP (1991) recommendations for limits of exposure for radiation workers for whole body dose set at 20 mSv/y. For pregnant women, however, the ICRP limit of dose is 2 mSv for the duration of pregnancy. Consequently, the study by NRL (1998) concludes that airline companies may apply a limit of 2 mSv for a pregnant member of the aircrew from the time of conception. Astronauts, who circle the earth in orbit for extended periods of

time, those who have traveled and plan to travel to the moon and back, and those who may travel to Mars have reason for concern of exposure to cosmic radiation where there is no protection from the earth's partially protective atmospheric shield. Fujitaka (2005) reports that a 1-week mission on the space shuttle will result in a radiation dose of 3.5 mSv, while astronauts would accumulate a dose of 43 mSv during a trip to the moon. Travel to Earth to Mars would take 280 days and the return trip 256 days during which time astronauts would accumulate 1850 mSv, and a stay on Mars for 439 days would expose astronauts to an additional 410 mSv whereby each astronaut would accumulate a grand total of 2.26×10^3 mSv (Paschoa and Steinhäusler (2010)). A very interesting and stimulating note for thought is reported by Fujitaka (2005) that space travel to Pluto, which is at the boundaries of our solar system would expose astronauts to a cosmic radiation dose of 70 Sv or 70,000 mSv, which is enough radiation to kill every cell in the human body. This may be so at current speeds of space travel, as NASA's New Horizons Mission spacecraft to Pluto was launched in June 2006, and it is expected to arrive at Pluto after nine years, sometime in 2015. However, with the proper thrust systems, high speeds of space travel in a manned spacecraft would be possible (Westmoreland, 2010 and Walter, 2006), which would minimize space travel time well out of our solar system and thus keep cosmic radiation dose to acceptable limits.

For further information on radiation dosimetry, the reader is invited to peruse books dedicated to this subject matter such as those by Bevelacqua (2010), Stabin (2009) and Cember and Johnson (2008).

XIV. STOPPING POWER AND LINEAR ENERGY TRANSFER

Previous sections in this chapter provide information on the mechanisms of interaction of radiation with matter. In summary, we can state that the principal mechanisms of interaction of charged particles with matter, which result in significant charged-particle energy loss, are (i) ionization via Coulombic interactions of the charged particles with atomic electrons of the absorbing medium, (ii) electron orbital excitation of the medium, which occurs when the energy transfer through Coulombic interaction is not sufficient to actually eject an electron from an atom, and (iii) the radial emission of energy as bremsstrahlung (x-radiation) when a charged particle decelerates as it is deflected by an atomic nucleus. Release of particle energy by bremsstrahlung radiation becomes increasingly significant as the charged particle (*e.g.*, beta-particle) energy and absorber atomic number increase. On the other hand, electromagnetic radiation dissipates its energy in matter via three mechanisms, namely, (i) the photoelectric effect, (ii) Compton scattering, and (iii) pair production. The photoelectric effect and Compton scattering generate ion pairs directly within the absorbing medium, whereas pair production results in the creation of charged particles (positrons and negatrons) that will subsequently dissipate their energy via ionization, electron excitation, and, in the case of positrons, annihilation. Also, we have seen that energetic neutrons will dissipate their energy in

matter through elastic collisions with atomic nuclei of the absorbing medium. When hydrogen is present in the absorbing material, the bulk of fast-neutron energy is passed on to the hydrogen nuclei. In turn, the kinetic energy of these protons is absorbed in the medium via ionization and excitation processes. We have seen also that low- and high-energy neutrons are absorbed principally via inelastic neutron reactions, which can result in the production of charged particles and gamma radiation.

The radiation properties (*e.g.*, charge, mass, and energy) and mechanisms of interaction previously described govern the rate of dissipation of energy and consequently the range of travel of the nuclear radiation in the absorber. This brings to bare the concepts of stopping power and linear energy transfer (LET), which are described subsequently.

A. Stopping Power

Stopping power is defined by The International Commission on Radiation Units and Measurements (ICRU) as the average energy dissipated by ionizing radiation in a medium per unit path length of travel of the radiation in the medium (Taylor et al, 1970). It is, of course, impossible to predict how a given charged-particle will interact with any given atom of the absorber medium. Also, when we consider that the Coulombic forces of charged particles will interact simultaneously with many atoms as it travels through the absorbed medium, we can only predict an average effect of energy loss per particle distance of travel. Taking into account the charge, mass, and speed (energy) of the particle, and the density and atomic number of the absorbing medium, Bethe (1933) and Bethe and Ashkin (1953) derived the formula for calculating the stopping power resulting from Coulombic interactions of heavy charged particles (*e.g.*, alpha particles, protons, and deuterons) traveling through absorber media. Röhrlich and Carlson (1954) have refined the calculations to include energy losses via bremsstrahlung radiation, significant when high-energy electrons and beta particles interact with absorbers of high atomic number. Also, refinements to the stopping power formulas in the low-energy ranges of heavy particles have been made by several researchers, including Bohr and Lindhard (1954), Lindhard and Scharff (1960, 1961), Northcliffe, 1963, and Mozumder et al. (1968). Derivations of stopping power formulas can be obtained from texts by Evans (1955), Friedlander et al (1964), Roy and Reed (1968), and Segré (1968). Stopping power and range tables for electrons and protons over the energy range of 10^{-3} – 10^5 MeV and for helium ions over the energy range of 10^{-3} – 10^3 MeV in 74 materials are available from Berger (1993) and Berger et al (2005), and these can be calculated on-line at the website of the National Institute of Standards and Technology (NIST), *i.e.*, <http://www.nist.gov/physlab/data/star/index.cfm>, for electrons in any user-specified materials, and for protons and helium ions in 74 materials (NIST, 2010).

The formulas for the stopping power of charged particles due to Coulombic or collisional interactions (*i.e.*, ionization and

electron orbital excitation) are clearly defined by Tsoulfanidis (1995) as the following:

1. for heavy charged particles (e.g., protons, deuterons, and alpha particles),

$$\frac{dE}{dx} = 4\pi r_0^2 z^2 \frac{mc^2}{\beta^2} NZ \left[\ln \left(\frac{2mc^2}{I} \beta^2 \gamma^2 \right) - \beta^2 \right] \quad (1.392)$$

2. for electrons or negatrons (negative beta particles),

$$\frac{dE}{dx} = 4\pi r_0^2 \frac{mc^2}{\beta^2} NZ \left\{ \ln \left(\frac{\beta \gamma \sqrt{\gamma - 1}}{I} mc^2 \right) + \frac{1}{2\gamma^2} \left[\frac{(\gamma - 1)^2}{8} + 1 - (\gamma^2 + 2\gamma - 1) \ln 2 \right] \right\} \quad (1.393)$$

and

3. for positrons (positive beta particles),

$$\frac{dE}{dx} = 4\pi r_0^2 \frac{mc^2}{\beta^2} NZ \left\{ \ln \left(\frac{\beta \gamma \sqrt{\gamma - 1}}{I} mc^2 \right) - \frac{\beta^2}{24} \left[23 + \frac{14}{\gamma + 1} + \frac{10}{(\gamma + 1)^2} + \frac{4}{(\gamma + 1)^3} \right] + \frac{\ln 2}{2} \right\} \quad (1.394)$$

where dE/dx is the particle stopping power in units of MeV/m, r_0 is the classical electron radius = 2.818×10^{-15} m, z is the charge on the particle ($z = 1$ for p, d, β^- , β^+ and $z = 2$ for α), mc^2 is the rest energy of the electron = 0.511 MeV (see Section X.C), N is the number of atoms per m^3 in the absorber material through which the charged particle travels ($N = \rho(N_A/A)$ where ρ is the absorber density in units of g/cm^3 , N_A is Avogadro's number = 6.022×10^{23} atoms per mol, A is the atomic weight (not the mass number) of the absorber material, and Z is the atomic number of the absorber, $\gamma = (T + mc^2)/mc^2 = 1/\sqrt{1 - \beta^2}$ where T is the particle kinetic energy in MeV and m is the particle rest mass (e.g., proton = 938.2 MeV/ c^2 , deuteron = 1875.6 MeV/ c^2 , alpha particle = 3727.3 MeV/ c^2 , and β^- or $\beta^+ = 0.511$ MeV/ c^2 , and β the relative phase velocity of the particle = v/c , that is, the velocity of the particle in the medium divided by the speed of light in a vacuum = $\sqrt{1 - (1/\gamma^2)}$ (see also Chapter 15 for a treatment on β), and I is the mean excitation potential of the absorber in units of eV approximated by the equation

$$I = (9.76 + 58.8Z^{-1.19})Z, \quad \text{when } Z > 12 \quad (1.395)$$

where pure elements are involved as described by Tsoulfanidis (1995). However, when a compound or mixture of elements is concerned, a mean excitation energy, $\langle I \rangle$, must be calculated according to Bethe theory as follows:

$$\langle I \rangle = \exp \left\{ \frac{\sum_j w_j (Z_j/A_j) \ln I_j}{\sum_j w_j (Z_j/A_j)} \right\} \quad (1.396)$$

where w_j , Z_j , A_j , and I_j are the weight fraction, atomic number, atomic weight, and mean excitation energy, respectively, of the j th element (Seltzer and Berger, 1982a). See Anderson et al. (1969), Sorensen and Anderson (1973), Snow et al. (1973), Janni (1982), Seltzer and Berger (1982a,b, 1984), Berger and Seltzer (1982), and Tsoulfanidis (1995) for experimentally determined values of I for various elements and thorough treatments of stopping power calculations. Values of mean excitation potentials, I , for 100 elements and many inorganic and organic compounds are provided by Seltzer and Berger (1982a, 1984).

An example of the application of one of the above equations would be the following calculation of the stopping power for a 2.280 MeV beta particle (E_{max}) emitted from ^{90}Y traveling through a NaI solid scintillation crystal detector. This would be a practical example, as the NaI detector is used commonly for the measurement of ^{90}Y . The solution is as follows:

Firstly, the calculation of relevant variables are

$$\gamma = \frac{2.280 \text{ MeV} + 0.511 \text{ MeV}}{0.511 \text{ MeV}} = 5.462$$

$$\beta = \sqrt{1 - \frac{1}{\gamma^2}} = 0.9831 \quad \text{and} \quad \beta^2 = 0.9665$$

The atomic weight A for NaI would be the average atomic weight (A_{av}) based on the weight fraction w_{Na} for Na (15.3%) and w_I for I (84.7%) in NaI or

$$\begin{aligned} A_{av} &= (0.153)(A_{Na}) + (0.847)(A_I) \\ &= (0.153)(23) + (0.847)(127) = 111 \end{aligned}$$

Also, on the basis of the weight averages for Na and I, the atomic number Z would be the effective atomic number Z_{ef} calculated according to the following equation described by Tsoulfanidis (1995) and Andreo et al (2005):

$$Z_{ef} = \frac{\sum_{i=1}^L (w_i/A_i) Z_i^2}{\sum_{i=1}^L (w_i/A_i) Z_i} \quad (1.397)$$

where L is the number of elements in the absorber, w_i is the weight fraction of the i th element, A_i is the atomic weight of the i th element, Z_i is the atomic number of the i th element, and $w_i = N_i A_i / M$ where N_i is the number of atoms of the i th element and M is the molecular weight of the absorber. If we apply Eqn (1.397) to the absorber NaI, we find

$$\begin{aligned} Z_{ef} &= \frac{(0.153/22.989)(11)^2 + (0.847/126.893)(53)^2}{(0.153/22.989)(11) + (0.847/126.893)(53)} \\ &= 45.798 \end{aligned} \quad (1.398)$$

For pure elements, the value of the mean excitation potential, I , can be calculated according to the empirical formula provided by Eqn (1.395). However, for the compound NaI, the mean excitation energy, $\langle I \rangle$, will be calculated according to Eqn (1.196) as follows:

$$\begin{aligned} \langle I \rangle &= \exp \left\{ \frac{\left[(0.153)(11/22.989) \ln 149 \right] + \left[(0.847)(53/126.893) \ln 491 \right]}{\left[(0.153)(11/22.989) \right] + \left[(0.847)(53/126.893) \right]} \right\} = 400 \text{ eV} \end{aligned} \quad (1.399)$$

where the values of the mean excitation energy, J_i , for the elements Na and I of 149 and 941 eV, respectively, were obtained from Steltzer and Berger (1982a). From Eqn (1.393), the stopping power, due to collisional interactions, for the 2.280 beta particle traveling through a NaI crystal, is calculated as

$$\begin{aligned} \frac{dE}{dx} &= 4(3.14)(2.818 \times 10^{-15} \text{ m})^2 \left(\frac{0.511 \text{ MeV}}{0.9665} \right) (3.67 \text{ g/cm}^3) \\ &\times \left(\frac{6.022 \times 10^{23} \text{ atoms/mol}}{111 \text{ g/mol}} \right) \left(\frac{10^6 \text{ cm}^3}{\text{m}^3} \right) \times (45.798) \\ &\times \left\{ \ln \left(\frac{(0.9831)(5.462)\sqrt{4.462}}{400 \text{ eV}} (0.511 \text{ MeV})(10^6 \text{ eV/MeV}) \right) \right. \\ &\left. + \frac{1}{2(5.462)^2} \left[\frac{(4.462)^2}{8} + 1 - (5.462^2 + 2(5.462) - 1) \ln 2 \right] \right\} \\ &= 460.4 \text{ MeV/m} \end{aligned} \tag{1.400}$$

The term $(10^6 \text{ cm}^3/\text{m}^3)$ is included in the above calculation to maintain consistency of units, thus converting the units of density expressed in g/cm^3 to g/m^3 . In SI units, the stopping power can be expressed in units of J/m or

$$(460.4 \text{ MeV/m})(1.602 \times 10^{-13} \text{ J/MeV}) = 7.38 \times 10^{-11} \text{ J/m} \tag{1.401}$$

The stopping power is often expressed in units of $\text{MeV cm}^2/\text{g}$ or $\text{J m}^2/\text{kg}$, which provides values for stopping power without defining the density of the absorber medium (Taylor et al, 1970 and Tsoulfanidis, 1995). In these units the above calculation can be expressed as

$$\frac{1}{\rho} \left(\frac{dE}{dx} \right) = \frac{4.604 \text{ MeV/cm}}{3.67 \text{ g/cm}^3} = 1.25 \text{ MeV cm}^2/\text{g} \tag{1.402}$$

This calculated value of stopping power due to collision or Coulombic interactions agrees closely to the on-line computer-calculated value of $1.20 \text{ MeV cm}^2/\text{g}$ for a 2.280 MeV beta particle or electron in NaI (See NIST, 2011).

Eqn (1.393) used above to calculate the stopping power for the 2.280 MeV beta particle from ^{90}Y in NaI accounts only for energy of the beta particle lost via collision interactions resulting in ionization and electron-orbital excitations. The equation does not account for radiative energy loss via the production of bremsstrahlung radiation, which can be very significant with beta particles of high energy and absorber materials of high atomic number. Thus, a complete calculation of the stopping power must include also the radiative energy loss via bremsstrahlung as described by Eqn (1.175), that is,

$$\left(\frac{dE}{dx} \right)_{\text{total}} = \left(\frac{dE}{dx} \right)_{\text{col.}} + \left(\frac{dE}{dx} \right)_{\text{rad.}} \tag{1.403}$$

where $(dE/dx)_{\text{total}}$ is the rate of total beta particle or electron energy loss in an absorber, $(dE/dx)_{\text{col.}}$ is the rate of energy loss due to collision or ionization interactions, and $(dE/dx)_{\text{rad.}}$ is the rate of radiative energy loss due to bremsstrahlung production. We must keep in mind that each stopping-power calculation, such as the above example, provides values for only one beta particle or electron energy. Beta particles, on the other hand, are

emitted from decaying radionuclides with a broad spectrum of energies from zero to E_{max} , the majority of which may possess an average energy, E_{av} , of approximately one-third of E_{max} .

The ratio of beta-particle energy loss via radiative energy emission as bremsstrahlung to energy loss via collision interactions causing ionization and excitation is described by the approximation

$$\frac{E_{\text{brems.}}}{E_{\text{ion.}}} \approx \frac{EZ}{750} \tag{1.404}$$

where E is the beta-particle energy in MeV and Z is the atomic number of the absorber material (Evans, 1955, Friedlander et al, 1964, and Faw and Schultis, 2004). From Eqns (1.403) and (1.404), we can approximate the radial energy loss for the 2.280 MeV beta particle in NaI using the previously calculated ionizational energy loss Eqn (1.400) as

$$\begin{aligned} \left(\frac{dE}{dx} \right)_{\text{rad.}} &\approx \frac{ZE}{750} \left(\frac{dE}{dx} \right)_{\text{col.}} \\ &\approx \frac{(45.798)(2.280)}{750} (4.604 \text{ MeV/cm}) \\ &\approx 0.641 \text{ MeV/cm} \end{aligned} \tag{1.405}$$

This radiative energy loss expressed in units of $\text{MeV cm}^2/\text{g}$ would be

$$\frac{1}{\rho} \left(\frac{dE}{dx} \right) = \frac{0.641 \text{ MeV/cm}}{3.67 \text{ g/cm}^3} = 0.17 \text{ MeV cm}^2/\text{g} \tag{1.406}$$

This agrees closely to the on-line computer calculated value of $0.16 \text{ MeV cm}^2/\text{g}$ for the radiative energy loss a 2.280 MeV beta particle or electron in NaI (See NIST, 2011). The total stopping power of the 2.280 MeV beta particle in NaI according to Eqn (1.403) is calculated as

$$\begin{aligned} \left(\frac{dE}{dx} \right)_{\text{total}} &= \left(\frac{dE}{dx} \right)_{\text{col.}} + \left(\frac{dE}{dx} \right)_{\text{rad.}} \\ &= 4.60 \text{ MeV/cm} + 0.64 \text{ MeV/cm} \\ &= 5.24 \text{ MeV/cm} \end{aligned} \tag{1.407}$$

Beta-particle loss via bremsstrahlung radiation of the 2.280 MeV beta particles from ^{90}Y is significant in NaI, namely, $0.641/5.24$ or 12.2% of the total energy loss. Consequently, NaI solid scintillation detectors are at times used for the analysis of ^{90}Y (Coursey et al, 1993). The actual detection efficiencies reported by Coursey et al (1993) for the solid scintillation analysis of ^{90}Y fall in the range of 9.9–18% depending on sample and detector counting geometries. The detection efficiencies exceed the above-calculated 12.2% energy loss via bremsstrahlung production, because the NaI detector will also respond to collision-excitation energy of the beta particle in addition to bremsstrahlung radiation excitation. Caution is warranted in making correlations between detector response to beta-particle radiation and stopping-power calculations, because we must keep in mind that each stopping-power calculation, such as the above example, provides values for only one beta-particle energy. Beta particles, on the other hand, are emitted with a broad spectrum of energies from zero to E_{max} .

Bremsstrahlung production will increase as the absorber atomic number (Z) and beta-particle or electron energy increase. Bremsstrahlung is highly penetrating electromagnetic radiation, and thus low atomic number absorbers such as aluminum or plastic (high in carbon and hydrogen) may be used as shields against beta-particle radiation. Shielding material containing high-atomic-number elements, such as lead glass, against high-energy beta particles will yield high levels of bremsstrahlung radiation. The effect of atomic number (Z) and beta-particle or electron energy (E) on the ratio of energy loss via bremsstrahlung production to ionization energy is illustrated in Fig. 1.92. The effective atomic numbers of compounds, such as polyethylene ($-C_2-H_4)_n$, $Z_{ef} = 5.28$), water ($Z_{ef} = 6.60$) and air ($Z_{ef} = 7.3$), included as absorbers in Fig. 1.92, are a function of the weight fraction of each element in the compound calculated according to Eqn (1.397). As illustrated in Fig. 1.92, absorbers of low atomic number yield less bremsstrahlung radiative energy loss from high-energy beta-particle or electron interactions in matter.

B. Linear Energy Transfer

The International Commission on Radiation Units and Measurements (ICRU) defines linear energy transfer (L) of charged particles in a medium as

$$L = \frac{dE_L}{dl} \tag{1.408}$$

where dE_L is the average energy locally imparted to the medium by a charged particle of specified energy in traversing a distance dl (Taylor et al, 1970). The term "locally imparted" refers either to a maximum distance from the particle track or to a maximum value of discrete energy loss by the particle beyond which losses are no longer considered as local. Linear energy transfer or LET is generally measured in units of keV/ μ m. The ICRU recommends, when a restricted form of LET is

desired, that the energy cutoff form of LET be applied, because this can be evaluated using restricted stopping-power formulas (Taylor et al, 1970). The energy-restricted form of LET or L_Δ is therefore defined as that part of the total energy loss of a charged particle which is due to energy transfers up to a specified energy cutoff value:

$$L_\Delta = \left(\frac{dE}{dl} \right)_\Delta \tag{1.409}$$

where the cutoff energy (Δ) in eV units must be defined or stated. If no cutoff energy is applied, then the subscript ∞ is used in place of Δ , where L_∞ would signify the value of LET, which includes all energy losses and would therefore be equal to the total mass stopping power.

Fig. 1.93 illustrates charged particle interactions within an absorber involved in the measurement of LET. The possible types of energy loss, ΔE , of a charged particle of specified energy, E , traversing an absorber over a track length dl is illustrated, where O represents a particle traversing the observer without any energy loss, U is the energy transferred to a localized interaction site, q is the energy transferred to a short-range secondary particle when $q \leq \Delta$, and Δ is a selected cutoff energy level (e.g., 100 eV), Q' is the energy transferred to a long-range secondary particle (e.g., formation of delta rays) for which $Q' > \Delta$, γ is the energy transferred to photons (e.g., excitation fluorescence, Cherenkov photons, etc.), r is a selected cutoff distance from the particle's initial trajectory or path of travel, and θ is the angle of particle scatter. The interactions q , Q , and γ are subdivided in Fig. 1.93 when these fall into different compartments of the absorber medium. See Taylor et al, (1970) for methods used for the precise calculations of LET. Some examples of LET in water for various radiation types are given in Table 1.25. The table clearly illustrates that radiation of a given energy with shorter range in a medium will yield higher values of LET than radiations of the same energy with longer

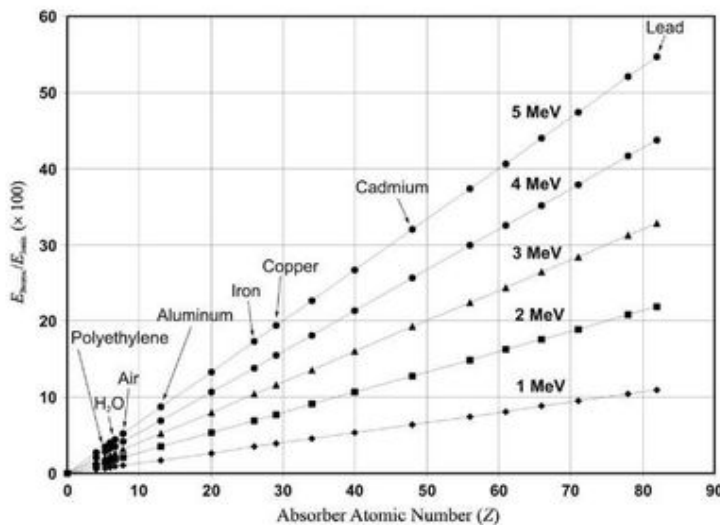


FIGURE 1.92 Ratio of energy loss via radiative bremsstrahlung production to energy loss via ionization or collision energy loss, expressed as a percent and calculated according to the approximation $E_{brem}/E_{ion} = EZ/750$, for beta particles or electrons of energies E ranging from 1 to 5 MeV as a function of atomic number (Z) of the absorber material. Some common absorbers are identified above data points corresponding to their atomic number (Z) or effective atomic number (Z_{ef}) for absorbers that are compounds. (From L'Annunziata, 2007, reprinted with permission of Elsevier © 2007.)

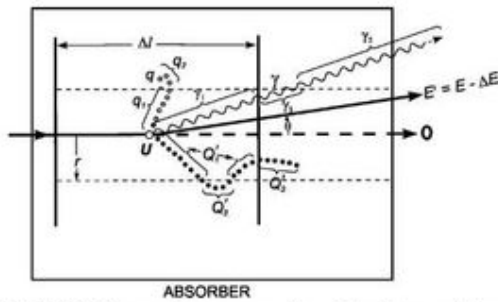


FIGURE 1.93 Diagram of the passage of a particle of energy E through a thickness Δl of material illustrating the several types of energy loss that may occur. (From Taylor et al., (1970) reprinted with permission from ICRU © 1970.)

ranges in the same medium. This may be intuitively obvious, because the shorter the range of the radiation, the greater is the energy dissipated per unit path length of travel. We can take this further and generalize that the following radiation types will yield LET values of decreasing orders of magnitude (the heavier charged particles are considered here to be of the same energy for purposes of comparison) according to the sequence:

Decreasing LET:

- Fission Products
- Alpha Particles
- Deuterons
- Protons
- Low-energy x Rays and Beta Particles
- High-energy x Rays and Beta Particles
- Gamma Radiation and High-energy Beta Particles

Although the electromagnetic x- and gamma radiations are not charged particles, these radiations do have the

characteristics of particles (photons) that produce ionization in matter. They are, therefore, included in the above sequence and among the radiations listed in Table 1.25.

The term delta rays (δ -rays), referred to in the previous paragraph, is used to identify high-energy electrons that produce secondary ionization. When a charged particle, such as an alpha particle, travels through matter, ionization occurs principally through Coulombic attraction of orbital electrons to the positive charge on the alpha particle with the ejection of electrons of such low energy that these electrons do not produce further ionization. However, direct head-on collisions of the primary ionizing particle with an electron does occur occasionally whereby a large amount of energy is transferred to the electron. The high-energy electron will then travel on in the absorbing matter to produce secondary ionization. These high-energy electrons are referred to as delta rays. Delta rays form ionization tracks away from the track produced by the primary ionizing particle (Horowitz, 2006 and Cucinotta et al, 1998). Also, most of the muon-induced background in Ge gamma spectrometers is caused by bremsstrahlung radiation of delta electrons (Povinec et al, 2008).

When we compare particles of similar energy, we can state that the ranges of particles of greater mass and charge will obviously be shorter and the magnitude of their LET values would be consequently higher in any given medium. The relationship between mass, charge, energy, and the range of particles and their corresponding LET values can be appreciated from Table 1.26. The LET values in Table 1.26 are estimated by dividing the radiation energy by its range or path length in the medium. Such a calculation provides only an estimate of the LET, because the energy dissipated by the radiation will vary along its path of travel, particularly in the case of charged particles, more energy is released when the particle slows down before it comes to a stop as illustrated in Fig. 1.29, when energy liberated in ion-pair formation is the highest. Nevertheless, the LET values

TABLE 1.25 Track-average Values of LET (L_Δ) in Water Irradiated with Various Radiations^a

Radiation	Cut-off energy, Δ (eV)	L_Δ (keV/ μ m)
⁶⁰ Co gamma rays	Unrestricted	0.239
	10,000	0.232
	1,000	0.230
	100	0.229
22-MeV x-rays	100	0.19
2-MeV electrons (whole track)	100	0.20
200-kV x-rays	100	1.7
³ H beta particles	100	4.7
50-kV x-rays	100	6.3
5.3 MeV alpha particles (whole track)	100	43

^aFrom Taylor et al., (1970). Reprinted with permission from ICRU © 1970.

TABLE 1.26 Range and Approximate LET Values for Various Charged-Particle Radiations in Water in Order of Decreasing Mass and Charge^a

Nuclide	Radiation, energy (MeV)	Range in water (mm)	Average LET in water (keV/μm)
Thorium-232	α, 4.0	0.029 ^b	138
Americium-241	α, 5.5	0.048 ^b	114
Thorium-227	α, 6.0	0.055 ^b	109
Polonium-211	α, 7.4	0.075 ^b	98
—————	d, 4.0	0.219 ^c	18.3
—————	d, 5.5	0.377 ^c	14.6
—————	d, 6.0	0.440 ^c	13.6
—————	d, 7.4	0.611 ^c	12.1
—————	p, 4.0	0.355 ^d	11.3
—————	p, 5.5	0.613 ^e	9.0
—————	p, 6.0	0.699 ^f	8.6
—————	p, 7.4	1.009 ^g	7.3
Tritium	β ⁻ , 0.0186 (E _{max})0.00575 ^h		3.2 ^h
Carbon-14	β ⁻ , 0.156 (E _{max}) 0.280 ^h		0.56 ^h
Phosphorus-32	β ⁻ , 1.710 (E _{max}) 7.92 ^h		0.22 ^h
Yttrium-90	β ⁻ , 2.280 (E _{max}) 10.99 ^h		0.21 ^h

^aThe deuteron (d) and proton (p) energies were arbitrarily selected to correspond to the alpha-particle (α) energies to facilitate the comparison of the effects of particle mass and charge on range and LET.
^bCalculated according to Eqns (1.99) and (1.100).
^cThe deuteron range is calculated from the equation $R_{2,αE} = (M/Z^2)R_{p,E/M}$. The equation provides the range of a particle of charge Z, mass M, and energy E, where $R_{p,E/M}$ is the range in the same absorber of a proton of energy E/M (Friedlander et al., 1964).
^dCalculated according to Eqns (1.97), (1.99) and (1.100), $R_{de} = 28.5 \text{ mg/cm}^2$ (Fig. B.1, Appendix B).
^eCalculated according to Eqns (1.97), (1.99) and (1.100), $R_{de} = 49.5 \text{ mg/cm}^2$ (Fig. B.1).
^fCalculated according to Eqns (1.97), (1.99) and (1.100), $R_{de} = 56.5 \text{ mg/cm}^2$ (Fig. B.1).
^gCalculated according to Eqns (1.97), (1.99) and (1.100), $R_{de} = 62.0 \text{ mg/cm}^2$ (Fig. B.1).
^hCalculations are based on the maximum energy (E_{max}) of the beta particles. The range was calculated according to the empirical formula $R = 0.412E^{1.27-0.0954 \ln E}$ available from the curve provided in Fig. B.3, Appendix B.

provided in Table 1.26 give good orders of magnitude for comparative purposes.

The concept of LET and the calculated values of LET for different radiation types and energies can help us interpret and sometimes even predict the effects of ionizing radiation on matter. For example, we can predict that heavy charged particles, such as alpha radiation, will dissipate their energy at shorter distances within a given absorber body than the more penetrating beta- or gamma radiations. Also, low-energy x-radiation can produce a similar effect as certain beta radiations. The order of magnitude of the LET will help us predict the penetration power and degree of energy dissipation in an

absorber body, which is critical information in studies of radiation chemistry, radiation therapy, and dosimetry, among others. For additional information on linear energy transfer and its applications, the reader is referred to works by Jones et al (2010), Paschoa and Steinhäusler (2010), Pickrell (2009), Choudhuri et al (2007), Azab et al. (2006), Ehman and Vance (1991), Spinks and Woods (1990), and Farhatziz and Rodgers (1987).

XV. RADIONUCLIDE DECAY, INGROWTH, AND EQUILIBRIUM

The activity of a radioactive source or radionuclide sample is, by definition, its strength or intensity or, in other words, the number of nuclei decaying per unit time (e.g., dpm or dps). The activity decreases with time as a result of radionuclide decay. A unit of time in which there is an observable change in the activity of a given quantity of radionuclide may be very short, of the order of seconds, or very long, of the order of years. The rate of decay of some nuclides is so slow that it is impossible to measure any change in radioactivity during our lifetime.

A. Half-Life

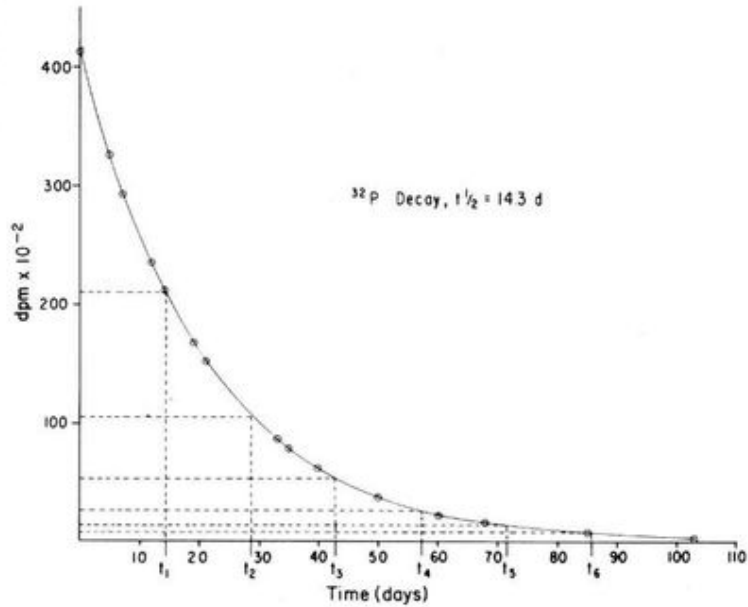
Rates of radionuclide decay are usually expressed in terms of half-life. This is the time, *t*, required for a given amount of radionuclide to lose 50 % of its activity. In other words, it is the time required for one-half of a certain number of nuclei to decay. The decay curve of ³²P (Fig. 1.94) illustrates the concept of half-life. In Fig. 1.94, the activity of the ³²P is plotted against time in days. It can be seen that, after every interval of 14.3 days, the radioactivity of the ³²P is reduced by half. Thus, the half-life, *t*_{1/2}, of ³²P is 14.3 days. It is not possible to predict when one particular atom of ³²P will decay; however, it is possible to predict statistically for a large number of ³²P radionuclides that one-half of the atoms would decay in 14.3 days.

The phenomenon of radioactivity decay and its measurement in terms of half-life was first observed by Ernest Rutherford (1900). He published his observations on the rate of decay of a certain isotope of thorium in the *Philosophical Magazine* in January 1900 less than four years after Henri Becquerel first reported the existence of radioactivity to the French Academy of Sciences in February and March 1896. Rutherford (1900) measured the rate of decay by the level of ionization that the radiation would produce in air as a function of time, and he noted the following:

...the intensity of the radiation has fallen to one-half its value after an interval of about one minute. The rate of leak [meaning rate of decay or rate of ionization caused by the radiation] due to the emanation was too small for measurement after an interval of 10 minutes [i.e., 10 half-lives]...The current [produced by the ionization] reaches half its value in about one minute — a result which agrees with the equation given, for $e^{-2t} = 1/2$ when $t = 60$ seconds.

In his original paper, Rutherford (1900) did not use the term 'half-life', but he defined mathematically the concept of half-life. As we shall see subsequently in Eqn (1.415) that the ratio of the number of radionuclides, *N*, in a sample at a given time, *t*, to

FIGURE 1.94 Decay of ^{32}P represented as a linear plot of activity in disintegrations per minute (dpm) against time in days. Horizontal and vertical lines between the ordinate and abscissa delineate ^{32}P activities (dpm) after six half-lives identified by the symbols $t_1, t_2, t_3, \dots, t_6$. (From L'Annunziata, M. F., 1965, unpublished work.)



the original number of nuclides, N_0 , in that sample at time $t = 0$, is equal to $e^{-\lambda t}$ where e is the base to the natural logarithm, λ is a decay constant of that radionuclide, and t is the interval of time.

When radionuclide decay can be recorded within a reasonable period of time, the half-life of a nuclide can be determined by means of a semi-logarithmic plot of activity versus time, as shown in Fig. 1.95. Radionuclide decay is a logarithmic relation, and the straight line obtained on the semi-logarithmic plot permits a more accurate determination of the half-life.

Ernest Rutherford and Frederick Soddy (1902) in the *Philosophical Magazine* summarized their findings on radioactivity and radionuclide decay as follows:

Turning from the experimental results to their theoretical interpretation, it is necessary to first consider the generally accepted view of the nature of radioactivity. It is well established that this property is the function of the atom and not of the molecule. Uranium and thorium, to take the most definite cases [example], possess the property in whatever molecular condition they occur...So far as the radioactivity of different compounds of different density and states of division can be compared together, the intensity of the radiation appears to depend only on the quantity of active element [radioisotope] present.

The above statement by Rutherford and Soddy in 1902 that "the intensity of the radiation appears to depend only on the quantity of active element present" is defined subsequently in mathematical terms.

The number, ΔN , of atoms disintegrating in a given time, Δt , is proportional to the number, N , of radioactive atoms present. This relationship may be written as

$$\Delta N / \Delta t = \lambda N \tag{1.410}$$

or

$$dN / dt = -\lambda N \tag{1.411}$$

where λ is a proportionality constant, commonly referred to as the decay constant, and the negative sign signifies a decreasing number of radionuclides with time.

One condition must be fulfilled for Eqn (1.410) to be rigorously applicable: the total number of radioactive atoms being considered must be large enough to make statistical methods valid. For example, in the case of a single isolated atom of ^{32}P , there is no way to predict when the atom will decay. In fact, the atom might decay in the first second after $t = 0$ (the moment observations are initiated) or it might decay days or weeks later. The concept of half-life is a statistical one, which, when applied to a large number of atoms, as is usually the case, allows an accurate calculation of the activity of radionuclides after a given time interval.

For radionuclide decay calculations, Eqn (1.411) must be transformed into a more suitable form and may be expressed as

$$dN / N = -\lambda dt, \tag{1.412}$$

which can be integrated between the limits N_0 and N and between t_0 and t , where t_0 is 0 (the moment observations are initiated), N_0 is the number of atoms originally present at time t_0 , and N is the number of atoms remaining after time t :

$$\int_{N_0}^N dN / N = -\lambda \int_{t_0}^t dt \tag{1.413}$$

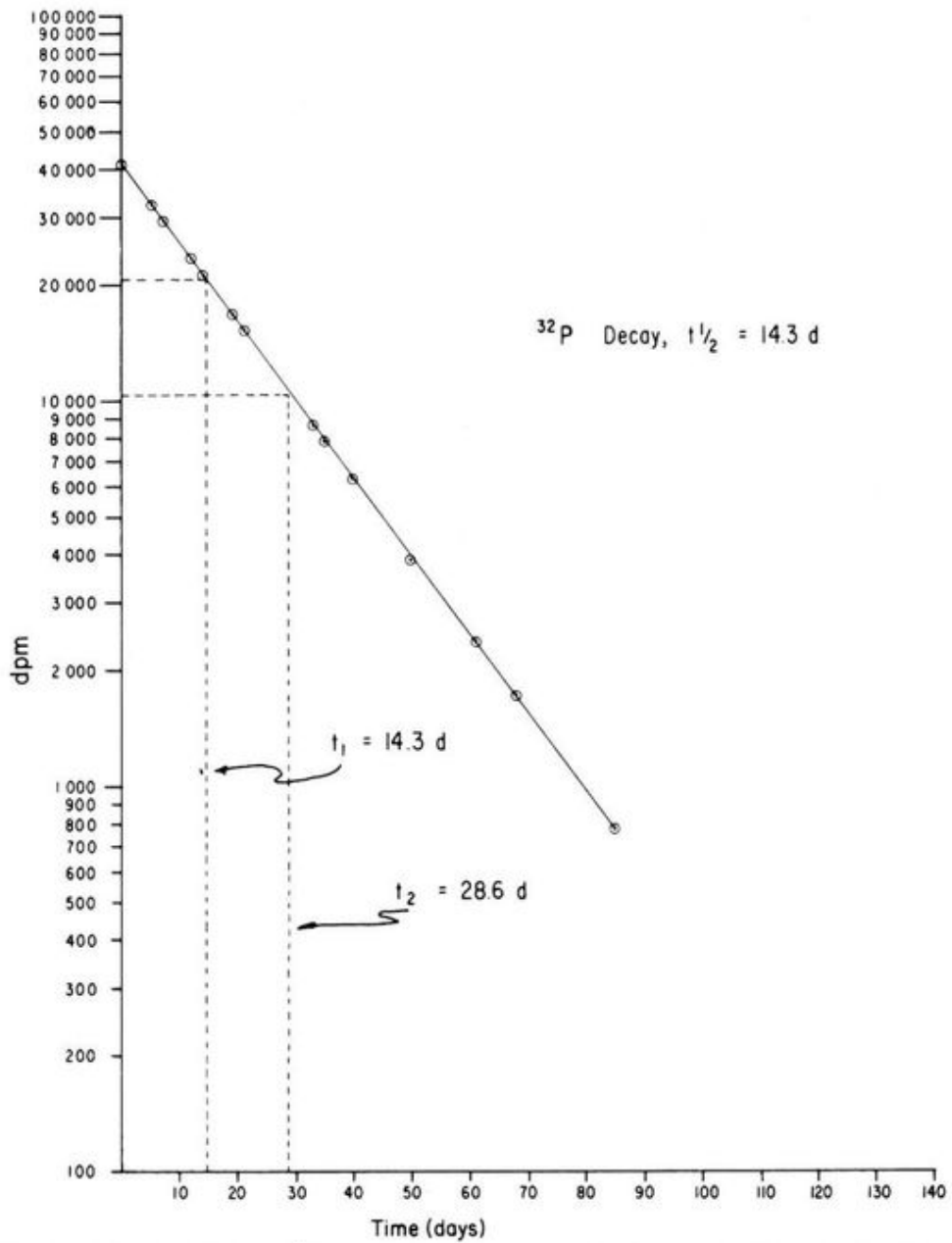


FIGURE 1.95 Semi-logarithmic plot of the decay of ^{32}P . Two half-lives (t_1 and t_2) are delineated by horizontal and vertical lines between the ordinate and abscissa. (From L'Annunziata, M. F., 1965, unpublished work.)

to give

$$\ln N/N_0 = -\lambda t \tag{1.414}$$

Eqn (1.414) may be written in exponential form as

$$N = N_0 e^{-\lambda t} \tag{1.415}$$

where e is the base of the natural logarithm, λ is the decay constant, and t is the interval of time. Eqn (1.415) is the form used to determine the decay of a radionuclide sample after a given time interval. To use Eqn (1.415), the value of the decay constant λ must be known, and this is different for each radionuclide. To determine λ for a particular radionuclide, a relationship between the decay constant and the half-life may be derived from the decay Eqn (1.414), which may be transposed to

$$\ln N_0/N = \lambda t \tag{1.416}$$

By definition, we know that, after an interval of time corresponding to the half-life, half of the original activity remains. Therefore, we may assign the original activity N_0 as unity whereby after one-half-life the remaining activity N would be one-half of unity, and Eqn (1.416) would become

$$\ln 1/(1/2) = \lambda t_{1/2} \tag{1.417}$$

or

$$\ln 2 = \lambda t_{1/2} \tag{1.418}$$

and

$$0.693 = \lambda t_{1/2} \tag{1.419}$$

The decay constant can then be defined as

$$\lambda = 0.693/t_{1/2} \tag{1.420}$$

The value of λ can be calculated easily from the half-life of an isotope with Eqn (1.420). The units used for λ are expressed in reciprocal time, s^{-1} , m^{-1} , h^{-1} , d^{-1} , or y^{-1} , depending on the half-life of the radionuclide and also on the time interval t used in Eqn (1.415). For example, if ^{32}P , which has a half-life of 14.3 days, is used in an experiment, λ may be expressed in d^{-1} . The unit of the decay constant must agree with the time interval t of Eqn (1.415).

The following example illustrates the use of Eqn (1.415) to calculate the decay of a radionuclide sample within any time interval.

If a sample contained 3.7 MBq of ^{32}P on a given date and an investigator wished to determine the amount remaining after a 30-day period, he would first determine the decay constant for ^{32}P according to Eqn (1.420) and then calculate the activity after the specified time period using the decay Eqn (1.415) as follows. The decay constant in units of d^{-1} is determined by

$$\lambda = 0.693/t_{1/2} = 0.693/14.3d = 4.85 \times 10^{-2}d^{-1}$$

With the calculated value of λ and the known time interval t , the activity of the remaining ^{32}P is determined according to Eqn (1.415) expressed in terms of activity (A) or

$$A = A_0 e^{-\lambda t} \tag{1.421}$$

and

$$\begin{aligned} A &= 3.7 \times 10^6 \text{ dps} \left(e^{-[(4.85 \times 10^{-2} \text{ day}^{-1})30 \text{ days}]} \right) \\ &= 3.7 \times 10^6 \text{ dps} (e^{-1.455}) \\ &= 3.7 \times 10^6 (0.2334) \\ &= 8.64 \times 10^5 \text{ dps} = 0.864 \text{ MBq} \end{aligned}$$

where A is the activity of the radionuclide in units of decay rate (e.g., dps) after time t and A_0 is the initial activity at time t_0 or $A_0 = 3.7 \text{ MBq} = 3.7 \times 10^6 \text{ dps}$ since by definition $1 \text{ MBq} = 1 \times 10^6 \text{ dps}$. Thus, after the 30-day period, the activity of ^{32}P decayed from an initial activity of 3.7 MBq to 0.864 MBq.

The decay equation has many practical applications, as it can be used also to calculate the time required for a given radionuclide sample to decay to a certain level of activity. Let us consider the following example:

A patient was administered intravenously 600 MBq of ^{99m}Tc methylene diphosphate, which is a radiopharmaceutical administered for the purposes of carrying out a diagnostic bone scan. The doctor then wanted to know how much time would be required for the ^{99m}Tc radioactivity in the patient's body to be reduced to 0.6 MBq (0.1% of the original activity) from radionuclide decay alone ignoring any losses from bodily excretion. The half-life $t_{1/2}$ of ^{99m}Tc is 6.00 hours. To calculate the time required, we can write Eqn (1.421) as

$$A/A_0 = e^{-\lambda t} \tag{1.422}$$

where A is the activity in dps (disintegrations per second) after time t and A_0 is the initial activity at time t_0 . Eqn (1.422) can be transposed to

$$\ln A_0/A = \lambda t \tag{1.423}$$

or

$$t = \frac{1}{\lambda} \ln \frac{A_0}{A} \tag{1.424}$$

By definition Eqn (1.420) the decay constant λ of ^{99m}Tc is $0.693/t_{1/2}$ or $0.693/6.00 \text{ h}$. Solving Eqn (1.424) after inserting the value of λ and the relevant activities of ^{99m}Tc gives

$$\begin{aligned} t &= (6.00 \text{ h}/0.693) \ln(600 \text{ MBq}/0.6 \text{ MBq}) \\ &= 59.8 \text{ hours} = 2.5 \text{ days} \end{aligned}$$

In the case of a mixture of independently decaying radionuclides, the rate of decay of each nuclide species does not change. However, the rate of decay of the overall sample is equal to the sum of the decay rates of the individual nuclide species. The cumulative decay of a mixture of independently decaying nuclides from the most simple case of a mixture of two nuclides to a more complex case of n number of nuclides is described by

$$N = N_1^0 e^{-\lambda_1 t} + N_2^0 e^{-\lambda_2 t} + \dots + N_n^0 e^{-\lambda_n t} \tag{1.425}$$

where N is the number of atoms remaining after time t , and N_1^0 , N_2^0 , and N_n^0 are the number of atoms originally present at time t_0 of 1, 2, and n number of nuclide species, respectively.

The semi-logarithmic decay plot of a mixture of two independently decaying nuclides is not a straight line, contrary to pure

radionuclide samples, but is a composite plot, as in the case of a mixture of ^{32}P and ^{45}Ca (see Fig. 1.96). If the half-lives of the two nuclides are significantly different, the composite curve may be analyzed so that these may be determined. If the decay of the composite mixture can be observed over a reasonable period of time, the composite curve will eventually yield a straight line representing the decay of the longer-lived nuclide after the disappearance of the shorter-lived nuclide (depicted in Fig. 1.96). This straight line may be extrapolated to time $t = 0$ so that the activity (dpm) of this nuclide at $t = 0$ can be found. The difference between the activity at $t = 0$ of the longer-lived nuclide and the total activity of the sample at $t = 0$ gives the activity at $t = 0$ of the shorter-lived nuclide. Likewise, further subtraction of points of the extrapolated decay curve from the composite curve yields the decay curve of the shorter-lived nuclide.

The half-lives of the two radionuclides are determined from the slopes of the two decay curves isolated from the composite curve. Eqn (1.416), which is expressed in natural logarithms, may be transformed to logarithms to the base 10 by

$$2.30 \log(N_1/N_2) = \lambda(t_2 - t_1) \quad (1.426)$$

or

$$\log(N_1/N_2) = \frac{\lambda}{2.30}(t_2 - t_1) \quad (1.427)$$

where N_1 and N_2 are the numbers of atoms or activity of the sample at times t_1 and t_2 , respectively. As $\lambda/2.30$ of Eqn (1.427) is equal to the slope, the decay constant, λ , may be calculated from a graphical determination of the slope. With a calculated value of λ , the half-life of the nuclide is then calculated from Eqn (1.420).

Many radionuclides have very long half-lives, which make the graphic representation of their decay impossible. Some examples are ^3H ($t_{1/2} = 12.3$ y), ^{14}C ($t_{1/2} = 5.73 \times 10^3$ y), ^{40}K ($t_{1/2} = 1.3 \times 10^9$ y), and ^{174}Hf ($t_{1/2} = 2 \times 10^{15}$ y) (see Appendix A.). In such cases, the half-lives can be calculated from Eqns (1.411) and (1.420). The decay rate or activity, A , in disintegrations per year (DPY) of a given nuclide sample, defined by dN/dt of Eqn (1.411), is measured experimentally. The number of atoms of the radioassayed sample, defined by N of Eqn (1.411), must be known or determined. This is simple for pure samples. For example, the number of atoms of ^{40}K in a pure sample of KCl is easily calculated from Avogadro's number (6.022×10^{23} molecules/mol) and the percentage natural abundance of ^{40}K (0.012 %). Samples of unknown purity and isotopic abundance require a quantitative analysis of the element such as that provided by a mass spectral analysis of the isotopic abundance. The value of λ in y^{-1} is calculated as

$$\lambda = \frac{dN/dt}{N} = \frac{A}{N} = \frac{\text{CPM}/E}{N} (5.25 \times 10^5 \text{ min/year}) \quad (1.428)$$

where A is the sample nuclide activity in DPY, N is the number of atoms of the nuclide in the sample, CPM is the sample count rate provided by the instrument radioactivity detector, E is the instrument counting efficiency, and $5.25 \times 10^5 \text{ min/year}$ is the factor used to convert counts per minute (CPM) to counts per year (CPY). The half-life can then be

calculated according to Eqns (1.420) and (1.428), both of which define the value of λ .

Let us look at a practical example of the use of the above equations to determine the half-life of ^{40}K taken from the work of Grau Malonda and Grau Carles (2002). The accurate determination of the half-life of ^{40}K has very practical implications, as it is currently used by geologists to date a rock's formation based on the measurement of the quantity of the stable daughter nuclide ^{40}Ar . Grau Malonda and Grau Carles (2002) report the accurate determination of the half-life of ^{40}K by measuring the activity of ^{40}K in a sample of pure KNO_3 and applying the relationships of half-life to λ according to Eqns (1.420) and (1.428). They measured the ^{40}K specific activity in KNO_3 by the very accurate CIEMAT/NIST efficiency tracing liquid scintillation standardization method (see Chapter 7) to be $12.24 \pm 0.014 \text{ Bq/g}$. Also, applying the known isotopic concentration of ^{40}K in KNO_3 of 0.01167% and the value of Avogadro's number 6.022×10^{23} atoms per mole, they could calculate the number of atoms of ^{40}K in 1 g of KNO_3 as follows:

$$\left(\frac{6.022 \times 10^{23} \text{ atoms K/mole KNO}_3}{(101.103 \text{ g KNO}_3/\text{mole KNO}_3)} \right) \left(\frac{0.01167 \text{ atoms } ^{40}\text{K}}{100 \text{ atoms K}} \right) = 6.951 \times 10^{17} \text{ atoms } ^{40}\text{K/g KNO}_3$$

From Eqns (1.420) and (1.428), we can write

$$\frac{1}{\lambda} = \frac{t_{1/2}}{0.693} = \frac{N}{A} \quad (1.429)$$

or

$$t_{1/2} = 0.693 \left(\frac{N}{A} \right) \quad (1.430)$$

From the specific radioactivity of ^{40}K in KNO_3 (i.e., $\text{dps } ^{40}\text{K/g KNO}_3$) determined by the very accurate CIEMAT/NIST efficiency tracing liquid scintillation standardization method, and the calculated number of atoms of ^{40}K per gram of KNO_3 , Grau Malonda and Grau Carles (2002) calculated the half-life of ^{40}K as

$$t_{1/2} = 0.693 \left(\frac{6.951 \times 10^{17} \text{ atoms } ^{40}\text{K/g KNO}_3}{(12.24 \text{ dps } ^{40}\text{K/g KNO}_3)(60 \text{ s/m})(5.25 \times 10^5 \text{ m/y})} \right)$$

and

$$t_{1/2} = 1.248 \times 10^9 \text{ y}$$

From the mean of nine determinations, Grau Malonda and Grau Carles (2002) were able to assign the value of the half-life ($t_{1/2}$) of ^{40}K to be $(1.248 \pm 0.004) \times 10^9 \text{ y}$ at a 95% confidence level.

Other radionuclides have very short half-lives such as ^{209}Ra ($t_{1/2} = 4.6 \text{ s}$), ^{215}At ($t_{1/2} = 1.0 \times 10^{-4} \text{ s}$), and ^{212}Po ($t_{1/2} = 2.98 \times 10^{-7} \text{ s}$). Half-lives of such short duration can be determined by delayed-coincidence methods (Jakubek et al, 2010, Kurtukian-Nieto, et al, 2008, Morozov et al, 2006, 2002 and 1998, Schwarzschild, 1963, Oms, 2004, Petkov et al, 2003, and Ohm et al, 1990), which involve the use of scintillation and semiconductor detectors with detector response times as short

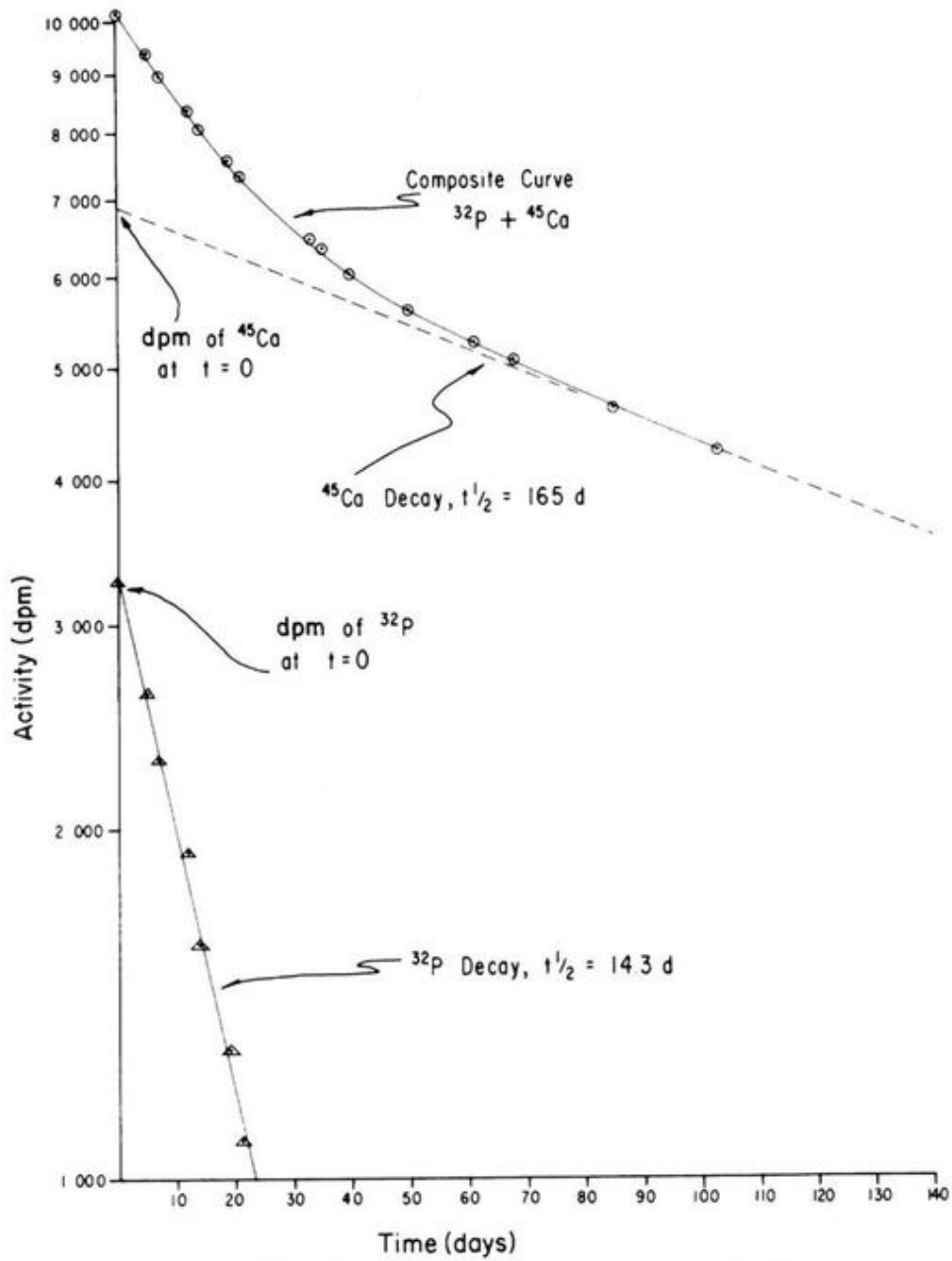


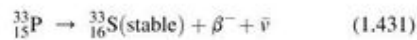
FIGURE 1.96 Semi-logarithmic decay curves of ^{32}P and ^{45}Ca isolated from a composite decay curve of a mixture of $^{32}\text{P} + ^{45}\text{Ca}$. (From L'Annunziata, M. F., 1965, unpublished work.)

as 10^{-11} seconds. The technique has also been applied to the measurement of the half-lives of excited nuclear states, such as the 8.7 ns and 98.1 ns half-lives of the 14.4 and 136.5 keV excited states of ^{57}Fe daughter nuclides, that emit gamma radiation, following the decay of ^{57}Co (Morozov et al, 2006, 2002). Radiation detectors with resolving times of fractions of a microsecond are set electronically so that a delay circuit will detect a radiation-induced pulse from the parent in coincidence with a radiation pulse produced from the daughter. Varying the delay time of the coincidence circuit results in a delay of the coincidence pulse rate from which a decay curve of the very short-lived daughter nuclide can be plotted and the half-life determined.

B. General Decay Equations

The simplest decay relationship between parent and daughter nuclides that can be considered is that of a parent nuclide which decays to form a stable daughter nuclide.

The decay of the radionuclide ^{33}P serves as an example. The parent nuclide ^{33}P decays with a half-life of 25 days with the production of the stable daughter ^{33}S , as indicated by



Numerous radionuclides, such as ^3H , ^{14}C , ^{32}P , ^{35}S , ^{36}Cl , ^{45}Ca , and ^{131}I (see Appendix A), decay by this simple parent–daughter relationship.

However, numerous other radionuclides produce unstable daughter nuclides. The simplest case would be that in which the parent nuclide A decays to a daughter nuclide B, which in turn decays to a stable nuclide C:



In such decay chains, the rate of decay and production of the daughter must be considered as well as the rate of decay of the parent. The decay of the parent is described by the simple rate equation

$$-dN_A/dt = \lambda_A N_A \quad (1.433)$$

which is integrated to the form

$$N_A = N_A^0 e^{-\lambda_A t} \quad (1.434)$$

where N_A^0 is the number of atoms of the parent at the time $t = 0$ and N_A is the number of atoms after a given period of time $t = t_1$.

The decay rate of the daughter is dependent on its own decay rate as well as the rate at which it is formed by the parent. It is written as

$$-dN_B/dt = \lambda_B N_B - \lambda_A N_A \quad (1.435)$$

where $\lambda_B N_B$ is the rate of decay of the daughter alone and $\lambda_A N_A$ is the rate of decay of the parent or rate of formation of the daughter. Eqns (1.434) and (1.435) may be transposed into the linear differential equation

$$dN_B/dt + \lambda_B N_B - \lambda_A N_A^0 e^{-\lambda_A t} = 0 \quad (1.436)$$

which is solved for the number of atoms of daughter, N_B , as a function of time to give

$$N_B = \frac{\lambda_A}{\lambda_B - \lambda_A} N_A^0 (e^{-\lambda_A t} - e^{-\lambda_B t}) + N_B^0 e^{-\lambda_B t} \quad (1.437)$$

Although unnecessary in this treatment, the solution to Eqn (1.436) is given by Friedlander et al (1964).

In decay schemes of this type, the following three conditions may predominate: (1) secular equilibrium, (2) transient equilibrium, and (3) the state of no equilibrium. Each of these cases will now be considered in detail.

C. Secular Equilibrium

The phenomenon of radioisotope decay equilibrium was first observed by Ernest Rutherford and Frederick Soddy in 1902, which they reported in their classic paper on “The Cause and Nature of Radioactivity”. They reported their observations as follows:

Radioactivity is shown to be accompanied by chemical changes in which new types of matter are being continuously produced. These reaction products are at first radioactive, the activity diminishing regularly from the moment of formation. Their continuous production maintains the radioactivity of the matter producing them at a definite equilibrium value.

Secular equilibrium is a steady-state condition of equal activities between a long-lived parent radionuclide and its short-lived daughter. The important criteria upon which secular equilibrium depends are:

1. the parent must be long-lived, that is, negligible decay of the parent occurs during the period of observation, and
2. the daughter must have a relatively short half-life. The relative difference in half-life in this latter criterion is further clarified by

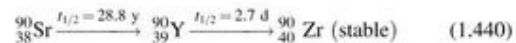
$$\lambda_A/\lambda_B \leq \sim 10^{-4} \quad (1.438)$$

that is,

$$\lambda_A \ll \lambda_B \quad (1.439)$$

where λ_A and λ_B are the respective decay constants of the parent and daughter nuclides. The importance of these two requirements can be clearly seen, if the ^{90}Sr (^{90}Y) equilibrium is taken as an example.

The nuclide ^{90}Sr is the parent in the decay scheme



The long half-life of ^{90}Sr definitely satisfies the first requirement for secular equilibrium, because over a quarter of a century is needed for it to lose 50 % of its original activity. As will be seen, less than 3 weeks are required for secular equilibrium to be attained and, in this interim period, negligible decay of ^{90}Sr occurs.

To satisfy the second requirement, the decay constants for ^{90}Sr and ^{90}Y , λ_A and λ_B , respectively, must be compared. The decay constants for ^{90}Sr and ^{90}Y are easily calculated from their half-lives and Eqn (1.420), and the values are $6.60 \times 10^{-5} \text{ d}^{-1}$

and $2.57 \times 10^{-1} \text{ d}^{-1}$, respectively. Consequently, in the comparison $\lambda_A/\lambda_B = 2.57 \times 10^{-4}$, and this is in agreement with the order of magnitude required for secular equilibrium.

An equation for the growth of daughter atoms from the parent can be obtained from Eqn (1.437) by consideration of the limiting requirements for secular equilibrium. Since $\lambda_A \approx 0$ and $\lambda_A \ll \lambda_B$, $e^{-\lambda_A t} = 1$ and λ_A falls out of the denominator in the first term. If the daughter nuclide is separated physically from the parent (L'Annunziata, 1971), $N_B^0 = 0$ at time $t = 0$ (time of parent–daughter separation) and the last term would fall out of Eqn (1.437). Thus, in the case of secular equilibrium, the expression of the ingrowth of daughter atoms with parent can be written as

$$N_B = \frac{\lambda_A N_A^0}{\lambda_B} (1 - e^{-\lambda_B t}) \quad (1.441)$$

If the observation of the ingrowth of the daughter is made over many half-lives of the daughter, it is seen that the number of atoms of daughter approaches a maximum value $\lambda_A N_A^0/\lambda_B$, which is the rate of production of daughter divided by its decay constant. The final form of Eqn (1.441) to be used for the calculation of the ingrowth of daughter can be expressed as

$$N_B = (N_B)_{\text{max}} (1 - e^{-\lambda_B t}) \quad (1.442)$$

Since the activity of the daughter atoms, A_B , is proportional to the number of daughter atoms, or $A_B = k\lambda_B N_B$, where k is the coefficient of detection of the daughter atoms, Eqn (1.442) may also be written as

$$A_B = (A_B)_{\text{max}} (1 - e^{-\lambda_B t}) \quad (1.443)$$

Rutherford and Soddy (1902) were the first to write and interpret Eqns (1.442) and (1.443) when they studied the equilibrium existing between radioactive thorium and a daughter radionuclide. They noted the following:

The radioactivity of thorium at any time is the resultant of two opposing processes: 1. The production of fresh radioactive material at a constant rate by the thorium compound, and 2. The decay of the radiating power of the active material with time. The normal or constant radioactivity possessed by thorium is an equilibrium value, where the rate of increase of radioactivity due to the production of fresh active material [daughter nuclide] is balanced by the rate of decay of radioactivity of that already formed...The experimental curve obtained with the hydroxide [This was the chemical form they used to separate the parent nuclide from the daughter.] for the rate of rise of its activity from a minimum to a maximum value will therefore be approximately expressed by the equation $I_t/I_0 = 1 - e^{-\lambda t}$, where I_0 represents the amount of activity recovered when the maximum is reached, and I_t the activity recovered after time t , λ being the same constant as before.

(Notice the similarity of Rutherford and Soddy's equation, which may be transposed to read $I_t = (I_0)(1 - e^{-\lambda t})$ and Eqns (1.442) and (1.443).)

Let us take an arbitrary example of equal activities of 100 dpm of parent ^{90}Sr and 100 dpm of daughter ^{90}Y , in secular equilibrium. From these activities, we can calculate and graphically represent the ingrowth of ^{90}Y with its parent and also the decay of ^{90}Y subsequent to the separation of parent and daughter nuclides (L'Annunziata, 1971). Identical activities

of ^{90}Sr and ^{90}Y are arbitrarily chosen, because their activities are equal while in secular equilibrium prior to their separation. Fig. 1.97 illustrates the calculated growth of ^{90}Y as produced by ^{90}Sr (curve B) using Eqn (1.443) with $(A_B)_{\text{max}} = 100$. The decay of separated ^{90}Y (curve A) is plotted by simple half-life decay ($t_{1/2} = 2.7 \text{ d}$). The dashed line (line C) represents the decay of ^{90}Sr , which is negligible during the period of observation ($t_{1/2} = 28.8 \text{ y}$). The total activity (curve D) is the result of both ^{90}Sr decay and the ingrowth of ^{90}Y after the separation of the latter, and it is obtained by the addition of curve B to line C. It may be noted from Fig. 1.97 that after approximately six half-lives of ^{90}Y (~18 d), the activity of ^{90}Y has increased to essentially the same activity of ^{90}Sr , after which both nuclides decay with the same half-life that of the parent ^{90}Sr (28.8 y).

Ernest Rutherford and Frederick Soddy in their classic paper on "The Cause and Nature of Radioactivity" in 1902 in the *Philosophical Magazine* made the first published observation of what is now known as secular equilibrium. They were studying the radioactivity of an isotope of thorium and a daughter isotope, which they called ThX. The term 'daughter isotope' for an isotope decay product was not then established, because knowledge of radioactivity was only then at its infancy. They summarized their findings with the following:

The foregoing experimental results may be briefly summarized. The major part of the radioactivity of thorium – ordinarily about 54 percent – is due to a non-thorium type of matter, ThX, possessing distinct chemical properties, which is temporarily radioactive, its activity falling to half value in about four days. The constant radioactivity of thorium is maintained by the production of this material at a constant rate. Both the rate of production of the new material and the rate of decay of its activity appear to be independent of the physical and chemical condition of the system.

(We now know that the activity of parent and daughter nuclides are equal in secular equilibrium and the value of 'about 54 percent' reported by Rutherford and Soddy was precisely 50 percent.)

As an example of the practical utility of this phenomenon, the application of secular equilibrium theory to the analysis of ^{90}Sr in the environment is discussed.

One method reported by the Los Alamos National Laboratory (see Gautier, 1995) entails the initial chelation (complex formation) of the sample strontium with the sodium salt of ethylenediaminetetraacetic acid (EDTA). The complexed strontium is then isolated by elution on an ion-exchange column. The eluted strontium is then precipitated as a carbonate. The activity of radioactive strontium, which will include $^{89}\text{Sr} + ^{90}\text{Sr}$ in the sample, is determined by low-background counting. Low-background liquid scintillation counting is most often used for the total $^{89}\text{Sr} + ^{90}\text{Sr}$ analysis, as described by Passo and Cook (1994). The isolated radiostromium is then allowed to remain in the sample without further treatment for a period of about 2 weeks to allow ingrowth of ^{90}Y . About 2 weeks are needed to ensure that the parent and daughter radionuclides are in secular equilibrium before the chemical separation of yttrium from strontium. From Eqn (1.443) it is calculated that after 2 weeks, the activity of ^{90}Y grows to 97.4 % of its original level. Carrier yttrium is then

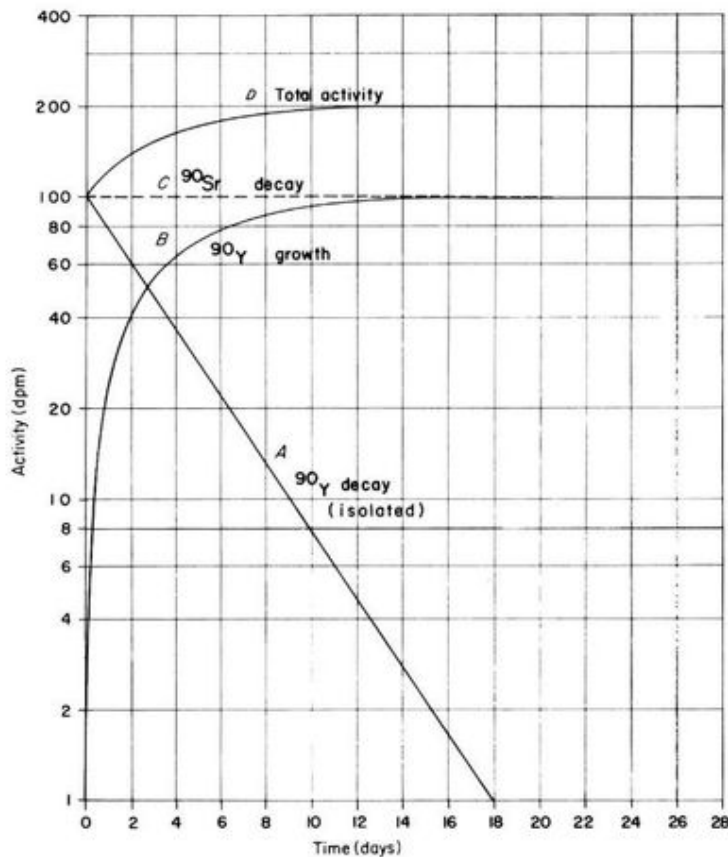


FIGURE 1.97 Growth and decay curves following the separation of ^{90}Sr (^{90}Y) in secular equilibrium. (A) Decay of isolated ^{90}Y . (B) Ingrowth of ^{90}Y with ^{90}Sr . (C) Decay of isolated ^{90}Sr . (D) Total activity from isolated ^{90}Sr , representing both ^{90}Sr decay and ^{90}Y growth until secular equilibrium is attained. (From L'Annunziata, 1971, reprinted with permission © 1971 American Chemical Society.)

added to the dissolved radiostrontium, and the yttrium is precipitated as the hydroxide, redissolved, and reprecipitated as an oxalate (see Section XVI.C for a discussion of the concepts of carrier and carrier-free radionuclides). The step involving the precipitation of yttrium from the sample results in the separation of ^{90}Y from the radiostrontium. The separated ^{90}Y can then be assayed by suitable low-background counting using liquid scintillation or Cherenkov counting (Passo and Cook, 1994 and L'Annunziata and Passo, 2002). The ^{90}Sr activity in the sample is determined from the activity of ^{90}Y by calculating the ^{90}Y decay from the time of separation (precipitation) of yttrium from strontium. This is possible because the parent and daughter radionuclides were at secular equilibrium (i.e., ^{90}Sr dpm = ^{90}Y dpm) at time $t = t_0$ when the precipitation and separation of yttrium from strontium were carried out. The ^{89}Sr activity in the sample is determined from the difference between the total radiostrontium activity ($^{89}\text{Sr} + ^{90}\text{Sr}$) and the measured activity of ^{90}Sr . A review of radioanalytical methods for the analysis of radioactive isotopes of strontium including ^{90}Sr , which involves the concept of secular equilibrium, is provided by Vajda and Kim (2010).

Certain chemical processes in natural and biological systems can preferentially select either the parent or daughter nuclide

and, in this manner, separate the two. For example, a research investigator could administer nuclides in secular equilibrium to a soil and plant system. At the time of administration, the nuclides are in secular equilibrium, that is, both the parent and daughter activities are equal. However, if in the course of the experiment the investigator obtains a plant sample for radioassay, which had preferably absorbed either the parent or daughter, problems ensue if the equilibrium phenomenon is not considered. Radioassay of plant tissue that had selectively concentrated the parent could show an initial progressive rise in radioactivity due to ingrowth of daughter, whereas a selective concentration of daughter would result in a sample showing an initial decrease in radioactivity. In cases such as these, it is necessary to isolate the parent radionuclide chemically and wait for a period of time sufficient to permit secular equilibrium to be reached [~2 weeks for the ^{90}Sr (^{90}Y) example] before the radiochemical analysis of a sample.

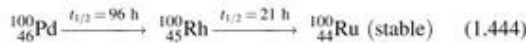
D. Transient Equilibrium

Like secular equilibrium, transient equilibrium is a steady-state condition between the parent and daughter nuclides. However, in transient equilibrium the parent–daughter nuclides do not

possess the same activities, but rather they decay at the same half-life, that of the parent nuclide.

The criterion upon which transient equilibrium rests is that the parent nuclide must be longer-lived than its daughter, but not of the order of magnitude described by Eqn (1.438); that is, it is necessary that $\lambda_A < \lambda_B$. However, the ratio λ_A/λ_B should fall within the limits $10^{-4} < \lambda_A/\lambda_B < 1$.

The decay chain of ^{100}Pd serves as an example of parent–daughter nuclides that may attain transient equilibrium. ^{100}Pd decays by electron capture to ^{100}Rh with a half-life of 96 h. The daughter nuclide ^{100}Rh decays by electron capture and positron emission to the stable nuclide ^{100}Ru . The half-life of the daughter nuclide is 21 h. The decay scheme may be represented as



The first criterion for transient equilibrium is satisfied in this case; the half-life of the parent nuclide is greater than that of the daughter. If the decay constants λ_A and λ_B are now calculated, we can determine whether or not the second criterion ($10^{-4} < \lambda_A/\lambda_B < 1$) is satisfied.

The value of λ_A , given by 0.693/96 h, is $7.2 \times 10^{-3} \text{ h}^{-1}$, and that of λ_B , given by 0.693/21 h, is $3.3 \times 10^{-2} \text{ h}^{-1}$. Consequently, the ratio $\lambda_A/\lambda_B = 2.2 \times 10^{-1}$ and lies within the limits of the second criterion.

If the general decay Eqn (1.437) of the daughter nuclide is considered, the term $e^{-\lambda_B t}$ is negligible compared with $e^{-\lambda_A t}$ for sufficiently large values of t . Thus, the terms $e^{-\lambda_B t}$ and $N_B^0 e^{-\lambda_B t}$ may be dropped from Eqn (1.437) to give

$$N_B = \frac{\lambda_A}{\lambda_B - \lambda_A} (N_A^0 e^{-\lambda_A t}) \quad (1.445)$$

for the decay of the daughter nuclide as a function of time. Because $N_A = N_A^0 e^{-\lambda_A t}$, Eqn (1.445) may be written as

$$N_B/N_A = \frac{\lambda_A}{\lambda_B - \lambda_A} \quad (1.446)$$

From Eqn (1.446), it can be seen that the ratio of the number of atoms or the ratio of the activities of the parent and daughter nuclides is a constant in the case of transient equilibrium.

Since $A_A = k_A \lambda_A N_A$ and $A_B = k_B \lambda_B N_B$, where A_A and A_B are the activities of the parent and daughter nuclides, respectively, and k_A and k_B are the detection coefficients of these nuclides, Eqn (1.446) may be written in terms of activities as

$$\frac{A_B}{k_B \lambda_B} (\lambda_B - \lambda_A) = \frac{A_A}{k_A \lambda_A} \lambda_A \quad (1.447)$$

or

$$A_B/A_A = \frac{k_B \lambda_B}{k_A (\lambda_B - \lambda_A)} \quad (1.448)$$

If equal detection coefficients are assumed for the parent and daughter nuclides, Eqn (1.448) may be written as

$$A_B/A_A = \frac{\lambda_B}{(\lambda_B - \lambda_A)} \quad (1.449)$$

Thus, for transient equilibrium Eqn (1.449) indicates that the activity of the daughter is always greater than that of the parent by the factor $\lambda_B/(\lambda_B - \lambda_A)$. Eqn (1.449) may likewise be written as

$$A_A/A_B = 1 - \lambda_A/\lambda_B \quad (1.450)$$

whereby the ratio A_A/A_B falls within the limits $0 < A_A/A_B < 1$ in transient equilibrium.

If an activity of 100 dpm is arbitrarily chosen for the daughter nuclide ^{100}Rh in transient equilibrium with its parent ^{100}Pd , the activity of ^{100}Pd can be found using either Eqns (1.449) or 1.450. Eqn (1.449) gives

$$100 \text{ dpm}/A_A = \frac{3.3 \times 10^{-2} \text{ h}^{-1}}{3.3 \times 10^{-2} \text{ h}^{-1} - 7.2 \times 10^{-3} \text{ h}^{-1}}$$

or

$$A_A = 78 \text{ dpm}$$

With the use of Eqn (1.449) or (1.450), the decay of the daughter nuclide may be calculated as a function of parent decay in transient equilibrium. The ^{100}Pd – ^{100}Rh parent–daughter decay in transient equilibrium is illustrated by curves A and B, respectively, of Fig. 1.98. The parent and daughter nuclides are shown to have respective activities of 78 dpm and 100 dpm at time $t = 0$. As curves A and B show, the parent and daughter nuclides in transient equilibrium decay with the same half-life, that corresponds to the half-life of the parent.

If the parent and daughter nuclides were to be separated, the daughter nuclide would decay according to its half-life as indicated by curve C. The isolated parent nuclide would, however, show an increase in activity with time owing to the ingrowth of daughter until transient equilibrium is attained. Curve D of Fig. 1.98 shows the ingrowth of daughter nuclide from a freshly isolated parent. Because $N_B^0 = 0$ at time $t = 0$ (time of separation of parent and daughter), the last term of Eqn (1.437) falls out to give

$$N_B = \frac{\lambda_A N_A^0}{\lambda_B - \lambda_A} (e^{-\lambda_A t} - e^{-\lambda_B t}) \quad (1.451)$$

The term $\lambda_A N_A^0/(\lambda_B - \lambda_A)$ describes the rate of production of the daughter divided by the difference between the daughter and parent decay constants, which may be written as

$$N_B = (N_B)_{\text{max}} (e^{-\lambda_A t} - e^{-\lambda_B t}) \quad (1.452)$$

similar to the case of Eqn (1.442). Since the activity, A_B , of the daughter atoms is proportional to the number of daughter atoms, or $A_B = k_B \lambda_B N_B$, where k is as defined previously, Eqn (1.452) may also be written as

$$A_B = (A_B)_{\text{max}} (e^{-\lambda_A t} - e^{-\lambda_B t}) \quad (1.453)$$

Because the maximum daughter activity in this sample is 100 dpm, Eqn (1.453) may be used to calculate the ingrowth of daughter nuclide with $(A_B)_{\text{max}} = 100$.

Curve E of Fig. 1.98 illustrates the activity of the isolated parent and daughter nuclides. It is found by summing curves A and D and consequently accounts for the simultaneous decay of the parent nuclide and the ingrowth of the daughter. Notice that the slopes of curves A, B, and E are identical when transient

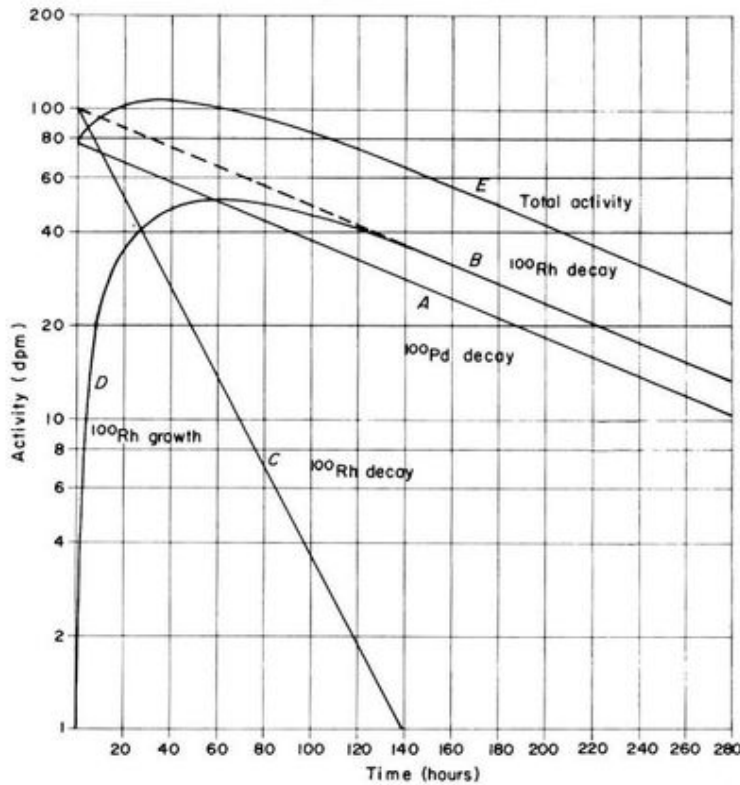


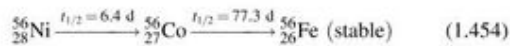
FIGURE 1.98 Growth and decay curves following the separation of ^{100}Pd (^{100}Rh) in transient equilibrium. (A) Decay of isolated parent nuclide ^{100}Pd . (B) Decay of ^{100}Rh daughter nuclide in transient equilibrium. The dashed portion of this curve represents ^{100}Rh decay if parent and daughter nuclides were not separated. (C) Decay of ^{100}Rh after separation from its parent. (D) The ingrowth of ^{100}Rh with the isolated parent ^{100}Pd . (E) Total activity from the isolated ^{100}Pd representing both ^{100}Pd decay and ^{100}Rh growth until transient equilibrium is attained. (From L'Annunziata, 1987; reprinted with permission from Elsevier © 1987.)

equilibrium is attained, that is, the rates of decay of both the parent and daughter are identical.

Practical examples of decay and ingrowth calculations in addition to those provided in the previous Sections XV.C and XV.D may be obtained from Harnes and Jerome (2004).

E. No Equilibrium

The cases of secular equilibrium and transient equilibrium, which involve decay schemes whereby the parent nuclide is longer lived than its daughter, were just considered. In other cases in which the daughter nuclide is longer-lived than its parent, $\lambda_A > \lambda_B$, no equilibrium is attained. Instead, the parent nuclide of shorter half-life eventually decays to a negligible extent, leaving only the daughter nuclide, which decays by its own half-life. The following decay scheme of ^{56}Ni serves as an example:

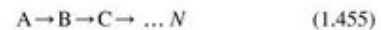


The parent nuclide ^{56}Ni decays by electron capture with a half-life of 6.4 d, whereas its daughter ^{56}Co decays with the longer half-life of 77.3 d by electron capture and β^+ emission. Curve A of Fig. 1.99 illustrates the decay of the ^{56}Ni parent nuclide. The decay of initially isolated ^{56}Ni is followed by the ingrowth (production) of the ^{56}Co daughter nuclide, shown by curve B.

The ingrowth of daughter is calculated from Eqn (1.437), of which the last term, $N_B^0 e^{-\lambda_B t}$, falls out because $N_B^0 = 0$ at time $t = 0$. The number of daughter atoms N_B of Eqn (1.437) may be converted to activity, A_B , by the term $A_B = k_B \lambda_B N_B$ as discussed previously. The total activity illustrated by curve C of Fig. 1.99 depicts both the simultaneous decay of parent nuclide and the growth and decay of daughter determined by summing curves A and B. Notice from Fig. 1.99 that the parent nuclide activity in this example becomes negligible after around 55 d, after which the total activity, curve C, has a slope corresponding to the decay rate of the daughter nuclide.

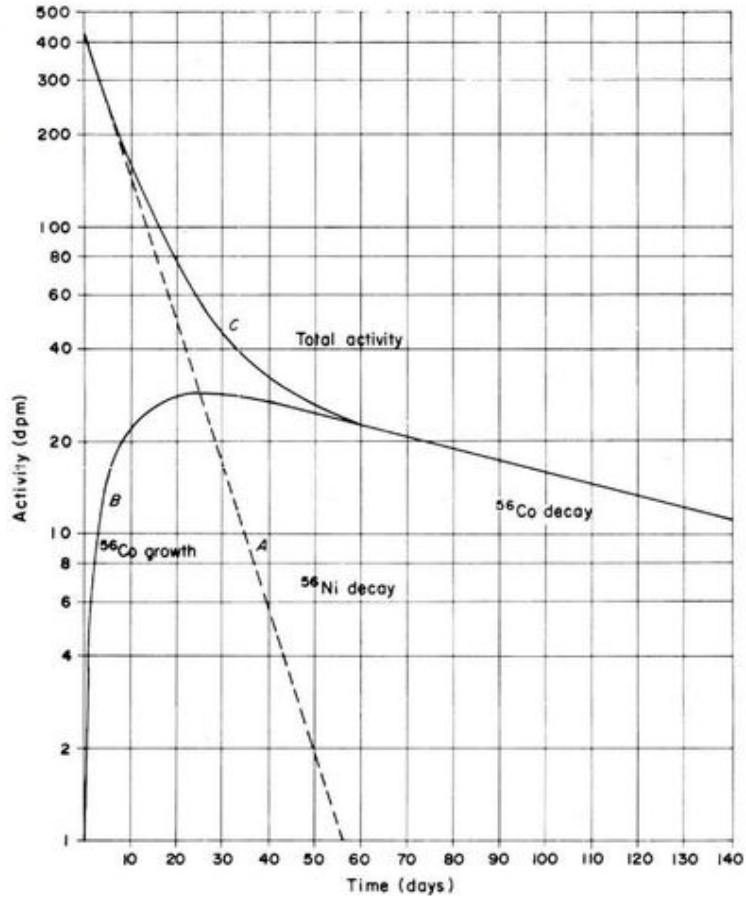
F. More Complex Decay Schemes

Other decay schemes exist that involve a chain of numerous nuclides such as

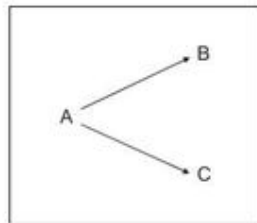


where nuclides A, B, and C are followed by a chain of a number N of decaying nuclides. Long-decay chains of this type may be observed in the complex decay schemes of high-atomic-number natural radionuclides such as the ^{232}Th , ^{238}U , and ^{235}U natural decay chains illustrated previously in Figs 1.19, 1.20, and 1.21. These decay schemes are described by the general Eqn (1.455). However, within each of the natural decay schemes, illustrated

FIGURE 1.99 Growth and decay curves of the ^{56}Ni (^{56}Co) parent-daughter nuclides following the isolation or fresh preparation of the parent nuclide ^{56}Ni . (A) Decay of the parent nuclide ^{56}Ni . (B) Ingrowth of daughter nuclide ^{56}Co . (C) Total activity representing both ^{56}Ni decay and the simultaneous growth and decay of ^{56}Co daughter. (From L'Annunziata, 1987; reprinted with permission from Elsevier © 1987.)



in Figs 1.19, 1.20, and 1.21, there are one or more branching decays of the type.



For example, in Fig. 1.19, ^{212}Bi , within the ^{232}Th natural decay chain, is the parent of the two daughter nuclides ^{212}Po and ^{208}Tl . The half-life of the parent nuclide in branching decays is a function of the two decay processes and may be written as

$$t_{1/2} = 0.693 / (\lambda_A + \lambda_B) \quad (1.456)$$

where λ_A and λ_B are the decay constants of the two separate decay processes.

XVI. RADIOACTIVITY UNITS AND RADIONUCLIDE MASS

A. Units of Radioactivity

The units used to define radioactivity or, in other words, the activity of a sample are written in terms of the number of atoms, N , disintegrating per unit of time, t . We can use Eqn (1.410), previously discussed in this chapter, to calculate the activity of any given mass of radionuclide. The equation, namely $\Delta N / \Delta t = \lambda N$, defines the proportionality between the rate of decay of a radionuclide and the number of atoms of the radionuclide in a sample. As an example, we may use Eqn (1.410) to calculate the activity of 1 g of ^{226}Ra as follows:

$$\begin{aligned} \Delta N / \Delta t &= \lambda N \\ \Delta N / \Delta t &= (0.693 / t_{1/2})(N) \end{aligned} \quad (1.457)$$

where $\lambda = 0.693 / t_{1/2}$ as derived previously Eqn (1.420). If we take the half-life, $t_{1/2}$, of ^{226}Ra to be 1599 y and substitute for N , in the preceding equation, the number of atoms per mol of ^{226}Ra , we can write

$$\Delta N/\Delta t = (0.693/1599\text{y})(6.022 \times 10^{23} \text{ atoms}/226 \text{ g}) \quad (1.458)$$

where, according to Avogadro's number, there are 6.022×10^{23} atoms per gram mole of substance. If we now convert the half-life of ^{226}Ra from units of years to minutes, we can calculate the number of atoms of ^{226}Ra disintegrating per minute (dpm) per gram according to

$$\Delta N/\Delta t = \left[\frac{0.693}{(1599 \text{ y})(365 \text{ d/y})(24 \text{ h/d})(60 \text{ min/h})} \right] \times \left(\frac{6.022 \times 10^{23} \text{ atoms}}{226 \text{ g}} \right) \quad (1.459)$$

$$\begin{aligned} \Delta N/\Delta t &= \left(\frac{0.693}{8.404 \times 10^8 \text{ min}} \right) (2.665 \times 10^{21} \text{ atoms/g}) \\ &= 2.19 \times 10^{12} \text{ atoms per minute per gram} \end{aligned}$$

The activity of 1 g of ^{226}Ra is the basis of the unit of radioactivity known as the curie (Ci). One curie is almost equal to the activity of 1 g of ^{226}Ra or, by definition,

$$1 \text{ Ci} = 2.22 \times 10^{12} \text{ dpm} = 3.7 \times 10^{10} \text{ dps} \quad (1.460)$$

Therefore, one curie of activity or any multiple of the curie of any radionuclide defines the number of atoms disintegrating per unit of time in minutes or seconds.

The rate of decay in terms of time in seconds gives rise to the Système International d'Unités (SI) unit of activity, which is the Becquerel (Bq), where by definition

$$1 \text{ Bq} = 1 \text{ dps} \quad (1.461)$$

Therefore, we can interrelate the curie and Becquerel as follows:

$$1 \text{ Ci} = 2.22 \times 10^{12} \text{ dpm} = 3.7 \times 10^{10} \text{ dps} = 37 \text{ GBq} \quad (1.462)$$

Likewise, smaller units of the curie, namely the millicurie (mCi) and microcurie (μCi), may be interrelated with the becquerel as follows:

$$1 \text{ mCi} = 2.22 \times 10^9 \text{ dpm} = 3.7 \times 10^7 \text{ dps} = 37 \text{ MBq} \quad (1.463)$$

and

$$1 \mu\text{Ci} = 2.22 \times 10^6 \text{ dpm} = 3.7 \times 10^4 \text{ dps} = 37 \text{ kBq} \quad (1.464)$$

Another unit of activity recommended in the early 1960s by the International Union of Pure and Applied Physics, but less frequently used, is the rutherford, where 1 rutherford = 10^6 dps and 1 microrutherford would be equivalent to 1 dps or 1 Bq (Buttlar, 1968; Das and Ferbel, 1994).

B. Correlation of Radioactivity and Radionuclide Mass

From Eqn (1.457) and calculations made in Section XVI.A, we can see that, for samples of a given level of activity,

radionuclides of shorter half-life will contain a smaller number of radioactive atoms than radionuclides of longer half-life.

We can use Eqn (1.457) again to compare two radionuclides of relatively short- and long half-lives to see the magnitude of the differences in radionuclide masses we would encounter for any given level of radioactivity. For example, we may take the radionuclide ^{32}P of 14.3-day half-life and the radionuclide ^{14}C of 5730-year half-life and calculate the activity per gram (e.g., dpm/g) and grams per curie (e.g., g/Ci) of each radionuclide for comparative purposes. These calculations are as follows.

1. ^{32}P , half-life = 14.3 days

$$\begin{aligned} \Delta N/\Delta t &= (0.693/t_{1/2})(N) \\ &= \left[\frac{0.693}{(14.3 \text{ d})(24 \text{ h/d})(60 \text{ m/h})} \right] \left(\frac{6.022 \times 10^{23}}{32 \text{ g}} \right) \\ &= 6.32 \times 10^{17} \text{ dpm/g } ^{32}\text{P} \end{aligned} \quad (1.465)$$

If, by definition, 1 curie = 2.22×10^{12} dpm, we can convert the above calculated activity per gram of ^{32}P to grams ^{32}P per curie as follows:

$$\begin{aligned} \frac{2.22 \times 10^{12} \text{ dpm/Ci}}{6.32 \times 10^{17} \text{ dpm/g } ^{32}\text{P}} &= 3.51 \times 10^{-6} \text{ g } ^{32}\text{P per Ci} \\ &= 3.51 \times 10^{-6} \text{ mg } ^{32}\text{P per mCi} \end{aligned} \quad (1.466)$$

2. ^{14}C , half-life = 5730 years

$$\begin{aligned} \Delta N/\Delta t &= (0.693/t_{1/2})(N) \\ &= \left[\frac{0.693}{(5730 \text{ y})(365 \text{ d/y})(24 \text{ h/d})(60 \text{ m/h})} \right] \\ &\quad \times \left(\frac{6.022 \times 10^{23}}{14 \text{ g}} \right) \\ &= 9.90 \times 10^{12} \text{ dpm/g } ^{14}\text{C} \end{aligned} \quad (1.467)$$

This activity per gram of ^{14}C is converted to grams ^{14}C per curie as follows:

$$\begin{aligned} \frac{2.22 \times 10^{12} \text{ dpm/Ci}}{9.90 \times 10^{12} \text{ dpm/g } ^{14}\text{C}} &= 0.224 \text{ g } ^{14}\text{C per Ci} \\ &= 0.224 \text{ mg } ^{14}\text{C per mCi} \end{aligned} \quad (1.468)$$

The calculated mass of ^{32}P in 1 curie of activity is almost a million fold less than the calculated mass of ^{14}C in 1 curie of activity. In general, research with radionuclides often involves the applications and analysis of lower levels of radioactivity in microcuries, and picocuries, and so on. The masses of radioactive atoms in the micro-, and picocurie levels of radioactivity are obviously much smaller than encountered at the curie or millicurie level. It is important, therefore, to be aware of the order of magnitude of

radioactive atom masses involved, which leads us to the concept of "carrier-free" samples of radionuclides, discussed subsequently.

C. Carrier-Free Radionuclides

A carrier-free radionuclide sample is, by definition, a sample in which all of the atoms of a particular element consist of the radioactive isotope, that is, no stable isotope of that element is present. A stable isotope of the particular element is referred to as carrier. Carrier-free radioisotopes are commonly used in research in the bio-, medical, and chemical sciences (Elmore, 2009, Lin and Chao, 2009, Li and Deutscher, 2008, Steinman and Mulholland, 2007, Buchtela, 2005, and Horányi, 2004). Often chemical compounds are labeled as carrier free, but are not literally carrier free. Commercial suppliers of radionuclides and radioisotope-labeled compounds used in research will specify the specific activity of the radionuclide, which is the activity in disintegration rate per mass, *e.g.*, dpm/g, dps/g, Ci/g, Bq/g, or Bq/mol, etc. Organic compounds labeled with ^{14}C or ^3H are generally not carrier free, and such compound labels with high specific-activity radioisotopes may contain $>80\%$ ^{14}C and $>50\%$ tritium (Elmore, 2009). In the previous section, Eqns (1.465) and (1.467) were used to calculate the specific activities of carrier-free radioisotopes ^{32}P and ^{14}C , respectively. It is important, therefore, to be aware of the masses of radioactive isotope in a given sample and any consequences that may be involved when very small quantities (*e.g.*, 10^{-6} to 10^{-12} g or smaller) of radioactive nuclide may be involved.

For example, in Section XVI.B, we calculated that there was only 3.51×10^{-6} g of ^{32}P per curie of radioactivity. A millicurie of carrier-free ^{32}P , which is a level of activity commonly procured from a radioisotope supplier, would contain only 3.51×10^{-9} g of ^{32}P and possibly a small percentage of stable phosphorus. It is a common procedure to dilute the carrier-free ^{32}P to the microcurie level of activity prior to working with the radionuclide, such as in tracer studies. One microcurie of carrier-free ^{32}P would contain only 3.51×10^{-12} g of phosphorus. Obviously, therefore, we should consider the consequences of working with such small amounts of phosphorus in solution. Over the past 45 years of working with carrier-free radioactive nuclides sources, the author has experienced the absorption of significant quantities of radionuclides onto the surface of glassware. If we consider the ionic characteristics of the chemical forms of certain radionuclide sources and the minute quantities these may possess in the carrier-free form, significant quantities of certain radionuclides could be lost from solution by absorption onto the surface of glassware, onto the surface of precipitates, and so forth. The addition of carrier (*i.e.*, stable isotope or organic compound without the radioisotope label) may be added to a high specific activity sample to facilitate radioisotope tracer studies. For example, when working with sources of high specific activity, if a particular experiment calls for the addition of carrier, the author will add carrier to the radionuclide source during the dilution procedure. If carrier is not desired, the procedure recommended by Chase

and Rabinowitz (1968) can be utilized. For example, if it is desired to dilute a carrier-free solution of $\text{NaH}_2^{32}\text{PO}_4$ in a volumetric flask, it is best to treat the flask first with a 1% solution of NaH_2PO_4 prior to the addition of the carrier-free solution. The volumetric flask and any other glassware used in the dilution may be rinsed with the 1% NaH_2PO_4 . Alternatively, the volumetric flask may be filled with the 1% NaH_2PO_4 solution and allowed to sit for several hours. The flask is then rinsed with deionized water to remove unabsorbed phosphorus. The flask can then be used to prepare a dilution of carrier-free or high specific activity $\text{NaH}_2^{32}\text{PO}_4$. It is important, however, to rinse the flask with a solution of the same chemical form as the radioisotope, if it is desirable to prevent contamination of the radioisotope with another chemical form.

REFERENCES

- "Readers may view, browse, and/or download material for temporary copying purposes only, provided these uses are for noncommercial personal purposes. Except as provided by law, this material may not be further reproduced, distributed, transmitted, modified, adapted, performed, displayed, published, or sold in whole or in part, without prior permission from the American Physical Society or other organizations that own copyright to the material in the references listed herein."
- Abbe, J.C., Marques-Netto, A., 1975. Szilard-Chalmers effects in hafnium complexes. *J. Inorg. Nucl. Chem.* 37, 2239–2242.
- Abele, H., 2000. The standard model and the neutron β -decay. *Nucl. Instrum. Methods Phys. Res. Sect. A* 440, 499–510.
- Abele, H., 2002. Is the uncertainty of the quark-mixing-CKM-matrix violated in neutron beta-decay? *Phys. Rev. Lett.* 88, 211801.
- Adloff, J.P., 1989. Radioactive disequilibrium in nature: origin, facts and applications. *Int. J. Radiat. Applic. Instrum. Part C* 33 (3), 257.
- Adriani, O., Barbarino, G.C., Bazilevskaia, A., Bellotti, R., Boezio, M., Bogomolov, E.A., Bonechi, L., Bongi, M., Bonvicini, V., and Borisov, S. et al. PAMELA Collaboration (2010). PAMELA results on the cosmic-ray antiproton flux. *Phys. Rev. Letts.* (In Press), arXiv:1007.0821v [astro-ph.HE].
- Aguiar, M., Alcaraz, J., Allaby, J., Alpat, B., Ambrosi, G., Anderhub, H., Ao, L., Arefiev, A., Azzarello, P., Babucci, E., et al., AMS Collaboration, 2002. The alpha magnetic spectrometer (AMS) on the international space station: part I – results from the test flight on the space shuttle. *Phys. Rep.* 366 (6), 331–405.
- Alfassi, Z.B., Kurhelevsky, A.P., Wolf, W., 1986. Optimization of the production of Na^{18}F by use of the Szilard–Chalmers reaction following irradiation of fluorine compounds with 14 MeV neutrons. *J. Radioanal. Nucl. Chem.* 100 (2), 263–268.
- Allard, D., Parizot, E., Olinto, A.V., 2007. On the transition from galactic to extragalactic cosmic-rays: spectral and composition features from two opposite scenarios. *Astropart. Phys.* 27 (1), 61–75.
- Alvarez, L.W., 1938. The capture of orbital electrons by nuclei. *Phys. Rev.* 54 (7), 486–497.
- Amaldi, E., Fermi, E., 1935. Absorption of slow neutrons. *Ricerca Sci.* 6, 344–347.
- Amaldi, E., Fermi, E., 1936a. Groups of slow neutrons. *Ricerca Sci.* 7 (1), 310–313.
- Amaldi, E., Fermi, E., 1936b. Diffusion of slow neutrons. *Ricerca Sci.* 7 (1), 393–395.
- Amaldi, E., D'Agostino, O., Fermi, E., Pontecorvo, B., Rasetti, F., Segre, E., 1935. Artificial radioactivity produced by neutron bombardment. II. *Proc. Roy. Soc. London A* 149 (868), 522–558.
- AMS Collaboration, 2000. Cosmic protons. *Phys. Lett.* B490, 27–35.
- Amsler, C., et al., 2008. Particle data group. Review of particle physics. *Phys. Letts.* B 667, 1–1340.
- Andersen, H.H., Sørensen, H., Vadja, P., 1969. Excitation potentials and shell corrections for the elements $Z_2 = 20$ to $Z_2 = 30$. *Phys. Rev.* 180, 373–380.

- Anderson, C.D., 1932. The apparent existence of easily detectable positives. *Science* 76, 238.
- Anderson, C.D., 1933a. The positive electron. *Phys. Rev.* 43, 491–498.
- Anderson, C.D., 1933b. Free positive electrons resulting from the impacts upon atomic nuclei of the photons from ThC. *Science* 77, 432.
- Anderson, C.D., 1936. The production and properties of positrons. Nobel lecture, december 13, 1939. In: Nobel Lectures, Physics, 1922–1941. Elsevier Publishing, Amsterdam (1965).
- Anderson, C.D., Neddermeyer, S.H., 1933. Positrons from gamma rays. *Phys. Rev.* 43, 1034–1035.
- Anderson, C.D., Neddermeyer, S.H., 1936. Cloud chamber observations of cosmic rays at 4300 meters elevation and near sea-level. *Phys. Rev.* 50, 263–271. <http://prola.aps.org/toc/PR/v50/i4>.
- Anderson, H.L., Fermi, E., Hanstein, H.B., 1939a. Production of neutrons in uranium bombarded by neutrons. *Phys. Rev.* 55, 797–798.
- Anderson, H.L., Fermi, E., Szilard, L., 1939b. Neutron production and absorption in uranium. *Phys. Rev.* 56, 284–286.
- Andreo, P., Seuntjens, J.P., Podgorsak, E.B., 2005. Calibration of photon and electron beams. In: Podgorsak, E.B. (Ed.), *Review of Radiation Oncology Physics: A Handbook for Teachers and Students*, International Atomic Energy Agency (IAEA), Vienna, pp. 301–355.
- Angeli, I., Csatlós, M., 1977. Fine structure in the mass number dependence of rms charge radii. *Nucl. Phys. A* 288 (3), 480–492.
- Aponick Jr., A.A., Chesterfield, C.M., Bromley, D.A., Glendenning, N.K., 1970. Quadrupole and hexadecapole deformations in rare earth nuclei. *Nucl. Phys. A* 159 (2), 367–384.
- Araújo, H.M., Blockley, J., Bungau, C., Carson, M.J., Chagani, H., Daw, E., Edwards, B., Ghag, C., Korolkova, E.V., Kudryavtsev, V.A., et al., 2008. Measurements of neutrons produced by high-energy muons at the boubly underground laboratory. *Astropart. Phys.* 29, 471–481.
- Argonne National Laboratory, 1963. *Reactor Physics Constants*, ANL-5800, second ed. United States Atomic Energy Commission, Washington, DC.
- Arison, G., et al., UA1 Collaboration, 1983a. Experimental observation of isolated large transverse energy electrons with associated missing energy at $\sqrt{s} = 540$ GeV. *Phys. Lett.* 122B, 103–116.
- Arison, G., et al., UA1 Collaboration, 1983b. Experimental observation of lepton pairs of invariant mass around 95 GeV/c² at the CERN SPS collider. *Phys. Lett.* 126B, 398–410.
- Arzumanov, S., Bondarenko, L., Chernyavsky, S., Drexel, W., Fomin, A., Geltenbort, P., Morozov, V., Panin, Yu., Pendlebury, J., Schreckenbach, K., 2000a. Neutron lifetime measured by monitored storing of ultra-cold neutrons. *Nucl. Instrum. Methods Phys. Res., Sect. A* 440, 511–516.
- Arzumanov, S., Bondarenko, L., Chernyavsky, S., Drexel, W., Fomin, A., Geltenbort, P., Morozov, V., Panin, Yu., Pendlebury, J., Schreckenbach, K., 2000b. Neutron lifetime measured by monitored storing of ultra-cold neutrons with detection of inelastically scattered neutrons. *Phys. Letts. B* 483, 15–22.
- Arzumanov, S., Bondarenko, L., Geltenbort, P., Morozov, V., Nesvizhevsky, V.V., Panin, Yu., Strepetov, A., 2009. A new project to measure the neutron lifetime using storage of ultracold neutrons and detection of inelastically scattered neutrons. *Nucl. Instrum. Methods Phys. Res., Sect. A* 611, 186–188.
- Asaro, F., Perlman, I., 1953. Patterns in alpha spectra of even-even nuclei. *Phys. Rev.* 91, 763–764.
- Ashley, R.P., Kulcinski, G.L., Santarius, J.F., Krupakar Murali, S., Piefer, G., Radel, R., 2000. Steady-state D–³He Proton Production in an IEC Fusion Device. Fusion Technology Institute, University of Wisconsin, Madison, UWFD-1144 pp. 6.
- Audi, G., Wapstra, A.H., Thibault, C., 2003. The AME2003 atomic mass evaluation (II) tables, graphs, and references. *Nucl. Phys. A* 729, 337–676.
- Audiotore, L., Barnà, R.C., De Pasquale, D., Italiano, A., Trifirò, A., Trimarche, M., 2005. Study of a 5 MeV electron linac based neutron source. *Nucl. Instrum. Methods Phys. Res. Sect. B* 229, 137–143.
- Auger, P., 1923. Secondary β rays produced in a gas by X-rays. *Compt. Rend.* 177, 169–171.
- Auger, P., 1925a. Sur les rayons β secondaires produits dans un gaz par des rayons-X. *Compt. Rend.* 180, 65–68.
- Auger, P., 1925b. Sur l'effect photoélectrique compose. *J. de Physique Radium* 6, 205–208.
- Auger, P., Maze, R., 1938. Les grandes gerbes cosmiques de l'atmosphère. *C. R. Acad. Sci. Ser. B* 207, 228–230.
- Auger, P., Maze, R., 1939. Extension et pouvoir pénétrant des grandes gerbes de rayons cosmiques. *Compt. Rend.* 208, 1641–1643.
- Auslender, V.L., Bukin, A.D., Voronin, L.A., Kokin, E.N., Korobeinikov, M.V., Krainov, G.S., Lukin, A.N., Radchenko, V.M., Sidorov, A.V., Tkachenko, V.O., 2004. Bremsstrahlung converters for powerful industrial electron accelerators. *Radiat. Phys. Chem.* 71, 295–297.
- Avignone III, F.T. (2010). The Majorana ⁷⁶Ge double-beta decay project. *Progress in Particle and Nucl. Phys.* 64 (2), 258–260.
- Aydin, E.G., Tel, E., Kaplan, A., Aydin, A., 2008. Equilibrium and pre-equilibrium calculations of neutron production in medium-heavy targets irradiated by protons up to 100 MeV. *An. Nucl. Energy* 35, 2306–2312.
- Azab, A.K., Abu Ali, H., Srebnik, M., 2006. Boron neutron capture therapy. *Studies in Inorganic Chemistry* 22, 337–366.
- Bacon, G.E., 1969. *Neutron Physics*. Wykeham Publications, London.
- Bagnaia, P., et al., UA2 Collaboration, 1983. Evidence for $Z^0 \rightarrow e^+e^-$ at the CERN $\bar{p}p$ collider. *Phys. Lett.* 129B, 130–140.
- Bailey, J., Borer, K., Combley, F., Drumm, H., Krienen, F., Lange, F., Picasso, E., von Ruden, W., Farley, F.J.M., et al., 1977. On muon lifetimes and time dilation. *Nature* 268 (5618), 301–305.
- Bailey, J., Borer, K., Combley, F., Drumm, H., Eck, C., Farley, F.J.M., Field, J.H., Flegel, W., Hattersley, P.M., Krienen, F., et al., 1979. Final report of the CERN muon storage ring including the anomalous magnetic moment and the electric dipole moment of the muon, and the direct test of relativistic time dilation. *Nucl. Phys. B* 150, 1–75.
- Bainbridge, K.T., 1952. Effect of chemical combination of radioactivity confirmed. *Chem. Eng. News* 30, 654.
- Baker, C.P., Holloway, M. G., King, L. O., and Schreiber, R. E., 1943. Cross Section for the Reaction $20(230,240)10$. Los Alamos Technical Report, LAMS-2, p. 63.
- Balasubramanian, P.S., 1997. Anodically oxidized aluminum layer as a useful substrate for the fabrication of ¹⁴⁷Pm sources for beta-ray thickness gauges. *J. Radioanal. Nucl. Chem.* 223 (1–2), 79–81.
- Balasubramanian, P.S., 1998. A simple procedure for the fabrication of high activity beta-radiation sources of ¹⁴⁷Pm for use in beta-ray thickness gauges. *J. Radioanal. Nucl. Chem.* 229 (1–2), 157–160.
- Bambynek, W., Crasemann, B., Fink, R.W., Freund, H.U., Mark, H., Swift, C.D., Price, R.E., Rao, P.V., 1972. X-ray fluorescence yields, Auger, and Coster-Kronig transition probabilities. *Rev. Mod. Phys.* 44, 716–813. http://rmp.aps.org/abstract/RMP/v44/i4/p716_1.
- Banner, M., et al., UA2 Collaboration, 1983. Observation of single isolated electrons of high transverse momentum in events with missing transverse energy at the CERN $\bar{p}p$ collider. *Phys. Lett.* 122B, 476–485.
- Barabash, A.S., Hubert, Ph., Nachab, A., Kononov, S.I., Vanyushin, I.A., Umatov, V., 2008. Search for β^+EC and ECEC processes in ¹¹²Sn and $\beta^-\beta^-$ decay of ¹²⁴Sn to the excited states of ¹²⁴Te. *Nucl. Phys. A* 807 (3–4), 269–281.
- Barabash, A.S., Hubert, Ph., Nachab, A., Umatov, V., 2007. Search for β^+EC and ECEC processes in ⁷⁴Se. *Nucl. Phys. A* 785 (3–4), 371–380.
- Barkla, C.G., 1917. Characteristic Röntgen radiation. In: Nobel Lectures, Physics 1901–1921, (1967). Elsevier Publishing Company, Amsterdam.
- Barnes, R.K., Boot, D., Sorby, P.J., 1986. Polarographic quantification of the specific activity of copper-64 produced by Szilard–Chalmers reactions. *Appl. Radiat. Isot.* 37, 1241.
- Barthakur, N.N., 1983. The β -ray gauge as a leaf surface wetness detector. *Int. J. Appl. Radiat. Isot.* 34 (11), 1549–1552.
- Basini, G. et al., 1999. The flux of cosmic-ray antiprotons from 3.7 to 24 GeV. *Proc. 26th Int. Cosmic Ray Conf. Salt Lake City* 3, 101.
- Bayanov, B., Burdakov, A., Chudaev, V., Ivanov, A., Konstantinov, S., Kuznetsov, A., Makarov, A., Malyshkin, G., Mekler, K., Sorokin, I., Sulyaev, Y., Taskaev, S., 2009b. First neutron generation in the BINP accelerator based neutron source. *Appl. Radiat. Isot.* 67, S285–S287.
- Bayanov, B., Burdakov, A., Kuznetsov, A., Makarov, A., Sinitskii, S., Sulyaev, Y., and Taskaev, S., 2010. Dosimetry and spectrometry at accelerator based neutron source for boron neutron capture. *Radiat. Meas.* 45 (10), 1462–1464.

- Bayanov, B., Kashaeva, E., Makarov, A., Malyshekin, G., Samarin, S., Taskaev, S., 2009a. A neutron producing target for BINP accelerator-based neutron source. *Appl. Radiat. Isot.* 67, S282–S284.
- Bé, M.-M., Chisté, V., Dulieu, C., 2006. Detailed calculation of *K*- and *L*-Auger electron emission intensities following radioactive disintegration. *Appl. Radiat. Isot.* 64, 1435–1439.
- Beach, A.S., Beatty, J.J., Bhattacharyya, A., Bower, C., Coutu, S., DuVernois, M.A., Labrador, A.W., McKee, S., Minnick, S.A., Müller, D., et al., 2001. Measurement of the cosmic-ray antiproton-to-proton abundance ratio between 4 and 50 GeV. *Phys. Rev. Lett.* 87 (27), 271101.
- Beatty, J.J., Bhattacharyya, A., Bower, C., Coutu, S., DuVernois, M.A., McKee, S., Minnick, S.A., Müller, D., Musser, J., Nutter, S., et al., 2004. New measurement of the cosmic-ray positron fraction from 5 to 15 GeV. *Phys. Rev. Lett.* 93, 241102.
- Beck, M., 2010. The KATRIN experiment. *J. Phys. Conf. Series* 203 (1), 012097.
- Beckerly, J.G., 1945. What is the “Geiger-Nuttall law”? *Am. J. Phys.* 13 (3), 158–159.
- Becquerel, A.H., 1896a. On the rays emitted by phosphorescence. *Comptes Rendus Acad. Sci. Paris* 122, 420.
- Becquerel, A.H., 1896b. On the invisible rays emitted by phosphorescent bodies. *Comptes Rendus Acad. Sci. Paris* 122, 501.
- Becquerel, A.H., 1901. The radio-activity of matter. *Nature* 63, 396–398.
- Becquerel, A.H., 1903. On radioactivity, a new property of matter. Nobel lecture, december 11, 1903. “Nobel Lectures, Physics, 1901–1921.” (1967). In: *Science Incorporated Elsevier* (Ed.), *Nobel Lectures in Physics, 1901–1970*, vol. 1. Elsevier Publishing, Amsterdam.
- Behr, T., Bebe, M., Lohr, M., Sgourou, G., Angerstein, C., Wehrmann, E., Nebendahl, K., Becker, W., 2000. Therapeutic advantages of Auger electron-over beta emitting radiometals or radioiodine when conjugated to internalizing antibodies. *Eur. J. Nucl. Med.* 27 (7), 753–765.
- Bellotti, R., et al., 1996. Measurement of the negative muon spectrum between 0.3 and 40 GeV/c in the atmosphere. *Phys. Rev. D* 53 (1), 35–43. http://pd.aps.org/abstract/PRD/v53/i1/p35_1.
- Bellotti, R., Cafagna, F., Cirrella, M., De Marzo, C.N., Golden, R.L., Stochaj, S.J., De Pascale, M.P., Morselli, A., Picozza, P., Stephens, S.A., et al., 1999. Balloon measurements of cosmic-ray muon spectra in the atmosphere along with those of primary protons and helium nuclei over midlatitude. *Phys. Rev. D* 60 (5) 052002.
- Berger, M.J., 1993. Stopping-Power and Range Tables for Electrons, Protons, and Helium Ions. NISTIR 4999, National Institute of Standards and Technology, Gaithersburg, MD.
- Berger, M.J., Hubbell, J.H., 1997. Photon attenuation coefficients. In: Lide, D.R., Frederikse, H.P.R. (Eds.), *Handbook of Chemistry and Physics, seventy-seventh ed.* CRC Press, Boca Raton, pp. 10–250 to 10–254.
- Berger, M.J., Seltzer, S.M., 1982. Stopping Powers and Ranges of Electrons and Positrons. Nat. Bureau Standards Publ. NBSIR 82–2550, p. 168.
- Berger, M.J., Coursey, J.S., Zucker, M.A., Chang, J., ESTAR, PSTAR, ASTAR, 2005. Computer Programs for Calculating Stopping-Power and Range Tables for Electrons, Protons, and Helium Ions (Version 1.2.3) [Online] available. National Institute of Standards and Technology, Gaithersburg, MD. <http://www.nist.gov/physlab/data/star/index.cfm>.
- Berger, M.J., Hubbell, J.H., Seltzer, S.M., Chang, J., Coursey, J.S., Sukumar, R., Zucker, D.S., 2010. XCOM: Photon Cross Sections Database 8 (XGAM). The National Institute of Standards and Technology (NIST). <http://www.nist.gov/pml/data/xcom/index.cfm>.
- Bethe, H.A., 1937. Nuclear physics. B. Nuclear dynamics, theoretical. *Rev. Mod. Phys.* 9, 69–244.
- Bethe, H.A., Ashkin, J., 1953. Passage of radiations through matter. In: Segré, E. (Ed.), *Experimental Nuclear Physics*, vol. 1. J. Wiley, New York.
- Bethe, H.A., Bacher, R.F., 1936. Nuclear physics A, stationary states of nuclei. *Rev. Mod. Phys.* 8, 82–229.
- Bethe, H.A., 1933. Quantenmechanik der ein- und zwei-electronen-probleme. In: Geiger, H., Scheel, K. (Eds.), *Handbuch der Physik*, Second ed. vol. 24. Springer, Berlin Part I.
- Bevilacqua, J.J., 2010. *Basic Health Physics: Problems and Solutions*. Wiley-VCH, Hoboken, p. 768.
- Bevilacqua, R., Giannini, G., Calligaris, F., Fontanarosa, D., Longo, F., Scian, G., Totaro, P., Vittor, K., Vallaza, E., Severgnini, M., et al., 2007. PhoNeS: a novel approach to BNCT with conventional radiotherapy accelerators. *Nucl. Instrum. Methods Phys. Res., Sect. A* 572, 231–232.
- Bhattacharjee, P., Sigl, G., 2000. Origin and propagation of extremely high-energy cosmic rays. *Phys. Rep.* 327, 109–247.
- Birattari, C., Bonardi, M., Groppi, F., Gini, L., 2001. Review of cyclotron production and quality control of “high specific activity” radionuclides for biomedical, biological, industrial, and environmental applications at INFN-LASA. In: Marti, F. (Ed.), *Cyclotrons and Their Applications 2001. Proceedings of Sixteenth International Conference*, American Institute of Physics, Melville, New York.
- Bird, D.J., Corbató, S.C., Dai, H.Y., Elbert, J.W., Green, K.D., Huang, M.A., Kieda, D.B., Ko, S., Larsen, C.G., Loh, E.C., et al., 1995. Detection of a cosmic ray with measured energy well beyond the expected spectral cutoff due to cosmic microwave radiation. *Astrophys. J.* 441, 144–150.
- Blackett, P.M.S., Occhialini, G.P.S., 1933. Some photographs of the tracks of penetrating radiation. *Proc. Roy. Soc. London* 139A, 699–726.
- Blasi, P., 2008. Origin of high energy cosmic rays: a short review. *Nucl. Instrum. Methods Phys. Res. Sect. A* 588, 166–170.
- Blendowske, R., Fliessbach, T., Walliser, H., 1987. Microscopic calculation of the ^{14}C decay of Ra nuclei. *Nucl. Phys. A* 464, 75–89.
- Blümer, J., Engel, R., Hörandel, J.R., 2009. Cosmic rays from the knee to the highest energies. *Prog. Part. Nucl. Phys.* 63, 293–338.
- Bodei, L., Kassis, A.I., Adelstein, S.J., Mariani, G., 2003. Radionuclide therapy with iodine-125 and other Auger-emitting radionuclides: experimental models and clinical applications. *Cancer Radiother. Radiopharm.* 18, 861–877.
- Boehm, F., Wu, C.S., 1954. Internal bremsstrahlung and ionization accompanying beta decay. *Phys. Rev.* 93, 518–523.
- Boezio, M., Carlson, P., Francke, T., Weber, N., Suffert, M., Hof, M., Menn, W., Simon, M., Stephens, S.A., Bellotti, R., et al., 1999. The cosmic-ray proton and helium spectra between 0.2 and 200 GeV. *Astrophys. J.* 518 (1), 457–472.
- Boezio, M., et al., 2000a. The cosmic-ray proton and helium spectra between 0.2 and 200 GeV. *Astrophys. J.* 518, 457.
- Boezio, M., et al., 2000b. Measurements of the flux of atmospheric muons with the CAPRICE94paratus. *Phys. Rev. D* 62, 032007.
- Bohr, A., 1951. On the quantization of angular momenta in heavy nuclei. *Phys. Rev.* 81, 134–138.
- Bohr, A., 1992. Rotational motion in nuclei. In: Lundqvist, S. (Ed.), *Nobel Lectures, Physics 1971–1980*. World Scientific Publishing, Singapore.
- Bohr, A., Mottelson, B.R., 1953a. Interpretation of isomeric transitions of electric quadrupole type. *Phys. Rev.* 89, 316–317.
- Bohr, A., Mottelson, B.R., 1953b. Rotational states in even-even nuclei. *Phys. Rev.* 90, 717–719.
- Bohr, N., 1913. On the constitution of atoms and molecules. *Philos. Mag.* 26 (6), 1–25.
- Bohr, N., 1914. On the spectrum of hydrogen (address to the physical society of Copenhagen, dec. 20, 1913). *Physik Tidsskrift* 12, 97, translated by A.D. Udden “The Theory of Spectra and Atomic Constitution – Three Essays 1922.” In: Moulton, F.R., Schifferes, J.J. (Eds.), *Autobiography of Science*. Doubleday, New York 1950.
- Bohr, N., 1921a. Atomic structure. *Nature* 107, 104–107.
- Bohr, N., 1921b. Atomic structure. *Nature* 108, 208–209.
- Bohr, N., 1922. The structure of the atom. Nobel lecture, december 11, 1922. In: *Nobel Lectures, Physics 1922–1941*. Elsevier Publishers, Amsterdam (1965).
- Bohr, N., 1928. The quantum postulate and the recent development of atomic theory. *Nature* 121, 580–591.
- Bohr, N., Lindhard, J., 1954. Electron capture and loss by heavy ions penetrating through matter. *Kgl. Danske Videnskab Selskab, Mat.-Fys. Medd.* 28 (7), 1–30.
- Bonardi, M.L., Birattari, C., Groppi, F., Gini, L., Mainardi, H.S.C., 2004. Cyclotron production and quality control of “high specific activity” radionuclides in no-carrier added form for radioanalytical applications in the life sciences. *J. Radioanal. Nucl. Chem.* 250 (3) 425–419.
- Bonetti, R., Guglielmetti, A., 1999. Measurements of cluster radioactivity. In: Greiner, W., Gupta, R.K. (Eds.), *Heavy Elements and Related New Phenomena*, vol. II. World Scientific, Singapore, p. 1168.

- Bonetti, R., Carbonini, C., Guglielmetti, A., Hussonnois, M., Trubert, D., Le Naour, C., 2001. Cluster decay of ^{230}U via Ne emission. *Nucl. Phys. A* 686, 64–70.
- Bonn, J., Bornschein, L., Bornschein, B., Fickinger, L., Flatt, B., Kazachenka, O., Kovalik, A., Kraus, Ch., Otten, E.W., Schnall, J.P., Ulrich, H., Weinheimer, Ch., 2001. The Mainz neutrino mass experiment. *Nucl. Phys. B–Proc. (Suppl. 91)* (1–3), 273–279.
- Borisenko, V.E., Ossicini, S., 2004. What is What in the Nanoworld: A Handbook on Nanoscience and Nanotechnology. Wiley-VCH Verlag GmbH & Co. KgaA, Weinheim.
- Born, M., 1926a. The quantum mechanics of the impact process. *Z. Physik* 37 (12), 863–867.
- Born, M., 1926b. Quantum mechanics in impact process. *Z. Physik* 38 (11/12), 803–840.
- Born, M., 1926c. Zur wellenmechanik der stossvorgänge. *Göttingen Nachr. Math. Phys. Kl.* 146–160.
- Born, M., 1926d. The adiabatic principle in the quantum mechanics. *Z. Physik* 40 (3/4), 167–192.
- Born, M., Fock, V., 1928. Beweis des adiabatsatzes. *Z. Physik* 51, 165–180.
- Born, M., Oppenheimer, R., 1927. Quantum theory of molecules. *Ann. Physik* 84 (20), 457–484.
- Born, M., Heisenberg, W., Jordan, P., 1926. Quantum mechanics II. *Z. Physik* 35 (8/9), 557–615.
- Brasch, A., Lange, F., Waly, A., Banks, T.E., Chalmers, T.A., Szilard, L., Hopwood, F.L., 1934. Liberation of neutrons from beryllium by x-rays: radioactivity induced by means of electron tubes. *Nature* 134, 880.
- Bressan, A., Dalla Torre, S., Gobbo, B., Tessarotto, F., 2008. Proceedings of the sixth international workshop on ring imaging Cherenkov detectors. *Nucl. Instrum. Methods Phys. Res. Sect. A* 595 (1), 1–281.
- Brien, M., Kitching, J.E., Lee, J.K.P., Hinrichsen, P.F., 1972. States of ^{87}Sr populated by deuteron pick-up from ^{89}Y . *Nucl. Phys. A* 185, 289–302.
- Brink, D.M., 2005. Nuclear fission and fusion. In: Bassani, G., Liedl, G., Wyder, P. (Eds.), *Encyclopedia of Condensed Matter Physics*. Academic Press/Elsevier, Amsterdam, pp. 113–118.
- Browne, E., Firestone, R.B., Shirley, V.S., 1986. Table of Radioactive Isotopes. John Wiley & Sons, New York.
- Bryne, J., 1994. Neutrons, Nuclei and Matter, an Exploration of the Physics of Slow Neutrons. Institute of Physics, London.
- Buchtele, K., 2005. Radiochemical methods: overview, pp. 1–8. In: *Encyclopedia of Analytical Science*, 2nd ed. Elsevier, Amsterdam, p. 468.
- Buck, B., Merchant, A.C., 1989. Cluster model calculations of exotic decays from heavy nuclei. *Phys. Rev. C* 39, 2097–2100.
- Burhop, E.H.S., Asaad, W.N., 1972. The Auger effect. In: Bates, D.R., Esterman, I. (Eds.), *Advances in Atomic and Molecular Physics*, vol. 8. Academic Press, New York, pp. 163–184, pp. 299.
- Buttler, H.V., 1968. *Nuclear Physics, an Introduction*. Academic Press, New York.
- Campbell, D.B., Vetter, K., Henning, R., Lesko, K., Chan, Y.D., Poon, A.W.P., Perry, M., Hurley, D., Smith, A.R., 2008. Evaluation of radioactive background rejection in ^{76}Ge neutrino-less double-beta decay experiments using a highly segmented HPG detector. *Nucl. Instrum. Methods Phys. Res. Sect. A* 587, 60–67.
- Canberra Nuclear, 1996. Neutron detection and counting. In: *Canberra Nuclear Instruments Catalog*, ninth ed. Canberra Industries, Meriden, CT, pp. 37–39.
- Capello, A., Krenning, E., Breeman, W., Bernard, B., de Jong, M., 2003. Peptide receptor radionuclide therapy in vitro using [^{111}In -DTPA(0)] octreotide. *J. Nucl. Med.* 44 (1), 98–104.
- Caso, C., et al., 1998. Particle Physics Group Review of particle physics. *Eur. Phys. J. C* 3 (1–4), 1–783.
- Celiktas, C., 2011. A method to determine the gamma-ray linear attenuation coefficient. *Ann. Nucl. Energy* 38 (9), 2096–2100.
- Cember, H., Johnson, T., 2008. *Introduction to Health Physics*, fourth ed. McGraw-Hill Medical, New York, p. 864.
- Cengiz, A., Almaz, E., 2004. Internal bremsstrahlung spectra of β^- particle emitters using the Monte Carlo method. *Radiat. Phys. Chem.* 70, 661–668.
- Chadwick, J., 1932a. Possible existence of a neutron (Received Feb. 27, 1932). *Nature* 129, 312.
- Chadwick, J., 1932b. The existence of a neutron (Received May 10, 1932). *Proc. Roy. Soc. A* 136, pp. 692–708.
- Chadwick, J., 1935. The neutron and its properties. Nobel lecture, december 12, 1935. In: *Nobel Lectures, Physics 1922–1941* (1965). Elsevier Publishers, Amsterdam.
- Chase, G.D., Rabinowitz, J.L., 1968. *Principles of Radioisotope Methodology*, third ed. Burgess Publishing Company, Minneapolis, 140–143.
- Chen, P., Wang, J., Hope, K., Jin, L., Dick, J., Camron, R., Brandwein, J., Minden, M., Reilly, R., 2006. Nuclear localizing sequences promote nuclear translocation and enhance the radiotoxicity of the anti-CD33 monoclonal antibody HuM195 labeled with In-111 in human myeloid leukemia cells. *J. Nucl. Med.* 47 (5), 827–836.
- Cherenkov, P.A., 1934a. Visible light from clear liquids under the action of gamma radiation. *C.R. DOKL. AKAD. NAUK, SSSR* 2 (8), 451–454.
- Cherenkov, P.A., 1934b. Sichtbares leuchten von reinen flüssigkeiten unter der einwirkung von γ -strahlen. *C.R. Dokl. Akad. Nauk, SSSR* 2 (8), 455–457.
- Cherenkov, P.A., 1936. Die wirkung eines magnetfeldes auf das durch gammastrahlen hervorgerufene sichtbare leuchten der flüssigkeiten. *Dokl. Akad. Nauk, SSSR* 3 (9), 413–416.
- Cherenkov, P.A., 1958. Nobel lecture: radiation of particles moving at a velocity exceeding that of light, and some of the possibilities for their use in experimental physics. Stockholm, December 11, 1958. In: *Nobel Foundation Staff (Ed.), Nobel Lectures, Physics, 1942–62*. Elsevier Publishing, Amsterdam (1964).
- Cherenkova, E., 2005. Pavel Cherenkov – a person and a physicist – through the eyes of his daughter. *Nucl. Instrum. Methods Phys. Res. Sect. A* 553, 1–8.
- Cherenkova, E.P., 2008. The discovery of the Cherenkov radiation. *Nucl. Instrum. Methods Phys. Res. Sect. A* 595, 8–11.
- Chiavassa, A., 2011. Studies of the knee of the cosmic rays primary spectrum through measurements in the 10^{16} – 10^{18} eV energy range. *Nucl. Instrum. Methods Phys. Res. Sect. A*, 630 (1), 183–188.
- Choppin, G.R., Liljenzin, J.O., Rydberg, J., 2002. *Radiochemistry and Nuclear Chemistry*, third ed. Elsevier, Amsterdam, p. 720.
- Choudhuri, S., Arvidson, K., Chanderbhan, R., 2007. Carcinogenesis: mechanisms and models. 343–359. In: Gupta, R.C. (Ed.), *Veterinary Toxicology: Basic and Clinical Principles*. Academic Press, p. 1224.
- Chourasia, A.R., Chopra, D.R., 1997. Auger electron spectroscopy. In: Settle, F.A. (Ed.), *Handbook of Instrumental Techniques for Analytical Chemistry*. Prentice Hall, Upper Saddle River, New Jersey, pp. 791–808.
- Cipitii, B.B., Kulcinski, G.L., 2005. The production of ^{13}N using beam-target $\text{D}-^3\text{He}$ fusion reaction. *Fusion Sci. Techn.* 47, 1245–1249.
- Clapp, T.G., Titus, K.J., Olson, L.H., Dorrity, J.L., 1995. The on-line inspection of sewn seams. *National Textile Center Annual Report (August)*, 221–230.
- Clay, J. (1928). Penetrating radiation. *Proc. Royal Acad. Amsterdam* 31, 1091.
- Cleland, M.R., Thompson, C.C., Kato, H., Odera, M., Morrissey, R.F., Herring, C.M., O'Neill, M.T., Wilcott, T.R., Masefield, J., Hansen, J.M., Saylor, M.C., Sloan, D.P., 1991. Evaluation of a new X-ray processing facility. *Nucl. Instrum. Methods Phys. Res. Sect. B* 56–57 (2), 1242–1245.
- Clem, J.M., Evenson, P.A., 2002. Positron abundance in galactic cosmic rays. *Astrophys. J.* 568, 216–219.
- Cline, D., 1993. Quadrupole and octupole shapes in nuclei. *Nucl. Phys. A* 557, 615–634.
- Coakley, K.J., 2001. Neutron lifetime experiments using magnetically trapped neutrons: optimal background correction strategies. *Nucl. Instrum. Methods Phys. Res. Sect. A* 469, 354–363.
- Coakley, K.J., 2007. Optimal proton trapping strategy for a neutron lifetime experiment. *Nucl. Instrum. Methods Phys. Res. Sect. A* 577, 702–707.
- Cohen, D.D., Stelcer, E., Siegle, R., Ionescu, M., Prior, M., 2008. Experimental bremsstrahlung yields for MeV proton bombardment of beryllium and carbon. *Nucl. Instrum. Methods Phys. Res. Sect. B* 266, 1149–1153.
- Compton, A.H., 1923a. A quantum theory of the scattering of x-rays by light elements. *Phys. Rev.* 21 (5), 483–502.
- Compton, A.H., 1923b. The spectrum of scattered x-rays. *Phys. Rev.* 22 (5), 409–413.
- Compton, A.H., 1932. Variation of the cosmic rays with latitude. *Phys. Rev.* 41, 111–113.
- Compton, A.H., 1933. A geographic study of cosmic rays. *Phys. Rev.* 43, 387–404.
- Constantini, D.L., Chan, C., Cai, Z., Vallis, K.A., Reilly, R.M., 2007. ^{111}In -labeled trastuzumab (herceptin) modified with nuclear localization

- sequences (NLS): an Auger electron-emitting radiotherapeutic agent for HER2/neu-amplified breast cancer. *J. Nucl. Med.* 48 (8), 1357–1368.
- Coster, D., Kronig, R. de L., 1935. A new type of Auger effect and its influence on the x-ray spectrum. *Physica* 2 (1–12), 13–24.
- Coursey, B.M., Calhoun, J.M., Cessna, J.T., 1993. Radioassays of yttrium-90 used in nuclear medicine. *Nucl. Med. Biol.* 20 (5), 693–700.
- Coutu, S., Beatty, J.J., DuVernois, M.A., Barwick, S.W., Schneider, E., Bhattacharyya, A., Bower, C.R., Musser, J.A., Labrador, A., Müller, D., Swordy, S.P., et al., 2000. Energy spectra, altitude profiles and charge ratios of atmospheric muons. *Phys. Rev. D* 62 (3) 032001.
- Cowan Jr., C.L., Reines, F., Harrison, F.B., Kruse, H.W., McGuire, A.D., 1956. Detection of the free neutrino: a confirmation. *Science* 124, 103–104.
- Cronin, J.W., 1999. Cosmic rays: the most energetic particles in the universe. *Rev. Mod. Phys.* 71 (2), S165–S172.
- Csikai, J., 1987. *CRC Hand Book of Fast Neutron Generators*, Vol. 1. John Wiley and Sons, New York, p. 256.
- Cucinotta, F.A., Nikjoo, H., Goodhead, D.T., 1998. The effects of delta rays on the number of particle-track traversals per cell in laboratory and space exposures. *Rad. Res.* 150, 115–119.
- Curie, M., 1911. Radium and the new concepts in chemistry. Nobel Lecture on December 11, 1911. In: Nobel Foundation Staff (Eds.), *Nobel Prize Lectures in Chemistry, 1901–1970*, 1967, vol. 1, 1901–1921, vol. 2, 1922–1941, vol. 3, 1942–1962. Elsevier Science, Amsterdam.
- Curie, P., 1905. Radioactive substances, especially radium. nobel lecture on June 6, 1905. In: *Science Incorporated Elsevier* (Ed.), *Nobel Lectures in Physics, 1901–1970*, Vol. 1. Elsevier Publishing, Amsterdam “Nobel Lectures, Physics, 1901–1921.” (1967).
- Dalrymple, G.B., 2001. The age of the earth in the twentieth century: a problem (mostly) solved. Geological Society, London. *Special Publications* January 1, 190, 205–221.
- Daraktchieva, Z., and the NEMO Collaboration, 2009. Search for neutrinoless double beta decay with NEMO 3 experiment. *Nucl. Phys. A* 827, 495c–497c.
- Das, A., Ferbel, T., 1994. *Introduction to Nuclear and Particle Physics*. John Wiley & Sons, New York.
- Daudel, R., 1947. Alteration of radioactive periods of the elements with the aid of chemical methods. *Rev. Sci.* 85, 162.
- Davis, D.W., Krogh, T.E., 2000. Preferential dissolution of ^{234}U and radiogenic Pb from α -recoil-damaged lattice sites in zircon: implication for thermal histories and Pb isotopic fractionation in the near surface environment. *Chem. Geol.* 172, 41–58.
- Davis Jr., R., 1952. Nuclear recoil following neutrino emission from beryllium 7. *Phys. Rev.* 86 (6), 976–985.
- de Broglie, L., 1923a. Waves and quanta. *Nature* 112, 540.
- de Broglie, L., 1923b. Ondes et quanta. *Compt. Rend.* 177, 507–510.
- de Broglie, L., 1923c. Quanta de lumière, diffraction et interférence. *Compt. Rend.* 177, 548–550.
- de Broglie, L., 1924. Recherches sur la théorie des quantas. Thesis, Paris.
- de Broglie, L., 1925. Recherches sur la théorie des quantas. *Ann. Phys. (Paris)* 3 (10), 22–128.
- Dean, J.A., 1995. *Analytical Chemistry Handbook*. McGraw-Hill, New York.
- Dewey, M., Coakley, K., Gilliam, D., Greene, G., Laptev, A., Nico, J., Snow, W., Wietfeldt, F., Yue, A., 2009. Prospects for a new cold neutron beam measurement of the neutron lifetime. *Nucl. Instrum. Methods Phys. Res. Sect. A* 611, 189–192.
- Dirac, P.A.M., 1933. Theory of electrons and positrons. Nobel lecture, December 12, 1933. In: *Nobel Lectures, Physics, 1922–1941*. Elsevier Publishing, Amsterdam (1965).
- Dirac, P.A.M., 1928a. The quantum theory of the electron. *Proc. Royal Soc. (London) A* 117, pp. 610–612.
- Dirac, P.A.M., 1928b. The quantum theory of the electron, Part II. *Proc. Royal Soc. (London) A* 118, 351–361.
- Dolan, T.J., 1982. *Fusion Research: Principles, Experience and Technology*. Pergamon Press, New York.
- Donahue, R.J., Fassó, A., 2002. Radioactivity and radiation protection. In: Hagiwara, et al. (Eds.), *Phys. Rev. D* 66 01001–1.
- Dowdall, M., O’Dea, J., 2002. $^{226}\text{Ra}/^{238}\text{U}$ disequilibrium in an upland organic soil exhibiting elevated natural radioactivity. *J. Environ. Radioact.* 59, 91–104.
- Dracos, M., 2009. Possibility of detecting neutrinoless double beta decays using nuclear emulsions. *Rad. Measurements* 44, 729–732.
- Drumm, H., Krienen, F., Lange, F., Picasso, E., von Ruden, W., Farley, F.J.M., et al., 1977. On muon lifetimes and time dilation. *Nature* 268 (5618), 301–305.
- Drury, L.O.’C., 1983. An introduction to the theory of diffuse shock acceleration of energetic particles in tenuous plasmas. *Rep. Prog. Phys.* 46, 973–1027.
- Durrani, S.A., Bull, R.K., 1987. *Solid State Nuclear Track Detection: Principles, Methods, and Applications*. Pergamon Press, Oxford, pp. 304.
- Eckelman, W.C., Volkert, W.A., Bonardi, M., 2008. True radiotracers: are we approaching theoretical specific activity with Tc-99m and I-123? *Nucl. Med. Biol.* 35, 523–527.
- Ehman, W.D., Vance, D.E., 1991. *Radiochemistry and Nuclear Methods of Analysis*. John Wiley & Sons, New York.
- Einstein, A., 1905. Über einen die erzeugung und verwandlung des liches betreffenden heuristischen gesichtspunkt. *Annalen der Physik, Leipzig* 17, 132–148.
- ElBaradei, M., 2004. Nuclear power, an evolving scenario. *IAEA Bulletin* 46 (No. 1), 4–8.
- Elliott, S.R., Vogel, P., 2002. Double beta decay. *Ann. Rev. Nucl. Part. Phys.* 52, 115–151.
- Elliott, S.R., Hahn, A.A., Moe, M.K., 1986. Experimental investigation of double-beta decay in ^{76}Se . *Phys. Rev. Lett.* 56, 2582–2585.
- Elliott, S.R., Hahn, A.A., Moe, M.K., 1987. Direct evidence for two-neutrino double-beta decay in ^{76}Se . *Phys. Rev. Lett.* 59, 2020–2023.
- Elliott, S.R., Gehman, V.M., Kazkaz, K., Mei, D.-M., Young, A.R., 2006. Pulse shape analysis in segmented detectors as a technique for background reduction in Ge double-beta decay experiments. *Nucl. Instrum. Methods Phys. Res. Sect. A* 558, 504–510.
- Elmore, C.S., 2009. The use of isotopically labeled compounds in drug discovery. pp 515–524. In: Maacor, J. (Ed.), *Annual Reports in Medicinal Chemistry*, vol. 44. Academic Press, p. 736.
- Elster, J., Geitel, H., 1903. Über die durch radioactive emanation erregte scintillierende phosphoreszenz der sidot-blende. *Phys. Z.* 4, 439–440.
- Elton, L.R.B., 1958. A semi-empirical formula for the nuclear radius. *Nucl. Phys.* 5, 173–178.
- Engelfried, J., Paic, G., 2005. Proceedings of the fifth international workshop on ring imaging Cherenkov detectors. *Nucl. Instrum. Methods Phys. Res. Sect. A* 553 (1–2), 1–380.
- Eshwarappa, K.M., Sanjeev, G., Siddappa, K., Kashyap, Y., Sinha, A., Sarkar, P.S., Godwal, B.K., 2007. Comparison of photoneutron yield from beryllium irradiated with bremsstrahlung radiation of different peak energy. *An. Nucl. Energy* 34, 896–901.
- Eskandari, M.R., Kashian, S., 2009. Design of moderator and multiplier systems for D-T neutron source in BNCT. *An. Nucl. Energy* 36, 1100–1102.
- Evans, R.D., 1955. *The Atomic Nucleus*. McGraw-Hill, New York, p. 972.
- Ezhov, V.F., Andreev, A.Z., Ban, G., Bazarov, B.A., Geltenbort, P., Hartman, F.J., Glushkov, A.G., Groshev, M.G., Knyazhkov, V.A., Kovrizhnykh, N.A., et al., 2009. Magnetic storage of UCN for a measurement of the neutron lifetime. *Nucl. Instrum. Methods Phys. Res. Sect. A* 611, 167–170.
- Fantidis, J.G., Nicolaou, G.E., Tsagas, N.F., 2009. A transportable neutron radiography system based on a SbBe neutron source. *Nucl. Instrum. Methods Phys. Res. Sect. A* 606, 806–810.
- Farhatziz, Rodgers, M.A.J., 1987. *Radiation Chemistry, Principles and Applications*. VCH Publishers, Inc., New York.
- Farkas, J., 2004. Food irradiation, pp. 785–812. In: Mozumder, A., Hatano, Y. (Eds.), *Charged Particle and Photon Interactions with Matter*. Marcel Dekkar, New York.
- Farkas, J., 2006. Irradiation for better foods. *Trends Food Sci. Techn.* 17, 148–152.
- Farkas, J., Mohácsi-Farkas, C., 2011. History and future of food irradiation. *Trends Food Sci. Techn.* 22 (2–3), 121–126.
- Faw, R.E., Shultis, J.K., 2004. Radiation sources, pp. 613–631. In: Meyers, R.A. (Ed.), *Encyclopedia of Physical Science and Technology*. Academic Press.
- Feather, N., 1938. Further possibilities for the absorption method of investigating the primary β -particles from radioactive substances. *Proc. Cambridge Phil. Soc.* 34, pp. 599–611.
- Feather, N., 1940. Lord Rutherford. Blackie & Son, Ltd.
- Feinberg, G., Paul, M., Arenstam, A., Berkovits, D., Kijel, D., Nagler, A., Silverman, I., 2009. LiLiT – a liquid lithium target as an intense neutron

- source for nuclear astrophysics at the Soreq applied research accelerator facility. *Nucl. Phys. A* 827, 590c–592c.
- Feld, B.T., Weiss Szilard, G. (Eds.), 1972. *The Collected Works of Leo Szilard: Scientific Papers*. MIT Press, Cambridge, p. 642.
- Fenyves, E., Haiman, O., 1969. *The Physical Principles of Nuclear Radiation Measurements*. Academic Press, New York.
- Fermi, E., 1934a. Versuch einer theorie der β -Strahlen. *Z. Phys.* 88, 161–177.
- Fermi, E., 1934b. Attempt at a theory of beta rays. *Nuovo Cimento*, 11, 1–21.
- Fermi, E., 1934c. Radioactivity induced by neutron bombardment. *Nature* 133, 757.
- Fermi, E., 1934d. Possible production of elements of atomic number higher than 92. *Nature* 133, 898–899.
- Fermi, E., 1938. Artificial radioactivity produced by neutron bombardment. Nobel Lecture, December 12, 1938. In: "Nobel Lectures, Physics, 1922–1941. Elsevier Publishing, Amsterdam (1965).
- Fermi, E., 1940a. Reactions produced by neutrons in heavy elements. *Science* 92, 269–271.
- Fermi, E., 1940b. Reactions produced by neutrons in heavy elements. *Nature* 146, 640–642.
- Fermi, E., 1949. On the origin of the cosmic radiation. *Phys. Rev.* 75 (8), 1169–1174.
- Fermi, E., Amaldi, E., Wick, G.C., 1938. On the albedo of slow neutrons. *Phys. Rev.* 53, 493.
- Fermi, E., Amaldi, E., D'Agostino, O., Rasetti, F., Segre, E., 1934. Artificial radioactivity produced by neutron bombardment. *Proc. Roy. Soc. London A146(857)*, pp. 483–500.
- Fermi, E., Amaldi, E., 1936. On the absorption and the diffusion of slow neutrons. *Phys. Rev.* 50, 899–928.
- Fernandes, H.M., Lamego Simoes Filho, F.F., Perez, V., Ramalho Franklin, M., Gomiero, L.A., 2006. Radioecological characterization of a uranium mining site located in a semi-arid region in Brazil. *J. Environ. Radioact.* 88, 140–157.
- Feshbach, H., 1952. The coulomb scattering of relativistic electrons and positrons by nuclei. *Phys. Rev.* 88 (2), 295–297.
- Fiore, K., 2006. Nuclear energy and sustainability: understanding ITER. *Energy Policy* 34, 3334–3341.
- Fiorini, E., 2007. Neutrinoless double beta decay. *Nucl. Phys. B – Proc. Supplements* 168, 11–16.
- Fiorini, E., 2008. Double beta decay. *Nucl. Phys. A* 805, 313c–319c.
- Firestone, R.B., Shirley, V.S., Baglin, C.M., Frank Chu, S.Y., Zipkin, J., 1996. *Table of Isotopes*, eighth ed., vols. I and II. John Wiley & Sons, New York.
- Flammersfeld, A., 1946. Eine beziehung zwischer energie und reichweite für betastrahlen kleiner und mittlerer energie. *Naturwissenschaften* 33, 280–281.
- Fowler, W.A., Oppenheimer, J., 1938. Scattering and loss of energy of fast electrons and positrons in lead. *Phys. Rev.* 54 (5), 320–324.
- Frank, I.M., 1958. Optics of light sources in refractive media. Nobel Lecture, December 11, 1958. In: Nobel Foundation Staff (Ed.), *Nobel Lectures, Physics, 1942–62*. Elsevier Publishing, Amsterdam (1964).
- Frank, I., Tamm, I.g., 1937. Coherent visible radiation of fast electrons passing through matter. *Dokl. Akad. Nauk, SSSR* 14 (3), 109–114.
- Freitas, E.D.C., Monteiro, C.M.B., Ball, M., Gómez-Cadenas, J.J., Lopes, J.A.M., Lux, T., Sánchez, F., dos Santos, J.M.F., 2010. Secondary scintillation yield in high-pressure xenon gas for neutrinoless double beta decay ($0\nu\beta\beta$) search. *Phys. Letters B* 684, 205–210.
- Friedlander, G., Kennedy, J.W., Miller, J.M., 1964. *Nuclear and Radiochemistry*, Second ed. John Wiley & Sons, New York, p. 585.
- Fujitaka, K., 2005. High-level doses brought by cosmic rays. *Int. Congr. Ser.* 1276, 124–128.
- Fukuda, Y., Izawa, T., Koshio, Y., Moriyama, S., Namba, T., Shiozawa, M., 2010. InP solid state detector for measurement of low energy solar neutrinos. *Nucl. Instrum. Methods Phys. Res. A*, 623 (1), 460–462.
- Gaisser, T.K., 2001. Origin of cosmic radiation. *Astron. AIP Conf. Proc.* 558, 27–42.
- Gaisser, T.K., Maurer, R.H., 1973. Cosmic \bar{p} production in interstellar pp collisions. *Phys. Rev. Lett.* 30, 1264–1267.
- Gaisser, T.K., Schaefer, R.K., 1992. Cosmic-ray secondary antiprotons: a closer look. *Astrophys. J.* 394, 174–184.
- Gaisser, T.K., Stanev, T., 2002. Cosmic rays. In: Hagiwara, et al. (Eds.), *The Review of Particle Physics*. University of California, Lawrence Berkeley Laboratories, pp. 23.1–23.19. *Physical Review D*66.
- Gamow, G., 1928. Zur quantentheorie des atomkernes. *Zeit. f. Phys.* 51, 204–212.
- Gamow, G., 1930. Mass defect and nuclear constitution. *Proc. Roy. Soc. Lond., A*, 126, pp. 632–644.
- Gamow, G., with Rutherford, E. (Chair), Aston, F.W., Chadwick, J., Ellis, C.D., Fowler, R.H., Richardson, O.W., and Hartree, D.R., 1929. Discussion on the Structure of Atomic Nuclei. *Proc. Roy. Soc. Lond., A*, April 6, 123, pp. 373–390.
- Gardner, R.P., Metwally, W.A., Shehata, A., 2004. A semi-empirical model for a ^{90}Sr beta-particle transmission thickness gauge for aluminum alloys. *Nucl. Instrum. Methods Phys. Res. B* 213, 357–363.
- Gautier, M.A. (Ed.), 1995. *Health and Environmental Chemistry: Analytical Techniques, Data Management, and Quality Assurance*. Los Alamos National Laboratory, Los Alamos, NM, Manual LA-10300-M, vol. III, UC-907, pp. WR190–1 - WR190–16.
- Gautreau, R., Savin, W., 1999. *Theory and Problems in Modern Physics*. McGraw-Hill, New York.
- Gehman, V.M., Elliott, S.R., Mei, D.-M., 2010. Systematic effects in pulse shape analysis of HPGe detector signals for $0\nu\beta\beta$. *Nucl. Instrum. Methods Phys. Res. Sect. A* 615, 83–92.
- Geiger, H., Nuttall, J.M., 1911. The range of alpha particles from various substances and a relationship between range and period of transformation. *Phil. Mag.* 22, 613–621.
- Gell-Mann, M., 1964. A schematic model of baryons and mesons. *Phys. Lett.* 8, 214–215.
- Ghassoun, J., Mostacci, D., Molinari, V., Jehouani, A., 2010. Detailed dose distribution prediction of Cf-252 brachytherapy source with boron loading dose enhancement. *Appl. Radiat. Isot.* 68 (2), 265–270.
- Gibbs, W.W., 1998. A massive discovery. *Sci. Am.* 279 (2), 18–20.
- Gibson, J.A.B., Piesch, E., 1985. *Neutron Monitoring for Radiological Protection*. Technical Report Series No. 252, International Atomic Energy Agency, Vienna.
- Gielow, P., 1990. Preparation of ^{64}Cu -labelled diethyl-HIDA. *Appl. Radiat. Isot.* 41 (2), 237–238.
- Giller, M., 2008. Cosmic rays between the knee and the ankle. *J. Phys. G* 35 (2) 023201.
- Glasser, R.G., Seeman, N., Stiller, B., 1961. Mean lifetime of the neutral pion. *Phys. Rev.* 123, 1014–1020.
- Glendenin, L.E., 1948. Determination of the energy of beta particles and photons by absorption. *Nucleonics* 2, 12–32.
- Glover, R.N., Jones, A.D.W., 1966. Stripping and pick-up reactions on the carbon isotopes. *Nucl. Phys.* 84, 673–682.
- Goepfert-Mayer, M., 1935. Double beta-disintegration. *Phys. Rev.* 48, 512–516.
- Goepfert-Mayer, M., 1948a. On Closed Shells in Nuclei. United States Atomic Energy Commission, AECD – 1818. Argonne National Laboratory, p. 5.
- Goepfert-Mayer, M., 1948b. On closed shells in nuclei. *Phys. Rev.* 74, 235–239.
- Goepfert-Mayer, M., 1949. On closed shells in nuclei, II. *Phys. Rev.* 75, 1969–1970.
- Goepfert-Mayer, M., 1964. The shell model. *Science* 145, 999–1006.
- Goepfert-Mayer, M., 1972. The shell model. Nobel Lecture given on December 12, 1963. In: *Nobel Lectures, Physics 1963–1970*. Elsevier Publishing, Amsterdam.
- Goepfert-Mayer, M., Jensen, J.H.D., 1955. *Elementary Theory of Nuclear Shell Structure*. John Wiley & Sons, New York, p. 269.
- Goepfert-Mayer, M., Jensen, J.H.D., 1955. The shell model. I. shell closure and jj coupling. In: Siegbahn, K. (Ed.), *Alpha, Beta- and Gamma-ray spectroscopy*. North Holland Publishing, Amsterdam, p. 557.
- Golden, R.L., et al., 1979. Evidence for the existence of cosmic-ray antiprotons. *Phys. Rev. Lett.* 43, 1196–1199.
- Golden, R.L., Mauger, B.G., Nunn, S., Horan, S., 1984. Energy dependence of the \bar{p}/p ratio in cosmic rays. *Astrophys. Lett.* 24, 75–83.
- Gómez, H., Cebrián, S., Morales, J., Villar, J.A., 2007. Background reduction and sensitivity for germanium double beta decay experiments. *Astroparticle Phys.* 28, 435–447.
- Gould, C.R., Davis, E.D., Wilets, L., Siemens, P.J., 2004. Nuclear physics, pp. 721–738. In: Meyers, R.A. (Ed.), *Encyclopedia of Physical Science and Technology*. Academic Press, Orlando.
- Gratta, G., Wang, Y.F., 1999. Towards two-threshold, real-time solar neutrino detectors. *Nucl. Instrum. Methods Phys. Res. Sect. A* 438, 317–321.

- Grau Carles, A., Grau Malonda, A., 2006. Computational aspects in modeling the interaction of low-energy X-rays with liquid scintillators. *Appl. Radiat. Isot.* 64, 1515–1519.
- Grau Carles, A., Kossert, K., 2009. Monte Carlo simulation of Auger electron spectra. *Appl. Radiat. Isot.* 67, 192–196.
- Grau Malonda, A., Grau Carles, A., 2002. Half-life determination of ^{40}K by LSC. *Appl. Radiat. Isot.* 56, 153–156.
- Grau Malonda, A., Grau Carles, A., Garcia, G., 2006. Mean values of LMM Auger transition in a KLM model. *Appl. Radiat. Isot.* 64, 1485–1491.
- Green, J.H., Maddock, A.G., 1949. (n, γ) recoil effects in potassium chromate and dichromate. *Nature* 164, 788–789.
- Greenberg, O.W., 1964. Spin and unitary spin independence in a paraquark model of baryons and mesons. *Phys. Rev. Lett.* 13, 598–602.
- Greiner, W., Ivascu, M., Poenaru, D.N., Sandulescu, A., 1985. An exotic nuclear decay of ^{223}Ra by emission of ^{14}C nuclei. *Z. Phys. A* 320, 347–348.
- Grieder, P.K.F., 2001. *Cosmic Rays at Earth: Researcher's Reference Manual and Data Book*. Elsevier, Amsterdam, pp. 1093.
- Grimani, C., 2005. Upper limit to the cosmic-ray positron flux generated at the pulsar polar cap. In: *Proc. of the 29th Int. Cosmic Ray Conf. (Pune, India, 3–10 August 2005)*, 3, pp. 9–12.
- Grimani, C., 2009. Origin of cosmic-ray positrons. In: *Proc. of the 31st Int. Cosmic Ray Conf. (Łódź, Poland, 7–15 July 2009)*.
- Groom, D.E., Mokhov, N.V., Striganov, S.I., 2001. Muon stopping power and range tables 10 MeV to 100 TeV. *Atomic Data Nucl. Data Tables* 78, 183–356.
- Gullstrand, A., 1925. Presentation speech, the Nobel prize in physics 1924. In: *Nobel Lectures, Physics 1922–1941*. Elsevier Publishing, Amsterdam (1965).
- Gurney, R.W., Condon, E.U., 1928. Wave mechanics and radioactive disintegration. *Nature* 122, 439.
- Hahn, O., Meitner, L., 1924. Das β -strahlenspektrum von radium und seine deutung. *Z. Phys.* 26, 161–168.
- Hahn, O., Strassmann, F., 1939a. Über den nachweis und das verhalten der bei bestrahlung des urans mittels neutronen entstehenden erdalkalimetalle. *Naturwissenschaften* 27, 11–15.
- Hahn, O., Strassmann, F., 1939b. Nachweis der entstehung activer bariumisotope aus uran und thorium durch neutronenbestrahlung; nachweis weiterer aktiver bruchstücke bei der uranspaltung. *Naturwissenschaften* 27, 89–95.
- Halpern, A., 1988. *Schaum's 3000 Solved Problems in Physics*. McGraw-Hill, New York.
- Hammer, G.P., Zeeb, H., Tveten, U., Blettner, M., 2000. Comparing different methods of estimating cosmic radiation exposure of airline personnel. *Radiat. Environ. Biophys.* 39, 227–231.
- Han, M.Y., Nambu, Y., 1965. Three-triplet model with double SU(3) symmetry. *Phys. Rev.* 139, B1006–B1010.
- Harbottle, G., 1954. Szilard-Chalmers reaction in crystalline compounds of chromium, radiochemical analysis. *J. Chem. Phys.* 22, 1083.
- Harms, A.V., Jerome, S.M., 2004. On the integrated decay and ingrowth equations used in the measurement of radioactive decay families: the general solution. *Appl. Radiat. Isot.* 61, 367–372.
- Hasselberg, K.B., 1908. Presentation speech of the Nobel prize in chemistry 1908. In: *Nobel Lectures, Chemistry 1901–1921*. Elsevier Publishing, Amsterdam (1966).
- Hawryluk, R.J., Adler, H., Alling, P., Ancher, C., Anderson, H., Anderson, J.L., Ascroft, D., Barnes, C.W., Barnes, G., 1994. Confinement and heating of a deuterium-tritium plasma. *Phys. Rev. Lett.* 72, 3530–3533.
- Haxel, O., Jensen, J.H.D., Suess, H.E., 1949. On the "magic numbers" in nuclear structure. *Phys. Rev.* 75, 1766.
- Hayashida, N., Honda, K., Honda, M., Imaizumi, S., Inoue, N., Kadota, K., Kakimoto, F., Kamata, K., Kawaguchi, S., Kawasumi, N., 1994. Observation of a very energetic cosmic ray well beyond the predicted 2.7 K cutoff of the primary energy spectrum. *Phys. Rev. Lett.* 73, 3491–3494.
- He, G., Luo, J., Liu, Z., Kong, X., 2006. Cross-section measurements for ($n, 2n$), (n,p) and (n,α) reactions on strontium isotopes at the neutron energy about 14 MeV. *Annals Nucl. Energy* 33 (1), 37–42.
- Heisenberg, W., 1926a. Quantum mechanics. *Naturwissen.* 14, 989–994.
- Heisenberg, W., 1926b. Multi-boson problem and resonance in the quantum mechanics. *Z. Phys.* 38 (6/7), 411–426.
- Heisenberg, W., 1926c. Fluctuation appearances and quantum mechanics. *Z. Phys.* 40 (7), 501–506.
- Heisenberg, W., 1927. Über den anschaulichen Inhalt der quantentheoretischen Kinematik und Mechanik. *Z. Phys.* 43, 172–198.
- Heisenberg, W., 1929. The development of the quantum theory 1918–1928. *Naturwissen.* 17, 490–496.
- Heisenberg, W., 1934. Considérations théoriques générales sur la structure du noyau, pp. 316. In: *Institut International de Physique Solvay, "Structure et Propriétés des Noyaux Atomiques: Rapports et Discussions du Septième Conseil de Physique tenu a Bruxelles du 22 au Octobre 1933*. Gauthier-Villars, Paris.
- Hertz, H., 1887. Über einen einfluss des ultravioletten liches auf die elektrische entladung. *Sitz-ber. Berl. Akad.* 9 June, also *Wied. Ann. Physik* vol. 31.
- Hertz, K.L., Hilton, N.R., Lund, J.C., Van Scyoc, J.M., 2003. Alpha-emitting radioisotopes for switchable neutron generators. *Nucl. Instrum. Methods Phys. Res. A* 505, 41–45.
- Hess, V.F., 1912. Über beobachtungen der durchdringenden strahlung bei sieben freiballonfahrten. *Phys. Z.* 13, 1084–1091.
- Hess, V.F., 1936. Unsolved problems in physics; tasks for the immediate future in cosmic rays studies. Nobel Lecture, December 12, 1939. In: *Nobel Lectures, Physics, 1922–1941*. Elsevier Publishing, Amsterdam (1965).
- Hess, V.F., 1940. The discovery of cosmic radiation. *Thought (Fordham Quarterly)* 15, 225–236.
- Hetherington, E.L., Sorby, P.J., Camakaris, J., 1986. The preparation of high specific activity copper-64 for medical diagnosis. *Appl. Rad. Isot.* 37 (12), 1242–1243.
- Heyde, K.L.G., 2004. *Basic Ideas and Concepts in Nuclear Physics, An Introductory Approach*, third ed. Institute of Physics Publishing, Bristol, p. 360.
- Higashi, T., Tomizawa, T., Daino, M., Yamamoto, Y., 2003. Preliminary results of low pressure discharge experiments of a cylindrical inertial electrostatic confinement fusion device aimed for a small neutron source. *Fusion Sci. Techn.* 44, 544–548.
- Hirsh, R.L., 1967. Inertial-electrostatic confinement of ionized fusion gases. *J. Appl. Phys.* 38 (11), 4522–4535.
- Hof, M., Menn, W., Pfeifer, C., Simon, M., Golden, R.L., Stochaj, S.J., Stephens, S.A., Basini, G., Ricci, M., Massimo Brancaccio, F., et al., 1996. Measurement of cosmic-ray antiprotons from 3.7 to 19 GeV. *Astrophys. J. Lett.* 467 (1), L33–L37.
- Holden, N.E., 1997a. Table of isotopes. In: *Lide, D.R. (Ed.), CRC Handbook of Chemistry and Physics, seventy-seventh ed.* CRC Press, Boca Raton, FL, pp. 11–38–11–143.
- Holden, N.E., 1997b. Neutron scattering and absorption properties. In: *Lide, D.R. (Ed.), CRC Handbook of Chemistry and Physics, seventy-seventh ed.* CRC Press, Boca Raton, FL, pp. 11–144–11–158.
- Holloway, M.G., and Baker, C.P., 1944. Note on the origin of the term "barn". Los Alamos Technical Report LAMS-523, p. 4.
- Holloway, M.G., Baker, C.P., 1972. How the barn was born. *Phys. Today* 25 (7), 9.
- Honda, T., Horie, H., Kudo, Y., Ui, H., 1965. Nuclear direct interaction in the $^{12}\text{C}(\alpha)^{11}\text{B}$ reaction. *Nucl. Phys.* 62, 561–574.
- Hörandel, J.R., 2008a. Cosmic-ray composition and its relation to shock acceleration by supernova remnants. *Adv. Space Res.* 41, 442–463.
- Hörandel, J.R., 2008b. The origin of galactic cosmic rays. *Nucl. Instrum. Methods Phys. Res. Sect. A* 588, 181–188.
- Hörandel, J.R., 2010. Cosmic rays at the highest energies. *Prog. Part. Nucl. Phys.* 64, 351–359.
- Horányi, G., 2004. Advantages of the radiotracer technique, pp. 5–8. In: *Horányi, G. (Ed.), Interface Science and Technology, Radiation Studies of Interfaces, vol. 3*. Elsevier, Amsterdam, p. 435.
- Horowitz, Y., 2006. *Microdosimetric Response of Physical and Biological Systems to Low- and High-LET Radiations*. Elsevier, Amsterdam, p. 500.
- Hubbell, J.H., 1969. Photon Cross Sections, Attenuation Coefficients, and Energy Absorption Coefficients from 10 keV to 100 GeV. *NSRDS-NBS 29*, Natl. Stand. Ref. Data Ser., National Bureau of Standards (U.S.), p. 80.
- Huh, C.-A., 1999. Dependence of the decay rate of ^7Be on chemical forms. *Earth Planetary Sci. Lett.* 171, 325–328.
- Huisman, H., Bacelar, J.C.S., van Goethem, M.J., Harakeh, M.N., Hoefman, M., Kalantar-Nayestanaki, N., Löhner, H., Messchendorp, J.G.,

- Ostendorf, R.W., Schadmand, S., Scholten, O., Simon, R.S., Timmermans, R.G.E., Volkerts, M., Wilschut, H.W., 2000. Dynamical effects in proton-proton bremsstrahlung for non-coplanar geometries. *Phys. Letts. B* 476, 9–14.
- IAEA, 2006. Directory of Cyclotrons used for Radionuclide Production in Member States. IAEA-DCRP/CD, International Atomic Energy Agency, Vienna.
- IAEA, 2007. Nuclear Technology Review. GC(951)/INF/3, International Atomic Energy Agency, Vienna, p. 32.
- IAEA, 2009. Nuclear Technology Review. GC(53)/INF/3, International Atomic Energy Agency, Vienna, p. 41.
- Ianni, A., Montanino, D., Villante, F.L., 2005. How to observe ^8B solar neutrinos in liquid scintillator detectors. *Phys. Letts. B* 627, 38–48.
- ICRP, 1991. Publication 60, "1990 Recommendation of the International Commission on Radiological Protection. Pergamon Press.
- ICRU Report 63, 2000. Nuclear Data for Neutron and Proton Radiotherapy and for Radiation Protection. ISBN 0-913394-62-9.
- Ilić, R., Durrani, S.A., 2003. Solid state nuclear track detectors. pp.179–237. In: L'Annunziata, M.F. (Ed.), *Handbook of Radioactivity Analysis*, second ed. Elsevier, Amsterdam, p. 1273.
- Isotope Products Laboratories, 1995. Californium-252 fission foils and neutron sources. In: *Radiation Sources for Research, Industry and Environmental Applications*. Isotope Products Laboratories, Burbank, CA, p. 55.
- Ivanovich, M., 1994. Uranium series disequilibrium: concepts and applications. *Radiochim. Acta* 64, 81–94.
- Ivanovich, M., Harmon, R.S., 1992. Uranium Series Disequilibrium: Applications to Earth, Marine and Environmental Sciences. Clarendon Press, Oxford, p. 910.
- Iwashita, Y., Nagae, T., Tanimori, T., Fujioka, H., Shimizu, H.M., 2011. Satellite pulsed tiny neutron source at Kyoto University, Sakyō. *Nucl. Instrum. Methods Phys. Res. Sect. A*, 634 (1, Suppl.1), S97–S99.
- Jaklevic, J.M., Madden, N.W., Wiegand, C.E., 1983. A precision beta gauge using a plastic scintillator and photomultiplier detector. *Nucl. Instrum. Methods* 214, 517–518.
- Jakubek, J., Platkevic, M., Granja, C., Köster, U., Pospisil, S., 2011. Direct observation of decay of radioactive nuclei with spatial and time coincidence technique. *Nucl. Instrum. Methods Phys. Res. Sect. A*, 633 (Suppl.1), s203–s205.
- Janczyszyn, J., Pohorecki, W., Domańska, G., Loska, L., Taczanowski, S., Shvetsov, V., 2006. Measurement and calculation of cross section for (p, x) reactions on natural Fe for 650 MeV protons. *Annals Nucl. Energy* 33 (7), 633–639.
- Janni, J.F., 1982. Proton range-energy tables, 1 keV – 10 GeV. *Atomic Data Nucl. Data Tables* 27, 147–339.
- Jansen, J.A., Peerdeman, R.Th., De Vries, C., 1971. Nuclear charge radii of ^{12}C and ^9Be . *Nucl. Phys. A* 188 (2), 337–352.
- Janson, E., Westlin, J., Ohrvall, U., Oberg, K., Lukinius, A., 2000. Nuclear localization of In-111 after intravenous injection of [In-111-DTPA-D-Phe(1)]-octreotide in patients with neuroendocrine tumors. *J. Nucl. Med.* 41 (9), 1514–1518.
- J.E.T., Team, 1992. Fusion energy production from a deuterium-tritium plasma in the JET tokamak. *Nucl. Fusion* 32, 187–201.
- Jia, W., Ehrhardt, G.J., 1997. Enhancing the specific activity of Re-186 using an inorganic Szilard-Chalmers process. *Radiochim. Acta* 79 (2), 131–136.
- Johansson, A., Wilkin, C., 2009. Hard bremsstrahlung in the $pp \rightarrow p\bar{p}\gamma$ reaction. *Phys. Letts. B* 673, 5–8.
- Johansen, G.A., Jankson, P., 2004. Isotope Gauges for Industrial Process Measurements. John Wiley & Sons Ltd, Chichester, UK. doi: 10.1002/0470021098.fmatter.
- Joliot-Curie, I., Joliot, F., 1934a. Artificial production of a new kind of radioelement. *Nature* 133, 201.
- Joliot-Curie, I., Joliot, F., 1934b. Un nouveau type de radioactivité. *Comptes Rendus* 198S, 254–256.
- Joliot-Curie, I., Joliot, F., 1934c. Séparation chimique des nouveaux radioéléments émetteurs d'électrons positifs. *Comptes Rendus* 198S, 559–561.
- Jones, H.G., 1973. Estimation of plant water status with the beta-gauge. *Agric. Meteorology* 11, 345–355.
- Jones, J.A., Casey, R.C., Karoia, F., 2010. Ionizing radiation as a carcinogen. In: McQueen, C. (Ed.), *Comprehensive Toxicology*, second ed. Elsevier Science, Amsterdam, pp. 181–228, 250.
- Karelin, Y.A., Gordeev, Y.N., Karasev, V.I., Radchenko, V.M., Schimbarev, Y.V., Kuznetsov, R.A., 1997. Californium-252 neutron sources. *Appl. Radiat. Isot.* 48 (10–12), 1563–1566.
- Kaschl, G.Th., Wagner, G.J., Mairle, G., Schmidt-Rohr, U., Turek, P., 1970. Proton pick-up from ^{19}F , ^{20}Ne and ^{22}Ne . *Nucl. Phys. A* 155, 417–442.
- Katz, L., Penfold, A.S., 1952. Range-energy relations for electrons and the determination of beta-ray end-point energies by absorption. *Rev. Mod. Phys.* 24 (1), 28–44.
- Kazkaz, K., the Majorana Collaboration, 2005. The Majorana search for neutrinoless double-beta decay. *Nucl. Phys. B – Proc. Supplements* 143, 550.
- Kearns, E., Kajita, T., Totsuka, Y., 1999. Detecting massive neutrinos. *Sci. Am.* 281 (2), 64–71.
- Kelley, K.C., Hertel, N.E., Pitcher, E.J., Devlin, M., Mashnik, S.G., 2005. ^{149}Gd production cross section measurements for 600- and 800-MeV protons on tantalum, tungsten, and gold. *Nucl. Phys. A* 760 (3–4), 225–233.
- Kesterbaum, D., 1998. Neutrinos throw their weight around. *Science* 281 (5383), 1594–1595.
- Khachan, J., Samarian, A., 2007. Dust diagnostics on an inertial electrostatic confinement device. *Phys. Letts. A* 363, 297–301.
- Kim, H.S., Park, S.H., Ha, J.H., Song, T.Y., Cho, S.Y., Kim, Y.K., 2009. Development of a beta gauge system for a fabric density measurement. *Appl. Radiat. Isotopes* 67, 1213–1215.
- Kim, I.J., Jung, N.S., Jung, H.D., Hwang, Y.S., Choi, H.D., 2008. A D–D neutron generator using a titanium drive-in target. *Nucl. Instrum. Methods Phys. Res. Sect. B* 266, 829–833.
- Klarsfeld, S., Martorell, J., Oteo, J.A., Nishimura, M., Sprung, D.W.L., 1986. Determination of the deuteron mean square radius. *Nucl. Phys. A* 456 (3), 373–396.
- Knapp, A.K., Abrams, M.D., Hulbert, L.C., 1985. An evaluation of beta attenuation for estimating aboveground biomass in a tallgrass prairie. *J. Range Manag.* 38 (6), 556–558.
- Knipp, J.K., Uhlenbeck, G.E., 1936. Emission of gamma radiation during the beta decay of nuclei. *Physica* III(6), 425–439.
- Koch, L., 1995. Radioactivity and fission energy. *Radiochim. Acta* 70/71, 397–402.
- Kolhinen, V.S., Elomaa, V.-V., Eronen, T., Hakala, J., Jokinen, A., Kortelainen, M., Suhonen, J., Äystö, J., 2010. Accurate Q value for the ^{74}Se double-electron-capture decay. *Phys. Letters B* 684 (Issue 1), 17–21.
- Kossert, K., Grau Carles, A., 2008. Study of a Monte Carlo rearrangement model for the activity determination of electron-capture nuclides by means of liquid scintillation counting. *Appl. Radiat. Isot.* 66, 998–1005.
- Kossert, K., Grau Carles, A., 2010. Improved method for the calculation of the counting efficiency of electron-capture nuclides in liquid scintillation samples. *Appl. Radiat. Isot.* 68, 1482–1488.
- Kostroun, V.O., Chen, M.S., Crasemann, B., 1971. Atomic radiation transition probabilities to the 1s state and theoretical K-shell fluorescence yields. *Phys. Rev. A* 3, 533–545.
- Krane, K.S., 1988. *Introductory Nuclear Physics*. John Wiley & Sons, New York.
- Krappe, H.J., Wahsweiler, H.G., 1967. Stability of nuclei against pear-shaped deformations. *Nucl. Phys. A* 104 (3), 633–641.
- Krása, A., Wagner, V., Majerle, M., Křížek, F., Kugler, A., Svoboda, O., Adam, J., Krivopustov, M.L., 2010. Neutron production in a Pb/U-setup irradiated with 0.7–2.5 GeV protons and deuterons. *Nucl. Instrum. Methods Phys. Res. Sect. A* 615, 70–77.
- Kraus, Ch., Bornschein, B., Bornschein, L., Bonn, J., Flatt, B., Kovalik, A., Ostrick, B., Otten, E.W., Schall, J.P., Thümler, Th., Weinheimer, Ch., 2005. Final results from phase II of the Mainz neutrino mass search in tritium decay. *Eur. Phys. J. C* 40 (4), 447–468.
- Kristiansen, J.R., La Vuccha, G., Colombo, L.P.L., Mainini, R., Bonometto, S.A., 2010. Coupling between cold dark matter and dark energy from neutrino mass experiments. *New Astronomy* 15, 609–613.
- Kudo, H., 1995. Radioactivity and fusion energy. *Radiochim. Acta* 70/71, 403–412.
- Kurtukian-Nieto, T., Benlliure, J., Schmidt, K.-H., 2008. A new analysis method to determine β -decay half-lives in experiments with complex background. *Nucl. Instrum. Methods Phys. Res. Sect. A* 589, 472–483.
- Kushnir, M.M., Rockwood, A.L., Nelson, G.J., 2004. Simultaneous quantitative analysis of isobars by tandem mass spectrometry from unresolved chromatographic peaks. *J. Mass Spectrom.* 39 (5), 532–540.

- Labidi, S., Mahjoubi, H., Essafi, F., Ben Salah, R., 2010. Natural radioactivity levels in mineral, therapeutic and spring waters in Tunisia. *Radiat. Phys. Chem.* 79, 1196–1202.
- Lacoste, V., 2010. Review of radiation sources, calibration facilities and simulated workplace fields. *Radiat. Meas.* 45 (10), 1083–1089.
- Lakosi, L., Nguyen, C.T., 2008. Neutron interrogation of high-enriched uranium by a 4 MeV linac. *Nucl. Instrum. Methods Phys. Res. Sect. B* 266, 3295–3301.
- Lal, D., 2009. Cosmogenic isotopes. In: Steele, J., Thorpe, S., Turekian, K. (Eds.), *Encyclopedia of Ocean Sciences*. Academic Press/Elsevier Science Publishers, Amsterdam, pp. 678–687.
- Lal, D., Peters, B., 1967. Cosmic ray produced radioactivity on the earth. *Handbuch der Physik* 46 (2), 551–612.
- Landowne, S., Dasso, C.H., 1986. Novel aspects of the carbon decay mode of radium. *Phys. Rev. C* 33, 387–389.
- L'Annunziata, M.F., 1971. Birth of a unique parent-daughter relation: secular equilibrium. *J. Chem. Educ.* 48, 700–703.
- L'Annunziata, M.F., 1987. *Radionuclide Tracers, Their Detection and Measurement*. Academic Press, London, p. 505.
- L'Annunziata, M.F., 2007. *Radioactivity: Introduction and History*. Elsevier Science, Amsterdam, p. 609.
- L'Annunziata, M.F., Passo Jr., C.J., 2002. Cherenkov counting of yttrium-90 in the dry state: correlations with phosphorus-32 Cherenkov counting data. *Appl. Radiat. Isot.* 56, 907–916.
- Lawrence, E.O., 1935. Transmutation of sodium by deuterons. *Phys. Rev.* 47, 17–27.
- Lawrence, E.O., 1951. The evolution of the cyclotron. Nobel Lecture given on December 11, 1951 in Stockholm, Sweden. In: *Nobel Lectures, Physics, 1922–1941*. Elsevier Publishing, Amsterdam (1965).
- Lawrence, E.O., Alvarez, L.W., Brobeck, W.M., Cooksey, D., Corson, D.R., McMillan, E.M., Salisbury, W.W., Thornton, R.L., 1939. Initial performance of the 60-inch cyclotron of the William H. Crocker Radiation Laboratory, University of California. *Phys. Rev.* 56, 124.
- Lawrence, E.O., Cooksey, D., 1936. On the apparatus for the multiple acceleration of light ions to high speeds. *Phys. Rev.* 50, 1131–1140.
- Lawrence, E.O., Edlefsen, N.E., 1930. The production of high-speed protons without the use of high voltages. *Science* 72, 376–377.
- Lawrence, E.O., Livingston, M.S., 1931a. The production of high-speed protons without the use of high voltages. *Phys. Rev.* 37, 1707.
- Lawrence, E.O., Livingston, M.S., 1931b. The production of high-speed protons without the use of high voltages. *Phys. Rev.* 38, 834.
- Lawrence, E.O., Livingston, M.S., 1932. The production of high-speed light ions without the use of high voltages. *Phys. Rev.* 40, 19–35.
- Lawrence, E.O., Livingston, M.S., 1934. The multiple acceleration of ions to very high speeds. *Phys. Rev.* 45, 608–612.
- Lederer, M.C., Shirley, V.S., 1978. In: Brown, E., Dairiki, J.M., Doebler, R.E., Shihab-Eldin, A.A., Jardim, L.J., Tuli, J.K., Buyn, A.B. (Eds.), *Table of Isotopes*, seventh ed. John Wiley & Sons, New York.
- Lee, K.K.M., Steinle-Neumann, G., 2008. Ab-initio study of the effects of pressure and chemistry on the electron-capture radioactive decay constants of ${}^7\text{Be}$, ${}^{22}\text{Na}$ and ${}^{60}\text{K}$. *Earth Planetary Sci. Lett.* 267, 628–636.
- Lee, T.D., Yang, C.N., 1956. Question of parity conservation in weak interactions. *Phys. Rev.* 104, 254–258.
- Leighton, R.B., Wanlass, S.D., Anderson, C.D., 1953. The decay of V^0 particles. *Phys. Rev.* 89, 148–177. http://prola.aps.org/abstract/PR/v89/i1/p148_1.
- Leung, K.K.H., Zimmer, O., 2009. Proposed neutron lifetime measurement using a hybrid magnetic trap for ultra-cold neutrons. *Nucl. Instrum. Methods Phys. Res. Sect. A* 611, 181–185.
- Levinger, J.S., 1953. Effects of radioactive disintegrations on inner electrons of the atom. *Phys. Rev.* 90, 11–25.
- Li, Z., Deutscher, M.P., 2008. Analyzing the decay of stable RNAs in *E. coli*, pp. 31–45. In: Maquat, L.E., Arraiano, C.M. (Eds.), *Methods in Enzymology*, vol. 447. Elsevier, Amsterdam, p. 364.
- Licciardi, J.M., Denoncourt, C.L., Finkel, R.C., 2008. Cosmogenic ${}^{36}\text{Cl}$ production rates from Ca spallation in Iceland. *Earth Planetary Sci. Lett.* 267, 365–377.
- Lide, D.R., 2010. *CRC Handbook of Chemistry and Physics*, ninetyfirst ed. CRC Press, Taylor & Francis Group, Boca Raton, p. 2610.
- Lilley, J., 2001. *Nuclear Physics, Principles and Applications*. John Wiley & Sons, Ltd., West Sussex, pp. 393.
- Lin, C.C., Chao, J.H., 2009. Radiochemistry of iodine: relevance to health and disease, p. 171–182. In: Preedy, V., Burrow, G., Watson, R. (Eds.), *Comprehensive Handbook of Iodine*. Academic Press, p. 1334.
- Lindhard, J., Scharff, M., 1960. Recent developments in the theory of stopping power. I. Principles of the statistical method. In: *Penetration of Charged Particles in Matter*. National Academy of Sciences-National Research Council, vol. 752, Publication, 49.
- Lindhard, J., Scharff, M., 1961. Energy dissipation by ions in the keV region. *Phys. Rev.* 124, 128–130.
- Lindote, A., Araújo, H.M., Kudryavtsev, V.A., Robinson, M., 2009. Simulation of neutrons produced by high-energy muons underground. *Astropart. Phys.* 31, 366–375.
- Linsley, J., 1963. Evidence for a primary cosmic-ray particle with energy 10^{20} eV. *Phys. Rev. Lett.* 10 (4), 146–148.
- Lipkin, H.J., White, M.G., 1950. Scattering of positrons and electrons by nuclei. *Phys. Rev.* 79 (5), 892L–893L, erratum 80 (4), 770L.
- Litherland, A.E., Tomskii, I., Zhao, X.-L., Cousins, L.M., Doupe, J.P., Javahery, G., Kieser, E.E., 2007. Isobar separation at very low energy for AMS. *Nucl. Instrum. Methods Phys. Res. Sect. A* 259 (1), 230–235.
- Liu, L., Huh, C.-A., 2000. Effect of pressure on the decay rate of ${}^7\text{Be}$. (2000). *Earth Planetary Sci. Lett.* 180, 163–167.
- Lobashev, V.M., Aseev, V.A., Belesev, A.I., Berlev, A.I., Geraskin, E.V., Golubev, A.A., Golubev, N.A., Kazachenko, O.V., Kuznetsev, Yu.E., Ostroumov, R.P., et al., 2000. Neutrino mass and anomaly in the tritium beta-spectrum. In: *Proceedings the XIX International Conference on Neutrino Physics and Astrophysics (Neutrino-2000)*, Sudbury, Canada, June 16–21, 2000.
- Lobashev, V.M., Aseev, V.A., Belesev, A.I., Berlev, A.I., Geraskin, E.V., Golubev, A.A., Kazachenko, O.V., Kuznetsev, Yu. E., Ostroumov, R.P., Rivkis, L.A., et al., 1999a. Direct search for mass of neutrino and anomaly in the tritium beta-spectrum. *Phys. Lett. B* 460, 227–235.
- Lobashev, V.M., Aseev, V.A., Belesev, A.I., Berlev, A.I., Geraskin, E.V., Golubev, A.A., Golubev, N.A., Kazachenko, O.V., Kuznetsev, Yu. E., Ostroumov, R.P., et al., 1999b. Neutrino mass and anomaly in the tritium beta-spectrum. Results of the “Troitsk ν -mass” experiment. *Nucl. Phys. B (Proc. Suppl.)* 77, 327–332.
- Lobashev, V.M., Belesev, A.I., Berlev, A.I., Geraskin, E.V., Golubev, A.A., Kazachenko, O.V., Kuznetsev, Yu. E., Rivkis, L.A., Stern, B.E., Titov, N.A., et al., 1999c. Neutrino rest mass and anomaly in the tritium β spectrum. *Nucl. Phys. A* 654, 982c–987c.
- Loeber, C.R., 2002. *Building the Bombs: A History of the Nuclear Weapons Complex*. Sandia National Laboratories, Albuquerque, p. 262.
- Loveland, W., 2004. Nuclear chemistry, pp. 597–615. In: Myers, R.A. (Ed.), *Encyclopedia of Physical Science and Technology*, third ed. Elsevier, Amsterdam.
- Luo, N., Ragheb, M., Miley, G.H., 2010. Proton bremsstrahlung and its radiation effects in fusion reactors. *Fusion Eng. Design* 85, 39–45.
- Macfarlane, R.D., Kohman, T.P., 1961. Natural alpha radioactivity in medium-heavy elements. *Phys. Rev.* 121, 1758–1769.
- Madani, J.H., Ahmad, I., Alvi, M.A., 2010. Microscopic study of deuteron-nucleus total reaction cross section at medium energies. *Nucl. Phys. A* 839 (1–4), 42–50.
- Mahboub, K., 2008. A simple theoretical approach to the liquid drop model. *Ann. Nucl. Energy* 35, 1381–1385.
- Mahjour-Shafiei, M., Amir-Ahmadi, H.R., Bacelar, J.C.S., Castelijns, R., Ermisch, K., van Garderen, E.D., Gasparić, I., Harakeh, M.N., Kalantar-Nayestanaki, N., Kis, M., Löhner, H., Scholten, O., 2006. Proton-proton bremsstrahlung towards the elastic limit at 190 MeV incident beam energy. *Phys. Letts. B* 632, 480–484.
- Majorovits, B., 2010. Segmented HPG detectors for the search of neutrinoless double beta-decay. *Progress in Particle and Nucl. Phys.*, 64 (2), 264–266.
- Malik, S.S., Gupta, R.K., 1989. Theory of cluster radioactive decay and of cluster formation in nuclei. *Phys. Rev. C* 39, 1992–2000.
- Mameli, A., Greco, F., Fidanzio, A., Fusco, V., Cilla, S., D'Onofrio, G., Grimaldi, L., Augelli, B.G., Giannini, G., Bevilacqua, R., et al., 2008. CR-39 detector based thermal neutron flux measurements, in the photo

- neutron project. Nucl. Instrum. Methods Phys. Res. Sect. B 266, 3656–3660.
- Manjunatha, H.C., Rudraswamy, B., 2009. Exposure of bremsstrahlung from beta-emitting therapeutic radionuclides. Rad. Meas. 44, 206–210.
- Manjunatha, H.C., Rudraswamy, B., 2010. Bremsstrahlung exposure of tissues from beta-therapeutic nuclides. Nucl. Instrum. Methods Phys. Res. Sect. A 621, 581–589.
- Mapleston, P., 1997. Film thickness gauges meet market needs for quality, cost. Mod. Plastics 74, 73–76.
- Marcelli, L., 2011. Identification of the light nuclei component of cosmic rays with the PAMELA experiment. Nucl. Instrum. Methods Phys. Res. Sect. A. 630 (1), 58–62.
- Markowicz, A.A., VanGrikin, R.E., 1984. Composition dependence of bremsstrahlung background in electron-probe X-ray microanalysis. Anal. Chem. 56, 2049–2051.
- Marques-Netto, A., Abbe, J.C., 1975. Szilard-Chalmers effects in hafnium chelates. J. Inorg. Nucl. Chem. 37, 2235–2238.
- Martin, B., Shaw, G., 2004. Particle physics, elementary, pp. 617–648. In: Meyers, R.A. (Ed.), Encyclopedia of Physical Science and Technology. Academic Press, Orlando.
- Martin, R.C., Knauer, J.B., Baló, P.A., 2000. Production, distribution and applications of californium-252 neutron sources. Appl. Radiat. Isot. 53, 785–792.
- Martin, R.C., Laxon, R.R., Miller, J.H., Wierzbicki, J.G., Rivard, M.J., Marsh, D.L., 1997. Development of high-activity ^{252}Cf sources for neutron brachytherapy. Appl. Radiat. Isot. 48 (10–12), 1567–1570.
- Martínez, S.A., Barquero, R., Gómez-Ros, J.M., Lallena, A.M., Andrés, C., Tortosa, R., 2010. Evaluation of neutron production in new accelerators for radiotherapy. Radiat. Meas. 45 (10), 1402–1405.
- Mason, T.E., Abernathy, D., Anderson, I., et al., 2006. The spallation neutron source in oak ridge: a powerful tool for materials research. Physics B 385–386, 955–960.
- Masuda, K., Yoshikawa, K., Ohishi, T., Ogawa, S., Zen, H., Takamatsu, T., 2006. Spatial distribution of D–D/D– ^3He advanced fuels fusion reactions in an inertial electrostatic confinement device. Proceedings of the 21st IAEA Conference on Fusion Energy, Chengdu, 16–21 October 2006. IAEA-CN-149, pp. 1–8. IC/P7–9.
- Materne, S., Picker, R., Altarev, I., Angerer, H., Franke, B., Gutmiedl, E., Hartmann, F.J., Müller, A.R., Paul, S., Stoepler, R., 2009. PENELOPE—on the way towards a new neutron lifetime experiment with magnetic storage of ultra-cold neutrons and proton extraction. Nucl. Instrum. Methods Phys. Res. Sect. A 611, 176–180.
- Mausner, L.F., Mirzadeh, S., Srivastava, S.C., 1992. Improved specific activity of reactor produced ^{117m}Sn with the Szilard–Chalmers process. Appl. Radiat. Isot. 43 (9), 1117–1122.
- Mavunda, R.D., Assiamah, M., Nam, T.L., Keddy, R.J., 2004. Bremsstrahlung spectra from diagnostic X-rays. Radiat. Phys. Chem. 71, 991–992.
- McGrath, J., Fulton, B.R., Joshi, P., Davies, P., Muenstermann, D., Schulz, O., Zuber, K., Freer, M., 2010. Detecting multi-hit events in a CdZnTe coplanar grid detector using pulse shape analysis: A method for improving background rejection in the COBRA $0\nu\beta\beta$ experiment. Nucl. Instrum. Methods Phys. Res. Sect. A 615, 57–61.
- McLane, V., Dunford, C.L., Rose, P.F., 1988. Neutron Cross Sections. In: Neutron Cross Section Curves, vol. 2. Academic Press, San Diego.
- McMillan, E., Abelson, P.H., 1940. Radioactive element 93. Phys. Rev. 57, 1185–1186.
- Mederski, H.J., 1961. Determination of internal water by beta gauging technique. Soil Sci. 92, 143–146.
- Mederski, H.J., Alles, W., 1968. Beta gauging leaf water status: influence of changing leaf characteristics. Plant Physiol. 43, 470–472.
- Mehta, K., Kojima, T., Sunaga, H., 2003. Applicability study on existing dosimetry systems to high-power bremsstrahlung irradiation. Radiat. Phys. Chem. 68, 959–962.
- Meitner, L., 1923. Das beta-strahlenspektrum von UX_1 und seine deutung. Z. Phys. 17, 54–66.
- Meitner, L., 1924. Über die Rolle der γ -strahlen beim atomzerfall. Z. Phys. 26, 169–177.
- Meitner, L., Frisch, O.R., 1939. Disintegration of uranium by neutrons: a new type of nuclear reaction. Nature 143, 239–240 (February 11, 1939).
- Meitner, L., Strassmann, F., Hahn, O., 1938. Künstliche erwandlungsprozesse bei bestahlung des thoriums mit neutronen; auftreten isomer reihen durch absaltung von α -Strahlen. Z. Phys. 109, 538–552.
- Melhorn, W., 1998. 70 years of Auger spectroscopy, a historical perspective. J. Electron Spect. Related Phenomena 93 (1), 1–15.
- Melhus, C.S., Rivard, M.J., 2006. Towards HDR ^{252}Cf brachytherapy: shielding assessment of a linear accelerator vault. Brachytherapy 5 (2), 83–84.
- Menn, W., Hof, M., Reimer, O., Simon, M., Davis, A.J., Labrador, A.W., Mewaldt, R.A., Schindler, S.M., Barbier, L.M., Christian, E.R., Krombel, K.E., et al., 2000. The absolute flux of protons and helium at the top of the atmosphere using IMAX. Astrophys. J. 533 (1), 281–297.
- Mercer, J.A., Hussein, E.M.A., Waller, E.J., 2007. A non-intrusive neutron device for in situ detection of petroleum contamination in soil. Nucl. Instrum. Methods Phys. Res. Sect. B 263, 217–220.
- Messier, M.D., 2006. Review of neutrino oscillation experiments. Flavor Phys. and CP Violation Conf. Vancouver 2002, hep-ex/0606013v1 5 Jun 2002.
- Michel, R., Brechbiel, M., Mattes, M., 2003. A comparison of 4 radionuclides conjugated to antibodies for single-cell kill. J. Nucl. Med. 44 (4), 632–640.
- Miley, G.H., Sved, J., 1997. The IEC – A plasma-target-based neutron source. Appl. Radiat. Isot. 48 (10–12), 1557–1561.
- Miley, G., Yang, Y., Webber, J., Shaban, Y., Momota, H., 2005. RF ion source-driven IEC design and operation. Fusion Sci. Techn. 47, 1233–1237.
- Miller, R.B., 2003. Food irradiation using bremsstrahlung X-rays. Radiat. Phys. Chem. 68, 963–974.
- Miller, R.B., 2005. Food Irradiation. Springer, Berlin, New York, London, p. 246.
- Mitchell, J.W., Barbier, L.M., Christian, E.R., Krizanec, J.F., Krombel, K., Ormes, J.F., Streitmatter, R.E., Labrador, A.W., Davis, A.J., Mewaldt, R.A., et al., 1996. Measurement of 0.25–3.2 GeV antiprotons in the cosmic radiation. Phys. Rev. Lett. 76 (17), 3057–3060.
- Moe, M.K., 1986. Double-beta decay in ^{82}Se , ^{128}Te , and ^{130}Te . AIP Conf. Proc. 150, 1012–1016.
- Moe, M.K., Rosen, S.P., 1989. Double-beta decay. Scient. Amer., 48–55 (November).
- Möller, P., Nix, J.R., Myers, W.D., Swiatecki, W.J., 1995. Nuclear ground-state masses and deformations. Atomic Data Nucl. Data Tables 59, 185–381.
- Morozov, V.A., Churin, I.N., Morozova, N.V., 1998. Nuclear experimental techniques – three-dimensional delayed coincidence single-crystal scintillation time spectrometer. Instrum. Exp. Tech. 41 (5), 609.
- Morozov, V.A., Morozova, N.V., Budica, T., Cata-Danil, Gh., Ghita, D., Popescu, I.V., 2006. Measurement of the half-life for two ^{57}Fe excited states by a single-crystal scintillation time spectrometer. Nucl. Instrum. Methods Phys. Res. Sect. A 566, 448–451.
- Morozov, V.A., Morozova, N.V., Narseev, Yu. V., Sereeter, Zh., Zlokazov, V.B., 2002. High-sensitivity delayed-coincidence spectrometer to search for short-lived nuclear states. Nucl. Instrum. Methods Phys. Res. Sect. A 484, 225–232.
- Moseley, H.G.J., 1913. The high frequency spectra of the elements. Philos. Mag. 26 (1), 1024–1034.
- Moseley, H.G.J., 1914. The high frequency spectra of the elements. Philos. Mag. 27 (2), 703–713.
- Moussavi-Zarandi, A., 2008. Determination of beryllium by use of photonuclear activation techniques. Appl. Radiat. Isot. 66, 158–161.
- Mozumber, A., Chatterjee, A., Magee, J.L., 1968. Theory of radiation chemistry, IX. Mode and structure of heavy particle tracks in water. Amer. Chem. Soc. Series Adv. in Chem. 1, 27.
- Mukoyama, T., Shimizu, S., 1974. The effect of pressure on orbital electron capture. Phys. Lett. 50A (4), 258–260.
- Müller, A.R., Altarev, I., Angerer, H., Gutmiedl, E., Hartmann, F.J., Materne, S., Paul, S., Picker, R., 2009. A low-temperature proton detector for a neutron lifetime experiment. Nucl. Instrum. Methods Phys. Res. Sect. A 611, 289–292.
- Munger, M.L., Peterson, R.J., 1978. Proton stripping reactions on ^{194}Pt , ^{196}Pt and ^{198}Pt . Nucl. Phys. A303, 199–216.
- Murin, A.N., Nefedov, V.D., 1955. Concentration of artificial radioactive isotopes of groups IV and V by method of recoil atoms. Primenenie Mechenykh Atomov v Anal. Khim., Akad. Nauk S.S.S.R., 75–78. UCRL Trans.
- Murray, R.L., 2009. Nuclear Energy. An Introduction to the Concepts, Systems, and Applications of Nuclear Processes, sixth ed. Elsevier Publishers, Amsterdam, p. 497.

- Nagano, M., Watson, A.A., 2000. Observations and implications of the ultra-high-energy cosmic rays. *Rev. Mod. Phys.* 72, 689–732.
- Nakahata, M., 2000. Neutrinos underground. *Science* 289 (5482), 1155–1156.
- Nakayama, F.S., Ehrler, W.L., 1964. Beta ray gauging technique for measuring leaf water content changes and moisture status of plants. *Plant Physiol.* 39, 95–98.
- Nambu, Y., 1966. A systematics of hadrons in subnuclear physics. In: de Shalit, A., Feshbach, H., Van Hove, L. (Eds.), *Preludes in Theoretical Physics*. North Holland, Amsterdam and John Wiley, New York, pp. 133–142.
- Nico, J.S., Dewey, M.S., Gilliam, D.M., Wielfeldt, F.E., Fei, X., Snow, W.M., Greene, G.L., Pauwels, J., Eykens, R., Lamberty, A., Van Gestel, J., Scott, R.D., 2005. Measurement of the neutron lifetime by counting trapped protons in a cold neutron beam. *Phys. Rev. C* 71 (5) 055502.
- Nielsen, D.R., Cassel, D.K., 1984. Soil water management. In: L'Annunziata, M.F., Legg, J.O. (Eds.), *Isotopes and Radiation in Agricultural Sciences*, vol. 1. Academic Press, San Diego, pp. 37–43.
- NIST, 2011. Stopping-Power and Range Tables for Electrons, Protons, and Helium Ions [Online]. National Institute of Standards and Technology, Gaithersburg, MD. <http://www.nist.gov/pml/data/star/index.cfm>.
- NNDC, 2010a. Q-value Calculator (QCalc). National Nuclear Data Center, Brookhaven National Laboratory. <http://www.nndc.bnl.gov/qcalc/>.
- NNDC, 2010b. Nuclear Decay Data (NuDat). National Nuclear Data Center, Brookhaven National Laboratory. Decay Radiation Data, NuDat 2.5. <http://www.nndc.bnl.gov/nudat2/>.
- Noborio, K., Yamamoto, Y., Ueno, Y., Konishi, S., 2006. Confinement of ions in an inertial electrostatic confinement fusion (IECF) device and its influence on neutron production rate. *Fusion Eng. Design* 81, 1701–1705.
- Northcliffe, L.C., 1963. Passage of heavy ions through matter. *Ann. Rev. Nucl. Sci.* 13, 67–102.
- NRL, 1998. The exposure of New Zealand aircrew to cosmic radiation. National Radiation Laboratory, Information Sheet 19, February 1998, p. 6, Christchurch, New Zealand.
- Obregewitsch, R.P., Rolston, D.E., Nielsen, D.R., Nakayama, F.S., 1975. Estimating relative leaf water content with a simple beta gauge calibration. *Agron. J.* 67, 729–732.
- Occhialini, G.P.S., Powell, C.F., 1947. Nuclear disintegrations produced by slow charged particles of small mass. *Nature* 159, 186–190.
- Occhialini, G.P.S., Powell, C.F., 1948. Observations on the production of mesons by cosmic radiation. *Nature* 162, 168–173.
- Ochiai, K., Sato, S., Wada, M., Kubota, N., Kondo, K., Yamauchi, M., Abe, Y., Nishitani, T., Konno, C., 2007. Thin slit streaming experiment for ITER by using D-T neutron source. *Fusion Eng. Design* 82, 2794–2798.
- Ogando, J., 1993. Nuclear web gauging keeps pace with processor needs. *Plastics Technol.* 39, 46–49.
- Ohm, H., Liang, M., Molnár, G., and Sistemich, K., 1990. Delayed-coincidence measurement of subnanosecond lifetimes in fission fragments. "The Spectroscopy of Heavy Nuclei 1989 Proceedings of the International Conference on the Spectroscopy of Heavy Nuclei, Agia Pelagia, Crete, June 25-July 1, 1989. Institute Physics Conference Series, No. 105, 323–328. Adam Hilger, Ltd., Bristol.
- Ohnishi, M., Osawa, H., Furukawa, T., Suma, T., 2007. Development of convergent D–D fusion neutron generator with large pulse current. *Fusion Sci. Technol.* 52, 1101–1104.
- O'Leary, G.J., Incerti, M., 1993. A field comparison of three neutron moisture meters. *Aust. J. Exp. Agric.* 33, 59–69.
- Olzem, J., Gast, H., Schael, S., 2007. Cosmic-ray positron identification through bremsstrahlung conversion. *Nucl. Phys. B (Proc. Suppl.)* 173, 51–55.
- Oms, J., 2004. Lifetime extraction from delayed-coincidence experiments by a direct deconvolution method. *Nucl. Instrum. Methods Phys. Res. Sect. A* 527, 598–603.
- O'Shaughnessy, C.M., Golub, R., Schelhammer, K.W., Swank, C.M., Seo, P.-N., Huffman, P.R., Dzhosyuk, S.N., Mattoni, C.E.H., Yang, L., Doyle, J.M., Coakley, K.J., Thompson, A.K., Mumm, H.P., Lamoreaux, S.K., McKinsey, D.N., Yang, G., 2009. Measuring the neutron lifetime using magnetically trapped neutrons. *Nucl. Instrum. Methods Phys. Res. Sect. A* 611, 171–175.
- Ott, E.W., Weinheiner, C., 2008. Neutrino mass limit from tritium β decay. *Rep. Prog. Phys.* 71 (8), 6201.
- Paces, J.B., Ludwig, K.R., Peterman, Z.E., Neymark, L.A., 2002. $^{234}\text{U}/^{238}\text{U}$ evidence for local recharge and patterns of ground-water flow in the vicinity of Yucca Mountain, Nevada, USA. *Appl. Geochem.* 17, 751–779.
- Pachoa, A.S., Steinhäusler, F., 2010. Cosmic radiation, including its effects on airline crew, frequent flyers, and space travel, pp. 87–121. In: *Radioactivity in the Environment*, vol. 17. Elsevier, Amsterdam, p. 244.
- Park, Y.J., Song, B.C., Im, H.-J., Kim, J.-Y., 2009. Performance characteristics of a prompt gamma-ray activation analysis (PGAA) system equipped with a new compact D–D neutron generator. *Nucl. Instrum. Methods Phys. Res. Sect. A* 606, 243–247.
- Passo Jr., C.J., Cook, G.T., 1994. *Handbook of Environmental Liquid Scintillation Spectrometry. A Compilation of Theory and Methods*. Packard Instrument Company, Meriden, CT.
- Patil, B.J., Chavan, S.T., Pethe, S.N., Krishnan, R., Dhole, S.D., 2010a. Measurement of angular distribution of neutron flux for the 6 MeV race-track microtron based pulsed neutron source. *Appl. Radiat. Isot.* 68, 1743–1745.
- Patil, B.J., Chavan, S.T., Pethe, S.N., Krishnan, R., Bhoraskar, V.N., Dhole, S.D., 2010b. Simulation of e– γ –n targets by FLUKA and measurement of neutron flux at various angles for accelerator based neutron source. *An. Nucl. Energy* 37, 1369–1377.
- Paul, S., 2009. The puzzle of neutron lifetime. *Nucl. Instrum. Methods Phys. Res. Sect. A* 611, 157–166.
- Paul, W., Steinwedel, H., 1955. Interaction of electrons with matter. In: Siegbahn, K. (Ed.), *Beta- and Gamma-ray Spectroscopy*. North-Holland, Amsterdam.
- Pauli, W., 1924. Zur Frage der theoretischen deutung der satelliten einiger spektrallinien und ihrer beeinflussung durch magnetische felder. *Naturwiss.* 12, 741–743.
- Pauli, W., 1925. Über den zusammenhang des abschlusses der electronengruppen in atom der komplexstruktur der spectren. *Z. Phys.* 31, 765–783.
- Pauli, W., 1946. Exclusion principle and quantum mechanics. Nobel Lecture, December 13, 1946. In: Nobel Foundation Staff (Ed.), *Nobel Lectures, Physics, 1942–62*. Elsevier Publishing, Amsterdam (1964).
- Perlman, I., Ypsilantis, T.J., 1950. Consistency of nuclear radii of even-even nuclei from alpha-decay theory. *Phys. Rev.* 79, 30–34. http://prola.aps.org/abstract/PR/v79/i1/p30_1.
- Perlman, I., Ghiorso, A., Seaborg, G.T., 1950. Systematics of alpha radioactivity. *Phys. Rev.* 77 (1), 26–50.
- Petkov, P., Möller, O., Tonev, D., Dewald, A., von Brentano, P., 2003. Lifetime determination in delayed-coincidence experiments using the differential decay-curve approach. *Nucl. Instrum. Methods Phys. Res. Sect. A* 500, 379–385.
- Pichlmaier, A., Butterworth, J., Geltenbort, P., Nagel, H., Nesvizhevsky, V., Neumaier, S., Schreckenbach, K., Steichele, E., Varlamov, V., 2000. MAMBO II: neutron lifetime measurement with storage of ultra-cold neutrons. *Nucl. Instrum. Methods Phys. Res. Sect. A* 440, 517–521.
- Pickrell, J.A., 2009. Radiation and health effects, pp. 381–392. In: Gupta, R.C. (Ed.), "Handbook of Toxicology of Chemical Warfare Agents". Academic Press, p. 1168.
- Piefer, G.R., Santarius, J.F., Ashley, R.P., Kulcinski, G.L., 2005. Design of an ion source for ^3He fusion in a low pressure IEC device. *Fusion Sci. Technol.* 47, 1255–1259.
- Pierre Auger Collaboration, 2010. A study of the effect of molecular and aerosol conditions in the atmosphere on air fluorescence measurements at the Pierre Auger Observatory. *Astropart. Phys.* 33, 108–129.
- Planck, M., 1900. Zur theorie des gesetzes der energieverteilung im normal-spectrum. In: *Verhandlungen der Deutschen Physikalischen Gesellschaft im Jahre 1900*. Johann Ambrosius Barth, Leipzig, pp. 237–245. Jahrg. 2, Nr. 17.
- Pläß, W.R., Dickel, T., Czok, U., Geissel, H., Petrick, M., Reinheimer, K., Scheidenberger, C., Yavor, M.I., 2008. Isobar separation by time-of-flight mass spectrometry for low-energy radioactive ion beam facilities. *Nucl. Instrum. Methods Phys. Res. Sect. B* 266 (19–20), 4560–4564.
- Poenaru, D.N., Greiner, W., Depta, K., Ivascu, M., Mazilu, D., Sandulescu, A., 1986. Calculated half-lives and kinetic energies for spontaneous emission of heavy ions from nuclei. *Atomic Data Nuclear Data Tables* 34, 423–538.

- Poenaru, D.N., Ivascu, M., Sandulescu, A., Greiner, W., 1985. Atomic nuclei decay modes by spontaneous emission of heavy ions. *Phys. Rev. C* 32, 572–581.
- Potgieter, M.S., 2008a. Solar cycle variations and cosmic rays. *J. Atmosph. Solar-Terr. Phys.* 70, 207–218.
- Potgieter, M.S., 2008b. Challenges to cosmic ray modeling: From beyond the solar wind termination shock. *Adv. Space Res.* 41, 245–258.
- Potgieter, M.S., 2010. The dynamic heliosphere, solar activity, and cosmic rays. *Adv. Space Res.* 46, 402–412.
- Povinec, P.P., Vojtyla, P., Comanducci, J.-F., 2008. Monte Carlo simulation of background characteristics of gamma-ray spectrometers – a comparison with experiment. *Radioact. Environ.* 11, 163–208.
- Price, P.B., 1989. Heavy particle radioactivity. *Ann. Rev. Nucl. Part. Sci.* 39, 19–42.
- Price, P.B., 1994. Recent advances in cluster radioactivities. In: Scheid, W., Sandulescu, A. (Eds.), *Frontier Topics in Nuclear Physics*. Plenum Press, New York, p. 510.
- Rachinhas, P.J.B.M., Simões, P.C.P.S., Lopes, J.A.M., Dias, T.H.V.T., Morgado, R.E., dos Santos, J.M.F., Stauffer, A.D., Conde, C.A.N., 2000. Simulation and experimental results for the detection of conversion electrons with gas proportional scintillation counters. *Nucl. Instrum. Methods Phys. Res. Sect. A* 441, 468–478.
- Radchenko, V.M., Ryabinin, M.A., Andreytchuk, N.N., Gavrilov, V.D., Karelin, Ye. A., 2000. Curium-248 standard neutron source. *Appl. Radiat. Isot.* 53, 833–835.
- Radel, R.F., Kulcinski, G.I., Ashley, R.P., Santarius, J.F., Emmert, G.A., Piefer, G.R., Sorebo, J.H., Boris, D.R., Egle, B., Zenobia, S.J., Aklerson, E., Donovan, D.C., 2007. Detection of highly enriched uranium using a pulsed D–D fusion source. *Fusion Sci. Techn.* 52, 1087–1091.
- Raghaven, R.S., 1976. Inverse β decay of $^{115}\text{In} \rightarrow ^{115}\text{Sn}^+$: a new possibility for detecting solar neutrinos from the proton-proton reaction. *Phys. Rev. Lett.* 37, 259–262.
- Rahaman, S., Elomaa, V.-V., Eronen, T., Hakala, J., Jokinen, A., Julin, J., Kankainen, A., Saastamoinen, A., Suhonen, J., Weber, C., Åystö, J., 2008. Q values of the ^{76}Ge and ^{100}Mo double-beta decays. *Phys. Letters B* 662, 111–116.
- Rahmani, F., Shahriari, M., 2010. Hybrid hpononeutron source optimization for electron accelerator-based BNCT. *Nucl. Instrum. Methods Phys. Res. Sect. A* 618, 48–53.
- Rainwater, J., 1950. Nuclear energy level argument for a spheroidal nuclear model. *Phys. Rev.* 79, 432–434.
- Ray, A., Das, P., Saha, S.K., Das, S.K., Sethi, B., Mookerjee, A., Basu Chaudhuri, C., Pari, G., 1999. Observation of large change of ^7Be decay rate in Au and Al_2O_3 and its implications. *Phys. Lett. B* 455, 69–76.
- Ray, A., Das, P., Saha, S.K., Goswami, A., De, A., 2009. Observation of enhanced orbital electron-capture nuclear decay rate in a compact medium. *Phys. Lett. B* 679, 106–110.
- Reines, F., 1960. Neutrino interactions. *Ann. Rev. Nucl. Sci.* 10, 1–26.
- Reines, F., 1979. The early days of experimental neutrino physics. *Science* 203, 11–16.
- Reines, F., 1994. 40 years of neutrino physics. *Prog. Part. Nucl. Phys.* 32, 1–12.
- Reines, F., Cowen Jr., C.L., 1956. The neutrino. *Nature* 178, 446–449.
- Reines, F., Cowen Jr., C.L., 1957. Neutrino physics. *Phys. Today* 10 (8), 12–18.
- Rhodes, R., 1986. *The Making of the Atomic Bomb*. Touchstone/Simon & Schuster, New York, p. 886.
- Robson, J.M., 1950a. Radioactive decay of the neutron. *Phys. Rev.* 77, 747A.
- Robson, J.M., 1950b. Radioactive decay of the neutron. *Phys. Rev.* 78, 311–312.
- Roentgen, W.C., 1895. Über eine neue art von strahlen. *Sitzungsberichte der Würzburger Physik-medice Gesellschaft.* 9, 132–141.
- Roentgen, W.C., 1896. On a new kind of rays. *Nature* 53 (No. 1369), 274–276.
- Rohrlich, F., Carlson, B.C., 1954. Positron-electron differences in energy loss and multiple scattering. *Phys. Rev.* 93, 38–44.
- Ronen, Y., 1997. Systematic behaviour in cluster radioactivity. *Ann. Nucl. Energy* 24 (2), 161–164.
- Ronen, Y., 2004. Indications of the validity of the liquid drop model for spontaneous fission half-lives. *Ann. Nucl. Energy* 31, 323–329.
- Rose, H., Jones, G.A., 1984. A new kind of natural radioactivity. *Nature* 307, 245.
- Rossi, B., Hall, D.B., 1941. Variation of the rate of decay of mesotrons with momentum. *Phys. Rev.* 59, 223–228.
- Rowe, D.J., Wood, J.L., 2010. *Fundamentals of Nuclear Models*. World Scientific, Hackensack, NJ, p. 676.
- Roy, R.R., Reed, R.D., 1968. *Interactions of Photons and Leptons with Matter*. Academic Press, New York.
- Royer, G., 2008. On the coefficients of the liquid drop model mass formulae and nuclear radii. *Nucl. Phys. A* 807 (3–4), 105–118.
- Rutherford, E., 1899. Uranium radiation and the electrical conduction produced by it. *Phil. Mag* 47 (Ser. 5), 109–163.
- Rutherford, E., 1900. A radioactive substance emitted from thorium compounds. *Phil. Mag* 49 (Ser. 5), 1–14.
- Rutherford, E., 1903. The magnetic and electric deviation of the easily absorbed rays from radium. *Phil. Mag* 6 (Ser.), 177–187.
- Rutherford, E., 1906. Retardation of the alpha particle from radium in passing through matter. *Phil. Mag* 12 (Ser. 6), 134–146.
- Rutherford, E., 1908. The chemical nature of the alpha particles from radioactive substances. Nobel Lecture. In: *Nobel Lectures, Chemistry, 1901–1921 (1966)*. Elsevier Publishing, Amsterdam.
- Rutherford, E., 1911. The scattering of α and β particles by matter and the structure of the atom. *Phil. Mag* 21 (Ser. 6), 669–688.
- Rutherford, E., 1913. The structure of the atom. *Nature* 92 (No. 2302), 423.
- Rutherford, E., 1919. Collision of α -particles with light atoms. *Nature (London)* 103, 415–418.
- Rutherford, E., 1920a. Bakerian lecture: nuclear constitution of atoms. *Proc. Royal Soc. London* 97A, 374–401.
- Rutherford, E., 1920b. Nuclear constitution of atoms. *Proc. Royal Soc. London* 97A, 374–401.
- Rutherford, E., 1927. Structure of the radioactive atom and origin of the alpha rays. *Phil. Mag.* 4 (22), 580–605.
- Rutherford, E., 1929. Annual address to the royal society. *Proc. Royal Soc. London* 122A, 1–23.
- Rutherford, E., 1936. The development of the theory of atomic structure. In: Needham, J., Pagel, W. (Eds.), *Background to Modern Science*. Macmillan Company, New York, pp. 61–74.
- Rutherford, E., Soddy, F., 1902. The cause and nature of radioactivity. *Phil. Mag.* 4, 370–396.
- Samec, K., Milenković, S., Dementjevs, S., Ashrafi-Nik, M., Kalt, A., 2009. Design of a compact high-power neutron source—the EURISOL converter target. *Nucl. Instrum. Methods Phys. Res. Sect. A* 606, 281–290.
- Samios, N.P., Plano, R., Prodel, A., Schwartz, M., Steinberger, J., 1962. Parity of the neutral pion and the decay $\pi^0 \rightarrow 2e^+ + 2e^-$. *Phys. Rev.* 126, 1844–1849. http://prola.aps.org/abstract/PR/v126/i5/p1844_1.
- Sandulescu, A., Greiner, W., 1977. Mass asymmetry in fission, fusion and mass transfer due to the fragmentation in valleys. *J. Physics G* 3 (8), L189.
- Sandulescu, A., Poenaru, D.N., Greiner, W., Hamilton, J.H., 1985. Comment on “exotic nuclear decay of ^{223}Ra by emission of ^{14}C nuclei”. *Phys. Rev. Lett.* 54, 490.
- Santhosh, K.P., Biju, R.K., Sahadevan, S., 2010. Cluster formation probability in the trans-tin and trans-lead nuclei. *Nucl. Phys. A* 838, 38–49.
- Sanuki, T., Motoki, M., Matsumoto, H., Seo, E.S., Wang, J.Z., Abe, K., Anraku, K., Asaoka, Y., Fujikawa, M., Imori, M., 2000. Precise measurement of cosmic-ray proton and helium spectra with the BESS spectrometer. *Astrophys. J.* 545 (2), 1135–1142.
- Scherini, V., 2011. Search for ultra-high energy photons with the Pierre Auger Observatory. *Nucl. Instrum. Methods Phys. Res. Sect. A*, 630 (1), 226–229.
- Schrödinger, E., 1926a. Quantisierung als eigenwertproblem I. *Annalen der Physik* 79 (4), 361–376.
- Schrödinger, E., 1926b. Quantisierung als eigenwertproblem II. *Annalen der Physik* 79 (6), 489–527.
- Schrödinger, E., 1926c. Über das verhältnis der Heisenberg-Born-Jordan’schen quantenmechanik zu der meinen. *Annalen der Physik* 79 (8), 734–756.
- Schrödinger, E., 1926d. Quantisierung als eigenwertproblem III. *Annalen der Physik* 80 (13), 437–490.
- Schrödinger, E., 1926e. Quantisierung als eigenwertproblem IV. *Annalen der Physik* 81 (18), 109–143.
- Schwarzschild, A., 1963. A survey of the latest developments in delayed coincidence measurements. *Nucl. Instrum. Methods* 21, 1–16.

- Seaborg, G.T., 1937. The interaction of fast neutrons with lead. PhD Dissertation, Chemistry, University of California, Berkeley.
- Seaborg, G.T., 1951. The transuranium elements: present status. In: Nobel Lectures, (1964) Chemistry 1942–1962. Elsevier Publishing Company, Amsterdam.
- Seaborg, G.T., 1995. Transuranium elements: the synthetic actinides. *Radiachim. Acta* 70/71, 69–90.
- Seaborg, G.T., McMillan, E.M., Kennedy, J.W., Wahl, A.C., 1946a. Radioactive element 94 from deuterons on uranium. *Phys. Rev.* 69, 366–367 (submitted January 28, 1941).
- Seaborg, G.T., Wahl, A.C., Kennedy, J.W., 1946b. Radioactive element 94 from deuterons on uranium. *Phys. Rev.* 69, 367 (submitted March 7, 1941).
- Segré, E., 1947. Possibility of altering the decay rate of a radioactive substance. *Phys. Rev.* 71, 274–275.
- Segré, E., 1968. *Nuclei and Particles*. W. A. Benjamin, New York.
- Sekine, T., Kimura, K., Yoshihara, K., 1986. Application of nuclear recoil to radioisotope enrichment of copper-64. *J. Nucl. Sci. Technol.* 23 (12), 1064–1068.
- Seltzer, S.M., Berger, M.J., 1982a. Evaluation of the collision stopping power of elements and compounds for electrons and positrons. *Int. J. Appl. Radiat. Isot.* 33, 1189–1218.
- Seltzer, S.M., Berger, M.J., 1982b. Procedure for calculating the radiation stopping power for electrons. *Int. J. Appl. Radiat. Isot.* 33, 1219–1226.
- Seltzer, S.M., Berger, M.J., 1984. Improved procedure for calculating the collision stopping power of elements and compounds for electrons and positrons. *Int. J. Appl. Radiat. Isot.* 35 (7), 665–676.
- Selwyn, R.G., Nickless, R.J., Thomadsen, B.R., DeWerd, L.A., Micka, J.A., 2007. A new internal pair production ratio of ^{90}Y : the development of a non-destructive assay for ^{90}Y and ^{90}Sr . *Appl. Radiat. Isot.* 65, 318–327.
- Serebrov, A., Varlamov, V., Kharitonov, A., Fomin, A., Pokotilovski, Y., Geltenbrot, P., Butterworth, J., Krasnoschekova, I., Lasakov, M., Tal'daev, R., Vassiljev, A., Zherebtsov, O., 2005. Measurement of the neutron lifetime using a gravitational trap and a low-temperature Fomblin coating. *Phys. Lett. B* 605, 72–78.
- Serway, R.A., Moses, C.J., Moyer, C.A., 2005. *Modern Physics*, third ed. Brooks/Cole – Thomson, Belmont, CA, p. 600.
- Shanmugam, G., Kamalaharan, B., 1988. Application of a cubic barrier in exotic-decay studies. *Phys. Rev. C* 38, 1377–1381.
- Sharma, S.K., Jakhar, S., Shukla, R., Shyam, A., and Rao, C.V.S., 2010. Explosive detection system using pulsed 14 MeV neutron source. *Fusion Eng. Design*, 85 (7–9), 1562–1564.
- Shelfield, J., 2001. The future of fusion. *Nucl. Instrum. Methods Phys. Res. Sect. A* 464, 33–37.
- Shi, Y.J., Swiatecki, W.J., 1985. Estimate of radioactive decay by the emission of nuclei heavier than α -particles. *Nucl. Phys. A* 438, 450–460.
- Shu, W.M., Matsuyama, M., Suzuki, T., Nishi, M.F., 2004. Characteristics of a promising tritium process monitor detecting bremsstrahlung X-rays. *Nucl. Instrum. Methods Phys. Res. Sect. A* 521, 423–429.
- Shu, W.M., Matsuyama, M., Suzuki, T., Nishi, M.F., 2006. Monitoring of tritium in diluted gases by detecting bremsstrahlung X-rays. *Fusion Eng. Design* 81, 803–808.
- Sick, I., 1982. Precise nuclear radii from electron scattering. *Phys. Lett. B* 116 (4), 212–214.
- Sick, I., Trautmann, D., 1998. On the rms radius of the deuteron. *Nucl. Phys. A* 637 (4), 559–575.
- Šimković, F., 2010. Double beta decay: A problem of particle, nuclear and atomic physics. *Progress in Particle and Nucl. Phys.*, 64 (2), 219–227.
- Simpson, J.A., 1948. The latitude dependence of neutron densities in the atmosphere as a function of altitude. *Phys. Rev.* 73, 1389–1391.
- Simpson, J.A., 1951. Neutrons produced in the atmosphere by cosmic radiations. *Phys. Rev.* 83, 1175–1188.
- Simpson, J.A., 1983. Elemental and isotopic composition of the galactic cosmic rays. *Ann. Rev. Nucl. Part. Sci.* 33, 323–381.
- Simpson, J.A., 2001. The cosmic radiation. In: Bleeker, J.A.M., Geiss, J., Huber, M.C.E. (Eds.), *The Century of Space Science*, vol. 1. Kluwer Academic Publishers, Dordrecht, The Netherlands, pp. 117–151.
- Simpson, J.A., Fonger, W., Treiman, S.B., 1953. Cosmic ray intensity-time variations and their origin: neutron intensity variation method and meteorological factors. *Phys. Rev.* 90, 934–950. http://prola.aps.org/abstract/PR/v90/i5/p934_1.
- Singh, B., Batra, R.K., 1987. A method for calculating mass attenuation coefficients of beta particles. *Appl. Radiat. Isot.* 38 (12), 1027–1031.
- Skidmore, M.S., Ambrosi, R.M., O'Brien, R.C., 2009. Neutron sources for in-situ planetary science applications. *Nucl. Instrum. Methods Phys. Res. Sect. A* 608, 403–409.
- Slowinski, B., 2003. Spallation reactions and accelerator-driven systems. *Appl. Energy* 75, 129–136.
- Snell, A.H., Miller, L.C., 1948. On the radioactive decay of the neutron. *Phys. Rev.* 74, 1217–1218.
- Snell, A.H., Pleasonton, F., McCord, R.V., 1950. Radioactive decay of the neutron. *Phys. Rev.* 78, 310–311.
- Snow, W.M., Chowdhuri, Z., Dewey, M.S., Fei, X., Gilliam, D.M., Greene, G.L., Nico, J.S., Sørensen, H., Andersen, H.H., 1973. Stopping power of Al, Cu, Ag, Au, Pb, and U for 5–18 MeV protons and deuterons. *Phys. Rev. B* 8, 1854–1863.
- Snow, W.M., Chowdhuri, Z., Dewey, M.S., Fei, X., Gilliam, D.M., Greene, G.L., Nico, J.S., Wietfeldt, F.E., 2000. A measurement of the neutron lifetime by counting trapped protons. *Nucl. Instrum. Methods Phys. Res. Sect. A* 440, 528–534.
- Soddy, F., 1913a. Inter-atomic charge. *Nature* 92, 399–400.
- Soddy, F., 1913b. Radioactivity. *Chem. Soc. Annual Reports* 10, 262–288.
- Soddy, F. (1922). The origins of the conceptions of isotopes. Nobel Lecture, December 12, 1922. In “Nobel Lectures, Chemistry 1901–1921” (1966), Elsevier Publishing Co., Amsterdam.
- Spano, H., Kahn, M., 1952. Enrichment of tin activity through the Szilard-Chalmers separation. *J. Amer. Chem. Soc.* 74, 568–569.
- Spinks, J.W.T., Woods, R.J., 1990. *An Introduction to Radiation Chemistry*, third ed. John Wiley & Sons, Inc, New York.
- Stabin, M.G., 2009. “Radiation Protection and Dosimetry” An Introduction to Health Physics. Springer, New York, p. 396.
- Steinman, A.D., Mulholland, P.J., 2007. Phosphorus limitation, uptake, and turnover in Benthic stream algae, pp. 187–212. In: Hauer, F.R., Lamberti, G.A. (Eds.), *Methods in Stream Ecology*, second ed. Elsevier, Amsterdam, p. 877.
- Stone, J.O., Allan, G.L., Fifield, L.K., Cresswell, R.G., 1996. Cosmogenic chlorine-36 from calcium spallation. *Geochim. Cosmochim. Acta* 60 (4), 679–692.
- Strachan, J.D., Adler, H., Barnes, C.W., Barnes, G., et al., 1994. Fusion power production from TFTR plasmas fueled with deuterium and tritium. *Phys. Rev. Lett.* 72, 3526–3529.
- Strömholm, D., Svedberg, T., 1909a. Untersuchungen über die chemie der radioactiven grundstoffe. I. *Z. Anorg. Chem.* 61, 338–346.
- Strömholm, D., Svedberg, T., 1909b. Untersuchungen über die chemie der radioactiven grundstoffe. II. *Z. Anorg. Chem.* 63, 197–206.
- Stuewer, R.H., 1997. Gamow, alpha decay, and the liquid-drop model of the nucleus, pp. 30–43. In: Harper, E., Parke, W.C., David Anderson (Eds.), *George Gamow Symposium*, vol. 129. Astronomical Society of the Pacific, San Francisco ASP Conference Series.
- Sundaesan, M.K., 2001. *Handbook of Particle Physics*. CRC Press, Boca Raton, FL, p. 446.
- Suzuki, T., Kanungo, R., Bochkarev, O., Chulkov, L., Cortina, D., et al., 1999 (numerous authors). Nuclear radii of $^{17,19}\text{B}$ and ^{14}Be . *Nucl. Phys. A* 658 (4), 313–326.
- Szilard, L., Chalmers, T.A., 1934a. Chemical separation of the radioactive element from its bombarded isotope in the fermi effect. *Nature* 134, 462.
- Szilard, L., Chalmers, T.A., 1934b. Detection of neutrons liberated from beryllium by gamma rays: a new technique for inducing radioactivity. *Nature* 134, 494–495.
- Szilard, L., Chalmers, T.A., 1935. Radioactivity induced by neutrons. *Nature* 135, 98.
- Szucs, Z., van Rooyen, J., Zeevaert, J.R., 2009. Recoil effect on β -decaying in vivo generators, interpreted for $^{103}\text{Pd}/^{103m}\text{Rh}$. *Appl. Radiat. Isot.* 67, 1401–1404.
- Tait, W.H., 1980. *Radiation Detection*. Butterworths, London.
- Takahashi, Y., Misawa, T., Masuda, K., Yoshikawa, K., Takamatsu, T., Yamauchi, K., Yagi, T., Pyeon, C.H., Shiroya, S., 2010. Development of landmine detection system based on the measurement of radiation from landmines. *Appl. Radiat. Isot.*, 68 (12), 2327–2334.
- Takamatsu, T., Masuda, K., Kyunai, T., Tokui, H., Yoshikawa, K., 2006. Inertial electrostatic fusion device with an ion source using a magnetron discharge. *Nucl. Fusion* 46, 142–148.

- Tanaka, H., Sakurai, Y., Suzuki, M., Masunaga, S., Kinashi, Y., Kashino, G., Liu, Y., Mitsumoto, T., Yajima, S., Tsutsui, H., Maruhashi, A., Ono, K., 2009a. Characteristics comparison between a cyclotron-based neutron source and KUR-HWNIF for boron neutron capture therapy. *Nucl. Instrum. Methods Phys. Res. Sect. B* 267, 1970–1977.
- Tanaka, H., Sakurai, Y., Suzuki, M., Takata, T., Masunaga, S., Kinashi, Y., Kashino, G., Liu, Y., Mitsumoto, T., Yajima, S., Tsutsui, H., Takada, M., Maruhashi, A., Ono, K., 2009b. Improvement of dose distribution in phantom by using epithermal neutron source based on the $\text{Be}(p,n)$ reaction using a 30 MeV proton cyclotron accelerator. *Appl. Radiat. Isot.* 67, S258–S261.
- Tanihata, I., Hamagaki, H., Hashimoto, O., Nagamiya, S., Shida, Y., Yoshikawa, N., Yamakawa, O., Sugimoto, K., Kobayashi, T., Greiner, D.E., Takahashi, N., Nojiri, Y., 1985. Measurement of interaction cross sections and radii of He isotopes. *Phys. Lett. B* 160 (6), 380–384.
- Taylor, L.S., Tubiana, M., Wyckoff, H.O., Allisy, A., Boag, J.W., Chamberlain, R.H., Cowan, E.P., Ellis, F., Fowler, J.F., Fränzl, H., et al., 1970. Linear Energy Transfer. ICRU Report 16. International Commission on Radiation Units and Measurements, Washington, D.C.
- Thisgaard, H., Jensen, M., 2009. Production of the Auger emitter ^{119}Sb for targeted radionuclide therapy using a small PET-cyclotron. *Appl. Radiat. Isot.* 67, 34–38.
- Thompson, K.A., 2004. Relativity, special. In: Meyers, R.A. (Ed.), *Encyclopedia of Physical Science and Technology*, third ed. Elsevier, Amsterdam, pp. 117–141.
- Thomsen, K., 2007. A compound target concept for pulsed spallation sources. *Nucl. Instrum. Meth. Phys. Res. A* 580, 1597–1599.
- Thomson, J.J., 1897. Cathode rays. *Philos. Mag.* 44, 293–316.
- Titus, K.J., Clapp, T.G., Zhu, Z., 1997. A preliminary investigation of a beta-particle transmission gauge for seam quality determination. *Textile Res. J.* 67, 23–24.
- Tolhoek, H.A., Brussaard, P.J., 1954. On the theory of alpha disintegration and the determination of nuclear radii. *Physica* 21 (1–5), 449–470.
- Tomar, B.S., Steinebach, O.M., Terpstra, B.E., Bode, P., Wolterbeek Th. H., 2010. Studies on production of high specific activity ^{99}Mo and $^{99\text{m}}\text{Tc}$ by Szilard Chalmers reaction. *Radiochim. Acta* 98, 499–506.
- Tomaschitz, R., 2004. Cosmic rime dilation: the clock paradox revisited. *Chaos Solutions Fractals* 20, 713–717.
- Tomiyasu, K., Yokoyama, K., Watanabe, M., Hotta, E., 2010. Particle-in-cell simulation of magnetic-assisted electrostatic confinement device. *Fusion Eng. Design* 85 (5), 728–733.
- Tossell, J.A., 2002. Does the calculated decay constant for ^7Be vary significantly with chemical form and/or applied pressure? *Earth Planetary Sci. Lett.* 195, 131–139.
- Tracz, G., Drozdowicz, K., Gabańska, B., Krynicka, E., 2009. Pulsed thermal neutron source at the fast neutron generator. *Appl. Radiat. Isot.* 67, 1148–1155.
- Tsoufanidis, N., 1995. *Measurement and Detection of Radiation*, second ed. Taylor and Francis, Washington, DC.
- Tsybin, A.S., 1997. New physical possibilities in compact neutron sources. *Appl. Radiat. Isot.* 48 (10–12), 1577–1583.
- Tueros, M., Sciutto, S., 2010. TIERRAS: A package to simulate high energy cosmic ray showers underground, underwater and under-ice. *Comp. Phys. Commun.* 181, 380–392.
- Tumul'kan, A.D., 1991. Typical calibration curves for beta thickness gauges. *Measurement Techniques* 34 (1), 24.
- Turner, J.E., 1995. *Atoms, Radiation and Radiation Protection*, second ed. John Wiley & Sons, New York.
- U.S. Public Health Service, 1970. *Radiological Health Handbook*, Publ. No. 2016. Bureau of Radiological Health, Rockville, MD.
- Vajda, N., Kim, C.-K., 2010. Determination of radiostrontium isotopes: a review of analytical methodology. *Appl. Radiat. Isot.* 68, 2306–2326.
- Van Elteren, J.T., Kroon, K.J., Woroniecka, U.D., De Goij, J.J.M., 1999. Voltammetry detection of copper in high specific activity ^{64}Cu . *Appl. Radiat. Isot.* 51, 15–19.
- Van Rooyen, J., Szuics, Z., Zeevaert, J.R., 2008. A possible in vivo generator $^{100}\text{Pd}/^{103\text{m}}\text{Rh}$ — Recoil considerations. *Appl. Radiat. Isot.* 66, 1346–1349.
- Vandendael, I., 2010. *Use of Auger Electron Spectroscopy to Study an Industrial Process*. Lambert Academic Publishing, p. 228.
- Villard, P., 1900a. Sur la réflexion et la refraction des rayons cathodiques et des rayons déviables du radium. *Compt. Rendus Acad. Sci., Paris* 130, 1010–1012.
- Villard, P., 1900b. Sur le rayonnement du radium. *Compt. Rendus Acad. Sci., Paris* 130, 1178–1179.
- Villard, P., 1900c. Rayonnement du radium. *Séances de la Société Française de Physique*, 45–46.
- Vogel, P., 1967. On the nuclear octupole deformation in the $218 \leq A \leq 232$ region. *Phys. Letts. B* 25 (2), 65–67.
- Vogel, P., 1968. On nuclear octupole deformations. *Nucl. Phys. A* 112 (3), 583–593.
- Volkerts, M., Bacelar, J.C.S., van Goethem, M.J., Harakeh, M.N., Hoefman, M., Huisman, H., Kalantar-Nayestanaki, N., Löhner, H., Messchendorp, J.G., Ostendorf, R.W., Schadmand, S., Simon, R.S., Wagner, V., Wilschut, H.W., 2001. Proton-deuteron bremsstrahlung at 190 MeV. *Nucl. Phys. A* 684, 510e–512e.
- von Weizsäcker, C.F., 1935. Zur theorie der kernmassen. *Zeit. Physik.* 96, 431–458.
- Walstrom, P.L., Bowman, J.D., Penttilä, S.I., Morris, C., Saunders, A., 2009. A magneto-gravitational trap for absolute measurement of the ultra-cold neutron lifetime. *Nucl. Instrum. Methods Phys. Res. Sect. A* 599, 82–92.
- Walter, U., 2006. Relativistic rocket and space flight. *Acta Astronaut.* 59, 453–461.
- Wang, C., Martin, R., Fontanesi, J., Joiner, M., Martinez, A.A., Ebling, R., 2008. Development of a new Cf-252 source for remote afterloading neutron brachytherapy: Implications and applications. *Brachytherapy* 7 (2), 161–162.
- Wapstra, A.H., Audi, G., Thibault, C., 2003. The AME2003 atomic mass evaluation (I). Evaluation of input data, adjustment procedures. *Nucl. Phys. A* 729, 129–336.
- Webber, W.R., Potgieter, M.S., 1989. The artificial production of nuclear gamma-radiation. *Astrophys. J.* 344, 779.
- Westmoreland, S., 2010. A note on relativistic rocketry. *Acta Astronaut.* 67, 1248–1251.
- Wilkinson, D.H., 2007. Super-allowed Fermi beta-decay: the neutron lifetime; GA/GV. *Nucl. Instrum. Methods Phys. Res. Sect. A* 574, 1–2.
- Woan, G., 2000. *The Cambridge Handbook of Physics Formulas*. Cambridge University Press, Cambridge, p. 219.
- Wüstling, S., Armbrust, T., Steidl, M., Zadorozhny, S., 2006. A large, 64-pixel PIN-diode detector for low-energy beta-electrons. *Nucl. Instrum. Methods Phys. Res. Sect. A* 568, 382–387.
- Yamauchi, K., Ohura, S., Watanabe, M., Okino, A., Kohno, T., Hotta, E., Yuura, M., 2006. Performance of neutron/proton source based on ion-source-assisted cylindrical radially convergent beam fusion. *IEEJ Trans.-Fund. Mat.* 126, 1177–1182.
- Yang, Y., Li, Y., Wang, H., Li, T., Wu, B., 2007. Explosives detection using photoneutrons produced by X-rays. *Nucl. Instrum. Methods Phys. Res. Sect. A* 579, 400–403.
- Yi, C.Y., Han, H.S., Jun, J.S., Chai, H.S., 1999. Mass attenuation coefficients of β^- -particles. *Appl. Radiat. Isot.* 51, 217–227.
- Yoshikawa, K., Masuda, K., Takamatsu, T., Hotta, E., Yamauchi, K., Shiroya, S., Misawa, T., Takahashi, Y., Ohnishi, M., Osawa, H., 2007b. Research and development on humanitarian landmine detection system by use of a compact D–D fusion neutron source. *Fusion Sci. Technol.* 52, 1092–1095.
- Yoshikawa, K., Masuda, K., Takamatsu, T., Shiroya, S., Misawa, T., Hotta, E., Ohnishi, M., Yamauchi, K., Osawa, H., Takahashi, Y., 2007a. Research and development of a compact discharge-driven D–D fusion neutron source for explosive detection. *Nucl. Instrum. Methods Phys. Res. Sect. B* 261, 299–302.
- Yoshiyuki, S., Hiroshi, T., 1999. Development of a small-sized painting thickness gauge based on a beta-ray transmission technique. *Radioisotopes* 48 (3), 163–171.
- Yukawa, H., 1935. On the interaction of elementary particles. I. *Proc. Phys.-Math. Soc. Japan* 17, 48–57.
- Yukawa, H., 1949. Meson theory in its developments. Nobel Lecture, December 12, 1949. In: *Nobel Foundation Staff (Ed.), Nobel Lectures, Physics, 1942–62. (1964) Elsevier Publishing, Amsterdam.*
- Zahn, U., 1967a. A study of the recoil behavior of ^{56}Mn atoms in dilute solutions of manganese carbonyl compounds. *Radiochim. Acta* 7, 170–175.
- Zahn, U., 1967b. Recoil reactions in crystalline ^{56}Mn carbonyls. *Radiochim. Acta* 8, 177–178.

- Zamani, M., Fragopoulou, M., Stoulos, S., Krivopustov, M.I., Sosnin, A.N., Brandt, R., Westmeier, W., Manolopoulou, M., 2008. A spallation neutron source based on Pb target surrounded by U blanket. *Radiat. Meas.* 43, S151–S155.
- Zavrtanik, D., 2011. Results from the Pierre Auger Observatory. *Nucl. Instrum. Methods Phys. Res. Sect. A*, 630 (7) 166–170.
- Zeeman, P., 1897. The effect of magnetism on the nature of light emitted by a substance. *Nature* 55 (1424), 347.
- Zeisler, S.K., Weber, K., 1998. Szilard-Chalmers effect in holmium complexes. *J. Radioanal. Nucl. Chem.* 227, 105–109.
- Zhou, F., Xue, X., Kong, X., Yuan, S., Huang, H., Li, Y., 2010. Measurements of the $^{89}\text{Y}(n,\gamma)^{90\text{m}}\text{Y}$ cross-section in the neutron energy range of 13.5–14.6 MeV. *Nucl. Instrum. Methods Phys. Res. Sect. B* 268 (9), 1367–1369.
- Zinn, W.H., Szilard, L., 1939. Emission of neutrons by uranium. *Phys. Rev.* 56, 619–624.
- Zito, R.R., Schiferl, D., 1987. Electron capture decay in Jovian planets. *ICARUS* 72, 647–649.
- Zuber, K., 2003. Spectroscopy of low energy solar neutrinos using CdTe detectors. *Phys. Letts. B* 571, 148–154.
- Zweig, G., 1964. CERN Report No. 8419 TH 412 (unpublished), reprinted. In: Lichtenberg, D.B., Rosen, S.P. (Eds.), *Developments in the quark theory of hadrons*. Hadronic Press, Nonantum, MA (1980).

Radioactivity Counting Statistics

Agustín Grau Malonda

CIEMAT, Avda. Complutense 22, 28040, Madrid, Spain

Agustín Grau Carles

Instituto de Física Fundamental, (CSIC), Serrano 113b, 28006 Madrid, Spain

Chapter Outline

I. Introduction	163	1. Variance of a Population	173
II. Statistical Distributions	164	2. Variance of Two Populations	174
A. The Poisson Distribution	164	V. Regression	176
B. The Gaussian Distribution	165	A. Linear Regression	176
III. Analysis of a Sample of Results	167	1. Confidence Intervals and Hypothesis Testing	177
A. Best Estimate of the True Value	167	VI. Detection Limits	177
B. Best Estimate of Precision	168	A. Critical Levels	177
C. Error Propagation	168	B. Gamma-Spectra	179
D. Accuracy of the Mean Value	169	1. High-Resolution Gamma-Spectra	179
E. Combination of Measurements	170	2. Low-Resolution Gamma-Spectra	182
F. The Statement of the Results	171	VII. Metrology Applications	183
1. Combined Standard Uncertainty	171	A. Uncertainty Budget	183
2. Rules for Expressing Results	171	B. Uncertainty Calculation	184
IV. Statistical Inference	172	1. Uncertainty Transmission in Eqn (2.109)	184
A. Hypothesis Testing	172	2. Numerical Calculation of Uncertainty	186
B. Confidence Intervals	173	References	188
C. Statistical Inference	173	Relevant Statistical References Tables	189

I. INTRODUCTION

In the measurement process, the object to be observed is always affected by an undetermined interaction between the observer and the observed. As a result, the measured magnitudes are always reproduced with a certain inherent uncertainty caused by the instrument. This uncertainty in the measurements makes the use of error theory essential. When we measure radioactive substances, the situation becomes even more complicated, because the radioactivity decay is a random process. In radioactivity, counting two types of fluctuations are basically generated, one related to the activity of the sample, when the half-life of the radionuclide is short, and another caused by the random nature of radioactivity decay, which modifies the disintegration rates with time. Since the measurement of radioactivity involves values with different degrees of reliability

and validity, the principles of counting statistics must be applied (Larson, 1969, and Eadie et al. 1971).

In many types of measurement, such as mass, volume, time, length, etc., the measured quantity has a given value and only the measurement conditions introduce statistical variations. The situation is different, however, in radioactivity measurements. The radioactive decay process follows Poisson statistics, so a sample's activity value is not a specific value but a mean value that varies with time. If we measure the emission of a radioactive source, as shown in Table 2.1, repeated measures are not equal. But there is a clear condition: if the measuring equipment does not introduce a perturbation, the emission and measurement rates must follow the same statistical law, so their mean and variance rates are equal from a statistical perspective.

Example 2.8 represents a detailed analysis of the set of measurements shown in Table 2.1. We see that they are not

TABLE 2.1 Counting Rates of a Radioactive Sample

Measure	Counts
1	214
2	222
3	217
4	210
5	243
6	238

affected by the counter. Example 2.9 presents another case in which the counting rates are affected by the counter even though the differences between measurements are smaller.

II. STATISTICAL DISTRIBUTIONS

In this section, we shall study all basic characteristics of both the Poisson and the normal (or Gaussian) distributions, and their relation to radioactivity counting statistics. Although the Poisson distribution involves all processes of radioactivity decay, and therefore the detection of particles and radiation, the normal distribution is applied more often by far and is better known in the majority of cases. Since the application of the Poisson distribution to counting statistics may be tedious and time consuming, and considering that both distributions give identical results, when the total number of counts becomes large, our final objective will be the determination of some characteristic parameters, which will allow one to exchange the Poisson distribution by the normal one.

A. The Poisson Distribution

The Poisson distribution describes a random process for which the occurrence probability of a certain event is constant and small. This distribution not only concerns radioactivity counting statistics (Helstrom, 1968) or nuclear decay, but is also applied to evaluate, in a more or less approximate way, many other processes Garwood (1936), Grau Malonda (1999). Some examples of daily life that verify Poisson statistics are, for example, the number of phone calls received at a phone switchboard several minutes before noon, the number of annual strikes in a factory, the number of misprints on a book page, the number of times a piece of a machine fails in a given period of time, and the number of fatal traffic accidents each week in a city. Przyborowski and Wilenski (1935) present an application of Poisson law and construct rules to minimize the chance of errors in tests and samples.

In radioactivity decay four aspects are fulfilled: all radioactive nuclei have the same decay probability for a given time period, the decay process of one nucleus is not affected by the decay of other nuclei, the total number of nuclei and measurement time intervals are sufficiently large, and the nuclei half-life is long compared with the detection pulse. Therefore, the radioactivity decay is a random process, in which a discontinuous random variable is

defined as the number of times a decay event takes place in a continuous period of time t . Additionally, the probability of one decay event occurring in a time increment Δt must be asymptotically proportional to Δt , independently of the time value in the interval Δt and all previous decay events. Under these conditions, the Poisson distribution takes the form

$$P_x(t) = \frac{e^{-at}(at)^x}{x!} \quad x = 0, 1, 2, \dots \quad (2.1)$$

where $P_x(t)$ is the probability that a number of x decay processes take place in time t and a is a constant to be determined. The expression (2.1) may be derived in three different ways: by approximation from the binomial distribution (Hoel, 1984 and Eadie et al. (1971)), considering first principles (Evans, 1972), or basing all calculations on a Markov process (Feller, 1968; Rozanov, 1977).

Three important properties derived from Eqn (2.1) are the following:

$$\sum_{x=0}^{\infty} P_x = 1 \quad (2.2)$$

$$\sum_{x=0}^{\infty} xP_x = at \quad (2.3)$$

$$\sum_{x=0}^{\infty} (x - at)^2 P_x = at \quad (2.4)$$

The normalization condition (2.2) states that the summation of all possible probabilities P_x of the Poisson distribution is one. The expression (2.3) defines the parameter a as the average value of the distribution divided by t , i.e., the number of decay processes per unit of time. The third expression (2.4) refers to the identity relation between the variance and the mean, when the Poisson distribution is applied. The most important consequence derived from the three properties (2.2) to (2.4) is that the single parameter a enables one to determine the first- and second-order moments (i.e., $\sum_{x=0}^{\infty} xP_x$ and $\sum_{x=0}^{\infty} x^2P_x$) of the Poisson distribution. By defining the average number of decay processes in time t as the product $\mu = at$, the Poisson distribution can be expressed as

$$P_x = \frac{e^{-\mu}\mu^x}{x!} \quad (2.5)$$

The Poisson distribution is asymmetric, and its shape depends on the parameter μ , which is a real value greater than zero.

Example 2.1 The measurement of a radioactive sample of ^{238}U ($T_{1/2} = 4.47 \times 10^9$ years) during three days gives a total number of counts 133,747. (a) Evaluate the average counting rate, and compute the probability of counting: (b) less than one count in one second, (c) exactly one count, (d) less than 3 counts, (e) a number of counts between 1 and 4, and (f) more than 3 counts.

a. The average counting rate is

$$\mu = \frac{133,747}{3 \times 24 \times 60 \times 60} = 0.516 \text{ counts/s}$$

- b. The probability of counting less than one count is computed as follows:

$$P(X < 1) = P_0 = e^{-0.516} = 0.597$$

- c. The probability of counting exactly one count:

$$P(X = 1) = \frac{\mu^1 e^{-\mu}}{1!} = 0.516 \times e^{-0.516} = 0.3$$

- d. The probability of counting less than 3 counts is the addition of the probabilities of counting none, one and 2 counts

$$\begin{aligned} P(X < 3) &= \sum_{x=0}^2 P_x = P_0 + P_1 + P_2 = e^{-\mu} + \mu e^{-\mu} + \frac{\mu^2}{2} e^{-\mu} \\ &= e^{-\mu} \left(1 + 0.516 + \frac{0.516^2}{2} \right) = 0.984 \end{aligned}$$

- e. The probability of counting a number of counts between 1 and 4 is the addition of the probabilities of counting exactly 2 and 3 counts

$$\begin{aligned} P(1 < X < 4) &= P_2 + P_3 = \frac{\mu^2 e^{-\mu}}{2!} + \frac{\mu^3 e^{-\mu}}{3!} \\ &= e^{-\mu} \left(\frac{\mu^2}{2!} + \frac{\mu^3}{3!} \right) \\ &= e^{-0.516} \left(\frac{0.516^2}{2} + \frac{0.516^3}{6} \right) = 0.093 \end{aligned}$$

- f. The probability of counting more than 3 counts is

$$\begin{aligned} P(X > 3) &= \sum_{x=4}^{\infty} P_x = 1 - \sum_{x=0}^3 P_x \\ &= 1 - (P_0 + P_1 + P_2 + P_3) \\ &= 1 - e^{-\mu} \left(1 + \mu + \frac{\mu^2}{2!} + \frac{\mu^3}{3!} \right) \\ &= 1 - e^{-0.516} \left(1 + 0.056 + \frac{0.516^2}{2} + \frac{0.516^3}{6} \right) \\ &= 0.00196 \end{aligned}$$

It should be remarked that a linear combination of the two random variables X and Y , which both follow the Poisson distribution, gives a third random variable, which does not necessarily follow the Poisson distribution. For the following three random variables $Y = aX$, $Z = Z + Y$, and $W = X - Y$, only Z follows the Poisson distribution.

B. The Gaussian Distribution

In general, it is assumed that the random variable X follows a normal distribution of mean m and variance σ^2 , when the probability density function of a set of measured values x yields the function

$$p(x) = \frac{1}{\sigma\sqrt{2\pi}} \exp \left[-\frac{(x-\mu)^2}{2\sigma^2} \right] \quad (2.6)$$

where $(-\infty < x < \infty)$, $(-\infty < \mu < \infty)$ and $(0 < \sigma^2 < \infty)$.

Frequently, in the course of a number of measurements, we are interested in evaluating the probability that a new measurement of the random variable X verifies a certain condition relative to the value x . This probability is computed in terms of the accumulated distribution function, which is defined as follows:

$$P(X \leq x) = \frac{1}{\sigma\sqrt{2\pi}} \int_{-\infty}^x \exp \left[-\frac{(t-\mu)^2}{2\sigma^2} \right] dt \quad (2.7)$$

Geometrically, the integral (2.7) is interpreted as the area under the curve between the limits of the interval $-\infty \leq X \leq x$. Since each pair of values (μ, σ^2) defines a different distribution, there is no simple way to tabulate the accumulated distribution function. This inconvenience is partially resolved by defining the normalized random variable Z

$$Z = \frac{X - \mu}{\sigma}, \quad (2.8)$$

for which the probability density and the accumulated distribution functions can be defined as follows:

$$p(z) = \frac{1}{\sqrt{2\pi}} \exp \left(-\frac{z^2}{2} \right) \quad (2.9)$$

$$P(Z \leq z) \equiv \Phi(z) = \frac{1}{\sqrt{2\pi}} \int_{-\infty}^z \exp \left(-\frac{t^2}{2} \right) dt \quad (2.10)$$

Although the tabulated values of the accumulated distribution function (2.10) are found in the majority of statistics manuals, the symmetric character of the distribution makes two different criteria of tabulation possible, which may cause confusion. For instance, Triola (2010) assumes the integration interval $0 \leq Z \leq z$, while Newbold (2009) and Abramowitz and Stegun (1972) consider $-\infty < Z \leq z$. These intervals are shown in Fig. 2.1. Since the normal distribution is normalized to one, both criteria of tabulation make the values simply differ in 0.5. Bevington (1969) defines the normalized random variable Z as the absolute value of the difference between the means $|X - \mu|$ divided by the standard deviation

$$Z = \frac{|X - \mu|}{\sigma}$$

The integration interval is $-\infty < Z < \infty$ and the values of $\Phi(Z)$ are two times the values for the interval $0 < Z < \infty$.

Example 2.2 By searching in Table 2.2, calculate the accumulated distribution function Φ for the following limits of the standard random variable Z : (a) $0 \leq Z \leq 1.75$, (b) $-1.75 \leq Z \leq 0$, (c) $Z \geq 1.85$, (d) $Z \leq 1.10$, and (e) $Z \leq -1.45$.

- a. The second column in Table 2.2 shows the accumulated distribution function Φ for the values of z listed in the first column. The remaining columns, from third to eleventh, list the intermediate values of Φ when z is incremented in 0.01.

FIGURE 2.1 Integration intervals corresponding to two different criteria for tabulation.

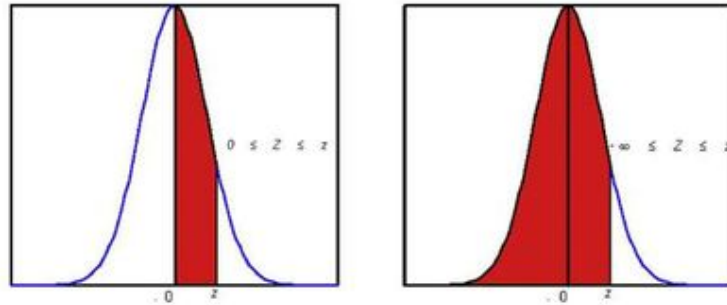
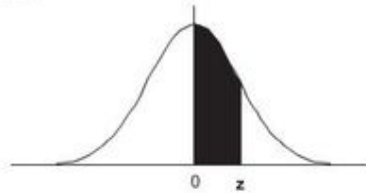


TABLE 2.2 The Standard Normal Distribution



z	0.00	0.01	0.02	0.03	0.04	0.05	0.06	0.07	0.08	0.09
0.0	0.0000	0.0040	0.0080	0.0120	0.0160	0.0199	0.0239	0.0279	0.0319	0.0359
0.1	0.0398	0.0438	0.0478	0.0517	0.0557	0.0596	0.0636	0.0675	0.0714	0.0753
0.2	0.0793	0.0832	0.0871	0.0910	0.0948	0.0987	0.1026	0.1064	0.1103	0.1141
0.3	0.1179	0.1217	0.1255	0.1293	0.1331	0.1368	0.1406	0.1443	0.1480	0.1517
0.4	0.1554	0.1591	0.1628	0.1664	0.1700	0.1736	0.1772	0.1808	0.1844	0.1879
0.5	0.1915	0.1950	0.1985	0.2019	0.2054	0.2088	0.2123	0.2157	0.2190	0.2224
0.6	0.2257	0.2291	0.2324	0.2357	0.2389	0.2422	0.2454	0.2486	0.2517	0.2549
0.7	0.2580	0.2611	0.2642	0.2673	0.2704	0.2734	0.2764	0.2794	0.2823	0.2852
0.8	0.2881	0.2910	0.2939	0.2967	0.2995	0.3023	0.3051	0.3078	0.3106	0.3133
0.9	0.3159	0.3186	0.3212	0.3238	0.3264	0.3289	0.3315	0.3340	0.3365	0.3389
1.0	0.3413	0.3438	0.3461	0.3485	0.5308	0.3531	0.3554	0.3577	0.3599	0.3621
1.1	0.3643	0.3665	0.3686	0.3708	0.3729	0.3749	0.3770	0.3790	0.3810	0.3830
1.2	0.3849	0.3869	0.3888	0.3907	0.3925	0.3944	0.3962	0.3980	0.3997	0.4015
1.3	0.4032	0.4049	0.4066	0.4082	0.4099	0.4115	0.4131	0.4147	0.4162	0.4177
1.4	0.4192	0.4207	0.4222	0.4236	0.4251	0.4265	0.4279	0.4292	0.4306	0.4319
1.5	0.4332	0.4345	0.4357	0.4370	0.4382	0.4394	0.4406	0.4418	0.4429	0.4441
1.6	0.4452	0.4463	0.4474	0.4484	0.4495	0.4505	0.4515	0.4525	0.4535	0.4545
1.7	0.4554	0.4564	0.4573	0.4582	0.4591	0.4599	0.4608	0.4616	0.4625	0.4633
1.8	0.4641	0.4649	0.4656	0.4664	0.4671	0.4678	0.4686	0.4693	0.4699	0.4706
1.9	0.4713	0.4719	0.4726	0.4732	0.4738	0.4744	0.4750	0.4756	0.4761	0.4767
2.0	0.4772	0.4778	0.4783	0.4788	0.4793	0.4798	0.4803	0.4808	0.4812	0.4817

Therefore, the sought value of $\Phi(1.75) = 0.4599$ is given in column seven.

- b. Taking into account the symmetry of the curve with respect to the origin, we have

$$\Phi(-1.75 \leq Z \leq 0) = \Phi(0 \leq Z \leq 1.75) = 0.4599$$

- c. Since the total area under the curve is 1, we obtain

$$P(Z \geq 1.85) = 0.5 - P(0 \leq Z \leq 1.85) = 0.5 - 0.4678 = 0.0322$$

- d. Since the area under the curve for the interval $-\infty < Z \leq 0$ is 0.5, we have

$$P(Z \leq 1.10) = 0.5 + P(0 \leq Z \leq 1.10) = 0.5 + 0.3643 = 0.8643$$

- e. By applying both the normalization and symmetry properties of the curve, we obtain

$$\begin{aligned} P(Z \leq -1.45) &= 0.5 - P(-1.45 \leq Z \leq 0) \\ &= 0.5 - P(0 \leq Z \leq 1.45) \\ &= 0.5 - 0.4265 = 0.0735 \end{aligned}$$

In practice, the random variable Z has no physical meaning. For this reason, the notation $N(\mu, \sigma^2)$ is adopted preferably in those statistical problems that apply the normal distribution. However, to perform calculations, the tabulated values of the standard normal distribution are still valid. The following examples make it clear how to manage Table 2.2, when the notation $N(\mu, \sigma^2)$ is adopted.

Example 2.3 Consider the random variable X that follows the normal distribution $N(16, 16)$. Compute the accumulated distribution probability $P(X \geq 17)$ from Table 2.2

The average and the standard deviation are $\mu = 16$ and $\sigma = 4$, respectively. The limits of the interval for the standard random variable Z are obtained from equation (2.8):

$$Z = \frac{X - \mu}{\sigma} = \frac{17 - 16}{4} = 0.25$$

Hence,

$$\begin{aligned} P(X \geq 17) &= P(Z \geq 0.25) = 0.5 - P(0 \leq Z \leq 0.25) \\ &= 0.5 - 0.0987 = 0.4013 \end{aligned}$$

Example 2.4 The normal distribution $N(20, 4)$ has the accumulated distribution probability 0.30 for $X \leq x_0$. Compute x_0 .

Since $P(Z \leq z_0) = 0.30 < 0.5$, z_0 must be negative. By making use of Table 2.2, we find $z_0 = -0.84$. Now, from equation (2.8), $-0.84 = (x_0 - 20)/2$. Thus, $x_0 = 20 - 1.68 = 18.32$.

In contrast to the Poisson distribution, the linear combination of the two random variables X and Y , which are characterized by the normal distribution, generates a new random variable $W = aX + bY$, which always follows the normal distribution. This important property clearly indicates how advantageous the

TABLE 2.3 Probability for Different Intervals

Interval	Probability
$\mu \pm 0.67\sigma$	0.50
$\mu \pm \sigma$	0.68
$\mu \pm 1.64\sigma$	0.90
$\mu \pm 2\sigma$	0.95
$\mu \pm 3\sigma$	0.997

application of the normal distribution compared to the Poisson distribution may be. For large average values of μ , the Poisson distribution is generally approximated to the normal distribution $N(\mu, \mu)$. In such a case, the accumulated distribution satisfies the equation

$$P(X \leq x) = e^{-\mu} \sum_{n=0}^x \frac{\mu^n}{n!} \approx \Phi\left(\frac{x + \frac{1}{2} - \mu}{\sqrt{\mu}}\right) \quad (2.11)$$

This approximation sets the standard deviation of the normal distribution equal to the standard deviation of the Poisson distribution, and yields results commonly denoted as $\mu \pm \sigma$, where $\sigma = \sqrt{\mu}$. Since the area under the curve for the interval $(\mu - \sigma, \mu + \sigma)$ is 68% of the total area, the probability that new measurements give results lying in the interval $(\mu - \sigma, \mu + \sigma)$ is 68%. Table 2.3 shows such a probability for different intervals.

III. ANALYSIS OF A SAMPLE OF RESULTS

Both the Poisson and normal distributions are applied to analyze the results of experiments with a large number of observed events. In practice, however, that is not the case, and the observed events in an experiment are frequently limited in number. All statistical information of one experiment is contained in the population distribution (or limit distribution). When a radioactive sample is analyzed, the amount of accumulated results depends on the counting rate and the measuring time, but what about the true value? This section will try to answer this and other questions relative to the analysis of a statistical sample of results.

A. Best Estimate of the True Value

For a symmetric distribution, the best estimate of the true value is given by the center of symmetry of the distribution. This center of symmetry is by definition the single value that agrees with its symmetrical position in the distribution. Since the mean, median, and mode all represent the center of symmetry of the distribution, nothing can be concluded about which one is the best to describe the true value.

For an asymmetric distribution, the mean, median, and mode take on different values. Therefore, the best estimate of the true value may be selected among these three possibilities by considering the requirements of the problem. Certain special

cases may lead one to choose the median or the mode as the best estimate, but the mean of the population distribution is the one preferred in the majority of situations.

Let us assume the average of a sample \bar{x} as the best estimate of the true value for a sample of results x_1, x_2, \dots, x_n that follow an unknown distribution

$$\bar{x} = \frac{1}{n} \sum_{i=1}^n x_i \quad (2.12)$$

Obviously, when the total number of measurements $n \rightarrow \infty$, the sample of results conforms to the population distribution, and the true value X agrees with the mean value of the distribution μ . Eisenhart (1963) analyzes the concepts of true value and uncertainty in measurement instruments.

B. Best Estimate of Precision

The analysis of the results of an experiment makes it necessary to define the concept of uncertainty. The width of the distribution shows graphically the uncertainty in symmetrical distributions. The two simplest expressions that represent the uncertainty are the absolute mean deviation τ and the standard deviation σ :

$$\tau = \int_{-\infty}^{\infty} |x - X| p(x) dx \quad (2.13)$$

$$\sigma^2 = \int_{-\infty}^{\infty} (x - X)^2 p(x) dx \quad (2.14)$$

where X is the true value of the distribution, commonly associated with the mean of the distribution.

To define the absolute average deviation, the absolute differences between x and the true value X are multiplied by the relative frequencies of x in the distribution, and integrated for all possible values of x . On the other hand, Eqn (2.14) squares the difference instead of taking the absolute value. In both cases, the result of integration is a positive number that becomes larger with the distribution width.

The difference between the terms error and uncertainty have been widely discussed in the literature (Burns et al., 1973; Campion et al., 1973; Rabinovich, 2005). An easy description of error theory is given in Beers (1957). The term error is generally applied to describe the difference between the measured and the true values, while the term uncertainty is related to the inaccuracy of the measurements, and is always accompanied with the corresponding confidence probability. The International Vocabulary (1993) defines uncertainty as 'an interval having a stated level of confidence'. We illustrate the difference between the two definitions with an example such that the error can be 1%, whereas the uncertainty is $\pm 1\%$ with a level of confidence of 95% (observe how the error can be +1% or -1%, but never $\pm 1\%$).

The simplest counting statistics is when we have only one counting result and we are interested in associating with it an uncertainty. This is possible because the radioactive emission follows Poisson statistics and, if the measurement does not

perturb the process, the standard deviation of the total counts is its square root.

When the counting statistics includes n measurements x_1, x_2, \dots, x_n , the sample variance is given by the expression

$$s_n^2 = \frac{1}{n-1} \sum_{i=1}^n (x_i - \bar{x})^2, \quad (2.15)$$

which coincides with the variance (2.14) for $n \rightarrow \infty$.

C. Error Propagation

In radioactivity counting statistics, the Poisson distribution gives the uncertainty in the total number of counts. Other related quantities, e.g., counting rate or the number of counts without background, are obtained by error propagation (Natrella, 2005; Nicholson 1966).

Suppose the triple measurement of one radioactive sample gives the three independent results x, y , and z for the total number of counts, then the respective standard deviations are $\sigma_x = \sqrt{x}, \sigma_y = \sqrt{y}, \sigma_z = \sqrt{z}$, and the standard deviation of a function of these three variables x, y , and z , when these are independent, is given by

$$\sigma_u^2 = \left(\frac{\partial u}{\partial x}\right)^2 \sigma_x^2 + \left(\frac{\partial u}{\partial y}\right)^2 \sigma_y^2 + \left(\frac{\partial u}{\partial z}\right)^2 \sigma_z^2 \quad (2.16)$$

On the other hand, when the three variables x, y , and z are correlated, we have

$$\begin{aligned} \sigma_u^2 = & \left(\frac{\partial u}{\partial x}\right)^2 \sigma_x^2 + \left(\frac{\partial u}{\partial y}\right)^2 \sigma_y^2 + \left(\frac{\partial u}{\partial z}\right)^2 \sigma_z^2 + 2\rho_{xy} \left(\frac{\partial u}{\partial x}\right) \left(\frac{\partial u}{\partial y}\right) \sigma_x \sigma_y \\ & + 2\rho_{yz} \left(\frac{\partial u}{\partial y}\right) \left(\frac{\partial u}{\partial z}\right) \sigma_y \sigma_z + 2\rho_{xz} \left(\frac{\partial u}{\partial x}\right) \left(\frac{\partial u}{\partial z}\right) \sigma_x \sigma_z \end{aligned} \quad (2.17)$$

where ρ_{xy}, ρ_{xz} , and ρ_{yz} , are the correlation coefficients for the variables xy, xz , and yz , respectively. These coefficients are defined by

$$\rho_{xy} = \frac{1}{(n-1)\sigma_x\sigma_y} \left(\sum_{i=1}^n x_i y_i - n\bar{X}\bar{Y} \right) \quad (2.18)$$

$$\rho_{xz} = \frac{1}{(n-1)\sigma_x\sigma_z} \left(\sum_{i=1}^n x_i z_i - n\bar{X}\bar{Z} \right) \quad (2.19)$$

$$\rho_{yz} = \frac{1}{(n-1)\sigma_y\sigma_z} \left(\sum_{i=1}^n y_i z_i - n\bar{Y}\bar{Z} \right) \quad (2.20)$$

The corresponding correlation coefficient for two independent variables is $\rho = 0$, while for two completely correlated variables it is given by $\rho = \pm 1$. Table 2.4 shows several common functions and their respective partial derivatives. To compute the standard deviations for the counting parameters listed in column 1 of Table 2.5, the application of the error propagation equations in Table 2.4 is required.

Example 2.5 Two students are discussing how to apply the error propagation equations of Table 2.4 on function $u = 2x$ to obtain the standard deviation. Student A considers the standard

TABLE 2.4 Error Propagation

Equation	Standard Deviation
$u = ax$	$\sigma_u = a\sigma_x$
$u = x \pm y$	$\sigma_u = \sqrt{\sigma_x^2 + \sigma_y^2}$
$u = a + bx + cy$	$\sigma_u = \sqrt{b^2\sigma_x^2 + c^2\sigma_y^2}$
$u = xy/z$	$(\sigma_u/u)^2 = (\sigma_x/x)^2 + (\sigma_y/y)^2 + (\sigma_z/z)^2$
$u = \log x$	$\sigma_u = \sigma_x/x$

deviation $\sigma_u = 2\sigma_x$ the best, while student B, after transforming the function into $u = x + x$, obtains the standard deviation $\sigma_u = \sqrt{2}\sigma_x$. Then a third student C joins the discussion arguing that the standard deviation is $\sigma_u = 2\sqrt{5}\sigma_x$ by transforming the function into $u = z - v$, where $z = 4x$ and $v = 2x$. Explain the discrepancies in the standard deviations obtained by the three students.

Only the standard deviation given by student A is correct. The assumption of student B is not valid, because the two terms into which the function u has been separated are correlated. Therefore, from (2.17) we have

$$\sigma_u^2 = \sigma_x^2 + \sigma_x^2 + 2\sigma_x\sigma_x = (\sigma_x + \sigma_x)^2 = 4\sigma_x^2$$

so

$$\sigma_u = 2\sigma_x$$

in agreement with the result given by student A. The argument of student C is also devoid of the correlation concept. To be correct, the standard deviation should be expressed as

$$\begin{aligned} \sigma_u^2 &= \sigma_z^2 + \sigma_v^2 - 2\sigma_z\sigma_v = 16\sigma_x^2 + 4\sigma_x^2 - 2 \times 4\sigma_x \times 2\sigma_x \\ &= (4\sigma_x - 2\sigma_x)^2 = 4\sigma_x^2 \end{aligned}$$

so

$$\sigma_u = 2\sigma_x$$

which also agrees with the result obtained by student A.

Error propagation is of great interest in planning experiments. Optimization of experiments allows one to reduce to a minimum the uncertainties of experimental results. A good example is the optimization in isotopic dilution as is shown by

Angoso et al. (1973). Optimization of the figure of merit to obtain the best compromise between sample and background counts can be seen in the papers of Loevinger and Berman (1951), Thomas (1950), Jaffey (1960), Reynolds (1964), Donn and Wolke (1976), and Wyld (1970).

D. Accuracy of the Mean Value

In the previous sections, the mean value m of a distribution of infinite events was taken as the best estimate of the true value X . In practice, however, the number of available measurements is finite, and frequently low. Since this number varies depending on the experiment, one question that immediately arises is: How can we approximate the mean value to the true value? In other words, how many measurements are necessary to obtain an accuracy better than a certain value?

The verification of one experiment by repeating the same sequence of measurements should provide similar average values X_n , and be in good agreement with the true value X , when the total number of measurements is large. The average value for a sequence of n independent measurements is given by

$$X_n = \frac{1}{n}(x_1 + x_2 + \dots + x_n) \tag{2.21}$$

By applying the error propagation theory to Eqn (2.21), the following standard deviation of the mean is obtained:

$$\sigma(X_n) = \left(\frac{\sigma^2(x_1)}{n^2} + \frac{\sigma^2(x_2)}{n^2} + \dots + \frac{\sigma^2(x_n)}{n^2} \right)^{1/2} \tag{2.22}$$

Since x_1, x_2, \dots, x_n come from measuring the same quantity, we have

$$\sigma^2(x_1) = \sigma^2(x_2) = \dots = \sigma^2(x_n) = \sigma^2(x) \tag{2.23}$$

thus

$$\sigma(X_n) = \frac{\sigma(x)}{\sqrt{n}} \tag{2.24}$$

By taking the average quadratic deviation (2.15) as the best estimate of the measurements, we obtain

$$S_n = \sigma(X_n) = \frac{(\sum_{i=1}^n (x_i - X)^2)^{1/2}}{\sqrt{n(n-1)}} = \frac{\sigma_n(x)}{\sqrt{n-1}} = \frac{s_n(x)}{\sqrt{n}} \tag{2.25}$$

TABLE 2.5 Application of Uncertainty Transmission to Different Counting Results

Result	Equation	Standard deviation
Counting rate	$b = C_B/t_B$	$\sigma(b) = \sigma(C_B)/t_B = \sqrt{C_B}/t_B$
Net gross counting	$C_S = C_{S+B} - C_B$	$\sigma(C_S) = \sqrt{\sigma^2(C_{S+B}) + \sigma^2(C_B)}$ $= \sqrt{C_{S+B} + C_B}$
Net counting rate	$c_S = C_{S+B}/t_{S+B} - C_B/t_B$	$\sigma(c_S) = \sqrt{\sigma^2(C_{S+B})/t_{S+B}^2 + \sigma^2(C_B)/t_B^2}$ $= \sqrt{C_{S+B}/t_{S+B}^2 + C_B/t_B^2}$
Channels ratio	$Q = N_A/N_B$	$(\sigma(Q)/Q)^2 = (\sigma(N_A)/N_A)^2 + (\sigma(N_B)/N_B)^2$ $= 1/N_A + 1/N_B$

which indicates the degree of accuracy of the mean value X_n . The standard deviation S_n in Eqn (2.25) is called the **standard error**, and gives the best estimate of the true value when written as

$$X = X_n \pm S_n \quad (2.26)$$

where S_n is a function of the total number of counts and measurements. The increment of the number of measurements makes the accuracy improve proportionally with the square root.

Frequently the best estimate of one experiment is computed from the mean values instead of directly from the measurements. Suppose X_n and Y_n are the corresponding mean values of two sets of n and m measurements, then the mean value of the new variable $z = x \pm y$ is $Z_{nm} = X_n \pm Y_m$, and its standard deviation is given by

$$\sigma(Z_{nm}) = \sqrt{\sigma^2(X_n) + \sigma^2(Y_m)} \quad (2.27)$$

so

$$S_{nm} = \sqrt{S_n^2 + S_m^2} = \sqrt{\frac{\sigma_n^2(x)}{n-1} + \frac{\sigma_m^2(x)}{m-1}} \quad (2.28)$$

E. Combination of Measurements

We are by now quite familiar with the computation of the uncertainty of nonmeasured quantities from the uncertainty of directly measured quantities by error propagation. However, how can we combine results from experiments in which we have applied different methods?

Suppose that the successive measurements carried on one radioactive sample give $X_n \pm S_n$ by applying one procedure and $X_m \pm S_m$ by applying another. If both methods were of similar precision, a good estimate of the true value could be

$$X_{n,m} = \frac{X_n + X_m}{2} \quad (2.29)$$

In practice, however, one procedure may be more precise than the other, and the best estimate of the true value is given by the weighted mean

$$X_{n,m} = \alpha X_n + (1 - \alpha) X_m \quad \text{where } 0 \leq \alpha \leq 1 \quad (2.30)$$

The numerical value of the weight α is computed from S_n and S_m . By applying error propagation to Eqn (2.30) we obtain the equation

$$S_{n,m}^2 = \alpha^2 S_n^2 + (1 - \alpha)^2 S_m^2 \quad (2.31)$$

The error function $S_{n,m}$ becomes minimum when the derivatives vanishes

$$\frac{dS_{n,m}^2}{d\alpha} = 2\alpha S_n^2 - 2(1 - \alpha) S_m^2 = 0 \quad (2.32)$$

That is, when

$$\alpha = \frac{S_n^{-2}}{S_n^{-2} + S_m^{-2}} \quad \text{and} \quad 1 - \alpha = \frac{S_m^{-2}}{S_n^{-2} + S_m^{-2}} \quad (2.33)$$

Hence, the best estimate of the true value will be given by

$$X_{n,m} = \frac{1}{S_n^{-2} + S_m^{-2}} \left(\frac{X_n}{S_n^2} + \frac{X_m}{S_m^2} \right) \quad (2.34)$$

and the standard deviation

$$S_{n,m}^2 = \frac{S_n^{-2} + S_m^{-2}}{(S_n^{-2} + S_m^{-2})^2} = \frac{S_n^2 S_m^2}{S_n^2 + S_m^2} \quad (2.35)$$

so

$$S_{n,m}^{-2} = S_n^{-2} + S_m^{-2} \quad (2.36)$$

The subsequent generalization of Eqns (2.34) and (2.36) to more than two procedures generates the following equations:

$$X_{n,m,p,\dots} = \frac{1}{S_n^{-2} + S_m^{-2} + S_p^{-2} + \dots} \left(\frac{X_n}{S_n^2} + \frac{X_m}{S_m^2} + \frac{X_p}{S_p^2} + \dots \right) \quad (2.37)$$

and

$$S_{n,m,p,\dots}^{-2} = S_n^{-2} + S_m^{-2} + S_p^{-2} + \dots \quad (2.38)$$

Frequently, these equations are written applying the following notation:

$$X = \sum_{n=1}^N \frac{x_n}{S_n^2} / \sum_{n=1}^N \frac{1}{S_n^2} \quad (2.39)$$

$$S_m^2(X) = 1 / \sum_{n=1}^N \frac{1}{S_n^2} \quad (2.40)$$

the subscript *in* denotes an inner type standard deviation. On the other hand, the subscript *out* is used for outer standard deviations that verify

$$S_{out}(X) = \left[\frac{\sum_{i=1}^N (x_i - X)^2 / S_i^2}{(N - 1) \sum_{i=1}^N 1 / S_i^2} \right]^{1/2} \quad (2.41)$$

Both types of standard deviation, S_{out} and S_{in} , are equal for samples taken from the same normal population. However, in many situations, the ratio S_{out}/S_{in} differs from unity, adopting the expression defined by Topping (1972):

$$Z = \frac{S_{out}}{S_{in}} = \left[\frac{\sum_{i=1}^N (x_i - X)^2 / \sigma_i^2}{N - 1} \right]^{1/2} \quad (2.42)$$

The observed data can only be considered consistent when the value of Z does not differ significantly from unity. In such a case, the best value for the error of the weighted average is given by the greatest of the two values S_{out} or S_{in} . On the other hand, when Z differs significantly from unity, the conclusion is that systematical errors are present in the measurements. This leads to weights that do not verify the Eqn (2.33), and depend more on other conditions such as the right performance of the experiment.

Example 2.6 The measurement of the energy emitted by one of the gamma-ray transitions of ^{60}Co was carried out by five different methods. The resulting energies and their respective uncertainties are shown in Table 2.6. Find the mean value and the inner and outer standard deviations. Also, compute the value of Z and analyze the consequences of its proximity to unity.

TABLE 2.6 Energy and Uncertainty of ⁶⁰Co Gamma Ray

E_γ [keV]	Uncertainty
1332.483	0.046
1332.560	0.050
1332.540	0.040
1332.509	0.015
1332.508	0.015

The computation of the weighted average gives

$$X = \frac{\sum_{n=1}^5 x_n/S_n^2}{\sum_{n=1}^5 1/S_n^2} = \frac{1.3840098 \times 10^7}{1.0386478 \times 10^4} = 1332.511 \text{ keV}$$

For the inner and outer type standard deviations we have

$$S_{in} = \frac{1}{\sqrt{\sum_{n=1}^5 1/S_n^2}} = \frac{1}{\sqrt{1.0386478 \times 10^4}} = 0.0098$$

and

$$S_{out} = \left[\frac{\sum_{n=1}^5 (x_n - X)^2/S_n^2}{(5 - 1) \sum_{n=1}^5 1/S_n^2} \right]^{1/2} = \left(\frac{1.914313}{4 \times 1.0386 \times 10^4} \right)^{1/2} = 0.0068$$

respectively.

For the value of Z we obtain

$$Z = \frac{\sigma_{out}}{\sigma_{in}} = \frac{0.0068}{0.0098} = 0.69$$

By applying the F -test in the way shown in Example 2.9, we conclude that we have no reasons to think of different standard deviations.

F. The Statement of the Results

The concept of uncertainty is commonly applied to evaluate the degree of feasibility in the results of one experiment. The uncertainty considers two limits to determine how the best estimate may deviate from the true value in terms of probability. The uncertainty of the results of a measurement is generally determined by several components, which may be grouped in two categories, according to the procedure used to determine the numerical values:

- Uncertainties evaluated following statistical procedures (type A evaluation).
- Uncertainties evaluated by means of other procedures (type B evaluation).

There is no correspondence between the classification of the uncertainty components in the two categories A and B and the usual classification into random and systematic errors. A detailed discussion on systematic uncertainties is given by Eisenhart (1963). The nature of an uncertainty is conditioned by the use of the corresponding quantity or, more clearly, the way in which the quantity appears in the model describing the

measuring process. When the corresponding quantity is used in different ways, the random component may be transformed into systematic or vice versa. Therefore, the terms accidental and systematic uncertainties may be misleading when they are used in practice. An alternative nomenclature sometimes used is:

"uncertainty component arising from a random effect"

"uncertainty component arising from a systematic effect"

In these statements, the random effect generates a possible random error in the process of measurement, while a systematic effect may generate a possible systematic error. A clear description of the different uncertainties involved in sample standardization is presented in the paper of Zimmerman et al. (2001).

Each uncertainty component, which contributes to the resultant uncertainty of a measurement by means of an estimated standard deviation, is referred to as the **standard uncertainty** and denoted by u_i . The u_i value is the positive square root of the estimated variance u_i^2 .

The uncertainty component of category A is represented by means of statistics: The estimated standard deviation s_i , which is equal to the positive value of the square root of the estimated variance s_i^2 and the number ν_i of the associated degrees of freedom. For this component, the standard uncertainty is $u_i = s_i$. The computation of the uncertainty by means of the statistical analysis of an observed set is referred to as **type A uncertainty** computation, which may be considered as an approximation to the corresponding standard deviation.

In a similar way the **type B uncertainty** component, denoted by u_j , may be considered as an approximation to the corresponding standard deviation. To understand the background of the statement of uncertainty, we refer to the paper of Müller (1979).

1. Combined Standard Uncertainty

The combined standard uncertainty, u_c , of a measurement is obtained from the individual standard uncertainties, obtained from type A and B evaluations. The rules given in the error transmission section will be applied here.

The combined standard uncertainty is used in the determination of fundamental constants, in fundamental metrology research and in comparisons.

On the other hand, for commercial, industrial, or regulatory applications, the required uncertainties must define an interval with a high probability that the result falls within it. In this case, it is convenient to introduce the concept of **expanded uncertainty**, U , obtained from multiplying u_c by a **coverage factor**, k , so that $U = ku_c$. Generally, the value of the coverage factor k is chosen so that we select a confidence level associated with the interval defined by $U = ku_c$. Two often used coverage factors, when the quantity is described by a normal distribution, are $k = 2$ and $k = 3$, which define intervals of confidence of 95.5% and 99.7%, respectively. Evaluation of precision and accuracy in instrument calibration systems is given by Eisenhart (1968).

2. Rules for Expressing Results

In this section, we follow the NIST recommendations given by Taylor and Kuyatt (1994); this guide is consistent with the

guidelines of the Guide to the Expression of Uncertainty in Measurement (GUM) (JCGM 100, 2008). The result of a measurement may be followed by the sign \pm and the corresponding uncertainty. The U value and the k factor or the applied u_c must always be specified. A complete uncertainty description for activity concentration for three measurement systems, liquid scintillation, ionization chambers, and $4\pi\gamma$ spectrometers, is presented in the work of Zimmerman et al. (2001). It is recommended that the following information be included:

A list of all the components of the standard uncertainty with the appropriate degrees of freedom and the resulting value u_c . The uncertainty components should be identified in agreement with the method used to estimate the numerical values: type A or B. A detailed description of how each component of the standard uncertainty has been evaluated must be presented. When we take $k \neq 2$, a description of how k has been chosen should be given. As an example we present three different forms of writing the energy and the associated uncertainty for the gamma-ray energy of ^{51}Cr :

1. $E = (320.08419 \pm 0.00042)$ keV. The number after \pm symbol is the numerical value of the expanded uncertainty $U = ku_c$, with $u_c = 0.00021$ keV, and a coverage factor $k = 2$. We assume that the estimated values of a sample follow a normal distribution with a standard deviation u_c . The unknown energy value is believed to be in the interval defined by U with a level of confidence of 95%.
2. $E = (320.08419 \pm 0.00052)$ keV, where the number following the \pm symbol is the numerical value of the expanded uncertainty, $U = ku_c$, and a coverage factor based into a t distribution for $\nu = 9$ degrees of freedom. U defines an interval containing the unknown energy value with a confidence level of 95%.
3. $E = 320.08419$ keV with a combined standard deviation $u_c = 0.00021$ keV. We assume that the possible estimated energy values are distributed following a normal distribution with a standard deviation u_c . The unknown energy value is in the interval $E \pm u_c$ with an approximated confidence level of 68%.

IV. STATISTICAL INFERENCE

From a very general point of view, we can consider statistical inference as a form of decision based on probability. In a more limited sense, however, one can say that the statistical inference allows estimation or prediction from the data. Statistical inference gives responses to three types of problems: First, it permits one to test if a statement about the value of a parameter is correct. Second, it allows one to calculate the value of a parameter. Finally, it allows one to see whether some relationship exists between two or more variables and, in the affirmative case, to determine this relationship. In this section, we analyze the hypothesis testing and the estimation techniques.

A. Hypothesis Testing

A statistical hypothesis is an assertion about the probability density function of a random variable. Thus, the assertion that

a random variable possesses a Poisson distribution is an example of a statistical hypothesis. The statement that the mean of a normal distribution is 5 is also a statistical hypothesis.

A test of a statistical hypothesis is a procedure for deciding whether to accept or reject the hypothesis. Before carrying out the test, we define a hypothesis called a **null hypothesis**, denoted by H_0 . A null hypothesis is a statement about a population parameter that is being tested by the use of sample results and a decision-making process. This hypothesis must be contrasted with another called the **alternative hypothesis**, denoted by H_1 . An alternative hypothesis is a statement to be accepted if the null hypothesis is rejected. The alternative hypothesis utilizes the same parameter as the null hypothesis but gives motivation for the rest of the test procedure. This is the statement we want to accept. Both hypotheses define complementary regions. The **critical region** is the portion of a distribution that provides values for the sample results causing the rejection of H_0 . In other words, the critical region is the acceptance region for the alternative hypothesis. The critical value is the value that determines the critical region. Once the null and the alternative hypotheses have been established, we proceed to carry out the experiment and obtain the statistical sample to quantify the statistics of the test. If this one belongs to the critical region, we reject the null hypothesis and accept the alternative.

The result of our decision implies the possibility to guess correctly or make a mistake. We do not know with certainty what the true result is. To understand the meaning of a hypothesis test and the decision table established before carrying out the experiment, we consider the particular case of a sample, which may be radioactive. Only after carrying out the measurement experiment, may the analyst decide if the sample is or is not radioactive. Two correct and two incorrect decisions can be taken as is shown in Table 2.7

The interpretation of Table 2.7 is the following:

- If the null hypothesis is certain and it is accepted, the decision is correct.
- If the null hypothesis is certain and it is rejected, the decision is incorrect and the error made is type I. Its probability is represented by α .
- If the alternative hypothesis is certain and it is accepted, the decision is correct.
- If the alternative hypothesis is certain and it is rejected, the decision is incorrect and the error made is type II. Its probability is represented by β .

TABLE 2.7 Possible Consequences of a Final Decision

Decisions	Reality	
	H_0 true	H_1 true
Accept H_0	Correct decision	Type II error
Reject H_0	Type I error	Correct decision

Therefore:

$$\begin{aligned}\alpha &= P(\text{Type I error}) = P(\text{reject } H_0 \text{ being certain}) \\ &= P(\text{accept } H_1 \text{ when } H_0 \text{ is certain})\end{aligned}$$

$$\begin{aligned}\beta &= P(\text{Type II error}) = P(\text{accept } H_0 \text{ being uncertain}) \\ &= P(\text{accept } H_0 \text{ when } H_1 \text{ is certain})\end{aligned}$$

The power of the test is defined as $1 - \beta$, the probability of rejecting a false null hypothesis:

$$1 - \beta = P(\text{accept } H_1 \text{ when it is certain})$$

Example 2.7 To decide if a sample is radioactive, we accept the following null hypothesis: " $H_0; \mu_s = 0$ (the sample is not radioactive)". a) What cases can be given? b) Which is the type of error? c) Which is the type II error? d) Which error is more dangerous? e) What do you prefer: α small and β large or α large and β small?

a. The following cases can be given:

The activity of the sample is null and the analyst decides that it is not radioactive. The decision is correct.

The activity of the sample is null and the analyst decides that it is radioactive. The decision is incorrect and a type I error is made.

The sample is radioactive and the analyst decides that the sample has radioactivity. The decision is correct.

The sample is radioactive and the analyst decides that the sample has no radioactivity. The decision is incorrect and a type II error is made.

b. A type I error is made when the analyst decides that the sample is radioactive and it is not radioactive.

c. A type II error is made when the analyst decides that the sample is not radioactive and it is radioactive.

d. In this case, it is more serious to make a type II error than a type I error. A type I error obliges one to take unnecessary precautions with the sample. On the other hand, a type II error makes us consider the sample as nonradioactive when in fact it is radioactive. That produces a situation with radiation risk.

e. It is preferable to have α large and β small than the reverse.

It is not convenient to make α or β equal to zero. The most advisable is to choose a value for α equal to 0.01 or 0.05; when we examine a situation where H_0 is true, 1% or 5%, respectively, of the times we make incorrect decisions. The selected value for α will be determined by the severity of the circumstances of making an error. We have centered our attention on α because the objective of hypotheses testing is to test the truth of the statement contained in H_0 and to make a decision related to the rejection of this hypothesis.

The value of α is equal to the area under the curve corresponding to the rejection region. It is usual to nominate α as the significant value or the size of the critical region. Therefore, the level of significance is the probability α of a type I error. When we say that the results of a study are statistically significant we indicate that a value α has been chosen and the hypothesis testing leads to the rejection of the null hypothesis.

When we give α , the area of the rejection region for the distribution is known. For one-tail tests, the application of α is immediate. In two-tail tests, we must take into account that $\alpha/2$ corresponds to each tail, so that the sum of the areas of the two regions is α . When one knows the area of a region of the normal or t distributions, the value of z or t is obtained directly from tables.

Up to here we have chosen a level of significance before solving the problem. This procedure allows one to obtain a decision in a clear and fast way, defining previously a value for α . Another strategy consists of using what is known as the p -value to express the level of significance achieved by the data. The p -value is defined as the probability of obtaining a statistical test more extreme than z^* if H_0 is true; in other words, the p -value = $P(z > |z^*|)$ where $|z^*|$ is the absolute value of z^* .

B. Confidence Intervals

Interval estimators very probably contain the unknown population parameter. To formalize these statements it is necessary to express them in terms of probability. Let us suppose that θ is the parameter to be estimated. Let us also suppose that we have extracted a random sample and from the sample information it is possible to find two random variables X_1 and X_2 , such that $X_1 < X_2$. If these random variables have the property that $1 - \alpha$ is the probability that X_1 is smaller than θ and that X_2 is larger than θ , we can write

$$P(X_1 < \theta < X_2) = 1 - \alpha \quad (2.43)$$

where α is a number between 0 and 1. Then the interval X_1 and X_2 is an interval estimator of θ at $100(1 - \alpha)\%$ of confidence. If we call x_1 and x_2 the realizations of both random variables, the interval x_1 and x_2 is the confidence interval at $100(1 - \alpha)\%$ for θ . The quantity $1 - \alpha$ is the level of confidence for the interval. In other words, if we take random samples from the population a large number of times, the parameter θ will be contained in $100(1 - \alpha)\%$ of the calculated intervals. Confidence intervals are written as $x_1 < \theta < x_2$.

C. Statistical Inference

1. Variance of a Population

A problem that frequently appears in statistics is determining if the standard deviation of a sample corresponds to the standard deviation of a population. If we take random samples of size n from a normal distribution with variance σ^2 , we know that the random variable χ^2 allows us to study σ or σ^2 from the probabilities of the curve χ^2 .

In radioactivity measurements with pulse counters it is assumed that a good counter does not perturb measurements and therefore the standard deviation of the total counting is equal to the standard deviation of radioactivity disintegration. To test the reliability of a counter it is very useful to apply the χ^2 test. It allows one to check if a set of experimental data follows a preset statistical law. More details about the application of the χ^2 -test

in radioactivity measurements is given by Evans (1972). The χ^2 value is defined by the equation

$$\chi^2 = \frac{\sum_{i=1}^n [(observed\ value)_i - (expected\ value)]^2}{expected\ value} \quad (2.44)$$

where n is the total number of independent classifications i in which the data have been grouped. The expected value is computed from Poisson frequency distribution and corresponds to the mean $\mu \approx \bar{x}$. The measured values x_i are the results of the counting; they should be at least 5. The previous expression is now

$$\chi^2 = \frac{\sum_{i=1}^n (x_i - \bar{x})^2}{\bar{x}} \quad (2.45)$$

We will compare $\sigma = \sqrt{\bar{x}}$ with $s = \sqrt{\frac{\sum_{i=1}^n (x_i - \bar{x})^2}{n-1}}$, where n is the number of measurements. The null hypothesis is

$$H_0 : \sigma = s \quad (2.46)$$

and the alternative is

$$H_1 : \sigma \neq s \quad (2.47)$$

From the alternative hypothesis we conclude that the test is bilateral. Therefore, we will reject the null hypothesis if we obtain

$$\chi^2 > \chi_{n-1, \alpha/2}^2 \quad \text{or} \quad \chi^2 < \chi_{n-1, 1-\alpha/2}^2 \quad (2.48)$$

Example 2.8 A radioactive sample was measured with a Geiger counter 6 times. The duration of each measurement was 5 minutes. Check if the counter works well taking the measurements from Table 2.9.

The average value of the number of counts accumulated in 5 minutes is

$$\bar{x} = \frac{\sum_{i=1}^6 x_i}{n} = \frac{1344}{6} = 224$$

The distribution standard deviation is

$$\sigma = \sqrt{\bar{x}} = \sqrt{224} = 15.0$$

The observed standard deviation is

$$s = \sqrt{\frac{\sum_{i=1}^n (x_i - \bar{x})^2}{n-1}} = \sqrt{\frac{906}{5}} = 13.5$$

The null hypothesis is

$$H_0 : \sigma = s$$

The alternative hypothesis is

$$H_1 : \sigma \neq s$$

The rejection region is obtained from Table 2.8 for $f = n - 1 = 5$ and $\alpha = 0.05$. The critical values are $\chi_{5,0.025}^2 = 12.83$ and $\chi_{5,0.975}^2 = 0.831$. From the experimental data we have

$$\chi^2 = \frac{\sum_{i=1}^n (x_i - \bar{x})^2}{\bar{x}} = \frac{906}{224} = 4.04$$

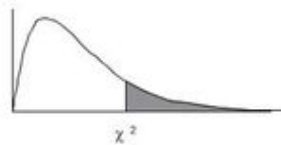
The rejection region is $\chi^2 > 12.83$ and $\chi^2 < 0.831$. As χ^2 is outside the rejection region we do not reject the null hypothesis and we conclude that the counter works correctly. Other examples for the application of the χ^2 -test to counters with anomalies are available in Grau Carles and Grau Malonda (2000).

2. Variance of Two Populations

Comparing variances requires the introduction of a new statistical test, the **F ratio**. Two population variances are compared by forming a ratio of their corresponding sample variance. The null hypothesis is $H_0 : \sigma_1^2 = \sigma_2^2$ and the statistical test is

$$F = \frac{s_1^2}{s_2^2} \quad (2.49)$$

TABLE 2.8 Chi-square (χ^2) Distribution



F	α									
	0.995	0.990	0.975	0.95	0.90	0.10	0.05	0.025	0.01	0.005
1	—	—	0.001	0.004	0.016	2.706	3.841	5.024	6.635	7.879
2	0.010	0.020	0.050	0.103	0.211	4.605	5.991	7.378	9.210	10.60
3	0.072	0.115	0.216	0.325	0.584	6.251	7.815	9.348	11.34	12.84
4	0.207	0.297	0.484	0.711	1.064	7.779	9.488	11.14	13.28	14.86
5	0.412	0.554	0.831	1.145	1.610	9.236	11.07	12.83	15.09	16.75
6	0.676	0.872	1.237	1.635	2.204	10.64	12.59	14.45	16.81	18.55

TABLE 2.9 Counts of a Radioactivity Sample

measure	Counts	Δ	Δ^2
1	214	-10	100
2	222	-2	4
3	217	-7	49
4	210	-14	196
5	243	19	361
6	238	14	196

The F -statistics is described by the F -distribution depending on the degrees of freedom. Now we have two samples and one degree of freedom for each sample: $f_1 = n_1 - 1$ is the degree of freedom for the numerator and $f_2 = n_2 - 1$ for the denominator. We write these as

$$f = (n_1 - 1, n_2 - 1) \tag{2.50}$$

Since s_1^2 and s_2^2 can never be negative, the F curves start at 0 and are skewed to the right as is shown in Table 2.10. The total area under the curve is equal to 1.

The null hypothesis does not establish an order for σ_1^2 and σ_2^2 . When we write $\sigma_1^2 = \sigma_2^2$, we could also write $\sigma_2^2 = \sigma_1^2$. It does not matter which sample variance goes in the numerator of F . When $H_0: \sigma_1^2 = \sigma_2^2$ is true, under ideal circumstances,

$F = s_1^2/s_2^2 = 1$. Thus, to carry out a hypothesis test, we must see how far the computed values of F deviate from 1.

If we observe the sketch of Table 2.10 we can appreciate that this table gives critical values larger than 1 for the right-hand tail. This decision simplifies our work but it forces us to compromise such that the larger values of s must be in the numerator. If we accept this criterion, we can ignore the F -values on the left-hand tail.

Let us examine in detail Table 2.10 corresponding to $F_{\alpha/2} = F_{0.025}$ or $\alpha = 0.05$. The rows of the table indicate the number of degrees of freedom of the numerator and the columns the number of degrees of freedom of the denominator. The critical value is in the intersection of the appropriate row and column. When the value of the degrees of freedom is not explicit in the table, the following approach must be used: 1) choose the next degree of freedom, and 2) if the degree of freedom in the table is halfway with that of the sample, the largest critical value will be taken.

Example 2.9 In Example 6, the internal ($S_{in} = 0.0098$) and external ($S_{ex} = 0.0068$) uncertainties were obtained. Find if these uncertainties are different at the 95% level of confidence.

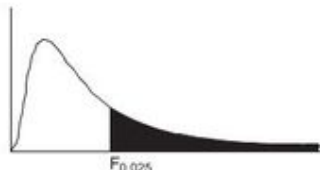
We assume that there is no difference between the variances:

$$H_0 : S_{in}^2 = S_{ex}^2$$

The alternative hypothesis indicates that the variances are different

$$H_1 : S_{in}^2 \neq S_{ex}^2$$

TABLE 2.10 F -Distribution



f .deno.	f . numerator								
	1	2	3	4	5	6	7	8	9
1	647.79	799.50	864.16	899.58	921.85	937.11	948.22	956.66	963.28
2	38.51	39.00	39.17	39.25	39.30	39.33	39.36	39.37	39.39
3	17.44	16.04	15.44	15.10	14.89	14.74	14.62	14.54	14.47
4	12.22	10.65	9.98	9.60	9.36	9.20	9.07	8.98	8.90
5	10.00	8.43	7.76	7.39	7.15	6.98	6.85	6.76	6.68
6	8.81	7.26	6.60	6.23	5.99	5.82	5.70	5.60	5.52
7	8.07	6.54	5.89	5.52	5.29	5.12	4.99	4.90	4.82
8	7.57	6.06	5.42	5.05	4.82	4.65	4.53	4.43	4.36
9	7.21	5.71	5.08	4.72	4.48	4.32	4.20	4.10	4.03
10	6.94	5.46	4.83	4.47	4.24	4.07	3.95	3.85	3.78

This alternative hypothesis indicates that the contrast is bilateral with $\alpha = 0.05$. The degrees of freedom are $f_{in} = f_{ex} = n - 1 = 4$. From Table 2.10 we obtain the critical value $F_{\alpha/2} = F_{0.025} = 9.60$. The rejection region is then $F_{0.025} > 9.60$. The computed value for $F_{0.025}^*$ is

$$F_{0.025}^* = \frac{S_{in}^2}{S_{ex}^2} = \frac{0.0098^2}{0.0068^2} = 2.08$$

As the computed value is less than the critical one ($F_{0.025}^* < F_{0.025}$), the null hypothesis cannot be rejected. Therefore, we conclude that there is no reason to think that S_{ex} and S_{in} are different.

V. REGRESSION

The problems analyzed so far were characterized to have one or two independent random variables. In this section, we consider the case of two or more random variables related to each other. The form of the relationship may be highly varied and unknown, but, in many cases, it is possible to guess, with good justification, a linear relationship. In other words, we consider two random variables X and Y , and we assume that the observations tend to be grouped in a straight line. In this case, we say that a linear relationship exists between the two random variables. Once a relationship has been established, we must obtain the function relating the random variables by means of a regression.

A. Linear Regression

The degree of association between two random variables is obtained by applying the correlation between them. This correlation is symmetrical since it is indifferent to the correlation between X and Y or between Y and X . In this section, we study the effect on the random variable Y when the random variable X takes a specific value. We limit our analysis to the simplest mathematical structure relating X and Y : the linear relationship. Variations of the problem of fitting a function to a set of data: curvilinear relationships, weighted least squares, nonlinear squares, etc. are analyzed by Draper and Smith (1998). Since we are working with random variables, over time for each value of X a distribution of Y values is obtained; therefore, we will use the concept of conditional distribution. An essential characteristic of this distribution is the mean or the expected value. We denote the expected value of the random variable Y with $E[Y|X = x]$, when the random variable X takes the specific value x . Our assumption of linearity implies that the conditional expected value has a linear dependence on x ,

$$E[Y|X = x] = \alpha + \beta x \tag{2.51}$$

where α and β determine the correct line. The interpretation of each one of these constants is immediate. When $x = 0$ we have

$$E[Y|X = 0] = \alpha \tag{2.52}$$

where α is the expected value for the dependent variable Y when the independent variable X takes the value 0.

Let us suppose now that X is increased by 1 unit so that x becomes $x+1$, then

$$E[Y|X = x + 1] = \alpha + \beta(x + 1) \tag{2.53}$$

and

$$E[Y|X = x + 1] - E[Y|X = x] = \alpha + \beta(x + 1) - (\alpha + \beta x) = \beta \tag{2.54}$$

Therefore, β , the slope of the line, is the expected increase in Y when X increases by unit.

In fact, the equations given previously are not verified exactly. Let us suppose that the independent variable takes the value x_i . If we represent by Y_i the corresponding value of the dependent random variable, the expected value is

$$E[Y_i|X = x_i] = \alpha + \beta x_i \tag{2.55}$$

But, in practice, the value of Y_i will deviate from the expected value. If the difference between the observed and the expected value is denoted by ϵ_i , we can write

$$\epsilon_i = Y_i - E[Y_i|X = x_i] = Y_i - (\alpha + \beta x_i) \tag{2.56}$$

so that

$$Y_i = \alpha + \beta x_i + \epsilon_i \tag{2.57}$$

where the random variable ϵ_i has a mean of 0. The last equation is known as the **population regression line** of data (x_i, Y_i) .

We have just described the regression model illustrated in Fig. 2.2. For each possible value of the independent variable, the value of the dependent variable may be represented by means of a random variable whose mean is on the regression line. The regression line is drawn through the means of the distributions. For a value of x_i , the independent variable, the deviation of the dependent variable Y_i from the regression line is the error term ϵ_i .

The regression line is an interesting theoretical construction but, in practice, as we always work with samples of observations, we will never be able to obtain this one exactly. Instead of α and β we obtain their estimators: the numbers a and b . The estimated line has as equation

$$y = a + bx \tag{2.58}$$

Let us suppose that we have a sample of n pairs of observations $(x_1, y_1), (x_2, y_2), \dots, (x_n, y_n)$. We are interested in obtaining the line that best fits to those data. We know that the value x_i produces the value y_i obtained from equation $a + bx_i$, but the

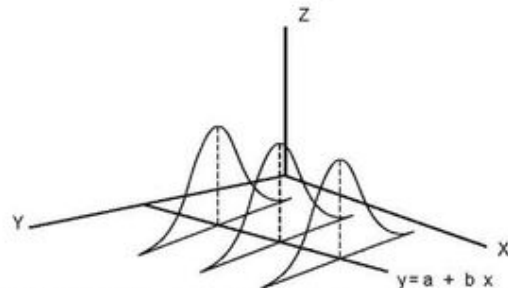


FIGURE 2.2 Probability density functions of the dependent variable for given values of x .

exact value for the dependent variable is y_i . The difference between the two is

$$e_i = y_i - (a + bx_i) \quad (2.59)$$

The values of e_i may be positive or negative. If we want to give the same weight to the positive and negative values of the same quantity, a possibility is to work with the square of e_i . The sum of squared differences from the point to the line is

$$SQ = \sum_{i=1}^n e_i^2 = \sum_{i=1}^n (y_i - a - bx_i)^2 \quad (2.60)$$

The least squares method allows one to estimate the line of a population regression for which the sum of the squares is a minimum. The parameter b can be obtained from the equation

$$b = \frac{\sum_{i=1}^n x_i y_i - n \bar{x} \bar{y}}{\sum_{i=1}^n x_i^2 - n \bar{x}^2} \quad (2.61)$$

and a with the equation

$$a = \bar{y} - b \bar{x} = \frac{\bar{y} \sum_{i=1}^n x_i^2 - \bar{x} \sum_{i=1}^n x_i y_i}{\sum_{i=1}^n x_i^2 - n \bar{x}^2} \quad (2.62)$$

where \bar{x} and \bar{y} are the respective means of the sample. The line

$$y = a + bx \quad (2.63)$$

is the **sample regression** line of Y on X .

The least squares method is a good procedure to estimate the regression line for the population. This procedure is the most appropriate when the regression line for the population

$$Y_i = \alpha + \beta x_i + e_i \quad (2.64)$$

is required. This must fulfill the following conditions:

- Each value of x_i is a fixed number, which is equivalent to saying that the realization of a random variable X_i is independent of the error term e_i .
- Errors are random variables with an expected value equal to zero:

$$E[e_i] = 0 \quad (i = 1, 2, \dots, n) \quad (2.65)$$

- All the random variables e_i have the same variance σ_e^2 :

$$E[e_i^2] = \sigma_e^2 \quad (i = 1, 2, \dots, n) \quad (2.66)$$

- The random variables e_i are not correlated:

$$E[e_i e_j] = 0 \quad \text{for all } i \neq j$$

Bacon (1953) describes the least squares method of fitting a line for different conditions and analyzes the goodness-of-fit results from different experiments.

1. Confidence Intervals and Hypothesis Testing

We will analyze the problems of interval construction and the hypothesis testing for the regression parameters of a population. Suppose that the regression line is

$$Y_i = \alpha + \beta x_i + e_i \quad (2.67)$$

and the conditions of the previous section are fulfilled. If σ_e^2 is the common variance for the error terms e_i , an unbiased estimator of σ_e^2 is

$$s_e^2 = \frac{\sum_{i=1}^n e_i^2}{n-2} \quad (2.68)$$

where e_i are the residuals of the least squares. These residuals substitute the error terms e_i , which are unknown. We divide by $n-2$ because we lose two degrees of freedom when estimating the parameters α and β .

If we designate with b the least squares estimate of the slope of the population regression line, the estimator of β is unbiased and the variance is

$$\sigma_b^2 = \frac{\sigma_e^2}{\sum_{i=1}^n (x_i - \bar{x})^2} = \frac{\sigma_e^2}{\sum_{i=1}^n x_i^2 - n \bar{x}^2} \quad (2.69)$$

An unbiased estimator of σ_b^2 is provided by

$$s_b^2 = \frac{s_e^2}{\sum_{i=1}^n (x_i - \bar{x})^2} = \frac{s_e^2}{\sum_{i=1}^n x_i^2 - n \bar{x}^2} \quad (2.70)$$

In both cases, we assume that the conditions of the previous section are fulfilled.

Although the slope is the most interesting parameter, we give also the equation to compute the estimator of the variance of the ordinate on the origin. We substitute β , b , and s_b^2 for α , a , and s_a^2 to have

$$s_a^2 = s_e^2 \left(\frac{1}{n} + \frac{\bar{x}^2}{\sum_{i=1}^n x_i^2 - n \bar{x}^2} \right) \quad (2.71)$$

VI. DETECTION LIMITS

Radioactivity measurements are characterized by a variable zero level due to background. This situation obliges one to work with detection and determination limits when the radioactivity of the source is very low.

In this section, we analyze the problem of obtaining the detection limits for very low radioactivity measurements. A complete discussion of the detection limits, in a measurement process, requires the introduction of two specific levels: i) a **decision limit** that allows one to deduce whether the result of the analysis indicates that the sample is or is not radioactive and ii) a **detection limit** that indicates if an analytical process leads to a quantitative detection. The relationships between these limits and the equations to compute them are also given.

In a general way, two types of devices are considered: counters, characterized to accumulate the information in one channel, and spectrometers, where information is distributed in numerous channels. In the latter case, we distinguish between high-resolution detectors, such as Ge, and low-resolution detectors, such as NaI(Tl).

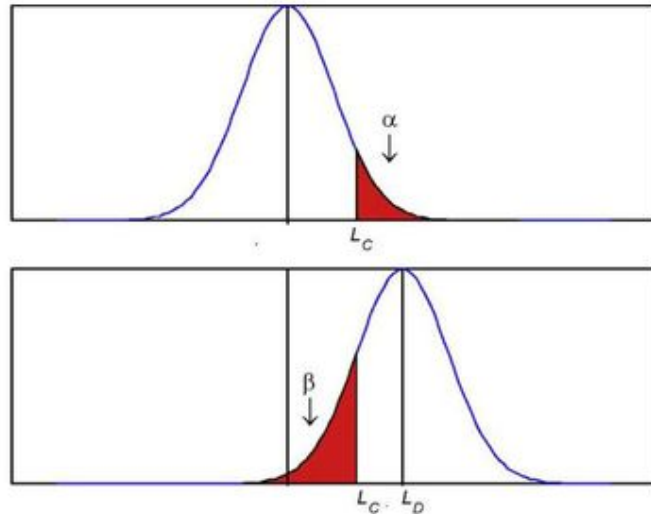
A. Critical Levels

We will distinguish two fundamental problems in the measurement of very low radioactivity sources: i) given an observed net signal, S , to decide whether a real signal has been detected or, in other words, to decide whether the sample is

indeed radioactive. ii) Is $\mu_S > 0$? This question can be addressed by the statistical theory of hypothesis testing, in which one first formulates a test hypothesis. In our case, the null hypothesis H_0 for μ_S is $\mu_S = 0$. This hypothesis and the alternative hypothesis H_1 ($\mu_S > 0$) are mutually exclusive. Together they cover all possible values of μ_S . As a consequence of the intrinsic statistical variation in the counting rates, we can arrive at one of the following two types of judgment errors: i) the error of the first kind or type I error states that true activity is greater than zero when, in fact, it is zero or ii) the error of the second kind or type II error states that the true activity is zero when, in fact, it is greater than zero. The probability of making a type I error is denoted by α and depends on the test procedure. The maximum value of α and the standard deviation of the net signal σ_0 , when $\mu_S = 0$, allow one to establish the critical level L_C . An observed signal, S , must exceed L_C to yield the decision "detected." The probability distribution of possible outcomes, when the true net signal is zero, intersects L_C such that the factor $1 - \alpha$ corresponds to the correct decision "nondetected." Whereas the probability of making a type II error, denoted by β , also depends on the size of the measured quantity, in the case of radioactive measurements it depends on the amount of radioactivity of the tested material. The most relevant papers about low-level detection limits are Altshuler and Pasternack (1963), Currie (1968), (1995), and Donn and Wolke (1977).

When the critical level L_C has been established, an *a priori* detection limit L_D may be established by specifying L_C , the acceptable level β , for a type II error and the standard deviation σ_D , characterizing the probability distribution of the net signal when its true value μ_S is equal to L_D . Fig. 2.3 shows the type I and II error curves and the critical levels L_C and L_D . The mean μ_S may be between zero and L_D . When μ_S is between 0 and L_C we agree that there is no radiation from the sample. When μ_S is between L_C and L_D there may be radioactivity but when $\mu_S = L_D$ the type II error is minimum. Therefore, for $L_C < \mu_S < L_D$ although we can have detection, such detection cannot be considered reliable given that the type II error is not a minimum.

FIGURE 2.3 Type I and II errors.



The critical level L_C is given by

$$L_C = k_\alpha \sigma_0 \tag{2.72}$$

and the detection limit by

$$L_D = L_C + k_\beta \sigma_D \tag{2.73}$$

where $k_\alpha \equiv z_\alpha$ and $k_\beta \equiv z_\beta$ are the $k \equiv z$ scores of the standardized normal distribution corresponding to probability levels $1 - \alpha$ and $1 - \beta$, respectively.

When we analyze the pulses due to radioactivity emission, we can assume that the distributions of background and background + source follow the Poisson distribution. When the count number is sufficiently large, the distributions are approximately normal. Under such circumstances, the variance of the net counting is given by

$$\sigma^2 = \sigma_{S+B}^2 + \sigma_B^2 = \mu_S + \mu_B + \frac{\mu_B}{n} \tag{2.74}$$

where σ_B is obtained from n measurements without the source. Note that σ depends on the signal level.

If σ_0^2 is the variance when $\mu_S = 0$, and σ_D^2 is the variance for $\mu_S = L_D$, we have

$$L_C = k_\alpha \sigma_0 = k_\alpha (\mu_B + \sigma_0^2)^{1/2} \tag{2.75}$$

and

$$\sigma_D^2 = \sigma_{S+B}^2 + \sigma_B^2 = \mu_S + \mu_B + \sigma_0^2 = L_D + \sigma_0^2 \tag{2.76}$$

From Eqn (2.73) we get

$$L_D = L_C + k_\beta (L_D + \sigma_0^2)^{1/2} \tag{2.77}$$

Solving Eqns (2.75) and (2.77), we obtain

$$L_D = L_C + \frac{k_\beta^2}{2} \left\{ 1 + \left[1 + \frac{4L_C}{k_\beta^2} + \frac{4L_C^2}{k_\alpha^2 k_\beta^2} \right]^{1/2} \right\} \tag{2.78}$$

The mean value and the standard deviation without the source allow one to compute L_C and L_D for selected values of α and β by means of Eqns (2.75) and (2.78). If $k_\alpha = k_\beta = k$, we obtain a considerable simplification of Eqn (2.73), which is reduced to the form

$$L_D = k^2 + 2L_C \quad (2.79)$$

Example 2.10 Background and a source-plus-background are measured and the counting rates obtained are $C_B = 203$ counts/h and $C_{B+S} = 235$ counts/h. Previously, the background was measured for 200 hours, accumulating a total of 40 000 counts (counting rate $B = 200$ counts/h). Compute the values of L_C and L_D when $\alpha = 0.025$ and $\beta = 0.050$, in the following two cases: a) when we know that the background does not change and we can use the value of B and b) when we cannot apply B because the background changes.

The values $k_\alpha = 1.96$ when $\alpha = 0.025$ and $k_\beta = 1.645$ when $\beta = 0.050$ are obtained from Table 2.2 as follows: Given that $k_\alpha = z_{1-\alpha} = 0.975$, the value considered in Table 2.2 is $0.975 - 0.5 = 0.475$. This value corresponds to row 1.9 and column 0.06, thus $k_\alpha = 1.96$. In the same way, $k_\beta = z_{1-\beta} = 0.95$ and the value to be carried to Table 2.2 is $0.95 - 0.5 = 0.45$. This value is not included in the table; however, it is between 0.4495 and 0.4505, at row 1.6 and columns 0.04 and 0.05 (mean 0.045). Therefore, $k_\beta = 1.645$.

The background counting rate is $C_B = 203$ counts/h. As the expected background counting rate is $B = 200$ counts/h, it seems that the background has not changed. The net counting rate is

$$C_S = C_{B+S} - B = 235 - 200 = 35 \text{ counts/h}$$

and the critical counting rate is

$$L_C = k_\alpha \sqrt{\mu_B + \sigma_B^2} \approx k_\alpha \sqrt{B} = 1.96 \times \sqrt{200} = 27.7 \text{ counts/h}$$

Since 35 is greater than 27.7, our decision is that there is activity in the sample. The minimum significant measured counting rate is 27.7 counts/h.

The minimum detectable counting rate from Eqn (2.78) is

$$\begin{aligned} L_D &= L_C + \frac{k_\beta^2}{2} \left\{ 1 + \left[1 + \frac{4L_C}{k_\beta^2} + \frac{4L_C^2}{k_\alpha^2 k_\beta^2} \right]^{1/2} \right\} \\ &= 27.7 + \frac{1.645^2}{2} \left\{ 1 + \left[1 + \frac{4 \times 27.7}{1.645^2} + \frac{4 \times 27.7^2}{1.96^2 \times 1.645^2} \right]^{1/2} \right\} \\ &= 53.9 \text{ counts/h} \end{aligned}$$

and applying the approximate equation

$$L_D = (k_\alpha + k_\beta) \sqrt{B} = (1.96 + 1.645) \sqrt{200} = 51.0 \text{ counts/h}$$

When the background changes we cannot use the mean number B . The net counting rate is obtained applying the following expression

$$C_S = C_{S+B} - C_B = 235 - 203 = 32 \text{ counts/h}$$

and

$$\begin{aligned} L_C &= k_\alpha \sqrt{\mu_B + \sigma_B^2} = k_\alpha \sqrt{\mu_B + \mu_B} = k_\alpha \sqrt{2\mu_B} \approx k_\alpha \sqrt{2C_B} \\ &= 1.96 \sqrt{2 \times 203} = 39.49 \text{ counts/h} \end{aligned}$$

Since the net counting rate is less than the critical net counting rate, our conclusion is that there is no significant radioactivity in the sample. The minimum detectable counting rate is

$$\begin{aligned} L_D &= L_C + \frac{k_\beta^2}{2} \left\{ 1 + \left[1 + \frac{4L_C}{k_\beta^2} + \frac{4L_C^2}{k_\alpha^2 k_\beta^2} \right]^{1/2} \right\} = 39.49 \\ &\quad + \frac{1.645^2}{2} \left\{ 1 + \left[1 + \frac{4 \times 39.49}{1.645^2} + \frac{4 \times 39.49^2}{1.96^2 \times 1.645^2} \right]^{1/2} \right\} \\ &= 75.6 \text{ counts/h} \end{aligned}$$

and applying the approximate equation

$$\begin{aligned} L_D &= (k_\alpha + k_\beta) \sqrt{2C_B} = (1.96 + 1.645) \sqrt{2 \times 203} \\ &= 72.6 \text{ counts/h} \end{aligned}$$

B. Gamma-Spectra

Ge detectors allow the experimental spectroscopists to obtain gamma- and X-ray spectra with high resolution compared with that obtained with NaI(Tl) detectors. This excellent resolution facilitates the qualitative and quantitative analyses of radionuclide mixtures for high and medium activities. However, for low-level samples the low efficiency and the similarity of the small peaks to the fluctuations of the background can make the discrimination between true and false peaks difficult.

Since NaI(Tl) detectors have larger volume and lower resolution than Ge detectors, the detection of low activity peaks is different for each detector. Each one of the Ge peaks can be analyzed taking the two independent constituent parts: the peak and the Compton contribution. On the other hand, the NaI(Tl) peaks force us to consider the overlap contribution of the different spectral components in each of the peaks.

In this section, we analyze the determination and detection limits for Ge detectors. Based upon the acceptable risk of committing a type I error, a minimum significant measured area for a peak is defined and, for a type II error, a minimum detectable true area is introduced. The study of complete response of the NaI(Tl) detector is carried out taking into account the contribution of the different spectral components.

1. High-Resolution Gamma-Spectra

In an experimental Ge gamma spectrum, the minimum detectable area of a peak is the minimum number of photopeak counts that make it detectable. The value of this minimum depends on the spectral background under the peak, but the background usually does not coincide with the detector background. The minimum is predetermined by the statistical risk of including an observed peak when it is not a real peak or concluding that a real peak is not present when it is really there.

The procedures to discern between real and false peaks are based on the assumption that real peaks show a Gaussian shape. This procedure gives good results when the peaks are sufficiently defined and the Gaussian hypothesis is valid; however, when the peaks are small they can be taken as statistical fluctuations with Gaussian appearance. Therefore, a computational procedure dedicated to determining very small peaks must be able to detect false peaks.

There is a probability that a false peak is accepted as a true peak. This is called a type I error. Based upon the acceptable risk of committing a type I error we define a **minimum significant measured area**. It is assumed that all the peaks in the spectrum whose measured areas are smaller than this limit are discarded and considered as false peaks. This is the type II error. Consequently, we can define a minimum detectable real peak area such that if the actual photopeak area is at least this large, the risks of committing type I or type II errors are less than some preselected values.

An application of this analysis consists of determining the minimum time required to be sure that the risk of making a type I or II error does not exceed acceptable values. This allows one to predict the time required to assure the detection of small peaks.

a. Distribution of False Peaks

Following Head (1972), to know the distribution of false peaks, it is necessary to carry out an experiment and have a peak identification computer program. In essence, the experiment consists of preparing "background" spectra with an average measure of 50–50 000 counts/channel. For the purpose of the experiment, the background in the energy range of 80–500 keV can be simulated by the Compton tails of the two ⁶⁰Co gamma lines, in order to determine false peaks. By means of another gamma source with peaks in the range given above we can produce the real peaks. ¹³³Ba can be used to generate real peaks. The objective is clear: The ⁶⁰Co Compton distribution produces the "background" and ¹³³Ba gives the true peaks for each background. For a certain background level and several resolution values (1.0, 1.5, 2.0, 2.5, and 3.0 channels, for a real resolution of 1.5 channels), we obtain the number of false and acceptable peaks. From the different analyzed backgrounds, we obtain the curves shown in Fig. 2.4, where the average area of the false peaks detected \bar{A} and the widths $\sigma_{\bar{A}}$ of these areas as a function of the background B under the peak areas (due to the Compton tails of ⁶⁰Co gamma lines) are represented.

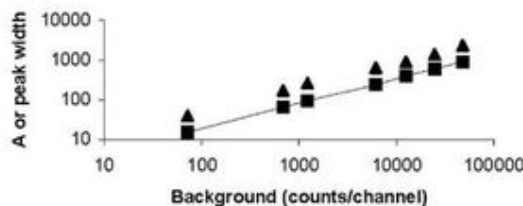


FIGURE 2.4 Average of the peak count area (triangles) and width of the peaks (squares) as a function of background. (From Head, 1972, reprinted with permission of Elsevier © 1972).

b. Minimum Significant Area

The probability of committing a type I error or of concluding that a peak corresponds to a gamma ray, when in fact it is a false peak, depends upon the peak selection procedure and upon the level of the background under the peak. A minimum significant measured area A_I can be defined by the expression

$$\alpha = P\{\text{Measured area of a false peak} \geq A_I\} \quad (2.80)$$

A peak whose area is equal or larger than A_I is retained and all peaks whose area is less than A_I are rejected. If we do not have any additional information about the peak, the probability that it is false is α , or, in other words, the risk of accepting a false peak as true is α .

If we assume that the false peak area distribution is normal, the minimum significant area for committing a type I error, for a given risk, is given by the equation

$$A_I = \bar{A} + z_\alpha \sigma_{\bar{A}} \quad (2.81)$$

where z_α is related to α by the equation

$$\alpha = \int_{z_\alpha}^{\infty} \frac{1}{\sqrt{2\pi}} \exp(-u^2/2) du \quad (2.82)$$

\bar{A} and $\sigma_{\bar{A}}$ may be obtained by interpolation in Fig. 2.4 for a given background B , the value of the minimum significant area A_I , for a risk α , may be computed from Eqn (2.81).

c. Minimum Detectable Area

Assume that we have obtained A_T counts in the photopeak of a given gamma ray. When we compute the area by means of a fitting program, the fitted area A_F will seldom be equal to A_T . Due to statistical fluctuations, the measured area for a peak will usually be distributed about the real area ($\bar{A}_F = A_T$) with a width σ_F . As we have seen in the last section, all peaks with mean areas lower than A_I will be discarded as not significant. A type II error is committed when a real peak $A_T \geq A_I$, due to the spread in the fitted area, gives $A_F < A_I$ and consequently the peak is discarded.

The probability of committing a type II error depends upon the value of A_I and the fitted area A_F . We define the minimum detectable area A_{II} as

$$\beta = P\{\text{Fitted area } A_F < A_I, \text{ when the true area is } A_T = A_{II}\} \quad (2.83)$$

As the fitted area is normally distributed with variance σ_F^2 we have

$$A_{II} = A_I + k_\beta \sigma_F \quad (2.84)$$

where the relationship between β and k_β is the same as that between α and k_α . In this case, σ_F^2 is the variance of the fitted area distribution when $\bar{A}_F = A_T = A_{II}$.

We introduce a hypothesis that allows us to solve the problem with the data we have. We suppose that the variance of the fitted area distribution is similar to the variance of the false peak area distribution ($\sigma_F^2 \approx \sigma_{\bar{A}_I}^2$). As A_{II} is very close to A_I we assume that $\sigma_F^2 \approx \sigma_{\bar{A}_I}^2 \approx \sigma_{\bar{A}_I}^2 \approx \sigma_{\bar{A}_I}^2$, consequently

$$A_{II} = A_I + k_\beta \sigma_{\bar{A}} \quad (2.85)$$

or

$$A_H = \bar{A} + (k_\alpha + k_\beta)\sigma_{\bar{A}} \quad (2.86)$$

\bar{A} and $\sigma_{\bar{A}}$ may be obtained interpolating in Fig. 2.4.

Example 2.11 The background spectrum has $B = 10000$ counts/channel. Obtain the values of \bar{A} and $\sigma_{\bar{A}}$. Compute A_I and A_{II} for $\alpha = 10\%$ and $\beta = 1\%$.

For a background $B = 10000$ we obtain from Fig. 2.4

$$\bar{A} = 840 \text{ counts and } \sigma_{\bar{A}} = 320 \text{ counts}$$

The values of k_α and k_β , for $\alpha = 0.10$ and $\beta = 0.01$, are

$$k_\alpha = 1.28 \text{ and } k_\beta = 2.33$$

Therefore

$$A_I = \bar{A} + k_\alpha\sigma_{\bar{A}} = 840 + 1.28 \times 320 = 1250 \text{ counts}$$

and

$$A_{II} = \bar{A} + (k_\alpha + k_\beta)\sigma_{\bar{A}} = 840 + (1.28 + 2.33) \times 320 = 1995 \text{ counts}$$

The relationship between A_I , A_{II} , and B is

$$A_{II} = K_{\alpha\beta} B^{0.619} \quad (2.87)$$

The exponent is obtained from the graphical representation of A_I and A_{II} as a function of B . The factor $K_{\alpha\beta}$ is a parameter independent of B containing all the information related to the type I and II error risks that influence A_{II} . In fact, $K_{\alpha\beta}$ is a risk factor depending functionally on α , β , and B . From Eqns (2.86) and (2.87), we obtain

$$K_{\alpha\beta} = \frac{A_{II}}{B^{0.619}} = \frac{\bar{A} + (k_\alpha + k_\beta)\sigma_{\bar{A}}}{B^{0.619}} \quad (2.88)$$

It is observed that $K_{\alpha\beta}$ is symmetric in α and β .

d. Minimum Counting Time

We have just concluded that we may calculate a minimum area, A_{II} , so that a peak with this area cannot be false with a risk α and a real peak cannot be discarded as false with a risk β . It has been supposed that the background and the peak grow evenly during data accumulation by the spectrometer. In this situation, we may compute the counting duration to assure that the peak is detectable with the risks α and β .

Let us suppose that a is the true counting rate for the peak, expressed in counts/h. If $t_{\alpha\beta}$ is the time required, in hours, assuming that the risks for the type I and II errors do not exceed α and β , respectively, we can write

$$A_{II} = at_{\alpha\beta} \quad (2.89)$$

$$B = bt_{\alpha\beta} \quad (2.90)$$

taking these expressions to Eqn (2.87), we have

$$at_{\alpha\beta} = K_{\alpha\beta}(bt_{\alpha\beta})^{0.619} \quad (2.91)$$

the minimum counting time is given by

$$t_{\alpha\beta} = (K_{\alpha\beta}/a)^{2.62} b^{1.62} \quad (2.92)$$

TABLE 2.11 Experimental Values of B , \bar{A} , and $\sigma_{\bar{A}}$

B	\bar{A}	$\sigma_{\bar{A}}$
100	50	18.8
500	135	50.9
1000	208	78.1
5000	563	211.6
10000	865	324.9
20000	1328	499.0
40000	2040	766.4

(From Head (1972) reprinted with permission of Elsevier 1972)

Example 2.12 Table 2.11 shows the experimental values of B , \bar{A} , and $\sigma_{\bar{A}}$. Find the relationship between A_{II} and B when $\alpha = 0.10$ and $\beta = 0.01$ or 0.5 . Show that $A_{II} = K_{\alpha\beta} B^c$ and compute $K_{\alpha\beta}$ and c . It is assumed that $K_{\alpha\beta}$ is a parameter independent of B .

Table 2.12 shows the values of A_{II} for different values of B .

Equation $A_{II} = K_{\alpha\beta} B^c$ may be fitted taking logarithms

$$\log A_{II} = \log K_{\alpha\beta} + c \log B$$

This is a linear equation

$$y = a + cx$$

where

$$y = \log A_{II}$$

and

$$x = \log B$$

Applying least square fitting to the quantities of Table 2.12, when $\alpha = 0.10$ and $\beta = 0.01$, we get $K_{\alpha\beta} = 6.81$ and $c = 0.619$, and when $\alpha = 0.10$ and $\beta = 0.50$, we get $K_{\alpha\beta} = 4.28$ and $c = 0.619$. As c takes the same values, we may compute $K_{\alpha\beta}$ applying the equation

$$K_{\alpha\beta} = \frac{\bar{A} + (k_\alpha + k_\beta)\sigma_{\bar{A}}}{B^{0.619}}$$

The values of B , \bar{A} , and $\sigma_{\bar{A}}$ may be values of Table 2.11 or interpolated logarithmically from Table 2.12; e.g. for $\alpha = 0.01$

TABLE 2.12 Values of B and A_{II} for Different α and β Values

$\alpha = 0.10, \beta = 0.01$		$\alpha = 0.10, \beta = 0.50$	
B	A_{II}	B	A_{II}
100	118	100	74
500	319	500	201
1000	490	1000	308
5000	1327	5000	834
10000	2038	10000	1281
20000	3130	20000	1967
40000	4806	40000	3021

and $\beta = 0.015$, when $B = 1000$, $\bar{A} = 208$, and $\sigma_{\bar{A}} = 78$, we have

$$K_{\alpha\beta} = \frac{208 + (2.33 + 1.96) \times 78}{1000^{0.619}} = 7.55$$

Example 2.13 Compute the values of $t_{\alpha\beta}$ when $\alpha = 0.01$ and $\beta = 0.025$, the background counting rate is $b = 100$ counts/h and $a = 20$ counts/h.

From Eqn (2.92), taking into account that $K_{\alpha\beta} = 7.55$ from the last example we have

$$t_{\alpha\beta} = \left(\frac{7.55}{20}\right)^{2.62} 100^{1.62} = 135 \text{ h}$$

2. Low-Resolution Gamma-Spectra

Nal(Tl) detectors generate spectra with very poor resolution compared with the spectra obtained with Ge detectors. Consequently, the procedure described in the previous section is not generally applicable to low-resolution spectra. Isolated peaks cannot be analyzed due to interference from other spectral components. In this section, we introduce a more general procedure based on considering the complete spectral response. This procedure introduces a larger complication in calculations but it is inevitable when we have radionuclide mixtures and the spectrum of one of the radionuclides overlaps the other spectra and vice versa. In this situation, the background must be considered as an independent spectrum. A standard procedure for estimating the radionuclide concentration from gamma-ray spectrometer data is the method of weighted least squares fitting. In this case, it is assumed that the net spectrum of a radionuclide mixture is equivalent to some linear combination of the net characteristic spectra of the radionuclides existing in the sample. The concentration of these radionuclides is represented by the coefficients of the linear combination estimate. Consequently, the estimation of these coefficients is equivalent to the determination of their concentrations.

The solution of least squares is a function $\theta' = (\theta_1, \theta_2, \dots, \theta_m)$, which minimizes the sum of the squares of the count differences between observed and fitted channels. This sum of squares is denominated a residual variation. We define the following n -dimensional vectors:

- $\mathbf{x} = (x_1, x_2, \dots, x_n)$ net counting rate corresponding to channels 1, 2, ..., n
- $\mathbf{y} = (y_1, y_2, \dots, y_n)$ gross counts (sample + background) in channels 1, 2, ..., n .
- $\mathbf{b} = (b_1, b_2, \dots, b_n)$ background counts in channels 1, 2, ..., n .

If t is the counting time of the sample and r the counting time of the background, we may define the elements w_{jj} of the diagonal matrix \mathbf{W} as

$$w_{jj} = \frac{y_j}{t^2} + \frac{b_j}{r^2} \tag{2.93}$$

The solution obtained by weighted least squares method is given by the estimator

$$\hat{\theta} = (\mathbf{A}\mathbf{W}^{-1}\mathbf{A}')^{-1}\mathbf{A}\mathbf{W}^{-1}\mathbf{x} \tag{2.94}$$

where \mathbf{A} is an $m \times n$ matrix called the calibration matrix. The dimension m corresponds to the number of calibration spectra and n to the number of channels of each spectrum.

The variance of the estimated concentration parameter for the i th radionuclide is the i th diagonal element of the matrix $(\mathbf{A}\mathbf{W}^{-1}\mathbf{A}')^{-1}$. In order to test the goodness of fit we use the residual mean square

$$s^2 = \frac{1}{n-m} (\mathbf{x} - \mathbf{A}'\hat{\theta})\mathbf{W}^{-1}(\mathbf{x} - \mathbf{A}'\hat{\theta}) \tag{2.95}$$

which is distributed as a chi-square random variable. A review of methods currently used to unfold particle spectra for measured pulse-height distributions is presented by Matzke (2002).

a. Sample with a Single Radionuclide

To illustrate the procedure described in the previous section, we consider a simple case: the limit of detection determination when the sample has only one radionuclide and we use a two-channel counter. Eqn (2.94) becomes

$$\hat{\theta}_1 = \left\{ \frac{a_{11}^2}{y_1/t^2 + b_1/r^2} + \frac{a_{12}^2}{y_2/t^2 + b_2/r^2} \right\}^{-1} \times \left\{ \frac{a_{11}(y_1/t - b_1/r)}{y_1/t^2 + b_1/r^2} + \frac{a_{12}(y_2/t - b_2/r)}{y_2/t^2 + b_2/r^2} \right\} \tag{2.96}$$

the standard error is given by

$$S(\hat{\theta}_1) = \left\{ \frac{a_{11}^2}{y_1/t^2 + b_1/r^2} + \frac{a_{12}^2}{y_2/t^2 + b_2/r^2} \right\}^{-1/2} \tag{2.97}$$

and the detection limit is given by

$$L_D = (k_\alpha + k_\beta) \left\{ \frac{a_{11}^2}{y_1/t^2 + b_1/r^2} + \frac{a_{12}^2}{y_2/t^2 + b_2/r^2} \right\}^{-1/2} \tag{2.98}$$

If the counter has only one channel, the estimate is

$$\hat{\theta}_1 = \left\{ \frac{a_{11}^2}{y_1/t^2 + b_1/r^2} \right\}^{-1} \times \left\{ \frac{a_{11}(y_1/t - b_1/r)}{y_1/t^2 + b_1/r^2} \right\} = \frac{y_1/t - b_1/r}{a_{11}} \tag{2.99}$$

and

$$S(\hat{\theta}_1) = \sqrt{\frac{y_1/t^2 + b_1/r^2}{a_{11}^2}} \tag{2.100}$$

The detection limit is

$$L_D = (k_\alpha + k_\beta) \sqrt{\frac{y_1/t^2 + b_1/r^2}{a_{11}^2}} \tag{2.101}$$

b. Sample with Two Radionuclides

Consider now a radioactive sample with two radionuclides and a counter with two channels. The standard error of the estimated concentrations for radionuclide 1 is $S(\hat{\theta}_1)$ and $S(\hat{\theta}_2)$ for the

second radionuclide. It is straightforward to demonstrate the following equations

$$S(\hat{\theta}_1) = \left\{ \frac{1}{d} \left(\frac{a_{21}^2}{y_1/t^2 + b_1/r^2} + \frac{a_{22}^2}{y_2/t^2 + b_2/r^2} \right) \right\}^{-1/2} \quad (2.102)$$

and

$$S(\hat{\theta}_2) = \left\{ \frac{1}{d} \left(\frac{a_{11}^2}{y_1/t^2 + b_1/r^2} + \frac{a_{12}^2}{y_2/t^2 + b_2/r^2} \right) \right\}^{-1/2} \quad (2.103)$$

where d denotes the determinant of the matrix $\mathbf{AW}^{-1}\mathbf{A}'$.

The individual estimate of concentrations is impossible when the shape of pulse distributions in both channels is similar. In this situation, $d \rightarrow 0$.

The detection limit for radionuclide 1 is approximated by

$$L_D(1) = (k_\alpha + k_\beta) \left\{ \frac{1}{d} \left(\frac{a_{21}^2}{y_1/t^2 + b_1/r^2} + \frac{a_{22}^2}{y_2/t^2 + b_2/r^2} \right) \right\}^{-1/2} \quad (2.104)$$

and for radionuclide 2 by

$$L_D(2) = (k_\alpha + k_\beta) \left\{ \frac{1}{d} \left(\frac{a_{11}^2}{y_1/t^2 + b_1/r^2} + \frac{a_{12}^2}{y_2/t^2 + b_2/r^2} \right) \right\}^{-1/2} \quad (2.105)$$

c. Sample with Several Radionuclides

From the above discussion it is evident that the standard error of the parameter to estimate, the concentration of radionuclides, depends on the following factors: counting time of the sample and background, relationship between the spectral shape included in the library and the concentration of the radionuclides present in the sample.

According to the description of Pasternack and Harley (1971), in the multi-radionuclide and multi-channel situation we may consider three different detection limits:

A radionuclide is assumed to be in the sample and the library contains only this radionuclide.

The sample contains only one radionuclide but the library contains this and other radionuclides.

The sample and the library each contain the same radionuclides. The procedure to obtain the detection limits in case 1 is as follows: First we obtain the background spectrum of the system $\mathbf{b}' = (b_1, b_2, \dots, b_n)$ and the spectrum for a mock sample $\mathbf{y}' = (y_1, y_2, \dots, y_n)$. Generally we can use the background distribution \mathbf{b}' in the place of \mathbf{y}' . Then we apply the least squares analysis and compute the standard error $S(\hat{\theta}_1)$ from the square root of $(\mathbf{a}'_1 \mathbf{W}^{-1} \mathbf{a}_1)^{-1}$, where $\mathbf{a}_1 = (a_{11}, a_{12}, \dots, a_{1n})$ denotes the radionuclide library spectrum. Thus

$$S(\hat{\theta}_1) = \left\{ \sum_{j=1}^n \frac{a_{1j}^2}{y_j/t^2 + b_j/r^2} \right\}^{-1/2} \quad (2.106)$$

and

$$L_D = (k_\alpha + k_\beta) \left\{ \sum_{j=1}^n \frac{a_{1j}^2}{y_j/t^2 + b_j/r^2} \right\}^{-1/2} \quad (2.107)$$

When we take \mathbf{b}' in place of $\mathbf{y}'(t = r)$, the detection limit is

$$L_D = (k_\alpha + k_\beta) \left\{ \sum_{j=1}^n \frac{a_{1j}^2}{2b_j/r^2} \right\}^{-1/2} \quad (2.108)$$

For case 2, the procedure is the same but the matrix \mathbf{A} contains all the spectra of the library. For case 3, the procedure is again the same. It is recommended that the mock sample adequately simulates the sample absorption. When the library does not contain all the sample radionuclides, the estimate may be unacceptable. When the library contains more spectra than the sample a reduction in precision is observed and the standard error increases; however, the estimates remain unbiased. Explicit mathematical expressions for the bias and the loss of precision when using inadequate calibration matrices are given by Pasternack and Liuzzi (1965).

VII. METROLOGY APPLICATIONS

A. Uncertainty Budget

In all radionuclide standardization work we must present a table that lists the various quantified uncertainties. We will take as an example the determination of the activity concentration of a ^{133}Ba solution (Simpson and van Wyngaardt, 2008). As was customary at the time, Table 2.13 shows only the different components of uncertainty and the uncertainty for each component. Table 2.13 is a technical table directed to experts. Along with many published uncertainty budgets, Table 2.13 does not fully comply with the guidelines of the GUM (see section 7.1.4 of JCGM 100:2008), and would require an expert in the field using specialized knowledge to make an educated guess of

TABLE 2.13 Standard Uncertainty Budget for ^{133}Ba , in Percentage of the Activity Concentration

Component	Relative standard uncertainty multiplied by a sensitivity factor (%)
Counting statistics	0.08
Weighing	0.035
Dead time	0.04
Coincidence resolving time	0.002
Satellite pulses (afterpulsing)	0.10
Counting time	0.001
Background	0.01
Adsorption	0.002
Half-life	0.001
Extrapolation of efficiency curve	0.20
Combined uncertainty (in quadrature)	0.244

(From Simpson and van Wyngaardt, 2008, reprinted with permission from Elsevier © 2008)

the likely method of evaluation. In recent years, in the field of radionuclide metrology, a concerted effort is being made to include an explanation on how each uncertainty value was obtained in the uncertainty budget, similar to the remarks given in the following table. Here, we asked Simpson and van Wyngaardt to provide us a table for nonexperts with more details. Table 2.14 describes the procedures for obtaining the different uncertainties as well as the type of uncertainty (A or B). We must mention that in the past 3 years Dr. Simpson and the members of other laboratories have tried to include additional information in the uncertainty budget along the lines of Table 2.14.

B. Uncertainty Calculation

Wang et al. (2001) obtained the activity concentration of a ¹²⁵I solution measuring 10 samples and applying the equation

$$N_0 = T + \frac{N_\gamma N_{\alpha\beta}}{N_{\beta\gamma}(2N_{\alpha\alpha} + N_{\alpha\beta})} \times \left[N_\alpha + N_\beta - N_\gamma \left(\frac{N_{\alpha\beta}}{2N_{\beta\gamma}} + \frac{N_6}{N_{\beta\gamma}} - \frac{2N_{\alpha\alpha}}{N_{\alpha\beta}} \right) \right] \quad (2.109)$$

The values of different quantities are shown in Table 2.15. This table shows the activity of each of the samples (final column), the mean value of 10 samples, and the relative standard deviation.

There are two procedures for calculating the uncertainty activity obtained with Eqn (2.109). The traditional option is to

calculate the activity of each sample and then to obtain from them the standard deviation. This is the procedure followed by Wang et al. (2001). The results are shown in Table 2.15. The relative variance is

$$S = \sqrt{\frac{\sum_{i=1}^{10} (N_{0i} - \bar{N}_0)^2}{(10 - 1)}} = \sqrt{\frac{21.3}{9}} = 1.538$$

and

$$\frac{S}{\bar{N}_0} = \frac{1.538}{292.8} = 0.005$$

Another procedure (Taylor, 1997), which we follow in this section, is known as uncertainty transmission. It consists of calculating the standard deviation and correlation of the different quantities in order to determine the uncertainty introduced by using a specific equation to calculate the activity of ¹²⁵I.

1. Uncertainty Transmission in Eqn (2.109)

Consider uncertainty transmission for Eqn (2.109). Let

$$F_1 = \frac{N_\gamma N_{\alpha\beta} (N_\alpha + N_\beta)}{N_{\beta\gamma} (2N_{\alpha\alpha} + N_{\alpha\beta})}$$

$$F_2 = - \frac{N_\gamma^2 N_{\alpha\beta}}{N_{\beta\gamma} (2N_{\alpha\alpha} + N_{\alpha\beta})}$$

TABLE 2.14 Details of the ¹³³Ba Standard Uncertainty Budget, in Percentage of the Activity Concentration

Component	Relative standard uncertainty multiplied by a sensitive factor (%)	Remarks	Evaluation type (A or B)
Counting statistics	0.08	Statistical analysis of 5 extrapolation values (one value from each 5 counting sources)	A
Weighing	0.035	Mass ± 0.01 mg, for source preparation using Mettler M3 balance. Mass ± 1 mg, for dilution using Mettler B6 balance.	B
Dead time	0.04	Due to uncertainty in τ _D (typically ± 0.05 μs for all the threshold settings).	B
Coincidence resolving time	0.002	Uncertainty in τ _R was typically ± 0.001 μs.	B
Satellite pulses (afterpulsing)	0.10	θ ± 1σ (re-analyzed data by increasing/decreasing the afterpulse correction values by their measured uncertainties for each threshold setting).	B
Counting time	0.001	Calibration of timer	B
Background	0.01	A combination of: Background square root statistics applied. Different background data sets interchanged.	A B
Absorption	0.002	Accounts for uncertainties in the final result due to residual ¹³³ Ba remaining after 5 rinsing in the ampoule received, as measured with a NaI (Tl) detector.	B
Half-life	0.001	t _{1/2} = 10.540 ± 0.006 years	B
Extrapolation of efficiency curve	0.20	Alternative fits to data (activity conc. range/(2√3)), assuming the range to be uniformly distributed.	B
Combined uncertainty (in quadrature)	0.244	Quadratic sum of all uncertainty components (for k = 1).	

(From Simpson and van Wyngaardt, 2011).

TABLE 2.15 Data from First-time Measurements of the 10 Samples.

Sample no.	Weight (mg)	Count rates after correction ($T_{1/2} = 59.43$ days)								N_0 Bq/mg
		T	N_α	N_β	N_γ	$N_{\alpha\alpha}$	$N_{\alpha\beta}$	$N_6 = N_{\beta\beta} + N_{\alpha\gamma}$	$N_{\beta\gamma}$	
1#	46.18	199.52	93.56	23.66	7.15	24.5	13.0	5.22	1.012	290.4
2#	70.60	195.10	92.25	23.47	7.19	22.4	12.0	4.87	0.942	291.1
3#	75.01	194.29	92.46	23.58	7.21	22.0	11.8	4.77	0.913	292.5
4#	97.54	208.61	96.20	23.91	7.19	28.5	14.5	5.71	1.087	292.8
5#	117.68	201.90	94.88	23.88	7.24	25.2	13.3	5.33	1.025	292.6
6#	120.75	200.27	94.51	23.87	7.24	24.5	13.0	5.20	0.995	292.7
7#	142.10	203.91	94.55	23.85	7.26	26.1	13.4	5.29	1.005	293.0
8#	175.01	200.48	93.31	23.64	7.24	23.6	12.5	4.98	0.947	294.1
9#	98.26	201.59	94.43	23.84	7.25	24.7	13.0	5.14	0.976	293.5
10#	108.11	197.13	95.51	24.48	7.74	24.2	12.5	5.00	0.965	295.5
Average		200.3	94.19	23.82	7.27	24.56	12.89	5.15	0.987	292.8
Relative standard deviation (%)		2.1	1.4	1.2	2.3	7.5	5.9	5.2	5.0	0.5

(From Wang et al., 2001, reprinted with permission of Elsevier © 2001)

$$F_3 = \frac{N_{\alpha\beta}}{2N_{\beta\gamma}} + \frac{N_6}{N_{\beta\gamma}} - \frac{2N_{\alpha\alpha}}{N_{\alpha\beta}}$$

The expression to which we apply the uncertainty transmission is

$$N_0 = T + F_1 + F_2F_3$$

We deduce each of the partial derivatives relative to the various parameters. For convenience, we write the equations in tables. The left side of the equation is in the first row and the right side

is in the second. We numerically calculate each of these partial derivatives (Tables 2.16–2.20).

TABLE 2.16 Partial Derivatives of N_0 with Respect to T , N_α , N_β , and N_6

$\frac{\partial N_0}{\partial T}$	$\frac{\partial N_0}{\partial N_\alpha} = \frac{\partial N_0}{\partial N_\beta}$	$\frac{\partial N_0}{\partial N_6}$
1	$\frac{N_\gamma N_{\alpha\beta}}{N_{\beta\gamma}(2N_{\alpha\alpha} + N_{\alpha\beta})}$	$-\frac{N_\gamma^2 N_{\alpha\beta}}{N_{\beta\gamma}^2(2N_{\alpha\alpha} + N_{\alpha\beta})}$

TABLE 2.17 Partial Derivatives to Calculate $\partial N_0 / \partial N_{\alpha\beta}$

$\frac{\partial N_0}{\partial N_{\alpha\beta}}$	$\frac{\partial F_1}{\partial N_{\alpha\beta}}$	$\frac{\partial F_2}{\partial N_{\alpha\beta}}$	$\frac{\partial F_3}{\partial N_{\alpha\beta}}$
$\frac{\partial F_1}{\partial N_{\alpha\beta}} + \frac{\partial F_2}{\partial N_{\alpha\beta}} F_3 + \frac{\partial F_3}{\partial N_{\alpha\beta}} F_2$	$\frac{2N_{\alpha\alpha}N_\gamma(N_\alpha + N_\beta)}{N_{\beta\gamma}(2N_{\alpha\alpha} + N_{\alpha\beta})^2}$	$-\frac{2N_\gamma^2 N_{\alpha\alpha}}{N_{\beta\gamma}(2N_{\alpha\alpha} + N_{\alpha\beta})^2}$	$\frac{1}{2N_{\beta\gamma}} + \frac{2N_{\alpha\alpha}}{N_{\alpha\beta}^2}$

TABLE 2.18 Partial Derivatives to Calculate $\partial N_0 / \partial N_\gamma$

$\frac{\partial N_0}{\partial N_\gamma}$	$\frac{\partial F_1}{\partial N_\gamma}$	$\frac{\partial F_2}{\partial N_\gamma}$
$\frac{\partial F_1}{\partial N_\gamma} + \frac{\partial F_2}{\partial N_\gamma} F_3 + \frac{\partial F_3}{\partial N_\gamma} F_2$	$\frac{N_{\alpha\beta}(N_\alpha + N_\beta)}{N_{\beta\gamma}(2N_{\alpha\alpha} + N_{\alpha\beta})}$	$-\frac{2N_\gamma N_{\alpha\beta}}{N_{\beta\gamma}(2N_{\alpha\alpha} + N_{\alpha\beta})}$

TABLE 2.19 Partial Derivatives to Calculate $\partial N_0/\partial N_{\beta\gamma}$

$\frac{\partial N_0}{\partial N_{\beta\gamma}}$	$\frac{\partial F_1}{\partial N_{\beta\gamma}}$	$\frac{\partial F_2}{\partial N_{\beta\gamma}}$	$\frac{\partial F_3}{\partial N_{\beta\gamma}}$
$\frac{\partial F_1}{\partial N_{\beta\gamma}} + \frac{\partial F_2}{\partial N_{\beta\gamma}} F_3 + \frac{\partial F_3}{\partial N_{\beta\gamma}} F_2$	$-\frac{N_\gamma N_{\alpha\beta}(N_\alpha + N_\beta)}{N_{\beta\gamma}^2(2N_{\alpha\alpha} + N_{\alpha\beta})}$	$\frac{N_\gamma^2 N_{\alpha\beta}}{N_{\beta\gamma}^2(2N_{\alpha\alpha} + N_{\alpha\beta})}$	$-\frac{N_{\alpha\beta}}{2N_{\beta\gamma}^2} - \frac{N_6}{N_{\beta\gamma}^2}$

TABLE 2.20 Partial Derivatives to Calculate $\partial N_0/\partial N_{\alpha\alpha}$

$\frac{\partial N_0}{\partial N_{\alpha\alpha}}$	$\frac{\partial F_1}{\partial N_{\alpha\alpha}}$	$\frac{\partial F_2}{\partial N_{\alpha\alpha}}$	$\frac{\partial F_3}{\partial N_{\alpha\alpha}}$
$\frac{\partial F_1}{\partial N_{\alpha\alpha}} + \frac{\partial F_2}{\partial N_{\alpha\alpha}} F_3 + \frac{\partial F_3}{\partial N_{\alpha\alpha}} F_2$	$-\frac{2N_\gamma N_{\alpha\beta}(N_\alpha + N_\beta)}{N_{\beta\gamma}(2N_{\alpha\alpha} + N_{\alpha\beta})^2}$	$\frac{2N_\gamma^2 N_{\alpha\beta}}{N_{\beta\gamma}(2N_{\alpha\alpha} + N_{\alpha\beta})^2}$	$-\frac{2}{N_{\alpha\beta}}$

2. Numerical Calculation of Uncertainty

The values to be applied to the equations are the mean values of different magnitudes. These mean values are shown in Table 2.21.

To calculate the numerical value of the partial derivatives, we first calculate some combinations of values that are repeated in the calculations.

The calculated values of the partial derivatives are shown in Table 2.23

If the quantities are correlated, correlation coefficients have to be calculated. Correlation coefficient is defined as

$$\rho(x, y) = \frac{1}{(n-1)\sigma_x\sigma_y} \left(\sum_{i=1}^n x_i y_i - n\bar{x}\bar{y} \right)$$

where \bar{x} and \bar{y} are the mean of the random variables X and Y , respectively. Table 2.23 shows the values of the correlation coefficients for different pairs of variables:

TABLE 2.21 Mean Values

N_γ	N_α	N_β	N_γ	$N_{\alpha\alpha}$	$N_{\alpha\beta}$	N_6	$N_{\beta\gamma}$
200.280	94.196	23.818	7.271	24.570	12.900	0.987	5.151

TABLE 2.22 Numerical Values of Some Combinations of Values Repeated in the Calculation.

$N_\alpha + N_\beta$	$2N_{\alpha\alpha} + N_{\alpha\beta}$	F_1	F_2	F_3
118.01	62.01	180.687	-11.131	7.937

TABLE 2.23 Values of Partial Derivatives

$\frac{\partial N_0}{\partial N_\gamma}$	$\frac{\partial N_0}{\partial N_\alpha}$	$\frac{\partial N_0}{\partial N_\beta}$	$\frac{\partial N_0}{\partial N_\gamma}$	$\frac{\partial N_0}{\partial N_{\alpha\alpha}}$	$\frac{\partial N_0}{\partial N_{\alpha\beta}}$	$\frac{\partial N_0}{\partial N_6}$	$\frac{\partial N_0}{\partial N_{\beta\gamma}}$
1.0000	1.5322	1.5322	0.5127	-1.2475	-3.2695	-11.2911	39.2328

Variance and standard deviation equations ($\sigma_0 = \sigma_{N_0}$)

$$\begin{aligned} \sigma_0^2 = & \left(\frac{\partial N_0}{\partial T}\right)^2 \sigma_T^2 + \left(\frac{\partial N_0}{\partial N_{\alpha\beta}}\right)^2 \sigma_{\alpha\beta}^2 + \left(\frac{\partial N_0}{\partial N_\gamma}\right)^2 \sigma_\alpha^2 + \left(\frac{\partial N_0}{\partial N_\alpha}\right)^2 \sigma_\alpha^2 \\ & + \left(\frac{\partial N_0}{\partial N_\beta}\right)^2 \sigma_\beta^2 + \left(\frac{\partial N_0}{\partial N_{\beta\gamma}}\right)^2 \sigma_{\beta\gamma}^2 + \left(\frac{\partial N_0}{\partial N_{\alpha\gamma}}\right)^2 \sigma_{\alpha\alpha}^2 + \left(\frac{\partial N_0}{\partial N_6}\right)^2 \sigma_6^2 \\ & + 2\left(\frac{\partial N_0}{\partial N_T}\right)\left(\frac{\partial N_0}{\partial N_\alpha}\right)\rho(N_T, N_\alpha)\sigma_T\sigma_\alpha + 2\left(\frac{\partial N_0}{\partial N_T}\right)\left(\frac{\partial N_0}{\partial N_\beta}\right)\rho(N_T, N_\beta)\sigma_T\sigma_\beta \\ & + 2\left(\frac{\partial N_0}{\partial N_T}\right)\left(\frac{\partial N_0}{\partial N_\gamma}\right)\rho(N_T, N_\gamma)\sigma_T\sigma_\gamma + 2\left(\frac{\partial N_0}{\partial N_T}\right)\left(\frac{\partial N_0}{\partial N_{\alpha\alpha}}\right)\rho(N_T, N_{\alpha\alpha})\sigma_T\sigma_{\alpha\alpha} \\ & + 2\left(\frac{\partial N_0}{\partial N_T}\right)\left(\frac{\partial N_0}{\partial N_{\alpha\beta}}\right)\rho(N_T, N_{\alpha\beta})\sigma_T\sigma_{\alpha\beta} + 2\left(\frac{\partial N_0}{\partial N_T}\right)\left(\frac{\partial N_0}{\partial N_6}\right)\rho(N_T, N_6)\sigma_T\sigma_6 \\ & + 2\left(\frac{\partial N_0}{\partial N_T}\right)\left(\frac{\partial N_0}{\partial N_{\beta\gamma}}\right)\rho(N_T, N_{\beta\gamma})\sigma_T\sigma_{\beta\gamma} + 2\left(\frac{\partial N_0}{\partial N_\alpha}\right)\left(\frac{\partial N_0}{\partial N_\beta}\right)\rho(N_\alpha, N_\beta)\sigma_\alpha\sigma_\beta \\ & + 2\left(\frac{\partial N_0}{\partial N_\alpha}\right)\left(\frac{\partial N_0}{\partial N_\gamma}\right)\rho(N_\alpha, N_\gamma)\sigma_\alpha\sigma_\gamma + 2\left(\frac{\partial N_0}{\partial N_\alpha}\right)\left(\frac{\partial N_0}{\partial N_{\alpha\alpha}}\right)\rho(N_\alpha, N_{\alpha\alpha})\sigma_\alpha\sigma_{\alpha\alpha} \\ & + 2\left(\frac{\partial N_0}{\partial N_\alpha}\right)\left(\frac{\partial N_0}{\partial N_{\alpha\beta}}\right)\rho(N_\alpha, N_{\alpha\beta})\sigma_\alpha\sigma_{\alpha\beta} + 2\left(\frac{\partial N_0}{\partial N_\alpha}\right)\left(\frac{\partial N_0}{\partial N_6}\right)\rho(N_\alpha, N_6)\sigma_\alpha\sigma_6 \\ & + 2\left(\frac{\partial N_0}{\partial N_\alpha}\right)\left(\frac{\partial N_0}{\partial N_{\beta\gamma}}\right)\rho(N_\alpha, N_{\beta\gamma})\sigma_\alpha\sigma_{\beta\gamma} + 2\left(\frac{\partial N_0}{\partial N_\beta}\right)\left(\frac{\partial N_0}{\partial N_\gamma}\right)\rho(N_\beta, N_\gamma)\sigma_\beta\sigma_\gamma \\ & + 2\left(\frac{\partial N_0}{\partial N_\alpha}\right)\left(\frac{\partial N_0}{\partial N_{\alpha\alpha}}\right)\rho(N_\alpha, N_{\alpha\alpha})\sigma_\alpha\sigma_{\alpha\alpha} + 2\left(\frac{\partial N_0}{\partial N_\beta}\right)\left(\frac{\partial N_0}{\partial N_{\alpha\beta}}\right)\rho(N_\beta, N_{\alpha\beta})\sigma_\beta\sigma_{\alpha\beta} \\ & + 2\left(\frac{\partial N_0}{\partial N_\beta}\right)\left(\frac{\partial N_0}{\partial N_6}\right)\rho(N_\beta, N_6)\sigma_\beta\sigma_6 + 2\left(\frac{\partial N_0}{\partial N_\beta}\right)\left(\frac{\partial N_0}{\partial N_{\beta\gamma}}\right)\rho(N_\beta, N_{\beta\gamma})\sigma_\beta\sigma_{\beta\gamma} \\ & + 2\left(\frac{\partial N_0}{\partial N_\gamma}\right)\left(\frac{\partial N_0}{\partial N_{\alpha\alpha}}\right)\rho(N_\gamma, N_{\alpha\alpha})\sigma_\gamma\sigma_{\alpha\alpha} + 2\left(\frac{\partial N_0}{\partial N_\gamma}\right)\left(\frac{\partial N_0}{\partial N_{\alpha\beta}}\right)\rho(N_\gamma, N_{\alpha\beta})\sigma_\gamma\sigma_{\alpha\beta} \\ & + 2\left(\frac{\partial N_0}{\partial N_\gamma}\right)\left(\frac{\partial N_0}{\partial N_6}\right)\rho(N_\gamma, N_6)\sigma_\gamma\sigma_6 + 2\left(\frac{\partial N_0}{\partial N_\gamma}\right)\left(\frac{\partial N_0}{\partial N_{\beta\gamma}}\right)\rho(N_\gamma, N_{\beta\gamma})\sigma_\gamma\sigma_{\beta\gamma} \\ & + 2\left(\frac{\partial N_0}{\partial N_{\alpha\alpha}}\right)\left(\frac{\partial N_0}{\partial N_{\alpha\beta}}\right)\rho(N_{\alpha\alpha}, N_{\alpha\beta})\sigma_{\alpha\alpha}\sigma_{\alpha\beta} + 2\left(\frac{\partial N_0}{\partial N_{\alpha\alpha}}\right)\left(\frac{\partial N_0}{\partial N_6}\right)\rho(N_{\alpha\alpha}, N_6)\sigma_{\alpha\alpha}\sigma_6 \\ & + 2\left(\frac{\partial N_0}{\partial N_{\alpha\alpha}}\right)\left(\frac{\partial N_0}{\partial N_{\beta\gamma}}\right)\rho(N_{\alpha\alpha}, N_{\beta\gamma})\sigma_{\alpha\alpha}\sigma_{\beta\gamma} + 2\left(\frac{\partial N_0}{\partial N_{\alpha\beta}}\right)\left(\frac{\partial N_0}{\partial N_6}\right)\rho(N_{\alpha\beta}, N_6)\sigma_{\alpha\beta}\sigma_6 \\ & + 2\left(\frac{\partial N_0}{\partial N_{\alpha\beta}}\right)\left(\frac{\partial N_0}{\partial N_{\beta\gamma}}\right)\rho(N_{\alpha\beta}, N_{\beta\gamma})\sigma_{\alpha\beta}\sigma_{\beta\gamma} + 2\left(\frac{\partial N_0}{\partial N_6}\right)\left(\frac{\partial N_0}{\partial N_{\beta\gamma}}\right)\rho(N_6, N_{\beta\gamma})\sigma_6\sigma_{\beta\gamma} \end{aligned}$$

The numerical value of the uncorrelated variance is

$$\text{Var1} = 46.4319$$

and the variance of the correlation is

$$\text{Var2} = -44.2895$$

Therefore, the variance of the activity is

$$\sigma_0^2 \approx S_0 = \text{Var1} + \text{Var2} = 2.1424$$

and the standard deviation is

$$S_0 = 1.4637$$

Corresponding to the relative standard deviation

$$\frac{S_0}{N_0} = 0.00502 \approx 0.5\%$$

This value coincides with that obtained by the traditional method. The difference between the two procedures is that, in the first, measurements are independent and therefore there is no correlation between them. However, they may or may not be correlated in the second procedure. In our example, the quantities are not independent, so correlations are required, complicating the calculation. Whenever possible it is advisable to apply the first procedure, but there are situations where we need to apply the second. We emphasize that in uncertainty transmission the

TABLE 2.24 Correlation Coefficients

$\rho(x, y)$	$y = N_\alpha$	$y = N_\beta$	$y = N_\gamma$	$y = N_{tot}$	$y = N_{\alpha\beta}$	$y = N_6$	$y = N_{\beta\gamma}$
$x = N_\gamma$	0.7628	0.2130	-0.2119	0.9591	0.9668	0.9393	0.8834
$x = N_\alpha$		0.7789	0.4016	0.8660	0.8202	0.7964	0.7772
$x = N_\beta$			0.8731	0.3820	0.2923	0.2654	0.2768
$x = N_\gamma$				-0.0565	-0.1714	-0.2007	-0.1787
$x = N_{tot}$					0.9872	0.9714	0.9417
$x = N_{\alpha\beta}$						0.9935	0.9683
$x = N_6$							0.9809

quantities are not always correlated. Therefore, we only apply correlations when the quantities involved are not independent (Tables 2.22 and 2.24).

REFERENCES

- Abramowitz, M., Stegun, I.A., 1972. Handbook of Mathematical Functions with Formulas, Graphs and Mathematical Tables. NBS Applied Mathematical Series, vol. 55. Washington, p. 1046.
- Altshuler, B., Pasternack, B., 1963. Statistical measures of the lower limit of detection of a radioactivity counter. *Health Phys.* 9, 293–298.
- Angoso, M., Gimeno, F., Grau Malonda, A., Domínguez, G., 1973. Isotopic dilution determination of lebacid in oranges. *J. Radioanal. Chem.* 13, 149–154.
- Bacon, R.M., 1953. The best straight line among the points. *Am. J. Phys.* 28, 428–440.
- Beers, Y., 1957. Introduction to the Theory of Error. Addison-Wesley, Massachusetts, p. 66.
- Bevington, P.R., 1969. Data Reduction and Error Analysis for the Physical Sciences. McGraw, New York, p. 336.
- Burns, J.E., Campion, P.J., Williams, A., 1973. Error and uncertainty. *Metrologia* 9, 101–102.
- Campion, P.J., Burns, J.E., Williams, A., 1973. A Code of Practice for Detailed Statement of Accuracy. National Physical Laboratory, London, p. 51.
- Currie, L.A., 1968. Limits for quantitative detection and quantitative determination. *Anal. Chem.* 40, 586–593.
- Currie, L.A., 1995. Nomenclature in evaluation of analytical methods including detection and quantification capabilities. *Pure Appl. Chem.* 67, 1699–1723.
- Donn, J.J., Wolke, R.L., 1976. The practical design and statistical interpretation of background-dominant counting experiments. *Radiochem. Radioanal. Lett.* 25 (2), 57–66.
- Donn, J.J., Wolke, R.L., 1977. The statistical interpretation of counting data from measurements of low-level radioactivity. *Health Phys.* 32, 1–14.
- Draper, N.H., Smith, H., 1998. Applied Regression Analysis. John Wiley, New York, p. 736.
- Eadie, W.T., Drijard, D., James, F.E., Ross, M., Sadoulet, B., 1971. Statistical Methods in Experimental Physics. North Holland, Amsterdam, p. 296.
- Eisenhart, C., 1963. Realistic evaluation of precision and accuracy of instrument calibration systems. *J. Res.* 67C, 161–187.
- Eisenhart, C., 1968. Expression on the uncertainties of final results. *Science* 160, 1201–1204 (A detailed discussion on systematic errors).
- Evans, R.E., 1972. The Atomic Nucleus. Chap. 26–28 and Appendix G. McGraw Hill, New York, p. 972.
- Feller, W. (1968). An introduction to probability theory and applications. Vol. 1. John Wiley, New York, p. 509.
- Garwood, F., 1936. Fiducial limits for the Poisson distribution. *Biometrika* 28, 437–442.
- Grau Carles, P., Grau Malonda, A., 2000. Probabilidad Estadística Y Errores. Editorial Ciemat, Madrid, p. 437.
- Grau Malonda, A., 1999. Free Parameter Models in Liquid Scintillation Counting. Editorial Ciemat, Madrid, p. 416.
- Head, J.H., 1972. Minimum detectable photopeak in Ge(Li) spectra. *Nucl. Instrum. Methods* 98, 419–428.
- Helstrom, C.W., 1968. Statistical Theory of Signal Detection. Pergamon Press, Oxford, p. 364.
- Hoel, P.C., 1984. Introduction to Mathematical Statistics. John Wiley, New York.
- International Vocabulary of Basic and General Terms in Metrology, second ed., 1993 ISO.
- Jaffey, A.H., 1960. Statistical tests for counting. *Nucleonics* 18 (11), 180–184.
- JCGM 100, 2008. Evaluation of Measurement Data—Guide to the Expression of Uncertainty in Measurements. p. 134.
- Larson, H.J., 1969. Introduction to Probability Theory and Statistical Inference. John Wiley, New York, p. 435.
- Loevinger, R., Berman, M., 1951. Efficiency criteria in radioactivity counting. *Nucleonics* 9, 26–39.
- Matzke, M., 2002. Propagation of uncertainties in unfolding procedures. *Nucl. Instrum. Methods A476*, 230–241.
- Müller, J.W., 1979. Some second thoughts on error statements. *Nucl. Instrum. Methods* 163, 241–251.
- Natrella, M.G., 2005. Experimental Statistics. Dover, New York, p. 560.
- Newbold, P., 2009. Statistics for Business and Economics. Prentice Hall, New Jersey, p. 1008.
- Nicholson, W.L., 1966. Statistics of net-counting-rate estimation with dominant background corrections. *Nucleonics* 24, 118–121.
- Pasternack, B.S., Liuzzi, A., 1965. Patterns in residuals: a test for regression adequacy in radionuclide assay. *Technometrics* 7, 603–621.
- Pasternack, B.S., Harley, N.H., 1971. Detection limits for radionuclides in the analysis of multi-component gamma ray spectrometer data. *Nucl. Instrum. Methods* 91, 533–549.
- Przyborowski, J., Wilenski, H., 1935. Statistical principles of routine work in testing clover seed for dodder. *Biometrika* 27, 273–292.
- Rabinovich, S.G., 2005. Measurement Errors and Uncertainties. Theory and Practice. Springer, New York, p. 320.
- Reynolds, S.A., 1964. Choosing optimum counting. *Nucleonics* 22 (8), 104–105.
- Rozanov, Y.A., 1977. Probability theory: A concise course. Dover, New York, p. 148.
- Simpson, B.R.S., van Wyngaardt, W.M., 2008. Absolute activity of ^{133}Ba by liquid scintillation coincidence counting using the $4\pi(e, X)\text{-}\gamma$ extrapolation technique. *Appl. Radiat. Isot.* 66, 929–933.
- Simpson, B.R.S., van Wyngaardt, W.M., 2011. Private communication.
- Taylor, J.R., 1997. An introduction to Error Analysis. The Study of Uncertainties in Physical Measurements, second ed. University Science Books, California, p. 327.
- Taylor, B.N., Kuyatt, C.E., 1994. Guidelines for Evaluating and Expressing the Uncertainty of NIST Measurement Results. NIST Technical Note 1297. Washington.

- Thomas, A., 1950. How to compare counters. *Nucleonics* 6 (2), 50–53.
- Topping, T., 1972. *Errors of Observation and their Treatment*. Springer, New York, p. 119.
- Triola, M.F., 2010. *Elementary Statistics*. Addison Wesley, p. 896.
- Wang, Z., Zhang, X., Chang, Y., Liu, D., 2001. The determination of I-125 activity using sum-peak method with a well HPGGe-detector-based spectrometer. *Nucl. Instrum. Methods Phys. Res. A* 459, 475–481.
- Wyld, G.E.A., 1970. Statistical confidence in liquid scintillation counting. In: *The Current Status of Liquid Scintillation Counting*. Grune and Stratton, New York, p. 354.
- Zimmerman, B.E., Unterweger, M.P., Brodack, J.W., 2001. The standardization of ^{177}Lu by $4\pi\beta$ liquid scintillation spectrometry with ^3H -standard efficiency tracing. *App. Radiat. Isot.* 54, 623–631.
- Beyer, W.H., 1990. *CRC Standard Probability and Statistics Tables and Formulae*. CRC Press, Boca de Raton, Florida, p. 520.
- Hald, A., 1958. *Statistical Tables and Formulas*. John Willey and Sons, London, p. 97.
- James Rohlf, F., Sokal, R.R., 1994. *Statistical Tables*. Freeman, New York, p. 28.
- Kmietowicz, Z.W., Yannoulis, Y., 1976. *Mathematical, Statistical and Financial Tables for the Social Sciences*. Longman, London, p. 64.
- Lindley, D.V., Scott, W.F., 1995. *New Cambridge Statistical Tables*, second ed. Cambridge University Press, Cambridge, p. 96.
- Murdoch, J., Barnes, S.A., 1998. *Statistical Tables*, fourth ed. Macmillan Press, London, p. 79.
- Neave, H.R., 1998. *Elementary Statistical Tables*. Routledge, London, p. 48.
- Powel, F.C., 1982. *Statistical Tables for the Social Biological and Physical Sciences*. Cambridge University Press, London, p. 100.
- Zwillinger, D., Kokoska, S., 2000. *CRC Standard Probability and Statistics Tables and Formulae*. CRC Press, Boca de Raton, Florida, p. 200.

RELEVANT STATISTICAL REFERENCES TABLES

- Abramowitz, M., Stegun, I.A., 1965. *Handbook of Mathematical Functions: with Formulas, Graphs, and Mathematical Tables*. Dover, New York, p. 1046.

This page intentionally left blank

Gas Ionization Detectors

Georg Steinhauser and Karl Buchtela

Vienna University of Technology, Atominstitut, 1020 Vienna, Austria

Chapter Outline

I. Introduction: Principles of Radiation Detection by Gas Ionization	191		
II. Characterization of Gas Ionization Detectors	192		
A. Ion Chambers	192		
B. Proportional Counters	193		
C. Geiger–Müller Counters	193		
III. Definition of Operating Characteristics of Gas Ionization Detectors	193		
A. Counting Efficiency	194		
B. Energy Resolution	194		
C. Resolving Time	194		
D. Localization	194		
IV. Ion Chambers	194		
A. Operating Modes of Ion Chambers	195		
1. Ion Chambers Operating in the Current Mode	195		
2. Charge Integration Ionization Chambers	195		
3. Pulse-Mode Ion Chambers	195		
B. Examples and Applications of Ion Chambers	195		
1. Calibration of Radioactive Sources	195		
2. Measurement of Gases	196		
3. Frisch Grid Ion Chambers	196		
4. Radiation Spectroscopy with Ion Chambers	197		
5. Electret Detectors	199		
6. Fission Chambers	199		
V. Proportional Gas Ionization Detectors	200		
A. Examples and Applications of Proportional Counters	201		
		1. Gross Alpha–Beta Counting, Alpha–Beta Discrimination, and Radiation Spectroscopy Using Proportional Gas Ionization Counters	201
		2. Position-Sensitive Proportional Counters	203
		3. Low-Level Counting Techniques Using Proportional Gas Ionization Detectors	209
		4. Application in Environmental Monitoring, and Health Physics	210
		VI. Geiger–Müller Counters	214
		A. Designs and Properties of Geiger–Müller Counters	214
		1. Fill Gas	214
		2. Quenching	214
		3. Plateau	215
		4. Applications	215
		VII. Special Types of Ionization Detectors	216
		A. Neutron Detectors	216
		1. BF ₃ Tube Construction	217
		2. Detectors for Fast Neutrons	218
		3. Neutron Counting in Nuclear Analysis of Fissile Materials and Radioactive Waste	220
		4. Moisture Measurements	221
		B. Multiple Sample Reading Systems	221
		C. Self-Powered Detectors	222
		D. Self-Quenched Streamer	223
		E. Long-Range Alpha Detectors	223
		F. Liquid Ionization and Proportional Detectors	224
		G. Dynamic Random Access Memory Devices (DRAM)	224
		References	225

I. INTRODUCTION: PRINCIPLES OF RADIATION DETECTION BY GAS IONIZATION

When radiation penetrates matter, energy of the radiation is passed on to the matter and the radiation is shielded or even stopped. The atoms or molecules of matter are brought to a state of higher energy, an excited state, or they are ionized if the energy of the radiation is high enough.

Alpha, beta, and gamma rays are known as ionizing radiation. On passing through a gas, these radiations create positive ions and electrons. Those charged particles either cause chemical reactions or recombine, finally producing neutral specimens again. However, if an electric field is applied, the positive ions start to migrate to the cathode, and the electrons are attracted by the anode. If the field strength, the applied voltage per unit length, is high enough to prevent recombination during

migration of the ions and electrons, all of them arrive at the electrodes. They are collected at the electrodes, and by the detection of this electric charge using a suitable electric circuit, an indication of the presence of ionizing radiation is given.

Gas ionization detectors consist of a gas volume in an enclosure that is either sealed or constructed in such a way as to permit a continuous flow of the filling gas. Within that gas volume an electric field is applied across the electrodes. The outer wall frequently serves as one of the electrodes, the cathode, while a wire rod, a grid, or a plate in the middle of the gas volume serves as the anode.

Although there are many different variations in the design of gas ionization counters, a cylindrical system with a central wire or rod, called a "counting tube," is very common. Many designs with different shapes and geometries have been realized. Some of them are suitable for a very wide range of useful applications, some were designed for a very special investigation, and others have been realized only to learn more about the operating principles of ionization detectors in order to improve the performance of this type of radiation detection device.

In this chapter, a selection is given from numerous developments in the field of gas ionization detectors. It should be mentioned that radiation measurement methods today place emphasis mainly on radiation spectroscopy. Solid-state and scintillation detectors offer unique advantages in that field of applications. Nevertheless, a great deal of interesting and useful research work is still done using gas ionization detectors and new developments and applications are reported in the literature (Sauli 1998).

Many interesting developments have been made over the past decade or more in the field of position-sensitive gaseous detectors such as the microstrip gas chamber (MSGC) and gas electron multiplier (GEM) with good localization properties. These detectors are often referred to as micropattern gas detectors (MPGDs), because of their accurate position accuracy.

Although gas ionization detectors are extremely useful, problems and limitations have to be faced and careful planning of experiments to recognize and deal with those limitations is extremely important (Bateman et al., 1994). The suitability of gas ionization detector systems for a given kind and energy of radiation depends on the type (composition and pressure) of filling gas to be ionized; the applied field strength; the size, shape, and geometry of the detector volume and electrodes; and the type and thickness of the construction material that surrounds the detector gas volume. In addition, environmental factors such as temperature should not be entirely ignored. Finally, yet importantly, the design of the electric circuit that handles the output signal plays a very important role.

The geometric design of a detector also depends mainly on its application. The size and shape have to be chosen appropriately if small or large areas have to be surveyed by the detector; if it has to be submerged in a liquid; or if, by use of a suitably thin wall, alpha and low-energy beta particles are permitted to enter the detector volume; finally, if radiation energy has to be determined or if the localization or distribution of the radioactive material in a given specimen is of primary importance.

There are three kinds of gas-filled detectors: ion chambers, proportional counters, and Geiger-Müller counters. They differ

mainly in the strength of the electric field applied between their electrodes. Their common and different characteristics are discussed in this chapter.

II. CHARACTERIZATION OF GAS IONIZATION DETECTORS

A. Ion Chambers

Gas ionization detectors can be characterized by the effects created by different field strengths between the charge-collecting electrodes. The relationship between the pulse size produced and the potential applied across the electrodes of a gas ionization detector is shown in Fig. 3.1. The pulse size depends on the field strength and also on the type of radiation that enters the detector volume and creates ions.

At low field strength, many slowly migrating ion pairs still have the opportunity to recombine. This recombination region is not used for radioactivity detectors. As more voltage is applied, more ions and electrons produced by the ionizing radiation are collected at the electrode. Finally, a field strength is reached at which now rapidly migrating ions do not have a chance to recombine. Thus, a saturation region is reached where all the ions produced directly by the radiation event, the primary ions, are collected at the electrodes. A further increase of field strength cannot attract more ions because all of them have already been collected. Ion chambers operate in this region. The amount of charge collected at the electrodes directly shows the ionization effects of the incident radiation.

The design of ion chambers can be tailored for a special type of radiation and information about radiation energies can be provided. Since the output signal is directly related to the ionization effect, ion chambers are very useful in radiation dosimetry.

Alpha particles produce a great amount of ions along a short path length of travel (high linear energy transfer). They are easily detected, because they provide a high output signal. Beta particles and gamma rays produce a very low signal, and rather sophisticated circuits are sometimes needed for amplification of such low-voltage signals.

The following short calculation provides an example of the signal requirement of electronic circuits combined with ion chambers:

It is assumed that a radioactive source emits one alpha particle per second (activity 1 Bq) with an energy of 5 MeV, and all the energy of the alpha particles is deposited in the gas volume (air) of the counting chamber. The average ionization energy of that gas is 32.5 eV/ion pair. The rate of ion-pair formation in the gas is calculated as

$$\frac{5 \text{ MeV/alpha particle}}{32.5 \text{ eV/ion pair}} = 1.5 \times 10^5 \text{ ion pairs/alpha particle}$$

Thus 1.5×10^5 ion pairs or 1.5×10^5 electrons are produced by one alpha particle per second, corresponding to an electric charge of

$$(1.5 \times 10^5 \text{ electrons/s})(1.6 \times 10^{-19} \text{ C}) = 2.4 \times 10^{-14} \text{ C/s} \\ = 2.4 \times 10^{-14} \text{ A}$$

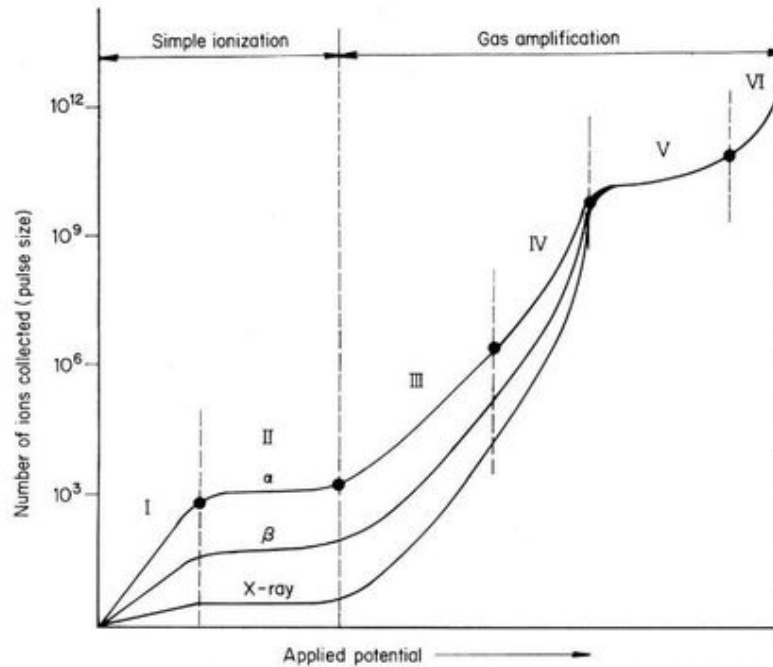


FIGURE 3.1 Relationship between the pulse size produced and the potential applied across the electrodes of a gas ionization chamber exposed to alpha, beta, and gamma radiation. Various regions are labeled by Roman numerals as follows: region I, recombination region; region II, simple ionization region; region III, proportional region; region IV, limited proportional region; region V, Geiger–Müller region; region VI, continuous discharge region. (From *L'Annunziata*, 1987. Reprinted with Permission from Elsevier © 1987)

B. Proportional Counters

If the field strength is increased further, additional ionization starts to occur because of the higher kinetic energy of the migrating primary ions. These primary ions, now being accelerated to a higher energy than the ionization energy of the detector gas, produce secondary ions by impact. With increasing field strength, a great number of additionally produced ions are accelerated, the number still being proportional to the number of primary ions. This gas ionization detector region (see Fig. 3.1) is called the proportional region. In that region, radiation with different abilities to produce primary ions (alpha, beta, or gamma radiation) can still be discriminated, or they are registered by “gross counting” without separation. Also, radiation of the same type but with different energies can be discriminated (Garcia-Leon et al., 1984).

With further gas multiplication due to higher field strength, some nonlinearities will be observed. This effect marks the beginning of the limited proportional region.

C. Geiger–Müller Counters

As the field strength is increased further, excitations of atoms and molecules are observed that, by the emission of ultraviolet light, can start additional ionization processes. In this region, referred to as the Geiger–Müller region, the total number of ions produced is independent of the number of primary ions

and, therefore, also independent of the type and energy of radiation. A further increase of the field strength causes a continuous discharge (see Fig. 3.1).

In the Geiger–Müller region, all primary ionization effects produce the same maximum response in the detector. Geiger–Müller counting tubes operate in this region and thus provide no direct information about the type and energy of radiation. Information related to the type and energy of radiation can be provided only by observing shielding effects related to this radiation. Alpha particles are stopped by a thin layer of matter, beta particles show a maximum range in penetrating a shielding material before they enter the detector, and photons show a somehow logarithmic decrease in intensity with increasing thickness of the material. In the earlier days of radiation measurements, such experimental setups were frequently used for rough determination of radiation type and energy (Chase and Rabinowitz, 1967).

III. DEFINITION OF OPERATING CHARACTERISTICS OF GAS IONIZATION DETECTORS

In the case of ionization detectors, as well as other detector types, some operating parameters are important for characterizing their capabilities: efficiency, resolution, and resolving time of the

detector. For some special detector designs, the position-sensitive detectors, also the capability to give precise information regarding the spatial distribution of particles or photons entering the detector volume is of importance.

A. Counting Efficiency

The efficiency refers to the number of particles or photons emitted by a radiation source related to the number of interactions registered by the counting system. This is usually called the absolute efficiency:

$$\text{Absolute efficiency} = \frac{\text{number of signals recorded by the detector}}{\text{number of particles or photons emitted by the source}}$$

All particles striking the detector volume may not be registered. Therefore, another kind of efficiency is used, which is called the intrinsic efficiency, and defined as

$$\text{Intrinsic efficiency} = \frac{\text{number of signals recorded by the detector}}{\text{number of particles or photons striking the detector}}$$

With ionization detectors, the absolute efficiency of charged particles can go up to nearly 100%. For gamma rays and X-rays, the efficiency is frequently much lower, because of the relatively poor interaction of the radiation with the gaseous detection volume of the ionization counters. Therefore, a higher density of the gaseous volume can sometimes be obtained by using a counting gas of high atomic number (xenon) and by increasing the gas pressure inside the ionization detector.

B. Energy Resolution

The energy resolution characterizes the ability of the detector to discriminate between two types of radiation with energies that are different but rather close to each other. A characteristic figure is given by the full width at half-maximum (FWHM), the width of a peak in a radiation energy spectrum display halfway between the baseline and top of the peak. If E_0 is the energy at the peak maximum and ΔE is the full width at half-maximum, the resolution is given as

$$R = \Delta E/E_0, \text{ which can also be recorded as a percentage.}$$

The value of the FWHM is a measure of the resolution. The smaller its value for a given energy line, the greater is the potential of a detector to provide individual information related to two radiations of approximate energy. Because of the statistical nature of any interaction of radiation with matter, resolution can never be perfect. In addition, electronic noise contributes to the deterioration of resolution.

Not all detectors can provide information about radiation energy.

C. Resolving Time

The resolving time refers to the minimum time interval a detector needs to recover from the interaction with a radiation

event and be able to register a following event. For many counting devices, not the resolving time of the detector but the resolving time of the electronic system (e.g. the data handling and processing steps) sets the limits for dealing with high count rates. Counting losses induced by resolving time of a counting system can be a limiting factor in measurements. Several methods for resolving time determination and correction are presented in the literature (Gardner and Liu, 1997; Lee and Gardner, 2000; Vinagre and Conde, 2001).

D. Localization

Some detector designs can give information about the entrance region of particles or photons into the detector or about the distribution of radioactive material in a sample. They can give an image of a radioactive specimen by showing the longitudinal or even two-dimensional distribution of radioactivity.

Position-sensitive detectors based on proportional counting systems were developed by Nobel Laureate Georges Charpak in the 1960s, and these played a decisive role in many discoveries in particle physics. These types of detectors, providing the opportunity of "nuclear imaging," are nowadays very important also in many experiments in biology and medicine (Charpak, 1970; Charpak and Sauli, 1978; Geltenbort, 1994; Nickles et al., 2002; Shekhtman, 2004; van der Graaf, 2011; see also Chapter 19).

IV. ION CHAMBERS

Ionization chambers can be considered as one of the simplest devices for radioactivity measurements. They were used in the very early days of research dealing with the detection of ionizing radiation. But even today new designs for special purposes are developed.

The chamber is made of a nonporous material, the electrodes are usually parallel plates, and the filling gas may have a pressure from a few tenths up to some tens of bars. When ionizing radiation passes through the gas, ion pairs are created. If a sufficiently high-voltage gradient prevents recombination, these ions drift toward the electrodes. The output signal registered by the electric circuit can be a flow of current, a charge or voltage pulse, or a total collected amount of electrical charge. Thus, three types of ion chambers are known: ion chambers operating in the current mode, ion chambers operating in the pulse mode, and electrostatic or charge integration ion chambers.

With ion chambers operating in the current mode, an electrical current flow is registered, which is initiated by the electrons and ions collected at the electrodes during the time of observation. With the pulse-mode type of chamber, single signals, such as voltage pulses created by the ions arriving at the electrodes from a single ionization event, are registered by applying suitable electronic amplification circuits. Electrostatic or charge integration ion chambers are similar to electroscopes. A static electric charge is given to a system consisting of a thin foil or fiber that is suspended parallel to a solid support or to a second fiber or foil. Because of the repulsion of like charges, the fiber or foil will be bent to stay at some distance away from

the support of the second foil or fiber. Ionizing radiation gradually discharges the system, and this causes the foils or fibers to move back to their original position.

Because of their simple construction and relatively low cost, ion chambers still have many applications. Information related to the type and energy of radiation can be obtained, and the ion chambers can be designed for the detection of low as well as high radioactivity levels. Many kinds of gases can be used to fill the detector volumes.

A. Operating Modes of Ion Chambers

1. Ion Chambers Operating in the Current Mode

One of the most important applications of an ion chamber in everyday radiochemistry is as a portable survey instrument for radiation monitoring purposes. A volume of counting gas, mostly air, is enclosed within walls made of metal-lined plastic or aluminum. These types of walls are "air equivalent." Thus, accurate measurements can be made for gamma radiation if the energy of the gamma radiation is high enough to penetrate the walls without significant attenuation and also low enough to establish electronic equilibrium in these walls. Usually, for gamma radiation with energy lower than 50 keV, attenuation effects have a considerable impact on the efficiency of such detectors. With these instruments, the saturated ion current is measured by using an electrometer circuit that is battery powered. Converting the DC signal of an ion chamber to an AC signal provides a more stable amplification, such as with the vibrating-reed electrometer or dynamic capacitor.

2. Charge Integration Ionization Chambers

A frequently used type of ionization counter is operated on the charge integration principle. This type of ionization chamber is charged initially. The drop of charge during exposure to a radiation field can be measured using a charger-reader mechanism and provides information regarding the dose from the radiation field to which the ionization chamber was exposed.

A familiar device is the ionization pocket chamber. These ionization chambers are also charged initially, but they are equipped with a small integral quartz fiber electroscop. An initial charging sets the scale of the electroscop to zero. The total integrated dose can be read periodically by observing the migration of the quartz fiber. This can be done very simply by optical observation, just by holding the pen-shaped pocket chamber up to a source of light and looking at the scale of the fiber electroscop through a small integrated magnifying glass. The accuracy and sensitivity of these devices are limited by leakage current across the insulator material of the ionization chamber.

3. Pulse-Mode Ion Chambers

Like other ionization detectors, such as proportional counters and Geiger-Müller tubes, ionization counters can also be used in pulse mode, in which each separate alpha particle, beta particle, or gamma quantum creates a distinguishable pulse

signal. Advantages of pulse-mode ionization chambers are their sensitivity and the ability to measure the energy of radiation and thus to be applicable in radiation spectroscopy. Today, such pulse-mode ionization chambers have been mostly replaced by semiconductor detectors. Nevertheless, for special applications, such as neutron counting facilities, such chambers are still in use.

Pulse amplitudes from all types of ion chambers are relatively small. In theory, the maximum signal amplitude accumulated from the ion pairs produced by the interaction of, for example, an alpha particle in air along its track within the chamber is of the order of 10^{-5} V. Such a signal can be processed, but rather sophisticated electronic systems are required. Pulses from a single-photon interaction are a hundred times smaller, and successful and accurate amplification is difficult and at times even impossible. Internal amplification within the detector volume, which is described in the section of this chapter dealing with proportional counting tubes, helps to overcome these problems.

In any case, it has to be taken into account that for some filling gases, such as propane, the energy response to beams of heavy ions depends also on the atomic number of the observed ions and, as a consequence, deficits of the pulse heights are sometimes considerable. This is not only due to ion energy loss via elastic collisions in the filling gas (e.g. propane) but most probably also due to electron-ion recombination within the dense ionization column created by the incident ion beam. This may be of importance for many types of gas ionization detectors used for the spectroscopy of ion beams with higher atomic mass (Weijers et al., 2002).

B. Examples and Applications of Ion Chambers

1. Calibration of Radioactive Sources

Standardization of gamma-emitting radionuclides (e.g. in nuclear medicine applications) is frequently carried out by comparing the ion current from a material with unknown activity with the ion current produced by a standard material of the same radionuclide. In that way, one takes advantage of the excellent long-term stability and reproducibility of the ion current produced from the same type of radiation. When operating in the saturation region, the current depends only on the geometry and the activity of a given radioactive material. Chamber volumes can be up to several 1000 cm^3 , and the walls are made of solid materials, such as steel or brass. The collecting electrode in the inner part is made of a thin metal foil to avoid as much as possible attenuation of the radiation.

High sensitivity can be obtained if pressurized gas is used for the ionization chamber. Of course, this will cause the background current to increase but not be as great as that produced by radiation sources. Pressurized chambers are used for the measurement of gamma-emitting nuclides.

The ion chamber region is usually reached by adjusting the voltage for the electrodes. Saito and Suzuki (1999) used a multielectrode ion chamber for measuring absolute fluence rate of X-rays. They adjusted the ion chamber region by varying the gas pressure at a given voltage.

2. Measurement of Gases

Many radioactive gases can be incorporated into the filling gas of ionization detectors. Also, in ionization chambers a gas can be sampled on a continuous flow-through basis. The ionization current produced by a gas can be calculated simply and straightforwardly only if the radiation is fully absorbed in the gas volume of the ionization chamber. These types of flow-through ionization chambers are used for monitoring air that contains small amounts of radioactive gas. In any case, a number of difficulties arise if the air is subject to atmospheric changes. Such perturbations of air properties can be due to the content of aerosols, moisture, ions, etc. (Jalbert and Hiebert, 1971; Mustafa and Mahesh, 1978; Waters, 1974).

Some interesting examples of flow-through ionization chambers are the activity measurements of ^{76}Kr and ^{85}Kr (Cooper et al., 2004 and Yunoki et al., 2010). The flow-through gaseous radiochemical method (FGRM) was demonstrated by Lebedev et al. (2006) as a useful method for monitoring the release of radioactive inert gas molecules formed as a result of nuclear reactions. When a radioactive gas isotope is released from an ampoule-loaded target material, the radioactive gas, that is released, is transported by a carrier gas into a gas counter for flow-through measurements. Lebedev et al. (2006) demonstrated that the activity I in disintegrations per second (dps) of radioactive inert gas in the counter was related to the flux of ionizing radiation (e.g. proton beam)

$$I = \frac{V_C P_C N_0 \sigma \phi}{1.44 t L}$$

where V_C is the active volume of the gaseous counting chamber in cm^3 , P_C is the pressure of the counter in physical atmospheres, N_0 is the number of atoms of target material, t is the half-life of the radioactive inert gas in seconds, σ is the cross section of a nuclear reaction for the formations of a radioactive isotope of an inert gas averaging in a spectrum of ionizing radiation, ϕ is the flux of ionizing radiation in $\text{cm}^{-2} \text{s}^{-1}$, and L is the consumption of transport gas in cm^3/s .

Yakushev et al. (2004) used a flow-through ionization chamber as a valuable tool in the identification and measurement of the decay properties element 112. An Ar-CH₄ mixture was used as the carrier and counting gas used to transport element 112 into an ionization chamber 5000 cm^3 in volume. The IUPAC (2010) officially approved the name copernicium, with symbol Cn, for the element with $Z = 112$ on 19 February 2010.

The change of ionization current due to smoke particles is the operational basis for smoke detectors. In such smoke detectors, a built-in alpha source provides a constant ionization current under normal atmospheric conditions. A twin chamber with enclosed air without flow-through capability is used for the reference ion current.

The design of twin chambers can also be used for background compensation. A twin chamber filled with pure air records the background without flow through of the air to be monitored. In that way, compensation for a changing background can easily be achieved, for example, in case of a changing gamma ray background during air monitoring.

Current mode ion chambers have been very useful in the measurement of radon. The background is low and the counting efficiency high (practically 100%). Experiments have also been reported to provide data for the radon content of groundwater by placing an ion chamber together with a known amount of water for three hours in a leak-proof container. The amount of radon in the air can be related to the concentration of radon in the water sample (Amrani et al., 2000).

Tritium measurements using ion chambers present a problem if elastomeric seals are applied. Those elastomeric materials are irreversibly contaminated and the background of the ion chamber is increased. Colmenares (1974) constructed a chamber using ultra-high-vacuum metallic seals, a metal construction of negligible water adsorption capacity and sapphire as insulator material. The chamber is bakeable up to 450 °C and the contamination problems are avoided.

3. Frisch Grid Ion Chambers

Because of the slow ion mobility in gases and the slow drift of ions at the applied field strength in ion chambers, the use of pulse-type ion chambers is restricted to low pulse rates if signals are desired that are related accurately to the original charge of ions and electrons generated by the radiation. Pulse-shaping circuits designed for low frequencies also make these systems rather susceptible to interference from microphone signals produced by mechanical vibrations.

Therefore, pulse-type ion chambers are frequently operated in such a mode that they sense the collected electrons only, not the created positive ions, which migrate much slower than the electrons. In that case, the pulse amplitude is related to the drift of the electrons only. The signal therefore has a much faster rise time, and higher counting rates can be successfully registered. However, since the amplitude of the signal now depends also on the position of the interaction within the ion chamber gas, there is no well-defined information related to the total number of ions created, which means that no information about the energy of the radiation is provided. However, methods have been developed to overcome the problem of the dependence of the pulse amplitude on the position of the interaction within the chamber. The region of the chamber volume is divided into two parts by a grid. This grid is maintained at a potential between those of the cathode and anode. The mechanical construction of the grid should allow electrons to pass through; it should be as "transparent" to electrons as possible. By suitable positioning of the radiation source outside the chamber or by effective collimation of its radiation, the emitted particles or rays interact with the gas in the ion chamber in a well-defined region between this grid and the negative electrode of the chamber. Thus, positive ions simply migrate to the cathode. Electrons are attracted by the transparent grid initially but are further accelerated toward the anode, which is at a much more positive potential than the transparent grid.

Electronic circuits are designed in such a way that, with the electron migration from grid to anode, the voltage between grid and anode drops and a signal is created that depends only on the electron drift and not on the migration of both electrons and cations. Therefore, the slow rise related to ion drift is

eliminated. Also, since all electrons are accelerated by the same potential difference, the amplitude of the pulse is independent of the position of the interaction. The amplitude is proportional only to the number of ion pairs, the number of electrons produced along the path of the interacting particle or ray. This type of ion chamber is called a Frisch grid chamber after Otto Robert Frisch who designed the detector (Knoll, 2010). Such Frisch grid chambers have been extremely useful in studies dealing with particle physics.

Gridded ionization chambers are ideally suitable for studies related to nuclear fission, because such detectors not only have a practically 100% detection efficiency but can also provide information about fission fragment properties such as energy, mass, charge, and emission angle. Tutin et al. (2001) designed an efficient device for such investigations, consisting of a combination of two parallel plate ionization chambers with grids and a common central cathode plate. (Fig. 3.2). The central aluminum disk cathode has a hole of 78 mm diameter where two thin aluminum foils, covered with uniform layers of thorium-232 or uranium-238 (fissile upon high-energy neutron capture), are mounted back to back. The grids are mounted on aluminum annular disks with an inner diameter of 160 mm and consist of tungsten wires 0.1 mm in diameter spaced by 1.25 mm. The chamber is filled with 90% argon and 10% methane at atmospheric pressure without continuous gas flow. Fission fragments emitted from the cathode are stopped in the space between the cathode and anode, free electrons drift to the anode, whereas the slow ions can be treated as being static for a short interval of time. At the end of the electron drift, the

collected charges can be related to the emission angle of the fission fragments. In a continuation of these studies, a similar multisection Frisch-gridded ionization chamber was designed by Ryzhov et al. (2006) to measure neutron-induced fission cross section of various radionuclides.

There are also applications in the life sciences. Lohmann et al. (1998, 2003) used a detector system of the Frisch grid chamber type in angiography for the determination of contrast agent (iodine) by "dichromography." According to this method, two images with monochromatic X-rays just below and above the absorption edge of the contrast agent are simultaneously obtained and subtracted. Although monochromatic X-rays having suitable intensity to visualize arteries of 1 mm diameter are only provided by synchrotron radiation, the authors concluded that the requirements for application of intravenous coronary angiography are fulfilled with the Frisch-gridded detector.

4. Radiation Spectroscopy with Ion Chambers

Pulse-type ion chambers have attracted some interest again, after years during which most of the interest was focused on semiconductor detectors. Ion chambers can be designed and constructed in any shape and size, and for charged particles the pressure can be tailored to an optimum for a desired stopping power (Fulbright, 1979). Also, there is practically no deterioration or degradation due to irradiation, which may adversely affect the application of ion chambers in radiation fields, and ion chambers can be fabricated by using available workshop facilities without high expenses.

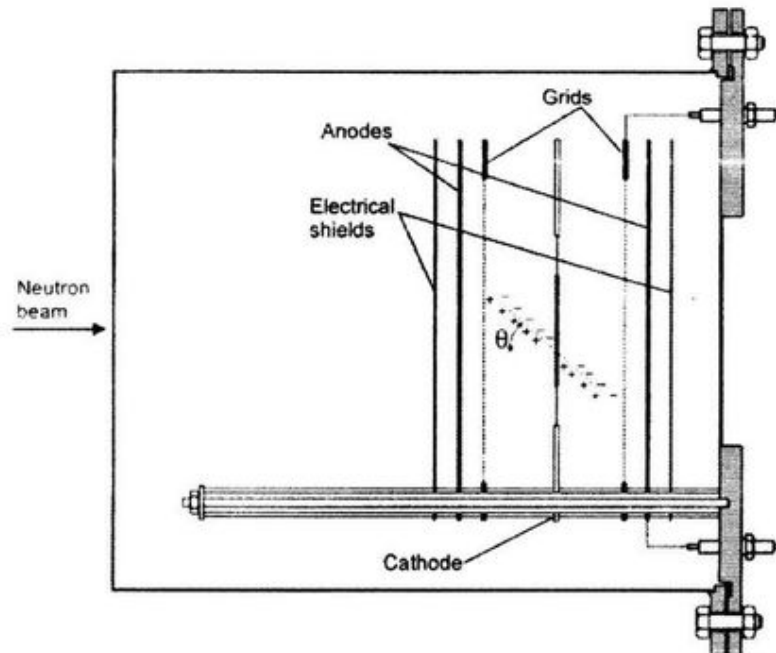


FIGURE 3.2 Schematic picture of a parallel gridded ionization chamber with one common cathode. (From Tutin et al., 2001. Reprinted with Permission from Elsevier © 2001)

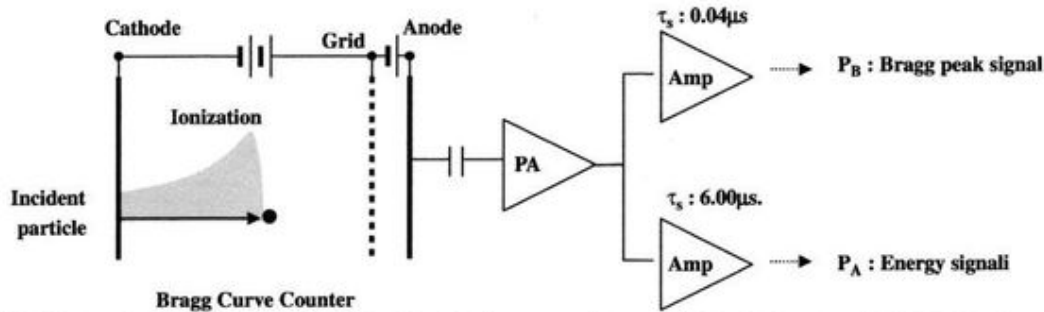


FIGURE 3.3 Schematic diagram of the electronic circuit to derive the incident energy and Bragg peak information from the anode of a BCC. The short and long shaping times are set to be 0.04 and 0.6 μ s, respectively. (From Hagiwara et al., 2008, Reprinted with Permission from Elsevier © 2008)

Pulse-type ion chambers have been applied in low-level alpha measurements, and good resolutions have been obtained that may even be comparable with the resolution of semiconductor detectors (Gruhn et al., 1982; Bertolini, 1984; Hoetzel and Winkler, 1984; Shenhav and Stelzer, 1985; Kotte et al., 1987; Nowack, 1987; Domnikov et al., 2001; Beck et al., 2009; Kada et al., 2010).

It was demonstrated that additional information regarding charged particle properties such as atomic number and charge state can be obtained by designing a chamber in such a way that particle pathways are parallel instead of perpendicular to the direction of the electric field. Thus, the drift time of electrons to the grid will be different for electrons created at the beginning of the track and those from the end of the path. The shape of the output pulse will therefore reflect the distribution of ion pairs along the track according to what is called a Bragg curve. With that technique, known as Bragg curve spectrometry, additional information such as atomic number and particle charge can be obtained. For that a detailed analysis of the pulse shape is necessary.

Hagiwara et al. (2008) developed a method to extend the energy acceptance of a Bragg curve counter (BCC) at the high-energy end. They applied this method to the measurement of lithium and beryllium ions emitted from carbon in the course of the bombardment by 70 MeV protons. A schematic diagram of the BCC and its signal-processing scheme, devised by Hagiwara et al. (2008), is illustrated in Fig. 3.3. A Bragg curve derived from the ionization intensity produced by an incident particle is illustrated in the figure by the shaded area above the particle path. From the Bragg curve, the Bragg peak signal PB and energy signal PE are obtained by the use of two pulse-shaping amplifiers with short (0.4 μ s) and long (6 μ s) shaping times, respectively. The long shaping time is longer than the drift time of the free electrons traveling from the cathode to the grid. A charge-sensitive preamplifier (PA) integrates and amplifies the original signals from the BCC before reaching the pulse-shaping amplifiers. Fig. 3.4 illustrates the 2-dimensional spectrum obtained when plotting PB versus PA (i.e. Bragg peak pulse height versus energy) illustrating clear

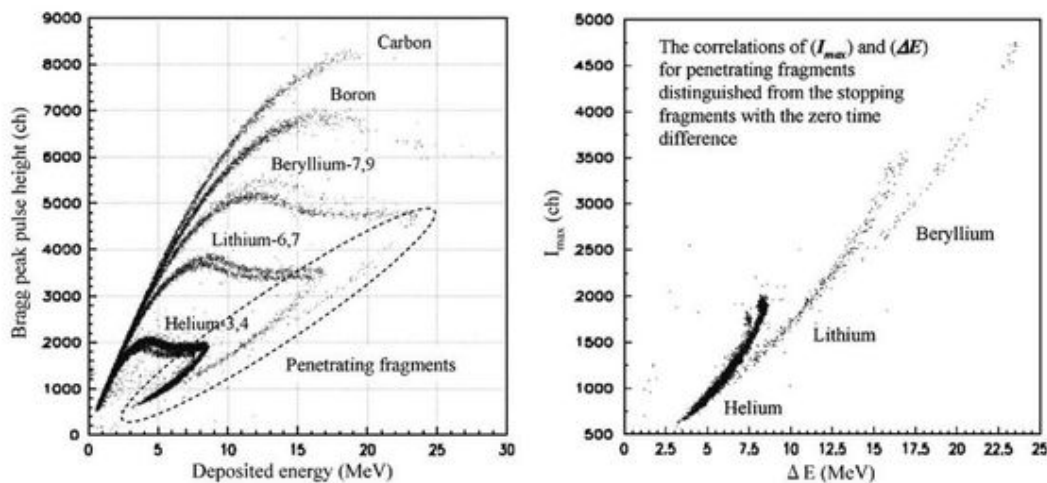


FIGURE 3.4 The two-dimensional spectrum of deposited energy versus Bragg peak of fragments emitted from a 4- μ m-thick polypropylene sample at 30° by 70-MeV proton-induced reaction. The dotted circle indicates the events of the penetrating fragments (i.e. those that pass through the BCC). The left-hand figure shows all events. The right-hand figure shows the correlations of I_{max} and ΔE for penetrating fragments from the fragments that stop within the active volume of the BCC. (From Hagiwara et al., 2008, Reprinted with Permission from Elsevier © 2008)

particle discrimination for particles that deposit all of their energy within the BCC (left-hand spectrum); however, interferences are observed due to high-energy particles capable of passing through the BCC (Fig. 3.4, dotted circle). Hagiwara et al. (2008) distinguished the high-energy particles (i.e. fragments) that penetrated the BCC counter by plotting I_{\max} (i.e. maximum ionization) against deposited energy (ΔE) as illustrated in Fig. 3.4.

Khriachkov et al. (2000) used an alpha particle spectrometer based on a Frisch grid chamber for studies of (n,α) -reactions induced by fast neutrons. Energy and emission angle of alpha particles could be determined.

Combinations of ionization chambers with position-sensitive ionization detector devices were used by Menk et al. (2000) for small-angle X-ray scattering (SAS) investigations. These systems are intended to be used for experiments in some European synchrotron centers.

Nariyama et al. (2004) developed a portable free-air ionization chamber for measurements of synchrotron radiation up to 150 keV. For high-energy X-rays, the plate separation becomes rather large and therefore the authors developed a special design to overcome that difficulty.

5. Electret Detectors

Electret types of ion chambers make use of the drop of surface voltage on a plastic material. The plastic specimen is a dielectric material, usually Teflon, which is quasi-permanently charged. It is called an electret and usually has the shape of a disk about 1 mm in thickness and 10 mm in diameter. Electrets are prepared by being heated and simultaneously exposed to an electric field. In this process, many dipoles in the material become oriented in a preferred direction. After heating, the material is "frozen" and keeps the position of its electric dipoles for a long period of time. A voltage gradient of several hundred volts can be maintained between the surfaces of the electret disk.

One surface of the electret is kept in contact with the wall of an ion chamber which builds up an electric field in the chamber. Ionizing radiation causes a decrease of charge in that system, resulting in a partial neutralization of the charge at the electret. Measurement of the electret voltage difference before and after irradiation allows determination of the amount of ionization. The system has to be calibrated and can be used for determination of environmental radiation doses.

Amrani et al. (2000) used an electret ion chamber for the determination of the radon content of groundwater. They put an electret ion chamber together with a known amount of water in a leak-proof container. The reading of the electret ion chamber provides the radon content in the air and this value could be related to the concentration of radon in the water sample. Electret detectors are commonly used as radon monitors in the environment including water and soil (Hamlat et al., 2003, Kitto et al., 2008, and Grossi et al., 2012), construction materials (Lavi et al., 2009), and in the public living and workplace (Denman et al., 2005; Righia et al., 2005; Papachristodoulou et al., 2010; Clouvas et al., 2011, and Okeji and Agwu, 2012). The electret ion chamber is simple in design. An example of an

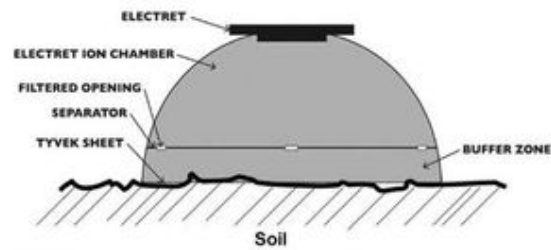


FIGURE 3.5 Scheme of an electret ion chamber for the measurement of radon flux from soil. The radon diffuses through the Tyvek® window and into the electret ion chamber. The radon activity (Bq/m^3) is proportional to the potential drop due to radon decay on the positively charged electret located at the top of the ion chamber. (From Grossi et al., 2012. Reprinted with Permission from Elsevier © 2012)

electret detector used for the measurement of radon flux from soil is illustrated in Fig. 3.5. Radon and thoron gas from the soil surface diffuse through the Tyvek filter into a buffer zone. Tyvek® is a brand of flash-spun high-density polyethylene fibers, impermeable to water, but permeable to gases. The radon and thoron enter into a buffer zone specifically designed to reduce any thoron that may be present (Kotrappa and Steck, 2009 and Grossi et al., 2012).

6. Fission Chambers

For power monitoring purposes in nuclear reactors, miniaturized ion chambers have been constructed that are equipped with stainless-steel walls lined with highly enriched uranium. Argon at a pressure of several bars is mainly used as a filling gas. Because of the high pressure, the dimensions of the detector volume can easily be kept larger than the range of the fission products created by the uranium-235 (n,f) reaction.

Long-term operation causes problems because of the burn-up of the fissile material (Böck and Balcar, 1975). To compensate for this, the so-called regenerative chambers have been designed. These chambers contain a combination of fertile (^{238}U , ^{234}U) and fissile (^{235}U , ^{239}Pu) material as a lining of the inner detector walls. Fission chambers may also show a memory effect after a prolonged period of operation in a reactor core. This is due to a buildup of fission products in the detector volume. Because of the fission product activity, some residual ionization still can be measured even without exposure to a flux of neutrons.

Because of the scarcity of conventional enriched uranium-235 material, fission detectors have been developed on the basis of uranium-233. Fig. 3.6 shows a schematic diagram of the uranium-233 fission chamber designed by Prasad and Balagi (1996). The chambers were filled with argon (97%) and nitrogen (3%) at 1 bar. Low and high sensitivities were obtained by using two kinds of electrode coatings. Low-sensitivity counters have a uranium-233 coating on the anode and high-sensitivity counters have a coating on the cathode. The main disadvantage of uranium-233 is its high specific alpha activity. This can cause pileup effects and spurious counts if the system is applied in pulse-mode operation.

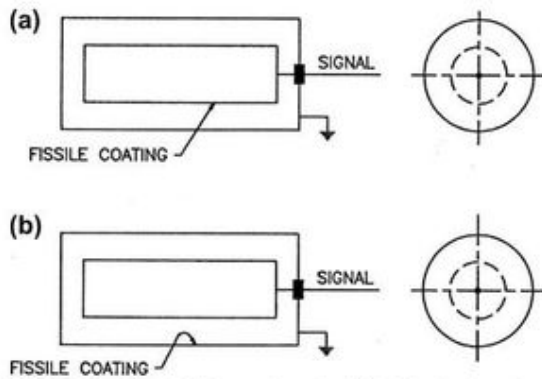


FIGURE 3.6 Schematic diagram of uranium-233 fission chambers. Low-sensitivity counters have a uranium-233 coating on the anode (a) and high-sensitivity counters have a coating on the cathode (b). The electrode spacings are 4 mm. (From Prasad and Balagi, 1996. Reprinted with Permission from American Institute of Physics © 1996)

Filliatre et al. (2008, 2009) found ^{242}Pu to be the best-suited fissile deposit for the fission chamber on-line measurement of the fast component of a high neutron flux ($\sim 10^{14} \text{ n cm}^{-2} \text{ s}^{-1}$) with significant thermal component. This was confirmed by Cabellos et al. (2010) with tests on the use of various fissionable materials in fission chambers. They found fission chambers with deposits of ^{242}Pu to be stable with fluences as high as 10^{22} n/cm^2 while satisfying high-sensitivity coefficients to fast neutrons.

A fission chamber of 3-mm diameter and $300 \mu\text{g}$ of ^{238}U deposit with argon filling gas at 5-atm pressure was used by Rapisarda et al. (2011) for the detection of fast neutrons in mixed neutron-gamma fields. The fission chamber was surrounded with a gadolinium (Gd) screen to cut off the thermal neutron component. The typical calculated neutron spectra at the position of the most sensitive part of the fission chamber with and without the Gd screen is illustrated in Fig. 3.7. The thermal neutron component is completely cut out by the Gd; however, the epithermal part (1 eV – 100 keV) is almost unaffected. The Gd screen obviously has a defined lifetime, due

to complete burn-up of the ^{155}Gd and ^{157}Gd isotopes, which are completely consumed for a 0.6-mm-thick Gd foil at a thermal neutron fluence of $2 \times 10^{21} \text{ n/cm}^2$.

Transmutation of transuranium elements by fast neutron-induced fission could be a promising way to reduce the long-term radiotoxicity of these materials in radioactive waste. In order to measure on-line, the fission rate of actinide targets a new generation of microfission chambers that have been constructed by Fadil et al. (2002) for the use at the high-flux reactor in Grenoble at a flux density of $10^{15} \text{ cm}^{-2} \text{ s}^{-1}$. To avoid pulse pileup, the chamber has to operate in current mode. Helium, a gas with high ionization potential, is used under such high flux conditions. Consequently, the problem of gas leakage during operation of the chamber at high temperatures has to be considered.

V. PROPORTIONAL GAS IONIZATION DETECTORS

Proportional gas ionization detectors operate at a higher-voltage gradient than ion chambers. The primary ion pairs created by ionizing radiation are accelerated much more and acquire a high kinetic energy. By colliding with other atoms or molecules along their drift, these ions and electrons induce secondary ionization. More ions and electrons are released with energy for further ionization of the filling gas. This multiplication process is called a Townsend avalanche or Townsend cascade. The anode wire must be very thin to obtain a region of sufficient field strength by applying a reasonable voltage. The gas amplification takes place mainly in the region of high-voltage gradient near the anode wire. Still, this amplification can be kept linearly proportional to the original ionization; the number of ions after gas amplification is proportional to the number of primary ions created by the ionizing radiation directly. Detailed explanations and descriptions of phenomena in gas ionization proportional counters are given by Charpak (1970) and Charpak and Sauli (1978).

Proportional counting tubes can be sealed, with the source of radiation kept outside the tube. A thin window permits radiation

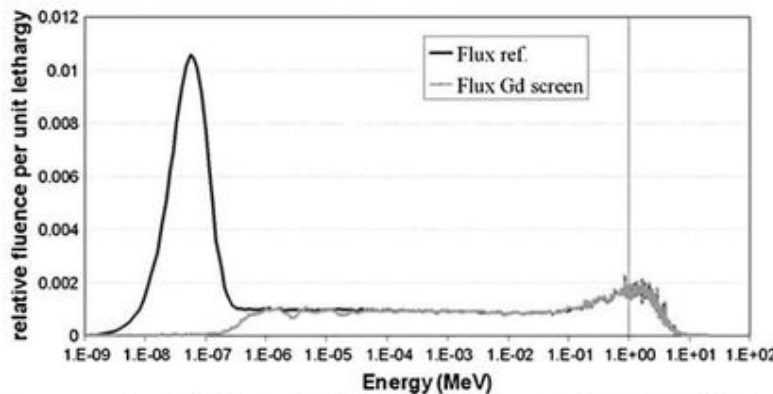


FIGURE 3.7 Calculated neutron spectra from a ^{238}U fission chamber with and without a Gd screen. (From Rapisarda et al., 2011. Reprinted with Permission from Elsevier © 2011)

penetration into the detector volume. Another configuration is designed for flow through of gas and the sample can be inserted into the detector volume. These “windowless” counting systems are useful for the detection of alpha particles and low-energy beta particles. A maximum counting efficiency of 50%, theoretically for a 2π counting geometry, is achieved. A 4π geometry can be achieved by using two flow-through tubes with the sample mounted on a thin foil between the tubes.

Proportional counters usually operate in the pulse mode.

For proportional counters, special gases or mixtures of gases have to be used. The filling gas should not form anions and should not contain components that attract electrons. The noble gases meet this requirement optimally. The formation of secondary Townsend avalanches should also be avoided. Such secondary avalanches are created by the emission of ultraviolet (UV) photons. This light is produced in the course of deexcitation of molecules or atoms of the filling gas. To prevent this effect, a component is added to the filling gas that absorbs the energy from the excited species. This additive must get rid of the energy through nonradiative modes, such as dissociation. By this mechanism, the ion cascade is localized near its origin and propagates only along the electric field. No other secondary avalanches are created. A frequently used filling gas consists of 90% argon and 10% methane and is called P10 gas (Alkhozov et al., 1967; Marouli et al., 2007, 2010, and Phillips et al., 2010).

Other gas mixtures (Penning gas) consist of a noble gas (neon or argon), the parent gas, with a small amount of an additive (e.g. methane, acetylene, or TMA) of lower ionization energy than the lowest excited state of the parent gas (Jarvinen and Sipila, 1984; Agrawal et al., 1989; Sakurai et al., 2003).

Gas amplification factors of 10^4 can easily be obtained. Therefore, rather simple electric circuits can be used for pulse amplification and pulse handling. Also, the effects of electronic noise can easily be avoided, because the output pulses created by that phenomenon are small.

Gas gain in proportional counting should be an exponential function of the applied high voltage. But in proportional counters filled with mixtures of argon and a low amount of a molecular gas, secondary avalanches develop and as a consequence gas gain increases faster than exponentially with the applied high voltage (Bronic and Grosswendt, 2001; Curzio et al., 2005).

Proportional counters, using the fast pulses from electron collection, have a short resolving time of less than 1 μ s. Proportional counters have a high intrinsic efficiency for alpha and beta particles. Photons are detected mainly by Compton effects produced in the walls of the counter. Thus, the intrinsic efficiency for gamma rays is rather low, especially for gamma photons with higher energies.

Counting losses with proportional counters are due to wall effects and to nondetection of beta particles with very low energy. Stanga et al. (2002) proposed a calculation model for the correction of counting losses. By means of such calculations, the accuracy of internal gas counting methods can be improved and tedious and time-consuming energy calibration procedures can be shortened or even avoided. Proportional counting (PC) is frequently applied to the preparation of reference sources by absolute activity measurements also referred to as radionuclide

standardization. Such radionuclide standardization methods involving joint proportional and solid scintillation detector arrangement [i.e. $4\pi\beta(\text{PC}) - \gamma\text{NaI}(\text{Tl})$ counting] counting are discussed in Chapter 14.

Aging effects in gas detectors under irradiation have been observed by Niebuhr (2006). The damage depends on the amount of radiation seen applied on the detector, but, in addition, many other parameters such as gas composition, gas quality, particle rate, and particle type play an important role.

Pulse-shape analysis can be used to reduce background effects or any undesirable events (Pandola et al., 2004). Background pulses frequently show a longer rise time than the desired signals of events to be measured.

A. Examples and Applications of Proportional Counters

1. Gross Alpha–Beta Counting, Alpha–Beta Discrimination, and Radiation Spectroscopy Using Proportional Gas Ionization Counters

With gross alpha–beta counting no attempt at any discrimination is made. Just the sum of all alpha and beta particles is detected. Gas proportional counting is one of the methods frequently used for gross counting (Passo and Kessler, 1992).

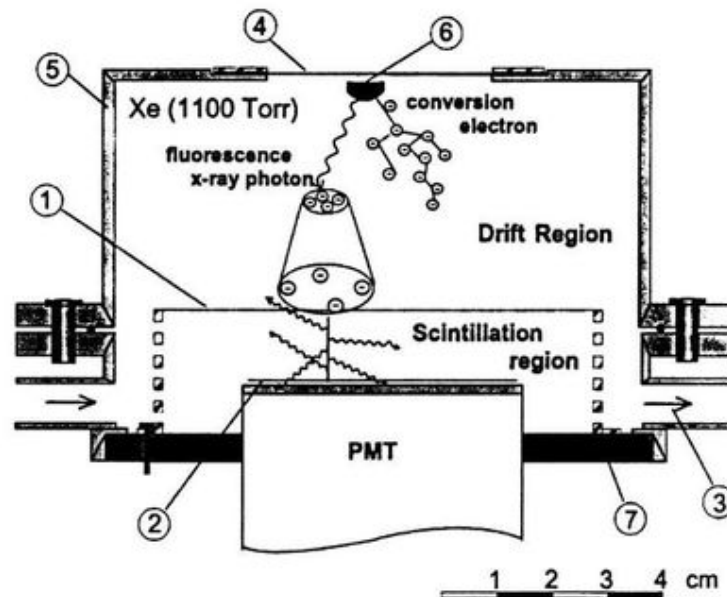
Proportional counters are also frequently used to distinguish between alpha and beta particles from a mixed source (Waples et al., 2003; Vasile et al., 2010; Dueñas et al., 2011, and Thakur and Mulholland, 2011). Alpha particles, with their high linear energy transfer, produce a high number of interactions with the gas in the detector volume. A beta particle produces a much lower number of ions per centimeter along its track than an alpha particle. The gas amplification factor is constant at a given voltage, so the output pulse is much higher for interactions of alpha particles compared with beta particles. With a suitable discriminator level or gate, the pulses created by alpha particles can be detected at a rather low-voltage setting. For the detection of beta particles, a higher voltage has to be used to overcome the discriminator level.

The alpha particles from a mixed source are registered at a lower voltage, the alpha plateau. At a higher voltage, alpha and beta particles are detected and gross alpha–beta counting is accomplished (L'Annunziata, 1987).

Alpha and beta radiation can also be discriminated according to the pulse length. Alpha pulses have a different pulse shape than beta pulses. Semkow and Parekh (2001) could demonstrate that alpha-radioactivity can be measured accurately in the presence of beta-radioactivity but the opposite is not always true due to alpha to beta cross-talk. This cross-talk depends mainly on the alpha-decay scheme and is due to the emission of conversion electrons, Auger electrons, and X-rays.

It is usually assumed that the counting efficiency of a 2π geometry alpha particle detector is 50%. Unfortunately, this is not true in practical measurements, because of self-absorption and backscattering. Several theories have been developed for the calculation of backscattering and self-absorption effects. Rodríguez et al. (1997) have presented a review on these topics and also developed new theories. Backscattering depends on the

FIGURE 3.8 Design of a gas proportional scintillation counter, 1. grid mesh with high electron transparency, 2. grid evaporated onto the photomultiplier, 3. to xenon gas purification system, 4. thin aluminized plastic window, 5. Stainless-steel enclosure, 6. Cd-109 source, 7. insulating material. (From Rachinhas et al., 2000, Reprinted with Permission from Elsevier(c) 2000)



atomic mass of the backing material of the radiation source. Corrections can be found experimentally by preparing samples of various thickness and extrapolation to zero sample thickness. But such determinations are only possible with a radioactive material with suitable long half-life.

To a limited extent, proportional counters can also be used for radiation spectroscopy (Jarvinen and Sipilä, 1984; Jahoda and McCammon, 1988). Pulse-height analysis can be applied for radiation spectroscopy for a given type of radiation. To perform pulse-height analysis properly, the particles or rays to be analyzed have to release their entire energy within the gas volume of the counter; that is, they must be totally absorbed within the counter. Proportional detectors are used for X-ray spectrometry in the field of X-ray fluorescence analysis, if high resolution is not required. Because of the gas amplification process, proportional counters have a poorer resolution than ion chambers. Today, mostly semiconductor detectors are used for X-ray spectroscopy (dos Santos et al., 1989, 2001).

Szaloki et al. (2000) have reviewed the essential progress in X-ray spectroscopy and they point out that although the gas-filled proportional detectors are not superior to semiconductor detectors in resolution, microstrip proportional counters are applied for many investigations including developments in the field of radioisotope-excited XRF analysis, especially at low-energy regions (X-rays below 10 keV).

Xenon gas proportional scintillation counters are used for the detection of X-rays when high detection efficiency and good energy resolution are required (Lopes et al., 2000, 2001; Monteiro et al., 2001, 2004; Simões et al., 2001; Covita et al., 2004; Coelho et al., 2007). An excellent example is the detector used by Rachinhas et al. (2000) for the identification of internal conversion electrons produced by the decay of

cadmium-109 and xenon-133 m to investigate details of the decay scheme of these radionuclides. The main aim was to selectively detect and identify conversion electrons of cadmium-109. Fig. 3.8 shows the design of the gas proportional scintillation counting device. The stainless-steel enclosure holds also a thin plastic window, which is aluminized on the inner side to provide a uniform field strength at the drift region. Drift and scintillation region are separated by a grid mesh with high electron transparency. A second grid is evaporated directly onto the photomultiplier and therefore the scintillation region is in direct contact with the photomultiplier and a high collection efficiency of the UV scintillation photons is guaranteed. Primary electron clouds are produced by ionizing radiation in the absorption region and these drift under the influence of a low electric field toward and through the first grid into the scintillation region, where due to a much higher field strength scintillations are produced in the xenon filling gas. The electric pulses of the photomultiplier are fed to an amplifier operating with very short shaping times, and, as a result, pulse shapes resemble very closely the scintillation light bursts. This produces an efficient pulse-shape discrimination and a very detailed interpretation of the pulse-height spectra (see Fig. 3.9).

As reliable detectors proportional counters are frequently used for the standardization of radionuclides. García-Toraño et al. (2002) compared three methods for the standardization of cesium-134: absolute counting with a 4π NaI(Tl) detector, liquid scintillation, and a proportional counter (argon and methane as counting gas at atmospheric pressure) in coincidence with a NaI(Tl) detector system. It was shown that all the results of the standardization have been consistent and that any of the three methods that were applied was well suited for this type of application. Pommé et al. (2005) and Stanga et al.

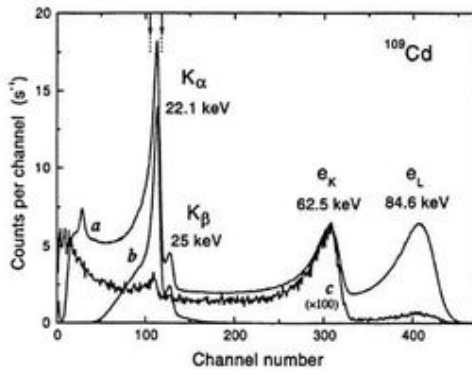


FIGURE 3.9 Pulse-height spectrum obtained from a Cd-109 source placed inside the gas proportional scintillation counter. Curve *a*: raw pulse-height distribution; curve *b* is obtained when pulses with duration outside the range from 3.6 to 4.0 μs are rejected. Curve *c* (values multiplied by 100) shows pulses that appear within a 20- μs interval after a 22.1-keV pulse within the range determined by curve *b*. (From Rachinhos et al., 2000. Reprinted with Permission from Elsevier © 2000)

(2006) also compared successfully gas proportional counting to other methods for the standardization of ^{125}I , which decays by electron capture with subsequent emission of conversion and Auger electrons, and the standardization of tritiated water, respectively.

The reliability of 4π pressurized gas proportions counters have been further demonstrated by Altizoglou et al. (2002) during their work dealing with the comparison of three methods to standardize a strontium-89 solution. Correction for self-absorption of the samples for gas proportional counting was obtained by plotting the activity concentration of the solution against the mass of radioactive sample. A new half-life value for strontium-89 (50.61 ± 0.05 days) was determined in this work.

International comparison and standardization programs frequently result not only in getting more accurate data of radiation properties but also in improving measurement procedures. Self-absorption corrections for beta measurements of solid samples have to be applied depending on the thickness of the specimen. Johansson et al. (2002) demonstrated that the self-absorption of beta particles from thallium-204 shows a linear relation to the logarithm of the dry mass of the source. They describe a way to minimize and correct for self-absorption in solid sources of thallium-204 of nuclides with similar decay properties. Also, a special device for source drying is described. Warm dry nitrogen jets (60°C) are blown on the rotating source material, which is mixed with colloidal silica (Ludox[®]) to decrease the crystal size of the solid deposit.

Improved gas proportional counting techniques for the standardization of negatron emitters (e.g. ^3H , ^{85}Kr) and positron emitters (e.g. ^{11}C) are described by Stanga and Cassette (2006), Marouli et al. (2010), and Phillips et al. (2010). The theory and principles of 4π proportional counting are provided in Section III.A of Chapter 14.

2. Position-Sensitive Proportional Counters

a. Single-Wire Proportional Counters

In a proportional counter, the position of the avalanche is limited to a small portion of the anode wire length. Some designs of proportional counters are capable of sensing the position of this avalanche and thus providing information about the position of an event taking place within the volume of the proportional counter. If the proportional counting tube is cylindrical with a central wire, electrons drift along the radial field lines. Thus, the position of the avalanche indicates the axial position of the initial ion pairs and the position of the entering radiation to be detected. Of course, if the incident radiation extends for some distance along the counting tube, only an approximate region of the incident radiation can be determined. The principle of charge division is most frequently used to determine the position of the ion avalanche. For that purpose, the central anode wire is made of a material having a rather high electric resistance per unit length (Ohsawa et al., 2000). By that means the charge that is collected at the wire electrode is divided between the amplifiers placed at both ends of the anode wire. The charges on those ends are collected in proportions related to the geometric position of the ion avalanche interacting with the wire electrode. A conventional output pulse is provided by summing up the response of the amplifiers and thus getting information about the total charge collected. A signal related to the position is provided by dividing the signal output of one amplifier by the output related to the total charge collected. The pulse height of this new signal indicates the relative position along the length of the central anode wire (Fischer, 1977; Westphal, 1976). Either analog signal handling or digital pulse processing techniques can be applied for this purpose.

Another method for position sensing uses pulse rise time measurements. With this technique, the relative rise times of the output pulses of the preamplifiers placed on both ends of the anode wire are determined. Interactions that take place far from one of the preamplifiers result in pulses with a much longer rise time than events close to the preamplifier position. From the rise time difference of the two preamplifiers, a signal can be created that is related to the position of the ion avalanche along the electrode wire. Good results regarding spatial resolution are observed. For well-collimated alpha particles, the FWHM can be 0.15 mm for a tube 200 mm long. Such position-sensitive proportional detectors have been applied for X-rays and neutrons, for magnetic spectroscopy of charged particles, and for localization of beta-emitting spots on thin layer or paper chromatograms (Goulianos et al., 1980).

b. Multiwire Proportional Counters

For many purposes, proportional counters with a number of anode wires instead of one central anode wire offer advantages. A grid of anode wires can be placed between two flat cathode plates. Near the cathode plate, the field is nearly uniform and electrons drift in that homogeneous field toward the anode wire grid. Near the wires the field strength increases and, as electrons approach this region, they are accelerated toward the nearest anode wire and an ion avalanche is created. Because of this,

the signal appears only at a single anode wire and the position of the primary ionizing event can be localized in the dimension perpendicular to the direction of the anode wires. This multiwire proportional counter was developed by Nobel Laureate Georges Charpak in the 1960s and played a decisive role, not only in many discoveries in particle physics but also in many experiments in biology and medicine (Charpak, 1970; Charpak and Sauli, 1978; Geltenbort, 1994). The technique for position-sensitive counting by using cathode wires of high resistivity has already been discussed. This technique can be used in addition to the plate and multiwire design and a two-dimensional signal pattern can be obtained. Another technique uses a detector construction with the cathode plate divided into narrow strips perpendicular to the anode wires. The induced charge to the nearest strip is recorded. Such position-sensing detectors with large areas are applied in high-energy particle research (Uozumi et al., 1993; Hayakawa and Maeda, 1994).

The relatively low signal amplitude is a disadvantage of these detectors. Therefore, for some applications, a hybrid detector system, between proportional and Geiger–Müller detectors, may be useful because of the much higher signal amplitude achieved; these are referred to as self-quenched streamer detectors (Knoll, 2010).

c. Microstrip and Micropattern Ionization Counters

Wire proportional chambers were mostly developed at CERN and have been a major step forward in particle detector technology. Even now the field of developing new varieties and improving available designs remains very active. Microstrip gas counters, micromesh designs, nonplanar variants of microstrip gas counters, such as the “compteur a trois (CAT),” secondary electron emission gas detectors, and some other varieties have been developed. A description of design with their special features and advantages is given by Fourme (1997). Christophel et al. (1998) present the development of a 2D microgap wire chamber. Such position-sensitive detectors can be used in other fields in addition to basic research in particle physics. Ortuño-Prados (1999) describes the use of a multiwire proportional counter as a potential detector for protein crystallography and other wide-angle diffraction experiments. Fried et al. (2002) describe a large curved 2D position-sensitive neutron detector which had been constructed for the protein crystallography station at Los Alamos National Laboratory; Babichev et al. (2001) report on their experience in medical radiography. The advantage of using multiwire proportional counters as high count rate detectors as well as their usefulness for producing dynamic images of high statistical quality is pointed out by Barr et al. (2002). A detailed summary on gas avalanche radiation detectors and their application in biomedical investigations is given by Breskin (2000) and Guillemot et al. (2007).

Microstrip gas chambers (MSGCs) are ionization counters in which anodes and cathodes are not single plates but are constructed as thin metal strips on a solid insulating support (Barbosa et al., 1992; Bouclier et al., 1992a, 1992b, 1992c, 1995; Oed, 1995; Pallares et al., 1992; Bellazzini et al., 2001, 2002; Clergeau et al., 2001; Sauli, 2001; Bateman et al., 2002; Mir et al., 2009). With such a system, the spot of the ionization

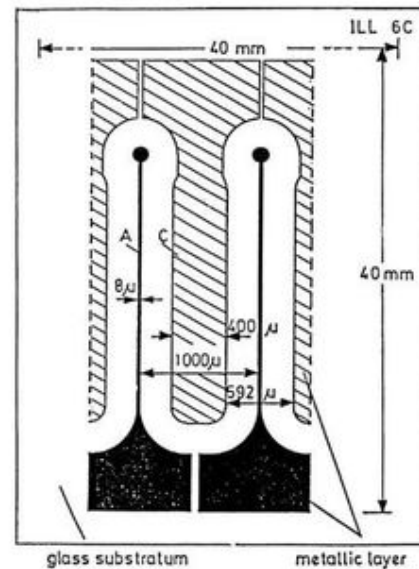


FIGURE 3.10 Structure of a microstrip plate. Electrode spacings are $400\ \mu\text{m}$ and the metallic layers on the glass support, the electrodes, have a thickness of $150\ \text{nm}$. The small strips are the anodes. (From Oed, 1995. Reprinted with Permission from Elsevier © 1995)

track can be localized, because ion production and migration and current flow take place in a well-defined single-electrode strip region. Thus, position-sensitive counting can be achieved. Such microstrip gas chambers can be obtained with very small spacing between the electrodes. A small pitch results in good resolution. Even at the beginning of their development, results were rather encouraging. At proportional gains above 10^4 good energy resolution (12% for 5.9 keV), position accuracies around $30\ \mu\text{m}$, and high rate capabilities were obtained. An example is shown in Fig. 3.10. This microstrip chamber was constructed by Oed (1995) using photolithographic techniques. The small strips are the anodes, and the electric field lines between the electrode strips are plotted in Fig. 3.11. An electron, that is set free in the gas volume in front of the microstrip plate and

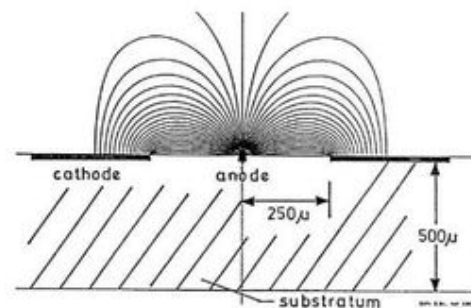


FIGURE 3.11 Plot of the electric field lines between the electrode strips of the microstrip plate. (From Oed, 1995. Reprinted with Permission from Elsevier (c) 1995)

reaches the microstrip plate, creates an avalanche in a very well defined small region.

Bateman et al. (2002) presented results of investigations dealing with energy resolution measurements using a microstrip gas counter (MSGC). The effects of gas filling, strip geometry, and other parameters have been examined in detail. A two-dimensional position-sensitive detector was realized by Barbosa et al. (1992). Two sets of microstrips are orthogonally oriented, forming a two-dimensional sensitive electrode, which is used in a multiwire proportional configuration as shown in Fig. 3.12. The two cathode systems are isolated by a silicon dioxide layer only $2\ \mu\text{m}$ thick and are therefore at practically the same distance (3 mm) from the anode wires. Therefore, the signals induced in both orthogonal electrodes are of the same amplitude. The authors aimed to define a two-dimensional X-ray detecting unit that also could be upgraded to a submillimeter spatial resolution detector.

There are some limitations to this design of detectors. One has to apply manufacturing techniques such as those used in the field of microelectronics. The total sensitive area of such counters seems to be limited. In addition, there are charge buildup effects of the supporting insulating materials. This can have a substantial influence on the gas gain at high fluxes. Ion avalanches can cause accumulation of electric charge on the insulating surface between the strips, which modifies the electric field around the electrodes and changes the gas multiplication characteristics. To avoid this, a surface conductivity of the insulating support can be created, for example, by ion implantation. However, the use of all these sophisticated manufacturing techniques imposes constraints on the size of such radiation detectors. In the beginning, glass and quartz were used for insulating support between the electrodes. Later

developments dealt with the application of plastic supports. These materials offer some advantages. They are flexible, and therefore nonplanar detectors can be designed. Cylindrical geometries with very small radii can be realized. Plastic materials not only have the advantage of lower atomic number of their constituents compared with glass but also can be made much thinner. Multiple scattering and photon conversion can be reduced. Plastic materials are also available with a wide range of electrical resistivities, and the design can be tailored to solve the problem of charge buildup. However, plastic materials have to meet the requirements of suitable mechanical stability. Bouclier et al. (1995) accomplished microstrip construction on plastic foils by applying a photolithographic etching technique on a layer of aluminum about $0.3\ \mu\text{m}$ thick on plastic. The distance between the electrodes was about $400\ \mu\text{m}$. This is somehow wider than the usually applied $200\ \mu\text{m}$ and is necessary because of the coarse optical quality of the plastic arrangements compared with glass support microstrips. Also, surface cleaning of plastic before vacuum evaporation of the aluminum cannot be done as perfectly as for glass supports.

Gains close to 10^3 could be reached with the equipment designed by Bouclier et al. (1995). Also, good energy resolution for low-energy X-rays was achieved.

The current tendency in the field of gaseous detectors is the replacement of wire chambers by advanced micropattern electron multipliers to obtain an improvement in spatial accuracy and counting rate capability. Electrode patterns are deposited by microlithographic techniques on insulating substrates. Due to the small distances between cathode and anode ($50\text{--}200\ \mu\text{m}$) these multipliers offer localization accuracy around a few tens of micrometers. The rapid collection of the ion avalanches

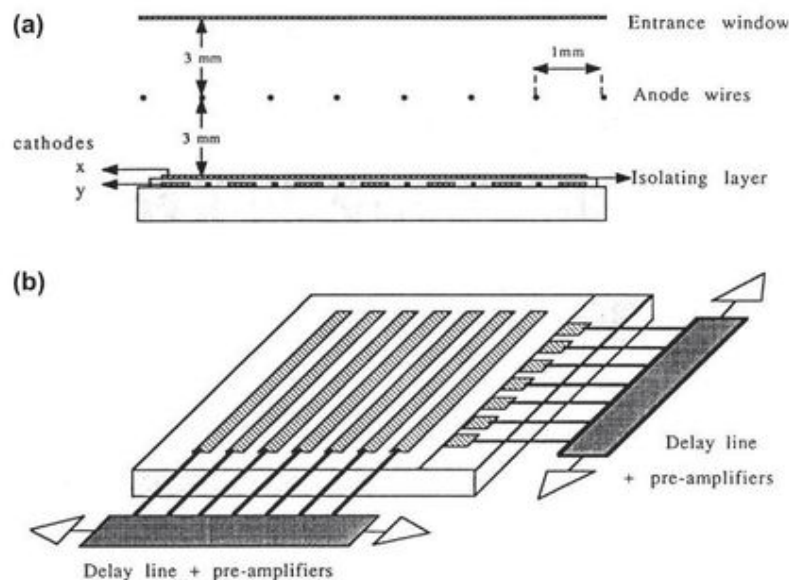


FIGURE 3.12 Two-dimensional position-sensitive detector arrangement. Two sets of microstrips at a distance of $2\ \mu\text{m}$ are orthogonally oriented and connected to delay lines. The anode wires are arranged between the microstrips and the entrance window at a distance of 3 mm. (From Barbosa et al., 1992. Reprinted with Permission from Elsevier © 1992)

considerably reduces space charge buildup, which influences the counting rate limitations. Many types of detectors in this family provide 2D localization in a single detector element.

Many new types of gas detectors with additional microstructures such as the gas electron multiplier system (GEM) and other designs continue under development (Levi et al., 1995; Clergeau et al., 2001; Sharma 2001; Horikawa et al., 2002; Sauli 2003, 2004a, 2007, 2010; Mörmann et al., 2004; Simon et al., 2009). These detectors are often referred to as micropattern gas detectors (MPGDs), because of their accurate position accuracy (Sauli 2001; Bellazzini et al. 2001, 2002; Mir et al. 2009).

The gas electrons multiplier (GEM) was introduced by Sauli (1997). A GEM detector consists of a thin polymer foil (25 μm), which is metal clad (18 μm) on both sides and perforated to yield a density of holes (70 μm diameter and 100 μm apart). Photolithographic techniques have been used for manufacturing. A voltage is applied onto the two faces of the metal clad foil and therefore the field is very strong inside the holes. The device is inserted in a gas detector on the path of drifting electrons. Primary electrons produced by ionization of the gas layer above the foil are sucked into the holes where an avalanche process takes place. By that process the charge drifting through the holes is amplified. Most of the secondary electrons produced in the avalanche are transferred to the region below the foil where these electrons are collected by an anode and cause a detection signal. Coupled to other devices such as multiwire or micropattern chambers, higher gains are obtained or an operation in less critical field-strength conditions is permitted. The fast response time generated by electrons is one of the main characteristic advantages of the GEM detector. The GEM detector has been originally developed for application in particle physics. But it has also been applied successfully in other fields of research. Two-dimensional GEM detectors have been used to obtain X-ray absorption images to show their applicability in medical diagnostics. Fig. 3.13 shows an absorption radiography of a small mammal using 8-keV X-rays. The real size of the image is 3 \times 6 cm. The position resolution depends on the photoelectron range in the gas. Presently, the application of this technique is mostly limited by the readout speed of the electronic system. Nevertheless, there are promising developments ongoing in this field (Sauli, 2001, 2003, 2004a, 2004b, 2010; Fraga et al., 2003; Tsyganov et al., 2008; Dalla Torre, 2011, and Villa et al., 2011).

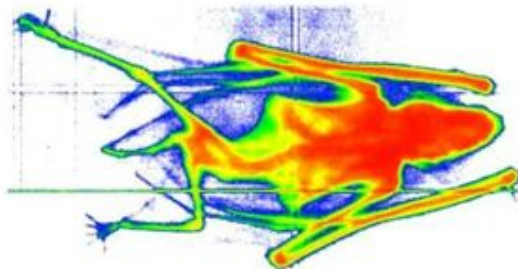


FIGURE 3.13 Absorption radiography of a small mammal recorded with a 2 D-GEM detector. (From Sauli, 2004b. Reprinted with Permission from Elsevier © 2004)

Gas electron multipliers have recently been included in a rather novel design of radiation detectors, which are constructed for applications in rare event experiments and, as the authors claim, will be of interest in neutrino-nucleus scattering, dark matter search, and probably also in nuclear imaging (Bondar et al. 2010, 2011). The authors describe experiments with a two-phase chamber, filled with liquid and gaseous argon and equipped with an assembly of THGEMs (thick gas electron multipliers). Ionization signals as well as signals from an attached avalanche photodiode (APD) are recorded. Other investigations rely on the information given by the photodiode only (e.g. Renker 2009; Kreslo et al., 2011). Photomultiplier tubes are frequently used in instrumentation for medical diagnosis such as with gamma cameras or CT equipment where light from large scintillator arrays has to be recorded. An alternative and probably more economic device for light detection and 2D recording would be the use of a thin solid photocathode combined with gas avalanche multipliers and a micropattern device (Fig. 3.14; Breskin, 2000). It is possible to include several GEMs to such a device in cascade (Sauli, 2001; Bachmann et al., 2002; Bondar et al., 2006; Aulchenko et al., 2009; Dalla Torre, 2011;). Each GEM operates at a low gain whereby a high total gain is achieved. In addition, the photocathode is shielded from photon feedback induced by ion avalanches (Fig. 3.15; Breskin, 2000).

Ongoing work is focused on the improvement of GEM detector performance (Assaf, 2002; Tsyganov et al., 2008, and Villa et al., 2011) and their quality control at the manufacture stage will be needed. Fraga et al. (2000) have shown that visible light emitted by the GEM avalanches can be successfully used for quality control of the material, to determine their uniformity and to identify local defects. It is much more effective than the normally performed optical inspection.

Bellazzini et al. (1999) introduced the WELL detector as a new type of position-sensitive gas proportional counter. The basic design is similar to the GEM detector. The main difference between the GEM and the WELL detector is that the GEM alone acts only as an amplifying stage, whereas the WELL detector has readout strips directly placed onto the insulating

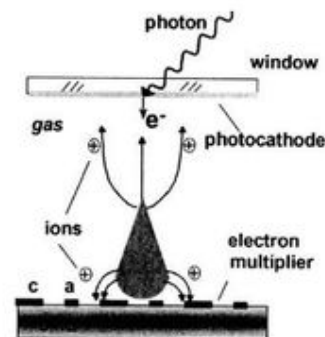


FIGURE 3.14 The principle of the gas avalanche photomultiplier: Photons stimulate the emission of electrons from the photocathode into the gas, avalanche multiplication takes place near the anodes of the micropattern device, ions are collected on neighboring cathodes, and some ions may drift to the photocathode. (From Breskin, 2000. Reprinted with Permission from Elsevier © 2000)

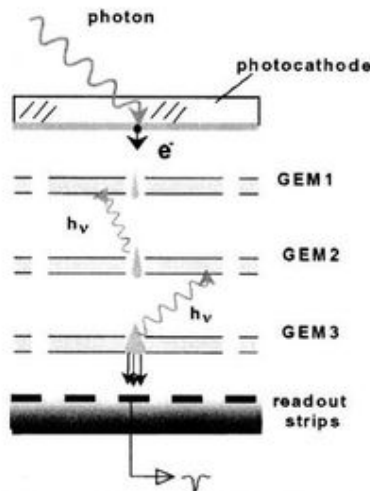


FIGURE 3.15 The multi-GEM photomultiplier concept, providing high total gain and 2D recording by a micropattern device. (From Breskin, 2000. Reprinted with Permission from Elsevier © 2000)

foil providing a position-sensitive compact system. Printed circuit board technology was employed to fabricate the amplifying structures (Bellazzini et al., 1999; Pitts and Martin, 2001).

Although the development of position-sensitive chambers are mainly dedicated for applications in high energy physics, these types of detectors are also instruments of choice for radiation detection and localization in other fields of basic and applied research. Breskin provides many examples for the application in biology and medicine. Among these are (i) the comparison of images obtained by autoradiographic techniques and ionization detectors, (ii) images of ionizing particle track patterns demonstrated as applications in nanodosimetry, and (iii) examples of the application of X-ray imaging and neutron imaging (Breskin, 2000).

Yu et al. (1999) designed a position-sensitive X-ray detector with curved electrodes for large-angle X-ray diffraction experiments at a synchrotron at Brookhaven National Laboratory. The detector can cover an angle of 45° and has an arc length of 20 cm with a radius of curvature of 25 cm.

Comprehensive reviews on the developments in gaseous detectors are presented by Hoch (2004), Tsyganov et al. (2008), Sauli (2010), and Dalla Torre (2011) and especially in the field of micropattern gas detectors by Sauli (1999, 2002, 2010), Oed (2001), Shekhtman (2002), Bellazzini et al. (2002), Titov (2007), and van der Graaf (2009, 2011).

Microstrip and micropattern gas chambers are filled with ^3He to be used as neutron counters (Iguchi et al., 1994; Hayakawa and Maeda, 1996; Radeka et al., 1998). The application of micropatterned devices for microdosimetry purposes was reviewed by Waker et al. (2009). By coating the cathode plane of a double-GEM detector with a 0.02- μm -thick layer of ^{10}B , Ohshita et al. (2010) demonstrated an efficient neutron detection, which could provide excellent two-dimensional images of neutron beam profiles. The neutron beam incident

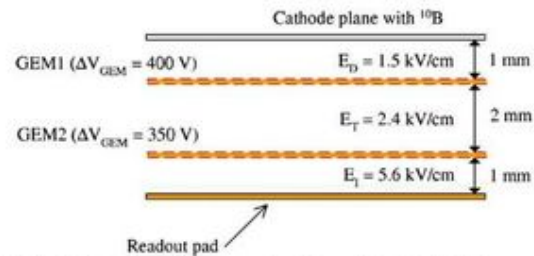
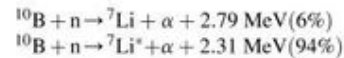


FIGURE 3.16 Schematic cross-sectional view of the double-GEM neutron detector. (From Ohshita et al., 2010. Reprinted with Permission from Elsevier © 2010)

on the GEM was imaged according to the following neutron reactions:



where $^7\text{Li}^*$ represents an excited particle, which spontaneously emits a 0.48-MeV gamma photon while returning to the ground state. Two GEMs were used for gas amplification as illustrated in Fig. 3.16 in a chamber gas mixture of Ar and CO_2 (70:30) providing a gas gain of approximately 400. The detector area was $100 \times 100 \text{ mm}$ with 120×120 readout channels. An example of two-dimensional neutron beam images taken at various distances from the beam collimator is illustrated in Fig. 3.17. Ohshita et al. (2010) measured the GEM detector position resolution at 1.2 mm in FWHM.

A triple-GEM neutron detector coupled to a CCD readout was devised by Fraga et al. (2002, 2003) for the detection of thermal neutrons. The detector was filled with ^3He and CF_4 . The ^3He in the GEM is used for thermal neutron conversion according to the reaction



which releases a 589-keV proton and 193-keV triton, and the CF_4 is needed to decrease the range of the triton and proton in the GEM detector. The He- CF_4 gas mixture scintillates in the GEM with an emission maximum at approximately 625 nm, which is imaged with a CCD coupled to a glass window at the floor of the GEM. A typical image of the proton-triton tracks imaged in the GEM following neutron capture by ^3He is illustrated in Fig. 3.18.

Roccaro et al. (2009) devised a gaseous detector for the determination of the neutron flux, energy distribution, and direction of neutron motion for both fast and thermal neutrons. The detector is filled with CF_4 at low pressure with one bar or more of ^4He to provide a target for fast neutrons through elastic scattering and a few Torr of ^3He to detect the thermal neutrons via neutron capture according to the reaction described above. The charged particles leave a trail of electrons along their tracks, and an electron avalanche occurs accompanied by the emission of scintillation light from the CF_4 . The light is then imaged by a lens coupled to a CCD camera, and the detector is referred to as an EMCCD camera (i.e. electron multiplier CCD camera). An example of images taken from events with

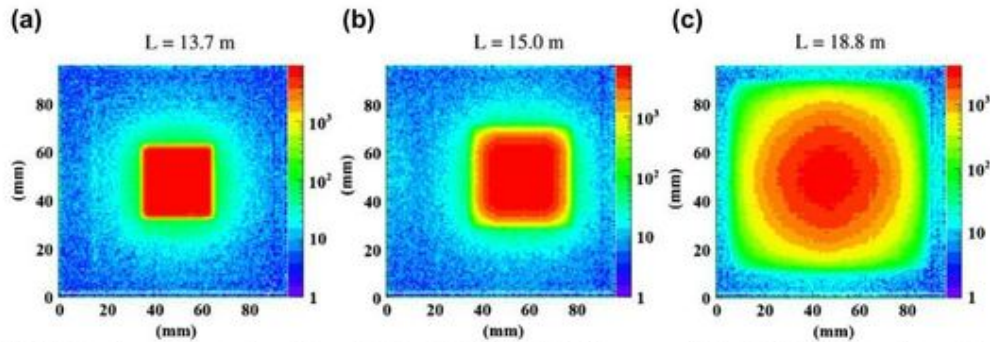


FIGURE 3.17 Neutron beam profiles at various distances (a) 13.7 m, (b) 15.0 m, and (c) 18.8 m measured by the double-GEM neutron detector. (From Ohshita et al., 2010. Reprinted with Permission from Elsevier © 2010)

14.1-MeV neutrons in the detector are illustrated in Fig. 3.19 where an inelastic reaction with ^{12}C of the CF_4 gas is observed.

For additional information on the application of multiwire and multipattern proportional counters applied in the biological sciences, see Chapter 19.

Multiwire proportional chambers originally have been designed for high rate applications; the applicability is mainly limited by the low ion drift velocity. Spatial resolutions are limited by wire spacing. In order to overcome these problems, the wires have been replaced by strips, printed on an insulating support. Developments include combinations and hybrids of the MSGC and GEM position-sensitive gaseous detectors such as the microhole and strip plate (MHSP) detector Natal da Luz et al. (2007a,b,c), the micro-pixel gas chamber (μ -PIC) and the microhole and strip plate (MHSP), and Micromegas detectors (Titov, 2007; Homma et al., 2009 and Veloso et al., 2000, 2001, 2010).

New structures of gas ionization detectors have been developed during the last years where the wires are replaced by a thin micromesh. Promising results were obtained with a very asymmetric two-stage parallel plate chamber with an arrangement that includes basically three electrodes: A large drift

region (about 1 kV/cm) between cathode and a micromesh and a small multiplication region with high field strength between micromesh and anode. Electrons formed in the drift region with moderate electric field pass through the mesh into the multiplication region where avalanches are produced. Typical gains are 10^3 – 10^4 , and, due to high field strength, fast pulses of a few nanoseconds duration are produced and high count rates can be managed. Positive ions from the avalanche are collected by the mesh. The authors use the name Micromegas (micromesh gas structure) for this detector arrangement (Giomataris et al., 1996). If the anode consists of a position-sensitive structure at the center, the avalanche can be spatially recorded. The Micromegas has been used mainly in high-energy particle detection and tracking but other applications such as the measurement of neutron radiation and imaging in the biological and medical sciences are also described (Derré et al., 2001; Delbart et al., 2001; Andriamonje et al., 2004; Pancin et al., 2007; Chefdeville et al., 2008; Donnard et al., 2009, Sauli, 2010; Fuitas et al., 2007 and Oger et al., in press).

Another variant of the parallel plate counter is a detector device named resistive plate chamber (RPC) (Sauli, 2010). The electrodes of this detector are not made of a metallic but of a plastic material which has a significant electrical resistivity (about 10^9 – 10^{13} ohm cm^{-1}). Avalanches do not grow too much and spark formation is avoided. The time resolution is better than 100 ps. Until now these devices have been used successfully in high-energy physics and further progress in developing this kind of detector can be expected (Santonic, 2003). Belli et al. (2007)



FIGURE 3.18 Superimposed proton–triton tracks obtained with an exposure time of 1 s with a CCD readout of a GEM-based neutron detector. (From Fraga et al., 2002. Reprinted with Permission from Elsevier © 2002)

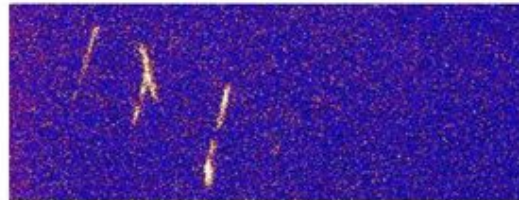


FIGURE 3.19 Image of three events with an EMCCD for 14.1-MeV neutrons from a neutron generator. The central event, appearing as an inverted Y, is considered the result of the inelastic reaction $^{12}\text{C}(n, n' + 3\alpha)$, which has an energy threshold of 7.9 MeV. (From Roccam et al., 2009. Reprinted with Permission from Elsevier © 2009)

studied possible applications of resistive plate counters for biomedical applications such as position emission tomography. Couceiro et al. (2007) described the application of position-sensitive resistive plate counters for animal PET investigations. Other applications (e.g. neutron counting) can be found in the reports of Abbrescia et al. (2004) and Hong et al. (2006).

For the first time a Micromegas counter has been used for in-core measurements in a nuclear reactor by Pancin et al. (2008).

A comprehensive review discussing new developments and future perspectives of gas ionization detectors is presented by Titov (2007). New designs of GEM, Micromegas, RPC, such as the coupling of GEM and Micromegas structures to a new type of detector are described. Advances in photolithography and microprocessing techniques in the chip industry have triggered a major transition in the field of gas ionization detectors from wire structure to micropattern devices (Sauli, 2010). It has to be mentioned at this point that most applications are related to charged particle physics, UV detection, and X-ray investigations rather than classical radioactivity analysis. Other review articles available in journals provide information regarding developments, achievements, trends, and future perspectives of position-sensitive gas ionization detectors (Sauli, 2001, 2003, 2010; Agosteo, 2010; Dalla Torre, 2011; van der Graaf 2011; Peskov et al., 2012).

3. Low-Level Counting Techniques Using Proportional Gas Ionization Detectors

For investigations involving low-level counting techniques, e.g. low-level radiocarbon dating experiments, a low and stable background is a necessity. Today this is achieved mostly by the application of "active shielding." The counting tube for the sample is surrounded by "guard tubes" which are combined with the sample counting tube by an anticoincidence circuit. Only the counts due to the sample counting tube alone are counted and not those registered by both counting systems simultaneously which are due to background radioactivity. In earlier times, this active shielding was a ring of sometimes more than 20 Geiger-Müller (GM) counting tubes. Later, umbrella-shaped guard tubes were designed. Those were in some cases displaced by liquid scintillator guards, which were specially designed for low-level anticoincidence shielding. The liquid scintillation solution is frequently based on a mineral oil solvent and especially suitable for large tanks. Within the guard chamber, several counters based on proportional detectors are sometimes installed. Some systems are equipped with pressure transmitters and temperature sensors to ensure constant conditions for the counting gas. In addition, measurement of the peak and median of the pulse-height spectrum is used to obtain information about the purity of the counting gas.

Several guard counter designs are described in the literature and a remarkable construction has been proposed and tested by Theodórsson and Heusser (1991). They suggest an arrangement of flat guard counters on the external sides of the main shield instead of the inner region of the shield as usual. In this way, the weight and space of the inner shield can be reduced. They also claim that the effects of secondary nuclear reactions causing background effects are considerably reduced.

A new detector type for low-level anticoincidence counting is designed and constructed by Zhang et al. (2002). A CdTe semiconductor counter is used as a guard detector, forming also the wall of the low-level proportional counting tube. This equipment is applied successfully to radiocarbon dating investigations and the authors suggest also other fields of application.

Background reduction by electronic circuit design can be accomplished by pulse-shape discrimination (Mäntynen et al., 1987; Äikää et al., 1992). By applying pulse-shape discrimination, the background is reduced by more than 70% and only 20% of the efficiency is lost. Figures of merit are improved by a factor of nearly 2. With a counting time of 44 h, measurable ages up to 56,000 years are achieved.

Carbon dioxide, being a "slower" gas than, for example, methane, is better suited for pulse-shape discrimination. On the other hand, purity requirements are much more severe for carbon dioxide. If pulse-shape discrimination for background reduction is used, the total length of the rising pulses is measured. The accumulated rise time of an irregular (i.e. a background) pulse is much longer than the rise time of a beta pulse. Yet, some background remains, for example, that arising from gamma-emitting radionuclides in the construction material. The factors necessary for all these improvements are provided by Äikää et al. (1992).

At present, three measurement methods for radiocarbon dating are available: accelerator mass spectrometry, low-level liquid scintillation counting, and low-level gas proportional counting. During the past several years, gas proportional counting methods had become less attractive for radiocarbon dating studies. Some authors are of the opinion that the application of gas proportional counting for radiocarbon dating should be reconsidered, although multidetector gas proportional counting systems offer some advantages.

A modern multidetector system has the advantage of parallel counting, which saves a great deal of time. Also, it takes less time to prepare carbon dioxide from a 1-g carbon sample than to carry out a benzene synthesis from the same amount of sample. This benzene is used as an additive to a liquid scintillation cocktail as discussed in Chapter 9. With parallel counting in a multidetector system based on ionization detectors, one of the samples is always a background sample, thus providing continuous monitoring of the background. Pulse rise discrimination techniques can be used in addition to reduce the number of background counts. If pulse rise analysis techniques are used to reject the slower rising background pulses, the counting efficiency is reduced by 18%, but at the same time the background is reduced by a factor of 3.3. A dramatic reduction of background counts is obtained by anticoincidence shielding. Like anticoincidence systems, liquid scintillation guard detectors are frequently used for active shielding.

According to the investigation of Theodórsson (1991), a multidetector gas proportional counting system seems to be highly competitive. Of course, the accelerator mass spectrometry technique has clear superiority over radiometric methods (Hou and Roos, 2008), especially for very small samples, but considering the high price of accelerator mass spectrometry equipment, it seems likely that accelerator mass spectrometry systems and gas proportional counting will be used in the future

and these will complement each other very well. Because of the potential of accelerator mass spectrometry, scientists hesitated to apply and further improve gas proportional counting.

Proportional counting devices still play an important role in radiocarbon dating investigations (e.g. Chiti et al., 2009, Facorellis et al., 2001).

Low-level liquid scintillation analyzers with active shielding can provide low background count rates of 0.3 cpm for ^{14}C measurements, making liquid scintillation an attractive method for ^{14}C dating. Chapters 7 and 9 of this book provide detailed information on low-level radiocarbon measurements by liquid scintillation analysis.

At the National Institute of Standards (NBS/NIST), tritium standards are calibrated regularly using liquid scintillation and gas proportional counting methods. Using the available data from measurement over 38 years, Unterweger and Lucas (2000) could obtain a more accurate and precise value for the half-life of that radionuclide (4504 ± 9 days).

The available data from international comparison projects have also been used to study the state of the art of tritium low-level measurement techniques. The objective was to find a realistic value for the sensitivity which could be demanded in ultra-low-level tritium investigations. Theodórsson (1999) reported that during intercomparison investigations only two laboratories could reach a standard deviation of ≤ 0.03 TU for weak samples. The achievement of a good level of sensitivity and accuracy for tritium measurement is a requirement, because otherwise the possibility of obtaining reliable hydrological information that tritium can give as a natural tracer would be severely limited. Improved future counting systems are discussed. It is again mentioned that gas proportional counting systems can be improved significantly by moving the guard counters to the outer surface of the shield as it had been already proposed by Theodórsson and Heusser (1991).

Measurements have been carried out also to verify theoretical aspects, such as the investigations of Kuzminov and Ose-trova (2000) on the shape of the carbon-14 beta-spectrum. Their examinations yielded results which are consistent with some of the theoretical predictions but which contradict the prediction of others. These findings may help researchers to arrive at more accurate theories.

4. Application in Environmental Monitoring, and Health Physics

a. Radon in Water

Zikovsky and Roireau (1990) have developed a simple method for the measurement of radon in water using proportional counters. The method is based on the purging of radon from water with argon, which is bubbled through the water sample and then directed to the counting tube. Argon picks up the radon that was dissolved in the water. A gas purification system removes humidity and oxygen. The high voltage is set for the alpha plateau and thus a very low background of less than 0.2 cpm and a counting efficiency of 25% are obtained, giving a detection limit of 0.02 Bq/L. This detection limit compares favorably with that of other methods developed for the determination of radon in water.

Radon daughters (polonium-218, lead-214, and polonium-214) contaminate the detector. Unless applying correction factors for the residual activities, a cooling period of at least one hour is essential to grant the decay of these daughter nuclides.

Beyond its relevance to health physics, the determination of radium and radon may also be essential for technical purposes. For example, the BOREXINO solar neutrino experiment at Laboratory Nazionali des Gran Sasso (LNGS, Italy) requires an extremely low radioactivity background (Simgen et al., 2003). Special care has to be taken to control ubiquitous radon in order to resolve the low solar neutrino event rate properly. The BOREXINO experiment is discussed in detail in Chapter 7. Simgen et al. (2003) developed a system for the detection of radium and radon based on miniaturized proportional counters with sensitivities of ~ 1 Bq/L (for radium-226) and ~ 0.1 Bq/L (for radon-222), respectively.

b. Measurement of Plutonium-241

Rosner et al. (1992) have built a proportional counting system that is especially suitable for the measurement of ^{241}Pu . Plutonium-241 is the only significant beta-emitting transuranium nuclide in the wastes from nuclear power plants. Quantitation of plutonium-241 in waste as well as in environmental samples is of interest because ^{241}Pu is a precursor of other transuranium nuclides that have longer half-lives, greater environmental mobility, and greater radiotoxicity. Alpha-emitting americium-241, with a half-life of 432 years, is the daughter product of plutonium-241 and has relatively high radiotoxicity.

Plutonium-241 can be determined indirectly by alpha spectroscopic measurements of its daughter nuclide americium-241. Measurements based on the ingrowth of the daughter radionuclide ^{241}Am can be done only after a long growth period. Even after 4 years the activity ratio $^{241}\text{Am}:^{241}\text{Pu}$ is only 1:166. Thus, a lower limit of detection for ^{241}Pu by direct measurement is desirable and has been achieved using proportional counting in the range of about 10 mBq according to the work of Rosner et al. (1992), whereas via ^{241}Am buildup, about 200 mBq is needed for detection.

Some authors have applied liquid scintillation counting to directly measure plutonium-241. Because of the rather high background of commonly available liquid scintillation equipment, this method can be applied only for samples with a relatively high content of plutonium-241. Investigations of that type have been carried out in regions with elevated fallout levels such as Scandinavia or with samples from the nuclear industry or weapons test sites. Lower limits of detection of 35–65 mBq have been reported. However, a low-level liquid scintillation analyzer equipped with a BGO detector guard and time-resolved liquid scintillation counting (TR-LSC) background discrimination electronics is capable of counting environmental ^{241}Pu at a low background of 2.4 cpm (L'Annunziata, personal communication).

However, because of the nonspecific character (i.e. continuous energy spectrum) of beta radiation, liquid scintillation and proportional counting require very pure samples for counting. Therefore, the chemical purity of the samples and the self-absorption due to the presence of matrix material in the counting sample are the critical points in the proportional

counting procedure. The effects of sample thickness, self-absorption, and energy loss in gas proportional counting were studied in detail by Martín-Sánchez et al. (2009).

For proportional counting special equipment is needed. This equipment can be obtained by modification of commercially available systems.

c. Measurement of Iron-55

For some radionuclides that are difficult to detect during radioprotection measures, gas ionization detectors still offer good possibilities. Iron-55 is formed by neutron capture of iron-54 and disintegrates *via* electron capture with a half-life of 2.7 years. Consequently, it is formed by the action of neutrons on steel and hence occurs in and around nuclear reactors. During planned repairs, the suspension and dispersion of this radioisotope of iron have to be monitored to avoid uptake by workers. The low-energy X-rays of iron-55 (5.9 keV) are stopped by most detector windows, which make its detection and quantification difficult. In the presence of other contaminating radionuclides, the measurement of iron-55 is further complicated. Surette and Waker (1994) have designed a monitoring system based on a sealed xenon-filled proportional counter with a thin beryllium window. The detector is combined with a single-channel analyzer and a shuttle mechanism that permits positioning of air filter or swipe media. For a counting time of 100 s, the detection limit is around 10 Bq. The thin window of the proportional counting tube (0.05 mm) allows more than 90% of photons with an energy of 3 keV or greater to pass through. The monitoring system is sufficiently sensitive to detect well below the maximum permissible level of surface contamination and also below the maximum permissible concentration in air of the facility for which it was designed.

The low X-ray energy of iron-55 suggests its application for testing the performance of new detection instruments and methods in the lower-energy region, see e.g. the work of Simões et al. (2003) and Masuda et al. (2002).

d. Tritium in Air

Proportional counters can also be used for tritium monitoring in air, as demonstrated by Aoyama (1990). Monitoring of tritium in air is required in the environment of 14-MeV neutron generators, heavy-water reactors, and reprocessing plants and will also be necessary at nuclear fusion reactors. Tritium must be detected separately from other radioactive volatile noble gases and air activation products. For occupational radiation protection and emission control, a real-time measurement and high sensitivity are necessary to meet the legal requirements for radiation protection and emission control. In order to respond to an accidental release, a wide range of detection is essential. High sensitivity can be obtained by using systems equipped with anticoincidence shielding or pulse-shape discrimination. Conventional proportional counters suffer from the disadvantage of requiring a counting gas and have a rather short operation range.

Aoyama (1990) described a method for tritium monitoring in air by the use of flow-through proportional counters with air as a counting gas. The counters need no counting gas other than the sampled air. The electronic equipment attached to the counting system comprises pulse-height discrimination, anticoincidence shielding, and background compensation. In that way, it is possible to detect and measure tritium in an external gamma background and also in alpha and beta backgrounds originating from other gaseous radioactive materials in the air sample. It was reported that a lower detection limit of 0.005 Bq/cm³ in the presence of natural background can be obtained in a counting time of 1 min. Also, a wide range of up to 5000 Bq/cm³ (up to six orders of magnitude) can be managed by this system. The proportional counting detector is rather complicated, consisting of an arrangement of anode wires and cathode meshes. A schematic illustration of this arrangement is shown in Fig. 3.20. Outer layers of the counter were used as guard counters to eliminate gamma background. Gaps between individual arrangements of anode and cathode were kept longer than the maximum range of tritium in air, thereby avoiding

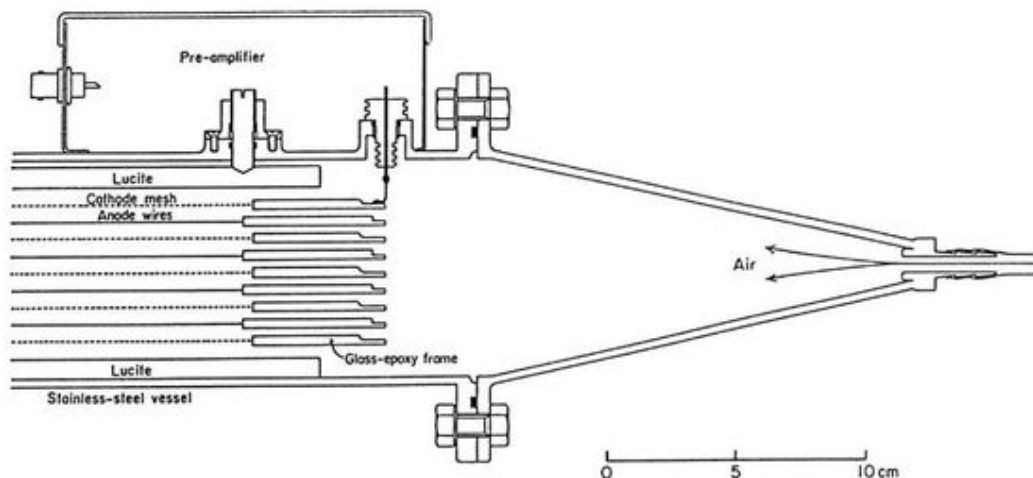


FIGURE 3.20 Cross section of a tritium monitor, which uses air as a counting gas. The detector consists of four layers of multiwire proportional counters. The air flows uniformly through the counter. (From Aoyama, 1990. Reprinted with Permission from IEEE © 1990)

coincidence effects caused by tritium. Such coincidence effects were used to exclude other beta rays. The alpha component from radon and its daughter nuclides was eliminated by pulse-height discrimination. Data derived from pressure, temperature, and humidity sensors were transferred to a computer and used to control the high voltage and to correct coincidence count rates. Loughlin and Lawrence (2007) carried out a thorough study of methods for the accurate monitoring of tritium in air in conjunction with the operation of the International Thermonuclear Experimental Reactor (ITER). They conclude a gas proportional counter is best suited for the measurement of HT and HTO when discriminating samplers are used at ventilation outlets from fusion reactions.

e. Positron Emitters in Air

The increasing demand of positron emitters such as fluorine-18, carbon-11, and oxygen-15 for medical applications (such as positron emission tomography, PET) has resulted in the commissioning of new cyclotron facilities. Marouli et al. (2007) studied the feasibility of using proportional counters for the monitoring of the emissions from the exhaust ducts at these facilities. The positrons were found to deposit 1.5–2.5 times more energy than negatrons to the counting gas, which affects the minimum detectable activity concentration in a positive way.

f. Monitoring of Gaseous Fission Products

Another important application of proportional counters is the verification of the Comprehensive Nuclear Test-Ban-Treaty (CTBT). The detection of fission products (most importantly ^{131}I and the xenon isotopes $^{134\text{m}}\text{Xe}$, $^{133\text{m}}\text{Xe}$, ^{133}Xe , and ^{135}Xe) or activation products [e.g. ^{37}Ar that can be produced from $^{40}\text{Ca}(n,\alpha)^{37}\text{Ar}$ or from $^{40}\text{Ar}(n,4n)^{37}\text{Ar}$] from a nuclear test remains as the only safe way to verify the nuclear nature of any (underground) explosion. Argon-37 disintegrates solely by electron capture with the emission of Auger electrons. The measurement of its low decay energy (2.8 keV) is done with special low-level gas proportional counters (Saey, 2007). Detection of radioxenon is also performed with the help of proportional counters, but usually in combination with other radioanalytical methods such as beta-gated gamma-coincidence counting, or high-resolution gamma spectrometry (Saey, 2009, 2010).

g. Radiostrontium

Low-level proportional counters are applied for quantitative radionuclide measurement after radiochemical separation procedures. Mateos et al. (2000) designed and constructed a semiautomatic analysis system for the determination of $^{90}\text{Sr}/^{90}\text{Y}$ in aqueous samples using a sequential injection method. The beta measurements are made twice within 24 h. From these results the initial activity of strontium-90 and yttrium-90 is calculated. Thus, the time-consuming yttrium milking method can be overcome.

Vaca et al. (2001) compared strontium-90 measurement methods using a Berthold LB770 counter and a Quantulus 1220 liquid scintillation spectrometer. The proportional counter had a passive shield of 20 cm thick lead and an active gas

proportional guard counter. The samples can be measured simultaneously by that device and a background from 0.3 to 0.6 cpm, depending on the detector location along the gas flow pathway is obtained. It is surprising that for gas proportional counting a minimum detectable activity of 0.13 Bq/kg is reported, for Cerenkov counting 0.37 Bq/kg.

Crown ether technologies were used by Scarpitta et al. (1999) to measure the strontium-90 content of Brookhaven National Laboratory groundwater samples. With gas proportional and liquid scintillation counting minimum detectable levels of 37 Bq/m³ were achieved using a processed sample of 1 L and a counting time of 1 h.

Proportional counting is also used for the determination of strontium-90 in human bones and teeth in Greece. Measurement was performed on yttrium-90 after equilibration with strontium-90 and liquid extraction using bis (2-ethyl-hexyl) hydrogen phosphate. The analyses unfolded an average of 30-mBq strontium-90 per gram calcium, which was found with only a small variation with respect to age and sex. From the variation of the activity in teeth it can be concluded that the contamination from atmospheric nuclear weapons tests exceeds by far that caused by the Chernobyl accident (Stamoulis et al., 1999).

In an extensive study, Degteva et al. (2006) investigated the dose resulting from external and internal exposure to radioactivity in the Techa River region, which was affected by the operation of the Mayak Production Association in the former Soviet Union. The internal dose was dominated by radiostrontium. Hence, investigation of thousands of teeth and bones was the method of choice in order to assess dose aspects. The authors found that the median doses to the red bone marrow and the bone surface was 0.21 and 0.37 Gy, respectively. For the maximum doses to the red bone marrow and bone surface, 2.0 and 5.2 Gy, respectively, were reported.

In an analytical and environmental study, the groundwater from the site of the nuclear power plant A1 Jaslovské Bohunice (Slovakia) was investigated (Ometáková et al., 2011). Several separation methods for the preconcentration of the radionuclides were tested. The ^{90}Y activity was determined by a low-level alpha–beta proportional counter and by Cerenkov liquid scintillation counting.

Much work has also been done to develop faster radioanalytical protocols for emergency response. Authors from Savannah River Nuclear Solutions developed methods for the determination of strontium-90 and alpha-emitting actinides in urine (Maxwell III and Culligan, 2009a), air filters (2010a), vegetation samples (2010b), milk, (Maxwell III and Culligan, 2009b), and water (Maxwell III and Culligan, 2009c). The authors use proportional counters for radiostrontium and alpha spectrometry for actinide determination.

Herranz et al. (2011) used a gas proportional counter to measure both ^{89}Sr and ^{90}Sr in environmental samples. The strontium is isolated first from the test sample, which also includes its isolation from the ^{90}Y daughter nuclide. Two counting times are required, one after the removal of ^{90}Y and a second count time selected after significant ingrowth of ^{90}Y . They used a proportional counter with a 5-cm diameter and 0.5- μm Mylar window. The detection efficiencies for ^{89}Sr ,

^{90}Sr , and ^{90}Y were 43%, 36%, and 44%, respectively, with uncertainties between 0.4% and 0.5% and a typical background count rate of 0.8 cpm.

h. Health Physics and Dosimetry

Tissue equivalent proportional counters (TEPCs) are a field with significant recent advances (Agosteo, 2010). They can be used to evaluate the radiation dose and dose equivalent for gamma rays, charged particles, and neutrons. Agosteo (2010) reports on the efforts toward miniaturization of TEPCs, which is important in radiation therapy, because conventional TEPCs are too large in comparison with the beam (especially for proton therapy of the eye) and hence suffer pulse pileup effects. TEPCs with cavities in the millimeter-range have been built to tackle this problem. An alternative approach consists of assessing the dose-mean linear energy through the variance method with a microdosimetric ion chamber operating in current mode. This method relies on the higher variance of the charge collected by an ionization chamber in a fixed time interval as the particle stopping power increases (Agosteo, 2010; ICRU, 1983; Hsu et al., 2008).

A mini-TEPC was developed by De Nardo et al. (2004a, b) for radiation therapy applications (Agosteo, 2010). Fig. 3.21 shows a sectional view of this detector. Its external diameter (2.7 mm) is the same as that of an 8-French (i.e. 2.7 mm) cannula, which is employed for mini-invasive surgery. The aim is to perform microdosimetric measurements directly inside the irradiated organ (for example, during the treatment of prostate tumors or proton radiotherapy of eye tumors; see De Nardo et al., 2010). The mini-TEPC sensitive volume is cylindrical (diameter and height 0.9 mm). The anode is a wire of gold-plated tungsten (diameter 10 μm). The cathode is made of Shonka A-150 plastic, 0.35 mm in thickness. The mini-TEPC is inserted in a titanium probe 2.7 mm in diameter, 170 mm in length, electrically grounded. The insulation between the conductive A-150 cathode and the titanium probe is ensured by a 0.35-mm-thick Rexolite cylinder. The propane-based tissue-equivalent gas flows continuously through the sensitive volume.

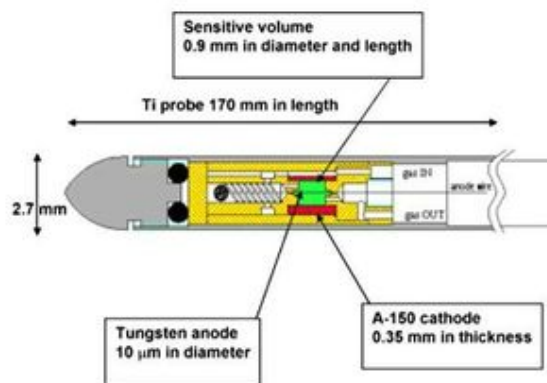


FIGURE 3.21 Cross-sectional view of a mini-TEPC used in radiation therapy. (From De Nardo et al., 2004a. Reprinted with Permission from Oxford University Press © 2004)

Another problem of conventionally sized TEPCs is their low sensitivity and energy response in low-dose rate applications (Waker et al., 2009). For low-energy neutrons, the range of the secondary charged particles is lower than the simulated site size of a TEPC. The instrument hence loses its spectrometric properties with respect to linear energy transfer (Agosteo, 2010). Waker et al. (2009) present and discuss the application of multielement and micropatterned devices to overcome these problems. Aslam et al. (2011) discuss their results on the investigation of the response of a commercially available spherical TEPC to mixed photon and neutron fields, which may affect the workers in nuclear power plants. They found that moderate dose rates, which do not result in dead times of more than 20–25% due to either of the component radiation or due to both components of a mixed field, generate acceptable results for radiation monitoring.

A tissue-equivalent proportional counter based on a thick gas electron multiplier (THGEM) has been proposed (Byun et al., 2009). The THGEM thickness ranges from the submillimeter to millimeter order, compared to standard GEM insulator foils with a thickness to 50 μm . This makes the THGEM more robust and practical for gas amplification in a two-dimensional microdosimeter (Agosteo, 2010).

Multielement TEPCs based on GEMs have been developed by Farahmand et al. (2003a, 2003b, 2004) and were reviewed by Agosteo (2010). This millimetric device consists of five cylindrical cavities of 4.3 mm³ in a sensitive volume sandwiched between two layers of A-150 plastic and filled with a tissue-equivalent gas. The GEM provides charge multiplication for the electrons from ion pair creation. The microdosimetric response of a TEPC–GEM to 14 MeV neutrons and a ^{252}Cf neutron source was measured by Farahmand et al. (2004) and found to be in good agreement with spectra available in the literature (Agosteo, 2010).

A twin miniaturized TEPC for application in boron neutron capture therapy was developed by Moro et al. (2006). Here, the wall of one TEPC is enriched in boron-10. For low-energy neutron fields below 500 keV, Waker and Aslam (2011a,b) developed a TEPC using a graphite-walled proportional counter. Miniaturization of TEPCs for low-energy neutron dosimetry has also been achieved successfully with the development of a compact multielement tissue-equivalent proportional counters (METEPCs) (Waker and Aslam, 2010).

Techniques to separate out the dose and energy spectra of neutrons and charged particles are necessary for health physics investigations in space shuttle conditions. Braby and Badhwar (2001) used a combination of a tissue equivalent and a hydrogen-free detector. Both have nearly the same response to photons, but the hydrogen-free detector is insensitive to neutrons below about 10 MeV. Thus, the neutron dose can be obtained by subtraction. Similar considerations are used also for the separation of charged particles and neutrons. Perez-Nunez and Braby (2011) report on the replacement of the TEPCs on the International Space Station and the improvements achieved with the new detectors.

Nanodosimetry will be of interest for investigations in microbiological radiation effects. Tamboul and Watt (2001) built a gridded parallel plate proportional counter, operating at

low pressure (1 Torr). This corresponds to a mean chord diameter of 1.8 nm. The device is designed to have a response to radiation simulating that of a bimolecular target of about the same sensitive volume, e.g. a double-stranded DNA molecule. A tissue-equivalent proportional counter on nanometric level was presented by Cesari et al. (2002). This "avalanche confinement TEPC" is characterized by a high gas gain and good energy resolution. It was defined to study sites in the nanometer scale down to 35 nm (Agosteo, 2010).

Thermoluminescence dating can be applied for objects that have been heated in the past such as bricks or pottery. In certain crystalline minerals, absorbed energy from ionizing radiation is re-emitted as light upon heating of the material. This method takes advantage of the fact that the dose received is proportional to the age (past the initial heating). As a consequence, for thermoluminescence dating the radiation dose the object had been exposed to must be known. Most frequently, this radiation dose is due to the content of alpha- and beta-emitting natural radionuclides within the material of the archeological specimen. Proportional counting techniques can be used to determine the activity of the material, and, from this analytical result, the radiation dose can be calculated. Troja et al. (1995) give an example for this type of activity measurements and dose calculations.

VI. GEIGER-MÜLLER COUNTERS

As already mentioned, with Geiger-Müller (GM) tubes much higher electric fields are applied than with ion chambers and proportional counters. Because of the high electric field, the intensity of an individual avalanche is enhanced. As a consequence of the emission of UV photons, which are released during deexcitation of atoms or molecules inside the tube, additional avalanches are created. One avalanche therefore can trigger another at a different position in the detector chamber volume. The number of avalanches grows exponentially. In addition, the number of slowly migrating positive ions increases. The increasing number of positively charged ions near the electrode causes the field strength to decrease, and further creation of avalanches is stopped, because ion pair multiplication requires a sufficiently high electric field strength. The discharge in a Geiger-Müller tube is terminated at about the same total produced charge, regardless of the amount of ions initially created by the radiation event. Therefore, all output pulses from a Geiger-Müller tube are of about the same size. The output-pulse amplitudes of GM tubes are very large compared with signals of ion chambers and proportional counters, usually of the order of several volts. Simple electronic circuits can be used to register Geiger-Müller output signals, but no information about the type and energy of the incident radiation can be obtained. Apart from this lack of information about the type and energy of radiation, Geiger-Müller tubes have a rather long resolving time compared with proportional counting tubes. Therefore, their use is limited to relatively low count rates, only a few hundred counts per second. Geiger and Müller (1928) hence originally proposed their instrument for the detection of "weakest activities." Resolving-time corrections can be applied, but the resolving time depends not only on the

field strength but also on the observed count rate (Jones and Holford, 1981).

The decaying source method is probably the most general and accurate of the methods for measuring the observed and true counting rates over the entire counting rate range of interest. For that a very pure radionuclide source of known half-life is essentially needed. True count rate and observed count rate differ considerably at high activity of the radioactive source; however, with time, the background-corrected observed count rate will approach the true count rate. This type of experimental determination of dead time is frequently used to test the usefulness of mathematically based models for correction (e.g. Gardner and Liu 1997; Lee and Gardner, 2000).

Counting losses induced by resolving time of a counting system can be a limiting factor in measurements. Vinagre and Conde (2001) presented an interesting method for the determination of resolving time of a counting system. They added an additional pulse to each pulse of the counting system and varied the delay time of this additional pulse. By observing the total count rate as a function of the delay time, good results for the resolving time could be obtained.

It warrants mention that Geiger-Müller tubes show a remarkable energy-dependent response for high-energy photons above 3 MeV. This was again pointed out by Neumann et al. (2002) to be a relevant factor in accurate dose determinations.

A. Designs and Properties of Geiger-Müller Counters

1. Fill Gas

The fill gas for Geiger-Müller counting tubes has to meet requirements similar to those for the fill gas of proportional counters. Argon and helium are most frequently used. The gas pressure is in the order of tenths of bars, and depending on the size and shape of the tubes a voltage in the order of hundreds of volts is applied. Geiger-Müller tubes are usually permanently sealed and operate at low gas pressure, although designs have been realized using atmospheric pressure and flow through to replenish the fill gas and flush out impurities.

2. Quenching

After the termination of the discharge, the slowly migrating positive ions of the fill gas finally arrive at the cathode, which is usually the outer wall of the counting tube. At this electrode, the cations capture electrons from the cathode surface and a corresponding amount of energy is liberated. If this liberated energy exceeds the ionization energy of the cathode material, additional electrons are set free from this electrode. These newly generated free electrons migrate to the anode and create another avalanche. This finally results in a continuous output of pulses. The probability of this additional electron drift is rather low, but because of the high number of cations at the field-strength conditions in a Geiger-Müller tube, this effect of multiple pulses is observed. With Geiger-Müller tubes special precautions have to be taken to prevent the formation of additional

avalanches. This can be done by reducing the bias voltage after the Geiger discharge. This external quenching can be achieved by using a suitable electronic circuit (resistor and capacitance) that determines the time of restoration of the high voltage following a Geiger discharge. The restoration time is usually on the order of milliseconds and therefore this design is suitable only for low count rates.

It is more common today to use internal quenching, which involves the addition of a suitable compound to the fill gas. The ionization energy for this additive to the fill gas (quench gas) must be lower than the ionization energy for the fill gas. Although confusing, the same expression, quench gas, is used for both the additive to a fill gas of proportional counters, which has to absorb UV photons, and the additive to a fill gas in the Geiger–Müller tube, which should be able to neutralize the drifting ions of the original filling gas by electron transfer. The ions of the quench gas migrate to the cathode and are also neutralized. However, the liberated ionization energy is now consumed by the quench gas and causes dissociation of the quench gas molecules. Some quench gases, such as halogens (e.g. chlorine or bromine), show spontaneous recombination; other quench gases, such as organic compounds (e.g. ethanol), are consumed, and therefore the lifetime of an organic-quenched Geiger–Müller tube is limited to about 10^9 counts. Quench gases are usually added at an amount of several percent to the fill gas of the Geiger–Müller tube.

A relatively long time is needed (100–500 μ s) to clean the positive ions that are formed during the avalanche propagation.

The transition from proportional mode to Geiger–Müller mode takes place at increasing field strength. Golovatyuk and Grancagnolo (1999) could demonstrate that this transition also depends on the concentration of a quenching gas. This fact may be of relevance if pulse-shape analysis is used for particle identification. If the concentration of quenching gas is low, gas amplification, as a function of high voltage, increases more rapidly and the boundary between the proportional region and the Geiger–Müller region may be crossed easily. Results of pulse-shape analysis may not be interpreted correctly.

3. Plateau

For the simple electronic circuits that are usually designed for use with Geiger–Müller tubes, a minimum pulse amplitude is required for count registering. At a given voltage, this minimum pulse amplitude is exceeded by all signals, as soon as that voltage, the Geiger discharge region, is reached. Therefore, on increasing the voltage while exposing the Geiger–Müller tube to a radioactive source of constant activity, pulse registering starts rather abruptly and the counts per unit of time remain relatively constant (plateau of a Geiger–Müller counter).

Geiger–Müller tubes are frequently rated on the basis of the slope of the plateau region. The slope of the plateau region of halogen-quenched tubes is usually less flat than that of organic-quenched tubes (2–3% per 100 v). However, halogen-quenched tubes can usually be operated at a lower voltage than organic-quenched tubes.

4. Applications

The design of Geiger–Müller tubes is usually similar to that of proportional tubes. But most frequently the end window type is used. Geiger–Müller tubes can also have the shape of “needle tubes,” in which the anode consists of a needle. In the vicinity of the needlepoint the field strength varies by $1/r^2$ instead of the $1/r$ variation near a wire or rod electrode. Therefore, counters with a very small active volume can be manufactured.

Since a Geiger discharge is created by a single ion pair, alpha and beta particles, once they penetrate the wall or window, are registered with very high efficiency. Gamma rays are detected by the electrons that are observed as a result of interaction of the gamma ray with the walls of the counting tube via the photoelectron effect or Compton effect. The efficiency of Geiger–Müller tubes for gamma rays is relatively low (in the order of a few percent over a wide energy range) and also depends on the atomic number of the material used to make the tubes. The range of medical or industrial applications of GM tubes could further be extended, provided the stopping power of the tubes can be improved. In a first approach to this problem, Meric et al. (2011a, b) applied Monte Carlo methods for the simulation of the stopping efficiencies of GM counters and benchmarked the results experimentally.

Currently, Geiger–Müller tubes are used most frequently for radiation monitoring and contamination control in day-to-day radiochemistry work.

Photon doses in mixed fields (neutrons/gamma) are frequently measured with Geiger–Müller counters. But it has to be mentioned that the response of Geiger–Müller detectors depends on photon energy, especially for photon energies above 3 MeV. Dealing with the analysis of neutron and photon components during calibration experiments, Neumann et al. (2002) point out that the knowledge of spectral distribution of the photons is essential for accurate dose determinations.

Beyond scientific value, Geiger–Müller counters are very suitable also for educational purposes. Blanco et al. (2009) show the application of Geiger counters for the detection of cosmic rays at different levels (from sea level, to mountains, to airplane cruise altitudes).

a. Environmental Radioassay

Radon. Bigu (1992) designed a fully automatic system for the unattended quantitation of radon-222 and radon-220 progeny. He used a GM beta particle detector with a pancake configuration. The instrument is a microprocessor-based system that consists of a sampling device, an electronic scaler, and a personal computer. The computer records all sampling and counting routines.

The sampling device consists of a filter about 5 cm in diameter facing the detector at a distance of about 0.5 cm. The airflow rate is 1.4 L/min. However, the measurement and data procedure are rather complex and requires a rather sophisticated computer program. Basically, the following steps are required:

- The sampling and counting for a given period provide results for the combined radon-222 and radon-220 progeny contribution.

- A counting period after the sampling records the beta particle activity versus time and thus permits assay of radon-222 daughter products.
- From the results of the preceding steps the contribution of radon-220 progeny can be calculated.

Difficulties may arise if measurements have to be made under transient conditions, for example, when there are rapid changes in the concentration of radon-222, or changes in the aerosol concentration or aerosol size distribution. This effect is related to the half-life of the radionuclides of interest. For radon-220 it is particularly acute, because of the long half-life of lead-212. The full effect of any of these changes (perturbations) is felt by the detectors after about one half-life of the dominating radionuclide of the decay chain.

Epstein et al. (2009) studied the health hazards caused by drinking water from "radium ore revigators" (water jars lined with a carnotite layer). Direct radiation exposure was measured with a GM tube. Radon and its progeny in water and air from the revigator were measured by liquid scintillation counting. Trace elements were determined by application of inductively coupled plasma mass spectrometry. Interestingly, Epstein et al. (2009) conclude that the potential hazard from the revigator was not radiation but rather the chemically toxic elements such as arsenic and uranium that were extracted into the water.

Fluorine-18. Papp and Uray (2002) used a very simple experimental setup for the determination of fluorine-18 attached to aerosol particles in a laboratory where syntheses for positron emission tomography are carried out. Aerosol samples were collected by drawing the air through a glass-fiber filter using a mobile high-volume air sampler. The filter disks were counted under an end-window Geiger–Müller tube (mica window 2 mg/cm² thickness and 35 mm diameter, background about 32 cpm). Following this very simple experimental procedure, subsequent measurements and a rather complicated computation using Bateman-type differential equations have to be carried out to distinguish between the radioactivity of the airborne natural radionuclides such as ²¹⁸Po, ²¹⁴Pb, ²¹⁴Bi, ²¹²Pb, ²¹²Bi, ²⁰⁸Tl, and fluorine-18. Therefore, the method cannot provide instantaneous results, but very low-activity concentrations, around 1 Bq/m³, corresponding to 160 atoms/m³ can be detected. This method can be applied also to the determination of any other airborne beta-emitting radionuclide, if its half-life differs sufficiently from those of the progenies of radon and thoron.

Radiostromtium. The beta counting of yttrium-90 after ingrowth to equilibrium with strontium-90 had been used during an extensive and remarkable investigation carried out by Russian and Norwegian scientists in the South Ural region near the site of the first weapon grade plutonium production reactor complex in Russia. Geiger–Müller counting tubes had been used for the determination of beta particles and Strand et al. (1999) reported that they found 720 kBq/kg of strontium-90 in sediments and 8–14 kBq/L in water.

Cosma (2000) carried out strontium-90 determinations in Romania without previous chemical separation procedures. He used aluminum plates to absorb low-energy beta particles and thereby detect only the high-energy beta radiation of yttrium-90.

He obtained values between 40 and 75 kBq/kg in sediments and soil in Romania after the Chernobyl accident.

Chu et al. (1998) compared three methods for the determination of radiostromtium, the nitric acid precipitation method, ion exchange, and crown ether separation procedures. They analyzed soil, tealeaves, rice, and milk powder. Their main statement is that by application of the crown ether method the time-consuming and hazardous nitric acid precipitation method is avoided. Measurements were carried out using gas flow Geiger–Müller tubes and Cerenkov counters. Data are given for strontium-89 and -90.

VII. SPECIAL TYPES OF IONIZATION DETECTORS

A. Neutron Detectors

Practically every type of neutron detector consists of a target material that is designed to produce charged particles by interaction with neutrons. Those charged particles can be detected by any suitable detector, such as an ionization detector. The nuclear interactions resulting in the production of charged particles are governed by the reaction cross section. This cross section depends strongly on the energy of the neutrons as described in Chapter 1. In searching for such nuclear reactions, one has to consider that the cross section should be as large as possible. Detectors with high efficiency and small dimensions can be designed in this way.

The most popular nuclear interaction for the measurement of neutrons is the ¹⁰B(n,α)⁷Li reaction. It can be used for the measurement of slow neutrons. The cross section decreases rapidly with increasing neutron energy as illustrated in Fig. 1.60 of Chapter 1. This reaction is very useful, because of the large cross section for thermal neutrons (3840 barns, see Table 1.16 in Chapter 1) and because of the relatively high isotopic abundance of the boron isotope with mass number 10 (19.8%). Usually, boron trifluoride is used as an additive to the host gas in proportional counting tubes.

The reaction ³He(n,p)³H has a significantly higher cross section for thermal neutrons, but the relatively high cost of ³He has somewhat limited the application of this target material for proportional neutron counting tubes. The ³He counters can be used for what is usually called a hostile environment, and they find application in well logging investigations (Glesius and Kniss, 1988). Glesius and Kniss provide a review of such applications for borehole measurements.

For the detection of delayed neutrons, Loaiza (1999) used an array of helium-3 counters embedded in polyethylene. High efficiency, low dead time, and gamma insensitivity were the requirements to be met by this counting device. The system was tested using an Am/Li source, the accuracy relative to a standard source embedded in graphite was about 3%, the efficiency 29%, and the dead time 0.46 μs. Most gamma pulses have been suppressed by proper setting of amplifier gain and discriminator. Thus, all the necessary requirements for the investigations could be fulfilled.

For experiments with spallation neutron sources, detectors are required with two-dimensional response, good time

resolution, and capability for neutron energy determination. Radeka et al. (1998) built multiwire chambers up to 50 cm × 50 cm with helium-3 and propane as filling gas mixture for the construction of a large curved detector for protein crystallography studies at a pulsed spallation source at the Los Alamos National Laboratory. The detector is designed to be placed 16 m from the neutron creation point, and thus a single neutron pulse time would act as a monochromator for neutrons.

Also, new detector designs, such as GEM detectors, have been introduced for neutron measurements. Lopes et al. (1999) combine the principles of proportional scintillation counters and gas electron multipliers; Fraga et al. (2002, 2003) and Roccaro et al. (2009) applied helium-3 as a filling gas in GEM detectors to determine neutrons as described previously in this chapter. Ohshita et al. (2010) used a 0.02- μm -thick layer of ^{10}B on the entrance window of a GEM detector for the measurement and imaging of neutrons beams.

The $^6\text{Li}(n,\alpha)^3\text{H}$ reaction cannot be used for gas ionization counters, because a lithium-containing gas for proportional counters is not available. But ^6Li counting scintillators are quite common as detectors for neutrons as described in Chapter 16.

The cross sections of uranium-233, uranium-235, and plutonium-239 for fission reaction with thermal neutrons are very large, and the fission products that form the “charged particles” to be detected in a proportional counting tube have very high kinetic energy (about 160 MeV). This facilitates discrimination from the alpha emission of the fissile materials that are neutron targets of the counting system. Little success was achieved in attempts to produce these neutron targets as a gaseous additive to the host gas of proportional counting tubes. Commonly, the surfaces of the electrodes are covered with a deposit of the fissile material. This system is frequently applied, for example, for fission chambers that are used for reactor as well as nonreactor applications.

As mentioned previously, the BF_3 proportional tube is the most widely used detector for slow neutrons. Somehow the boron trifluoride can serve both purposes, as a target for slow neutrons and as a proportional counting gas for the reaction products of the $^{10}\text{B}(n,\alpha)^7\text{Li}$ reaction. Although other boron-containing gases have been investigated, BF_3 offers good properties as a proportional gas and also a high boron content compared with other gaseous boron compounds. Usually, boron-10 is highly enriched for use in boron trifluoride counting tubes. Tubes with enriched boron-10 have about five times higher efficiency for thermal neutron counting than tubes filled with boron in its natural isotopic abundance.

According to the reaction $^{10}\text{B}(n,\alpha)^7\text{Li}$, the output signal handling may appear simple and straightforward for the application of boron-10 to the detection or even spectroscopy of neutrons. However, the energy spectrum and pulse processing for BF_3 tubes can be rather complicated in detail. Recoil ^7Li also contributes to the energy spectrum and the nuclear reaction leads to either a ground state (94%) or an excited state (6%) of ^7Li . In addition, the volume of the counting tube in general is not sufficiently large compared with the range of the alpha particles or even the range of ^7Li recoil atoms. Therefore, not the entire energy of these reaction products is deposited in the

gas volume, but interaction with the walls of the tube occurs instead. This results in distortion of the energy spectrum recorded from ionizing effects in the gaseous volume. Summarizing, one can say that the BF_3 tube is a detector from which, by differential pulse-height analysis, little useful information is obtained about the energy spectrum of the incident radiation. The pulse-height spectrum depends mainly on the size and shape of the detector. Therefore, counting is done only at a high voltage providing a flat region at a plateau and a discriminator setting is used at which all neutrons are counted but all low-amplitude effects are rejected. Low-amplitude effects are due mainly to gamma rays producing secondary electrons from wall interactions. But at very high gamma radiation fields, problems arise because of pileup effects. Also, BF_3 suffers from radiation decomposition in gamma fields of high intensity. Some authors try to absorb decomposition products of BF_3 by applying activated charcoal as an absorbent.

Position-sensitive neutron counters are essential for measuring the neutron flux distribution in critical assemblies. For that purpose neutron counting tubes with unusual dimensions may be constructed, such as a 1.2-m-long and 8-mm-diameter tube designed by Uritani et al. (1995). With that device, nonuniformities in a critical assembly could be detected and correction measures undertaken.

During the last years, new structures of detectors have been designed and these developments have also found their application in neutron counting (Fuitas et al., 2007). Resistive plate chambers using gadolinium as converters have been constructed by Abbrescia et al. (2004) and applied for neutron beam measurements with very encouraging results; resistive plate chambers have been used for low-energy neutron investigations by Hong et al. (2006).

Although neutron detectors usually rely on the technical principles of proportional counters, modified Geiger–Mueller counters can be also applied for this purpose. Etaati et al. (2010) studied the performance of an activation counter. In this device, neutrons are moderated in a polyethylene packing and activate a silver foil that surrounds the GM tube. The activation products of silver (silver-108 and -110) disintegrate with short half-lives under emission of β^- particles, which can be detected by the counter.

1. BF_3 Tube Construction

With increasing dimension of BF_3 counting tubes, the detection efficiency is improved and wall effects are suppressed. To some extent, increasing the gas pressure has the same effects. Some consideration has to be given to the materials used for tube construction to avoid radioactivation effects due to neutron capture by the materials used for tube wall construction. Because of its rather low neutron interaction, aluminum is frequently the material of choice; however, if a low background is essential, one has to keep in mind that aluminum contains a small amount of alpha-emitting nuclides. For such low-level investigations, stainless steel is preferred as a construction material for BF_3 tubes. Elevated temperature has some adverse effects on counting performance. Above 100–150 °C pulse amplitude and pulse-height resolutions are decreased, because

of desorption of impurities from construction materials inside the tube. Extensive studies of the temperature dependence of BF_3 proportional counters were carried out by Sakamoto and Morioka (1994). Some phenomena that depend on temperature were related to impurities in the enclosed gas and also to construction details of the electrodes.

Usually, BF_3 tubes are operated at a rather high voltage. Therefore, spurious pulses are possible due to leakage current through insulators, especially under conditions of high humidity. Also, detector microphonics have been observed, if the counting system is subject to shock or vibrations.

2. Detectors for Fast Neutrons

It has to be kept in mind that the gas ionization detectors previously described, namely BF_3 and ^3He detectors, which are based on the conversion of neutrons to directly detectable charged particles, are capable of detecting only slow neutrons. The cross section responsible for the $^{10}\text{B}(n,\alpha)^7\text{Li}$ and $^3\text{He}(n,p)^3\text{H}$ reactions decreases rapidly for neutrons with higher energies. To use these detectors for the determination of fast neutrons, the high-energy particles have to be slowed down, i.e. to be moderated. The low detection efficiency for high-energy neutrons of slow neutron detectors can be greatly improved by surrounding the detector volume with a layer of moderating material, for example, hydrogen- and carbon-containing materials such as paraffin. Fast neutrons lose part of their initial high kinetic energy by impact with the moderator molecules before reaching the sensitive volume of the detector. However, neutrons can escape from the moderator layer by scattering

without reaching the detector volume or can be captured by moderator materials. Thus, an increase of the thickness of the moderator layer will not proportionally increase the number of thermalized neutrons counted by the detector. A maximum counting efficiency will be observed at a specific moderator thickness. This optimal thickness depends on the initial energy of the fast neutrons to be detected and varies from a few centimeters for neutrons with energies of keV up to several tens of centimeters for neutrons having energies in the MeV range.

There is no general method for neutron spectrometry, especially around the eV region. The "slowing-down time" method can be applied for such investigations and conventional BF_3 tubes are used (Maekawa and Oyama, 1995a; 1995b; 1997).

Toyokawa et al. (1995) described a multipurpose neutron counter, applicable to the measurement of fluence, energy distribution, and radiation dose equivalent. This system consists of a spherical polyethylene moderator and three ^3He position-sensitive tubes inserted into the moderator orthogonally to each other. These three position-sensitive tubes provide information about the thermal neutron distribution in the spherical moderator, and from that information the foregoing parameters can be evaluated.

For neutron spectrometry in the MeV range, ^3He ionization chambers can be used. Iguchi et al. (1994) carried out investigations dealing with the application of these detectors in neutron spectrometry. Their ^3He detector consists of a cylindrical gridded ionization chamber (Fig. 3.22). Monte Carlo simulation was applied to estimate the detector response. Four kinds of reactions in the detector gas were considered in the

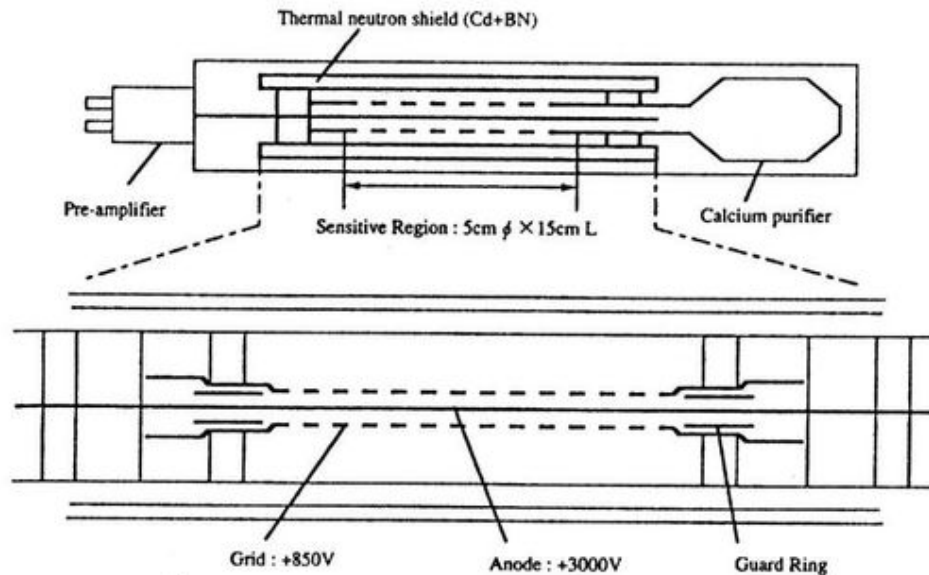


FIGURE 3.22 Schematic view of a ^3He gas ionization chamber. The detector consists of a cylindrical gridded ionization chamber. The sensitive volume is fixed to 5 cm in diameter and 15 cm in length by guard rings at both ends. The chamber is filled with helium-3, argon, and methane at a pressure of several bars. A calcium purifier in the chamber is used to remove hydrogen produced from the $^3\text{He}(n,p)^3\text{H}$ reaction from the detector gas. Thermal neutrons are shielded by a boron layer outside the tube. (From Iguchi et al., 1994. Reprinted with Permission from Elsevier © 1994)

calculations: ${}^3\text{He}(n,p)t$, ${}^3\text{He}(n,d)d$, ${}^3\text{He}(n,n')n'$, and ${}^1\text{H}(n,n')n'$ elastic scattering. Corresponding to these calculations, the response functions were measured with monoenergetic neutrons at various energy points.

Pulse height and rise time distribution analysis of signals from neutron proportional counters were used to reject undesirable signals of hydrogen-filled proton recoil counters, ${}^3\text{He}$ -filled counters, and BF_3 counters. Gamma ray background and wall effect pulses can be reduced by that method (Sakamoto and Morioka, 1993).

Neutron measurements in an environment with high gamma-radiation doses are of interest in the field of nuclear safeguards. Especially neutron–gamma coincidence counting is of particular interest for spent-fuel measurements for burn-up verification and in several steps of nuclear fuel reprocessing. The high gamma background has limited the selection of neutron detectors. Neutron fission chambers do not possess sufficient efficiency to be used in coincidence counting and BF_3 tubes suffer from radiation damage. Beddingfield et al. (1999, 2000) have carried out comprehensive research to optimize the helium-3 neutron proportional counter performance in high gamma ray dose environment. There are many parameters to be observed, such as tube size, gas pressure, gamma ray dose, gamma ray pileup, gamma ray energy, and radiation damage to the gas mixture and to the preamplifier system. There is no best option of counting tube design for all mixed field applications; however, from the presented amount of experimental data a good choice for a useful special design can be made.

An inexpensive sealed ${}^3\text{He}$ drift-tube neutron detector was designed by Wang et al. (2009) at the Los Alamos National Laboratory. In light of the limited supply and high cost of ${}^3\text{He}$, they developed a low pressure ${}^3\text{He}$ drift-tube neutron detector that takes advantage of the fraction of thermal neutrons scattered off a polyethylene moderator surface. The basic design of the drift-tube neutron detector is illustrated in Fig. 3.23. Wang et al. (2009) surrounded the tube with approximately 25-mm-thick high-density polyethylene sheet moderator. With a detector diameter of 5 cm and a specific gas mixture and pressure they could ensure that the full energy of the reaction ${}^3\text{He}(n,p){}^3\text{H}$ would be absorbed by gas ionization, which results in a prominent Q -value peak at 0.764 MeV in the pulse-height spectra and a detection efficiency of 5%. The detector was filled with 1 bar of total gas pressure with 25–300 mbar of ${}^3\text{He}$ with the remaining gas mixture consisting of C_2H_6 , ${}^4\text{He}$, CF_4 , and Ar.

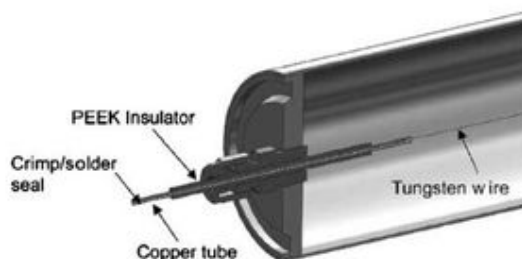


FIGURE 3.23 Schematic view of the drift-tube neutron detector construction. (From Wang et al., 2009. Reprinted with Permission from Elsevier © 2009)

Due to the relatively low pressure of ${}^3\text{He}$, the cost of the ${}^3\text{He}$ is not more than the cost of the other materials used to construct the detector. The wall of the detector consists of 0.89-mm-thick aluminum, and the tube length can be varied from 30 cm up to 6.1 m in length. The detector length was kept at a minimum of 30 cm (12 in.) to prevent domination of the detector by end effects. The anode wire consisted of 50- μm diameter gold-plated tungsten. The drift tube operates as a proportional counter at bias voltages ranging from 1400 V (300 mbar ${}^3\text{He}$) to 1800 V (25 mbar ${}^3\text{He}$). The detector was designed for fissile material detection, and the simple design permits the factor construction of 100 detectors by a 2-person team in 1 workday of 8 h.

a. Long Counter

Most neutron detector systems suffer from the disadvantage that the counting efficiency depends strongly on the energy of the neutrons to be detected. The so-called long counters try to avoid that disadvantage. A long counter consists of a neutron detector tube, most frequently a BF_3 tube, that is placed in the central region of a paraffin cylinder. The paraffin cylinder is covered with a layer of B_2O_3 and with an additional layer of paraffin. Only one end of the inner paraffin cylinder is not covered by the boron and additional paraffin. Thus, the device is sensitive only to neutrons coming from the direction of this end. Any neutron arriving from that direction is moderated and has a good chance of arriving at the central BF_3 tube. To give low-energy neutrons a better chance of reaching the tube, holes are drilled in the front end of the inner paraffin layer (Hunt and Mercer, 1978, Evans, 1982).

Because of the nearly energy-independent response of this type of counting tube, the long counter is also called a “flat response” detector. Many variations of such flat response detectors have been designed and constructed, some of them using ${}^3\text{He}$ tubes, pressurized filling gas, multiple tube arrangements, and so on (Tagziria and Thomas, 2000, Hu et al., 2009, Lacoste 2010, Lacoste and Gressier, 2010, Roberts et al., 2010, and Watanabe et al., 2011). One has to be aware that the counting efficiency of such neutron counting systems is rather low, sometimes much less than 1% (East and Walton, 1982, see Fig. 3.24).

As noted in the previous paragraph, many variations of long counters may be used; two examples of the most simple design and more complex design together with their response to a wide spectrum of neutron energies are illustrated in Figs. 3.24 and 3.25, respectively. The flat response neutron detector geometry illustrated in Fig. 3.24 is quite simple. The detector consists of a 20-cm-long ${}^3\text{He}$ position-sensitive proportional counter (PSPC) surrounded with polyethylene moderator. Polyethylene is often preferred over paraffin as moderator due, because it can be machined easily while also having a high content of hydrogen atoms. The neutrons enter from the left surface of the detector illustrated in Fig. 3.24. The peak positions in the spatial response of the 20-cm-long ${}^3\text{He}$ PSPC counter shift to deeper positions from the detector surface with increasing neutron energy, as illustrated in the lower part of Fig. 3.24.

A more complex design of a long counter, described by Lacoste and Gressier (2010) for the IRSN AMANDE facility in France, is illustrated in Fig. 3.25. It was modeled based on studies on the role and variation of different parameters, such as

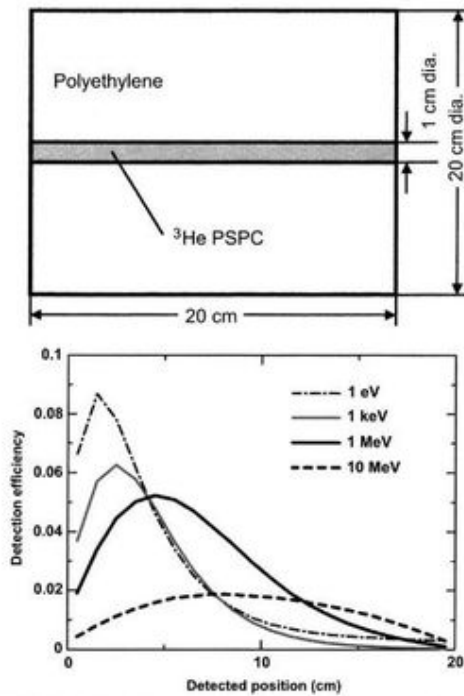


FIGURE 3.24 (Upper) Basic configuration of a flat response neutron detector. The neutrons enter the detector from the left side of the figure. (Lower) Calculated spectral response distribution (i.e. number of detected neutrons per incident neutron) of neutron detection position in the ³He PSC long counter for various incident neutron energies. (From Watanabe et al., 2011. Reprinted with Permission from Elsevier © 2011)

depth of holes in the front face and the position of the thermal neutron detector in the moderator. The long counter (PLC-IRSN), modeled with the Monte Carlo radiation transport code MCNPX, is illustrated in the upper portion of Fig. 3.25, and the response function of the counter over a wide range of neutron energies is illustrated in the lower portion of the figure. The detector measures approximately 40 cm in diameter and 45 cm in length. It is made of polyethylene and borated polyethylene, with a thin cadmium sheet in the front and at the rear. The front of the inner polyethylene layer is designed with an annulus of air and is 5 cm in depth and 3 cm in width. A polyethylene cylinder 6 cm in diameter and 7 cm in length is placed in front of the thermal neutron detector. The ³He gas was confined at a pressure of 10 atm. in an active volume 3.8 cm in diameter and 26.3 cm in length. The uniform response of the long counter to a wide range of neutron energies is illustrated in the lower portion of Fig. 3.25.

3. Neutron Counting in Nuclear Analysis of Fissile Materials and Radioactive Waste

Neutron counting tubes are also used in delayed neutron activation analysis. Some radionuclides follow a beta, n decay process; their beta emission is followed immediately by the

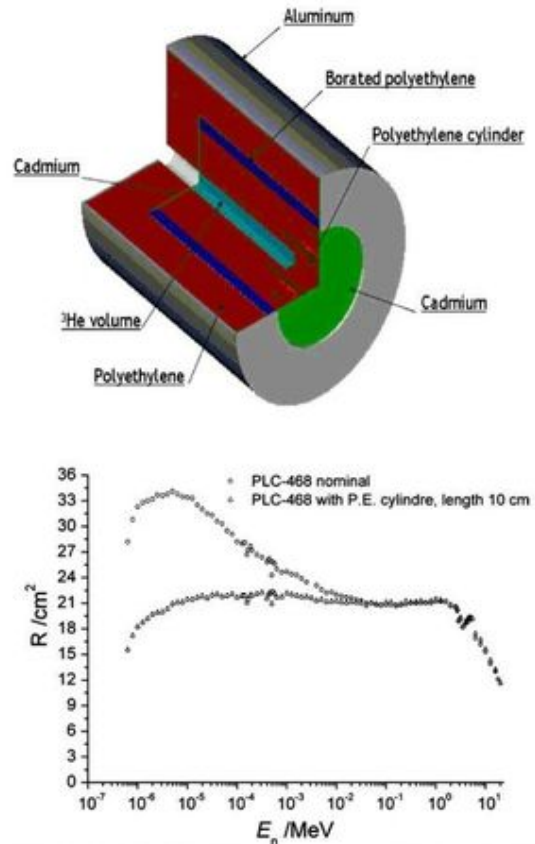


FIGURE 3.25 (Upper) PLC-468 long counter modeled with MCNPX. (Lower) Fluence response energy distributions of the PLC-468 long counter with and without a 10-cm-long cylinder of polyethylene inserted in front of the detector. The additional polyethylene cylinder decreases the sensitivity of the detector to the low-energy neutrons without affecting the detector response in the higher-energy range. (From Lacoste, 2010. Reprinted with Permission from Elsevier © 2010)

emission of neutrons. Such nuclides are produced by fission of heavy elements. Therefore, this procedure can be used for the analysis of fissile materials. Using thermal neutrons for fission is a specific method for the determination of uranium-235. With fast neutrons fission also occurs with uranium-238 and thorium-232.

Oxygen and calcium are interfering elements. Nitrogen-17 and potassium-48 are the products of fast neutron irradiation. But because those radionuclides have short half-lives (nitrogen-17, 4.2 s and potassium-48, 5.8 s) compared with the neutron-emitting products from uranium and thorium, the interference can be avoided by counting after a decay period of at least 20 s.

Delayed neutron activation analysis is carried out using a pneumatic transfer system at a neutron source of sufficient flux density, usually a reactor. The samples are first positioned near the reactor core by the transfer system, and after a suitable irradiation period (~60 s) and decay period (~20 s) samples are counted (~60 s) at a neutron detector assembly.

Thorium interference due to fast neutron-induced fission is overcome by irradiation with and without cadmium shielding. The delayed neutron activation analysis is used mainly for the determination of uranium and thorium at trace levels in minerals. Fully automatic systems are available, with detection limits in the range of 0.01 $\mu\text{g/g}$ for uranium and 1 $\mu\text{g/g}$ for thorium.

Neutron counters have been applied also to the determination of transuranium elements. A high-sensitivity neutron counting tube arrangement was used successfully for the determination of plutonium in radioactive waste drums at Lawrence Livermore National Laboratory (Hankins and Thorngate, 1993a; 1993b). It was reported that the sensitivity of this equipment is about 10 times better than the sensitivity of X-ray and gamma ray instruments that are normally used. Helium-3 counting tubes are arranged outside the waste package. These ^3He counters are covered with paraffin with an outside lining of cadmium. Fission neutrons passing the cadmium barrier are thermalized in the paraffin layer and detected by the ^3He tubes.

Another system uses a pulsed electron beam from a linear accelerator to produce high-energy photon bursts from a metallic converter. The photons induce fission in transuranium elements. When fission is induced in such material, delayed neutrons can be detected by a sensitive neutron counting system (Lyoussi et al., 1996).

A nanoparticle-doped micro-Geiger counter was designed to enable multispecies radiation detection, which is important for the detection of fissionable bomb-making materials (Whitney et al., 2009). In this forensic application, incoming radiation interacts with tailored nanoparticles, which release secondary charged particles into the fill gas. An array of multichanneled micro-GM tubes is formed to a counter platform. Each tube is doped with a nanoparticle from which the authors claim to achieve a possibility to discriminate alpha, beta, gamma/X-ray, and neutron radiation. Tungsten oxide nanoparticles convert beta particles to several electrons of lower energy; glass nanoparticles convert alphas to electrons; boron-10 converts neutrons to alphas; and lead oxide nanoparticles convert gammas/X-rays to photoelectrons. By analyzing the height of the resulting pulses of each individual channel under the same radioactive source, the type, location, and energy of the incoming radiation can be determined (Whitney et al., 2009).

Not only transuranium elements are determined in waste using neutron counting, but also moisture measurements of the radioactive waste are carried out. The thermalization of neutrons from an isotopic neutron source is detected by a proportional neutron counting tube. The moisture content of the waste is an important parameter that determines the combustibility of waste materials (Lentsch et al., 1996).

4. Moisture Measurements

Moisture measurements are based on the principle of neutron moderation by hydrogen atoms. In neutron water gauges, neutrons are most frequently produced through (α, n) reactions, e.g. $^9\text{Be}(\alpha, n)^{12}\text{C}$. These neutrons have a spectrum of energies from 0 to about 10 MeV. The neutrons of high energies are moderated (slowed down) by elastic scattering with hydrogen atoms from water. These slow neutrons are detected by

a counting device which is only sensitive for slow neutrons, e.g. a BF_3 counter. Modeling of the interactions of slow neutrons with different media, such as soils, is not easy and therefore a calibration is needed to convert the slow neutron counts to water content. Usually, a neutron moisture meter (NMM) device is combined with a density gauge.

Neutron moisture gauges are well-proven devices for soil water determination. Tolk and Evett (2009) compared the performance of an NMM and a lysimeter with respect to evapotranspiration determination of soil. They found a deviation of not more than 4% when comparing both methods. Although the NMM has served the need for this purpose, increasing regulatory burdens, including the requirement that the NMM not be left unattended, limit the usefulness of the method. Newer methods, which respond to soil electromagnetic (EM) properties, typically allow data logging and unattended operation, but with uncertain precision, accuracy, and volume of sensitivity. One major advantage of the NMM over EM devices is its insensitivity to temperature (Evett et al., 2006). In a later study on the same problem, Evett et al. (2009) conclude that the EM methods poorly reproduced the spatial and temporal behavior of NMM and gravimetric sampling and implied spatial variability of profile water content that was not evident in either the NMM or gravimetric data. The authors conclude that EM sensors were influenced not only by the mean water content in the sampling volume, but also by the smaller-scale structure of soil electrical properties.

The theory and practice of measuring the water content in large volumes of material by neutron thermalization and the measurement of thermal neutrons with BF_3 or ^3He detectors are reviewed by Nielsen and Cassel (1984) and Bacchi et al. (2002).

B. Multiple Sample Reading Systems

In radioassay methods in biochemistry and medicine, a high sample number throughput is frequently essential. Radioactivity quantitation on solid supports, and radioimmune, dot blot, cell proliferation, and receptor-binding assays require systems for counting a rather high number of samples in a given time. Simultaneous counting methods for a large number of samples are desirable. For these applications, multiple sample reading systems have been designed. Bateman (1994) has constructed a multipin detector. The pins are centered in holes in a metallic collimator system and 60 beta-sensitive positions are obtained.

A system with 96 individual detectors working in the Geiger-Müller region has also been manufactured (Roessler et al., 1993; Hillman et al., 1993a). A high sample throughput is achieved and the counting procedure is about 40 times faster than single-detector assay procedures. Of course, the counting efficiency for tritium is much lower than that achieved with liquid scintillation counting, but the background is reduced, because the GM detectors are very small.

Roessler et al. (1993) compared several methods for receptor-binding assays and compared the sample throughputs. Hillman et al. (1993b) applied the 96-sample measurement system for chromium-51 retention assays. Several other application examples can be found in the literature (Alteri, 1992; Hutchins, 1992).

Microplate assays related to investigations using radioactive tracers have attracted great interest during the past decade. For microplate assays radioactivity has to be measured from samples on a solid support that may hold 96 samples in an area of 8×12 cm. Cells or tissues are incubated in the presence of a radiolabeled substrate simultaneously in all positions of such a microplate. After the incubation, the nonincorporated components must be separated from the incorporated radioactive substrate at each position of the microplate. Applying conventional techniques, this was usually done by filtration and washing one sample after the other. The radioactive residue on the filters was counted using liquid scintillation counting (LSC) techniques. This was a rather time-consuming and expensive procedure. Great progress was achieved by developing a sample harvester that could harvest and wash 96 samples simultaneously, saving a great deal of time and work. This harvesting and washing procedure can be performed by a specially constructed fully automatic cell harvester from conventional microplates, or special filter bottom foils for these plates can be used. The application of a radioactivity reading system that can analyze 96 samples simultaneously greatly simplifies the microplate radioassay techniques.

Two different types of microplates can be chosen, those with and those without a removable bottom. The removable bottom consists of a membrane filter material that can be easily stripped from the bottom of the microplate.

These solid support samples can now be measured using either liquid scintillation counting (standard LSC or multidetector LSC) or ionization detector techniques, such as proportional ionization detector counting, position-sensitive proportional counter scanning, or multidetector avalanche gas ionization detector quantitation. See Chapters 7 and 16 of this book for a detailed description of scintillation analysis in the microplate sample format.

For position-sensitive proportional counter scanning, systems similar to those used for scanning thin layer chromatograms (TLC) or paper chromatograms (PC) are used. With a position-sensitive wire detector, 12 samples in a single row can be counted simultaneously. This method suffers from some disadvantages. This type of detector has a very low counting efficiency for low-energy beta emitters, and it is subject to high amounts of cross-talk when high-energy beta-emitting radionuclides such as phosphorus-32 are analyzed. Also, the efficiency is not uniform across the entire length of the wire. It seems that this technique is rather unsuitable for quantitative simultaneous multicounting applications. Therefore, systems with individual detectors in the format of the microplate were designed and manufactured. Open-end gas avalanche detectors are used and the systems are capable of quantitating tritium, carbon-14, phosphorus-32, sulfur-35, iodine-125, and many other beta emitters. Of course, the filter mat must be dry but there is no addition of cocktail. The filter is not destroyed and can be used for further investigations. Moreover, the amount of waste is minimized.

A detailed description and examples of applications are given by Kessler (1991). This technique can be applied to the radioassay of dot blots and labeled cell proliferation assays. With conventional autoradiography and densitometry, the range

of radioactivity measurements is much smaller than with a multidetector system, because an X-ray film shows a saturation effect in blackening. Also, the exposure time for X-ray films is much longer than the measurement time for ionization detectors. Other more quantitative imaging methods are described in Chapter 19. The ionization multidetector arrangement seems to be comparable to a liquid scintillation multidetector system (Kessler, 1991). However, commercially available high-sample-throughput multidetector microplate scintillation analyzers described in Chapter 7 provide higher counting efficiencies and higher sample throughput.

C. Self-Powered Detectors

Self-powered neutron detectors are fabricated with a material incorporated in the detector volume that has a high cross section for neutrons. By neutron capture, a beta-emitting radionuclide is formed. The detector operates by directly measuring the flow of current produced by the beta particles. No external bias voltage is needed. Other types of self-powered detectors (SPDs) for neutron counting are operated by the current that is produced by ionization due to gamma emission related to neutron capture during fission. The main advantages of these self-powered neutron detectors are their small size and the simple electronics necessary for this type of detector (Alex et al., 2004; Miller et al., 2004; Alex and Ghodgaonkar, 2007).

The basic design of the SPD is illustrated in Fig. 3.26. The detector (emitter, Fig. 3.26) measures only 2 mm in diameter and 21 cm in length. The emitter is housed in a high-purity alumina ceramic tube (2.2 mm ID \times 2.8 mm OD) and enclosed in a 3-mm ID and 3.5-mm OD Inconel 600 tube. One end of the emitter is coupled to a 2-mm diameter twin core mineral insulated cable with a length up to 12 m. The long cable permitted in-core neutron monitoring. The small size of the self-powered neutron detector allows for applications in nuclear medicine such as the implanting of the detector into patients for the on-line measurement of neutron flux during neutron capture therapy (Miller et al., 2004). Examples of some emitters that can be used in SPDs, their neutron and/or gamma response, and applications are listed in Table 3.1. From the table it can be seen that not all SPDs are responsive to neutrons. For example, bismuth ($Z = 83$) has a neutron absorption cross section of 0.014b exhibiting a negligible response to neutron flux, and it is essentially a pure gamma detector (Alex et al., 2004). Other emitters such as Pt yield nearly equal current contributions from neutrons and gamma rays.

Disadvantages are the low levels of the output signals, a slow response time, and sensitivity of the response to the neutron spectrum. Self-powered detectors have to be operated in the

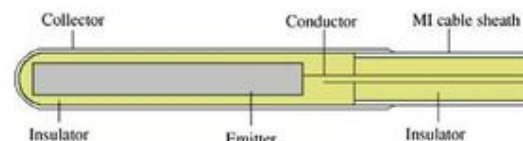


FIGURE 3.26 Schematic diagram of a self-powered neutron detector. (From Alex and Ghodgaonkar, 2007. Reprinted with Permission from Elsevier © 2007)

TABLE 3.1 Response Characteristics of SPDs

Emitter	Neutron response	Gamma response (γ , e)	Application
$^{105}_{43}\text{Rh}$	(n, β) (delayed)	Positive current	Flux mapping
$^{51}_{23}\text{V}$	Positive current	Negative current	
$^{59}_{27}\text{Co}$	(n, γ , e) (prompt)	Negative current	Reactor control
$^{195}_{78}\text{Pt}$	Positive current	Positive current	
$^{209}_{83}\text{Bi}$		Positive current	Gamma flux

(From Alex et al., 2004). Reprinted with Permission from Elsevier (c) 2004

current mode, because the signal created by a neutron can be only a single electron.

D. Self-Quenched Streamer

Traditionally, gas ionization detectors are categorized as ion chambers, proportional counters, and Geiger–Müller tubes. But another type of counting system based on ionization effects has been developed and applied. This is a type of gas multiplication detector that is somewhat different from proportional and Geiger–Müller counting systems. It is called a self-quenched streamer (SQS) or limited streamer detector and is frequently used in position-sensitive multiwire detector systems. In conventional proportional and Geiger–Müller counters, UV photons play a significant role in the propagation of an ion avalanche. If the propagation of the avalanche is kept small by the field strength or by absorption of UV, the system works in the proportional mode. If UV photons are able to create additional avalanches that may spread through the entire length of the anode wire and the whole process is terminated only by the creation of a space charge around the anode, the system works in the GM mode and the output signal does not depend on the original ionization effect (e.g. on the number of primary ions produced by the radiation event). In the self-quenched streamer mode, the ion avalanches are controlled in a special way. The counting tube is filled with a gas mixture that absorbs UV photons. Therefore, no additional avalanches far from the original avalanche pathway can be created through excitation by photon absorption. Avalanches, therefore, grow and propagate in the shape of a streamer. The streamers have a diameter of about 200 μm and extend a few millimeters from the anode. They terminate at low field strength at larger radii of the detector.

If the voltage is high enough, a single electron can create a streamer. The streamers have a final length that depends on the voltage applied. The formation of such streamers is supported by anode wires with relatively large diameters (0.1 mm).

SQS detectors have some properties of both proportional and Geiger–Müller detectors. The rather high internal gas amplification is useful for position-sensitive detectors. Position-sensitive detectors operating in the proportional region have much smaller signal amplitudes. However, as in the case of

Geiger–Müller tubes, the signal amplitudes in SQS detectors no longer provide information about the energy of the primary radiation event. Spreading of the avalanche along the total length of the anode wire is prevented. Thus, the resolving time is much shorter than with Geiger–Müller tubes (Knoll, 2010).

E. Long-Range Alpha Detectors

Traditional alpha detectors suffer from limitations related to the very short range of alpha particles in air. If sample and detector together are kept in a vacuum or sample and detector are operated in close proximity, reasonable efficiency is achieved. An alpha particle produces about 30,000 ions per 1 MeV of its particle energy (see Chapter 1). These ions can be transported over significant distances by a moving stream of air to a detector. For that purpose, a current of air can be generated by a small fan and the ions can be transported over a distance of several meters. The current of air is finally monitored by an ion chamber (Garner et al., 1994). By using air as the detector gas, alpha contamination on any complicated surface can be measured (MacArthur et al., 1992, 1993; Allander et al., 1994; Vu et al., 1994). Fig. 3.27 illustrates the principle of a long-range alpha detector. It is shown that the detector is sensitive to the ionized air molecules produced by the passage of an alpha particle rather than to the alpha particle itself. The detector consists mainly of two grids (see Fig. 3.28) across which an electric field is applied. One type of ion is attracted by the high-voltage (HV) grid, the other by the sense grid. Both possible polarities for the grids have been applied with equal sensitivity. The charge collected at the sense grid is measured by a suitable electronic circuit and used to determine the ionization, the number of alpha particles.

Instead of using airflow, the ions produced by alpha particles can be transported to the detector by an electrostatic field. At Los Alamos National Laboratory, long-range alpha detectors have been built for several applications, such as monitoring of soil surface and liquid effluents. A hand monitor has also been constructed. The method was applied to radon measurements (Bolton, 1994). Some effort has been made to use the long-range detectors for the measurement of beta contamination (Johnson et al., 1994).

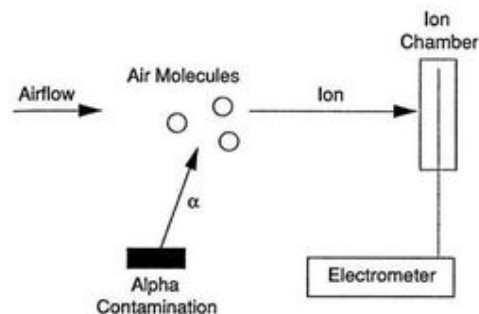


FIGURE 3.27 Principle of a long-range alpha detector operation. Ions created by alpha particles are transported to the detector by airflow. (From MacArthur et al., 1992. Reprinted with Permission from IEEE (c) 1992)

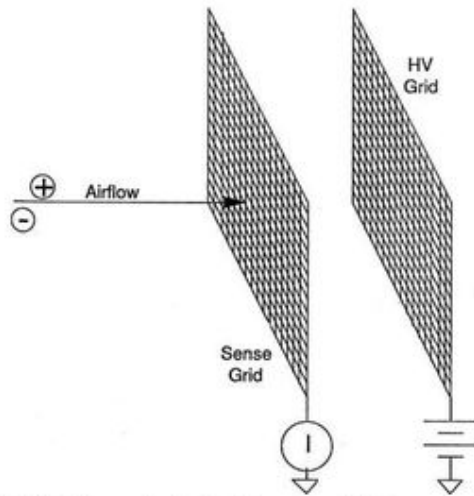


FIGURE 3.28 Construction detail of a long-range alpha detector. An electric field is applied across the grids. One type of ion is attracted by the HV grid, the other one by the sense grid. (From MacArthur et al., 1992. Reprinted with Permission from IEEE (c) 1992)

Real-time alpha activity monitoring is one of the applications for which the ionization detectors show several advantages. A monitoring system for real-time alpha monitoring was developed at Los Alamos and tested at the Radioactive Liquid Waste Treatment Facility as a means for real-time monitoring of liquid waste influent (Whitley et al., 1996). This system determines the alpha activity of the wastewater by measuring the ionization of ambient air above the surface at a rather long distance. The distance to the surface of the liquid described by Whitley et al. (1996) was about 4 inches. Sometimes this type of design causes problems because of changing levels of the surface to be monitored, for example, with liquids.

The ionization counting system consists of a metal enclosure and a signal plate that is maintained at 300 V DC. The box is maintained at ground potential. A highly sensitive electronic circuit is used to detect changes in current to the plate. Changes in alpha activity in the contaminated liquid at the 10 nCi/L level could be detected.

The authors claim that this kind of measurement equipment can be useful for monitoring low-level liquid streams before discharge into the environment. However, a more sensitive design will be necessary to ensure regulatory compliance and offer the opportunity for field application.

Ionization monitoring has one great advantage in simultaneous measurement of the entire body of a person. Air currents which are created by high-capacity fans can be drawn from all surfaces of the body of a person who is positioned in a monitoring chamber (size 91 cm × 91 cm × 213 cm). High airflow rate is essential because of the rather short "ion lifetime." Koster et al. (1998) describe a contamination measurement facility for alpha particle radionuclides, which is used at Los Alamos National Laboratory for test experiments.

Another example for the application of ionization monitoring is a portable swipe monitor, based on long-range alpha detection

(Whitley et al., 1998). This facility consists of two independent detection chambers. The swipe is placed in one chamber for the detection of the alpha contamination and the other chamber records signals due to the presence of radon or other background radionuclides. The response to beta contamination is about 100 times weaker compared to the same activity of alpha-emitting radionuclides. A unit applicable to rapid field measurements is available with dimensions of 28 cm × 13 cm × 14 cm, and weight of 5 kg.

F. Liquid Ionization and Proportional Detectors

Detector materials of high density offer some advantages, particularly for the detection of radiation with low linear energy transfer and high energy. Radiation spectroscopy in many cases can be carried out much more reliably using detector materials of higher density. Consequently, research related to liquid- and solid-state ionization detectors is carried out. Noble gases in the liquid or solid phase are dielectric materials where created electrons remain free if all electronegative impurities can be removed.

Among the noble gases, xenon has attracted much interest as a filling medium for ionization-type detectors, such as ion chambers and proportional counting systems. The start of the ion multiplication phenomenon is observed at a field strength of 10^8 V/m. At 10^5 V/m, the electron drift velocity is about 3×10^3 m/s. Main obstacles to the construction of such detectors are the requirements for operation at a low temperature and for extensive purification of the detector medium. Liquid xenon ionization chambers compared with sodium iodide (NaI) detectors have a similar gamma efficiency and a higher energy resolution (L'Annunziata, 1987). Of course, the energy resolution of semiconductor gamma detectors is still better.

The size of useful liquid or solid noble-gas ionization detectors depends on the purity of the filling material. Position sensing by large detectors can be carried out by measuring the electron drift time. Gridded versions of such ion chamber detectors have also been reported.

Liquid ionization chambers (Ar and Xe) are frequently used in basic nuclear physics, e.g. for the search for weakly interacting massive particles (WIMPs), such as the neutrinos predicted by supersymmetric theories (Ovchinnikov and Parusov, 1999).

Some information is available related to nonpolar liquids as ionization detectors at room temperature. Here, the purity that can be achieved and maintained for the applied material is extremely important. Research has been carried out using, for example, tetramethylsilane. This material was used for ion chambers working in pulse and current mode (Knoll, 2010).

G. Dynamic Random Access Memory Devices (DRAM)

Soft errors are induced to dynamic random access memory devices (DRAMs) and therefore Chou et al. (1997) studied their use as radiation detectors. Samples of DRAMs from several manufacturers, just off-the-shelf products, have been used for that study. Memory content of the DRAM was reset and then

after irradiation the number of flipped cells was determined. Once counted, the memory content is reset again. Experimental results using alpha particle radiation indicate that the soft error is linearly related to irradiation time as well as the radiation source intensity. This linearity could not be obtained with gamma radiation. Nevertheless, it can be assumed that high-density DRAMs may be promising counters for charged particle detections. They could also be used for the counting of neutrons, if the DRAMs are coated with a layer of neutron-sensitive materials.

REFERENCES

- Abbrescia, M., Paticchio, V., Ranieri, A., Trentadue, R., 2004. Resistive plate chambers as detectors for thermal neutrons. *Nucl. Instrum. Methods Phys. Res., Sect. A* 518, 440–442.
- Agosteo, S., 2010. Overview of novel techniques for radiation protection and dosimetry. *Radiat. Meas.* 45, 1171–1177.
- Agrawal, P.C., Ramsey, B.D., Weisskopf, M.C., 1989. Study of argon-based Penning gas mixtures for use in proportional counters. *Nucl. Instrum. Methods Phys. Res., Sect. A* 277, 557–564.
- Äikää, O., Mäntynen, P., Kankainen, T., 1992. High performance ^{14}C gas proportional counting system applying pulse shape discrimination. *Radiocarbon* 34, 414–419.
- Alex, M., Ghodgaonkar, M.D., 2007. Development of an inconel self powered neutron detector for in-core reactor monitoring. *Nucl. Instrum. Methods Phys. Res., Sect. A* 574, 127–132.
- Alex, M., Prasad, K.R., Kataria, S.K., 2004. Development of bismuth self-powered detector. *Nucl. Instrum. Methods Phys. Res., Sect. A* 523, 163–166.
- Alkhozov, G.D., Komar, A.P., Vorobev, A.A., 1967. Ionization fluctuation and resolution of ionization chambers and semiconductor detectors. *Nucl. Instrum. Methods* 48, 1–12.
- Allander, K.S., Bounds J.A., Mac Arthur D.W., 1994. Application of the long-range alpha detector (LRAD) to the detection of natural-occurring radioactive materials (NORM). *Proc. WM '94 Conf.*, Tucson, AZ.
- Alieri, E., 1992. Measurement of Reverse Transcriptase Activity of an HIV-1 Virus Stock Prepared in A 3.0i Lymphoblastoid Cells. *Matrix Application note*. Packard Instrument Company, Meriden, CT.
- Altizoglou, T., Denecke, B., Johansson, L., Sibbens, G., 2002. Standardisation of ^{89}Sr using different methods. *Appl. Radiat. Isot.* 56, 447–452.
- Amrani, D., Cherouati, D.E., Cberchali, M.E.H., 2000. Groundwater radon measurements in Algeria. *J. Environ. Radioact.* 51, 173–180.
- Andriamonje, S., Aune, S., Bignan, G., Blandin, C., Ferrer, E., Giomataris, L., Jammes, C., Pancin, J., 2004. New neutron detectors based on micromegas technology. *Nucl. Instrum. Methods Phys. Res., Sect. A* 525, 74–78.
- Aoyama, T., 1990. A tritium in-air monitor with compensation and additional recording of α , β and γ -backgrounds. *IEEE Trans. Nucl. Sci.* 37, 885–891.
- Aslam, Qashua, N., Waker, A.J., 2011. Study of the effect of high dose rate on tissue equivalent proportional counter microdosimetric measurements in mixed photon and neutron fields. *Nucl. Instrum. Methods Phys. Res., Sect. A* 652, 854–857.
- Assaf, J., 2002. High voltages influence on the response of two-stage GEM detector. *Radiat. Meas.* 35, 7–12.
- Aulchenko, V.M., Bobrov, A.V., Bondar, A.E., Shekhtman, L.I., Usov, E.V., Zhilich, V.N., Zhulanov, V.V., 2009. Triple-GEM detectors for KEDR tagging system. *Nucl. Instrum. Methods Phys. Res., Sect. A* 598, 112–115.
- Babichev, E.A., Baru, S.E., Groshev, V.R., Khabakhpashev, A.G., Kraimov, G.S., Leonov, V.V., Neustroev, V.A., Porosev, V.V., Savinov, G.A., Shekhtman, L.I., 2001. Usage of two types of high-pressure xenon chambers for medical radiography. *Nucl. Instrum. Methods Phys. Res., Sect. A* 461, 430–434.
- Bacchi, O.O., Reichardt, K., Calvache, M., Nielsen, D., Vachaud, G., Eaglesham, A., Chalk, P.M., Urquiaga, S., Zapata, F., Laurent, J.-P., Thony, J.L., Vauchlin, M., Moutonnet, P., 2002. Neutron and Gamma Probes: Their Use in Agronomy. *International Atomic Energy Agency Training Course Series No. 16 (IAEA-TCS-16)*, p. 75. IAEA, Vienna.
- Bachmann, S., Kappler, S., Ketzler, B., Müller, Th., Ropelewski, L., Sauli, F., Schulte, E., 2002. High rate X-ray imaging using multi-GEM detectors with a novel readout design. *Nucl. Instrum. Methods Phys. Res., Sect. A* 478, 104–108.
- Barbosa, A.F., Riekel, C., Wattecamps, P., 1992. Two dimensional X-ray detector based on microstrip and multiwire design. *Nucl. Instrum. Methods* A323, 247–251.
- Barr, A., Bonaldi, L., Carugno, G., Charpak, G., Iannuzzi, D., Nicoletto, M., Pepato, A., Ventura, S., 2002. A high-speed, pressurised multi-wire gamma camera for dynamic imaging in nuclear medicine. *Nucl. Instrum. Methods Phys. Res., Sect. A* 477, 499–504.
- Bateman, J.E., 1994. *Fundamentals of gas counters*. *Med. Radiat. Detect.* 1994, 89–99.
- Bateman, J.E., Sore, J., Knight, S.C., Bedford, P., 1994. A new gas counter for radioimmunoassay. *Nucl. Instrum. Methods Phys. Res., Sect. A* 348, 288–292.
- Bateman, J.E., Conolly, J.F., Derbyshire, G.E., Duxbury, D.M., Mir, J.A., Spill, E.J., Stephenson, R., 2002. Energy resolution in X-ray detection micro-strip gas counters. *Nucl. Instrum. Methods Phys. Res., Sect. A* 484, 384–395.
- Beck, T.R., Buchrüder, H., Schmidt, V., 2009. Performance tests for instruments measuring radon activity concentration. *Appl. Radiat. Isot.* 67, 876–880.
- Beddingfield, D.H., Johnson, N.H., Menlove, H.O., 2000. ^3He neutron proportional counter performance in high gamma-ray dose environments. *Nucl. Instrum. Methods Phys. Res., Sect. A* 455, 670–682.
- Beddingfield, D.H., Menlove, H.O., Johnson, N.H., 1999. Neutron proportional counter design for high gamma-ray environments. *Nucl. Instrum. Methods Phys. Res., Sect. A* 422, 35–40.
- Bellazzini, R., Bozzo, M., Brez, A., Gariano, G., Latronico, L., Lumb, N., Massai, M.M., Papanestis, A., Raffo, R., Spandre, G., Spezziga, M.A., 1999. A two-stage, high gain micro-strip detector. *Nucl. Instrum. Methods Phys., Res. Sect. A* 425, 218–227.
- Bellazzini, R., Bozzo, M., Brez, A., Gariano, G., Latronico, L., Lumb, N., Papanestis, A., Spandre, G., Massa, M.M., Raffo, R., Spezziga, M.A., 1999. The WELL detector. *Nucl. Instrum. Methods Phys. Res., Sect. A* 423, 125–134.
- Bellazzini, R., Brez, A., Gariano, G., Latronico, L., Lumb, N., Moggi, A., Reale, S., Spandre, G., Massai, M.M., Spezziga, M.A., Toropin, A., Costa, E., Soffitta, P., Pacella, D., 2001. Micropattern gas detectors: the CMS MSGC project and gaseous pixel detector application. *Nucl. Instrum. Methods Phys. Res., Sect. A* 471, 41–54.
- Bellazzini, R., Spandre, G., Lumb, N., 2002. Progress with micro-pattern gas detectors. *Nucl. Instrum. Methods Phys. Res., Sect. A* 478, 13–25.
- Belli, G., De Vecchi, C., Giroletti, E., Guida, R., Musitelli, G., Nardò, R., Necchi, M., Pagano, D., Ratti, S.P., Sani, G., Vicini, A., Vitulo, P., Viviani, C., 2007. RPCs in biomedical applications. *Nucl. Instrum. Methods Phys. Res., Sect. B* 158, 166–174.
- Bertolini, G., 1984. Alpha particle spectroscopy by gridded ionization chamber. *Nucl. Instrum. Methods* 223, 285–289.
- Bigu, J., 1992. Design and operation of an automated beta-particle counting system for the measurement of ^{220}Rn (and ^{222}Rn) progeny. *Appl. Radiat. Isot.* 43, 443–448.
- Blanco, F., La Rocca, P., Riggi, F., 2009. Cosmic rays with portable Geiger counters: from sea level to airplane cruise altitudes. *Eur. J. Phys.* 30, 685–695.
- Böck, H., Balcar, E., 1975. Long-time behaviour of regenerative in-core neutron detectors with ^{238}U - ^{239}Pu electrodes during power cycling. *Nucl. Instrum. Methods* 124, 563–571.
- Bolton, R.D., 1994. Radon monitoring using long-range alpha detector-based technology. *Nuclear Science Symposium*, Norfolk, VA.
- Bondar, A., Buzulutskov, A., de Oliveira, R., Ropelewski, L., Sauli, F., Shekhtman, L., 2006. *Nucl. Instrum. Methods Phys. Res., Sect. A* 556, 495–497.
- Bondar, A., Buzulutskov, A., Grebenuk, A., Sokolov, A., Akimov, D., Alexandrov, I., Breskin, A., 2010. Direct observation of avalanche scintillations in a THGEM-based two-phase Ar-avalanche detector using Geiger-mode APD. *J. Instrum.* 5, 20. P08002.
- Bondar, A., Buzulutskov, A., Grebenuk, A., Sokolov, A., Akimov, D., Alexandrov, I., Breskin, A., 2011. Geiger mode APD performance in

- a cryogenic two-phase Ar avalanche detector based on THGEMs. *Nucl. Instrum. Methods Phys. Res., Sect. A* 628, 364–368.
- Bouclier, R., Capeans, M., Evans, J., Garabatos, C., Manzin, G., Million, G., Ropelewski, L., Sauli, F., Shekhtman, L.I., Temmel, T., Fischer, G., 1995. Optimization of design and beam test of microstrip gas chambers. *Nucl. Instrum. Methods Phys. Res., Sect. A* 367, 163–167.
- Bouclier, R., Florent, J.J., Gaudaen, J., Million, G., Ropelewski, L., Sauli, F., 1992a. Microstrip gas chambers on thin plastic supports. *IEEE Trans. Nucl. Sci.* 39, 650–653.
- Bouclier, R., Florent, J.J., Gaudaen, J., Million, G., Pasta, A., Ropelewski, L., Sauli, F., Shekhtman, L., 1992c. High flux operation of microstrip gas chambers on glass and plastic supports. *Nucl. Instrum. Methods Phys. Res., Sect. A* 323, 240–246.
- Bouclier, R., Florent, J.J., Gaudaen, J., Sauli, F., Shekhtman, L., 1992b. Development of microstrip gas chambers on thin plastic supports. *Nucl. Instrum. Methods Phys. Res., Sect. A* 315, 521–528.
- Braby, L.A., Badhwar, G.D., 2001. Proportional counter as neutron detector. *Radiat. Meas.* 33, 265–267.
- Breskin, A., 2000. Advances in gas avalanche radiation detectors for biomedical applications. *Nucl. Instrum. Methods Phys. Res., Sect. A* 454, 26–39.
- Bronic, L.K., Grosswendt, B., 2001. Experimental study of gas mixtures in strong non-uniform electric fields. *Radiat. Phys. Chem.* 61, 477–478.
- Byun, S.H., Spirou, G.M., Hanu, A., Prestwich, W.V., Waker, A.J., 2009. Simulation and first test of a microdosimetric detector based on a thick gas electron multiplier. *IEEE Trans. Nucl. Sci.* 56, 1108–1113.
- Cabellos, O., Fernández, P., Rapisarda, D., García-Herranz, N., 2010. Assessment of fissionable material behaviour in fission chambers. *Nucl. Instrum. Methods Phys. Res., Sect. A* 618, 248–259.
- Cesari, V., Colausti, P., Magrin, G., De Nardo, L., Baek, W.Y., Grosswendt, B., Alkaa, A., Khamphan, C., Ségur, P., Tornielli, G., 2002. Nanodosimetric measurements with an avalanche confinement TEPC. *Radiat. Prot. Dosim.* 99, 337–342.
- Charpak, G., 1970. Evolution of the automatic spark chambers. *Annu. Rev. Nucl. Part. Sci.* 20, 195–254.
- Charpak, G., Sauli, F., 1978. Multiwire proportional chambers and drift chambers. *Nucl. Instrum. Methods* 162, 405–428.
- Chase, G., Rabinowitz, J., 1967. *Principles of Radioisotope Methodology*. Burgess Publishing Company, Minneapolis.
- Chefdeville, M., van der Graaf, H., Hartjes, F., Timmermans, J., Visschers, J., Blanco Carballo, V.M., Salm, C., Schmitz, J., Smits, S., Colas, P., Giomataris, I., 2008. Pulse height fluctuations of integrated micromegas detectors. *Nucl. Instrum. Methods Phys. Res., Sect. A* 591, 147–150.
- Chiti, T., Neubert, R.E.M., Janssens, I.A., Certini, G., Curiel Yuste, J., Sirignano, C., 2009. Radiocarbonating reveals different past managements of adjacent forest soils in the Campine region, Belgium. *Geoderma* 149, 137–142.
- Chou, H.P., Chou, T.C., Hau, T.H., 1997. Evaluation of high density DRAMs as a nuclear radiation detector. *Appl. Radiat. Isot.* 48, 1601–1604.
- Christophel, E., Dracos, M., Strub, R., 1998. The 2D-microgap wire chamber. *Nucl. Instrum. Methods Phys. Res., Sect. A* 419, 515–518.
- Chu, T.C., Wang, J.-J., Lin, Y.-M., 1998. Radiostrontium analytical method using crown — ether compound and Cerenkov counting and its application in environmental monitoring. *Appl. Radiat. Isot.* 49, 1671–1675.
- Clergeau, J.F., Covert, P., Feltin, D., Fischer, H.E., Guerard, B., Hansen, T., Manin, G., Oed, A., Palleau, P., 2001. Operation of sealed microstrip gas chambers at the ILL. *Nucl. Instrum. Methods Phys. Res., Sect. A* 471, 60–68.
- Clouvas, A., Xanthos, S., Takoudis, G., 2011. Indoor radon levels in Greek schools. *J. Environ. Radioact.* 102, 881–885.
- Coelho, L.C.C., Lopes, J.A.M., Covita, D.S., Conceição, A.S., Santos, J.M.F., 2007. Xenon GPSC high-pressure operation with large-area avalanche photodiode readout. *Nucl. Instrum. Methods Phys. Res., Sect. A* 575, 444–448.
- Colmenares, C.A., 1974. Bakeable ionization chamber for low level tritium counting. *Nucl. Instrum. Methods Phys. Res.* 150, 549.
- Cooper, J.R., Bernstein, L., McMahan, M.A., Powell, J., Wutte, D., Ahle, L., Benzer-Koller, N., Dashdorj, D., Kumbartzki, G., Mertziemakis, T.J., Schiller, A., Silver, C., Taylor, M.J., 2004. Production of a ^{79}Kr radioactive ion beam using a batch mode method. *Nucl. Instrum. Methods Phys. Res., Sect. A* 533, 287–294.
- Cosma, C., 2000. Strontium-90 measurement after the Chernobyl accident in Romanian samples without chemical separation. *Spectrochim. Acta Part B* 55, 1165–1171.
- Couceiro, M., Blanco, A., Ferreira, N.C., Ferreira Marques, R., Fonte, P., Lopes, L., 2007. RPC-PET: status and perspectives. *Nucl. Instrum. Methods Phys. Res., Sect. A* 580, 915–918.
- Covita, D.S., Simões, P.C.P.S., Fernandes, L.M.P., Freitas, E.D.C., Requeixa Ferreira, L.F., Veloso, J.F.C.A., dos Santos, J.M.F., 2004. The X-ray performance of a driftless gas proportional scintillation counter using short shaping-time constants for pulse analysis. *Nucl. Instrum. Methods Phys. Res., Sect. A* 516, 134–142.
- Curzio, G., Mazed, D., Ciolini, R., Del Gratta, A., Gentili, A., 2005. Effect of air on gas amplification characteristics in argon-propane (1%) —based proportional counters for airborne radon monitoring. *Nucl. Instrum. Methods Phys. Res., Sect. A* 537, 672–682.
- Dalla Torre, S., 2011. Status and perspectives of gaseous photon detectors. *Nucl. Instrum. Methods Phys. Res., Sect. A* 639, 111–116.
- De Nardo, L., Cesari, V., Donà, G., Colausti, P., Conte, V., Tornielli, G., 2004a. Mini TEPCs for proton therapy. *Radiat. Prot. Dosim.* 108, 345–352.
- De Nardo, L., Colausti, P., Héroult, J., Conte, V., Moro, D., 2010. Microdosimetric characterisation of a therapeutic proton beam used for conjunctival melanoma treatments. *Radiat. Meas.* 45, 1387–1390.
- De Nardo, L., Moro, D., Colausti, P., Conte, V., Tornielli, G., Cuttone, G., 2004b. Microdosimetric investigation at the therapeutic proton beam facility of CATANA. *Radiat. Prot. Dosim.* 110, 681–686.
- Degeva, M.O., Vorobiova, M.I., Tolstykh, E.I., Shagina, N.B., Shishkina, E.A., Anspaugh, L.R., Napier, B.A., Bougrov, N.G., Shved, V.A., Tokareva, E.E., 2006. Development of an improved dose reconstruction system for the Techa River population affected by the operation of the Mayak Production Association. *Radiat. Res.* 166, 255–270.
- Delbart, A., De Oliveira, R., Derré, J., Giomataris, Y., Jeanneau, F., Papadopoulos, Y., Rabourgeard, Ph., 2001. New development of Micro-megas detector. *Nucl. Instrum. Methods Phys. Res., Sect. A* 461, 84–87.
- Denman, A.R., Groves-Kirkby, C.J., Phillips, P.S., Crockett, R.G.M., Woolridge, A., Gillmore, G.K., 2005. The practical use of electrets in a public health radon remediation campaign. *J. Environ. Radioact.* 84, 375–391.
- Derré, J., Giomataris, Y., Zacccone, H., Bay, A., Perroud, J.-P., Ronga, F., 2001. Spatial resolution in Micromegas detectors. *Nucl. Instrum. Methods Phys. Res., Sect. A* 459, 523–531.
- Domnikov, V.N., Saltykov, L.S., Slusarenko, L.I., Shevchenko, S.V., 2001. About the effectiveness of spectrometry in alpha-activity monitoring of industrial air-borne particles. *Appl. Radiat. Isot.* 55, 543–547.
- Donnard, J., Berry, R., Carduner, H., Leray, P., Morteau, E., Provence, M., Servagent, N., Thers, D., 2009. The micro-pattern gas detector PIM: a multi-modality solution for novel investigations in functional imaging. *Nucl. Instrum. Methods Phys. Res., Sect. A* 610, 158–160.
- dos Santos, J.M.F., Dias, T.H.V.T., Reyes Cortes, S.D.A., Conde, C.A.N., 1989. Novel techniques for designing gas proportional scintillation counters for X-ray spectrometry. *Nucl. Instrum. Methods Phys. Res., Sect. A* 280, 288–290.
- dos Santos, J.M.F., Lopes, J.A.M., Veloso, J.F.C.A., Simões, P.C.P.S., Dias, T.H.V.T., dos Santos, F.P., Rachinhas, P.J.B.M., Ferreira, L.F.R., Conde, C.A.N., 2001. Development of portable gas proportional scintillation counters for X-ray spectrometry. *X-Ray Spectrom.* 30, 373–381.
- Dueñas, C., Fernández, M.C., Gordo, E., Cañete, S., Pérez, M., 2011. Gross alpha, gross beta activities and gamma emitting radionuclides composition of rainwater samples and deposition to ground. *Atmos. Environ.* 45, 1015–1024.
- East, L.V., Walton, B.B., 1982. Polythene moderated ^3He neutron detectors. *Nucl. Instrum. Methods Phys. Res.* 199, 643.
- Epstein, M.S., Miles Jr., D.G., Yu, L.L., 2009. What were they drinking? A critical study of the radium ore revigator. *Appl. Spectrosc.* 63, 1406–1409.
- Etaati, G., Amrollahi, R., Doust-Mohammadi, V., Ghal-Eh, N., Habibi, M., 2010. Calibration constant of a silver activated Geiger counter used for neutron efficiency measurements in plasma focus devices: theoretical vs. experimental studies. *J. Fusion Energy* 29, 381–386.
- Evans Jr., A.E., 1982. Energy dependence of the response of a ^3He long counter. *Nucl. Instrum. Methods* 199, 643–644.

- Evvett, S.R., Schwartz, R.C., Tolk, J.A., Howell, T.A., 2009. Soil profile water content determination: spatiotemporal variability of electromagnetic and neutron probe sensors in access tubes. *Vadose Zone J.* 5, 926–941.
- Evvett, S.R., Tolk, J.A., Howell, T.A., 2006. Soil profile water content determination: sensor accuracy, axial response, calibration, temperature dependence, and precision. *Vadose Zone J.* 5, 894–907.
- Facorellis, Y., Kyparissi-Apostolika, N., Maniatis, Y., 2001. The cave of Theopatra, Kalambaka: radiocarbon evidence for 50,000 years of human presence. *Radiocarbon* 43, 1029–1048.
- Fadil, M., Blandin, Ch., Christophe, S., Déruelle, O., Fioni, G., Marie, F., Mounier, C., Ridikas, D., Trapp, J.P., 2002. Development of fission microchambers for nuclear waste incineration studies. *Nucl. Instrum. Methods Phys. Res., Sect. A* 476, 313–317.
- Farahmand, M., Bos, A.J.J., van Eijk, C.W.E., 2003a. Gas electron multiplier (GEM) operation with tissue-equivalent gases at various pressures. *Nucl. Instrum. Methods Phys. Res., Sect. A* 506, 160–165.
- Farahmand, M., Bos, A.J.J., De Nardo, L., van Eijk, C.W.E., 2004. First microdosimetric measurements with a TEPC based on a GEM. *Radiat. Prot. Dosim.* 110, 839–843.
- Farahmand, M., Bos, A.J.J., Huizenga, J., De Nardo, L., van Eijk, C.W.E., 2003b. Design of a new tissue equivalent proportional counter based on a gas electron multiplier. *Nucl. Instrum. Methods Phys. Res., Sect. A* 509, 262–267.
- Filliatre, P., Oriol, L., Jammes, C., Vermeeren, L., 2008. Reasons why plutonium 242 is the best fission chamber deposit to monitor the fast component of a high neutron flux. *Nucl. Instrum. Methods Phys. Res., Sect. A* 593, 510–518.
- Filliatre, P., Oriol, L., Jammes, C., Vermeeren, L., 2009. Joint estimation of the fast and thermal components of a high neutron flux with a two on-line detector system. *Nucl. Instrum. Methods Phys. Res., Sect. A* 603, 415–420.
- Fischer, B.E., 1977. A digital processor for position sensitive detectors. *Nucl. Instrum. Methods* 41, 173–181.
- Fourme, R., 1997. Position sensitive gas detectors: MEPCs and their gifted descendants. *Nucl. Instrum. Methods Phys. Res., Sect. A* 392, 1–11.
- Fraga, F.A.F., Fetal, S.T.G., Ferreira Maques, R., Policarpo, A.P.L., 2000. Quality control of GEM detectors using scintillation techniques. *Nucl. Instrum. Methods Phys. Res., Sect. A* 442, 417–422.
- Fraga, F.A.F., Margato, L.M.S., Fetal, S.T.G., Fraga, M.M.F.R., Maques, R.F., Policarpo, A.J.P.L., Guerard, B., Oed, A., Manzini, G., van Vuure, T., 2002. CCD readout of GEM – based detectors. *Nucl. Instrum. Methods Phys. Res., Sect. A* 478, 357–361.
- Fraga, F.A.F., Margato, L.M.S., Fetal, S.T.G., Fraga, M.M.F.R., Ferreira Marques, R., Policarpo, A.J.P.L., 2003. Luminescence and imaging with gas electron multipliers. *Nucl. Instrum. Methods Phys. Res., Sect. A* 513, 379–387.
- Fried, J., Harder, J.A., Mahler, G.J., Makowiecki, D.S., Mead, J.A., Radeka, V., Schaknowski, N.A., Smith, G.C., Yu, B., 2002. A large, high performance, curved 2D position-sensitive neutron detector. *Nucl. Instrum. Methods Phys. Res., Sect. A* 478, 415–419.
- Fulbright, H.W., 1979. Ionization chambers. *Nucl. Instrum. Methods* 62, 21–28.
- García-León, M., García-Montaño, E., Madurga, G., 1984. Characterization of ⁹⁹Tc by shape of its plateau with a gas-flow proportional counter. *Int. J. Appl. Radiat. Isot.* 35, 195–200.
- García-Torales, E., Barquerro, R.L., Roteta, M., 2002. Standardization of ¹³⁴Cs by three methods. *Appl. Radiat. Isot.* 56, 211–214.
- Gardner, R.P., Liu, Linayan, 1997. On extending the accurate and useful counting rate of GM counter detector systems. *Appl. Radiat. Isot.* 48, 1605–1615.
- Garner, S.E., Bounds, J.A., Allander, K.S., Caress, R.W., Johnson, J.D., MacArthur, D.W., 1994. A compendium of results from long-range alpha detector soil surface monitoring: June 1992–May 1994. LA-12861-MS. Los Alamos National Laboratory Document.
- Geiger, H., Müller, W., 1928. Elektronenzählrohr zur Messung schwächster Aktivitäten (Electron counting tube for the measurement of weakest activities). *Naturwissenschaften* 16, 617–618.
- Geltenbort, P., 1994. Recent results with microstrip gas chambers. *Nucl. Instrum. Methods Phys. Res., Sect. A* 353, 168.
- Giomataris, Y., Rebourgeard, Ph., Robert, J.P., Charpak, G., 1996. MICRO-MEGAS: a high-granularity position-sensitive gaseous detector for high particle-flux environment. *Nucl. Instrum. Methods Phys. Res., Sect. A* 376, 29–35.
- Glesius, F.L., Kniss, T.A., 1988. He-3 neutron detectors for hostile environments. *IEEE Trans. Nucl. Sci.* 35, 867–871.
- Golovatyuk, V., Grancagnolo, F., 1999. Observation of transition between proportional and Geiger-Müller modes in helium-isobutane gas mixtures. *Nucl. Instrum. Methods Phys. Res., Sect. A* 428, 367–371.
- Goulianos, K., Smith, K.K., White, S.N., 1980. A simple electronic apparatus for the analysis of radioactively labeled gel electrophoretograms. *Anal. Biochem.* 103, 64–69.
- Grossi, C., Arnold, D., Adame, J. A., López-Coto, I., Bolívar, J. P., de la Morena, B. A., and Vargas, A., 2012. Atmospheric ²²²Rn concentration and source term at *El Arenosillo* 100 m meteorological tower in southwest Spain. *Radiat. Meas.*, 47, 149–162.
- Grossi, C., Vargas, A., Camacho, A., López-Coto, I., Bolívar, J.P., Xia, Yu, Conen, F., 2011. Inter-comparison of different direct and indirect methods to determine radon flux from soil. *Radiat. Meas.* 46, 112–118.
- Gruhn, C.R., Binimi, M., Legrain, R., Loveman, R., Pang, W., Loach, M., Scott, D.K., Shotter, A., Symons, T.J., Wouters, J., Zimmon, M., Devier, R., 1982. Bragg curve spectroscopy. *Nucl. Instrum. Methods* 196, 33–40.
- Guillemot, F., Brouillaud, B., Labrugère, C., Barthe, N., Durrieu, M.C., 2007. High resolution β -imager: a new tool for characterizing 2D peptide distribution on biomimetic materials? *IRBM* 28, 86–92.
- Hagiwara, M., Sanami, T., Oishi, T., Baba, M., Takada, M., 2008. Extension of energy acceptance of Bragg curve counter at the high-energy end. *Nucl. Instrum. Methods Phys. Res., Sect. A* 592, 73–79.
- Hamlat, M.S., Kadi, H., Djeflal, S., Brahimi, H., 2003. Radon concentrations in Algerian oil and gas industry. *Appl. Radiat. Isot.* 58, 125–130.
- Hankins, D. E., Thorngate, J. H., 1993a. A High Sensitive Neutron Counter and Waste Drum Counting with the High Sensitivity Neutron Instrument. UCRL-ID-111750. Document of the Lawrence Livermore National Laboratory, University of California.
- Hankins, D. E., Thorngate, J. H., 1993b. A Neutron Counting Instrument for Low Level Transuranic Waste. Document of the Lawrence Livermore National Laboratory, University of California, UCRL-ID-115887.
- Hayakawa, Y., Maeda, Y., 1994. Performance of a microstrip proportional counter. *Annu. Rep. Res. Reactor Inst. Kyoto Univ.* 27, 34–41.
- Hayakawa, Y., Maeda, Y., 1996. Microstrip gas chamber for X-rays and neutrons. *Jpn. J. Appl. Phys.* 35, 123–125.
- Herranz, M., Idoeta, R., Legarda, F., 2011. Analysis of uncertainties and detection limits for the double measurement method of ⁹⁰Sr and ⁹⁰Sr. *Radiat. Meas.* 46, 680–686.
- Hillman, G.G., Roessler, N., Fulbright, R.S., Edson Pontes, J., Haas, G.P., 1993a. Application of the direct beta counter Matrix 96 for cytotoxic assays: simultaneous processing and reading of 96 wells using a ⁵¹Cr retention assay. *Cancer Immunol. Immun.* 36, 351–356.
- Hillman, G.G., Roessler, N., Fulbright, R.S., Edson Pontes, J., Haas, G.P., 1993b. ⁵¹Cr release assay adapted to a 96-well format sample reading. *Biotechniques* 15, 744–749.
- Hoch, M., 2004. Trends and new developments in gaseous detectors. *Nucl. Instrum. Methods Phys. Res., Sect. A* 535, 1–15.
- Hoetzl, H., Winkler, R., 1984. Experience with large-area Frisch grid chambers in low-level alpha spectrometry. *Nucl. Instrum. Methods* 223, 290–295.
- Homma, Y., Ochi, A., Moriya, K., Matsuda, S., Yoshida, K., Kobayashi, S., 2009. Study of deposit associated with discharge in micro-pixel gas chamber. *Nucl. Instrum. Methods Phys. Res., Sect. A* 599, 47–52.
- Hong, B., Hong, S.J., Ito, M., Kang, T.I., Kim, B.I., Kim, H.C., Kim, J.H., Lee, K.B., Lee, K.S., Park, S., Ryu, M.S., Sim, K.S., 2006. Sensitivity of hybrid resistive plate chambers to low-energy neutrons. *Nucl. Instrum. Methods Phys. Res., Sect. B* 158, 161–165.
- Horioka, S., Inaba, S., Kawai, H., Matsumoto, T., Nakayama, H., Tajima, Y., Takamatsu, K., Tsurju, T., Yoshida, H.Y., 2002. Development of micro-gap wire chamber. *Nucl. Instrum. Methods Phys. Res., Sect. A* 481, 166–173.
- Hou, X., Roos, P., 2008. Critical comparison of radiometric and mass spectrometric methods for the determination of radionuclides in environmental, biological and nuclear waste samples. *Anal. Chim. Acta* 608, 105–139.

- Hsu, W.-H., Braby, L.A., Reece, W.D., 2008. Detection system built from commercial integrated circuits for real-time measurement of radiation dose and quality using the variance method. *Radiat. Prot. Dosim.* 128, 5–11.
- Hu, Q.Y., Li, B.J., Zhang, D., Guo, H.S., Yang, G.Z., Si, F.N., Liu, J., 2009. Optimizing the design of a moderator-based neutron detector for a flat response curve in the 2–14 MeV energy range. *Nucl. Instrum. Methods Phys. Res., Sect. A* 609, 213–216.
- Hunt, J.B., Mercer, R.A., 1978. The absolute calibration of a long counter by the associated activity techniques. *Nucl. Instrum. Methods* 156, 451–457.
- Hutchins, D., 1992. The Bioassay of Cytokines. Matrix application note. Packard Instrument Company, Meriden, CT.
- ICRU, 1983. International Commission on Radiation Units and Measurements. Microdosimetry. ICRU Report 36, ICRU, Bethesda, Maryland.
- Iguchi, T., Nakayama, N., Takahashi, H., Nakazawa, M., 1994. Neutron spectrometry using a ^3He gas ionization chamber. *Nucl. Instrum. Methods Phys. Res., Sect. A* 353, 152–155.
- Jahoda, K., McCammon, D., 1988. Proportional counters as low energy photon detectors. *Nucl. Instrum. Methods Phys. Res., Sect. A* 272, 800–813.
- Jalbert, R.A., Hiebert, R.D., 1971. Gamma insensitive air monitor for radioactive gases. *Nucl. Instrum. Methods* 96, 61–66.
- Järvinen, M.L., Sipilä, H., 1984. Improved proportional counters for practical application. *IEEE Trans. Nucl. Sci.* NS-31, 356–359.
- Johansson, L., Sibbens, G., Altizoglou, T., Denecke, B., 2002. Self-absorption correction in standardisation of ^{209}Tl . *Appl. Radiat. Isot.* 56, 199–203.
- Johnson, J.D., Allander, K.S., Bounds, J.A., Garner, S.E., Johnson, J.P., MacArthur, D.W., 1994. Long range alpha detector (LRAD) sensitivity to beta contamination and soil moisture. *IEEE Trans. Nucl. Sci.* 41, 755–757.
- Jones, A.R., Holford, R.M., 1981. Application of Geiger-Mueller counters over a wide range of counting rates. *Nucl. Instrum. Methods* 189, 503–509.
- Kada, W., Dwaikat, N., Datermichi, J., Sato, F., Murata, I., Kato, Y., Iida, T., 2010. A twin-type airflow pulse ionization chamber for continuous alpha-radioactivity monitoring in atmosphere. *Radiat. Meas.* 45, 1044–1048.
- Kessler, M.J., 1991. A new, rapid analysis technique for quantitation of radioactive samples isolated on a solid support. In: *Proceedings of the International Conference on New Trends in Liquid Scintillation Counting and Organic Scintillators 1989*. Lewis Publishers, Chelsea, MI.
- Khriachkov, V.A., Ketterov, V.V., Mitrofanov, V.F., Semenova, N.N., 2000. Low-background spectrometer for the study of fast neutron-induced (n,α) reactions. *Nucl. Instrum. Methods Phys. Res., Sect. A* 444, 614–621.
- Kitto, M.E., Fielman, E.M., Haines, D.K., Menia, T.A., Bari, A., 2008. Performance of a commercial radon-in-water measurement kit. *J. Environ. Radioact.* 99, 1255–1257.
- Knoll, G.F., 2010. *Radiation Detection and Measurement*. 4th ed. John Wiley & Sons, New York.
- Koster, J.E., Bounds, J.A., Kerr, P.L., Steadman, P.A., Whitley, C.R., 1998. Whole body personnel monitoring via ionization detection. *IEEE Trans. Nucl. Sci.* 45, 976–980.
- Kotrappa, P., Steck, D.J., 2009. Radon Flux Monitor for In Situ Measurement of Granite and Concrete Surfaces. Radon Symposium, 20–23 September. American Association of Radon Scientists and Technologists, Missouri.
- Kotte, R., Keller, H.J., Ortlepp, H.G., Strary, F., 1987. Bragg peak spectroscopy of low-energy heavy ions. *Nucl. Instrum. Methods Phys. Res., Sect. A* 257, 244–252.
- Kreslo, I., Badhrees, I., Delaquis, S., Ereditato, A., Janos, S., Messina, M., Moser, U., Rossi, B., Zeller, M., 2011. Pulse-shape discrimination of scintillation from alpha and beta particles with liquid scintillator and Geiger-mode multipixel avalanche diodes. *J. Instrum.* 6, 9, P07009.
- Kuzminov, V.V., Osetrova, N.J., 2000. Precise measurement of ^{14}C beta spectrum by using a wall-less proportional counter. *Phys. At. Nucl.* 63, 1292–1296.
- Lacoste, V., 2010. Design of a new long counter for the determination of the neutron fluence reference values at the IRSN AMANDE facility. *Radiat. Meas.* 45, 1250–1253.
- Lacoste, V., Gressier, V., 2010. Experimental characterization of the IRSN long counter for the determination of the neutron fluence reference values at the AMANDE facility. *Radiat. Meas.* 45, 1254–1257.
- L'Annunziata, M.F., 1987. *Radionuclide Tracers, Their Detection and Measurement*. Academic Press, New York.
- Lavi, N., Steiner, V., Alfassi, Z.B., 2009. Measurement of radon emanation in construction materials. *Radiat. Meas.* 44, 396–400.
- Lebedev, S.G., Akulinichev, S.V., Iljinov, A.S., Yants, V.E., 2006. A gaseous radiochemical method for registration of ionizing radiation and its possible applications in science and economy. *Nucl. Instrum. Methods Phys. Res., Sect. A* 561, 90–99.
- Lee, S.H., Gardner, R.P., 2000. A new G–M counter dead time model. *Appl. Radiat. Isot.* 53, 731–737.
- Lentsch, J.W., Babad, H., Stokes, T.I., Hanson, C.E., Vargo, G.F., Boechler, G.N., 1996. New instruments for characterization of high level waste storage tanks at the Hanford site. Presented at WM'96, Tucson, AZ.
- Louiza, D.J., 1999. High-efficiency ^3He proportional counter for the detection of delayed neutrons. *Nucl. Instrum. Methods Phys. Res., Sect. A* 422, 43–46.
- Lohmann, M., Besch, H.J., Dix, W.R., Dünger, O., Jung, M., Menk, R.H., Reime, B., Schildwächter, L., 1998. A high sensitive two-line detector with large dynamic range for intravenous coronary angiography. *Nucl. Instrum. Methods Phys. Res., Sect. A* 419, 276–283.
- Lohmann, M., Besch, H.J., Dix, W.-R., Metge, J., Reime, B., 2003. Demands on a detector for intravenous coronary angiography—experience after 379 patients. *Nucl. Instrum. Methods Phys. Res., Sect. A* 510, 126–137.
- Lopes, J.A.M., dos Santos, J.M.F., Conde, C.A.N., 2000. A large area avalanche photodiode as the VUV photosensor for gas proportional scintillation counters. *Nucl. Instrum. Methods Phys. Res., Sect. A* 454, 421–425.
- Lopes, J.A.M., dos Santos, J.M.F., Conde, C.A.N., Morgado, R.E., 1999. A new integrated photosensor for gas proportional scintillation counters based on the gas electron multiplier (GEM). *Nucl. Instrum. Methods Phys. Res., Sect. A* 426, 469–476.
- Lopes, J.A.M., dos Santos, J.M.F., Morgado, R.E., Conde, C.A.N., 2001. A xenon gas proportional scintillation counter with a UV-sensitive large-area avalanche photodiode. *IEEE Trans. Nucl. Sci.* 48, 312–319.
- Loughlin, M.J., Lawrence, G., 2007. Tritium monitoring in the ITER neutral beam test facility. *Fus. Eng. Des.* 82, 646–651.
- Lyoussi, A., Romeyer-Dheroy, J., Buisson, A., 1996. Low level transuranic waste assay system using sequential photon interrogation and on line neutron counting signatures. Presented at WM'96, Tucson, AZ.
- MacArthur, D. W., Allander, K. S., Bounds, J. A., Caress, R. W., Catlett, M. M., Rutherford, D. A., 1993. LRAD Surface Monitors. LA-12524-MS. Los Alamos National Laboratory Document.
- MacArthur, D.W., Allander, K.S., Bounds, J.A., Catlett, M.M., Meatee, J.L., 1992. Long-range alpha detector (LRAD) for contamination monitoring. *IEEE Trans. Nucl. Sci.* 39, 952–957.
- Maekawa, F., Oyama, Y., 1997. Measurement of neutron energy spectrum below 10 keV in an iron shield bombarded by deuterium tritium neutrons and benchmark test of evaluated nuclear data from 14 MeV to 1 eV. *Nucl. Sci. Eng.* 125, 205–217.
- Maekawa, F., Oyama, Y., 1995a. Neutron spectrum measurement in the energy region of eV with the slowing down time method. In: Miyajima, M., Sasaki, S., Iguchi, T., Nakazawa, N., Takebe, M. (Eds.), *Proceedings of the Ninth Workshop on Radiation Detectors and Their Uses*. KEK, Japan Nat. Inst. Phys.
- Maekawa, F., Oyama, Y., 1995b. Measurement of low energy neutron spectrum below 10 keV with the slowing down time method. *Nucl. Instrum. Methods Phys. Res., Sect. A* 372, 262–274.
- Miintynen, P., Äikää, O., Kankainen, T., Kiihola, L., 1987. Application of pulse shape discrimination to improve the precision of the carbon-14 gas proportional counting method. *Appl. Radiat. Isot.* 38, 869–873.
- Marouli, M., Dean, J.C.J., Sephton, J.P., Spyrou, N.M., 2010. Standardisation of positron-emitters in gas with the NPL primary gas counting system. *Appl. Radiat. Isot.* 68, 1378–1382.
- Marouli, M., Dean, J., Spyrou, N.M., 2007. Feasibility of using proportional gas counters as a primary standard for positron emitters in gas. *Nucl. Instrum. Methods Phys. Res., Sect. A* 580, 660–662.
- Martín Sánchez, A., Sáenz García, G., Jurado Vargas, M., 2009. Study of self-absorption for the determination of gross alpha and beta activities in water and soil samples. *Appl. Radiat. Isot.* 67, 817–820.

- Masuda, T., Sakurai, H., Inoue, Y., Gunji, S., Asamura, K., 2002. Optical imaging capillary gas proportional counter with Penning mixtures, *IEEE Transact. Nucl. Sci.* 49, 553–558.
- Mateos, J.J., Gomez, E., Garcias, F., Casas, M., Cerda, V., 2000. Rapid $^{90}\text{Sr}/^{90}\text{Y}$ determination in water samples using a sequential injection method, *Appl. Radiat. Isot.* 53, 139–144.
- Maxwell III, S.L., Culligan, B.K., 2009a. New column separation method for emergency urine samples, *J. Radioanal. Nucl. Chem.* 279, 105–111.
- Maxwell III, S.L., Culligan, B.K., 2009b. Rapid determination of radiostrontium in emergency milk samples, *J. Radioanal. Nucl. Chem.* 279, 757–760.
- Maxwell III, S.L., Culligan, B.K., 2009c. Rapid separation method for emergency water and urine samples, *J. Radioanal. Nucl. Chem.* 279, 901–907.
- Maxwell III, S.L., Culligan, B.K., Noyes, G.W., 2010a. Rapid separation method for actinides in emergency air filters, *Appl. Radiat. Isot.* 68, 2125–2131.
- Maxwell III, S.L., Culligan, B.K., Noyes, G.W., 2010b. Rapid separation of actinides and radiostrontium in vegetation samples, *J. Radioanal. Nucl. Chem.* 286, 273–282.
- Menk, R.H., Sarvestani, A., Besch, H.J., Walenta, A.H., Amenitsch, H., Bernstorff, 2000. Gas gain operations with single photon resolution using an integrating ionization chamber in small angle X-ray scattering experiment, *Nucl. Instrum. Methods Phys. Res., Sect. A* 440, 181–190.
- Meric, I., Johansen, G.A., Holstad, M.B., Gardner, R.P., 2011a. Monte Carlo modelling of gamma-ray stopping efficiencies of Geiger–Müller counters, *Nucl. Instrum. Methods Phys. Res., Sect. A* 636, 61–66.
- Meric, I., Johansen, G.A., Holstad, M.B., Lee, K.O., Calderon, A.F., Wang, J., Gardner, R.P., 2011b. A single scatter electron Monte Carlo approach for simulating gamma-ray stopping efficiencies of Geiger–Müller counters, *Nucl. Instrum. Methods Phys. Res., Sect. A* 654, 279–287.
- Miller, M.E., Mariãniþ, L.E., Szejnberg Gonçãlves-Carralves, M.L., Skumanieþ, M., Thorp, S.I., 2004. Implantable self-powered detector for on-line determination of neutron flux in patients during NCT treatment, *Appl. Radiat. Isot.* 61, 1033–1037.
- Mir, J.A., Conceição, A.S., Maia, J.M., Veloso, J.F.C.A., dos Santos, J.M.F., 2009. Comparative studies of MSGC and GEM for photon and electron detection at ambient conditions, *Nucl. Instrum. Methods Phys. Res., Sect. A* 598, 505–509.
- Monteiro, C.M.B., Morgado, R.E., dos Santos, J.M.F., Conde, C.A.N., 2004. A curved-grid gas proportional scintillation counter instrumented with a 25-mm active-diameter photosensor, *Nucl. Instrum. Methods Phys. Res., Sect. A* 522, 407–412.
- Monteiro, C.M.B., Lopes, J.A.M., Simões, P.C.P.S., dos Santos, J.M.F., Conde, C.A.N., 2001. An argon gas proportional scintillation counter with UV avalanche photodiode scintillation readout, *IEEE Trans. Nucl. Sci.* 48, 1081–1086.
- Mörmann, D., Breskin, A., Chechik, R., Shalem, C., 2004. Operation principles and properties of the multi-GEM gaseous photomultiplier with reflective photocathode, *Nucl. Instrum. Methods Phys. Res., Sect. A* 530, 258–274.
- Moro, D., Colautti, P., Gualdrini, G., Masi, M., Conte, V., De Nardo, L., Tomielli, G., 2006. Two miniaturised TPCs in a single detector for BNCT microdosimetry, *Radiat. Prot. Dosim.* 122, 396–400.
- Mustafa, S.M., Mahesh, K., 1978. Criterion for determining saturation current in parallel plate ionization chambers, *Nucl. Instrum. Methods* 150, 549–553.
- Nariyama, N., Kioshi, N., Ohnishi, S., 2004. Development of a portable free-air ionization chamber as an absolute intensity monitor for high-energy synchrotron radiation up to 150 keV, *Nucl. Instrum. Methods Phys. Res., Sect. A* 524, 324–331.
- Natal da Luz, H., Mir, J.A., Veloso, J.F.C.A., dos Santos, J.M.F., Rhodes, N.J., Schooneveld, E.M., 2007b. Micro-hole and strip plate (MHSP) operation in CF_4 , *Nucl. Instrum. Methods Phys. Res., Sect. A* 580, 286–288.
- Natal da Luz, H., Veloso, J.F.C.A., dos Santos, J.M.F., Mir, J.A., 2007c. A simple X-ray position detection system based on a MHSP, *Nucl. Instrum. Methods Phys. Res., Sect. A* 580, 1083–1086.
- Natal da Luz, H., Veloso, J.F.C.A., Mendes, N.F.C., dos Santos, J.M.F., Mir, J.A., 2007a. MHSP with position detection capability, *Nucl. Instrum. Methods Phys. Res., Sect. A* 573, 191–194.
- Neumann, S., Böttger, R., Guldbakke, S., Matzke, M., Sosaat, W., 2002. Neutron and photon spectrometry in mono energetic neutron fields, *Nucl. Instrum. Methods Phys. Res., Sect. A* 476, 353–357.
- Nickles, J., Bräuning, H., Bräuning-Demian, A., Dangendorf, V., Breskin, A., Chechik, R., Rauschnabel, K., Schmidt Böcking, H., 2002. A gas scintillation counter with imaging optics and large area UV-detector, *Nucl. Instrum. Methods Phys. Res., Sect. A* 477, 59–63.
- Niebuhr, C., 2006. Aging effects in gas detectors, *Nucl. Instrum. Methods Phys. Res. Sect. A* 566, 118–122.
- Nielsen, D.R., Cassel, D.K., 1984. Soil water management, In: L'Annunziata, M.F., Legg, J.O. (Eds.), *Isotopes and Radiation in Agricultural Sciences*, vol. 1. Academic Press, London and New York, pp. 35–65.
- Nowack, G.F., 1987. Electrical compensation method of mechanically induced disturbances in gas-filled radiation detectors, *Nucl. Instrum. Methods Phys. Res., Sect. A* 255, 217–221.
- Oed, A., 1995. Properties of micro-strip gas chambers (MSGC) and recent developments, *Nucl. Instrum. Methods Phys. Res., Sect. A* 367, 34–40.
- Oed, A., 2001. Micro pattern structures for gas detectors, *Nucl. Instrum. Methods Phys. Res., Sect. A* 471, 109–114.
- Oger, T., Chen, W.-T., Cussonneau, J.-P., Donnard, J., Duval, S., Lamblin, J., Lemaire, O., Mohamad Hadi, A.F., Leray, P., Morteau, E., Scotto Lavina, L., Stutzmann, J.-S., Thers, D., 2012. A liquid xenon TPC for a medical imaging Compton telescope, *Nucl. Instrum. Methods Phys. Res., Sect. A*, in press.
- Ohsawa, D., Masaoka, S., Katano, R., Isozumi, Y., 2000. Resolution of a position sensitive proportional counter with a resistive anode wire of carbon fiber, *Appl. Radiat. Isot.* 52, 943–954.
- Ohshita, H., Uno, S., Otomo, T., Koike, T., Murakami, T., Satoh, S., Sekimoto, M., Uchida, T., 2010. Development of a neutron detector with a GEM, *Nucl. Instrum. Methods Phys. Res., Sect. A* 623, 126–128.
- Okeji, M.C., Agwu, K.K., 2012. Assessment of indoor radon concentration in phosphate fertilizer warehouses in Nigeria, *Radiat. Phys. Chem.* 81, 253–255.
- Ometáková, J., Dulanská, S., Mátel, L., Remenc, B., 2011. A comparison of classical ^{90}Sr separation methods with selective separation using molecular recognition technology products AnaLig[®] SR-01 gel, 3 M Empore[™] Strontium Rad Disk and extraction chromatography Sr[®] Resin, *J. Radioanal. Nucl. Chem.* 290, 319–323.
- Ortuño-Prados, F., Bazzano, A., Berry, A., Budtz-Jørgensen, C., Hall, C., Helsby, W., Lewis, R., Parker, B., Ubertini, P., 1999. A high-pressure MWPC detector for crystallography, *Nucl. Instrum. Methods Phys. Res., Sect. A* 420, 445–452.
- Ovchinnikov, B.M., Parusov, V.V., 1999. A method for background reduction in an experiment for WIMP search with a Xe (Ar)-liquid ionization chamber, *Astropart. Phys.* 10, 129–132.
- Pallares, A., Barthe, S., Bergtold, A.M., Brom, J.M., Cailleret, J., Christophel, E., Coffin, J., Eberle, H., Fang, R., Fontaine, J.C., Geist, W., Kachelhoffer, T., 1992. High Throughput Screening of Samples Containing Alpha & Beta Radionuclides: An Overview of Methods, Application note, PerkinElmer Life and Analytical Sciences, Boston.
- Pancin, J., Andriamonje, S., Aune, S., Giganon, A., Giomataris, Y., Lecolley, J.F., Riallot, M., Rosa, R., 2008. Piccolo Micromegas: first in-core measurement in a nuclear reactor, *Nucl. Instrum. Methods Phys. Res., Sect. A* 592, 104–113.
- Pancin, J., Aune, S., Berthoumieux, E., Boyer, S., Delagnes, E., Macary, V., Pournarede, B., Safa, H., 2007. Neutron detection in high γ -background using a micromegas detector, *Nucl. Instrum. Methods Phys. Res., Sect. A* 572, 859–865.
- Pandola, L., Cattadori, C., Ferrari, N., 2004. Neural network pulse shape analysis for proportional counters events, *Nucl. Instrum. Methods Phys., Res. Sect. A* 522, 521–528.
- Papachristodoulou, C.A., Patiris, D.L., Ioannides, K.G., 2010. Exposure to indoor radon and natural gamma radiation in public workplaces in north-western Greece, *Radiat. Meas.* 45, 865–871.
- Papp, Z., Uray, I., 2002. Sensitive method for the determination of ^{18}F attached to aerosol particles in a PET centre, *Nucl. Instrum. Methods Phys. Res., Sect. A* 480, 788–796.
- Passo, C., Kessler, M., 1992. *The Essentials of Alpha/Beta Discrimination*. Packard Instrument Company, Meriden, CT.
- Perez-Nunez, D., Braby, L.A., 2011. Replacement tissue-equivalent proportional counter for the international space station, *Radiat. Prot. Dosim.* 143, 394–397.

- Peskov, V., Fonte, P., Martinengo, P., Nappi, E., Oliveira, R., Pietropaolo, F., Picchi, P., 2012. Advances in the development of micropattern gaseous detectors with resistive electrodes. *Nucl. Instrum. Methods Phys. Res., Sect. A* 661, S153–S155.
- Phillips, H.C., Johansson, L.C., Sephton, J.P., 2010. Standardisation of ^{85}Kr . *Appl. Radiat. Isot.* 68, 1335–1339.
- Pitts, W.K., Martin, M.D., 2001. Experience with laser microfabricated detectors at the University of Louisville. *Nucl. Instrum. Methods Phys. Res., Sect. A* 471, 268–271.
- Pommé, S., Altizoglou, T., Van Ammel, R., Sibbens, G., 2005. Standardisation of ^{125}I using seven techniques for radioactivity measurement. *Nucl. Instrum. Methods Phys. Res., Sect. A* 544, 584–592.
- Prasad, K.R., Balagi, V., 1996. Uranium-233 fission detectors for neutron flux measurement in reactors. *Rev. Sci. Instrum.* 67, 2197–2201.
- Rachinhas, P.J.B.M., Simões, P.C.P.S., Lopes, J.A.M., Dias, T.H.V.T., Morgado, R.E., dos Santos, J.M.F., Stauffer, A.D., Conde, C.A.N., 2000. Simulation and experimental results for the detection of conversion electrons with gas proportional scintillation counters. *Nucl. Instrum. Methods Phys. Res., Sect. A* 441, 468–478.
- Radeka, V., Schaknowski, N.A., Smith, G.C., Yu, B., 1998. High performance, imaging, thermal neutron detectors. *Nucl. Instrum. Methods Phys. Res., Sect. A* 419, 642–647.
- Rapisarda, D., Vermeere, L., García, Á., Cabellos, Ó., García, J.M., Ibarra, Á., Gómez-Rosa, J.M., Mota, F., Casal, N., Queral, V., 2011. Study on the response of IFMIF fission chambers to mixed neutron-gamma fields: PH-2 experimental tests. *Fus. Engin. Design* 86, 1232–1235.
- Renker, D., 2009. Geiger-mode avalanche photodiodes for Cherenkov detectors. *J. Instrum.* 5, 12, P01001.
- Righia, S., Lucialli, P., Bruzzi, L., 2005. Health and environmental impacts of a fertilizer plant – part II: assessment of radiation exposure. *J. Environ. Radioact.* 82, 183–198.
- Roberts, N.J., Thomas, D.J., Lacoste, V., Büttger, R., Loeb, S., 2010. Comparison of long counter measurements of monoenergetic and radionuclide source-based neutron fluence. *Radiat. Meas.* 45, 1151–1153.
- Roccaro, A., Tomita, H., Ahlen, S., Avery, D., Inglis, A., Baitat, J., Dujmic, D., Fisher, P., Henderson, S., et al., 2009. A background-free direction-sensitive neutron detector. *Nucl. Instrum. Methods Phys. Res., Sect. A* 608, 305–309.
- Rodriguez, P.B., Sánchez, A.M., Tomé, F.V., 1997. Experimental studies of self-absorption and backscattering in alpha-particle sources. *Appl. Radiat. Isot.* 48, 1215–1220.
- Roessler, N., Englert, D., Neumann, K., 1993. New instruments for high throughput receptor binding assays. *J. Receptor Res.* 13, 135–145.
- Rosner, G., Hötzel, H., Winkler, R., 1992. Determination of ^{241}Pu by low level beta proportional counting, application to Chernobyl fallout samples and comparison with the ^{241}Am build-up method. *J. Radioanal. Nucl. Chem.* 163, 225–233.
- Ryzhov, I.V., Tutin, G.A., Mityukhin, A.G., Oplavin, V.S., Soloviev, S.M., Blomgren, J., Renberg, P.-U., Meulders, J.P., El Masri, Y., Keutgen, Th., Prieels, R., Nolte, R., 2006. Measurements of neutron-induced fission cross-sections of ^{202}Tl , $^{204,206,207,208}\text{Pb}$ and ^{209}Bi with a multi-section Frisch-gridded ionization chamber. *Nucl. Instrum. Methods Phys. Res., Sect. A* 562, 439–448.
- Saey, P.R.J., 2007. Ultra-low-level measurements of argon, krypton and radon for treaty verification purposes. *ESARDA Bull.* 36, 42–56.
- Saey, P.R.J., 2009. The influence of radiopharmaceutical isotope production on the global radon background. *J. Env. Radioact.* 100, 396–406.
- Saey, P.R.J., 2010. Xenon. In: Atwood, D.A. (Ed.), *Radionuclides in the Environment*. John Wiley & Sons, Chichester.
- Saito, N., Suzuki, I.H., 1999. Absolute fluence rates of soft X-rays using a double ion chamber. *J. Electron Spectrosc. Relat. Phenom.* 101–103, 33–37.
- Sakamoto, S., Morioka, A., 1993. Pulse shape discrimination with proportional counters for neutron detection. In: Miyajima, M., Sasaki, S., Yoshimura, Y., Iguchi, T., Nakazawa, N. (Eds.), *Proceedings of the Seventh Workshop on Radiation Detectors and Their Uses*. Nat. Inst. Phys. KEK, Japan.
- Sakamoto, S., Morioka, A., 1994. Temperature dependence of BF_3 proportional counters. *Nucl. Instrum. Methods Phys. Res., Sect. A* 353, 160–163.
- Sakurai, H., Gunji, S., Tokanai, F., Maeda, T., Saitoh, N., Ujiie, N., 2003. Photoelectron track image of capillary gas proportional counter. *Nucl. Instrum. Methods Phys. Res., Sect. A* 505, 219–222.
- Santonico, R., 2003. RPCs: the challenges for the next two years. *Nucl. Instrum. Methods Phys. Res., Sect. A* 508, 1–5.
- Sauli, F., 1997. GEM: a new concept for electron amplification in gas detectors. *Nucl. Instrum. Methods Phys. Res., Sect. A* 386, 531–534.
- Sauli, F., 1998. Gas detectors: recent developments and future perspectives. *Nucl. Instrum. Methods Phys. Res., Sect. A* 419, 189–201.
- Sauli, F., 1999. Recent developments and applications of fast position-sensitive gas detectors. *Nucl. Instrum. Methods Phys. Res., Sect. A* 422, 257–262.
- Sauli, F., 2001. Gas detectors: achievements and trends. *Nucl. Instrum. Methods Phys. Res., Sect. A* 461, 47–54.
- Sauli, F., 2002. Micro-pattern gas detectors. *Nucl. Instrum. Methods Phys. Res., Sect. A* 477, 1–7.
- Sauli, F., 2004a. Progress with the gas electron multiplier. *Nucl. Instrum. Methods Phys. Res., Sect. A* 533, 93–98.
- Sauli, F., 2004b. From bubble chambers to electronic systems: 25 years of evolution in particle detectors at CERN (1979–2004). *Phys. Reports* 403–407, 471–504.
- Sauli, F., 2007. Imaging with the gas electron multiplier. *Nucl. Instrum. Methods Phys. Res., Sect. A* 580, 971–973.
- Sauli, F., 2010. Recent topics on gaseous detectors. *Nucl. Instrum. Methods Phys. Res., Sect. A* 623, 29–34.
- Sauli, F., 2003. Development and applications of gas electron multiplier detectors. *Nucl. Instrum. Methods Phys. Res., Sect. A* 505, 195–198.
- Scarpitta, S., Odlin-McCabe, J., Gaschott, R., Meier, A., Klug, E., 1999. Comparison of four ^{90}Sr groundwater analytical methods. *Health Phys.* 76, 644–656.
- Semkow, T.M., Parekh, P.P., 2001. Principles of gross alpha and beta radioactivity detection in water. *Health Phys.* 81, 567–573.
- Sharma, A., 2001. Detection of single electrons emitted by internal photocathodes with the gas electron multiplier (GEM). *Nucl. Instrum. Methods Phys. Res., Sect. A* 462, 603–606.
- Shekhtman, L., 2002. Micro-pattern gaseous detectors. *Nucl. Instrum. Methods Phys. Res., Sect. A* 494, 128–141.
- Shekhtman, L., 2004. Novel position-sensitive gaseous detectors for X-ray imaging. *Nucl. Instrum. Methods Phys. Res., Sect. A* 522, 85–92.
- Shenhav, N.J., Stelzer, H., 1985. The mass dependence of the signal peak height of a Bragg-curve. *Nucl. Instrum. Methods* 228, 359–364.
- Simgen, H., Buck, C., Heusser, G., Laubenstein, M., Rau, W., 2003. A new system for the ^{222}Rn and ^{226}Ra assay of water and results in the BOR-EXINO project. *Nucl. Instrum. Methods Phys. Res., Sect. A* 497, 407–413.
- Simões, P.C.P.S., Covita, D.S., Veloso, J.F.C.A., dos Santos, J.M.F., Morgado, R.E., 2003. A new method for pulse analysis of driftless-gas proportional scintillation counters. *Nucl. Instrum. Methods Phys. Res., Sect. A* 505, 247–251.
- Simões, P.C.P.S., dos Santos, M.F., Conde, C.A.N., 2001. Driftless gas proportional scintillation counter pulse analysis using digital processing techniques. *X-Ray Spectrom.* 30, 342–347.
- Simon, F., Kelsey, J., Kohl, M., Majka, R., Plesko, M., Sakuma, T., Smirnov, N., Spinka, H., Surrow, B., Underwood, D., 2009. Beam performance of tracking detectors with industrially produced GEM foils. *Nucl. Instrum. Methods Phys. Res., Sect. A* 598, 432–438.
- Stamoulis, K.C., Assimakopoulos, P.A., Ioannides, K.G., Johnson, E., Soucaco, P.N., 1999. Strontium-90 concentration measurements in human bones and teeth in Greece. *Sci. Total Environ.* 229, 165–182.
- Stanga, D., Cassette, P., 2006. Improved method of measurement for tritiated water standardization by internal gas proportional counting. *Appl. Radiat. Isot.* 64, 160–162.
- Stanga, D., Moreaub, I., Cassette, P., 2006. Standardization of tritiated water by two improved methods. *Appl. Radiat. Isot.* 64, 1203–1206.
- Stanga, D., Picolo, J.L., Coursol, N., Mitev, K., Moreau, I., 2002. Analytical calculations of counting losses in internal gas proportional counting. *Appl. Radiat. Isot.* 56, 231–236.
- Strand, P., Brown, J.E., Drozhko, E., Mokrov, Y., Salbu, B., Oughton, D., Christensen, G.C., Amundsen, I., 1999. Biogeochemical behaviour of ^{137}Cs and ^{90}Sr in the artificial reservoirs of Mayak PA, Russia. *Sci. Total Environ.* 241, 107–116.
- Surette, R.A., Waker, A.J., 1994. Workplace monitoring of swipes and air filters for ^{55}Fe . *IEEE Trans. Nucl. Sci.* 41, 1374–1378.

- Szalóki, I., Török, S.B., Ro, C.U., Injuk, J., Van Grieken, R.E., 2000. X-ray spectrometry. *Anal. Chem.* 72, 211–233.
- Tagziria, H., Thomas, D.J., 2000. Calibration and Monte Carlo modelling of neutron long counters. *Nucl. Instrum. Methods Phys. Res., Sect. A* 452, 470–483.
- Tamboul, J.Y., Watt, D.E., 2001. A proportional counter for measurement of the bio-effectiveness of ionising radiations at the DNA level. *Nucl. Instrum. Methods Phys. Res., Sect. B* 184, 597–608.
- Thakur, P., Mulholland, G.P., 2011. Monitoring of gross alpha, gross beta and actinides activities in exhaust air released from the waste isolation pilot plant. *Appl. Radiat. Isot.* 69, 1307–1312.
- Theodósson, P., 1991. Gas proportional versus liquid scintillation counting, radiometric versus AMS dating. *RadioCarbon* 33, 9–13.
- Theodósson, P., 1999. A review of low-level tritium system and sensitivity requirements. *Appl. Radiat. Isot.* 50, 311–316.
- Theodósson, P., Heusser, G., 1991. External guard counters for low-level counting systems. *Nucl. Instrum. Methods Phys. Res., Sect. B* 53, 97–100.
- Titov, M., 2007. New developments and future perspectives of gaseous detectors. *Nucl. Instrum. Methods Phys. Res., Sect. A* 581, 25–37.
- Tolk, J.A., Evett, S.R., 2009. Lysimetry versus neutron moisture meter for evapotranspiration determination in four soils. *Soil Sci. Soc. Am. J.* 73, 1693–1698.
- Toyokawa, H., Urotani, A., Mori, C., Takeda, N., Kudo, K., 1995. A multi-purpose spherical neutron counter. *IEEE Trans. Nucl. Sci.* 42, 644–648.
- Troja, S.O., Cro, A., Picouet, P., 1995. Alpha and beta dose-rate determination using a gas proportional counter. *Radiat. Meas.* 24, 297–308.
- Tsyganov, E., Antich, P., Parkey, R., Seliounine, S., Golovatyuk, V., Lobastov, S., Zhezher, V., Bazulatskov, A., 2008. Gas electron multiplying detectors for medical applications. *Nucl. Instrum. Methods Phys. Res., Sect. A* 597, 257–265.
- Tutin, G.A., Ryzhov, I.V., Eismont, V.P., Kireev, A.V., Condé, H., Elmgren, K., Olsson, N., Renberg, P.U., 2001. An ionization chamber with Frisch grids for studies of high-energy neutron - induced fission. *Nucl. Instrum. Methods Phys. Res., Sect. A* 457, 646–652.
- Unterwieser, M.P., Lucas, L.L., 2000. Calibration of the National Institute of Standards and Technology tritiated-water standards. *Appl. Radiat. Isot.* 52, 527–531.
- Uozumi, Y., Sakae, T., Matoba, M., Ijiri, H., Koori, N., 1993. Semi-microscopic formula for gas gain of proportional counters. *Nucl. Instrum. Methods Phys. Res., Sect. A* 324, 558–564.
- Uritani, A., Kuniya, Y., Takemaka, Y., Toyokawa, H., Yamane, Y., Mori, S., Kobayashi, K., Shiroya, S., Ichihara, C., 1995. A long and slender position-sensitive helium-3 proportional counter with an anode wire supported by a ladder shaped solid insulator. *J. Nucl. Sci. Technol.* 32, 719–726.
- Vaca, F., Manjón, G., Cuéllar, S., García-León, M., 2001. Factor of merit and minimum detectable activity for ^{90}Sr determinations by gas-flow proportional counting or Cherenkov counting. *Appl. Radiat. Isot.* 55, 849–851.
- van der Graaf, H., 2009. New developments in gaseous tracking and imaging detectors. *Nucl. Instrum. Methods Phys. Res., Sect. A* 607, 78–80.
- van der Graaf, H., 2011. Gaseous detectors. *Nucl. Instrum. Methods Phys. Res., Sect. A* 628, 27–30.
- Vasile, M., Benedik, L., Altitzoglou, T., Spasova, Y., Wätjen, U., González de Orduña, R., Hult, M., Beyermann, M., Mihalec, I., 2010. ^{226}Ra and ^{228}Ra determination in mineral waters—comparison of methods. *Appl. Radiat. Isot.* 68, 1236–1239.
- Veloso, J.F.C.A., dos Santos, J.M.F., Conde, C.A.N., 2000. A proposed new microstructure for gas radiation detectors: the microhole and strip plate. *Rev. Sci. Instrum.* 71, 2371–2376.
- Veloso, J.F.C.A., dos Santos, J.M.F., Conde, C.A.N., 2001. Gas proportional scintillation counters with a CsI-covered microstrip plate UV photosensor for high-resolution X-ray spectrometry. *Nucl. Instrum. Methods Phys. Res., Sect. A* 457, 253–261.
- Veloso, J.F.C.A., Silva, A.L.M., Oliveira, C.A.B., Gouvêa, A.L., Azevedo, C.D.R., Carramate, L., Natal da Luz, H., dos Santos, J.M.F., 2010. Energy resolved X-ray fluorescence imaging based on a micropattern gas detector. *Spectrochim. Acta B* 65, 241–247.
- Villa, M., Duarte Pinto, S., Alfonsi, M., Brock, I., Croci, G., David, E., de Oliveira, R., Ropelewski, L., Taureg, H., van Stenis, M., 2011. Progress on large area GEMs. *Nucl. Instrum. Methods Phys. Res., Sect. A* 628, 182–186.
- Vinagre, F.L.R., Conde, C.A.N., 2001. Method for effective dead time measurement in counting systems. *Nucl. Instrum. Methods Phys. Res., Sect. A* 462, 555–560.
- Vu, T.Q., Allander, K.S., Bolton, R.D., Bounds, J.A., Garner, S.E., Johnson, J.D., Johnson, J.P., MacArthur, D.W., 1994. Application of the long-range alpha detector for site-characterization technology. *Proceedings of the WM '94 Conference*, Tucson, AZ.
- Waker, A.J., Aslam, 2010. A preliminary study of the performance of a novel design of multi-element tissue equivalent proportional counter for neutron monitoring. *Radiat. Meas.* 45, 1309–1312.
- Waker, A.J., Aslam, 2011a. Study of microdosimetric energy deposition patterns in tissue-equivalent medium due to low-energy neutron fields using a graphite-walled proportional counter. *Radiat. Res.* 175, 806–813.
- Waker, A.J., Aslam, 2011b. An experimental study of the microdosimetric response of a graphite walled proportional counter in low energy neutron fields. *Nucl. Instrum. Methods Phys. Res., Sect. A* 652, 721–725.
- Waker, A.J., Dubeau, J., Surette, R.A., 2009. The application of micro-patterned devices for radiation protection dosimetry and monitoring. *Nucl. Technol.* 168, 202–206.
- Wang, Z., Morris, C.L., Makela, M.F., Bacon, J.D., Baer, E.E., Brockwell, M.J., Brooks, B.J., et al., 2009. Inexpensive and practical sealed drift-tube neutron detector. *Nucl. Instrum. Methods Phys. Res., Sect. A* 605, 430–432.
- Waples, J.T., Orlandini, K.A., Weckert, K.M., Edgington, D.N., Klump, J.V., 2003. Measuring low concentrations of ^{234}Th in water and sediment. *Marine Chem.* 80, 265–281.
- Watanabe, K., Otsuka, J., Shigeyama, M., Suzuki, Y., Yamazaki, A., Unitani, A., 2011. Flat-response neutron detector using spatial distribution of thermal neutrons in a moderator. *Nucl. Instrum. Methods Phys. Res., Sect. A* 652, 392–396.
- Waters, J.R., 1974. Precautions in the measurement of tritium concentration in air when using flow-through chambers. *Nucl. Instrum. Methods* 117, 39–43.
- Weijers, T.D.M., Ophel, T.R., Timmers, H., Elliman, R.G., 2002. A systematic study of the pulse height deficit in propane - filled gas ionization detectors. *Nucl. Instrum. Methods Phys. Res., Sect. A* 483, 676–688.
- Westphal, G.P., 1976. A high precision pulse-ratio circuit. *Nucl. Instrum. Methods* 134, 387–390.
- Whitley, C.R., Bounds, J.A., Steadman, P.A., 1998. A portable swipe monitor for alpha contamination. *IEEE Trans. Nucl. Sci.* 45, 533–535.
- Whitley, C.R., Johnson, J.D., Rawool-Sullivan, M., 1996. Real-time alpha monitoring of a radioactive liquid waste stream at Los Alamos National Laboratory. *WM 1996*, Tucson, AZ.
- Whitney, C., Pellegrin, S.M., Wilson, C., 2009. A nanoparticle doped micro-geiger counter for multispecies radiation detection. *J. Microelectromech. Syst.* 18, 998–1003.
- Yakushev, A.B., Zvara, I., Oganessian, Yu.Ts., Belozero, A.V., Dmitriev, S.N., Eichler, B., Hübener, S., Sokol, E.A., Türler, A., Yerebin, A.V., et al., 2004. Chemical identification and properties of element 112. *Nucl. Phys. A* 734, 204–207.
- Yu, B., Smith, G.C., Siddons, D.P., Pietraski, P.J., Zojceski, Z., 1999. Position sensitive gas proportional detectors with anode blades. *IEEE Trans. Nucl. Sci.* 46, 338–431.
- Yunoki, A., Yamada, T., Kawada, Y., Unno, Y., Sato, Y., Hino, Y., 2010. Activity measurement of ^{85}Kr diluted by a large volume balloon technique. *Appl. Radiat. Isot.* 68, 1340–1343.
- Zhang, L., Takahashi, H., Hinamoto, N., Nakazawa, M., Yoshida, K., 2002. Design of a hybrid gas proportional counter with CdTe guard counters for ^{14}C dating system. *Nucl. Instrum. Methods Phys. Res., Sect. A* 478, 431–434.
- Zikovskiy, L., Roireau, N., 1990. Determination of radon in water by argon purging and alpha counting with a proportional counter. *Appl. Radiat. Isot.* 41, 679–681.

This page intentionally left blank

Solid-State Nuclear Track Detectors

Shi-Lun Guo and Bao-Liu Chen

China Institute of Atomic Energy (CIAE), P. O. Box 275 (96), Beijing 102413, China

S.A. Durrani

School of Physics and Astronomy, University of Birmingham, Birmingham, B15 2TT, UK

Chapter Outline

Part 1 Elements	234		
I. Introduction	234		
II. Detector Materials and Classification of Solid-State Nuclear Track Detectors	236		
A. Crystalline Solids	236		
1. Muscovite Mica	237		
2. Apatite	237		
3. Zircon	238		
4. Sphene	239		
5. Olivine	239		
6. Pyroxene	239		
7. Other Crystalline Solids	240		
B. Glasses	240		
1. Man-Made Glasses	240		
2. Natural Glasses	241		
C. Plastics	241		
1. CR-39 (Polyallyldiglycol carbonate, PADC, PM-355, PM-500, PM-600)	241		
2. Polycarbonate (PC, Lexan, Makrofol, Taffak)	242		
3. Cellulose Nitrate (CN, LR-115, Daicel)	243		
4. Polyethylene Terephthalate (PET, Mylar, Cronar, Melinex, Lavsan, Terphane, Hostphan)	244		
5. CR-39—DAP Series	244		
6. Other New Track Detector Materials	245		
III. Recordable Particles with Solid-State Nuclear Track Detectors	245		
A. Protons	245		
1. Suitable Detectors for Proton Detection	246		
2. Proton Intensity Measurements	246		
3. Proton Energy Measurements	246		
4. Proton Spatial Distribution Measurements	247		
5. Applications of Proton Detection	247		
B. α -Particles	248		
1. Suitable Detectors for α -particle Measurements	248		
2. α -Intensity Measurements	248		
3. α -Particle Energy Measurements	250		
4. α -Spatial Distribution Measurements	250		
5. Applications of α Detection	251		
		C. Fission Fragments	251
		1. Suitable Detectors for Fission Fragments	252
		2. Fission Rate Determination	253
		3. Spatial Distribution of Fission and Fission Fragments	254
		4. Application of Fission Detection	254
		D. Heavy Ions ($Z \geq 3$)	254
		1. Suitable Detectors for Heavy Ions $Z \geq 3$	254
		2. Identification of Charge Z	255
		3. Identification of Mass A of Isotopes	255
		4. Heavy-Ion Energy Determination	255
		5. Applications of Heavy-Ion Detection	255
		E. Neutrons	255
		1. Principles of Neutron Detection	255
		2. Suitable Detectors for Neutron Detection	256
		3. Neutron Intensity Measurements	256
		4. Neutron Energy Measurements	256
		5. Neutron Dosimetry	256
		F. Exotic Particle Detection	257
		1. Suitable Detectors for Exotic Particle Detection	257
		2. Magnetic Monopole Detection	257
		3. Dark Matter Particle Detection	258
		IV. Track Formation Mechanisms and Criteria	258
		A. Introduction	258
		B. Track Formation Mechanisms	258
		1. Ion Explosion Spike for Inorganic Solids	258
		2. Chain Breaking Mechanism in High Polymers	258
		C. Criteria of Track Formation	259
		1. Primary Ionization Rate Criterion	259
		2. Restricted Energy Loss (REL) for Plastic Track Detectors	260
		3. Energy Deposition Model (E_e)	260
		D. Extended and Transitional Criteria	261
		1. Z_{eff}/β	261
		2. dE/dx Transitional Parameter	262
		V. Track Revelation	262
		A. Chemical Etching (CE)	262
		1. Etching Condition	262
		2. Track Etching Geometry	262
		3. Critical Angle of Etching	263

4. Techniques of Critical Angle Measurements	263	A. Cluster Radioactivities	273
5. Track Etching Geometry	264	B. Heavy-Ion Interactions	273
6. New Progress in Track Etching Geometry	264	1. Relativistic Projectile Fragmentation	273
B. Electrochemical Etching (ECE)	264	2. Sequential Fission after Inelastic Collisions	273
C. Track Etching Kinetics	265	C. Nuclear Fission and Neutron Physics	273
1. Objectives and Required Parameters	265	1. Nuclear Fission	273
2. Forward Calculation	266	2. Neutron Physics	275
3. Inverse Calculation	266	D. Plasma Physics	275
VI. Particle Identification	266	1. Laser Acceleration	275
A. Maximum Track Length Method	266	2. Inertial-Confinement-Fusion	276
B. Track-Etch Rate Versus Radiation Damage Density Method	266	E. Astrophysics and Cosmic Rays	276
C. Track-Etch Rate Versus Residual Range Method	266	F. Nuclear Technology	277
D. Track Diameter Method for Identification of Charge Z at High and Relativistic Energy	267	1. Nuclear Reactor Physics	277
E. Track Length Method for Identification of Charge Z at High and Relativistic Energy	269	2. Accelerator – Driven Subcritical Reactors (ADS)	278
VII. Track Fading and Annealing	269	3. Nuclear Forensic Analysis and Nuclear Safeguards	278
A. Track Fading and Annealing	269	G. Elemental Analysis and Mapping	280
B. Mechanisms of Track Fading	269	III. Earth and Planetary Sciences	280
C. Arrhenius Diagram	269	A. Fission Track Dating	280
D. Application of Track Fading and Annealing	270	1. Absolute Approach	280
1. Problems Resulting From Track Fading	270	2. Zeta Approach	282
2. Improving Analysis with the Aid of Track Annealing	270	3. Continental Drift and Ocean-Bottom Spreading	283
3. Apparent Fission Track Age and Its Corrections	270	4. Archaeology and Anthropology	283
4. Geothermal Chronology	271	5. Tectonic Up-Lift Rate Determination	285
VIII. Instrumentation	271	B. Geothermal Chronology	285
A. Size of Latent Tracks and Etched Tracks	271	C. U and Oil Exploration and Earthquake Prediction	286
B. Optical Microscope	271	IV. Life and Environmental Sciences	286
C. Track Image Analyzer	271	A. Radiation Protection Dosimetry	286
D. Electron Microscope	271	1. Radon and Thoron Monitoring and Dosimetry	286
E. Scanning Tunneling Microscope (STM) and Atomic Force Microscope (AFM)	271	2. Neutron Dosimetry	287
F. Spark Counter	272	B. Environmental Sciences	287
Part 2 Applications	272	1. Radioactive Fallout from Nuclear Accidents	287
I. Introduction	272	2. Drainage Contamination of Nuclear Plants	289
II. Physical Sciences and Nuclear Technology	272	V. NanoTechnology and Radiation Induced Material Modifications	289
		Acknowledgments	289
		References	289

PART 1 ELEMENTS

I. INTRODUCTION

Solid-state nuclear track detector (SSNTD) is a special type of radiation detector, which records tracks of heavy charged particles ($Z \geq 1$) in insulating or dielectric solids.

In a broad sense, nuclear emulsions (Barkas, 1963), special type of bubble detectors (BDs), and etch track detectors are all included in solid-state nuclear track detectors, because these detector materials are all solid substances and the recorded signals are trajectories (or visible tracks) of charged particles. In this handbook, solid-state nuclear track detectors refer to etch track detectors or dielectric track detectors. Track etching is the basic technique used to develop tracks in this type of track detector.

There are some other types of nuclear track detectors, such as cloud chamber, bubble chamber, and spark chamber (Wilson, 1951; Shutt, 1967); their detector materials are saturated vapors, superheated liquids, and ionizable gases, respectively. These mediums are not solid substances. They do not belong to solid-state nuclear track detectors, even though they can record nuclear particle tracks.

The historic stories of track etching to develop tracks in solid can be retraced to very early time. H. Baumhauer in 1894 etched apatite with diluted sulfuric acid and saw etched figures (fission-fragment tracks); but he did not know what they were because radioactivity was not discovered until two years later by Becquerel (1896a,b) and nuclear fission was discovered many years later (Hahn and Strassmann, 1939a,b and Meitner and Frisch, 1939). In a recent book, L'Annunziata (2007) provides a detailed historical account of the discoveries and research into nuclear radiation. Baumhauer (1894) published his results in a treatise on etch methods. Since the end of 19th century, etching techniques had become a traditional method to display dislocation in minerals. A. P. Hones in 1927, A. R. Patel and S. Tolansky in 1957, and L. C. Lovell in 1958 also showed etched figures (tracks) in minerals. None of them recognized the etchings as tracks (Fleischer, 1998). D. A. Young was the first scientist who intentionally revealed fission-fragment tracks in lithium fluoride (LiF) by etching in 1958 (Young, 1958). His discovery showed that radiation damage by heavy charged particles (fission fragments) could form tracks in crystal. After his early success he discontinued research in this field. E. C. H.

Silk and R. S. Barnes in 1959 observed fission-fragment tracks in muscovite mica with a transmission electron microscope (Silk and Barnes, 1959). This was the first direct observation of straight latent (un-etched) tracks of fission fragments in mica. They also noticed that latent fission-fragment tracks in muscovite mica disappeared (track fading) after a few seconds due to heating by the intensive electron beam of the microscope.

P. B. Price and R. M. Walker in 1961 found a way to circumvent the problem of the rapid fading of tracks in muscovite mica under the electron microscope. They stabilized and fixed the tracks by chemical etching. They also discovered that chemical etching could enlarge fission-fragment tracks continuously and the enlarged tracks could be visible under the ordinary optical microscope when the diameter of tracks was enlarged to micrometers (Price and Walker, 1962a, 1962b, 1962c). Their discoveries made fission-fragment tracks become sustainable records for continuous research, overcame the limitation of the electron microscope to survey only tiny volumes of solids, and made it possible for many difficult scientific problems to be easily tackled by very simple and popular instruments such as ordinary optical microscopes. Based on these discoveries, "a new track detector" was announced in 1962 by Price and Walker (1962d) and later was named the solid-state (nuclear) track detector (Walker, 1963; Fleischer et al., 1965c), which was similar to the cloud chamber, bubble chamber, and spark chamber, and superior to conventional nuclear emulsions in simplicity and ruggedness. At the same time, Price and Walker (1962d, 1963a) discovered fossil tracks in mica and invented fission track dating. They designed a low uranium determination technique (Price and Walker, 1963b) and suggested the idea to make nuclear track membrane.

R. L. Fleischer joined Price and Walker in 1962. By close cooperation they discovered that polymers and glasses could also record etchable tracks of heavy charged particles (Fleischer and Price, 1963a, 1963b). They extended nuclear track applications into nuclear physics (Price et al., 1963, Fleischer et al., 1964b), neutron detection (Walker et al., 1963), astrophysics (Price et al., 1968a,b), meteorite (Fleischer et al., 1967c), cosmic rays (Price et al., 1967, 1968; Fleischer et al., 1967a), tektites (Fleischer and Price, 1964), archaeology (Fleischer et al., 1965d), continental drift and ocean bottom spreading (Fleischer et al., 1968), Quaternary geology (Fleischer et al., 1969b), Crater dating (Fleischer et al., 1969e), dating of mechanical events and underground nuclear explosions (Fleischer et al., 1972, 1974), Lunar science (Fleischer and Hart, 1973), planetary science (Fleischer et al., 1965b), anthropology (Fleischer et al., 1965c, 1965d), search for magnetic monopoles (Fleischer et al., 1969a, 1969c), mapping of uranium (Fleischer, 1966), and radon monitoring (Alter and Price, 1968). They made the first practical polymer track membrane (Fleischer et al., 1964a).

Before 1967, etch track applications were basically limited to track counting. In 1967, P. B. Price and coworkers discovered a method of identification of charge (Z) of nuclear particles by measuring the etch rate along the trajectory of the particles. They found that track-etch rate along the trajectory of the particles is a function of radiation damage density for a specific track detector. Measuring residual range and track-etch rate, one

could determine the charge of the particle creating the track (Price et al., 1967; Price and Fleischer, 1971). This discovery greatly opened new fields of modern applications of solid-state nuclear track detectors to high-energy physics, astrophysics, cosmic-ray physics, nuclear fragmentation, exotic particles, and many other fields. These applications are discussed further on in this chapter.

Discovery of CR-39 as a track detector in 1978 was another important event (Cartwright et al., 1978). Up to now, CR-39 has been the most useful detector material compared with others.

Electrochemical etching was first reported by Tommasino (1970), which is an alternative way to develop tracks and is used widely in radiation dosimetry. The nuclear track spark counter was first devised by Cross and Tommasino (1970), which is an often used technique for rapid counting of nuclear tracks.

For track formation mechanism, Fleischer et al. (1964a) first suggested total energy loss rate as a criterion to judge whether a particle could be recorded by a specific detector material, but soon they found that this criterion could not fit the experimental data and they suggested another: primary ionization rate criterion (Fleischer et al., 1967). Benton and Nix (1969) suggested restricted energy loss criterion. Katz and Kobetich (1968) suggested total energy deposition criterion to judge the formation of tracks. The last three criteria were almost satisfied by track research, but none of them are perfect theoretically and experimentally. The most often used criteria are primary ionization rate and restricted energy loss rate. The calculation of total energy deposition criterion is more complicated; fewer researchers used it in practice.

Due to the obvious advantage of etch track detectors, many researchers joined in the study of etch track detectors, especially many nuclear emulsion scientists fully or partially turned to etch track detectors. This new interest was reflected in the name and topics of the international conferences on nuclear track detectors. At first, the name of the series of the conferences was on nuclear emulsions ("Corpuscular Photography"; "Nuclear Photography") from 1957 (the first international conference in Strasbourg) when the solid-state nuclear track detector was yet to be created. Since 1976 (the 9th international conference in Munchen), the name changed to "Solid State Nuclear Track Detector". This change reflected the rapid growth of the team of etch track detectors and the shift of scientific interest from emulsions to etch track detectors. Since 1992 (the 16th international conference in Beijing), the name changed to "Nuclear Tracks in Solids" for the reason that nuclear tracks can be used not only as nuclear particle detectors but also as nano- and microstructures applied to nanotechnology.

The split-off of the fission track dating workshop from the international conference on solid-state nuclear track detectors also showed the rapid expansion of the field of etch track detectors. A group of scientists who paid more attention to dating (including measurements of reactor neutrons, induced fission in nuclear reactors, and ancient spontaneous fission events) preferred to participate in fission track dating workshops.

Since 1978, a special journal entitled "Nuclear Track Detection" and later "Nuclear Tracks and Radiation

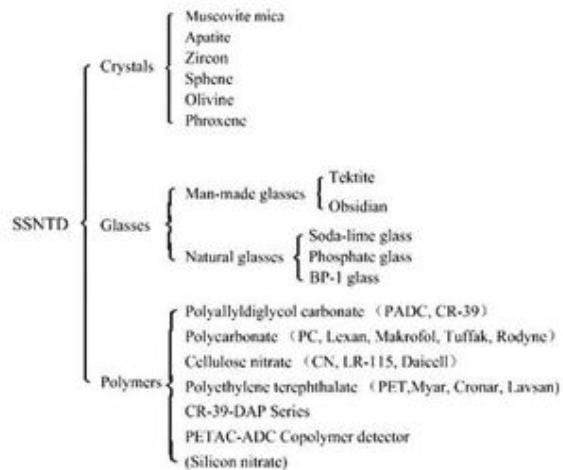
Measurements" and now "*Radiation Measurements*" was established to publish research papers on solid-state nuclear track detectors under the auspices of Elsevier Science publishers. All of the international conference proceedings on solid-state nuclear track detectors were published in the above journals or separately in the early years (1976, 1979, 1981) by Pergamon Press. The treatise works such as "Nuclear Tracks in Solids, Principles and Applications" by Fleischer et al. (1975), "Solid State Nuclear Track Detection" by Durrani and Bull (1987), "Ion Tracks and Microtechnology, Basic Principles and Applications" by Spohr (1990), "Fission Track Dating" by Wagner and Van den haute (1992), "Radon Measurements by Etch Track Detectors; Applications to Radiation Protection, Earth Sciences and Environment" by Durrani and Ilic (1997), and "Nuclear Track Detectors: Design, Methods and Applications" edited by Sidorov and Ivanov (2009) had given systematic details or specialized explanations on etch track detectors. The reader is referred to these reference books for additional information on nuclear track detectors.

II. DETECTOR MATERIALS AND CLASSIFICATION OF SOLID-STATE NUCLEAR TRACK DETECTORS

Nearly all kinds of transparent insulating solids can be used as solid-state nuclear track detectors (SSNTDs). These materials can be classified into natural and man-made solids. Natural solids include terrestrial and extraterrestrial ones. Terrestrial solids include all kinds of natural crystalline minerals and amorphous natural glasses. Tektites, obsidian, volcanic glasses, and impact glasses are examples of natural glasses. Extraterrestrial solids include meteorites and lunar rock. Most meteorites come from the asteroid belt between the orbits of Mars and Jupiter. Astronomers conjectured that there existed originally a planet in the asteroid belt. The planet broke at early time into many pieces or fragments. The fragments revolve round the sun on the original orbit of the planet but with some deviation. Some of the biased orbits intersect with the orbit of the earth. The fragments hit on the earth, forming meteorites. The lunar rocks were collected from the moon by astronauts of the USA in the early 1970s. Scientists from many countries participated in the research on lunar rocks with nuclear track techniques. The track lengths or diameters visible after etching under the optical microscope are usually several micrometers. Therefore, the lower limit of the sizes of the minerals or glasses for nuclear track studies is about 10 μm . Very large areas of natural muscovite mica up to $10 \times 10 \text{ cm}^2$ can be found and applied to nuclear physics studies. Man-made solids applied to as SSNTDs include man-made crystals (such as synthesized fluorophlogopite mica), man-made glasses (such as soda-lime glass and phosphate glass), and plastics (such as cellulose nitrate, polycarbonate, and polyallyldiglycol carbonate (CR-39)). Usually, man-made materials can be made very large for use as track detectors, especially in recording rare events such as cosmic-ray particles.

According to track formation mechanisms and etching behaviors, etch track detectors are usually classified as follows

with some examples of commonly used detector materials and newly developed materials:



In the following subsections, some basic knowledge on each detector material listed above will be given. For information about additional materials, the reader is referred to the monographs written by Fleischer et al. (1975), Durrani and Bull (1987) and Wagner and Van den haute (1992).

A. Crystalline Solids

Most of the transparent natural and man-made crystalline solids can be used as solid-state nuclear track detectors. Crystalline solids widely exist in the earth crust as mineral compositions of rocks, soils, and dust. Large-sized muscovite mica and quartz are examples of pure track detectors. The main compositions of granite are mica, feldspar, and quartz. All of them are transparent crystalline minerals and can be used as nuclear track detector materials. Many kinds of accessory minerals, such as apatite, zircon, and sphene, are also contained in granite. They are also transparent crystals with small sizes from about tens to hundreds of micrometers. They constitute about several percent of the total weight of the granite. These accessory minerals are very useful track detectors for fission track dating (FTD). After separation from the main compositions of the granite, each single grain of the accessory minerals can be used as track detectors. In many other types of rocks on the earth crust, similar situations exist, but the main and accessory minerals differ from rock to rock. One can select one or more special types of main minerals or accessory minerals as track detectors.

Each crystalline solid has a special crystal structure. The etch rates in different directions of the crystal usually vary. Therefore, etching proceeds anisotropically in crystals. The detection efficiencies of crystalline solid for charged particles (the ratio of recorded to incident particles) on different surfaces are usually diverse.

The most commonly applied crystalline solids and their properties are described below.

1. Muscovite Mica

Muscovite mica is a natural resource excavated from a mica mine. Large slabs of muscovite mica are found in pegmatite. It can be easily cleaved into thin flat pieces by a sharp needle or knife. The atomic composition of muscovite mica is $\text{KA}_3\text{Si}_3\text{O}_{10}(\text{OH})_2$ and density is $2.76\text{--}3.10\text{ g/cm}^3$ (the commonly quoted density is 2.8 g/cm^3). It has three refractive indices $n_a = 1.560$, $n_b = 1.594$, and $n_c = 1.598$ in three directions respectively. In track depth measurements under the optical microscope, the refractive index is taken as $n = 1.598$, that is n_c . Usually, the concentration of uranium in muscovite mica is very low ($\sim 10^{-9}\text{ g/g}$). It is about three orders of magnitude lower than that of the materials in the earth's crust ($\sim 2.7 \times 10^{-6}\text{ g/g}$). Therefore, muscovite mica is a good detector material with low concentration of uranium. It is suitable as a track detector for the determination of low uranium concentrations. The uranium concentration in muscovite mica varies. One must determine its uranium concentration before using it to determine the uranium concentration of other materials.

Muscovite mica is usually etched in hydrofluoric acid. For special purposes it can also be etched in hot concentrated NaOH solution (Khan et al., 1981; Guo et al., 1986a,b,c). The etching condition of fission-fragment tracks for optical microscope observation is listed in Table 4.1.

Figure 4.1(a) shows a microphotograph of fission-fragment tracks in muscovite mica taken with the ordinary optical microscope.

The etching condition is in 40% HF at 25°C for 500 min (Guo et al., 1982). Such an etching condition for muscovite mica was selected in order that the tracks were easily visible under optical microscope and the observed number of tracks was at the middle point of the flat response with respect to the change of etching time. Under this etching condition the detection efficiency of muscovite mica for fission fragments from induced fission of ^{235}U in 2π geometry is $(93.6 \pm 0.3)\%$ and critical angle is $3^\circ 41'$ (Guo et al., 1982). Muscovite mica has been widely applied to fission rate measurements (Li et al., 2001), neutron dose and energy-spectrum determination (Walker et al., 1963), fission track dating as external detectors (Fleischer et al., 1975; Durrani and Bull, 1987; Wagner and Van den haute, 1992;), uranium and plutonium concentration determinations (Price and Walker, 1963b), and multiprong sequential fission studies of heavy targets with heavy projectiles (Brandt, 1980; Vater et al., 1977, 1986; Gottschalk et al., 1983; Khan et al., 1987; Qureshi et al., 2005; Shahzad, 1995; Shahzad et al., 1999; Nasir et al., 2008; Khan et al., 2001; Baluch et al., 2006).

2. Apatite

Apatite is a sort of widespread accessory mineral, which exists ubiquitously in various rocks, such as plutonic, volcanic, metamorphic, and sedimentary rocks. It is the most frequently used mineral in fission track dating and geothermal chronology. Its atomic composition is $\text{Ca}_5(\text{F,Cl})(\text{PO}_4)_3$, density $3.16\text{--}3.22$ (usually 3.18) g/cm^3 , and refractive index $n_0 = 1.629\text{--}1.667$ in the direction of axis with average 1.648 , $n_c = 1.624\text{--}1.666$ in the direction perpendicular to the axis

TABLE 4.1 Etching Conditions of Common Nuclear Track Detectors for Optical Microscope Observation

Material	Etching condition	Reference
1. Crystalline solids		
Muscovite mica	48% HF, 23°C , 100 min–2 h	Price and Walker, 1962c
Apatite	0.1–5% HNO_3 , $20\text{--}25^\circ\text{C}$, 30 s–3 min	Fleischer and Price, 1964
Zircon	20 g NaOH + 5 g H_2O , 22°C , 15 min–4 h	Wagner and Van den haute, 1992
Sphene	37% HCl, 80°C , 80 min	Guo et al., 1980
Olivine	WN solution, boiling point, 5 h (1 g Liu et al., 1979 $\text{H}_2\text{C}_2\text{O}_4 \cdot 2\text{H}_2\text{O} + 1\text{ ml}$ $\text{H}_3\text{PO}_4 + 40\text{ g Na}_2\text{EDTA} +$ 100 ml $\text{H}_2\text{O} + \text{NaOH}$ until $\text{pH} = 8.0 \pm 0.3$)	
Pyroxene	60% NaOH, boiling point, 80 min	Liu et al., 1979
2. Glasses		
Soda-lime glass	48% HF, $20\text{--}25^\circ\text{C}$, 5–10 s	Fleischer and Price, 1963b
Phosphate glass	48% HF, $20\text{--}25^\circ\text{C}$, 5–20 s	Fleischer and Price, 1963b
BP-1 glass	49% HBF_4 , 50°C , 58–100 h	Wang et al., 1988
Tektite	48% HF, $20\text{--}25^\circ\text{C}$, 30 s	Fleischer and Price, 1964
Obsidian	48% HF, 23°C , 60 s	Fleischer and Price, 1964
3. Plastics (high polymers)		
CR-39	6.25N NaOH, 75°C , 6 h	Cartwright et al., 1978,
Polycarbonate (Lexan, Makrofol)	6.25N NaOH, 50°C , 20 min	Fleischer and Price, 1963a
Cellulose nitrate (LR-115)	6.25N NaOH, 23°C , 2–4 h	Fleischer et al., 1975
Polyethylene terephthalate	6.25N NaOH, 70°C , 10 min	Fleischer and Price, 1963a
4. New detector materials		
CR-39-DAP Series7N	NaOH, $70\text{--}90^\circ\text{C}$, 1–18 h	Kodaira et al., 2008
PETAC-ADC copolymer	6N NaOH, 70°C , 60 min (α) 30 min (FT)	Mandrekar et al., 2010
Silicon nitrate (Si_3N_4)	HF	Vlasukova et al., 2010

with average 1.645. Its hardness is five (5), quite easy to be ground and polished.

The track etching of apatite is very easy at room temperature and very fast (several seconds to several minutes) in concentrated or diluted nitric acid (see Table 4.1). Track-etch rate V_T bulk etch

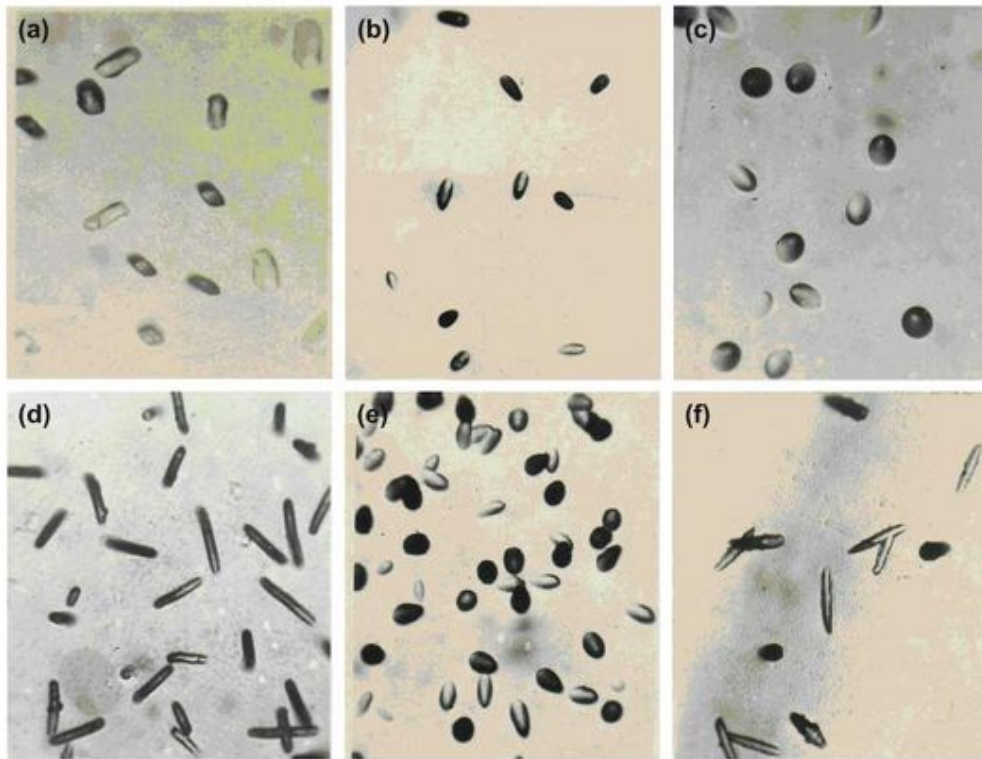


FIGURE 4.1 Microphotographs of fission-fragment tracks in (a) muscovite mica, (b) phosphate glass, (c) soda-lime glass, (d) polycarbonate, (e) quartz, and (f) polyester taken under an ordinary optical microscope. The etching conditions were selected such that the tracks were most clear and easy to observe under the optical microscope and the number of tracks was at the middle point of the constant part of the response curve for each type of the detector. For the color version of the figure, the reader is referred to the online version of the book.

rate V_B , and detection efficiency for fission-fragment tracks vary according to the orientation of apatite surfaces. The average detection efficiency of apatite for fission fragments of ^{252}Cf in 2π geometry is $(87.8 \pm 5.2)\%$ (Surinder Singh et al., 1986).

The uranium concentration in apatite is usually very high from about 1 to 100 ppm (parts per million = 10^{-6} g/g). (For comparison, the average concentration of uranium in the earth crust is about 2.7 ppm.)

Apatite has a relatively low thermal stability of fission tracks. Its partial annealing zone (PAZ) of fission tracks is in the range of about 60–125 °C (Gleadow and Duddy, 1981). The lower limit of temperature about 60 °C means that fission tracks in apatite can be treated as stable at temperature lower than 60 °C during the geologic time. Over the upper limit of the partial annealing zone (PAZ) about 125 °C, fission tracks will disappear after geological time. The closure temperature is $(100 \pm 20)^\circ\text{C}$ (Harrison et al., 1979). The relatively low partial annealing zone, which is almost consistent with the formation window of petroleum (hydrocarbon) 60–130 °C, makes apatite an important detector for the exploration of petroleum formation (Gleadow et al., 1983; Naeser and McCulloh, 1989; Green et al., 1989; Kang and Wang, 1991).

All the above advantages make apatite one of most useful mineral materials in fission track dating and geothermal chronology.

3. Zircon

Zircon, similar to apatite, as an accessory mineral exists ubiquitously in rocks of most types, and it is rich enough in uranium to permit age determinations down to million years or so. Its atomic composition is ZrSiO_4 , molecular weight 183.304 g/mol, $A/Z = 2.128$, and ionization potential $I = 209.5$ eV. The colorless zircon has a density 4.6–4.8 (usually 4.7) g/cm³, refractive index 1.925–1.984, and hardness 7–7.5. The green or dark brown zircon has a density of 3.9–4.1 g/cm³, refractive index 1.78–1.815, and hardness 6. Zircon can be etched by H_3PO_4 , or by NaOH, KOH, and their mixture at high-temperature. The etching condition 20 g NaOH:5 g H_2O (≈ 100 N) at 220 °C for 15 min to 4 h (see Table 4.1) is often adopted. For zircon etching, the grains of zircon are mounted on one surface of polyvinylidene fluoride (PVDF) sheet by pressing with a glass plate at high-temperature. The grains of zircon will be adhered and fixed onto the PVDF sheet. After grinding and polishing, the adhered

zircon is etched in a tightly closed container made of Teflon. The Teflon container is held by a steel container, which is placed in an electric oven for heating to 220 °C.

The uranium concentration of zircon is generally very high, between 300 and 600 ppm (Wagner and Van den haute, 1992) which is well suited for fission track dating and even for archaeological dating. The latent fission tracks in zircon are more thermal resistant than those in apatite. The track retention temperature of zircon is 210 ± 40 °C (Wagner and Van den haute, 1992).

Zircon and apatite often exist in the same geological body. The apparent age (age calculated by the simple age equation without taking track fading into account, see Section III. A. 1 of Part 2) of zircon and apatite reflects the years the geological body passed through their closure temperatures. From the depth–temperature relationship in the earth and the age difference between zircon and apatite, the uplift rate of the geological body can be derived. This technique of uplift rate determination is referred to as the mineral pair – closure temperature method or simply mineral pair method. Zircon is the second most commonly used mineral in fission track dating and geothermal chronology.

4. Spheue

Sphene (titanite) widely exists as an accessory mineral in plutonic and metamorphic rocks, but it is less common in pegmatite and volcanic rocks. Its atomic composition is $\text{CaTiO}[\text{SiO}_4]$, molecular weight 196.04 g/mol, $A/Z = 2.042$, ionization potential $I = 144.4$ eV, density 3.4–3.6 (usually 3.54) g/cm³, hardness 5.0–5.5, and refractive index 1.888–2.054.

The etching of sphene is easy to carry out with concentrated HCl at 90 °C for 30–90 min. The etching behavior of sphene exhibits a very strong anisotropic nature. The shapes of etched fission tracks are very different on different surfaces, depending on the orientation of the surfaces with respect to the crystal structure of the sphene and on the annealing before irradiation to fission fragments (Gleadow, 1978). The detection efficiency for fission tracks is also dependent on the orientation of the surface. The detection efficiency of annealed sphene can be down to one-half or even one-third compared with muscovite mica for spontaneous fission tracks. A calibration with annealed sphenes with random orientations showed that the ratio of detection efficiencies of the sphenes to muscovite mica is 0.516 ± 0.035 for fission fragments of ²³⁵U fission induced by thermal neutrons (Guo et al., 1980; Guo, 1982a). This value is much less than one. It means that the detection efficiency of annealed sphene for fission fragments is reduced.

Uranium concentration in sphene is usually rather high, between 100 and 1000 ppm. It is suitable for fission track dating and geothermal chronology. Thermal resistivity of fission tracks in sphene is higher than apatite and zircon. The effective track retention temperature (closure temperature) is 250 ± 50 °C (Wagner and Van den haute, 1992). Its partial annealing zone is 200–280 °C (Harrison et al., 1979).

Sphene has provided much data on geological dating (Naeser, 1967; Wagner and Van den haute, 1992) and also archaeological dating (Guo, 1982a; Guo et al., 1980, 1991).

5. Olivine

Olivine is a general composition of stone meteorites and stony-iron meteorites and exists in the earth crust. It contains plenty of information about radiation in space. It is a space radiation detector. It has been recording heavy charged particle tracks since its formation billions of years ago. Fossil tracks in extraterrestrial minerals were first found in olivine in a stony-iron meteorite (Fleischer et al., 1975).

The atomic composition of olivine is $(\text{Mg,Fe})_2\text{SiO}_4$, in which the ratio of Mg to Fe can be any value. The molecular weight is 140.708 g/mol for Mg_2SiO_4 and 203.778 g/mol for Fe_2SiO_4 , the average value 172.2335 g/mol is usually taken. Its density increases with increasing Fe content from 3.3 to 3.5 g/cm³, usually 3.35 g/cm³ is taken. Its hardness is 6.5–7.0 and refractive index 1.654–1.690. The $A/Z = 2.050$, and its ionization potential $I = 158.9$ eV.

The etching condition used by many workers is the following:

1 ml H_3PO_4 :1 g oxalic acid : 40 g disodium salt of EDTA : 100g H_2O : ~4.5 g NaOH, boiling temperature (~125 °C) for 5 h. Some amount of NaOH is added to make the pH value equal to 8.0 ± 0.3 of the etchant (Liu et al., 1979).

The uranium concentration of olivine is usually very low. It is $(0.046 \pm 0.004) \times 10^{-9}$ g/g in Jilin meteorite (Liu et al., 1979).

The tracks in olivine from meteorites or lunar rocks can provide information in the following fields:

1. Spontaneous fission of ²³⁸U and ²⁴⁴Pu. The latter nuclide is extinct in nature since its half-life is 8.08×10^7 a (year), which is much less than the age of the earth (4.6 ± 0.1) $\times 10^9$ a. It could exist only in the early era of the solar system. The tracks of spontaneous fission from both ²³⁸U and ²⁴⁴Pu in meteorites can provide information on the age of meteorites (Liu et al., 1979) as well as of lunar rocks.
2. Space radiation particles, including cosmic-ray particles and possible magnetic monopoles.
3. Records of interactions of cosmic-ray particles with nuclei in the meteorites and lunar rocks, such as high-energy spallation reactions and space neutron-induced fission.

From the above information, the origin of cosmic-ray particles and the phenomena occurring in cosmic-ray sources can be derived (Fleischer et al., 1975).

6. Pyroxene

Pyroxene is one of the main minerals in stone meteorites, stony-iron meteorites, and lunar rocks as well as in the earth crust. Its atomic composition is $\text{R}_2[\text{Si}_2\text{O}_6]$, where R represents Mg, Fe, or Ca; Mg and Fe are exchangeable. In some other pyroxenes, R represents Na, Li, Al, Fe, Ti, and the other elements. The basic structure of the above varieties of pyroxene is nearly the same; their properties are also very similar. For diopside $\text{CaMg}[\text{Si}_2\text{O}_6]$, its density is 3.28–3.40 (usually 3.29) g/cm³, refractive index 1.675–1.701, hardness 5.5–6, $A/Z = 2.000$, and ionization potential $I = 138.3$ eV. The etching condition for varieties of pyroxene (diopside, pigeonite, augite, enstatite, bronzite,

hypersthene, and ferrohypersthene) is 3g NaOH : 2g H₂O, boiling temperature, and 35–90 min (Lal et al., 1968). The uranium concentration in pyroxene is usually very low, for example, $(1.50 \pm 0.13) \times 10^{-9}$ g/g in Jilin meteorite (Liu et al., 1979) and $(0.95-15.0) \times 10^{-9}$ g/g in lunar mare basaltic fragments 70017–291 (Hu et al., 1982).

Pyroxene, similar to olivine, is an important mineral detector for retrieving space radiation information as described in II. E of Part 2 and in the classic book by Fleischer et al. (1975).

7. Other Crystalline Solids

Up to now, about 100 crystalline minerals have been successfully etched to show fission-fragment tracks (Fleischer et al., 1975; Wagner and Van den Haute, 1992). Besides the most commonly used minerals described above, quartz, feldspar, garnet, epidote, and whitlockite are also used frequently.

Quartz is one of the crystalline detectors with low uranium concentration. By using quartz as a track detector and irradiating samples in nuclear reactors, an atomic concentration of uranium as low as 10^{-12} can be determined (Fleischer et al., 1965a).

Feldspar is one of the main mineral compositions in meteorites and lunar rocks. Whitlockite is one of the rich accessory minerals in extraterrestrial studies. Both minerals have recorded large number of tracks of space radiation particles, which should undergo further detailed research.

For more information about the etching and applications of all of the crystalline minerals, the reader is referred to the monographs by Fleischer et al. (1975) and by Wagner and Van den haute (1992).

B. Glasses

Glasses, as nuclear track detectors, are a type of amorphous noncrystalline (uncrystallized) inorganic solid. It can be divided into natural glasses and man-made glasses. Natural glasses include terrestrial glasses and extraterrestrial glasses. Terrestrial glasses are formed in volcanic eruption, rock-melts solidification, tectonic frictional fusion, and meteoritic impactation. In other words, in all geological events in which the temperature dropped rapidly, the fused substance could not form crystalline structures, resulting in formation of glasses.

Volcanic glasses and tektites are examples of terrestrial glasses. Extraterrestrial glasses exist in meteorites and lunar rocks. When the meteoritic or lunar substances underwent cooling, some kinds of main mineral crystals, such as olivine, pyroxene, and feldspar, were first formed. The remaining substance with low crystallization temperature would form glassy substances by the rapid cooling process (Hu et al., 1982). Owing to the larger ionic radius of the uranium atom than that of other metallic ions, uranium atoms were pushed aside from the forming crystals into the gap substance, which were later formed in glassy interstitial materials. Therefore, glassy substance, distributed in the gaps of crystalline minerals, has a higher concentration of uranium than crystalline minerals.

Man-made glasses include different varieties, such as soda-lime glass, phosphate glass, BP-1 glass and others.

The common feature of glass track detectors is isotropic etching behavior. This feature results from the amorphous structure of glassy materials. Detailed explanation of etching of particle tracks in amorphous solids can be found in more recent publications (Nikezic and Kostic, 1997; Nikezic, 2000; Nikezic and Yu, 2003; Nikezic and Yu, 2004).

1. Man-Made Glasses

The atomic compositions of most man-made glasses vary according to their manufacture from place to place. For example, the compositions of soda-lime glasses are 23SiO₂:5Na₂O:5CaO:Al₂O₃ in the U. S. A (Fleischer et al., 1975), 67SiO₂:14Na₂O:14CaO:5Al₂O₃ in the U. K (Durrani and Bull, 1987), and 71SiO₂:15Na₂O:9CaO:3MgO:2Al₂O₃ in China (Guo et al., 1976b, 1982). All of these are commonly used as window glass, microscope slides, cover slips, etc. It is very convenient to place a slip of window glass or microscope slide in the beam of particles ($Z \geq 10$) at an accelerator to make an exposure for a certain time. Then, etch it in HF for a few seconds at room temperature and wash it immediately with water; the tracks of the particles as well as the flux and radial distribution of the particles from the accelerator can be determined easily. Similar determinations can be carried out within several minutes at nuclear reactors for flux and radial distributions of thermal neutron beams by folding a uranium foil with glass plate.

A microphotograph of fission-fragment tracks in soda-lime glass is shown in Fig. 4.1 (c). The critical angle of soda-lime glass for detecting fission fragments of ²³⁵U is $\theta_c = 37^\circ 21'$ and its detection efficiency in 2π geometry for isotropic emitted fission fragments from thin ²³⁵U foil is $(39.3 \pm 0.4)\%$ (Guo et al., 1982).

The advantage of soda-lime glass as a track detector is insensitivity to particles lighter than or equal to C ($Z = 6$). It can overcome intense background of α -particles in fission studies and intense accelerator beam particles in studies of nuclear reactions in the synthesis of transuranium elements (Flerov et al., 1964).

The composition of phosphate glasses is also varied, for example, 10P₂O₅:1.6BaO:Ag₂O:2K₂O:2Al₂O₃ in the U. S. A. (Fleischer et al., 1975), 34P₂O₅:7ZnO:4Al₂O₃:4BrO₃:SiO₂ in the U. K (Durrani and Bull, 1987), and 50LiPO₃:50Al(PO₃)₃:7AgPO₃:3B₂O₃ in China (Guo et al., 1976b, 1982).

The critical angle of Chinese phosphate glass for recording fission-fragment tracks is $7^\circ 6'$, while the 2π detection efficiency for isotropic ²³⁵U fission source is $87.6 \pm 0.5\%$, which is higher than soda-lime glasses (Guo et al., 1976b, 1982).

BP-1 glass is a special type of phosphate glass, which is composed of 65 wt% P₂O₅, 25 wt% BaO, 5 wt% Na₂O, and 5 wt% SiO₂ (Wang et al., 1988). BP-1 glass has been used in discoveries of several cluster radioactivities, studies of high-energy nuclear reactions, and measurements of isotopic compositions of manganese and nickel in galactic cosmic rays (GCRs). The latter measurements were carried out by using a stack of plates of BP-1 glass attached outside the Mir station for five years. The charge resolution was obtained being $\sigma_z = 0.08e$ for $Z = 69-79$, $E = 10.6$ AGeV for three individual

measurements over three sheets of glass. The mass resolution is $\sigma_m = 0.43\text{--}0.58$ amu for $Z = 25\text{--}28$, $A = 53\text{--}62$, and $E = 150\text{--}400$ AMeV for galactic cosmic rays. These are the highest charge and mass (isotope) resolutions yet obtained (Westphal et al., 1996).

BP-1 glass has been used in the identification of the emission of ^{23}F and ^{24}Na clusters from ^{231}Pa with branch ratios of 1×10^{-14} and 1.3×10^{-11} respectively. In this study, BP-1 glass only recorded the emitted nuclei ^{23}F and ^{24}Na without recording α (background), whose intensity is 10^{14} or 10^{11} times higher than that of the emitted nuclei (Price et al., 1992).

BP-1 glass has also been used in the measurement of fragmentation cross section of 160 AGeV Pb. Charge resolution is ~ 0.14 charge unit for one single cone measurement. For successive five sheets of glass, the $\sigma_z = -0.06e$. This charge resolution is more than adequate to identify fragments and hence to measure cross sections for charge-changing interactions. BP-1 glass is expected to be able to detect magnetic monopoles with charge $n=2$ and $\beta > 0.2$. No tracks of magnetic monopoles with $n=2$ were found.

2. Natural Glasses

Natural glasses were formed in the earth's crust or in meteorites or lunar rocks. Most important natural glasses are tektite and obsidian. Some other types are basaltic deep-sea glass and frictionite glass.

Tektite is a special type of glassy object, which distributes in four restricted areas in the world: (1) Southeast Asia and Australia (0.732 ± 0.039 Ma) (Guo et al., 1997), (2) Ivory Coast (1.08 ± 0.10 Ma) (Wagner, 1966), (3) Czech Republic (Moldova) (14.7 ± 0.4 Ma) (Wagner, 1966; Storzer and Wagner, 1977), and (4) North America (34.6 ± 0.7 Ma) (Storzer and Wagner, 1977). Many authors have dated the tektites and obtained results consistent with each other for each restricted area. The above ages in the brackets are given in order to show the time of their formation. Most acceptable hypothesis of the origin of tektites is that they were formed by impacts of meteoroids on the earth. During impact, a large kinetic energy of the meteoroid was transferred to the substance in the earth's crust and melted and sputtered the impacted substance to the sky; then the substance cooled down quickly to form glassy objects in sizes from several centimeters to less than 1 mm. The glassy objects drop down to the earth, forming tektites or microtektites. The chemical composition of tektites are similar to that of the earth crust, for example, 74.63%SiO₂, 12.19%Al₂O₃, 4.16%FeO, 2.32%K₂O, 1.87%CaO, 1.82%MgO, 1.36%Na₂O, 0.77%TiO₂, 0.54%Fe₂O₃, 0.09%MnO (Li Bin, 1982). The uranium concentration of tektites is also consistent with that of the average earth crust, for example, 1.74 ± 0.18 and 1.39 ± 0.15 ppm in the tektites found in Hainan island, China (Collaboration Group of China Institute of Atomic Energy and Guiyang Institute of Geochemistry, 1976).

The density of tektites is $2.32\text{--}2.5$ g/cm³ and refractive index $1.48\text{--}1.52$. Tektite is a suitable detector for fission track registration. Fission track dating of tektites can provide a variety of information in space research, stratigraphy, and paleoanthropology (Guo et al., 1997).

Obsidian is a special type of natural glassy detector to record fission-fragment tracks. Obsidian was formed during the young volcanism. When magma on the earth surface met with water in lakes or rivers, it rapidly cooled down at normal atmospheric pressure, forming obsidian glasses. Obsidian exists worldwide with volcanoes, such as around the Pacific and Mediterranean Oceans, west part of North and South America, New Zealand, Japan, Near East, East Africa, and Iceland. The sizes of obsidians vary from several hundred meters to centimeters or even as tephra. The refractive index of obsidian is $1.48\text{--}1.52$ (usually 1.49), density $2.33\text{--}2.41$ g/cm³, and hardness $5\text{--}5.5$. Its uranium concentration is $5\text{--}15$ ppm, which is suitable for fission track dating. Obsidian was used as sharp tools by ancient man, such as stone knives, saws, and arrow heads. It was a sort of object for commercial trade. By fission track techniques, the following information may be obtained: age and geographic provenance of obsidian raw materials, age of heating for manufacture of obsidian artifacts, age and uranium concentration of the obsidian are specific for each source of obsidian. Both can be criteria for judging the source (Bigazzi et al., 1990).

Other natural glasses, such as frictional glasses formed during fault displacement, impact glasses formed during the formation of a crater by meteorite bombardment, basaltic glasses formed during sea-floor spreading, are all useful for fission track measurements for many different purposes (Fleischer et al., 1975; Wagner and Van den haute, 1992).

C. Plastics

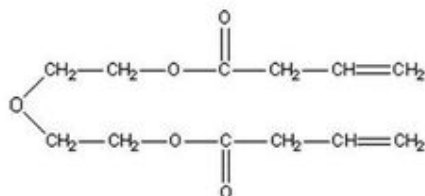
Since the discovery that polymers (plastics) can record etchable tracks of heavy charged particles (Fleischer and Price, 1963a), more than 30 types of polymer detectors have been successfully etched to reveal tracks. Compared with inorganic crystalline solids and glasses, plastic track detectors are more sensitive to heavy charged particles, such as the charge as low as $Z = 1$ (proton). The sensitivities of different polymers are different. CR-39 (polyallyldiglycol carbonate (PADC)) is the most sensitive detector in common use (the recordable charge $Z \geq 1$); amber is the most insensitive plastic detector (the lowest recordable charge is fission fragments, $Z > 30$).

1. CR-39 (Polyallyldiglycol carbonate, PADC, PM-355, PM-500, PM-600)

CR-39, as a unique sensitivity and high charge resolution detector, was discovered by Cartwright et al. (1978). CR-39 is the trade name of allyl diglycol carbonate. CR stands for "Columbia Resin". CR-39 plate (sheet) is produced by casting CR-39 monomer with some kinds of initiators in a frame. Kinoshita and Price (1980) found that IPP (di-isopropyl peroxydicarbonate) as initiator could produce a more smooth surface than the other initiators. Tarle et al. (1981) found that adding DOP (dioctyl phthalate) as plasticizer into the monomer before casting could reduce roughness after long etching. In order to meet the need of scientific research, many firms have made CR-39 sheets with special care. The most successful firms

include Intercast Europe in Italy¹, Page Molding in the UK², American Acrylic and Plastics in the USA³, Fukuvi Chemical Industry in Japan⁴, Tastrak in the UK⁵, and others (Pang Deling and Ma Guo-Cai, 1988).

The chemical composition of the monomer of CR-39 is $C_{12}H_{18}O_7$, with its molecular weight being 274.2707 g/mol. Its molecular structure is:



It has a chain-like structure. In polymerization of CR-39 monomers, the double bonds of allyl groups ($CH_2CH=CH_2$) in the structure of the monomers open and form a cross-linked net structure in three-dimensional directions with other molecules, forming polyallyldiglycol carbonate (PADC). In general, chain-like structures are more sensitive to radiation than the other structures, such as a benzene ring in polycarbonate. It is thus understandable why CR-39 is more sensitive than polycarbonate (Tsuruta et al., 2008).

The density of CR-39 is 1.32 g/cm³, refractive index $n = 1.504$, $A/Z = 1.877$, and its mean ionization potential $I = 70.2$ eV (Durrani and Bull, 1987). CR-39 track detectors can be etched with NaOH and KOH solutions. The recordable minimum ionizing particle is a 20 keV proton by etching with NaOH solution (Duan et al., 2009, 2010). The etched tracks of protons from 20 keV to 1.02 MeV are shown in Fig. 4.2 (Duan et al., 2010).

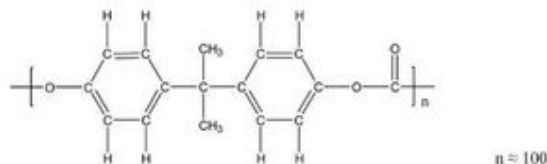
CR-39 detector can not only record track number N , positions (X, Y, Z), directions (zenith angle θ , azimuth angle ψ), but also derive particle charge Z , mass M , and energy E from the track parameters. It is the most widely used solid-state nuclear track detector.

2. Polycarbonate (PC, Lexan, Makrofol, Taffak)

Before the discovery of the CR-39 track detector in 1978, polycarbonate (PC) was the most commonly used track detector. Since CR-39 is more sensitive than polycarbonate, many of the measurements previously carried out with polycarbonate have been replaced by CR-39. But polycarbonate is still used frequently when proton tracks may be a strong background. For example, during nuclear reactor irradiation fast neutrons will produce background tracks of recoil protons in CR-39, but in polycarbonate the recoil protons will not be recorded as background tracks. In this case, polycarbonate is better than CR-39. Up to now, polycarbonate is preferred as an external detector in fission track dating. The flux of protons in cosmic rays at the top

of the atmosphere is over 10^2 times more than the sum of the other nuclei, as described in Chapter 1. Protons will produce a large background in CR-39, but will have no effect on polycarbonate. Therefore, polycarbonate is still used in satellites and balloons to collect data on heavy cosmic rays.

The composition of polycarbonate is $C_{16}H_{14}O_3$, with the molecular weight 254.2855 g/mol. Its molecular structure is



The benzene ring in the structure of polycarbonate has a tendency to absorb more radiation energy than the chain structure of CR-39 (Tsuruta et al., 2008; Chadderton et al., 1993). Therefore, polycarbonate is less sensitive to recording tracks than CR-39. The minimum recordable charge (atomic number) Z of particles by polycarbonate is 2 (α -particle). The ionization potential $I = 69.5$ eV, $A/Z = 1.896$, refractive index $n = 1.586$, and density = 1.29 g/cm³. Lexan is a commercial name of the product of Bisphenol-A polycarbonate foil made by General Electric Company. Lexan is one of the most widely used detectors in the polycarbonate series. Makrofol is a commercial name of Bisphenol-A polycarbonate foil produced by Bayer AG, Germany (Note: Bayer AG has stopped the production of Makrofol foil).

The properties of polycarbonate foils produced by different firms are similar but with noticeable differences. For example, the detection efficiency of polycarbonate foil produced in China for fission fragments of ^{235}U in 2π geometry is $(95.5 \pm 0.4)\%$ and the critical angle is $2^\circ 24'$; while the detection efficiency of Makrofol K from Bayer AG for the same source of fission fragments is $(93.6 \pm 0.7)\%$ and the critical angle is $3^\circ 40'$ (Guo et al., 1976b, 1982). The two results are close to each other, but not within statistical uncertainties. Similar situations occur for other types of plastic track detectors. For this reason, the parameters calibrated for a type of detector material cannot be used for another type of the detector when very precise results are required.

Experiences also show that the properties of different batches of the detector materials produced by the same firm with the same raw material are usually different. One must calibrate each batch of detectors before use. It does not mean one cannot use the results obtained by other workers. We just want to mention that the best way to get reliable results is to calibrate the detector for every batch and for each situation, if one needs high precision.

Tuffak is a commercial name of the polycarbonate foil produced by Rohm & Haas Company, USA. The density of

¹ Intercast Europe Srl., 10/A Via G. Natta, Area SPII, 43122 Parma, Italy. Tel: (+39) (0)521 607555; Fax: (+39)(0)521 607924. Web: <http://www.intercast.it>. E-mail: intercast@intercast.it.

² Pershore Mouldings Limited, Trade Estate, Poreshore, Worcestershire, WR10 2DH, England. Tel.: (+44)(0)386 553425.

³ American Acrylics and Plastics, Stratford, CT, USA.

⁴ BARYOTRAK, Fukuvi Chemical Industry, Tokyo, Japan.

⁵ Tastrak, Track Analysis Systems Ltd., c/o H. H. Wills Physics Laboratory, Bristol, UK.

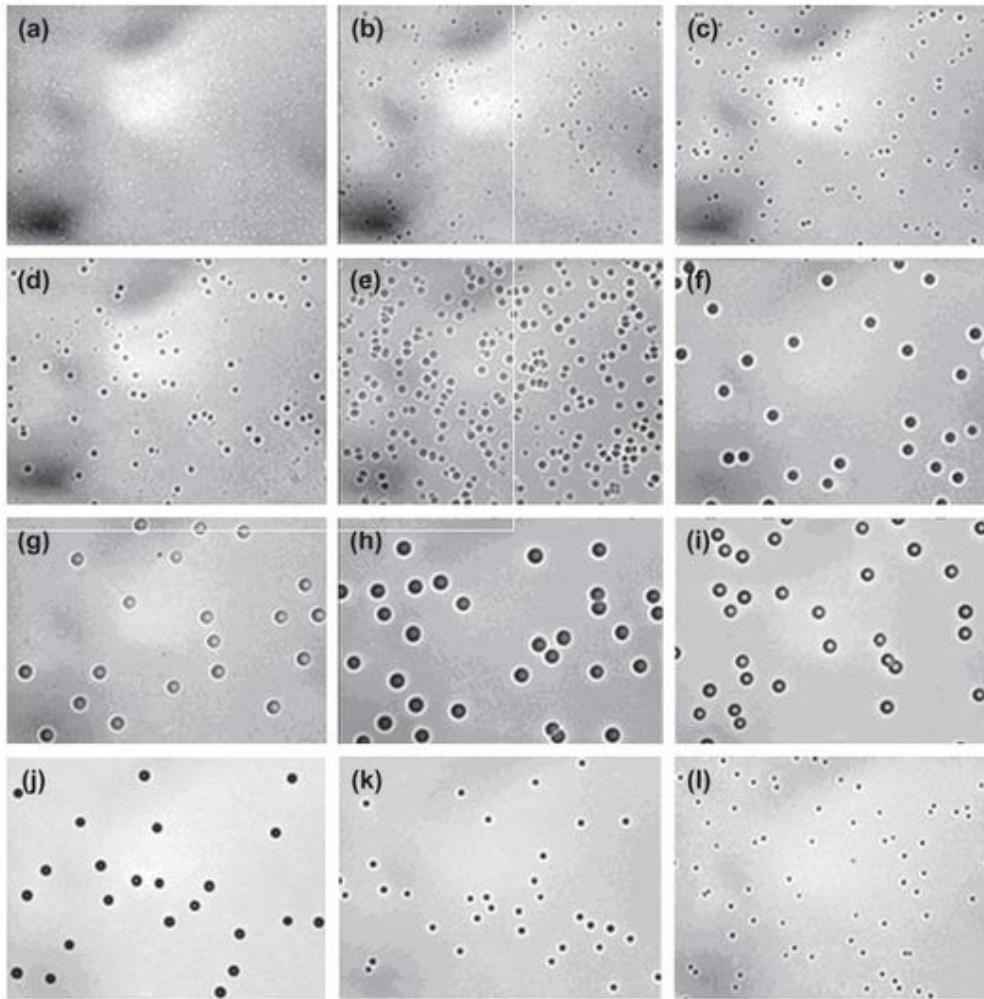


FIGURE 4.2 Microphotographs of tracks of monoenergetic protons of (a) 20, (b) 40, (c) 60, (d) 80, (e) 100, (f) 220, (g) 320, (h) 420, (i) 520, (j) 620, (k) 820 keV, and (l) 1.2 MeV, respectively, etched in 6 mol/L NaOH at 70 °C for 9 h. The minimum detectable energy of protons with CR-39 is ~20 keV. (From Duan et al., 2010. Reprinted with kind permission from *Acta Physica Sinica* © 2010)

Tuffak polycarbonate is 1.249 g/cm³ and refractive index is 1.586. The smoothness of the surface of Tuffak is much better than that of Lexan. A comparative study between Lexan and Tuffak showed that σ_D/\bar{D} values are 0.015 and 0.0034 for Lexan and Tuffak, respectively, for 955 MeV/u U tracks. \bar{D} is the average diameter of U tracks in Lexan or Tuffak. σ_D is the standard deviation of the track diameters. The value $\sigma_D/\bar{D} = 0.0034$ infers that by measuring a single track diameter, one can determine the charge Z with an uncertainty $\sigma_Z = 0.9e$ near the charge Z around 92 (U). In other words, by measuring the diameter of a single cone of the track in Tuffak, one can resolve uranium ion from the neighboring elements (O'Sullivan and Thompson, 1982; Ahlen et al., 1984; Salamon et al., 1985; Guo et al., 1984a).

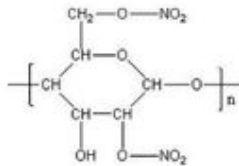
Polycarbonate track detectors have been used extensively in α radiography, neutron physics, heavy-ion studies, cosmic-ray research, and nuclear track membrane production (Fleischer et al., 1975; Durrani and Bull, 1987).

3. Cellulose Nitrate (CN, LR-115, Daicell)

Cellulose nitrate is one of the most sensitive nuclear track detector materials. Its sensitivity is just less than CR-39. The least ionizing ion is 0.55 MeV protons (Daicell). Fleischer (1981) showed that the least ionizing ion seen was 1.2 MeV protons for cellulose nitrate (VEB Eilenburg). In this case, the cellulose nitrate is more sensitive than CR-39.

Cellulose nitrate is made from absorbent cotton (cellulose) reacted with concentrated nitric acid. The three $-OH$ groups in the molecular structure of cellulose partly (1, 2 or all the 3 $-OH$ groups) are replaced by $-O-NO_2$ groups in the reaction.

The formed structure of cellulose nitrate with 2 $-O-NO_2$ groups is the following:



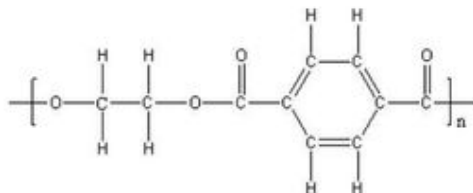
with formula $[C_6H_8O_9N_2]_n$ or $C_6H_8O_9N_2$ for short.

The density of CN is 1.4 g/cm^3 , $A/Z = 1.939$, and ionization potential $I = 81.1 \text{ eV}$.

LR-115 is a commercial name of cellulose nitrate detector made by Kodak-Pathe, or DOSIRAD, France. LR-115 type-II has an active layer of $12 \mu\text{m}$ red-dyed cellulose nitrate film coated on inert polyester base of $100 \mu\text{m}$ thickness. The thickness of $12 \mu\text{m}$ is designed for spark counting of α -particle tracks recorded in the film. LR-115 type-II is welcomed by radon scientists for the reason that α -particles emitted from radon progenies attached onto the surface of the detector cannot be developed by chemical etching for short etching times. The energies of the α -particles from the short-lived progenies are all higher than 6.0 MeV , which are beyond the energy window $0.06\text{--}6 \text{ MeV}$ of LR-115. In contrast, all the α -particles from the progenies can form etchable tracks in CR-39 by a short etching time. This is an advantage of LR-115 over CR-39 (Eappan and Mayya, 2004; Nikolaev and Ilic, 1999; Barillon, 2005; Yamauchi et al., 2008; Durrani and Bull, 1987; Durrani and Ilic, 1997; Narula et al., 2009a, 2009b; Nikezic et al., 2009; Sajo-Bohus et al., 2008, 2009; Boichichio et al., 2003, 2009).

4. Polyethylene Terephthalate (PET, Mylar, Cronar, Melinex, Lavsan, Terphane, Hostphan)

Polyethylene terephthalate (PET) is another commonly used track detector. Its molecular structure is:



The molecular formula is: $(C_{10}H_8O_4)_n$ or $C_{10}H_8O_4$ for short.

The density of PET is 1.397 g/cm^3 , refractive index $n = 1.640$, $A/Z = 1.915$, and ionization potential $I = 73.2 \text{ eV}$. The most commonly used etching condition is 6.25 N NaOH , 70°C , $10\text{--}40 \text{ min}$ for fission-fragment tracks.

PET is less sensitive than polycarbonate: PET cannot record tracks of α -particles. Therefore, PET is often used to selectively record heavy-ion tracks in the environments where intensive

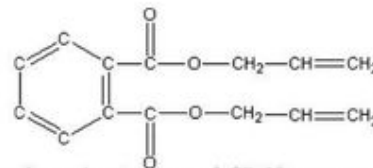
α -particles exist. Its charge and mass resolutions for several MeV/amu Ne ($Z = 10$) to Si ($Z = 14$) ions are good enough for the measurement of track parameters; thus, it was one of the detectors used in the discovery of cluster radioactivity (Barwick et al., 1985; Price, 1987; Tretyakova et al., 1985). See also Chapter 1 for a more detailed treatment of cluster radioactivity.

PET track detectors have also been used widely in many fields, such as heavy cosmic-ray analyses (Drach et al., 1987; Price and Drach, 1987), nuclear track membranes (Apel et al., 2008; Husaini et al., 2008; Zhu et al., 2004; Guo et al., 2008; Cao and Wang, 2009; Gomez Alvarez-Arenas et al., 2009), nano- and microstructure device manufacture (Spohr, 1990, 2008; Fink et al., 2008; Chakarvarti, 2009; Wang et al., 2009; Zagorski et al., 2009), and anti-counterfeiting techniques (Wang et al., 2008).

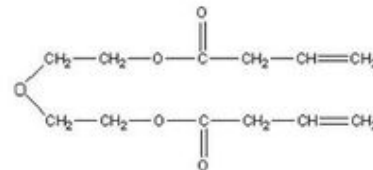
5. CR-39–DAP Series

Tsuruta (1999, 2000) found that the mixture of monomers of CR-39 and diallyl phthalate (DAP) can be copolymerized into a new type of track detector CR-39–DAP, whose property is in between that of CR-39 and DAP.

The structure of DAP monomer is:



For comparison, the structure of CR-39 monomer is copied here:



Similar to the CR-39 monomer, DAP monomer also has two groups of allyl ($-\text{CH}_2-\text{CH}=\text{CH}_2$), each of which has a double bond. When copolymerization starts, the double bond opens and connects with the opened bonds of CR-39 to form a three-dimensional structured copolymer CR-39–DAP.

In the DAP monomer there is a benzene ring, which has a tendency to adsorb radiation energy. For this reason, CR-39–DAP and DAP have a higher threshold than CR-39. Tsuruta et al. (2008) showed that the detection threshold of CR-39–DAP is lower than that of DAP and higher than that of CR-39, and the threshold increases as the percentage of DAP increases as follows:

$2 \text{ keV}/\mu\text{m}$ (water) (CR-39, DAP : CR-39 = 0 : 100), $40 \text{ keV}/\mu\text{m}$ (50 : 50), $88 \text{ keV}/\mu\text{m}$ (60 : 40), $108 \text{ keV}/\mu\text{m}$ (70 : 30), $125 \text{ keV}/\mu\text{m}$ (80 : 20), and $\sim 250 \text{ keV}/\mu\text{m}$ (DAP 100 : 0). They express the threshold as the total rate of energy loss in water on the right-hand side of the Bragg peak of the dE/dx curve. By the same expression, the thresholds of cellulose nitrate (CN) and polycarbonate (Lexan) are 110 and $330 \text{ keV}/\mu\text{m}$ (water),

respectively. It means that the sensitivity of CR-39–DAP is higher than that of Lexan and lower than that of CR-39; cellulose nitrate is nearly equal to the copolymer (70:30). These thresholds rank up as 2, 40, 88, 108, 125 and 250 keV/μm (water), which look like a spectrum of thresholds. This study opens up a new road to the development of nuclear track detectors, that is, to make a series of detectors with a rank of thresholds.

Doke (2008), Kodaira et al. (2008), and Ogura et al. (2006) confirmed the above development and suggested the application of these new types of detectors to the study of trans-iron nuclei in galactic cosmic rays at a space station or on long-duration balloon experiments.

6. Other New Track Detector Materials

One of the important tasks of nuclear track studies is to look for or synthesize new detector materials which have specific properties, such as a sensitivity higher than CR-39, or a threshold higher than that of the existing detector materials, or anti-annealing temperature of tracks higher than 1000 °C for days.

a. PETAC-ADC Copolymer Detector

Recently, Mandrek et al. (2010) claimed that a copolymer of pentaerythritol tetrakis (allyl carbonate) (PETAC) and allyl diglycol carbonate (ADC) in weight percent 4 : 6 shows that its maximum alpha sensitivity is almost double that of CR-39 under identical experimental conditions. The polymers can be conveniently etched by aqueous sodium hydroxide. In order to further verify the above conclusion, one should irradiate the copolymer and CR-39 sheets with heavy ions from accelerators to see at which energy the heavy ions can be recorded as tracks in each of the detectors.

b. Silicon Nitride (Si₃N₄) as Track Detector

Vlasukova et al. (2010) found that amorphous silicon nitride Si₃N₄ can record discontinuous tracks of W ($Z = 74$) with electron energy loss of 20.4 keV nm⁻¹ being maximum with etchant HF solution; Fe ($Z = 26$) and Kr ($Z = 36$) ions in the electron energy loss regime cannot form tracks in it. From the above results, one can see that the threshold of Si₃N₄ is quite high, but it is difficult to be used as a track detector at this stage due to its discontinuous tracks.

III. RECORDABLE PARTICLES WITH SOLID-STATE NUCLEAR TRACK DETECTORS

When a heavy charged particle enters an insulating solid, it produces radiation damage to materials in the solid along the trajectory of the particle. If the density of the damaged materials is high enough, the damaged materials can be selectively etched by a chemical reagent and result in an etched channel (hole) along the trajectory. The chemical reagent will continue to attack the bulk material of the solid from all directions. The inner diameter of the channel (hole) will increase in size. When the diameter of the channel increases to the size comparable with the wavelength of light, the channel becomes visible with an optical microscope. The visible channel is called an etched

track of the particle. The original radiation damage region along the trajectory before etching is called the latent track of the particle. In some types of very thin solid layers, latent tracks of particles have been observed under transmission electron microscopes (TEMs), such as muscovite mica. The diameter of latent tracks of fission fragments is several nanometers. If the radiation damaged materials are not dense enough, the damaged materials cannot be etched to form an etched track. In this case, the solid is not sensitive to the particle. The particle cannot be recorded by the solid. Conversely, when the solid is sensitive to the particle, it is recordable with the solid.

The density of radiation damaged materials is related not only to the species of particles (Z), but also to the velocity V (or energy E) of the particles. When the velocity (or energy) of a particle is very high, the time of interaction between the particle and the atomic electron of the atom in the solid is very short. The energy transferred from the particle to the electron is very little. In such a case, the resultant radiation damage is very low. The radiation damage region cannot be etched to become a track. As the velocity of the particle slows down, the interaction time increases gradually as described in Chapter 1. The density of the radiation damaged materials increases. Up to a certain density, the damaged materials become etchable to form a continuous track. As the charged particle is further slowed down, the particle will catch more and more electrons from the solid. The effective charge (Z_{eff}) of the particle gradually reduces. Its ability to produce damage also reduces. At some velocity, the density of damaged materials drops down to the least value required for etching. Afterward, the charged particle cannot produce an etchable track. The charged particle can produce an etchable track only in a limited region of velocity or energy. Above or below this region, the particle cannot leave etchable tracks in the solid. Here, we conclude that as long as the radiation damage density, even in a small region, can reach the etchable level, we consider the charged particle recordable with the solid (SSNTD).

Generally speaking, selecting appropriate detector materials, solid-state nuclear track detectors can record tracks of protons, α -particles, fission fragments, heavy ions, neutrons via its charged reaction products, α -recoil particles, exotic particles such as magnetic monopoles, dark matter, and fractional charge particles if they exist. In contrast, γ -rays, β -rays, and X-rays cannot be recorded by any kind of solid-state nuclear track detectors.

A. Protons

Proton measurements with solid-state nuclear track detectors have suddenly become an urgent need since the advent of laser acceleration and the latest advances in the study of laser inertial-confinement fusion. In these studies, the duration of a proton burst is about 10⁻¹² s or less for laser acceleration and about 10⁻⁹ s for a particle blast in laser fusion. In these cases, electronic detectors are blocked by dead time, but solid-state track detectors are superior in light of their advantages, which are the following: no dead time limitation, high detection efficiency, large dynamic range, good spatial, charge, mass, and energy resolutions, insensitivity to background radiation (neutrons, X- and γ -rays), and

insensitivity to electromagnetic disturbances. Therefore, CR-39 has become the key material for the detection of protons and other light nuclei produced in these studies (Duan et al., 2009, 2010; Szydłowski et al., 1999; Seguin et al., 2003).

The sources of protons, which are currently studied with solid-state nuclear track detectors, include:

- (1) Proton beams from laser acceleration;
- (2) Protons produced from an inertial-confinement fusion assembly and other plasma facilities;
- (3) Proton beams from particle accelerators;
- (4) Recoil protons from foil radiators for neutron spectrometry and dosimetry;
- (5) Recoil protons in hydrogen-containing plastic track detectors (CR-39); and
- (6) Protons from other nuclear reactions.

1. Suitable Detectors for Proton Detection

CR-39 is the most sensitive detector material in solid-state nuclear track detectors. It is the most suitable detector for recording proton tracks (Baiocchi et al., 1995; Bernardi et al., 1991; Cross, 1986; Cross et al., 1986; Jager et al., 1985; Sadowski et al., 1994; Szydłowski et al., 1999; Wang et al., 2002). The lowest recordable energy of protons in CR-39 is ~20 keV (Duan et al., 2009, 2010). The upper limit of energy of protons is ~6 MeV (Seguin et al., 2003). The tracks of protons from 20 keV to 1.020 MeV in CR-39 are shown in Fig. 4.2.

Cellulose nitrate (CN) detector is less sensitive than CR-39. It can also record proton tracks. The minimum energy of protons recordable in Daicell (CN) is 0.55 MeV (Fleischer, 1980).

2. Proton Intensity Measurements

Intensity usually refers to the number of specific particles that are produced from a source in unit time (second). To measure the intensity of a source, one needs to record the time (*t*) and to count the number of the particles (*N*) emitted from the source. The intensity is *N/t*. For proton intensity measurements with a solid-state nuclear track detector, one needs to record the time *t*, count the tracks *N* in a small area *S* of the detector, measure the distance *X* from the proton source to the detector, measure the angle *θ* between the proton direction and the normal of the detector, and know the detection efficiency *ε* of the detector to protons and the anisotropy *Φ(φ)* of the source. The proton intensity can be calculated according to following equation:

$$I = \frac{4\pi X^2 N}{S \cos \theta \Phi(\varphi) \epsilon t} \tag{4.1}$$

where *φ* is the angle of the detector position with respect to the proton source. For isotropic source, *Φ(φ)* = 1.

If particles (protons) from a source are collimated by apertures to become a beam such as that from particle accelerators, the particle (proton) intensity in these cases means particle flux, that is, the number of particles passed through a unit area (cm²) in unit time (second), also referred to as beam intensity.

Proton sources may be a point source, or an extended source. Any particle source has a definite size (extended source).

A so-called point source is a simple approximation, that the size of the source is negligible. Equation (4.1) is derived by an assumption that the particle source is a point source.

Placing a CR-39 sheet in the path of the protons and after counting the proton tracks, one can easily measure the intensity of the proton source or proton beam flux.

3. Proton Energy Measurements

a. Proton Diameter Method

In order to determine proton energy with a CR-39 or LR-115 detector, one must first calibrate the detector with mono-energetic protons. A detailed explanation of the calibration techniques with real mono-energetic protons (not by scattered protons through foil) can be found in the paper of Duan et al. (2009, 2010).

Figure 4.3 illustrates the results of a typical calibration with proton energies of 20, 40, 60, 80, and 100 keV:

In this energy region, it shows that the diameter of proton tracks increases monotonically with increasing proton energy in a defined etching condition. By measuring the track diameter of protons of unknown energy, one can immediately find the energy *E_p* of the protons from the calibration curve as illustrated in Fig. 4.3. The uncertainty *σ(E_p)* can be calculated from the following formula:

$$\sigma(E_p) = \frac{\sigma(D)}{\Delta D / \Delta E_p} \tag{4.2}$$

where *σ(D)* is the statistical deviation of the measurements of the track diameter and *Δ(D)/ΔE_p* is the slope of *D* versus *E_p* curve at the point of track diameter *D*.

b. Track Contrast (Gray Level) Method

Figure 4.4 illustrates the variation of track diameter *D* versus proton energy *E_p* in an extended range of energy.

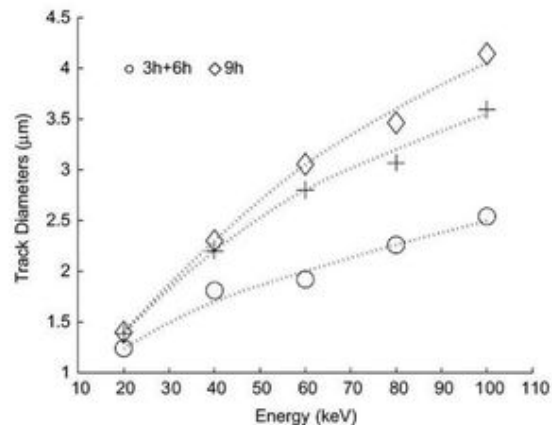


FIGURE 4.3 Relation between track diameter and proton energy in CR-39 etched in 6N NaOH, 70 °C for 3, 6, and 9 h. (From Duan et al., 2009; printed with permission from Elsevier © 2009)

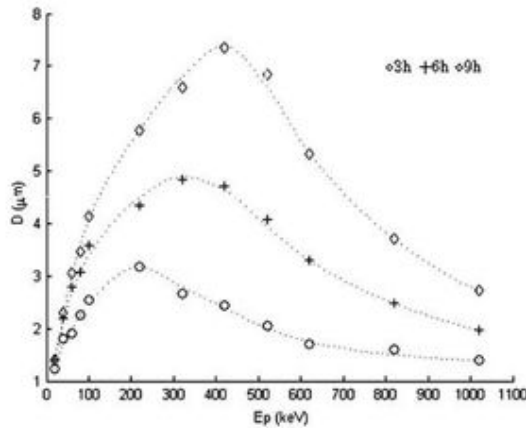


FIGURE 4.4 Relation between track diameter and energy of protons in CR-39 etched in 6N NaOH at 70 °C for 3, 6, and 9 h for proton energies from 20 keV to 1.2 MeV (Duan et al., 2009). Each track diameter corresponds to two proton energies. Track contrast or track gray level must be adopted in order to distinguish the energies of the protons. (From Duan et al., 2009. Reprinted with permission from Elsevier © 2009)

There are two proton energies corresponding to a given track diameter. In this case, the two proton energies can be distinguished by the track contrast or track gray levels. The tracks of the lower-energy protons are generally shallower and less dark due to the shallow and blunt etch-pits. The tracks of the higher energy protons are deeper and darker due to the deep and sharp etch-pits. This method of energy measurement of protons is practical with the use of the optical microscope and track image analyzers (Duan et al., 2009, 2010; Seguin et al., 2003; Nikezic and Yu, 2009).

c. Step Filter Method

The energy and energy spectrum of protons can be retrieved by the step filter method. If we let the protons pass through a plate of stopping material (filter of Al, Cu, or plastic sheet) and allow the protons to reach a CR-39 detector, and if the energy of the protons is in the energy window of the CR-39 registration (~20 keV–6 MeV), the protons will be recorded as tracks in the CR-39. The energy of protons on reaching the CR-39 can be obtained by measurement of track diameters. From the thickness of the stopping material (the filter) and the range–energy relation of protons in the material, one can further derive the energy of the protons arriving at the front surface of the filter. On the other hand, if a wedge-shaped filter is used to replace the plate filter, a wedge-range-filter (WRF) spectrometer is composed. This kind of filter can provide information on the proton energy spectrum of the source. Figure 4.5 is a schematic illustration of a wedge filter spectrometer used for measuring the proton energy spectrum.

The wedge can be composed of a series of films overlapping partly together. Different thicknesses of stopping material in the composed areas can be obtained. The wedge looks like a terraced field. The thickness of each part of the stopping material can be known precisely. This is the reason it is called a “step filter”.

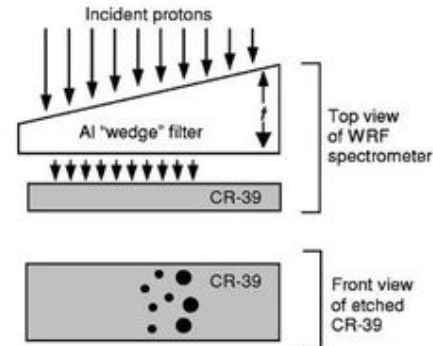


FIGURE 4.5 Schematic illustration of a wedge-shaped-filter spectrometer. In front of a CR-39 there is a wedge filter (Al). The thickness of the wedge changes gradually. Some of the protons incident on the filter are energetic enough to pass through it, and they impinge on the CR-39, forming tracks within the CR-39. The energy of the protons can be determined by the diameters of the tracks and the thickness of the filter at the track positions. A two-dimensional histogram of track number versus track diameter and versus the thickness of the filter can be converted to a histogram of proton number versus energy of the protons. (Seguin et al., 2003. Reprinted with permission from American Institute of Physics © 2003)

4. Proton Spatial Distribution Measurements

The solid-state nuclear track detector is a type of position sensitive detector. Its track diameter after etching is about several micrometers. Therefore, its spatial resolution is in the same range (several micrometers).

In some cases, the information of emission angles of protons is essential. For example, recoil protons from a thin hydrogen-containing foil, such as polyethylene (CH)_n, produced by elastic scattering of fast neutrons, can be recorded by a flat or curved CR-39 detector. The track coordinate on the detector reflects the recoil angle θ with respect to the direction of the incident neutron. The diameter of the track reflects the energy of the proton E_p (see Section III.A.3). The energy of the incident fast neutron can be calculated by the equation

$$E_n = E_p / \cos^2 \theta \quad (4.3)$$

This technique is often called the recoil proton method for neutron spectrum determination (Wan et al., 2003).

Another example of the measurement of proton spatial distribution is in laser acceleration. In order to determine the energy spectrum of protons accelerated in laser–plasma interaction, an electromagnetic spectrometer (Thomson spectrometer) is used to deflect the energetic protons produced in the interaction. Different energies of protons will be deflected to different angles. A flat or curved CR-39 sheet is placed behind the spectrometer to record the protons at different angles. Counting the proton tracks at different angles provides the energy spectrum of the protons after acceleration (Lan Xiaofei, 2009).

5. Applications of Proton Detection

Proton registration has become a budding and expanding field since the discovery of the laser acceleration mechanism and the

rapid advance in the study of laser-confinement fusion. In these fields, other detectors lost their advantages while the solid-state nuclear track detector is competent for proton analysis. The application of proton detection in these fields will be described in more detail in Subsection II.D.1 and II.D.2 of Part 2 of this chapter. See also Chapter 1 for a description of current studies on laser and inertial electrostatic confinement fusion.

B. α -Particles

Alpha particles are equivalent to helium (He) nucleus with kinetic energy. The following sources of α -particles are usually analyzed with solid-state nuclear track detectors:

- (1) α -Sources used in laboratories for calibration purposes;
- (2) U-bearing aerosol particles for nuclear safeguards;
- (3) Hot particles and fallouts from nuclear accidents;
- (4) Radon (Rn) and thoron dosimetry in dwellings, mines, and environments;
- (5) Radon (Rn) monitoring for exploration of uranium (U) and petroleum (oil), and prediction of earthquake and landslip;
- (6) $^{10}\text{B}(n,\alpha)^7\text{Li}$ reaction α -particle mapping for boron determination in metallurgy, agriculture, and cancer therapy (BNCT).

α -Particle registration is the most popular work in developing countries, because it does not require expensive equipment, such as nuclear reactors and particle accelerators. One only needs CR-39, LR-115, an optical microscope, etching bath, and chemicals, and it provides valuable research results for natural resources, human health, and scientific training.

1. Suitable Detectors for α -particle Measurements

CR-39 (polyallyldiglycol carbonate, PADC), LR-115 (cellulose nitrate, CN), and Lexan or Makrofol (polycarbonate, PC) are suitable detectors for recording α -particles.

a. CR-39

CR-39 is the most sensitive and popular detector for recording α -particles. Its energy window for recording α -particles is from ~ 0.1 to >20 MeV, or approximately from zero to infinite (Durrani and Bull, 1987). This means that no matter what is the medium between the source and the detector (CR-39), gas, liquid, or solid, the α -particles will create tracks in the detector as long as the α -particle can reach the detector, with the exception of the limitation of critical angle θ_c (see Section V.A.2).

b. LR-115

The sensitivity of cellulose nitrate LR-115 is less than CR-39. Its energy window for α -particles is about 1.2–3.9 MeV (Yu and Nikezie, 2009; Benton, 1968; Eappan and Mayya, 2004; Ilic and Durrani, 2003).

c. Lexan or Makrofol

Polycarbonate (Lexan, Makrofol, and Tuffak) is less sensitive than cellulose nitrate for recording α -particle tracks. In order to

reveal α -particles clearly, it is better to irradiate the detector with ultraviolet light before etching (Stern and Price, 1972; Benton and Henke, 1969a; Crawford et al., 1968; DeSorbo and Humphrey, 1970; DeSorbo, 1979; Fleischer et al., 1975; Durrani and Bull, 1987). The energy window of polycarbonate for recording α -particles is in between ~ 0.2 and 3 MeV (Durrani and Bull, 1987).

2. α -Intensity Measurements

α -Particle sources mainly have three states: solid, liquid, and gaseous. Solid α -sources are made on smooth plane surfaces of metals, such as stainless steel or aluminum. The plane sources can be divided into thin sources and thick sources. If the thicknesses of α -emitting material on the surfaces are less than about $100 \mu\text{g}/\text{cm}^2$, the sources may be considered thin sources. Because the ranges of α -particles of natural radioactivities in the source materials are in the range of about several to over $10 \text{ mg}/\text{cm}^2$ (see Chapter 1), the absorption loss or energy losses of α -particles in the thin source are negligible. Conversely, if the thicknesses are over $\sim 100 \mu\text{g}/\text{cm}^2$, the absorption losses or energy losses cannot be ignored.

Some α -emitting materials are dissolved or suspended in water or other solutions. Determination of α -concentration in the liquids are often required. Radon in air is an example of gaseous α -source.

a. Determination Techniques of α Intensity on Plane Surfaces

α -Intensity is defined as the number of α -particles emitted from a source in unit time (s^{-1}). Two types of techniques can be used in determination of α -intensity of plane sources: small sterad technique and 2π geometrical measurement.

Small Sterad Technique. The small sterad technique can give the most accurate and absolute determination of the intensity of α -particle sources. The α -plane source to be determined and a CR-39 sheet are put face to face, in a vacuum chamber with a distance 10–30 cm from each other, both surfaces being parallel with common axis. After pumping to remove air from the vacuum chamber, a shutter between the source and CR-39 sheet is opened, and α -recording starts. After some time, the shutter is closed, and α -recording stops. The α -tracks on the CR-39 sheet are etched in NaOH solution and counted with a microscope. The α -intensity I of the α -plane source can be calculated by the equations

$$I = \frac{N_T}{g\epsilon t} \quad (4.4)$$

and

$$g = \frac{1}{2} \left[1 - \frac{h}{\sqrt{h^2 + r^2}} \right] \left\{ 1 - \frac{3}{8} R^2 \left[\frac{h(h + \sqrt{h^2 + r^2})}{(h^2 + r^2)} \right] \right\}, \quad (R \ll h, r \ll h) \quad (4.5)$$

where N_T is the number of α -tracks on the CR-39 sheet, t is the α -recording time in seconds (s), g is the geometric factor for

recording α -particles with CR-39 sheet, h is the distance between the α -source and CR-39 detector (cm), R is the radius of the α -source (cm), r is the radius of the CR-39 detector (cm), and ε is the revealing efficiency of the α -particles in the CR-39 sheet.

If the CR-39 is shaped as a square with side a and all the tracks are counted as N_T , then r^2 in Eqn (4.5) should be replaced by a^2/π .

If one counts only a part of tracks in a small area S of CR-39 sheet, such as in several fields of view, one should replace r^2 in Eqn (4.5) by S/π . If the energy of the α -particles is in the energy window of the detector, $\varepsilon = 1$. Otherwise, $\varepsilon = 0$. If the energy of the α -particles is higher than the energy window of the detector, one can put a thin degrader foil in front of the detector to degrade the α -energy. The thickness of the degrader can be calculated by an empirical Bragg–Kleeman formula (L'Annunziata, 2003; Eappan and Mayya, 2004):

$$R_s(\text{cm}) = 3.2 \times 10^{-4} R_a A^{1/2} / \rho \quad (4.6)$$

where A is the mean atomic weight of the solid (g), ρ is density of the solid in g/cm^3 , R_s is the range of alpha particle in a given solid (the degrader foil), and R_a is the range of the alpha particle in air at an ambient temperature of 15 °C under pressure of 760 mmHg. R_a may be estimated through the relation

$$R_a(\text{cm}) = 0.324 E^{3/2} \quad (4.7)$$

where E is the energy of the alpha particle (MeV). The above equations for the calculation of alpha-particle ranges are the same as Eqn (1.94) and (1.95) in Chapter 1 where example calculations are provided.

When one has calculated the alpha-particle range, one can select a thickness of the degrader foil, which is thinner than the calculated range. The selected foil can be used as degrader. The thickness of α -sources for small sterad measurement should be thin, that is, at least less than half of the range of the alpha particles in the source material to ensure the accuracy of the measurement. In measurements utilizing the small sterad technique, other detectors can also be used, such as a surface barrier silicon detector or a scintillation detector. The advantage of the solid-state nuclear track detector (CR-39) is that it does not need the complicated electronic instrumentation.

2 π Geometrical Measurement. The 2π geometrical measurement is a simple technique for determining the intensity of an alpha-plane source. In this measurement, it is best that it be carried out as a relative measurement.

First, one should make a thin plane source of α -particles as a standard source and determine its intensity I_s by using other techniques, such as small sterad, surface-barrier detector, ionization chamber, or chemical analysis. Then the standard source is covered with a CR-39 detector (2π geometry), for a time t_s . After etching the CR-39 in NaOH solution, the alpha tracks are counted with an optical microscope (N_{T_s}). Afterward, an unknown α -source is covered with another CR-39 sheet of the same batch as that used for the standard source for a time t . The tracks are etched and counted (N_T) in the same manner,

as above. An approximation of the intensity I of the unknown source can be calculated by the following equation:

$$I = \frac{N_T t_s}{N_{T_s} t} I_s \quad (4.8)$$

In Eqn (4.8), the difference of detection efficiencies for the standard and unknown sources due to possible difference in thicknesses of the sources is ignored.

From Eqn (4.8) one can see that the intensity of the unknown source I can be calculated from the measured data N_T , N_{T_s} , t , t_s , and the known intensity I_s . The advantage of this relative measurement for plane sources is that one does not need to calibrate the detection efficiency of the CR-39 detector for the α -particles produced in the sources.

b. Determination Technique of α Intensity in Liquids

In the process of uranium production and nuclear disposal as well as in laboratories, various liquids having α -radioactivity have to be managed. The α -radioactivities in these liquids can be easily determined by using solid-state nuclear track detectors (CR-39 or LR-115) through the relative measurement. Here, we will give an example to illustrate how to determine the α -intensity of uranium in liquids. Some amount of uranium nitrate of natural uranium is dissolved in water. The uranium concentration in the solution can be calculated from the formula of uranium nitrate. The α -intensity I_x in a unit volume of solution is obtained by the isotopic ratio of ^{238}U (99.2745%), ^{235}U (0.720%), and ^{234}U (0.0055%) and the half-life of ^{238}U (4.468×10^9 a), ^{235}U (7.038×10^8 a), and ^{234}U (2.455×10^5 a). This solution can be used as a standard solution for the α -intensity determination. A piece of solid-state nuclear track detector, such as CR-39, is immersed into the solution for a certain time t_s . The CR-39 sheet can be cleaned by water. After etching the CR-39 sheet in NaOH solution (see Table 4.1), the track density N_{T_s} of α -particles is measured with an optical microscope. Afterward, another sheet of CR-39 of the same batch is immersed in the solution of unknown α -intensity for a time duration t_x . The track density N_{T_x} is measured. The α -intensity I_x in the unknown solution can be calculated by the equation

$$I_x = \frac{N_{T_x} t_s}{N_{T_s} t_x} I_s \quad (4.9)$$

Equation (4.9) is strictly valid only in the case that the composition and concentrations of the chemicals and α -energy are the same for the standard and unknown solutions. The variation of concentration will not affect the calculated value of I_x very seriously. The effect of α -energy can be corrected as inversely proportional to the range of the α -particles, that is,

$$I_x(\text{corrected}) = I_x \frac{R_s}{R_x} \quad (4.10)$$

The calibration result of CR-39 with standard solution can be treated as a constant c where

$$c = \frac{I_s t_s}{N_{T_s}} \quad (4.11)$$

Once the constant c is obtained, it can be used for follow-up determinations of unknown solutions with the same batch of detector.

The advantage of this relative determination of α -intensity in liquids is that one does not need to worry about the critical angles of α -particles in the CR-39. The effect of the critical angles will be canceled in the calculation. The distribution of tracks on the surface of the CR-39 is homogeneous in the case of a liquid source. One can select any place on the detector surface to measure the density of tracks and derive the α -intensity of the liquid source.

c. Determination of α Intensity in Air (Gaseous Substances)

The determination of the activities of radon (^{222}Rn), thoron (^{220}Rn), and ^{219}Rn in air is a typical example for α -intensity measurement in gaseous substances. This subject is important in earth science, environmental studies, health physics, and resource prospecting. LR-115 and CR-35 are traditionally used to carry out the research. It has become a special field of radon (Rn) monitoring (Jonsson, 1995; Ilic, 2005; Monnin et al., 1993; Segovia et al., 2005; Virk and Valia, 2001; Saad, 2008; Dwivedi et al., 2005; Mishra et al., 2005; Font, 2009; Font et al., 2008; Baixeras et al., 2005). More detailed explanation can be found in the Subsection Radon Measurement (Section IV.A.1 in Part 2 of this chapter).

3. α -Particle Energy Measurements

Three methods can be adopted in α -particle energy determination, namely, the track diameter method, the residual range method, and the stopping-foil method.

a. Track Diameter Method

The experimental determination of energy of α -particles with solid-state nuclear track detector by the track diameter method includes two steps. The first step is to calibrate the detector, such as CR-39 with mono-energetic α -particles from a particle accelerator or from an α -source, such as an ^{241}Am thin source (5.486 MeV (85.2%), 5.443 MeV (12.8%), other alpha energies are negligible). The energy of α -particles may be degraded by air or foils of various thicknesses. The α -particles impinge on the CR-39 detector perpendicularly. After etching of the CR-39 under certain etching conditions, the diameter of the α -tracks is measured with the optical microscope. A calibration curve will be obtained, which is the relationship between track diameter and the energy of the α -particles. The calibration curve is similar to that of protons (Fig. 4.3). The second step is to record the α -particles of unknown energy in normal incidence with the calibrated CR-39 detector (the detector produced in the same batch if possible). After etching under the same etching conditions, the track diameter is measured. By comparison of the track diameter with the calibration curve, one can obtain the energy of the α -particles. On the calibration curve, one diameter may correspond to two energies of α -particles (similar to Fig. 4.4). In this case, the gray level and the depth of track can be used to distinguish which energy is correct (see Section

III.A.3. Proton Energy Measurements); on the low-energy side, the track is shallower and the gray level is lower than that on the high-energy side.

b. Residual Range Method

The residual range method makes use of the range–energy relation (R – E relation) of α -particles in the detector materials. Measuring the residual range (R_0) allows one to retrieve the energy (E) of the particles. The range–energy relation can be calculated by the empirical Bragg–Kleeman formula, or by theoretical formulas (Bethe, 1930; Fano, 1964; Ahlen, 1980; Barkas and Berger, 1964; Benton and Henke, 1969b; Weaver, 2001; Henke and Benton, 1966), or by more popular computational codes SRIM (Ziegler and Biersack, 2003; Ziegler et al., 1985). The residual range of a particle is the distance from the point considered to the end point of the range. The coordinates of the end point of the range can be obtained by etching the track to a round blunt tip. The actual end point is at the point with a distance r to the etched tip where r is the radius of the blunt tip. When the residual range R_0 is measured, one can immediately obtain the energy from the range–energy relation (Few and Heshaw, 1982; Seguin et al., 2003).

c. Stopping-Foil or Range-Filter Method

A flat foil or wedge-like stopping material (range filter) and a CR-39 detector are used in this method, which is based on the range–energy relation of α -particles in stopping material (range-filter) to determine the energy of the α -particles. Only the α -particles whose range is larger than the thickness of the range-filter can be recorded as etchable tracks in the CR-39 detector behind the filter. The track diameter on the CR-39 sheet can give the energy of α -particles. From this energy and the thickness of the filter, one can derive the incident energy of the α -particle to the filter.

If one uses several filters of different thicknesses and CR-39 sheet, a series of energies (energy spectrum) can be obtained. If one uses a wedge-range-filter of appropriate thickness intervals, an accurate energy spectrum of α -particles may be obtained (Seguin et al., 2003; Kacenjar et al., 1982).

4. α -Spatial Distribution Measurements

The solid-state nuclear track detector is a position-sensitive detector. Its spatial resolution is normally about several micrometers for α -particles. Alpha spatical distribution measurements have two meanings. The first meaning relates to the measurement of the distribution of α -emitting nuclei on a surface or in a volume. This is a homogeneity measurement of an α -source. The second meaning relates to the measurement of the directions of an α -emission from a source. This is the angular distribution measurement of an α -source. For the first measurement, one needs to put a CR-39 or LR-115 sheet on the area or in the volume of the α -source for a certain time to allow enough number of α -particles to bombard the detector sheet. Afterward, the detector is etched, whereby one can see the distribution of tracks produced by the α -particles. Subsequently, one will be aware of the distribution of the source nuclei. The

following measurements belong to the first type of measurements: distribution of α -contaminations on surface of working places; the distribution of α -emitting nuclei, such as ^{239}Pu , ^{235}U , and ^{237}Np in organs of animals and human bodies; distributions of α -hot particles in the environments; uranium distribution in minerals; and boron distribution measurements in steels, leaves, and soils through (n, α) reaction-produced α -particles.

For the second type of spatial distribution measurement, one needs to deploy CR-39 or LR-115 sheets around the α -source in different directions. In laser inertial-confinement fusion studies, the CR-39 detector is the most useful detector to determine the yield and spatial distribution of α -particles from D + T, T + T, D + ^3He , and T + ^3He reactions (Seguin et al., 2003). By counting the tracks in unit area on the detectors in different directions, one will know the spatial distribution of the α -particles.

5. Applications of α Detection

Alpha-particle detection is one of the commonly applied domains of solid-state nuclear track detectors. Nearly all the fields where α -particles are produced can be studied by the track detectors. The particular fields requiring α -detection and where SSNTDs are particularly useful are as follows:

- Long-term radon and thoron monitoring.
- Nuclear fallout and hot particles
- Nuclear contamination around nuclear plants.
- Neutron spectrometry and dosimetry.
- Laser and plasma interactions.
- Uranium and petroleum exploration and earthquake prediction.
- Agriculture and metallurgy.
- α -Particle radiograph (Somogyi and Srivastava, 1970, 1971; Su, 1992, 1993).

The details of applications in these fields will be explained in the related subsections in Part 2 of this chapter.

C. Fission Fragments

A heavy nucleus can split into two nuclei, which is called nuclear fission. This process may occur automatically by the nucleus itself without any disturbance by other particles. This fission is called spontaneous fission. For example, the ^{238}U nucleus can split into two nuclei (the two new nuclei are called fission fragments; nuclear fission into three or more fission fragments is very rare (See Chapter 1 for a detailed treatment of nuclear fission)). The two fission fragments have different masses. The masses of light fragments of ^{238}U spontaneous fission are in the range $A = 85\text{--}105$ with an average $A = 97$. The heavy fragments have masses $A = 130\text{--}150$ with an average $A = 139$. The light fragments have an average kinetic energy of 97.6 ± 0.7 MeV. The heavy fragments have an average kinetic energy of 67.0 ± 1.2 MeV. The total kinetic energy is 164.6 MeV (Kase et al., 1978).

The rate of spontaneous fission of heavy nuclei is expressed by spontaneous fission decay constant λ_f . For ^{238}U spontaneous fission, one value of the decay constant $\lambda_f = 7.03 \times 10^{-17} \text{ a}^{-1}$ (Roberts et al., 1968) may be recommended. This value

corresponds to the half-life of ^{238}U spontaneous fission $T_{1/2} = 9.86 \times 10^{15} \text{ a}$ ($T_{1/2} = \ln 2 / \lambda_f \approx 0.693 / \lambda_f$).

It should be noted that more than 30 measurements on the decay constant of spontaneous fission of ^{238}U have been published (see the review articles: Bigazzi, 1981; Durrani and Bull, 1987; Wagner and Van den haute, 1992; Holden and Hoffman, 2000). A widespread of the results is apparent (λ_f from $1.7 \times 10^{-17} \text{ a}^{-1}$ to $11.8 \times 10^{-17} \text{ a}^{-1}$) from different measuring techniques. Most of the results are gathered to two groups. The largest group is peaked around $7 \times 10^{-17} \text{ a}^{-1}$, all of them were measured by solid-state nuclear track detectors. Another group is peaked around $8.46 \times 10^{-17} \text{ a}^{-1}$, which are measured mostly by the other techniques. A technical report on spontaneous fission half-lives for ground-state nuclides was published in 2000 by the International Union of Pure and Applied Chemistry, Analytical Chemistry Division, Commission on Radiochemistry and Nuclear Techniques (Holden and Hoffman, 2000), in which a value of ^{238}U spontaneous fission half-life $T_{1/2} = (8.2 \pm 0.1) \times 10^{15} \text{ a}$ was recommended, which corresponds to $\lambda_f = 8.45 \times 10^{-17} \text{ a}^{-1}$.

To obtain the recommended value, all the data of λ_f measured by solid-state nuclear track detectors were ruled out (16 out of 26 data in total). The reasons for ruling out the track data were explained in detail in the report. The basic reason is that most of the results of the λ_f measured by etch track detectors are lower than those by other detectors. The simplest way to get an average value is to throw away all the data from etch track measurements. The true reason for causing the large differences of λ_f values determined by different detectors might not have been exposed. Durrani and Bull (1987) suggested that if λ_f of ^{238}U spontaneous fission has been explicitly used in fission track dating, the value λ_f assumed must be stated in reporting results, so that valid comparisons can be made with other age determinations.

In addition to spontaneous fission, a heavy nucleus can split into two fission fragments upon bombardment with an incident particle, such as neutron, proton, heavy ion, γ -ray photon, and other elementary particle. For example, the ^{235}U nucleus bombarded by a thermal neutron will split into two fission fragments. This type of nuclear fission is called induced fission, as described in Chapter 1.

The mass distributions of ^{235}U fission induced by thermal neutrons are similar to those of ^{238}U spontaneous fission. The masses of light fragments are in the range of $A = 78\text{--}107$, with a peak value at $A = 95$. The heavy fragments are in the range of $A = 118\text{--}146$, with an average value $A = 140$ and a peak value $A = 134$. The charges of the light fragments are in the range $Z = 31\text{--}43$ with a peak value at $Z = 38$. The charges of the heavy fragments are $Z = 47\text{--}57$ with a peak at $Z = 52$. The charge Z and mass A of the fission fragments are in the range suitable for detection with solid-state nuclear track detectors.

The probability of nuclear reaction between a target nucleus and incident particle is described by the quantity reaction cross section. For example, the fission cross section σ_f of ^{235}U by thermal neutrons ($v = 2200 \text{ m/s}$, $E_n = 0.0253 \text{ eV}$) is 582 b ($1 \text{ b} = 10^{-24} \text{ cm}^2$). The fission cross section of ^{239}Pu by thermal neutrons is 738 b (Garber and Kinsey, 1976). The fission cross

section of ^{239}Pu is larger than that of ^{235}U for thermal neutrons. Both spontaneous and induced fission of heavy nuclei are important fields of research and application of solid-state nuclear track detectors.

1. Suitable Detectors for Fission Fragments

The energies of fission fragments of ^{235}U induced fission are about 1 and 0.5 MeV/amu for light and heavy fragments, respectively (MeV/amu = energy per atomic mass unit, nearly equal to energy per nucleon). These energies are around the peak regions of energy-loss rate (dE/dx), or restricted energy-loss rate (REL) or primary ionization (J) of nuclear particles in solids. Therefore, fission fragments are very easily recorded by solid-state nuclear track detectors. Even the most insensitive track detector of meteoritic minerals can record tracks of fission fragments. In other words, all of the known etch track detectors can be used to record tracks of fission fragments.

The track detectors for recording fission fragments can be classified into natural and man-made detectors. The most often used natural detectors include minerals (such as muscovite mica, apatite, zircon, sphene, olivine, pyroxene, and whitlockite) and natural glasses (such as tektite and obsidian). These detectors not only can record currently produced fission fragments but also have retained large number of fission-fragment tracks recorded since the formation of the detectors millions or billions of years ago. These detectors have been used in fission track dating, geothermal history, and paleoanthropology studies. If one wants to use these detectors to record newly produced particles in the laboratory, one should first anneal out the fossil tracks of fission fragments and other tracks to produce clean detectors (free from the backgrounds of the fossil tracks). If the annealing process had been made by ancient mankind by making fires, the newly recorded fission-fragment tracks after firing can provide the information of the age of the ancient man.

Man-made detectors for fission fragments can be classified into inorganic detectors and organic detectors. Inorganic detectors include synthetic mineral (such as synthetic phlogopite) and man-made glasses (such as soda-lime glass or window glass and phosphate glass). The advantage of these detectors is that these are free from background tracks. Organic detectors include polycarbonate, polyethylene terephthalate, CR-39, and cellulose nitrate (LR-115).

a. Muscovite Mica

Muscovite mica is an ideal track detector for the study of nuclear fission at the low-energy region. It can be cleaved into suitable thickness with a perfect smooth surface and cut to the required area. The lowest atomic number Z of particles recordable by muscovite mica is 10 (Ne). Alpha particles emitted from fission sources cannot be recorded as background tracks in mica. During irradiation with neutrons in nuclear reactors, the recoil nuclei and most of nuclear reaction products from the compositions of mica and from other materials cannot form background tracks in mica. Therefore, muscovite mica is a clean detector for the study of nuclear fission. In this respect,

muscovite mica is much better than plastic track detectors, such as polycarbonate, cellulose nitrate, cellulose acetate, polyethylene terephthalate, and CR-39.

In nuclear fission rate measurements, 2π geometry is often used. An amount of fissile material such as natural uranium (99.2745% ^{238}U , 0.720% ^{235}U , and 0.0055% ^{234}U) is electrodeposited onto a stainless steel plate. A muscovite mica overlaps on it, constituting a 2π geometry. If one places this combination on the beam of thermal neutrons from a nuclear reactor channel, one can record fission-fragment tracks with the muscovite mica. Because the angular distribution of fission fragment is isotropic in thermal neutron-induced fission and every fission event releases two fission fragments in opposite directions, the detection efficiency of the muscovite mica for the fission fragments can be written as follows (Guo et al., 1976b; 1982):

$$e = \begin{cases} 1 - \sin \theta_c & 0 \leq t \leq t_c \\ 1 - \sin \theta_c - \frac{(t - R \sin \theta_c)^2}{2Rt} & t_c \leq t \leq R \\ \frac{R}{2t} \cos^2 \theta_c & t \geq R \end{cases} \quad (4.12)$$

where e is the detection efficiency of muscovite mica for fission fragments, θ_c is the critical angle of track etching of fission fragments in the detector (see subsection V.A.3), R is the average range of fission fragments in the fission source (mg/cm^2), t is the thickness of the fission source (mg/cm^2), and t_c is the critical thickness of the fissile material, $t_c = R \sin \theta_c$.

For other track detectors and isotropic distribution of fission fragments, Eqn (4.12) can also be useful.

Many authors have determined the detection efficiency e and the critical angle θ_c of muscovite mica for fission fragments. For example, $e = (93.6 \pm 0.3)\%$ and $\theta_c = 3^\circ 41'$ for fission fragments of ^{235}U fission induced by thermal neutrons (Guo et al., 1976b, 1982), $e = 91.8\%$ and $\theta_c = 4^\circ 31'$ for fission fragments of ^{252}Cf spontaneous fission (Khan and Durrani, 1972), and $e = (94.8 \pm 0.53)\%$ for ^{244}Cm spontaneous fission (Gold et al., 1968).

In fission rate measurements with solid-state nuclear track detectors in 2π geometry, the backscattering effect of fission fragments from the substrate of fission source must be taken into consideration. For a thin fissile source attached to the surface of the detector, one fission fragment from each fission event will reach the surface of the detector and another fission fragment will go in the opposite direction and hit the substrate of the source. But there is a possibility that the fission fragment undergoes elastic scattering on the atoms in the substrate and changes its direction and enters into the detector. This fragment may also create a track in the detector. For this reason, one fission event may create two fission-fragment tracks in the detector. In other words, the number of tracks recorded in the detector is more than expected from the 2π geometry. For accurate determination of fission rate, one must make a backscattering correction for the number of tracks recorded by track detectors. A careful calibration showed that for gold-silicon substrate (Au-Si surface-barrier detector), 2.1% more tracks will be recorded by muscovite mica detectors and 2.1–2.7%

more tracks will be recorded by polycarbonate track detectors (Guo et al., 1976b, 1982).

Muscovite mica has been used in measurements of fission cross sections, angular distribution of fission fragments, neutron spectrometry and dosimetry, fission and neutron distribution in nuclear reactors, sequential fission in medium energy nuclear interaction, and fission track dating as external detectors. More details will be explained in Part 2 of this chapter.

b. Polycarbonate (Lexan, Makrofol, Tuffak)

The polycarbonate track detector is more sensitive than muscovite mica for fission fragments. Its least recordable particle is helium ($Z = 2$). However, it does not mean that full-energy α -particles emitted from uranium and plutonium can be recorded by polycarbonate. The α -particles can be recorded by polycarbonate detector only when the α -particles are slowed down within the detector to a very low energy (≤ 0.75 MeV/u) (Fleischer et al., 1975; Fleischer, 1981). In other words, by short etching, polycarbonate cannot show tracks of α -particles from natural α -radioactivity of uranium and plutonium and more heavier elements. For this reason, polycarbonate is also a clean detector in fission track measurements. It is comparable with muscovite mica. Therefore, the polycarbonate track detector is used wherever muscovite mica can be applied except for fossil tracks, or at high-temperature. In addition, polycarbonate is much cheaper (~ 100 times) than muscovite mica, more flexible and has a higher charge resolution.

Currently, polycarbonate is more popular than muscovite mica in fission track recording.

c. Polyethylene terephthalate (PET for short; Mylar, Chronar, Melinex, Terphane, Lavsan)

The sensitivity of polyethylene terephthalate is less than polycarbonate. The lowest recordable particles vary from Li ($Z = 3$) to B ($Z = 5$). Alpha particles and protons cannot be recorded as tracks in this detector. Therefore, PET is a clean detector for recording fission fragments of ^{235}U and ^{239}Pu .

d. CR-39

Even though CR-39 is sensitive to low Z heavy charged particles, it can be used safely to detect fission fragments induced by high-energy projectiles. At very high energies over several hundreds of MeV/amu, CR-39 can identify the charges of projectiles and distinguish the tracks of projectiles and fission fragments.

By measuring track diameters or track-etched lengths, the charge resolution achieves the separation of each element in the periodic table of elements. Therefore, CR-39 is one of the best detectors in studies of relativistic projectile fission and fragmentations.

e. Glasses

One of the advantages of glass track detectors is their short etching time for fission-fragment tracks. For example, several seconds to minutes are enough to develop fission-fragment tracks in soda-lime glass (e.g. window glass, microscope slide,

or cover glass) with 48% HF at room temperature. This advantage makes glass a convenient detector for the rapid testing of whether or not a fission source, such as ^{252}Cf , meets the requirements. For this purpose, one needs to put a piece of glass over the source at a distance for a certain time period, then etch the glass in HF for several seconds, wash it in water, dry it in air, and scan it with microscope, after which one will know the intensity of the fission source. In total, one needs less than 10 min for the test. If one wants to judge the flux or shape or distribution of neutrons in a beam, one needs to cover a plane of natural uranium source with a glass plate and put the uranium-glass combination in the beam to irradiate it for a certain time. The track of fission fragments of ^{235}U induced by thermal neutrons will be recorded in the glass. Glass detector plate is then etched, washed, dried, and scanned, after which one will see the shape of the neutron beam, the distribution of beam neutrons, and possibly measure the flux of neutrons from the nuclear reactor.

The detection efficiency of soda-lime glass (71SiO_2 : $15\text{Na}_2\text{O}$: 9CaO : 3MgO : $2\text{Al}_2\text{O}_3$) in 2π geometry for fission fragments from a thin layer of uranium source is $(39.3 \pm 0.4)\%$, which is less than that of muscovite mica and polycarbonate detectors (Guo et al., 1976b; 1982).

2. Fission Rate Determination

The solid-state nuclear track detector is a convenient detector for the determination of fission rates in a fission source. Fission sources can be classified into solid sources and liquid sources. Solid sources include plane sources and point sources. Plane sources include thin sources, thick sources, and infinite thickness sources (or called asymptotic sources). A plane (fission) source exposes a plane surface, which can be covered with a sheet of track detector.

Thin, thick, and infinite thickness sources are differentiated by the critical thickness t_c of the source and the average range R of fission fragments in the source material. t_c is a constant for a given fissile material: $t_c = R \sin \theta_c$ (Guo et al., 1976b, 1982). If $0 \leq t \leq t_c$, the detection efficiency e of the detector exposed or placed in contact with the fissile material will be equal to $1 - \sin \theta_c$, independent of the thickness t of the source. In other words, the detection efficiency is a constant, which is equal to that of a zero thickness source. Therefore, the source with thickness less than t_c is referred to as a thin source. If $t_c \leq t \leq R$, some fission fragments will stop in the fissile material, so that they cannot reach the detector. The detection efficiency changes as the thickness changes. The source in this thickness interval is referred to as a thick source. If $t \geq R$, only the fission fragments originating from the surface layer of the source material have the possibility of reaching the detector. Beyond the thickness R , no fission fragments can reach the detector. In this case, the thickness has reached an infinite thickness, or so-called asymptotic thickness. If one uses muscovite mica as fission detector for ^{235}U foil source, $\theta_c = 3^\circ 41'$. If the fission source material is uranium, $R \approx 7.5$ mg/cm², then $t_c \approx 482$ $\mu\text{g}/\text{cm}^2$. This means that the uranium fission source with thickness less than about 482 $\mu\text{g}/\text{cm}^2$ is a thin source. The source with a thickness

ranging from about 482 $\mu\text{g}/\text{cm}^2$ to about 7.5 mg/cm^2 is a thick source. The source with thickness larger than about 7.5 mg/cm^2 is an asymptotic source.

A point source is defined as a source whereby the size of the source in all directions is smaller than the range of fission fragments in the source material. In this case, all the fission fragments emitted toward the detector in a 2π geometry can reach the detector; no self-absorption loss occurs in such source material. Fine dust such as aerosol particles bearing uranium or plutonium are examples of point sources.

A liquid fission source is a source material in which the fissile material is dissolved or dispersed in a liquid. The rate of spontaneous or induced fission events is calculated according to the equation

$$A_f = \frac{N_f}{t\epsilon} \quad (4.13)$$

where A_f is the number of spontaneous or induced fission events that have occurred in unit time (s), N_f is the number of tracks recorded by the detector, ϵ is the detection efficiency of the detector for fission fragments (see Eqn (4.12)), and t is the time of irradiation of the detector to the fission fragments.

For a liquid fission source, a strip of track detector is immersed into the liquid to record the tracks of fission fragments during irradiation. The fission rate can be calculated by Eqn (4.13). In this case, the thickness of the fission source represented by " t " in Eqn (4.12) is unit thickness (1 cm). Compared with the average range of fission fragments in liquid ($R = 15.6 \mu\text{m}$ in water), the thickness " t " is larger than the range of fission fragments (R). Therefore, $\epsilon = \frac{R}{2t} \cos^2 \theta c$ with $t = 1\text{cm}$. The distribution of fission tracks on the surface of the detector is uniform. One does not need to count all the tracks on the detector. N_f should be considered as track density (number of tracks in unit area of the detector, cm^{-2}). The meaning of fission rate in a liquid is the fission number occurred in unit volume of the liquid (cm^{-3}).

For point fission sources, such as dusts or aerosol particles, or particles on swipes, one can move them to the surface of a track detector by micromanipulator or other means and stick them with diluted glue and cover them with another track detector for recording fission fragments from the source particles. The fission tracks gather like stars. If the tracks are not too crowded together, one can count the total tracks to know the number of fission that had occurred in the particle.

3. Spatial Distribution of Fission and Fission Fragments

The solid-state nuclear track detector is a passive position-sensitive detector. The spatial resolution is about several micrometers. It is suitable for the measurement of the distribution of fission events in a certain direction (one dimension) or on an area (two dimensions) or in a volume (three dimensions). The techniques of measurements are similar to those described in the previous subsections for protons. More detailed techniques and application can be found in Section II.C of Part 2 of this chapter.

4. Application of Fission Detection

Nuclear energy mainly has two sources: fission energy and fusion energy. The utilization of large amounts of fusion energy is now only in the promising stage, as described in Chapter 1. The application of fission energy is the main activity in the present era. Therefore, the detection and quantitative analysis of fission events are the main tasks of nuclear scientists and engineers.

Solid-state nuclear track detectors are vastly used in fission studies. As far as fission reactions are concerned, the following measurements have been carried out:

- (1) Incident particles: n, p, γ , π , α , heavy ion;
- (2) Target nuclei: U, Pu, Th, Bi, Pb, Tl, Hg, Au, Ho;
- (3) Energy range: Spontaneous fission; Low-energy fission ($E < 50 \text{ MeV}$); Medium-energy fission ($50 \text{ MeV} < E < 1000 \text{ MeV}$); High and relativistic energy fission ($E > 1000 \text{ MeV}$).

Solid-state nuclear track detectors have the following advantages for studying fission: (1) they can withstand intense low ionizing beam particles, (2) they can undergo a long duration of irradiation without the need for a power supply, (3) they have a high efficiency for fission fragments, (4) they are position sensitive for fission events, and (5) they exhibit a high charge resolution at high energy.

A very broad range of research fields utilizes track detectors. Very large areas of fission detection have been developed, which belong to the most important branches of nuclear science and technology, such as: (a) neutron physics and dosimetry; (b) nuclear reactor physics; (c) nuclear forensic analysis and safeguards; (d) fission track dating and geothermal chronology; and (e) uranium exploration.

For additional information, the reader is referred to books by Fleischer et al. (1975); Durrani and Bull (1987); and Wagner and Van den haute (1992) and the related Sections II.C, II.F.1, II.F.2, II.F.3, II.G, III.A, and III.B in Part 2 of this chapter.

D. Heavy Ions ($Z \geq 3$)

The origins of heavy ions are mainly the following:

- (1) Low-, medium-, and high-energy nuclear-interaction products,
- (2) Cosmic-ray nuclei,
- (3) cluster radioactivity emissions, and
- (4) heavy-ion accelerator beams.

1. Suitable Detectors for Heavy Ions $Z \geq 3$

The following are suitable detectors for heavy ions with $Z \geq 3$:

- a. Plastic track detectors, such as CR-39, CN, PC, and PET. These are the most sensitive group of track detectors.
- b. Glasses and minerals, such as muscovite mica, phosphate glass, BP-1 glass, soda-lime glass, and quartz. These are generally less sensitive than plastic track detectors.
- c. The criterion to select the most suitable detector is the capacity of the detector to discriminate against background — less ionizing particles if they exist. Otherwise, the detector should have the best potential to identify the charge Z and mass A of the beam and product heavy ions.

2. Identification of Charge Z

In the first several years after the discovery of solid-state nuclear track detectors, scientists were very disappointed that this type of detector could not distinguish particles of different charges (Z). In those early years, these track detectors were mainly used to count tracks of particles. It was Price et al. (1967), who first discovered that plastic track detectors could distinguish charge Z of particles. The principle of identification of charge Z is similar to that used for silicon surface-barrier detectors. This discovery opened up very broad applications of etch track detectors.

The techniques of identification of charge Z by etch track detectors can be classified as: maximum etchable track-length (L_{\max}) method, track-etch rate versus radiation damage density method, track-etch rate versus residual range method, track diameter method for relativistic energy, and track length method for relativistic energy.

Detailed explanations of these methods will be provided in Section VI of Part I of this chapter.

3. Identification of Mass A of Isotopes

Isotope identification is an extension of identification of charge Z (atomic number). It is based on the fact that the residual range R_0 of nuclei in a uniform substance is related to their mass A if their charge Z and phase velocity β ($=v/c$) are the same. By measuring the etch rate V_t (or etch track length L) and residual range R_0 , drawing a figure $V_t - R_0$, one can separate nuclei with different A (isotopes). The reader can refer to the monographs on track detectors (Fleischer et al., 1975; Durrani and Bull, 1987) for additional information on this subject.

4. Heavy-Ion Energy Determination

Energy determination of heavy ions is based on charge identification and range–energy relation. In order to determine the energy of heavy ions, one must first identify what kind of nuclei (Z) created the tracks, then solve the problem about what energy the heavy ions possesses. The techniques used to identify charge Z of the heavy ions, which created the tracks, have been explained in Subsection III.D.2. The range–energy relation of heavy ions in a nuclear track detector will be discussed in Subsection IV.D.2. When one has obtained the value of charge Z of the heavy ion, one can find the energy value E on the curve of range–energy relation of the special ion in the given detector material based on the residual range R_0 measured in the process of identification of charge Z .

5. Applications of Heavy-Ion Detection

Since the 1980s, great achievements have been made by using solid-state nuclear track detectors. The most important achievements are in the following two fields:

a. Heavy Ion Emission from Heavy Nuclei

Heavy nuclei can release not only α -, β -, γ -rays, but also heavy ions. Even though the first discovery of heavy-ion emission, that is, ^{14}C emission from the nucleus ^{223}Ra , was achieved by a silicon $\Delta E - E$ detector by Rose and Jones (1984), the similar

emission from other nuclei is not feasible to detect by the same detector, because of the more intense α -ray background. The solid-state track detector has taken the role of measuring the ions emitted from the other nuclei. Up to now, about 20 parent nuclei of heavy-ion emission have been discovered and measured (^{221}Fr , 221 , 222 , 223 , 224 , ^{226}Ra , ^{225}Ac , 228 , 230 , ^{232}Th , ^{231}Pa , 232 , 233 , 234 , ^{235}U , ^{237}Np , 236 , ^{238}Pu , ^{241}Am , ^{242}Cm , and ^{114}Ba) by nuclear track detectors. No other detectors can take the role in the subsequent discoveries (see Chapter 1 for a more detailed treatment of cluster radioactivity).

b. Relativistic Projectile Fragmentations and the Their Products

Since the first acceleration of heavy nuclei to relativistic energy at Bevalac at the Lawrence Berkeley National Laboratory in California in the early 1980s, the capability of charge resolution $\sigma_z < 1$ was achieved for heavy nuclei ($Z > 26$) with the use of a nuclear track detector and detector stacks. This capability made possible the charge determination of the products from relativistic fragmentation. A series of studies emerged, such as the search for fractional charge particles, measurements of charge pickup cross sections in nuclear interactions, projectile fission studies, electron capture and stripping process studies of ions in matters, charge-changing cross-section measurements of heavy ions in nuclear interactions, and measurements of the composition of ultraheavy cosmic rays. More detailed information can be found in the relevant sections in Part 2 of this chapter.

For other applications of heavy-ion detection with track detectors, the reader is referred to the books of Fleischer et al. (1975); Durrani and Bull (1987); and Benton et al., 1973; Hashemi - Nezhad and Durrani, 1986; Trautmann et al., 1998; Hou et al., 1990; Dunlop et al., 2007.

E. Neutrons

1. Principles of Neutron Detection

The neutron is a neutral particle. It cannot directly produce ionization and excitation of atoms. Therefore, it cannot be recorded directly by any kind of radiation detector, including etch track detectors. Neutrons are recorded through their recoil nuclei and reaction products with the atoms in or in front of the detector materials. Recoil nuclei H, C, O in CR-39 ($\text{C}_{12}\text{H}_{18}\text{O}_7$) can be recorded directly in the detectors. Polycarbonate ($\text{C}_{16}\text{H}_{14}\text{O}_3$) sheet can only record recoil C and O in itself. Recoil nuclei may come from a radiator, such as a thin foil polyethylene (CH_2) $_n$. The downstream detector such as CR-39 will record the recoil protons and carbon nuclei. The energy E of recoil nuclei follows the equation $E = \alpha E_n \cos^2 \varphi$, where E_n is the energy of incident fast neutrons and φ is the angle of the recoil nucleus with respect to the direction of the incident neutrons in the laboratory system. $\alpha = 4A/(A + 1)^2$, where A is the atomic number of the recoil nucleus. The nuclear reactions often used to record neutrons are (n, α) and (n, f) reactions, such as $^{10}\text{B}(n, \alpha)^7\text{Li}$, $^6\text{Li}(n, \alpha)^3\text{H}$, $^{235}\text{U}(n, f)$, $^{237}\text{Np}(n, f)$, $^{238}\text{U}(n, f)$, and $^{232}\text{Th}(n, f)$. Their threshold energies are $E = 0$ (^{10}B , ^6Li , ^{235}U), 0.4 MeV (^{237}Np), 1.1 MeV (^{238}U), and 1.17 MeV (^{232}Th).

To record neutron reaction product α -particles, usually CR-39 or LR-115 (cellulose nitrate) sheet is used. For recording neutron-produced fission fragments, muscovite mica, Lexan or Makrofol polycarbonate foil is used.

2. Suitable Detectors for Neutron Detection

a. CR-39

CR-39 is suitable for recording neutrons through (1) recoil nuclei, i.e. p, C, O in its own compositions (CR-39 sheet is used as both radiator and detector); (2) recoil nuclei, i.e. p and C from radiator polyethylene (CH₂)_n; in this case, CR-39 is used only as detector, but fast neutrons will produce nuclear recoils in the CR-39 as background; and (3) neutron reaction products, namely, α -particles and ⁷Li from the ¹⁰B(n, α)⁷Li reaction, and α -particles and tritium from the ⁶Li(n, α)³H reaction.

b. LR-115

LR-115 cellulose nitrate is nearly the same as CR-39 in neutron detection, but it is less sensitive than CR-39.

c. Lexan, Makrofol (polycarbonate)

Polycarbonate detector can be used as a nuclear recoil detector without radiator for fast neutron detection. Bare polycarbonate sheets will record recoil nuclei of oxygen and nitrogen produced in air by neutrons. Usually, an aluminum plate is placed in contact and in front of the detector to shield off the recoil nuclei from the air, or alternatively, to treat air as a radiator.

Polycarbonate sheets sandwiched with fissile foils can record fission fragments (fission rate measurement) and consequently derive the neutron fluences and neutron spectrum.

d. Muscovite Mica

Muscovite mica is the most ideal detector of neutrons with the help of fissile foils. It is insensitive to α -particles and β - and γ -rays. It is suitable for the measurement of neutrons in mixed radiation fields, where neutrons coexist with γ -rays.

3. Neutron Intensity Measurements

The advantages of the solid-state nuclear track detector in neutron intensity measurements are: (1) its small size and (2) it is insensitive to β - and γ -rays and to less ionizing nuclear particles. It can be inserted into small gaps to measure neutron intensities in nuclear facilities. A modern example is the measurement of the neutron production yield, neutron spatial distribution, and neutron spectrum in the study of accelerator-driven subcritical reactors (ADS) for the disposal of long-lived radioactive wastes (Brandt et al., 2005, 2008; Zamani et al., 2008; Fragopoulou et al., 2008; Wan et al., 2001, 2003). A variety of fields of neutrons have been studied with solid-state nuclear track detectors at different facilities (Zaki-Dizaji et al., 2008; Belafrites et al., 2008; Esposito et al., 2008; Bedogni et al., 2008; Al-Ghamdi et al., 2008; Al-Jarallah et al., 2002; Ohguchi et al., 2008; Abu-Jarad et al., 2002; Palfalvi, 2009; Guo et al., 1976a).

4. Neutron Energy Measurements

Early developments of neutron energy determination by track detectors have been reviewed and explained in books (Fleischer et al., 1975; Durrani and Bull, 1987). Here, only the basic techniques and new developments are pointed out.

a. Fission Foil and Track Detector Sandwich Techniques

The commonly used fission foils are ²³⁵U, ²³⁷Np, ²³⁸U, and ²³²Th with muscovite mica and polycarbonate track detectors.

b. Recoil Carbon and Oxygen Nuclei Method

By measuring the etched track parameters, the mouth and depth, one can calculate the REL spectrum. By computer simulation with the composition of the detector, the reaction cross sections of carbon and oxygen with fast neutrons, and the REL spectrum, one can obtain the neutron spectrum (Wang Yulan et al., 1998).

c. Radiator-Degrader-CR-39 Method

The radiator is a hydrogen-containing material, such as polyethylene (CH₂)_n thin foil. The degraders are Pb, Au, or Al in different thicknesses. CR-39 is the track detector to record the recoil protons with energy in the energy window of CR-39 (Aslam et al., 1988; Durrani et al., 1988; Dajko, 1990; Wan et al., 2003; Oda et al., 2009).

d. Bonner Sphere Spectrometers

More detailed explanation about Bonner sphere spectrometers will be given in Section IV.A.2 of Part 2 of this chapter.

5. Neutron Dosimetry

Neutron dosimeters are used in measurements of neutron dose. From the readings of neutron dosimeters, one can directly get the information of the dose received by a person. Accurate measurements of neutron dose are very difficult. Theoretically, the process of energy deposition of neutrons and its effects on the human body are very complicated. Recent renewal of the recommendations of the ICRP (International Commission on Radiological Protection) from publication 60 (1991) to Publication 103 (ICRP 103, 2007) reflects the progressive deepening of the understanding of neutron energy deposition and its effects on human health. Practically, ideal neutron dosimeters have not been found at the moment. All the existing neutron dosimeters cannot give accurate measurements of neutron dose owing to their intrinsic deficiencies.

The principle of neutron dose measurements includes two steps. The first step is to measure the fluence of neutrons Φ irradiated to the human body. The second step is to convert the neutron fluence Φ to dose equivalent $H(d)$ by using the documented conversion coefficients $H(d)/\Phi$ (ICRP Publication 74, 1996). New replacements for the ICRP 74 conversion coefficients will be published after having the ICRP recommendation 103. The procedure for the calibration of a neutron detector to become a neutron dosimeter is as follows: the neutron detector is put in the field of neutrons of known energy E_n ; the detector is irradiated with the neutrons to a certain

fluence Φ ; and readings M_c of the detector and the fluence Φ of neutrons with their energy E_n are recorded. Then, the response of neutrons M_c/Φ is obtained at the energy E_n of neutrons. Dividing M_c/Φ by the conversion coefficient $H(d)/\Phi$, the response of dose equivalent $M_c/H(d)$ is obtained. The conversion factor $H(d)/\Phi$ was documented in ICRP Publication 74 (1996) and will be replaced with a new one. The reciprocal of the response of dose equivalent is $H(d)/M_c$, the dose equivalent corresponding to one reading of the dosimeter. The above discussion is correct for monoenergetic neutrons of known energy. For a neutron spectrum of known energy distribution, the average conversion coefficient $H(d)/\Phi$ must be calculated from the neutron spectrum. For example, with an Am-Be neutron source, the dose equivalent received can be calculated from $H(d)/\Phi$ and Φ , where Φ is calculated from the distance between the detector (dosimeter) and the source and the intensity of the source.

An ideal neutron dosimeter should satisfy the following equations at all energies:

$$\frac{(M_c/\Phi)}{(H(d)/\Phi)} = c \quad (4.14)$$

or

$$\frac{M_c}{H(d)} = c \quad (4.15)$$

where c is a constant.

In other words, the two curves of M_c/Φ versus E_n and $H(d)/\Phi$ versus E_n can be overlapped if one of the curves is multiplied by a constant (c or $1/c$). In this case, one does not need to consider neutron energy E_n . One can directly obtain the dose equivalent $H(d)$ from the reading M_c . Up to now, a neutron dosimeter of this type has not been found. In other words, none of the existing neutron dosimeters is ideal.

CR-39 is a better neutron dosimeter than a nuclear emulsion plate (NTA) and thermoluminescence detector, but it is less efficient than a bubble detector (Guo et al., 2000) as a neutron dosimeter. Recently, a REM counter was designed by Agosteo et al. (2010) to measure neutron dose with CR-39 and ^{10}B converter by recording tracks of (n,α) reactions as a passive detector and with a ^3He proportional counter as active detector in the REM counter. It shows that both active and passive detectors in the REM counter can give relatively good agreement with the ideal $H(d)/\Phi$ curve, and the CR-39 + ^{10}B detector does not undergo deleterious signal saturation, pile-up effects, and the influence of intensive γ -rays as the active detector.

F. Exotic Particle Detection

Exotic particles include several hypothetical particles including the following:

- (1) Magnetic monopoles (MMs), which were predicted theoretically by Dirac (1931) and are required by the Grand Unification theories in theoretical physics.
- (2) Q-balls, which were predicted by supersymmetry theories to be a coherent state of squarks, leptons, and Higgs field.

Q-balls could be a candidate, among others, of cold dark matter which is proposed to solve the problem of the missing mass in the universe.

- (3) Nuclearites, which are known as strange quark matter (SQM). SQM is made up of approximately equal numbers of up, down, and strange quarks, and is surrounded by an electron cloud, forming a sort of atom. SQM could contribute to the cold dark matter in the universe.

1. Suitable Detectors for Exotic Particle Detection

CR-39, polycarbonate, phosphate glasses, and muscovite mica have been used to detect exotic particles.

2. Magnetic Monopole Detection

Magnetic monopoles are particles theoretically predicted by Dirac (1931). These particles are similar to protons or electrons or other charged particles, which can be separated into isolated particles from their opposite charge state. The magnetic charge of a monopole can be $g = ng_D = 68.5ne$, where $n = 1, 2, 3, \dots$, and g_D is the Dirac minimum charge: $g_D = hc/2e$.

From the relationship between magnetic charge g and electronic charge e , one can calculate the energy loss rate of a magnetic monopole passing through the stopping materials:

$$(dE/dx)_m \approx (g\beta/e)^2 (dE/dx)_e \quad \text{if } \beta \ll \alpha = \frac{1}{137}$$

$$(dE/dx)_m \approx (n^2/4) (dE/dx)_e = K\beta \quad \text{if } \beta \leq \alpha = \frac{1}{137}$$

$$(dE/dx)_m \approx 33 \text{ GeV/cm for plastic} \quad \text{if } n = 1 (g = g_D)$$

A very large value dE/dx (equivalent to the dE/dx of an heavy nucleus with charge $Z \approx 68.5e$ for $g = g_D$, and equivalent to that of a superheavy elemental ion with $Z \approx 137e$ for $g = 2g_D$) of monopoles classifies these as heavily ionizing particles, if they exist and consequently, these would be easy to detect with the use of nuclear track detectors, such as CR-39, polycarbonate (Lexan, Makrofol), BP-1 glasses, and UG-5 glasses (Derkaoui et al., 1999; Ahlen, 1980; Pinfold, 2009; Giacomelli and Patrizii, 2005; Kinoshita et al., 1992; Cecchini et al., 2005). Another important feature of energy loss of magnetic monopoles is that the electronic energy loss dE/dx decreases as the energy E of the magnetic monopole decreases in the entire electronic energy loss region, which is contrary to the feature of electrically charged particles. In the latter case (electrically charged particles), dE/dx gradually increases up to the Bragg peak as the energy of the particle decreases from $E \approx 3 \text{ GeV/amu}$.

The most sensitive etch track detector CR-39 has a threshold $Z/\beta \approx 5$. It allows the detection of a magnetic monopole with one unit Dirac charge ($g = g_D$) for a velocity $\beta (=v/c)$ of around 10^{-4} and $\beta > 10^{-3}$. The detector can record $g \geq 2g_D$ MM in all the velocity regions from $4 \times 10^{-5} < \beta < 1$ (Derkaoui et al., 1998, 1999). Lexan and Makrofol polycarbonate detectors have thresholds at $Z/\beta > 50$. They can record only relativistic MMs.

The phosphate glass detector (UG-5) is less sensitive. It can record only multiply charged magnetic monopoles.

The detection of magnetic monopoles can also be carried out by recording tracks of bound systems (dyons) of magnetic monopoles with a nucleus having a large nuclear magnetic moment, such as the proton, aluminum nucleus, and Mn nucleus. The energy loss of the bound system (MM + p, MM + Al, MM + Mn) is composed of the energy loss contributions of MM and the nucleus (Price et al., 1984; Derkaoui et al., 1999).

Up to now, no magnetic monopoles have been found (Pinfold, 2009).

3. Dark Matter Particle Detection

Great efforts have been made to detect various hypothetical dark matter particles by using solid-state track detectors. The solution to the problem of missing mass in the universe is of significance in theoretical physics, astrophysics, and cosmology. More detailed explanation of this subject is beyond the main scope of this handbook. The reader is referred to the articles written by Price (2005) and Cecchini and Patrizii (2008), from which more information can be obtained.

IV. TRACK FORMATION MECHANISMS AND CRITERIA

A. Introduction

Track formation mechanisms are studied to determine how etchable tracks of charged particles are formed in solids and what is the criterion or standard to expect which solids can record what particles.

The inferences we derive from the track formation mechanism and the criterion we use for the selection of solid-state nuclear track detectors must fit with the following facts:

- (1) Insulating solids and poor semiconductors with electrical resistivity higher than about 2000 Ω -cm are basically track-recording materials;
- (2) Metals and good semiconductors are not track-recording solids;
- (3) Electrons (β -rays), X-rays, and γ -rays cannot create etchable tracks in solids;
- (4) The sensitivities of different insulating solids are different, such as muscovite mica, which can record the nucleus of Ne ($Z = 10$) and heavier nuclei, but not a lighter nucleus of $Z < 10$. Polycarbonate can record α -particles, but not protons; CR-39 can record protons ($Z = 1$) and heavier particles. In other words, the solid-state nuclear track detector is a type of threshold detector.
- (5) Generally speaking, plastic or polymer detectors are more sensitive than inorganic solids;
- (6) Before etching, the recorded tracks in solids may be annealed out (i.e. track fading) at higher temperature.

What mechanisms can cause the above phenomena and what criterion can be used to judge the differences are essential questions for our understanding and application of nuclear track detectors.

B. Track Formation Mechanisms

1. Ion Explosion Spike for Inorganic Solids

The incident charged particle ionizes the atoms along its trajectory. Subsequently, the ionized ions with positive charges repel each other and are rejected into the region around the trajectory by Coulomb repulsion, forming a vacant region along the central line of the particle trajectory and interstitial atoms in the surrounding region as shown in Fig. 4.6.

The formed interstitial and vacant region relaxes elastically, straining the undamaged matrix. The long range of the strained region can be observed under a transmission electron microscope as a latent track and selectively etched by special etchant to form an etched track of the incident particle. The electrons in metals can diffuse very fast to reach the electrically positive ions and neutralize them. Therefore, no ion explosions occur in metal after the passage of heavy charged particle. For this reason, metal cannot be used as a solid-state nuclear track detector.

The positive ions formed by a charged particle in good semiconductors act as holes which move relatively fast and dissipate their charges before explosion of the ions. Therefore, good semiconductor material cannot record tracks of heavy charged particles.

2. Chain Breaking Mechanism in High Polymers

In a high polymer, molecular chains are broken by the passage of heavy charged particles. This process needs only about 2 eV of energy. This process occurs more readily in high polymers. The open ends of the chains are easily attacked by appropriate chemical reagents. This mechanism is shown in Fig. 4.7 (Fleischer, 1981).

The energy of about 2 eV required to break a chain of polymers is much less than that required to ionize an atom (at least 5–17 eV) for inorganic solids. Therefore, it needs less energy to create continuous damage sites in polymers than that in inorganic solids. This is the reason that higher polymers have a higher sensitivity than inorganic solids.

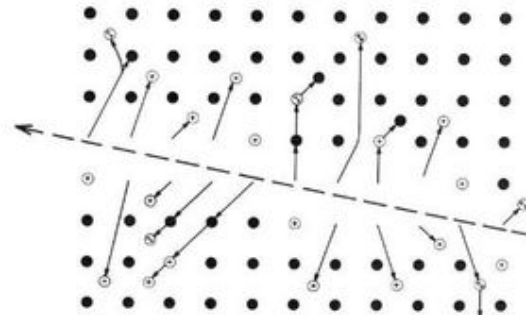


FIGURE 4.6 The ion explosion spike mechanism for track formation in inorganic solids. The incident heavy charged particle ionizes the atoms in the detector along its trajectory and forms a positively charged region. The positively charged ions repel each other by Coulomb force and are rejected to the surrounding region, forming a long vacant line along the trajectory and interstitial atoms around vacant line. These damaged materials easily react with appropriate chemicals and are dissolved in a chemical reagent, forming an etched track. (From Fleischer, 1998. Reprinted with kind permission from Springer Science + Business Media © 1998)

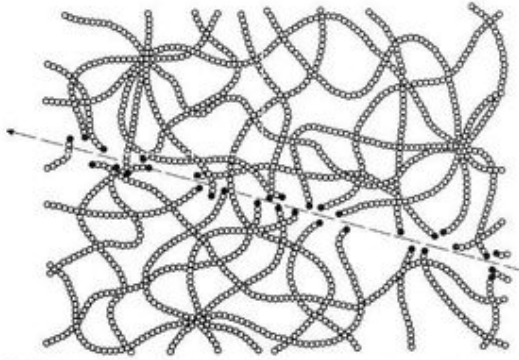


FIGURE 4.7 Chain-breaking mechanism in the formation of etchable tracks in higher polymers. Chain breaks by passage of a heavy charged particle allow preferential etching at a lower radiation damage density. For this reason, organic solids have a higher sensitivity to record tracks of heavy ions. (From Fleischer, 1998. Reprinted with kind permission from Springer Science + Business Media © 1998)

C. Criteria of Track Formation

The study of track formation criteria involves the search for a parameter or a quantity by which one can predict whether a particle can be recorded by a specific solid and describe quantitatively the threshold of the solid. This quantity is the property of the solid and has no relationship with any kind of charged particles. Several parameters have been proposed for the criteria, but none of these satisfactorily fit to all data. Every parameter is successful for certain properties but fail with respect to other properties of the solids.

1. Primary Ionization Rate Criterion

This criterion was suggested by Fleischer et al. (1967b). According to this criterion, the formation of etchable tracks is related to the number of primary ionizations produced along the trajectory of the particles.

a. Formulation

The formulation for calculation of primary ionization rate is given as follows:

$$J = \frac{2\pi n_e Z_{\text{eff}}^2 e^4 f_e}{mv^2 I_0} \left[\ln \frac{2mv^2}{I_0} - \ln(1 - \beta^2) - \beta^2 - \delta - K \right] \tag{4.16}$$

where n_e is the number of electrons in a unit volume of the detector, v is the velocity of incident particle, m is the mass of the electron, f_e is the effective fraction of the electrons in the detector in the most loosely bound state, I_0 is the ionization potential of the most loosely bound electrons in the detector, β is the particle velocity, i.e. v/c , where c is the speed of light in a vacuum, δ is a correction term for the effect of polarization of a medium at relativistic velocities, K is a constant depending on the composition of the stopping medium (detector), and Z_{eff} is the effective charge of the incident particle where

$Z_{\text{eff}} = Z[1 - \exp(-130\beta/Z^{2/3})]$, and Z is the atomic number of the incident particle.

The value of the adjustable constant K in Eqn (4.16) is selected by measuring track-etch rate V_T for at least two types of incident particles and adjusting the K value in Eqn (4.16) in order that for the same V_T , the corresponding J values are the same for all of the incident particles. This means that V_T is related only to J but not to the types of particles. By adopting $I_0 = 13$ eV for muscovite mica and $I_0 = 2$ eV for polycarbonate and cellulose nitrate, Fleischer et al. (1967b) adopted $K = 3.04$ to calculate J to fit the data well.

Figure 4.8 shows the relationships between J values and β or energy E of various incident charged particles as well as the thresholds of different types of detector materials.

b. Successes in Explanation of Thresholds

The criterion of primary ionization rate can give a good fit to the experimental results both for inorganic solids and for organic polymers. By adjusting the parameter K , a horizontal line

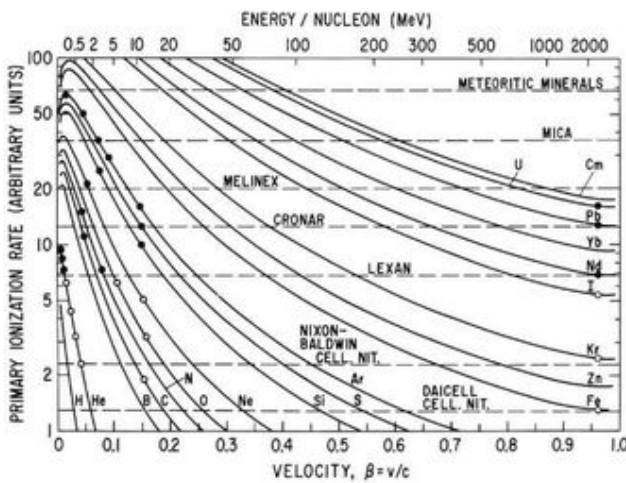


FIGURE 4.8 Relationship between primary ionization rate J and velocity β or energy E of various projectiles. The horizontal lines represent the thresholds of different types of track detectors. The solid circles denote etchable track formation in Lexan. The open circles denote that no etchable tracks were formed in Lexan. The minimum change Z , which can form tracks in muscovite mica, is Ne ($Z = 10$). The registration threshold of CR-39 lies below the x -axis. (Figure from Fleischer, 1998. Reprinted with kind permission from Springer Science + Business Media © 1998)

(threshold) can be obtained to separate the data of track formation from those of non-track formation.

c. Existing Problems

A number of problems exist with respect to primary ionization rate criterion, which are the following:

- (1) The main problem is that it does not consider the ionization induced by δ -rays.
- (2) Another problem is that the calculated primary ionization rate is only a relative value, and the formulation has not been approved scientifically.
- (3) The third problem is that in organic polymers, the parameter I_0 must be taken as small as about 2 eV. This energy is not enough to ionize any atoms even though a good fit can be obtained for an organic polymer. $I_0 \approx 2$ eV indicates that the tracks are formed by molecular chain breaking, not by primary ionization.

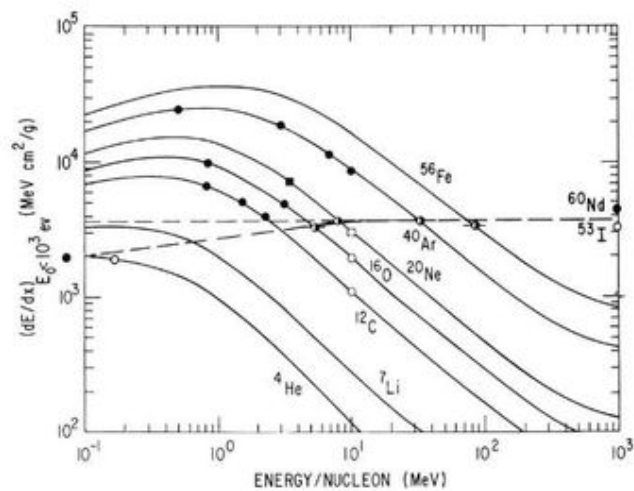
2. Restricted Energy Loss (REL) for Plastic Track Detectors

The restricted energy loss (REL) criterion was suggested by Benton (1967) and Benton and Nix (1969). The restricted energy loss is the portion of the total energy loss that produces δ -rays of less than some specified energy ω_0 . Not all of energy loss in solids contributes to track formation. A significant fraction of the energy transferred to electrons in a detector goes to electrons with sufficiently high energy and with range much larger than the scale of latent tracks. These higher-energy δ -rays will not contribute to the track formation. Only low-energy δ -rays with energy lower than ω_0 will contribute to the formation of etchable tracks.

a. Formulation

$$REL_{\omega_0} = \frac{2\pi n_e Z_{eff}^2 e^4}{mv^2} \left[\ln \frac{2mv^2 \omega_0}{I} - \ln(1 - \beta^2) - \beta^2 - \delta \right] \tag{4.17}$$

FIGURE 4.9 Restricted energy loss rate versus energy of the heavy charged particles in a Lexan polycarbonate track detector. The upper limit of the energy of δ -rays $\omega_0 = 1000$ eV was taken. Solid circles denote the formation of etchable tracks. Open circles denote no track formation. No horizontal line quite fits the measured data. (From Fleischer, 1981. Reprinted with permission from Elsevier © 1981)



where I is the mean ionization potential of the detector material and ω_0 is the upper limit of the δ -ray energy below which the deposited energy contributes to the formation of tracks.

The value of ω_0 has been taken as 200, 350, and 1000 eV by different authors. It plays the role of an adjustable parameter in the calculation of REL.

Figure 4.9 illustrates the relationships between REL and energy E of incident particles.

b. Successes in explanation of thresholds

The criterion of restricted energy loss rate has taken into account the insignificance of δ -rays with energy higher than ω_0 . Ideally, it is correct and easy to be accepted. For this reason, the horizontal line of the threshold fits to the data for the most part. Only in low energy region some deviation occurs.

c. Existing Problems

No horizontal line quite fits the measured data as shown in Fig. 4.9. Ahlen (1980) showed that REL cannot fit the V_T values in a straight line for particles with different charge Z .

3. Energy Deposition Model (E_v)

The energy deposition model (E_v) criterion was suggested by Katz and Kobetich (1968). It suggests that a charged particle will create an etchable track in a dielectric solid if the particle deposits energy E_v which reaches a critical dose (volume density) by δ -rays at a critical distance r from the path of the particle. The distance r from the path is 19 Å ($1 \text{ \AA} = 10^{-8} \text{ cm} = 10^{-10} \text{ m}$) for muscovite mica, 15 Å for cellulose nitrate, and 17 Å for Lexan polycarbonate. The critical energy density E_v deposited at the critical distance r of muscovite mica is $\sim 3.5 \times 10^9 \text{ erg/g}$.

a. Formulation

The calculations for obtaining E_v at a distance r by δ -rays are quite complicated. The reader is referred to the original articles by Katz and his coauthors (Katz and Kobetich, 1968; Kobetich and Katz, 1968).

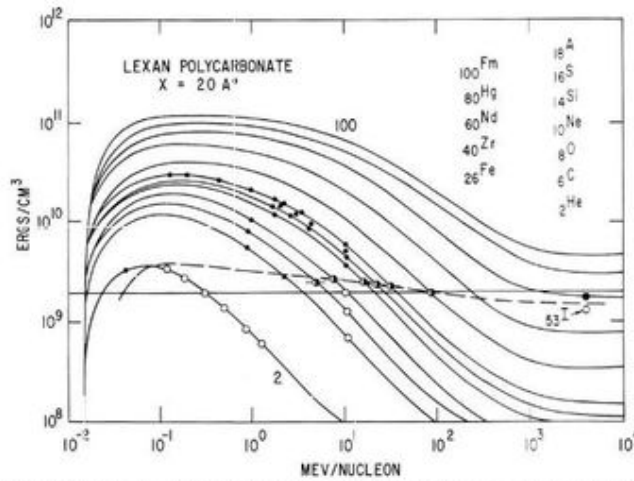


FIGURE 4.10 Energy deposition density E_v versus energy E of heavy charged particles (nuclei) in Lexan polycarbonate. Solid circles represent etchability in Lexan and open circles denote zero registration. The horizontal line denoting the threshold of Lexan is tilted toward the low energy region. (From Fleischer, 1981. Reprinted with permission from Elsevier © 1981)

Figure 4.10 shows the relationships between E_v and E of incident particles.

b. Successes in Explanation of Thresholds

This criterion has taken into account the energy density deposited by δ -rays and the critical radius from the trajectory of the particle, and the results can approximately predict the thresholds both for inorganic and organic solids.

c. Existing Problems

The obvious shortfall of this criterion is that it ignores the energy deposition of the primary incident particles. The second problem is that it cannot obtain a horizontal line to denote the existing threshold. The third problem is the sharp cutoff at low energy of incident particles, and it does not hold true for failure to detect very low energy incident particles.

D. Extended and Transitional Criteria

Besides the criteria explained in the previous sections, namely, J , REL , and E_v , there are two criteria often used by others, which are Z_{eff}/β and dE/dx . The value of Z_{eff}/β may be used as a criterion for track formation, but dE/dx can be used only as a transition parameter.

1. Z_{eff}/β

Ahlen (1980) compared the measured results of V_T of ^{28}Si , ^{56}Fe , and ^{20}Ne in a Lexan detector with REL and Z_{eff}/β . He concluded that Z_{eff}/β is preferred as a universal parameter over REL , and the experimental data are sufficiently good to rule out the REL model. The reason for Z_{eff}/β being a good parameter is that when the constant K in equation for J approaches infinity (∞), it is equivalent to, i.e. $J \propto (Z_{eff}/\beta)^2$. Therefore, $(Z_{eff}/\beta) \propto J^{1/2}$ will be another parameter as J to describe formation of etchable tracks.

Figure 4.11 illustrates the response $(V_T/V_T - 1)$ versus Z_{eff}/β of BP-1 glass etched by 48% HBF_4 at 50 °C, 49% HF at 20 °C,

and 6.25N NaOH at 50 °C (He et al., 1994). From the measured data, the authors found that the thresholds for formation of etchable tracks are related to the etching condition for the same detecting material. The threshold Z_{eff}/β values for BP-1 glass are 57 ± 1 , 68 ± 1 , and 78 ± 1 respectively for the above three etching conditions.

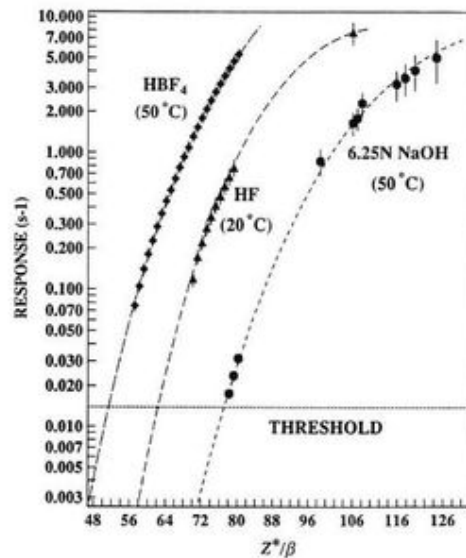


FIGURE 4.11 Response $(V_T/V_T - 1)$ versus Z_{eff}/β of BP-1 glass etched by 48% HBF_4 at 50 °C, 49% HF at 20 °C, and 6.25N NaOH at 50 °C where $s = V_T/V_B$, $Z^0 = Z_{eff}$. The solid points are measured data with an 11.4 AGeV ^{197}Au beam and its fragments in the three etching conditions. The horizontal dotted line denotes the threshold ($s - 1 \leq 0.015$) of track registration at normal incidence. The threshold $(Z_{eff}/\beta)_{th}$ values are given according to the lowest value of (Z_{eff}/β) in the figure, which are the lower limit of the instrument used. (From He et al., 1994; printed with permission from Elsevier © 1994)

a. Successes and Advantages of Z_{eff}/β as a Criterion of Track Formation

The Z_{eff}/β criterion of track formation has exhibited the following success and advantages:

- (1) It is easy to convert to the charge Z of relativistic heavy charged particles which can be recorded by the detector. For relativistic energy, $\beta \rightarrow 1$, $Z_{eff} \rightarrow Z$, and $Z_{eff}/\beta \rightarrow Z$. Therefore, $(Z_{eff}/\beta)_{th} = 26$ can be considered whereby relativistic Fe ions ($Z = 26$) in cosmic rays may be recorded by the detector.
- (2) It is easy to convert the registration threshold $(Z_{eff}/\beta)_{th}$ to primary ionization J and restricted energy loss (REL), since in all equations of J , REL , and dE/dx , $(Z_{eff}/\beta)^2$ is included. Other parameters in the equations can be obtained from the compositions of the detectors. Knowing the value of $(Z_{eff}/\beta)_{th}$, the thresholds of J , REL , and the transitional parameter dE/dx (see below) can be obtained for the detectors.
- (3) It is easy to determine the threshold of Z_{eff}/β of a detector by using different energies of at least one type of heavy ion, or different heavy ions.
- (4) The determined value of the threshold of Z_{eff}/β for each detector is absolute and fixed, not adjustable.

From the above advantages, one can see that the criterion Z_{eff}/β for track formation is convenient, straightforward, and easy to assigning a quantity, compared with other criteria suggested.

b. Existing problems

How to derive the threshold of track formation Z_{eff}/β for each type of detector remains to be solved.

2. dE/dx Transitional Parameter

Some authors still use total energy loss rate dE/dx to denote the thresholds of etch track detectors. This parameter has been demonstrated by extensive experiments that it cannot give a satisfied description of the thresholds. No horizontal line separates the ions that register from those that do not register. The lines that separate the experimental data for recording tracks from the nonrecording of tracks tilt up at the high-energy region. One cannot find a threshold value, which is independent of projectile charges (Z). However, the dE/dx value can be treated as a conditional reference mark, such as the "threshold" values for recording He ions are about 40 (50% CR-39), 88 (40%), 108 (30%), 125 (20%), and ~250 (0%) keV/ μm equivalent in water for CR-39-DAP plastics, where 50% CR-39 means the ratio of CR-39/DAP in the composition of CR-39-DAP is 50/50 (Tsuruta et al., 2008), since the dE/dx value of a particle of charge (Z) and energy (E) in a specific detector material can be determined or calculated very well. From the dE/dx value, one can trace back the energy E to calculate REL and J .

The formula used to calculate total energy loss rate is

$$\frac{dE}{dx} = \frac{4\pi n_e Z_{eff}^2 e^4}{mv^2} \left[\ln \frac{2mv^2}{I} - \ln(1 - \beta^2) - \beta^2 - \frac{C}{Z_2} - \frac{\delta}{2} \right] \quad (4.18)$$

where C/Z_2 is a shell correction term.

The other parameters in Eqn (4.18) are the same as in Eqn (4.16) and (4.17). The calculation methods of C/Z_2 and δ can be found in the review articles by Ahlen (1980), Iano (1964) and Barkas and Berger (1964).

V. TRACK REVELATION

Track revelation refers to the techniques used to reveal charged particle tracks in solids. The most successful and popularly used technique is track etching, which is the subject of this chapter. For other techniques of track revelation, the reader is referred to the treatise by Fleischer et al. (1975).

A. Chemical Etching (CE)

1. Etching Condition

Chemical etching is the basic technique used to reveal nuclear particle tracks in solids. The indispensable conditions for chemical etching are two, namely, etchant and etching device.

a. Etchant

An etchant is a particular chemical formulation which preferentially reacts with the damaged materials in the particle track resulting from the passage of a heavy charged particle in the solid-state nuclear track detector. One can find the etchants for different detector materials in the lists of etching conditions in the book by Fleischer et al. (1975) or by Wagner and Van den haute (1992). The etching conditions include three aspects: (a) compositions of the chemicals used as etchant; (b) temperature during etching; and (c) duration of the etching. The etchant is particular for each type of detector material. Selection of the wrong etchant will never reveal tracks. Usually, a higher concentration of etchant and higher temperature will etch tracks more rapidly; longer etching times will make the etched track larger in diameter.

b. Etching Device

Etching devices hold etchants and ensure the etching conditions. The etchant must be held in a closed container to prevent exchange of substances from inside or outside to ensure that the concentration of etchant remains constant. Homogeneous and constant temperatures in the whole volume of etchant are required in many studies. The etch rate increases exponentially with an increase in temperature. A small change in temperature will influence considerably the etch rate. In very precise measurements, such as in the identification of the charges of cosmic-ray particles, in the identification of masses of isotopes, and in nuclear track membrane production, the temperature must be controlled within ± 0.01 °C. When using the SSNTD for the counting of tracks with the optical microscope, a precision of temperature of ± 1 °C is sufficient in the temperature range of 10–100 °C. One or more stirrers are necessary to keep the etchant homogeneous in temperature (Guo, 1988).

2. Track Etching Geometry

The etching process includes two types of chemical reactions: (1) etchant with damaged material and (2) etchant with bulk

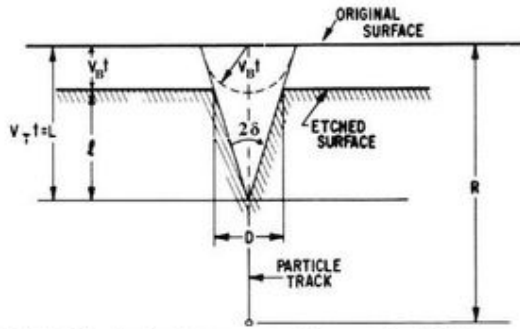


FIGURE 4.12 Track-etching geometry with constant V_T and V_B in an amorphous solid. The particle perpendicularly entered the solid and stopped at depth R below the surface. The etchant preferentially reacts with the damaged materials formed along the trajectory of the particle with a constant velocity V_T for a time t . The etchant attacks the bulk material from the original surface of the detector with a constant velocity V_B . After etching for a time t , an etch cone is formed along the trajectory with pit at depth $L = V_T t$ below the original surface. During time t , the surface layer with thickness $V_B t$ of the detector is removed by the etchant. The original surface moves to the new surface that is the etched surface. The visible track length is $l = (V_T - V_B)t$. (From Price and Fleischer, 1971. Republished with permission of Annual Review of Nuclear Science © 1971; permission conveyed through Copyright Clearance Center)

material of the detector. The first proceeds with velocity V_T along the trajectory, called track-etch rate. The second proceeds perpendicularly to the surface of the detector with velocity V_B called bulk etch rate. The etching process is a combined reaction of V_T and V_B .

Figure 4.12 shows the process of chemical etching in an amorphous solid having a track of particle perpendicularly incident to the detector.

3. Critical Angle of Etching

The track-etch rate V_T and bulk etch rate V_B sometimes are competitive with each other. The critical angle θ_c of etching is a result of the competition of V_B with V_T , which is shown in Fig. 4.13. The first particle entered the detector with incident angle θ (the angle between the direction of incident particle and the surface of the detector).

$V_T t$ is the etched track length at time t , $V_B t$ is the removed thickness from the surface of the detector, and θ is the incident angle of the particle (the angle between the particle direction and the detector surface). If $V_T t \sin \theta < V_B t$, the track will be

removed away by the etchant. No etched track is left in the detector after etching for the example illustrated in part (a) of Fig. 4.13. If $V_T t \sin \theta > V_B t$, a track cone will be left after etching (parts c and d). If $V_T t \sin \theta = V_B t$, it is the critical situation for formation of an etched track (part b). In this situation, the incident angle θ is denoted as θ_c . θ_c is the critical angle of etching. Then, one has

$$\theta_c = \arcsin \frac{V_B}{V_T} \quad (4.19)$$

4. Techniques of Critical Angle Measurements

a. Direct Measurement of Half Cone Angle

From Fig. 4.13(b) one can see $\theta_c = \delta$ where δ is the half angle of the etched track cone. This signifies that if one can measure the half angle δ of the etched cone, one can determine the critical angle θ_c and V_T , provided one knows the value of V_B .

b. Direct Measurement of Critical Angle

From Fig. 4.13(b) one can see that changing the beam angle θ of the incident particles, the etched tracks will start to appear at $\theta = \theta_c$. By this technique Khan and Durrani (1972) measured the critical angle θ_c of ^{252}Cf fission fragments in soda-lime glass ($35^\circ 30'$), U-2 Reference glass ($31^\circ 45'$), obsidian ($26^\circ 00'$), tektite ($25^\circ 45'$), quartz ($7^\circ 15'$), muscovite mica ($4^\circ 30'$), Makrofol polycarbonate ($3^\circ 00'$), and Lexan polycarbonate ($2^\circ 31'$).

c. Direct Measurement of Detection Efficiency

For a point source or thin plane source of given particles, one can directly measure the detection efficiency ϵ of the detector for the particles, that is, the ratio of the number of recorded tracks to the number of the emitted particles, to derive the critical angle θ_c by Eqn (4.20) for an isotropic source in 2π geometry (Fleischer et al., 1975):

$$\epsilon = 1 - \sin \theta_c \quad (4.20)$$

By this technique, Guo et al. (1976b) (see also Guo et al., 1982) measured the critical angle θ_c of fission fragments of ^{235}U -induced fission by thermal neutrons in muscovite mica ($3^\circ 41'$), phosphate glass ($7^\circ 6'$), silicate glass ($37^\circ 21'$), quartz ($16^\circ 2'$), polycarbonate (Chaoyang, China, $2^\circ 24'$), Makrofol K polycarbonate ($3^\circ 40'$), and polyester ($3^\circ 29'$).

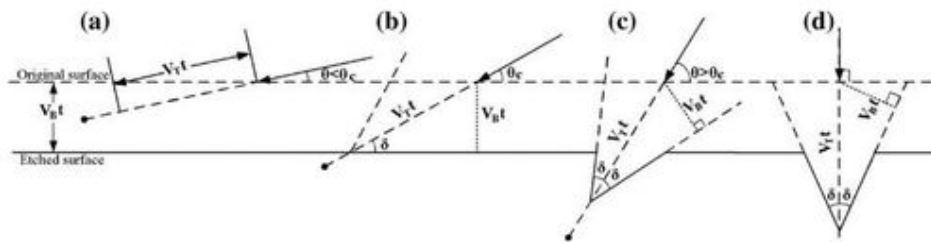


FIGURE 4.13 Existence of critical angle of etching for observation of etched tracks.

5. Track Etching Geometry

From Fig. 4.12 one can easily obtain the diameter of a track that perpendicularly enters the surface of detector ($\theta = 90^\circ$) according to the equation

$$d = 2V_B t \sqrt{\frac{V_T - V_B}{V_T + V_B}} \tag{4.21}$$

or

$$d = 2V_B t \sqrt{\frac{V - 1}{V + 1}} \tag{4.22}$$

where $V = (V_T/V_B)$. V is called the etch rate ratio.

For an incident angle $\theta \neq 90^\circ$ and constant track-etch rate V_T and bulk etch rate V_B , the major axis D of the opening of etched track is

$$D = \frac{2V_B t \sqrt{V^2 - 1}}{V \sin \theta + 1} \tag{4.23}$$

The minor axis of opening is

$$d = 2V_B t \sqrt{\frac{V \sin \theta - 1}{V \sin \theta + 1}} \tag{4.24}$$

For other parameters of etched tracks, one can find the formulas in the book written by Durrani and Bull (1987).

The equations of etched track geometry for constant V_T are only approximations to the true situation, because only for very few cases is V_T constant. Generally, V_T varies along the trajectory of a particle. Calculations based on a constant V_T often give results which are good enough for the studies of particles.

For track-etching geometry with varying V_T and for track-etching geometry in anisotropic solids, such as all crystalline minerals, the formulations can be found in the book by Durrani and Bull (1987).

6. New Progress in Track Etching Geometry

In recent years, the study on track-etching geometry has made tremendous progress. Nikezic and Kostic (1997) derived an analytical two-dimensional equation of etch pit wall in amorphous solid-state nuclear track detectors. Nikezic (2000) derived an analytical three-dimensional equation of track wall (for variable V_T ; conical track phase) described by the equation

$$\sqrt{x^2 + y^2} = \int_Z^L \frac{d\xi}{\sqrt{v^2(\xi) - 1}} \tag{4.25}$$

where Z is the axis along the particle track; (x, y) are the coordinates of a point on the track wall; v is etch rate ratio V_T/V_B ; L is the depth to which the chemical solution penetrates the detector material along the particle trajectory; and ξ is the parameter upon which v depends, such as, REL or others.

Nikezic and Yu (2003, 2004) extended the above track wall equation to over-etched tracks (or round-tip tracks). The whole set of equations can be used to calculate the track wall, track opening diameter, major axis, minor axis, and other parameters

for constant V_T , variable V_T , normal incidence, oblique incidence, sharp tip-etched tracks, and round-tip etched tracks. In summary, all parameters of tracks in amorphous solids can be calculated except the tracks in anisotropic crystalline minerals. For more information, the reader is referred to the original papers mentioned above.

B. Electrochemical Etching (ECE)

Electrochemical etching was first suggested by Tommasino (1970). A plastic detector foil with tracks of particles is used to divide a cell containing a suitable etchant, such as NaOH solution. A stainless steel electrode is placed in each half of the cell. A high-frequency oscillating voltage is connected to the two electrodes. The voltage is typically equivalent to $\sim 30\text{--}50 \text{ kV cm}^{-1}$ field strength. The frequency is ranged from several kHz to several tens of kHz. A 50 Hz 220 V sinusoidal supply can also work. Under the joint reactions of etchant and electric voltage, the tracks start to be etched. The forming track tip has a strong field, which makes the foil break down near the tip as shown in Fig. 4.14. The breakdown looks like a tree. The tree is a consequence of the charged particle track. Figure 4.15 shows microphotographs of ^{252}Cf fission-fragment tracks in CR-39 sheets of 485 μm in thickness.

Many researchers have studied the "treering" phenomenon (Tommasino et al., 1981; Sohrabi, 1981; Sohrabi and Mahdi, 1993; Li, 1993, 2008a, 2008b).

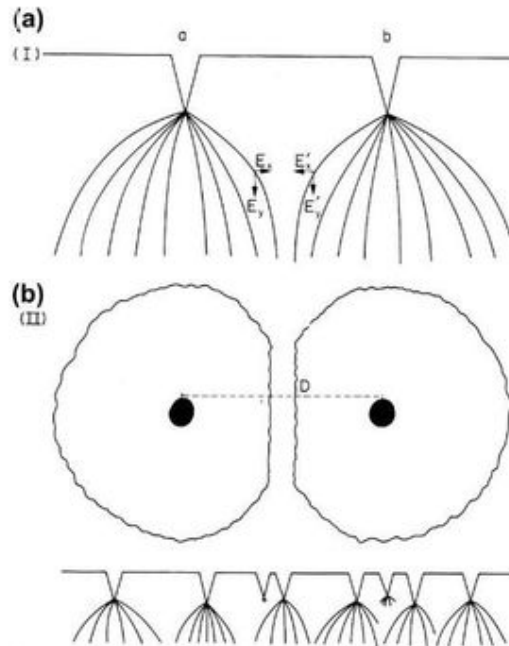


FIGURE 4.14 "Treering" phenomenon of electrochemical etching (ECE) of charged particle tracks in plastic foil. The sharp tips of etched cones have very strong field, which makes the foil break down, forming tree-like tracks. The breakdown spreads up to several hundred micrometers in width, which is easy to observe with a low-magnification optical microscope or even by the naked eye. (From Al-Najjar et al., 1979; printed with permission from Elsevier © 1979)

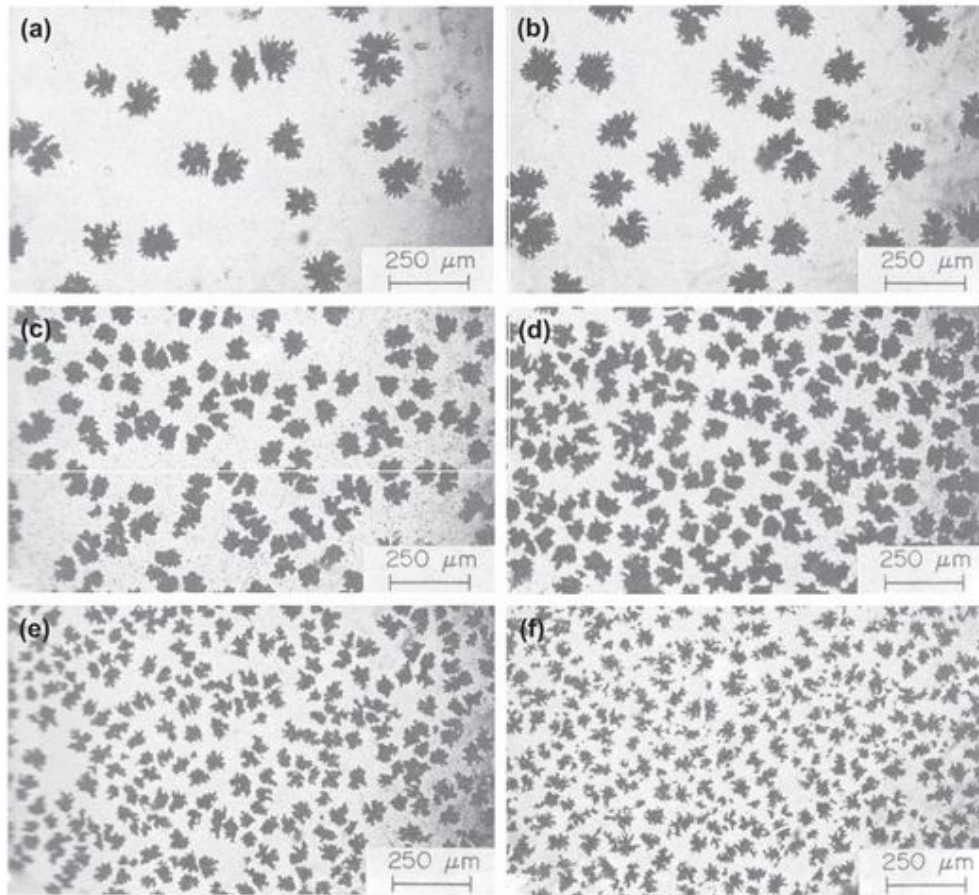


FIGURE 4.15 Microphotographs of electrochemically etched tracks of ^{252}Cf fission fragments recorded in CR-39 plates. The thickness of the CR-39 plate is 485 μm . The track densities are (1) 1.5×10^3 , (2) 3.0×10^3 , (3) 1.2×10^4 , (4) 2.4×10^4 , (5) 3.6×10^4 , and (6) $1.2 \times 10^5 \text{ cm}^{-2}$, respectively. The etching condition was 30 wt% KOH, 60 °C, 90 min. The electrical field condition was 15 kVcm^{-1} and 40 kHz. The track densities after ECE are the same as CE. The track size changes diminish as the density increases. (From Al-Najjar et al., 1979; printed with permission from Elsevier © 1979)

The advantage of electrochemical etching is that the size of the etched tracks is very large up to several hundreds of micrometers, which are easy to scan with an optical microscope or track image analyzer, or even can be seen with the naked eye. The disadvantage is that the track density must be lower than $\sim 10^5 \text{ cm}^{-2}$.

The applications of electrochemical etching are mainly in the detection of fission fragments, α -particles, and neutron-recoil tracks. The main fields of application are neutron dosimetry (Tanner et al., 2005; Dhairyawan et al., 2003; Zainali and Afkar, 2005; Hankins et al., 1989) and Rn monitoring (Zainali and Afkar, 2005).

C. Track Etching Kinetics

1. Objectives and Required Parameters

The ultimate purpose of the study of track-etching kinetics is to deduce the species of the particles from the tracks created by the particles.

For this purpose, two lines of calculations must be carried out.

- (1) First line of calculation – Calculation of track parameters from the parameters of the particles (Forward calculation);
- (2) Second line of calculation – Derivation of the parameters of the particles from the parameters of the etched tracks (Inverse calculation).

In the above calculation and derivation, the following parameters are required:

- (a) Particle parameters including atomic number Z_1 , mass M_1 , and energy E_1 (or velocity v_1);
- (b) Detector parameters including average atomic number Z_2 , average atomic mass M_2 , density ρ , and mean ionization potential I .
- (c) Radiation damage density parameter or threshold parameter, such as primary ionization rate J , or restricted energy loss rate REL , or $Z_{eff}\beta$, or others;

- (d) Track-etching parameter under special etching conditions, such as track-etch rate V_T and bulk etch rate V_B , or track-etch rate ratio $V = V_T/V_B$, or reduced etch rate $S = V_T/V_B - 1$, as a function of the radiation damage density, such as $V = f(REL)$, as well as the etching time t or the thickness h of removal on single surface of the detector.
- (e) Track parameters, such as track diameter d on the etched surface of the detector, major axis D and minor axis d of the mouth of tracks, and etched track length L , which are represented by equations as functions of track-etching parameters.

2. Forward Calculation

For the first line of calculation (forward calculation), Z_1 , M_1 , E_1 in (a) and Z_2 , M_2 , ρ , and l in (b) are known. One should select one of the threshold parameters in (c), such as REL , and know the relationship between the track-etch parameter and threshold parameter in (d), such as $V = f(REL)$, and use the equations of d , D and d , and L versus track-etching parameter in (e), such as $d = \varphi_1(V)$, $D = \varphi_2(V)$, and $L = \varphi_3(V)$. After calculation through the first line, a group of curves will be obtained of d , D (d), or L versus Z_1 , M_1 , or E_1 in the condition t or h . These curves can be used to identify the particles that created the tracks in the detector. These curves represent the relations between the tracks and particles.

The calculation through the first line is relatively easy and much progress has been made: Much work has been done along the first line on threshold parameters in (c) (Fleischer et al., 1975; Fleischer, 1981; Benton, 1967; Benton and Nix, 1969; Katz and Kobetich, 1968; Kobetich and Katz, 1968; Ahlen, 1980; see Section IV above). A large number of papers have been published on track-etching parameters in (d) (Hermsdorf, 2009; Hermsdorf and Reichet, 2010; Rana, 2008; Fromm et al., 1988; also the articles cited by these papers). Equations for calculating track parameters in (e) have been derived in amorphous solids for constant and variable V , for conic tracks, over-etched tracks, and round-tip tracks (Nikezic and Kostic, 1997; Nikezic, 2000; Nikezic and Yu, 2003, 2004, 2006, 2008b; Nikezic et al., 2008; Ditlov, 1995; Somogyi, 1980; Somogyi and Szalay, 1973; Henke and Benton, 1971).

Track evolution in anisotropic crystals is very complicated and less work has been done on this subject. This remains to be studied in detail in the future (Fleischer et al., 1975; Durrani and Bull, 1987; Somogyi, 1980; Henke and Benton, 1971).

3. Inverse Calculation

Inverse calculation by analytic formulations through the second line from the parameters of etched tracks to derive the parameters of the particles is more complicated than forward calculation. It should be possible, but no paper with this approach has appeared in the scientific journals.

In practice, experimental calibration of detectors by using accelerator beam particles is the current way to assign the correct charge Z_1 , mass M_1 , and energy E_1 of particles. These kinds of techniques have been used in the discoveries of cluster radioactivity of heavy nuclei (see Section II.A of Part 2 of this

chapter) and in many other physical and cosmic-ray studies (Fleischer et al., 1975; Durrani and Bull, 1987).

Experimental calibration is a more basic and straightforward way to retrace the particle parameters than the theoretical calculation through the track-etching kinetics.

VI. PARTICLE IDENTIFICATION

A. Maximum Track Length Method

The first method proposed for the identification of charges assumed that after a long etching time, the entire portion L_{\max} of the trajectory along which the density of radiation damage is higher than the critical (threshold) value is etched out. On this assumption, using appropriate curves of radiation damage density, a relationship between Z and L_{\max} could be calculated (Fleischer et al., 1965a). The "track-in-track" (TINT) and "track-in-cleavage" (TINCLE) techniques proposed by Lal et al. (1968) and Lal (1969) are based on this method.

B. Track-Etch Rate Versus Radiation Damage Density Method

This method is based on the fact that the etching rate along a track is a function of the radiation damage density. Track-etch rate can be represented by V_T along track (Price et al., 1967), or by etch cone length $L = V_T t$, where t is etching time (Price et al., 1967; Fleischer et al., 1975), or by the etch rate ratio $V = V_T/V_B$, where V_B is the bulk etch rate of the detector material (Fleischer et al., 1969d, 1975), or by the reduced track-etch rate $V - 1 = V_T/V_B - 1$ (Price, 1982). The radiation damage density is represented by the primary ionization rate J (Fleischer et al., 1967d), or restricted energy loss rate (REL) (Benton, 1967), or energy density E_v (Katz and Kobetich, 1968), or by $Z_{eff}\beta$ (Ahlen, 1980).

Figure 4.16 shows the curves of $V_T/V_B - 1$ versus $Z_{eff}\beta$ for CR-39 (DOP) and Tuffak polycarbonate. From these curves, one can see that V_T for both CR-39 and Tuffak increases steeply in the range $10 \leq Z_{eff}\beta \leq 99$ and $55 \leq Z_{eff}\beta \leq 105$, respectively (Salamon et al., 1985). CR-39 is more sensitive than Tuffak polycarbonate.

C. Track-Etch Rate Versus Residual Range Method

Figure 4.17 shows the relationship between track-reduced etch rates and residual ranges of some nuclei with different charge Z and A (isotopes) in phosphate glass (PSK-50, Schott Glass Technologies, Inc.).

The lines in Fig. 4.17 are fits to data for heavy ions of ^{28}Si , ^{24}Mg , and ^{20}Ne from the accelerator Superhilac in Berkeley, U. S. A. The curves show that the phosphate glass has excellent charge resolution in the region of Ne and Mg. The glass was used to record and identify Mg and Ne isotopes as well as spontaneous fission from a source of ^{234}U . The points in Fig. 4.17 are the measured results (Wang et al., 1987; Price, 1987). A similar identification technique of charge Z of heavy ions emitted from cluster radioactivity has been adopted by

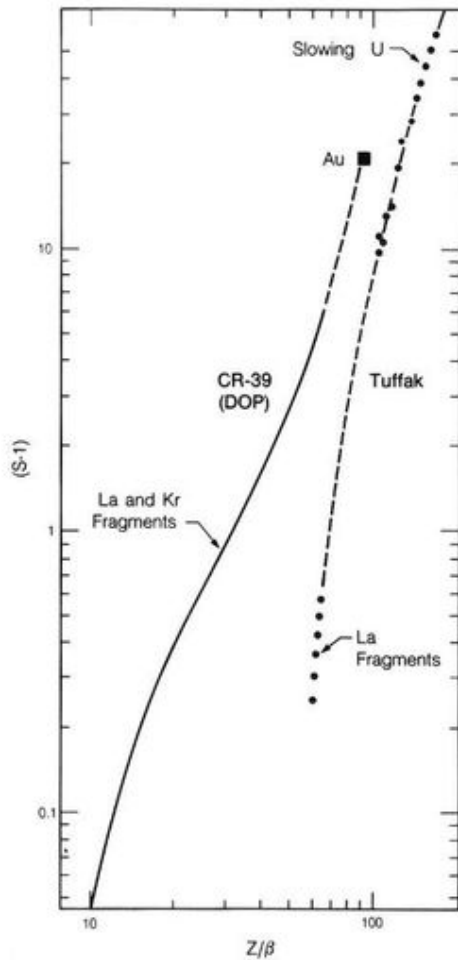


FIGURE 4.16 The curves of $V_T/V_B - 1$ versus Z_{eff}/β for CR-39 (DOP) and Tuffak polycarbonate. From these curves one can see that V_T for both CR-39 and Tuffak increases steeply in the range $10 \leq Z_{eff}/\beta \leq 92$ and $55 \leq Z_{eff}/\beta \leq 105$, respectively. Here $s = V_T/V_B$. (From Salamon et al., 1985; printed with permission from Elsevier © 1985)

using polycarbonate (Price et al., 1985), polyethylene terephthalate (Tretyakova et al., 1985; Barwick et al., 1985), barium phosphate glasses (Bonetti et al., 1993a, 1993b), BP-1 glass (Price et al., 1992), PSK-50 phosphate glass (Wang et al., 1987; Price et al., 1991; Moody et al., 1989, 1992; Bonetti et al., 1991), LG-750 phosphate glass (Wang et al., 1989; Moody et al., 1987), and phosphate glass (Tretyakova et al., 2001).

D. Track Diameter Method for Identification of Charge Z at High and Relativistic Energy

Experiments show that heavy ions (projectiles) with charge Z at high and relativistic energy will interact with nuclei in targets or detectors and form a series of projectile fragments with charge $Z - 1, Z - 2, \dots$. These fragments have nearly the same velocity

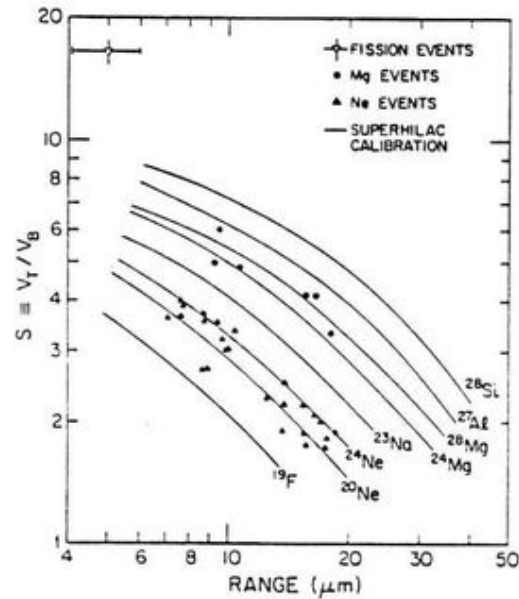


FIGURE 4.17 The relations between track-reduced etch rates and residual ranges of some nuclei with different charge Z and A (isotopes) in phosphate glass (PSK-50, Schott Glass Technologies, Inc.) (From Wang et al., 1987; printed with permission from Phys. Rev. C36, 2717-2720 (1987). Copyright 1987 The American Physical Society)

as the original projectiles. These interactions and their fragments can be used to calibrate the track detector, such as CR-39, to obtain its charge resolution σ_Z (standard deviation of charge Z) in charge identification.

The procedure of calibration of the track detector is as follows: (1) A thick stack of nuclear track detectors, such as CR-39, consisting of several or more than 10 sheets is irradiated with projectiles perpendicularly to the surface of the detectors to a dose of $\sim 10^6 \text{ cm}^{-2}$. (2) After etching the detectors at appropriate etching conditions, tracks of projectiles and fragments can be seen under an optical microscope. (3) The diameters of the tracks are scanned with an optical microscope or a track image analyzing instrument on one surface of the detector. The track diameter distribution is drawn as a histogram. If the scanned surface belongs to the sheet in the middle of the stack, the histogram of the track diameter distribution will show a series of peaks. The highest peak on the right hand (on larger diameter side) belongs to the projectiles (when matching the tracks with the tracks on the front surface of the first sheet, one will understand this conclusion). The charge corresponding to the highest peak is Z (the charge of the projectiles). The charge of the second peak (on the left side of the highest peak) is $Z - 1$, then, the third is $Z - 2$, and so on. (4) The average diameter \bar{D} and standard deviation σ_D are calculated from all the diameters of each peak. (5) The slope $\delta D/\delta Z$ is calculated in the figure of \bar{D} versus Z at each charge. (6) The charge resolution $\sigma_Z(1)$ is calculated from equation $\sigma_Z(1) = \sigma_D/(\delta D/\delta Z)$, where $\sigma_Z(1)$ is the charge resolution on a single surface for a given charge Z. (7) One can follow the same projectile to the next and the third and

more surfaces to measure the track diameters of the same projectile. Then, one can obtain a mean of the diameters in successive surfaces for the same projectile. When all the means for all the projectiles have been obtained, one can draw a new histogram of the distribution of the mean for all the projectiles averaged over all the surfaces. For example, in n surfaces, the peaks in the new histogram are narrower than those obtained on a single surface. One can calculate a new average diameter and its standard deviation $\sigma_D(n)$ for each peak. This $\sigma_D(n)$ is for n surfaces for each charge Z (each peak). A new δ_D/δ_z at each charge (or peak) can be obtained. The final charge resolution $\sigma_z(n) = \sigma_D(n)/(\delta_D/\delta_z)$ can be calculated, which is for all projectiles in each peak (each charge Z) averaged over all the surfaces. It has been shown that $\sigma_z(n) = \sigma_z(1)/\sqrt{n}$ is correct. The correctness shows that the energy loss in each sheet of the detector and in all the detectors for measuring the n track diameters is negligible compared with the total energy of the projectile. This means that the velocity ($\beta = v/c$) of the projectile approximates no change when the projectile is traveling through the stack which is measured. (8) One should point out that the correctness of the $1/\sqrt{n}$ relationship is conditional, which is as follows: When a heavy ion (projectile) is passing through the detectors (or stopping materials), it might pick up one or more electrons from the detector atoms to fill in its own inner shell orbits. The effective charge of the projectile changes to $Z - 1$ or $Z - 2$. This phenomenon disrupts the original charge state and makes the charge resolution become poorer than the $1/\sqrt{n}$ relation. This problem can be overcome by using stripping foils interleaved in the detector stack (Ahlen et al., 1984; Salamon et al., 1984; Guo et al., 1984a).

Figure 4.18 shows a histogram of charge distribution of nuclear interaction fragments from a 1.85 GeV/u ^{40}Ar beam in CR-39 (DOP) stack by track diameter measurement; after averaging over 16 cones on surfaces of eight sheets of the detector, the charge resolution $\sigma_z(16) = 0.06e$ (Price et al., 1983; Salamon et al., 1984).

It should be pointed out that the charge resolution of CR-39 is much higher than that of Si semiconductor detector with

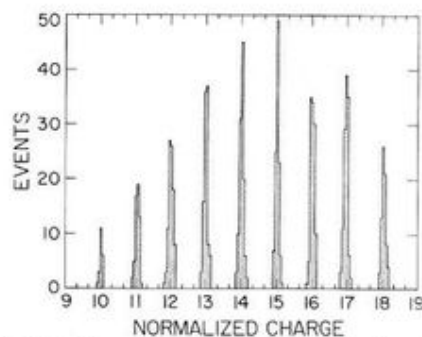


FIGURE 4.18 A histogram of charge distribution of nuclear interaction fragments from a 1.85 GeV/u ^{40}Ar beam in CR-39 (DOP) stack by track diameter measurement; after averaging over 16 cones on surfaces of eight sheets of the detector, the charge resolution $\sigma_z(16) = 0.06e$ (From Price et al., 1983; Salamon et al., 1984; Reprinted with permission © 1983 the American Physical Society. http://prj.aps.org/abstract/PRL/v50/i8/p566_1). CR-39 (DOP) is a special type of CR-39 (see Section II. C. 1. above).

equivalent thickness. Tarle et al. (1981) were the first to demonstrate that the etch track detector CR-39 has a charge resolution superior to semiconductor detectors of equivalent thickness. Ahlen (1980) theoretically predicted the superiority of the charge resolution of plastic track detectors to those of scintillator, nuclear emulsion, ionization chamber, and semiconductor detectors for high- and relativistic energy heavy ions. The reason for the higher charge resolution of plastic track detectors is as follows:

According to the restricted energy loss or the REL model (Benton, 1970), it is assumed that knock-on electrons with energy greater than ω_0 (350–1000 eV) are ineffective in causing the permanent radiation damage. The high-energy δ -rays deposit most of their energy quite far from the particle track. They do not contribute significantly to the primary track. Only the low-energy δ -rays deposit energy in the core region of the track, which is effective for etching. Ionization chambers and solid-state Si detectors correspond to total energy loss, including δ -rays of all energies. Scintillators and nuclear emulsions correspond to the δ -rays with energy higher than 1500 eV. Due to Poisson fluctuations in the collision frequency between the charged projectile and electrons within the detector medium, a large number of low-energy δ -rays are produced. The number of δ -rays then falls off rapidly as the δ -ray energy increases. The fluctuation of the number of high-energy δ -rays is the largest, which results in poor charge resolution of the scintillation detectors and nuclear emulsions. The fluctuation of the effective δ -rays is smaller in ionization chambers and Si detectors, which results in better charge resolution. The plastic track detectors correspond to δ -rays of low energy; the fluctuation is the least; thus, the charge resolution is the best for high- and relativistic energy heavy ions.

From a calibration with La, Kr, Fe, and Ar, Salamon et al. (1985) obtained the following empirical relation between charge resolution σ_z and Z/β of heavy ions for CR-39 (DOP) detector:

$$\sigma_z = \frac{1}{\sqrt{n}} \left[0.914 + 1.94 \times 10^{-3} \left(\frac{Z}{\beta} \right) + 4.35 \times 10^{-5} \left(\frac{Z}{\beta} \right)^2 \right] e \quad (4.26)$$

Similar calibrations have been made by several groups with similar results (Heinrich et al., 1995; Cecchini and Patrizii, 2008; Patrizii, 2001). From a calibration with Pb projectiles, Huntrup et al. (1997) achieved charge resolutions for a single etch cone $\sigma_z = 0.16e$ at $Z = 6$, $\sigma_z = 0.4e$ at $Z = 50$, and $\sigma_z = 1.0e$ at $Z = 82$ for a CR-39 detector.

He et al. (1994) found that BP-1 glass (Wang et al., 1989) has charge resolution $\sigma_z(1) = 0.19e$ with only a single ($n = 1$) measurement of an etch pit of ions with $Z = 79$ and $\beta = 0.997$. This charge resolution is equivalent to that of ~ 16 successive cone measurements in a CR-39 detector stack according to the law $\sigma_z(n) = \sigma_z(1)n^{-1/2}$. Better charge resolution of BP-1 glass can be achieved by measuring many successive track cones along the same particle trajectory. The unprecedented charge resolution of BP-1 glass opens up several fields of applications in nuclear physics, high-energy heavy-ion physics, and cosmic-ray astrophysics.

Track diameter identification of charges Z at relativistic energy has been used in many projects including the following:

- (1) Searching for fractionally charged particles such as charges of $Z + \frac{1}{3}$, $Z + \frac{2}{3}$ in projectile fragmentations (Price et al., 1983; Price, 2005; He and Price, 1991; Cecchini et al., 1993; Heinrich et al., 1995).
- (2) Measurements of charge pick-up cross section, in which the projectile picks up one or two charges (Ren et al., 1989; Jin et al., 1990; Price, 2008; Westphal et al., 1991).
- (3) Relativistic projectile fission studies (Guo et al., 1984b, 1986a).
- (4) Measurements of compositions of ultra-heavy cosmic rays (Westphal et al., 1998).
- (5) Cross sections for orbital electron capture and stripping of ions in stopping materials (Westphal and He, 1993).
- (6) Charge-changing fragmentation cross section (Cecchini and Patrizii, 2008, 2002; He and Price, 1994).

Compared with other types of radiation detectors, such as Au-Si-surface-barrier detectors ($\Delta E - E$ detectors), nuclear emulsions, and others, the solid-state track detector has also the following advantages (Price and Fleischer, 1970) for the identification of charge Z of particles:

- (1) Identification of heavy particles recorded during the ancient time.
- (2) Identification of very rare heavy particles such as those that occur at an extremely low rate as one per cm^2 per year (see Chapter 1, Section XII.A).
- (3) Identification of heavy particles in a high background of less heavily ionizing particles.
- (4) Identification of particles of very high ionization rate for which resolution of solid-state track detectors exceeds that of other detectors.
- (5) Cross sections for orbit electron capture and stripping of ions in stopping materials (Westphal and He, 1993).
- (6) Charge-changing fragmentation cross sections (Cecchini and Patrizii, 2008, 2002; He and Price, 1994).

E. Track Length Method for Identification of Charge Z at High and Relativistic Energy

This method is similar to the track diameter (D) method, whereby the length (L) of an etched cone at high and relativistic energy can also be used to identify charges Z (Giacomelli et al., 1998). The study shows that with a CR-39 sheet for one cone height (length) measurement, the charge resolution can reach $\sigma_z \approx 0.19-0.29e$ for $Z = 74-82$. In other words, one can separate nuclear fragments of high Z ($Z \geq 74$) by one cone length (L) measurement in a CR-39 detector. The track cone length (L) method has a better charge resolution in the charge region $74 \leq Z \leq 82$ than the track diameter (D) method (Giacomelli et al., 1998).

The track length method has been used to measure the charge-changing cross sections of $158 \text{ AGeV } ^{207}\text{Pb}$ with Bi, Al, Cu, and Pb targets. The data can be described by strong electromagnetic dissociation (Sher et al., 2007; Manzoor et al., 2000).

VII. TRACK FADING AND ANNEALING

This section describes the phenomenon of track fading and how to use this phenomenon to increase precision in the analyses of radioactivities.

A. Track Fading and Annealing

Latent tracks or radiation-damaged materials at higher temperature will gradually disappear. This process is called track fading. Track annealing fading is an intrinsic behavior of latent tracks or radiation-damaged materials. Track annealing describes the same behavior of latent tracks but stresses the existence of an external factor, such as laboratory heating or heated by magma intrusion in the earth's crust.

Track fading appears as (1) shortening of the etched track length; (2) reduction of the etched track opening; and (3) reduction of the number of tracks observable on internal surface compared with the fresh tracks of the same kind of particles.

B. Mechanisms of Track Fading

Track fading occurs presumably by the diffusion of atoms in the damaged region of inorganic solids or movements of molecular fragments within a polymer. Interstitial atoms can then recombine with lattice vacancies, and broken molecular chains may rejoin and the existed active species recombine. The activation energies of $\sim 1-2 \text{ eV}$ for track annealing support this conclusion.

From thermal dynamics, one can write

$$D = D_0 e^{-E_a/kT} \quad (4.27)$$

where D is the diffusion coefficient, E_a is the activation energy for annealing, k is the Boltzmann constant, and T is the absolute temperature.

The time to diffuse to some extent is inversely proportional to the diffusion coefficient D :

$$t \sim \frac{1}{D} \sim e^{E_a/kT} \quad (4.28)$$

From Eqn (4.28) one can see that the larger the activation energy E_a , the longer time it takes to remove the latent tracks; and the higher the temperature in the annealing device, the shorter will be the time it takes to erase the latent tracks.

C. Arrhenius Diagram

Equation (4.28) can be written as

$$\log t = c + \frac{E_a}{k} \frac{1}{T} \quad (4.29)$$

The relation between $\log t$ and $1/T$ can be drawn as a straight line as in Fig. 4.19.

From the slope of the straight line, one can derive the activation energy E_a for track annealing.

It should be noted that the activation energy E_a is related to the degree of annealing, that is, how large a percentage of the

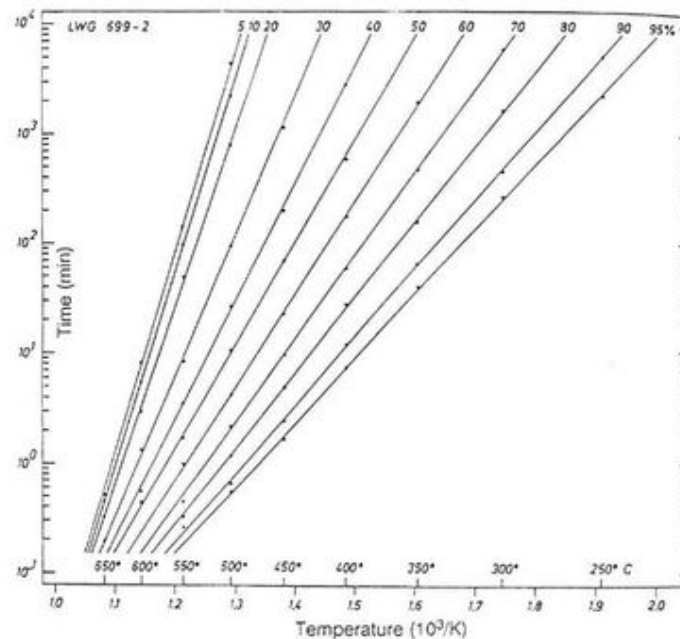


FIGURE 4.19 Arrhenius diagram between $\log(t)$ and $1/T$. The slope is E_a/k , from which one can determine the activation energy E_a for track annealing. (From Wagner and Van den haute, 1992. Reprinted with kind permission from Springer Science + Business Media © 1992)

tracks are annealed away, or how many of the tracks (percent) are lost in the annealing process on the internal surface of a mineral. Therefore, annealing time t , annealing temperature T , and annealing degree are three parameters; from any two, one can determine the third.

D. Application of Track Fading and Annealing

The track-fading phenomenon has two sides or characteristics. On one side, it can cause problems, and on the another side, it can provide new information or improve analytic accuracy.

1. Problems Resulting From Track Fading

The problems that may arise from track fading are the following:

- Particle tracks would be lost or partly lost if one carelessly manages the experiments or etching at an excessively high-temperature and etching that lasts for too long. Usually, for the etching tracks of plastic track detectors, the etching temperature should not exceed 70 °C in order that the annealing remains negligible.
- As elevated temperature speeds the annealing process, the temperature of irradiation environments should not be higher than that allowed by the detector. For example, the temperature for irradiation of plastic track detectors should not be higher than 70 °C. If the temperature is higher than 70 °C, one should use muscovite mica track detectors instead of plastic track detectors. Muscovite mica can retain 100% of the tracks up to 450 °C for 1 h (Fleischer et al., 1975).

2. Improving Analysis with the Aid of Track Annealing

Track annealing can be used to provide an experimental advantage, as described as follows:

- Muscovite mica is a fission detector, but it contains spontaneous fission tracks of ^{238}U . By annealing muscovite sheets over 600 °C, for more than 1 h, one can remove the spontaneous tracks from mica. Thus, one can produce very clean detectors without track background.
- In fission track dating, the detection efficiency of an external detector is usually different from that of the minerals to be dated. In this situation, one can use the same type of minerals as detectors for uranium determination. The detection efficiency will be equal to that of minerals for dating. In this case, one can anneal out all the latent spontaneous fission tracks in one aliquot of the minerals. This aliquot will be used to determine the uranium concentration of the minerals in a nuclear reactor by neutron-induced fission measurements. Another aliquot is left for the ^{238}U spontaneous fission number measurement. Both aliquots are mounted, ground, polished, and etched in the same condition. The detection efficiencies of the minerals for dating and for uranium determination will be equal to each other, which can be canceled in the age equation. In this way, the dating precision can be improved.

3. Apparent Fission Track Age and Its Corrections

Fission track dating is based on the number of ^{238}U spontaneous fission tracks accumulated in a mineral from the formation of the

mineral. If the temperature of the geological body containing the mineral was too high to retain fission tracks, the tracks formed in this period would be completely lost. After the geological body cooled down to some temperature (upper limit temperature of partial annealing zone (PAZ) of the mineral), ^{238}U spontaneous fission tracks would be retained, but they would be annealed partially by any higher temperature that existed later on. Only when the temperature cooled down to the lower limit temperature of the partial annealing zone, can the spontaneous fission track be retained completely. The tracks formed in the partial annealing zone (PAZ) would be shorter than the original tracks. This shortening of the tracks would reduce the number of tracks etched on the internal surface of the mineral, consequently reducing the measured age by fission track dating. The reduced fission track age is named apparent fission track age.

Apparent fission track age can be corrected to true age. There are three methods to make this correction: (1) track length correction method; (2) track diameter correction method; and (3) Plateau-age correction method. For a detailed treatment on these methods, the reader is referred to the books written by Fleischer et al. (1975), Durrani and Bull (1987) and Wagner and Van den haute (1992).

4. Geothermal Chronology

^{238}U spontaneous fission-fragment tracks are prints formed in minerals since the fission events occurred. Track annealing by follow-up thermal events makes secondary prints on fission tracks. Every track contains plentiful records of the thermal history which the mineral experienced since it was registered. The tracks were registered at different times (year or age). Comparisons, subtractions, and differentiations of the records contained in different tracks can retrieve the whole geothermal history from the time when the first spontaneous fission track was created in the minerals. Chambaudet et al. (1993) suggested a model coined as the "Smoke Convection Model" to retrieve the thermal history experienced by mineral, such as apatite. The authors claimed that it can retrieve the thermal history uniquely. Geothermal chronology has become a hot spot in geology and nuclear tracks in solids. For more information on this field of measurements, the reader is referred to review articles written by Reiners and Brandon (2006), Reiners and Ehlers (2005), and Bernet and Garver (2005).

VIII. INSTRUMENTATION

A. Size of Latent Tracks and Etched Tracks

The lower limit of the diameter of etchable latent tracks is about 30–40 Å (3–4 nm), and the etched track diameter can range from this size to more than 100 μm (Fleischer, 1981). The first instrument to study latent tracks was the transmission electron microscope (TEM; Silk and Barnes, 1959; Price and Walker, 1962a). The first instrument to study etched tracks was the optical microscope (Young, 1958; Price and Walker, 1962c).

Before the 1980s, there was no way to see the structures of latent and etched tracks in the range below the nanometer (nm). The dream of imaging subnanometer-size tracks was realized in

1982 by the discovery of the scanning tunneling microscope (SFM) (Binnig et al., 1982) and in 1986 after the discovery of the atomic force microscope (AFM) (Binnig and Quate, 1986).

B. Optical Microscope

The optical microscope can be used to analyze etched tracks in the size range of ~0.5 μm to several hundreds of μm. Optical microscopes are composed of (1) eyepiece (one or two), (2) objective (one or more), (3) stage, (4) condenser (transmitted light and reflected light), and (5) stand.

The accessories should include: (1) standard ruler, used to calibrate the scales; (2) reticule, which can be put in the eyepiece for measurement of track or field size; (3) reticulate, which is used as a standard area for the measurement of track density (tracks/cm²); (4) displacement transducer (one, two, or three), at least one for the measurement of depth (z-axis). Another two are for x- and y-axis measurements.

C. Track Image Analyzer

The composition of a track image analyzer includes (1) optical microscope, with x, y and z controllers; (2) CCD camera; (3) image plate; and (4) computer.

The parameters which can be reported by a track image analyzer are: (1) track number; (2) track width, major axis and minor axis; (3) track length; (4) track coordinates (x, y, z); (5) track orientation (Zenith angle θ , azimuth angle ϕ); (6) area of measurement; (7) areal density of tracks; and (8) gray level of tracks.

D. Electron Microscope

The electron microscope is operated in a vacuum. It can be classified into two types. One type is the transmission electron microscope (TEM), which requires a very thin solid as a track detector, such as a mica flake. Its resolution usually is about 1 nm–10 μm. Very high voltage and antivibration transmission electron microscopes can even resolve individual atoms. Another type is the scanning electron microscope (SEM), which can resolve about 2 nm–50 μm. When using a scanning electron microscope to measure tracks, it is best to have a sputter coater or a vacuum evaporation chamber to prepare a conductive layer on the surface of the etched detector so that the detector surface changes to be conductive to electrons.

E. Scanning Tunneling Microscope (STM) and Atomic Force Microscope (AFM)

The scanning tunneling microscope is used to scan electronic conductive substances, and the atomic force microscope (AFM) can measure insulating solids, which is characteristic of solid-state nuclear track detectors. The above microscopes are capable of resolving individual atoms. Figure 4.20 shows a photograph of an etched α -recoil etch pit taken by an atomic force microscope (AFM). In this photograph one can see three segments of track. Each segment represents one emission of α -particle. The ^{238}U nucleus and its progeny may have eight

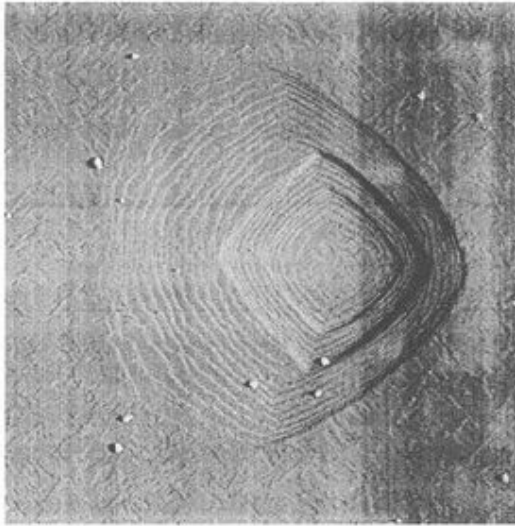


FIGURE 4.20 Photograph of an α -recoil track taken by an atomic force microscope (AFM). This track can be seen with three segments. Each segment was produced by one α -emission. Three segments are consecutively by three α -emissions. The ^{238}U nucleus and its progeny can have 8 α -emissions. At most it may leave 8 segments in the α -recoil track. ^{232}Th nucleus and its progeny can emit 6 α -particles. Their progeny nuclei are ^{226}Pa , ^{224}Ra , ^{220}Rn , ^{216}Po , ^{212}Pb , and ^{208}Pb , respectively. At most, it may leave 6 segments in the α -recoil track. (From Price, 1993; printed with permission from Elsevier © 1993)

α -particle emissions to decay to ^{208}Pb and at the most can create eight segments in an α -recoil track (Price, 1993). Each segment has several steps. Each step in the photograph is 2 nm in height.

Figure 4.21 shows a photograph taken by an atomic force microscope (AFM) of a 200 keV Ag etch pit showing 1 nm steps joining pairwise. One nm is the distance between the two neighboring layers of potassium (K) atoms in the structure of muscovite mica. The layers of K atoms are known as easily cleavage planes. These layers separate the tightly bound Si—O—Al structure, i.e. the TOT structure. Here T means tetrahedron structure within which one Si atom is in the center and three oxygen atoms at the four pinnacles of the tetrahedron. O means octahedron which is composed of Si—O or Al—O. The TOT structure is very rigid. This structure forms the step during etching. The pairing of two steps reflects the etching behavior of mica as explained by Price (1993).

From Figure 4.20 and 4.21, one can see that the atomic force microscope is a unique tool to study the etched track structure and track-etch kinetics.

F. Spark Counter

The spark counter was first devised by Cross and Tommasino (1968), which is a very simple device, and it is a very fast counter of tracks recorded in thin foils of track detectors. The advantages of this device are: (1) It is quite accurate in counting tracks. (2) The track spots sparked in the thin foil can be seen with the naked eye. The spot distribution reflects the particle distribution entered into the detector foil. (3) It is a fast counting device. Usually, it



FIGURE 4.21 Photograph of an etch pit of a 200 keV Ag track in muscovite mica. The black lines are etched steps bit by the HF etchant. The central part of the etch pit is the tip of the track. In certain directions, two steps join together. The height of one single step is 1 nm. The height of the joining step is 2 nm. The pairing of two steps reflects the etching property of muscovite mica by HF etchant. (From Price, 1993; printed with permission from Elsevier © 1993)

takes several seconds to 10 s to count all the tracks in a piece of track detector. This device is widely used in dosimetry of Rn and neutrons and in autoradiography (Eappan and Mayya, 2004).

For more information, the reader is referred to the original article by Cross and Tommasino (1968), and a book by Durrani and Bull (1987).

PART 2 APPLICATIONS

I. INTRODUCTION

Applications of nuclear track detectors are widespread in science and technology, among which the most important fields are as follows:

- (1) Physical sciences including low- and high-energy physics, astrophysics, cosmic-ray physics, plasma physics, nuclear reactor physics, and elemental analysis.
- (2) Earth and planetary sciences including fission track dating, geothermal chronology, meteorite studies, lunar and solar particles, uranium and petroleum exploration, and earthquake prediction.
- (3) Life and environmental sciences, which include radiation protection dosimetry, radon and thoron monitoring, neutron dosimetry, and radioactive contamination.
- (4) Nanotechnology and material sciences.

This chapter focuses on the most common and newly emerged fields of application.

II. PHYSICAL SCIENCES AND NUCLEAR TECHNOLOGY

Nuclear science is the first field of application of etch track detectors (Price and Walker, 1962e). A large number of

examples of research in the physical sciences with etch track detectors were reviewed in the journal articles and monographs (Fleischer et al., 1965a, 1975; Durrani and Bull, 1987). Some new research and results will be introduced below.

A. Cluster Radioactivities

Since the 1980s, the application of solid-state nuclear track detectors to heavy-ion detection has gained great success. One of the extremely exciting achievements is a series of discoveries in heavy-ion emission from nuclei called cluster radioactivity, or heavy-ion decay of nuclei. The first discovery of this type of nuclear decay ($^{223}\text{Ra} \rightarrow ^{14}\text{C} + ^{209}\text{Pb}$) was made with a silicon $\Delta E - E$ detector (Rose and Jones, 1984); however, for further discoveries in this field, the silicon detector cannot work well because the branching ratio of heavy-ion decay to α -decay is too low ($< 10^{-10}$). The solid-state nuclear track detector can be used to find and identify the tracks of the rare heavy ions in a very intensive α -track background. The branching ratio of ^{14}C decay from ^{223}Ra is $B = 3.98 \times 10^{-10}$ which already reaches the bare limit of detection of the silicon detector. For other nuclei with branching ratios below this limit, the nuclear track detector is the only capable detector for the discovery of this type of decay.

Up to now, more than 20 parent nuclei with $Z = 87-96$ and $Z = 56$ were discovered having cluster radioactivity. They are $Z = 87$ (^{221}Fr), $Z = 88$ ($^{221}, ^{222}, ^{223}, ^{224}, ^{226}\text{Ra}$), $Z = 89$ (^{225}Ac), $Z = 90$ ($^{228}, ^{230}, ^{232}\text{Th}$), $Z = 91$ (^{231}Pa), $Z = 92$ ($^{232}, ^{233}, ^{234}, ^{235}\text{U}$), $Z = 93$ (^{237}Np), $Z = 94$ ($^{236}, ^{238}\text{Pu}$), $Z = 95$ (^{241}Am), $Z = 96$ (^{242}Cm), and $Z = 56$ (^{114}Ba).

Up to now, 11 species of emitted heavy ions with $Z = 6, 8, 9, 10, 12,$ and 14 were discovered in this type of nuclear decay. The emitted heavy ions are: $Z = 6$ ($^{12}, ^{14}\text{C}$), $Z = 8$ (^{20}O), $Z = 9$ (^{23}F), $Z = 10$ ($^{24}, ^{25}, ^{26}\text{Ne}$), $Z = 12$ ($^{28}, ^{30}\text{Mg}$), and $Z = 14$ ($^{32}, ^{34}\text{Si}$).

In total, 11 species of daughter nuclei with $Z = 80, 81, 82, 83,$ and 50 were formed in the decay. They are: $Z = 80$ ($^{205}, ^{206}\text{Hg}$), $Z = 81$ (^{207}Tl), $Z = 82$ ($^{207}, ^{208}, ^{209}, ^{210}, ^{211}, ^{212}\text{Pb}$), $Z = 83$ (^{211}Bi), and $Z = 50$ (^{102}Sn). The daughters are the nuclei with magic number in Z (82, 50) or close to magic number in Z (80, 81, and 83 are close to magic number 82) (Price, 1993, 1994, 2005; Guglielmetti et al., 1995; Tretyakova et al., 1992). For a more detailed treatment of cluster radioactivity, see Section IV.E of Chapter 1.

The half-life $T_{1/2}$ and branching ratio B measured with nuclear track detectors for heavy-ion emission modes are listed in Table 4.2.

B. Heavy-Ion Interactions

1. Relativistic Projectile Fragmentation

Since the 1980s, another exciting application of solid-state nuclear track detectors in nuclear physics is the identification and study of heavy ions resulting from high and relativistic energy fragmentation of nuclei carried out in Berkeley (Bevalac), Brookhaven, and CERN.

These studies have opened a new branch of application in high-energy physics, astrophysics and cosmic rays (He and

Price, 1995; Price, 2005, 2008; Cecchini and Patrizzii, 2008; Manzoor et al., 2000; Grabez and Dragic, 2008).

It has been calibrated that the CR-39 has very high charge resolution $\sigma_Z \leq 0.5e/\sqrt{n}$ for relativistic nuclei of $10 \leq Z \leq 65$ by measuring etch pit diameters, where n is the number of successive etch pits measured along the trajectory of a nucleus, as illustrated in Fig. 4.22 (Salamon et al., 1985). The value of n can be larger than 10 for CR-39 with a detector thickness of 0.72 mm for each sheet. The charge resolution is high enough to assign the charges of fission fragments.

Owing to the high charge resolution of CR-39, relativistic projectile fission of 1 AGeV Au nuclei in CR-39 has been studied (Guo et al., 1984b). They observed that some Au projectiles were broken into two fragments in a CR-39 stack composed of 80 sheets each in size $15 \times 15 \times 0.072 \text{ cm}^3$ doped with 1% dioctyl phthalate. After a calibration of track diameter D to charge Z , they could determine the charge Z of each fragment in the fission events. By measuring the zenith and azimuth angles of each fission fragment with respect to the direction of the projectiles, they could determine the total energy release of each event and the interaction nature between the projectile and the target nucleus C, H, or O in the CR-39. They showed that the energy release in projectile fission is consistent with that of low-energy fission, and the transverse momentum transferred to fissioning species is consistent with a peripheral interaction. The mass distribution of fission fragments is very broad as that of fission of nuclei with $28 \leq Z \leq 83$ by 600 MeV and 1 GeV protons (Guo et al., 1986a).

The above example shows that CR-39 is one of the best detectors to possess the highest charge resolution for fission fragments at relativistic energy region.

2. Sequential Fission after Inelastic Collisions

The crystal structure of muscovite mica is anisotropic. The bulk etch rate by hydrofluoric acid parallel to the cleavage surface V_{\parallel} is much larger than that perpendicular to the cleavage V_{\perp} , that is $V_{\parallel} \gg V_{\perp}$, and the track-etch rate V_T for fission fragments is several thousand times larger than V_{\parallel} . These properties make the ranges of fission fragments stable after etching. Taking this advantage of muscovite mica, Brandt and co-workers opened up a new field of research on sequential fission of heavy nuclei, such as $\text{U} + \text{U}$, $\text{U} + \text{Pb}$, breaking into 3, 4, 5 pronged fission events in low-energy region (Brandt, 1980; Vater et al., 1977, 1986; Gottschalk et al., 1979, 1983; Khan et al., 1980; Qureshi et al., 1994, 1998a, 1998b, 2005; Khan, 1985; Shahzad et al., 1999).

In this field of research, the energy and mass of fission fragments cannot be derived from the shapes of tips, but by the ranges (lengths), zenith and azimuth angles of the fragment tracks and by mass and energy conservations (Gottschalk et al., 1983).

C. Nuclear Fission and Neutron Physics

1. Nuclear Fission

In nuclear fission, two fission fragments are emitted in opposite direction. (A small number of fission events ($< 1/300$)

TABLE 4.2 Cluster Radioactivity Nuclei Discovered or Confirmed by Solid-State Nuclear Track Detectors

Parent nucleus	Heavy ion emitted	Daughter nucleus	E_k (MeV)	Measured half-life $\log T$ (sec)	Branch ratio $-\log B$
^{221}Fr	^{14}C	^{207}Tl	29.28	14.5 ± 0.12	12.00 ± 0.12
^{221}Ra	^{14}C	^{207}Pb	30.34	13.0 ± 0.2	11.7 ± 0.2
^{222}Ra	^{14}C	^{208}Pb	30.97	11.0 ± 0.06	9.4 ± 0.06
^{223}Ra	^{14}C	^{209}Pb	29.85	15.2 ± 0.05	9.2 ± 0.05
^{224}Ra	^{14}C	^{210}Pb	28.63	15.8 ± 0.12	10.3 ± 0.12
^{225}Ac	^{14}C	^{211}Bi	28.57	17.16 ± 0.06	11.2 ± 0.06
^{226}Ra	^{14}C	^{212}Pb	26.46	21.3 ± 0.2	10.6 ± 0.2
^{228}Th	^{20}O	^{208}Pb	44.72	20.7 ± 0.08	12.9 ± 0.08
^{231}Pa	^{23}F	^{208}Pb	46.68	26	14
^{230}Th	^{24}Ne	^{206}Hg	51.75	24.6 ± 0.07	12.3 ± 0.07
^{232}Th	^{26}Ne	^{206}Hg	49.7	>27.9	>10.3
^{231}Pa	^{24}Ne	^{207}Tl	54.14	22.9 ± 0.05	10.9 ± 0.05
^{232}U	^{24}Ne	^{208}Pb	55.86	20.5 ± 0.03	11.1 ± 0.03
^{233}U	^{24}Ne	^{207}Pb	54.27	24.8 ± 0.03	12.1 ± 0.03
^{233}U	^{25}Ne	^{208}Pb	54.32		
^{234}U	^{24}Ne	^{210}Pb	52.81	25.9 ± 0.2	13.0 ± 0.2
^{234}U	^{26}Ne	^{208}Pb	52.87		
^{235}U	^{24}Ne	^{211}Pb	51.50	>27.4	>11.1
^{235}U	^{25}Ne	^{210}Pb	51.68		
^{233}U	^{20}Mg	^{205}Hg	65.32	>27.8	>15.1
^{234}U	^{20}Mg	^{206}Hg	65.26	25.7 ± 0.2	12.8 ± 0.2
^{237}Np	^{30}Mg	^{207}Tl	65.52	>27.4	>13.6
^{236}Pu	^{20}Mg	^{208}Pb	70.22	21.7 ± 0.3	13.7 ± 0.3
^{238}Pu	^{30}Mg	^{208}Pb	67.00	25.7 ± 0.25	16.3 ± 0.25
^{238}Pu	^{28}Mg	^{210}Pb	67.32		
^{238}Pu	^{32}Si	^{206}Hg	78.95	25.3 ± 0.16	15.9 ± 0.16
^{241}Am	^{34}Si	^{207}Tl	80.60	>25.3	>15.1
^{242}Cm	^{34}Si	^{208}Pb	82.88	>21.5	>14.4
^{114}Ba	^{12}C	^{102}Sn	~ 14.4	$T_c \geq 1.1 \times 10^3 \text{ s}$	$T \propto \geq 1.2 \times 10^2 \text{ s}$

release a third particle, called ternary fission or even release a fourth particle, quaternary fission, which is outside the scope of this chapter.) To which directions (orientations) the two fission fragments fly away from the point of fission is a primitive question. Experiments show that fission events induced by thermal neutrons are isotropic. Other fission events are all anisotropic, even in the center of mass system. The emitted fission fragments have some kind of preference in directions. In order to clarify the phenomenon of the anisotropic distribution, many experiments and theoretical studies have been carried out.

The solid-state nuclear track detector has been used in the measurements of angular distribution of fission fragments

emitted from fission. The angular distribution of fission fragments is dominated by the properties of the transit state at fission barrier of fissioning nuclei. In the transit state, fission occurs only through one or a few channels at low energy. The characteristics of the transit state will be reflected in the angular distribution of fission fragments. Solid-state nuclear track detectors, such as muscovite mica and polycarbonate (Lexan and Makrofol), can cover very large angles from -0° to -180° and can withstand the bombardments of intense light beam particles, such as γ -rays, neutrons, protons, α -particles, and nuclei even heavier than neons with higher energies. These detectors can clearly show the tracks of fission fragments and without background from the light particles of the

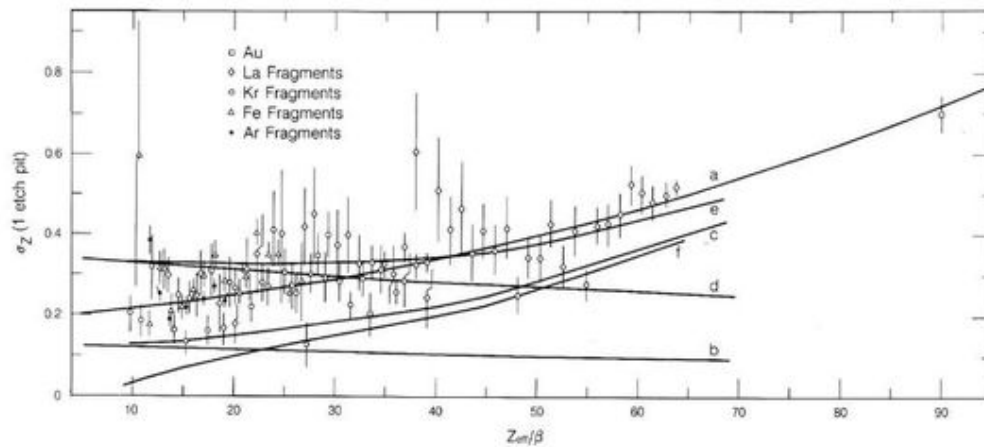


FIGURE 4.22 Measured charge resolution σ_z for a single etch pit ($n = 1$) as a function of Z_{eff}/β in CR-39. The curve a is a weighted least-squares quadratic fit to the data. (From Salamon, 1985; printed with permission from Elsevier © 1985)

beams. Because of the importance to fission physics, many scientists have carried out this research with SSNTDs (Vandenbosch and Huizenga, 1973).

A thin fission source in a small area supported by a thin foil is placed on the beam of incident particles in a vacuum chamber. A mica or polycarbonate strip is bent into a circular arc and supported by a frame of aluminum and placed around the source at a distance and stretched to a large angle from -0° – 90° with respect to the beam direction. Fission fragments emitted from the source are recorded by the track detector. Measuring the track density in the detector for a certain range of angles can provide the angular distribution of fission fragments in this special condition (Zhou et al., 1981; Guo, 1982b).

2. Neutron Physics

The neutron is an uncharged particle. It cannot be recorded by direct ionization in detecting material, but it can be detected through its recoil nuclei or nuclear reaction products, which are energetic charged particles. Nuclear fission is the first reaction used for the detection of neutrons by solid-state nuclear track detector (Walker et al., 1963). ^{235}U , ^{237}Np , ^{238}U , and ^{232}Th are often used as the fissile materials. Figure 4.23 shows their relationships between fission cross sections and neutron energy.

The threshold energies for fission are respectively: ^{235}U (0), ^{237}Np (~ 0.1 MeV), ^{238}U (1.0 MeV), and ^{232}Th (1.17 MeV). The accurate data of the cross sections can be found in BNL 325, Third Edition, Volume II (1976). The fissile sources of ^{235}U , ^{237}Np , and ^{238}U can be electrolytically deposited on metal foils. The ^{232}Th source can be made by pressure in a mold from ThO_2 powder (Guo et al., 1976a). The effective thickness of the pressed ThO_2 tablet for recording fission fragments with muscovite mica covering on its surface has been calibrated (Guo et al., 1976a) to be: $\frac{1}{2}mR\cos^2\theta_c = 2.32 \pm 0.07 \text{ mgTh/cm}^2$, where m is the mass of ThO_2 in unit volume of tablet, R is the average range of fission fragments in the tablet, and θ_c is the

critical angle of muscovite mica for recording fission fragments ($3^\circ 41'$, see Guo et al., 1982).

The above fissile material mica sandwiches can be used separately to measure the flux or fluence of monoenergetic fast neutrons from accelerator neutron sources, or measure the neutron dose. Four sandwiches of detectors can be put together to measure the neutron spectrum by dividing the whole range of energy into intervals (Durrani and Bull, 1987).

D. Plasma Physics

1. Laser Acceleration

Since the year 2000, table-top accelerators of proton and heavy-ion beam have become a focus of interest in scientific research. It is expected that table-top accelerators based on laser–plasma interactions might replace the current heavy-ion accelerators, which are large in size and length up to more than several tens of meters or even more than several kilometers. A high-intensity laser beam could produce a >50 MeV proton beam. This result has attracted worldwide researchers to join in this new research field. The solid-state nuclear track detector, CR-39, has become the most important tool to study this phenomenon. The possible mechanism of proton acceleration by laser–plasma interaction is called Target Normal Sheath Acceleration (TNSA) whereby a high-intensity laser beam hits on a solid target (foil); the prepulse of the laser (the small pulse before the main pulse of laser shoot) creates a thin plasma layer at the surface of the foil. Then, the intense part of the pulse (the main pulse) of the laser shoot interacts with the thin plasma layer, which accelerates the electrons toward the foil by the ponderomotive force. Finally, the electron beam reaches the rear surface (the opposite surface to the laser irradiation) and creates a strong electrostatic field which first ionizes and then accelerates protons to high energy. When the electrons have passed the foil, they act as a sheath with negative charge. The electron sheath moves very quickly. It attracts

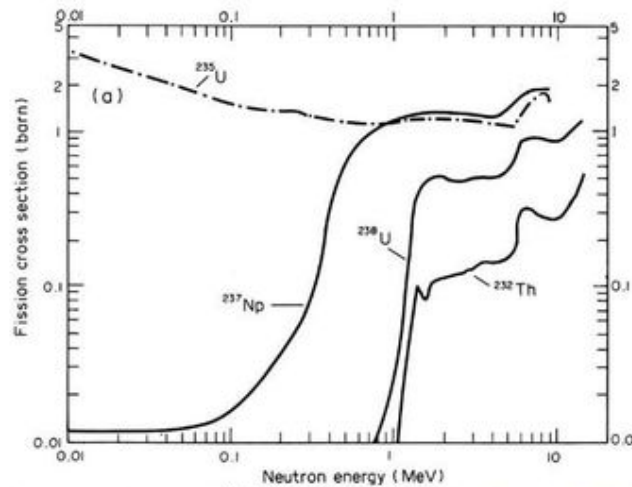


FIGURE 4.23 Fission cross sections versus neutron energy of ^{235}U , ^{237}Np , ^{238}U , and ^{232}Th . (From Durrani and Bull, 1987, reprinted with permission from Elsevier © 1987)

the positive protons to go to the same direction (normal to the surface of the foil). Following the electron sheath, the protons can reach a very high energy depending on the parameters of the laser and the foil. The target foil may be varied, and most accelerated particles are protons. These protons come from H_2O or hydrocarbon adsorbed on the surface of the foil.

The proton beam accelerated by laser-plasma interaction has the following properties: (1) The direction of the proton beam is normal to the surface of the target. The beam spread is less than 20° . It is nearly a collimated beam of protons. (2) The maximum proton energy is related to the laser intensity. Therefore, the proton energy is controllable by the laser beam. (3) The intensity of proton beams can reach 10^9 – 10^{13} protons per pulse. The usual frequency is about 10 pulses per second. It is strong enough for many applications. (4) The size of the beam source is about $10\ \mu\text{m}$, which is much smaller than that of the current heavy-ion accelerators.

Due to the above properties, laser acceleration is expected to feasibly replace some types of current big accelerators, to work as proton beam medical accelerators or spallation neutron sources.

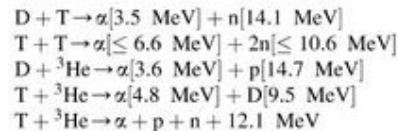
In laser acceleration, the proton beam duration is less than 10^{-12} s. In this very short time, more than 10^9 protons will reach the detector. Electronic detectors have a dead time. It is difficult to record a single proton and analyze its energy. In this case, the CR-39 is the best detector for recording a single proton and obtaining its energy.

Many laboratories are now carrying out laser acceleration studies with CR-39 track detectors (Snively et al., 2000; Ceccotti et al., 2007; Duan et al., 2009, 2010; Li et al., 2007; McKenna et al., 2005; Hicks et al., 2001).

2. Inertial-Confinement-Fusion

In inertial-confinement-fusion (ICF) induced by pulsed laser with high intensity and short time, the following primary fusion

reactions in the capsules will take place, in which α -particles are produced:



where D and T are the original compositions of the fuel in the capsule, and ${}^3\text{He}$ is the direct product of $\text{D} + \text{D} \rightarrow {}^3\text{He}$ [$0.82\ \text{MeV}$] + n [$2.45\ \text{MeV}$] reaction.

The best detector for recording α -particles in these reactions is CR-39 nuclear track detector (Seguin et al., 2003). The first actual instrument for measuring the charge-particle spectra in these fusion reactions was designed with electronic detectors, but it was eventually implemented with CR-39 detectors. The reasons for the big change of detector are due to the advantages of CR-39 detector, which are as follows: (1) The detection efficiency for the formed particles is high (about 100% for normal incidence). (2) The area coverage of CR-39 detector can be large and at various angles ($\sim 2\pi$ geometry being possible if necessary). (3) The energy resolution is higher by CR-39 than electronic detectors. (4) The immunity of CR-39 is superior to electromagnetic radiations (X-ray, γ -ray, and electric transients accompanied by shooting of the laser). (5) There is no overloading for less than $\sim 10^7\ \text{cm}^{-2}$ particles and no dead time compared with electronic detectors. (6) The detector has the ability to distinguish the types and energies of individual particles. CR-39 detector is used in many laser-plasma fusion laboratories throughout the world (Kacencar et al., 1982; Szydowski et al., 2009).

E. Astrophysics and Cosmic Rays

Astrophysics and cosmic-ray research is the oldest field of application since the discovery of solid-state nuclear track

detectors (Price and Walker, 1962c). Great achievements were made in the past 50 years with SSNTDs in research on the following:

- (1) Galactic cosmic rays
- (2) Solar particles
- (3) Ancient cosmic rays
- (4) Search for super-heavy elements in cosmic rays
- (5) Elementary and exotic particles

These studies with etch track detectors have been reviewed in the monographs of Fleischer et al. (1975) and Durrani and Bull (1987). Recent achievements are conveyed by the following authors: O'Sullivan (1995); Zhou et al. (2009); Doke (2008); Westphal et al. (1998); Hasebe et al. (2009); Yasuda et al. (2008); Weaver (2001); Weaver and Westphal (2002); Price (2005, 2008).

F. Nuclear Technology

1. Nuclear Reactor Physics

The basic physical processes in nuclear reactors are neutron-induced fission and the consequent fission release of neutrons. These processes continue as chain reactions. To study neutron number, flux, spatial distribution, and energy spectrum is one part of the work in reactor physics. Solid-state nuclear track detectors are used in these studies.

a. Determination of Neutron Temperature

In a steady-state operation of a nuclear reactor, neutrons and other molecules in the reactor are in thermal equilibrium. This state is described by temperature as in thermodynamics. The temperature is a decisive factor for the neutron energy spectrum in the thermal energy region. The neutron energy spectrum is considered to follow Maxwell energy distribution.

The principle of the determination of neutron temperature in a nuclear reactor is based on Westcott equation:

$$\tilde{\sigma} = \sigma_0 \left(g + r \sqrt{\frac{T_n}{T_0}} S_0 \right) \quad (4.30)$$

where $\tilde{\sigma}$ is the effective fission cross section of a given fissile nucleus for neutrons in the reactor; σ_0 is the fission cross section of the given nucleus for neutrons with velocity of 2200 m/s (for ^{235}U , $\sigma_0 = 582.6$ b; for ^{239}Pu , $\sigma_0 = 748.1$ b); g is a correction factor for non- $1/v$ fission cross section of the given nucleus in Maxwell neutron spectrum; $r\sqrt{T_n/T_0}$ is the relative ratio of epithermal neutrons (epithermal index); and S_0 is the correction factor for resonance absorption of the nucleus (resonance parameter). The variables g and S_0 are functions of neutron temperature T_n .

The track number N_T recorded on a track detector is described by equation

$$N_T = N\tilde{\sigma}\phi_0\varepsilon \quad (4.31)$$

where N is the number of the specific nuclei of fissile species; ϕ_0 is the integrated neutron flux (fluence) equivalent to 2200 m/s; and ε is the detection efficiency of the detector for fission fragments (see (Eqn 4.12));

Substituting Eqn (4.30) into Eqn (4.31) gives

$$N_T = N\sigma_0 \left(g + r \sqrt{\frac{T_n}{T_0}} S_0 \right) \phi_0 \varepsilon \quad (4.32)$$

In Eqn (4.32) for a combination of fissile species and a track detector, such as ^{235}U and mica, N , σ_0 , and ε are known, and N_T can be measured by track counting; only ϕ_0 and the variable T_n of g and S_0 are unknown. If one uses a second fissile species, such as ^{239}Pu plus mica, one has two equations and two unknowns. One can solve the equations to find ϕ_0 and T_n where T_n is the neutron temperature in a nuclear reactor. From T_n one can calculate the neutron energy distribution from the Maxwell equation (Liu and Su, 1971).

The advantages of the track detector for the measurement of the temperature of neutrons in nuclear reactor are the following:

- (1) The measurements are simple and convenient to perform;
- (2) One can determine small disturbances to the nuclear reactor and to the neutron energy spectrum;
- (3) The neutron fluence irradiated to the fissile materials can be obtained as a by-product of the measurements. One does not need to measure the neutron fluence with other techniques.
- (4) If one uses thin sources of both fissile materials, the detection efficiency ε for both sources will be canceled in the calculation. The uncertainty of the final result T_n will not be affected by ε .
- (5) No background effects come from α -, β -, or γ -rays.

The main sources of uncertainty are: track counting, numbers of the atoms of the two fissile materials, and the parameters of g , r , and S_0 as functions of the two species of nuclei.

The determination shows that the neutron temperatures at different positions in nuclear reactor are different. The temperature in core region is higher than that in the thermal column.

b. Determination of Fast Fission Factor in Nuclear Reactors

In thermal neutron reactors, the ^{235}U nucleus absorbs a thermal neutron and goes to fission. On the average, ν_5 neutrons will be produced. These neutrons in the beginning are fast neutrons with an average energy about 2 MeV. The fast neutrons have a probability to be absorbed by ^{238}U nuclei and the formed compound nuclei probably go to fission and release on the average ν_8 neutrons, and the new neutrons may induce ^{238}U nuclei to go to fission again. As a result of the above process, there will be in total $\varepsilon \nu_5$ neutrons produced ($\varepsilon > 1$) where ε is called the fast neutron fission factor or fast fission factor. In the design of thermal neutron reactors, the knowledge of the fast fission factor is of practical importance. For this purpose, Shi and Li (2001) have developed a method for the determination of the fast fission factor ε with solid-state nuclear track detectors. The procedure is as follows:

Two fission sources are electrolytically deposited on two Ni disks, one of which is natural uranium, another is enriched uranium. The thicknesses of the natural and enriched uranium

are $200 \mu\text{g}/\text{cm}^2$ and $20 \mu\text{g}/\text{cm}^2$, respectively; both are thinner than the critical thickness (See Subsection III.C.2). The Ni disk is $30 \mu\text{m}$ in thickness. The two uranium fission sources were covered with solid-state nuclear track detector sheets. The sizes of the sources and track detectors were the same as the cross section of the fuel element. The two fission sources and their detectors were packed together back to back, and inserted into the fuel element assembly. After irradiation in a heavy water zero power reactor (HWZPR), the track numbers recorded on the track detectors were counted. From the two track numbers and the atom numbers of ^{235}U and ^{238}U in the natural uranium source, enriched uranium source, and fuel element, they obtained the fast fission factor ϵ ($=1.050$) which is in agreement with the theoretical calculation (1.071). The detailed formulations to calculate ϵ from the above-mentioned data of measurements are provided by Shi and Li (2001).

c. Measurement of Reactor Fission Rate and Reactor Power by Track Detector

The decisive factor of nuclear reactor power is how many fission events occur in the whole reactor in 1 s, that is, the fission rate in the whole reactor. One way of measuring nuclear reactor power is to determine the fission rate in the whole nuclear reactor. Basically, it is difficult to measure fission rate in the whole reactor with conventional detectors. However, with the advent of the solid-state nuclear track detector, the measurement of fission rate in the whole reactor becomes quite easy. Li et al. (2001) sandwiched track detector foils on the fuel elements, which are regularly at different heights and different radius in the core of a miniature neutron source reactor. In total 80 track foils were collocated. The distribution of fission rate at each place as well as in the whole volume of reactor is obtained. By this method, they obtained the reactor power (29.9 kW), which was in agreement with that of the thermal-hydraulic method (30.9 kW) and gold foil activation method (27.7 kW) (Li et al., 2001). The conversion factor from the whole fission rate F to reactor power P is P_0 , $P = P_0 F$, where $P_0 = 0.321 \times 10^{-10} \text{ W/fission} = 200 \text{ MeV/fission}$. The advantages of the track detector technique for measuring reactor fission rate are by its absolute nature, simplicity, and applicability at low reactor power.

2. Accelerator – Driven Subcritical Reactors (ADS)

The accelerator-driven subcritical reactor is a new type of proposed nuclear reactor. It has the following characteristics:

- (1) A subcritical nuclear reactor. It is stable and without any obvious nuclear reactions in it.
- (2) Reaching critical condition only when an accelerator provides enough neutrons to it. When the accelerator stops, the criticality vanishes. It is a controllable reactor without any potential of a Chernobyl-type accident.
- (3) Generation of electricity from nuclear fission. It will be a nuclear power plant.

- (4) A breeder reactor. ^{238}U nuclei after capture of fast neutrons may turn to ^{239}Pu nuclei.
- (5) Transmuting long-lived isotopes into stable or short-lived nuclide.

The ADS was first proposed by Bowman et al. (1992), and Rubbia et al. (1997) gave a more clear explanation. Up to now, nobody knows what target materials and beam particles of the accelerator should be used to produce neutrons, what are the adequate fuel elements to release fission energy, how to exchange heat from the core region to the coolant, and what is the appropriate structure for the whole reactor. A few prototypes have been built. Some of them are quite simple, including special target material and size, special beam and energy, and special reactor core and blanket (Brandt et al., 2008; Hashemi-Nezhad et al., 2008).

The solid-state nuclear track detector, being thin pieces, small in size, nearly no disturbance to neutron fields, easy to insert into gaps in the testing reactors, being able to measure neutron flux, energy and distributions in three dimensions, has been applied to studies on accelerator-driven critical reactors. Zamani et al. (2008) used $^6\text{Li}_2\text{B}_4\text{O}_7 + \text{LR-115, CR-39}$, and CR-39 covered with Cd foil to measure thermal-epithermal and intermediate-fast neutrons. Adloff et al. (1999) investigated the production of thermal neutrons with thin ^{235}U targets on Lexan track detectors and ^{232}Th targets on Lexan detectors for neutron energies $E_n > 2 \text{ MeV}$. Dwivedi et al. (1993) used gold foils and track detectors to measure neutrons of energy $E_n > 30 \text{ MeV}$ (Wan et al., 2001). Zhuk et al. (2008) and Perelygin et al. (2001) used Pb foils and mica and PET foil to measure proton beam profiles and neutrons of energy $E_n > 30 \text{ MeV}$. Hashemi-Nezhad et al. (2008) used Pb foils and mica to measure neutrons and compared the results with Monte Carlo predictions using MCNPX code. Guo et al. (2001) used CR-39 sheets to measure neutrons and come to conclusions that the Hg target is disadvantageous compared to U(Pb) and Pb targets for neutron yield. In order to obtain a uniform field of neutrons in an adequate target size, the energy of protons from accelerators should not be lower than 1 GeV for ADS developments.

3. Nuclear Forensic Analysis and Nuclear Safeguards

a. Nuclear Forensics

For the requirements of the arms control and nonproliferation of nuclear weapons, a new research field gave birth in the 1990s. It was named as strengthened nuclear safeguards (Donohue, 2002). In this field of science, environmental samples within and outside nuclear facilities are collected to disclose undeclared nuclear material and expose undeclared nuclear activities.

Nuclear materials for weapons are mainly ^{235}U and ^{239}Pu . The abundance of $^{235}\text{U} \geq 90\%$ and the ratio of $^{240}\text{Pu}/^{239}\text{Pu} \leq 6\%$ are requirements for nuclear weapons. Lower abundances of $^{235}\text{U} \leq 5\%$ and the ratio of $^{234}\text{U}/^{239}\text{Pu} \geq 20\%$ are for commercial uses. Enriched ^{234}U comes from a uranium-enriching plant. The existence of enriched ^{234}U particles indicates that there is a uranium-enriching plant. Existence of

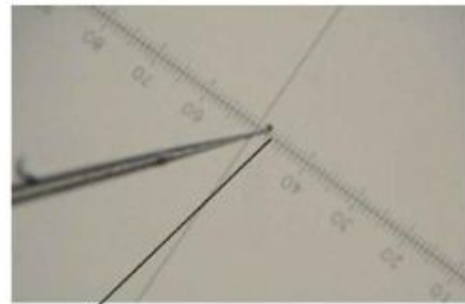
^{236}U indicates the existence of a nuclear fuel reprocessing plant. The analysis of isotopic compositions of uranium and plutonium in microscopic single particles has become a decisive method in nuclear safeguards and nuclear forensic analysis to disclose the undeclared activities. See Chapter 21 for a more comprehensive treatment of nuclear forensics.

b. Fission Track Technique

The fission track (FT) technique has been regarded as a feasible method to search for, locate, and transfer uranium-bearing particles from swipe samples. These particles are transferred to a thermal ionization mass spectrometer (TIMS) or secondary ion mass spectrometer (SIMS), or inductively coupled plasma mass spectrometer (ICP-MS) for analysis of isotopic abundances.

The fission track (FT) technique includes the following steps:

- (1) **Picking up uranium-bearing particles.** Swipe particles are transferred onto a Lexan polycarbonate detector of size $2 \times 2 \text{ cm}^2$. The Lexan detector with the particles is covered with a newly cleaved clean surface of mica detector. The sandwich formed of Lexan–mica is marked with a needle at three points (A, B, and C) coincident to each other on the outer surfaces of the Lexan and mica. The marked sandwich is tightly pressed together.
- (2) **Irradiation.** The sandwich of Lexan–mica is irradiated with thermal neutrons in a nuclear reactor to a neutron fluence about $10^{15}–10^{16} \text{ cm}^{-2}$. The neutrons induce fission of ^{235}U in the swipe particles. The fission fragments are recorded by the Lexan and mica track detectors.
- (3) **Etching.** After irradiation in the nuclear reactor, the mica detector is etched in HF and track stars will be seen under an optical microscope.
- (4) **Searching for and locating uranium-bearing particles.** Put the Lexan sheet on the mica back to back with the particles on the upper surface and the marks A, B, and C on both detectors overlapping each other. The particle on the upper surface of the Lexan coincident with the track star on the bottom surface of mica will be the uranium particle which produces the star. In this way, uranium-bearing particles are found. The coordinates (X_U, Y_U) of each particle as well as the coordinates (X_A, Y_A) , (X_B, Y_B) , and (X_C, Y_C) of the marks are recorded by the instruments connected with the stage of the microscope.
- (5) **Relocating particles and isotope analysis.** After coating with carbon or aluminum on the Lexan sheet by sputtering or vacuum evaporation, the Lexan sheet is placed under a scanning electron microscope (SEM) or secondary ion mass spectrometer (SIMS). By a mathematic formulation of relocation (see below), one can easily and quickly find the uranium-bearing particle. Further analyses on the elemental and isotopic composition of the particle can be carried out.
- (6) If TIMS is used to analyze the isotopic composition of the particle, one should use a micromanipulator (see Fig. 4.24) to pick up the particle and transfer it to a TIMS rhenium filament for analysis.
- (7) If ICP-MS is used for isotopic analysis, one should prepare a proper solution dissolving the particle for the



Uranium-bearing particle

FIGURE 4.24 Microphotograph of glass needle adhering to a uranium-bearing particle at its tip by static electricity. The tip diameter of the needle is about $1 \mu\text{m}$. The movement of the needle is controlled by micromanipulator (NARISHIGE, TYPE MO-202D). The precision of movement of the micromanipulator is $0.5 \mu\text{m}$. The glass needle was made by using an instrument (Puller, type PC-10, NARISHIGE). For the color version of the figure, the reader is referred to the online version of the book.

measurement. A micromanipulator is also needed to transfer the particle to the solvent.

c. Mathematical Formula of Relocation

For relocation of a uranium-bearing microparticle on the surface of a track detector or on other substrate such as a graphite planchet, one needs two or three reference points such as the marks made on the Lexan or mica. The reference points must be very easy to be found in the instruments. For locating and relocating the particle, one should first record the coordinates of the reference points A (X_A, Y_A) , B (X_B, Y_B) , and C (X_C, Y_C) and the coordinates of the uranium-bearing particle U (X_U, Y_U) in the first instrument. After putting the sample or planchet in the second instrument, one should first find the reference points and record the coordinates A (X'_A, Y'_A) and B (X'_B, Y'_B) . The uranium-bearing particle can be found easily at the position U (X'_U, Y'_U) calculated by the following formula (Guo et al., 2008):

$$X'_U = \overline{AU} \times R \times \cos \phi' + X'_A \quad (4.33)$$

$$Y'_U = \overline{AU} \times R \times \sin \phi' + Y'_A \quad (4.34)$$

where \overline{AU} is the distance between A and U, R is the ratio of the readings of the same distance in the second instrument to that in the first instrument:

$$R = \frac{\sqrt{(X'_B - X'_A)^2 + (Y'_B - Y'_A)^2}}{\sqrt{(X_B - X_A)^2 + (Y_B - Y_A)^2}} \quad (4.35)$$

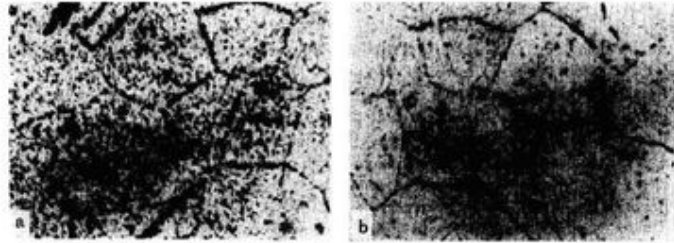
And ϕ' is the angle between AU and the X' -axis in the second instrument:

$$\phi' = \alpha' + \theta' \quad (4.36)$$

where α' and θ' are the angles between AU and AB and between AB and the X' -axis in the second instrument, respectively:

$$\alpha' = \alpha \quad (4.37)$$

FIGURE 4.25 Track microphotograph of MnTiB steel (a) and its corresponding microphotograph of the steel (b). After turning 180° of (a), the two microphotographs can be matched together.



where α is the angle between AU and AB in the first instrument:

$$\alpha = \begin{cases} \operatorname{Arctg} \frac{Y_U - Y_A}{X_U - X_A} - \operatorname{Arctg} \frac{Y_B - Y_A}{X_B - X_A}, & X_U > X_A, X_B > X_A, \text{ or} \\ & X_U < X_A, X_U < X_A \\ \operatorname{Arctg} \frac{Y_U - Y_A}{X_U - X_A} - \operatorname{Arctg} \frac{Y_B - Y_A}{X_B - X_A} + \pi, & X_U < X_A, X_B > X_A, \\ \operatorname{Arctg} \frac{Y_U - Y_A}{X_U - X_A} - \operatorname{Arctg} \frac{Y_B - Y_A}{X_B - X_A} - \pi, & X_U > X_A, X_B < X_A, \\ \frac{\pi}{2} - \operatorname{Arctg} \frac{Y_B - Y_A}{X_B - X_A}, & X_U = X_A, Y_U > Y_A, \\ -\frac{\pi}{2} - \operatorname{Arctg} \frac{Y_B - Y_A}{X_B - X_A}, & X_U = X_A, Y_U < Y_A, \\ \operatorname{Arctg} \frac{Y_U - Y_A}{X_U - X_A} - \frac{\pi}{2}, & X_B = X_A, Y_B > Y_A, \\ \operatorname{Arctg} \frac{Y_U - Y_A}{X_U - X_A} + \frac{\pi}{2}, & X_B = X_A, Y_B < Y_A, \end{cases} \quad (4.38)$$

$$\theta' = \begin{cases} \operatorname{Arctg} \frac{Y'_B - Y'_A}{X'_B - X'_A}, & X'_B > X'_A \\ \operatorname{Arctg} \frac{Y'_B - Y'_A}{X'_B - X'_A} + \pi, & X'_B < X'_A \\ \frac{\pi}{2}, & X'_B = X'_A, Y'_B > Y'_A \\ -\frac{\pi}{2}, & X'_B = X'_A, Y'_B < Y'_A. \end{cases} \quad (4.39)$$

In other words, recording the coordinate of two reference points and the particle in the first instrument and the coordinates of the two reference points in the second instrument, one can immediately calculate the coordinates of the particle in the second instrument. If one uses three or more reference points, such as A, B, and C, every two reference points give a pair of coordinates (X'_U, Y'_U) of the particle. Averaging all the three coordinates X'_U as well as three Y'_U , one can achieve better accuracy of the coordinates in the second instrument.

Guo et al. (2008) made reference points on a graphite planchet by using a nuclear track membrane having a pore diameter of 10 μm and simulated particles having the same diameter.

A relocation testing in the second instrument (SEM, JEOL 6360 LV) showed that the relocation accuracy was $(5.8 \pm 2.6) \mu\text{m}$ compared with the coordinates calculated from the formula for 87 simulated particles. It is accurate enough to find the uranium-bearing particle in the second instrument for further analysis. More detailed information can be found in Guo et al. (2008).

In all the above analyses, the solid-state nuclear track detector plays important roles (Shen et al., 2008; Guo et al., 2008; Lipponen and Zilliacus, 2004, 2003; 2002; Esaka et al., 2004; Baude and Chiappini, 2002; Donohue, 2002).

G. Elemental Analysis and Mapping

Elemental mapping has been discussed in detail in the book of Fleischer et al. (1975). Here only an example will be presented on boron mapping in metallurgy.

Natural boron is composed of ^{11}B (80.1%) and ^{10}B (19.9%). ^{10}B has a large cross section ($3840 \pm 11 \text{ b}$) for thermal neutrons in nuclear reactors. The reaction products of the reaction $^{10}\text{B}(n, \alpha)^7\text{Li}$ consist of α -particles with energies of 1.47 MeV (93.7%) and 1.77 MeV (6.3%). Both of these are easy to be recorded by solid-state nuclear track detectors (CR-39, LR-115, and cellulose acetate).

In order to observe the boron distribution in steel, a small block of steel is ground and polished to expose a smooth surface. Then, the smooth surface is covered with a thick solution of cellulose acetate (in acetone or cyclohexanone). After drying the solution, the steel block with the cellulose acetate layer is placed outside the channel of thermal column of nuclear reactor for irradiation with thermal neutrons. The reaction products α - and Li particles will create tracks in the cellulose acetate. The microphotographs of tracks after etching and the microphotograph of the steel of the same area are shown in Fig. 4.25.

Boron is concentrated on the crystal boundaries and uniformly distributed within the crystal cells. The recipes, smelting temperature, and quench condition of the steel can be selected and improved through these microphotographs (Guo, 1995). A large quantity of special steels have been smelted.

III. EARTH AND PLANETARY SCIENCES

A. Fission Track Dating

1. Absolute Approach

Fission track dating was first devised by Price and Walker (1962). It has become one of the important dating techniques

in geology and archaeology (Fleischer et al., 1975; Durrani and Bull, 1987; Wagner and Van den haute, 1992; Dumitru, 2000).

The principle of fission track dating is the following:

The fragments of spontaneous fission of ^{238}U nuclei in minerals create radiation damage tracks which can be developed as etched tracks in the mineral and can be observed with an optical microscope. The number of spontaneous fission tracks (N_s) is proportional to the age (T) of the mineral and the uranium content (N_u) in the mineral. After counting the spontaneous fission tracks and measuring the uranium content in the mineral, one can determine the age of the mineral. The easiest way to determine the uranium content in the mineral is to irradiate the mineral with thermal neutrons in a nuclear reactor. Thermal neutrons induce fission of ^{235}U in the mineral. The induced fission will be recorded in the mineral. Counting the induced fission tracks (N_i) and measuring the neutron fluence (ϕ_0) irradiated to the mineral, one can derive the uranium content from the fission cross section ($\bar{\sigma}$) of ^{235}U and N_i and ϕ_0 . The equation of age of the mineral can be written as follows (Collaboration Group of Institute of Atomic Energy and Guiyang Institute of Geochemistry, Academia Sinica, 1976):

$$T = \frac{1}{\lambda_D} \ln \left\{ \frac{C_{235}}{C_{238}} \cdot \frac{\lambda_D}{\lambda_F} \cdot \frac{\rho_s}{\rho_i} \cdot \phi_0 \cdot \bar{\sigma} \left[\frac{GR_i \cos^2 \theta_{ci} + (1 - \sin \theta_{ci})l_i}{R_s \cos^2 \theta_{cs} + (1 - \sin \theta_{cs})l_s} + 1 \right] \right\} \quad (4.40)$$

where C_{235} is the relative abundance of ^{235}U ($=0.720\%$), C_{238} is the relative abundance of ^{238}U ($=99.2745\%$), λ_D is the total decay constant of ^{238}U ($=1.5514 \times 10^{-10} \text{ a}^{-1}$), λ_F is the spontaneous fission decay constant of ^{238}U , ρ_s is the spontaneous fission track density of ^{238}U (cm^{-2}), ρ_i is the induced fission track density of ^{235}U (cm^{-2}), R is the average etchable range of fission fragments in the mineral (cm), θ_c is the critical angle of fission fragments in the mineral, l is the thickness of the single surface layer removed by etchant (cm), s denotes that the quantity is for spontaneous fission fragments, i denotes that the quantity is for induced fission fragments, G is a geometry factor where $G = 1$, when an internal surface is used to record induced fission-fragment tracks, and $G = 1/2$, when an external surface is used to record induced fission-fragment tracks.

In a special case, one can assume that $R_i = R_s$, $\theta_{ci} = \theta_{cs}$, and $l_i = l_s = 0$. Then, eqn (4.40) is simplified to the equation

$$T = \frac{1}{\lambda_D} \ln \left\{ \frac{C_{235}}{C_{238}} \cdot \frac{\lambda_D}{\lambda_F} \cdot \frac{\rho_s}{\rho_i} \cdot \phi_0 \cdot \bar{\sigma} \cdot G + 1 \right\} \quad (4.41)$$

It should be pointed out that if the detector used for recording induced fission tracks is not the same kind of mineral as that to be dated (by spontaneous fission tracks), then $R_i \neq R_s$, $\theta_{ci} \neq \theta_{cs}$, and $l_i \neq l_s$. In this case, Eqn (4.41) cannot be used to calculate age T .

It is always necessary to calibrate the ratio of the detection efficiency of an external detector for induced fission fragments to that of the mineral for spontaneous fission fragments (Guo, 1982a; Guo et al., 1980; Durrani and Bull, 1987; Holden and Hoffman, 2000). Otherwise, the resulting age value of T calculated from the simplified Eqn (4.41) would be erroneous.

If $\lambda_D T \ll 1$ ($T \leq 2 \times 10^8 \text{ a}$), then Eqn (4.41) can be further simplified as follows:

$$T = \frac{1}{\lambda_F} \frac{C_{235}}{C_{238}} \frac{\rho_s}{\rho_i} \cdot \phi_0 \cdot \bar{\sigma} \cdot G \quad (4.42)$$

Equation (4.42) has the same limitations as Eqn (4.41) in addition to the condition $T \leq 2 \times 10^8 \text{ a}$.

The technique of fission track dating by using Eqn (4.40), (4.41), and (4.42) is called the absolute approach (Wagner and Van den haute, 1992; Hurford, 1990).

Two problems have been met with the absolute approach.

a. ^{238}U Spontaneous Fission Decay Constant λ_f

Up to now, more than 30 data of λ_f have been published in the literature (Wagner and Van den haute, 1992; Bigazzi, 1981; Durrani and Bull, 1987). The values of λ_f spread over a very broad range. No one can recommend an integrated value from them. In the year 2000, the International Union of Pure and Applied Chemistry (IUPAC) published a technical report on "Spontaneous fission half-lives for ground-state nuclides" (Holden and Hoffman, 2000) and gave a special treatment on the ^{238}U spontaneous fission decay constant λ_f .

The IUPAC did not include the results of all λ_f values of ^{238}U spontaneous fission measured by solid-state nuclear track detectors. They averaged the results measured by the other detectors (ionization chamber, double ionization chamber, rotating bubble chamber, fission products from ^{238}U , third-order coincidence, and multiple neutron coincidence) and gave a recommended half-life value $t_{1/2} = (8.2 \pm 0.1) \times 10^{15} \text{ a}$ of ^{238}U spontaneous fission, which is equivalent to a $\lambda_f = 8.45 \times 10^{-17} \text{ a}^{-1}$. They considered that the recommended value of $t_{1/2}$ is the correct spontaneous fission half-life of ^{238}U .

The reasons for not including the results measured by solid-state nuclear track detectors are the following:

- (1) The values of half-life derived from track detectors do not agree with those derived from other techniques. The specific activity (λ_f), in general, is lower than that determined from other detectors.
- (2) The lower λ_f values are related to special properties of track detectors. The lower λ_f values are suitable to fission track dating, in which the factors that cause the lower values can be compensated in age determination. For a detailed explanation, the reader is referred to the above-mentioned technical report.

It has been demonstrated that no trend can be found with respect to whether the zeta calibration (see below) or the decay constant of $7 \times 10^{-17} \text{ a}^{-1}$ was used in fission track dating. The results based on a decay constant of $8.46 \times 10^{-17} \text{ a}^{-1}$ tend to be low compared with the mean age obtained in an international comparison of fission track ages for the 1988 fission track workshop (Miller et al., 1990). It means that by using $\lambda_f = 6.85 \times 10^{-17} \text{ a}^{-1}$ (Fleischer and Price, 1964) or $7.03 \times 10^{-17} \text{ a}^{-1}$ (Roberts et al., 1968), the age values obtained are in agreement with that of age standard, or in agreement with

the mean value obtained by different techniques in fission track dating (population method, external detector method, and zeta calibration approach). By using $\lambda_f = 8.46 \times 10^{-17} \text{ a}^{-1}$, the results of ages are generally lower than those obtained by other techniques.

In the absolute approach of fission track dating, an important point is to state that which decay constant λ_f of ^{238}U spontaneous fission was used in calculation of age, so that other workers can make comparison with other age determination by substituting a new λ_f value (Durrani and Bull, 1987).

In dating with the absolute approach, the effect of track fading on age must be corrected. The correction techniques include: track diameter method (relation of track diameter d/d_0 to track density ρ/ρ_0 , where the subscript "0" signifies that for no fading of tracks), track length method (relation of track length l/l_0 to track density ρ/ρ_0), and plateau-age correction method (annealing spontaneous and induced tracks simultaneously before etching until ρ/ρ_i reaches a constant value; the age calculated by the constant ρ_i/ρ_i is the true age of the sample).

b. Neutron Fluence ϕ_0

Neutron fluence determination in nuclear reactors is a mature technique for reactor physicists. For thermal neutron determination, the often used technique is activation foil measurements. Co, Au, and Cu foils are most suitable for thermal neutron fluences of 1.5×10^{15} – 6×10^{15} , 1×10^{11} – 1×10^{14} , and 1×10^{12} – $1 \times 10^{15} \text{ cm}^{-2}$, respectively. Co foil is most suitable for fission track dating.

In the irradiation of dating samples in nuclear reactors, one must pay attention to the total thickness of the samples. If the sample package is too thick, the outlayer of the sample will absorb neutrons and reduce the expected fluence of neutrons for the central part of sample. In this case, one should insert more than one (at least two) activation foils to get an average value of neutron fluence. Similar attention must be paid to the thickness of the activation foils. If the thickness of the activation foil is too large, the surface layer of the foil will absorb a significant amount of neutrons and a reduced fluence of neutrons reaches the central part of the foil (self-shielding). In this case, the

fluence of thermal neutrons can be written as following equations:

$$\phi_0 = nv_0t = \frac{A_0t}{N\hat{\sigma}(1 - e^{-\lambda t})} \tag{4.43}$$

$$\hat{\sigma} = \sigma_0 \left(K_{th}g + r\sqrt{\frac{T_n}{T_0}} S_0K_r \right) \tag{4.44}$$

where n is the volume density of thermal neutrons in the nuclear reactor (cm^{-3}), v_0 is the neutron velocity (2200 m/s), K_{th} is the self-shielding factor of activation foil for thermal neutrons, K_r is the self-shielding factor of activation foil for epithermal neutrons, A_0 is the activity of the activation foil, t is the exposure time of the activation foil to the reactor thermal neutrons in seconds (s), and λ is the decay constant of the nuclei formed in the exposure (s^{-1}).

The nuclear parameters of the activation foils of ^{59}Co , ^{63}Cu , and ^{197}Au as well as the ^{235}U (n,f) reaction for thermal and epithermal neutrons in nuclear reactors are listed in Table 4.3. For example, 50 mg/cm² of Co foil will have ~3% ($K_{th} = 0.97$) and ~11% ($K_r = 0.885$) effects on thermal and epithermal neutrons, respectively. These effects will be brought to the fluence value. If one does not give a correction for these effects, the final value of fluence of thermal neutrons (ϕ_0) calculated from the Co foil activity A_0 will be ~3.6% smaller than the real fluence. This reduction of calculated ϕ_0 would result in a younger age of the sample as calculated from Eqn (4.40), (4.41), or (4.42).

2. Zeta Approach

In order to avoid direct measurements of fluence of thermal neutrons ϕ_0 in nuclear reactors and avert adoption of the decay constant λ_f of ^{238}U spontaneous fission in the calculation of age, the zeta approach was proposed (Fleischer et al., 1975) and advocated (Hurford and Green, 1982, 1983) and extensively accepted and adopted (Miller and Duddy, 1985; 1990; Van den haute and Chambaudet, 1990; Wagner and Van den haute, 1992; Durrani and Bull, 1987; Wang and Kang, 1993; Wang et al., 1993; Yang et al., 2003). The zeta approach of fission track dating is based on the adoption of standard uranium glass to

TABLE 4.3 Parameters of Activation Foils of ^{59}Co , ^{63}Cu , ^{197}Au , and ^{235}U (n,f) in a Thermal Neutron Field in Nuclear Reactors

Temperature °C	^{59}Co		^{63}Cu		^{197}Au		^{235}U (n,f)	
	g	S_0	g	S_0	g	S_0	g	S_0
20	1.000	1.736	1.000	0.795	1.0053	17.30	0.9759	-0.0502
60	1.000	1.851	1.000	0.848	1.0075	18.44	0.9665	-0.0324
100	1.000	1.959	1.000	0.897	1.0097	19.51	0.9581	-0.0169
140	1.000	2.061	1.000	0.943	1.0119	20.52	0.9507	-0.0039
180	1.000	2.159	1.000	0.992	1.0141	21.49	0.9441	+0.0066
$\sigma_0 (\times 10^{-24} \text{cm}^2)$	37.40 ± 0.03		4.3 ± 0.2		98.8 ± 0.3		582.6	
$\lambda (\text{s}^{-1})$ (activated nucleus)	4.1673×10^{-9}		1.5161×10^{-5}		2.976634×10^{-6}			